HRVATSKO DRUŠTVO
ZA STROJARSKE TEHNOLOGIJE

CROATIAN SOCIETY
FOR MECHANICAL TECHNOLOGIES

In association with:

University of Split
Faculty of Electrical Engineering, Mechanical Engineering and Naval Architecture

University of Split
Faculty of Chemistry and Technology

University of Split
University Department of Professional Studies

University of Zagreb
Faculty of Mechanical Engineering and Naval Architecture

Slovak Academy of Science
Institute of Materials and Machine Mechanics

Bulgarian Academy of Sciences

University of Zenica

Rogante Engineering Office

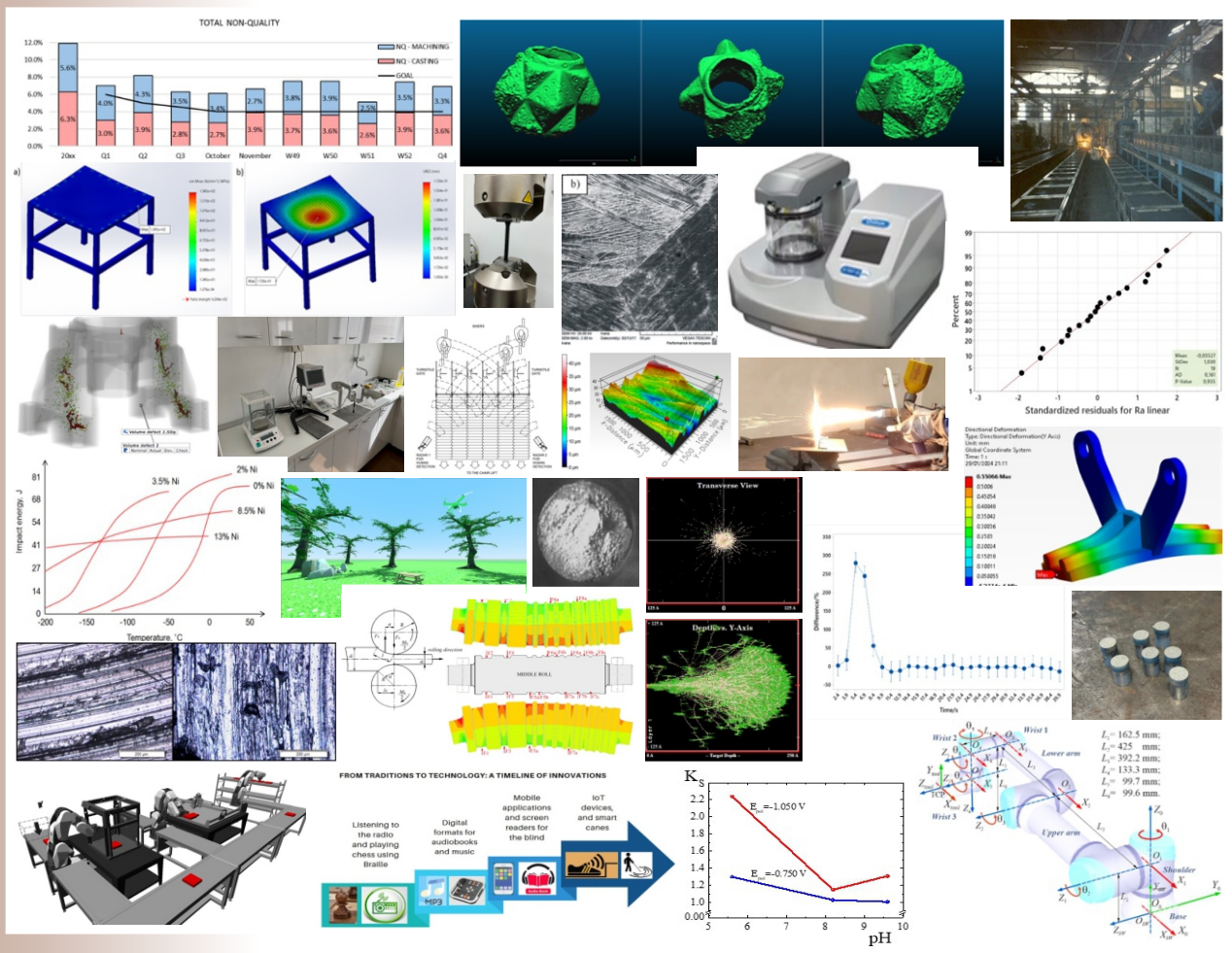
ISSN 1847-7917

14th International Conference

Mechanical Technologies and Structural Materials 2025

General sponsors:

University of Split - FESB, The City of Split,
Anton Paar Croatia d.o.o., Ansar - Analitika d.o.o., BELMET 97 d.o.o.,
Eurotehnika d.o.o., Mjerne tehnologije d.o.o., TOPOMATIKA d.o.o.



http://www.strojarska-tehnologija.hr

September, 18th - 19th, 2025.
FESB, Ruđera Boškovića 32, Split

CONFERENCE PROCEEDINGS

MECHANICAL TECHNOLOGIES AND STRUCTURAL MATERIALS

Split

Croatia

18 - 19 September 2025

ORGANIZED BY:

CROATIAN SOCIETY FOR MECHANICAL TECHNOLOGIES, Croatia

CO-ORGANIZERS:

UNIVERSITY OF SPLIT
FACULTY OF ELECTRICAL ENGINEERING, MECHANICAL ENGINEERING AND NAVAL ARCHITECTURE

UNIVERSITY OF SPLIT
FACULTY OF CHEMISTRY AND TECHNOLOGY

SLOVAK ACADEMY OF SCIENCE
INSTITUTE OF MATERIALS AND MACHINE MECHANICS

ROGANTE ENGINEERING OFFICE

BULGARIAN ACADEMY OF SCIENCES
INSTITUTE OF INFORMATION AND COMMUNICATION TECHNOLOGIES

UNIVERSITY OF ZENICA
MAŠINSKI FAKULTET

UNIVERSITY OF SPLIT
UNIVERSITY DEPARTMENT OF PROFESSIONAL STUDIES

UNIVERSITY OF ZAGREB
FACULTY OF MECHANICAL ENGINEERING AND NAVAL ARCHITECTURE

SPONSORS:

University of Split - FESB

CITY OF SPLIT

Anton Paar Croatia d.o.o.

Ansar - Analitika d.o.o.

BELMET 97 d.o.o.

Eurotehnika d.o.o.

Mjerne tehnologije d.o.o.

TOPOMATIKA d.o.o.

PUBLISHER:

CROATIAN SOCIETY FOR MECHANICAL TECHNOLOGIES, Croatia

HRVATSKO DRUŠTVO ZA STROJARSKE TEHNOLOGIJE, Hrvatska

c/o FESB, Ruđera Boškovića 32, 21000 SPLIT

tel.: +385 21 305 910; fax.: +385 21 463 877

e-mail: info@strojarska-tehnologija.hr

http://www.strojarska-tehnologija.hr

EDITORS:

PhD Nikša Čatipović, Assistant Professor
PhD Jure Krolo, Assistant Professor
PhD Nikola Gjeldum, Associate Professor

ISSN 1847-7917

ISSUE: 50

ORGANIZING COMMITTEE:

- Jure KROLO (Croatia) - President
- Marina CRNJAC ŽIŽIĆ (Croatia) - Vice President

- Amanda ALJINOVIĆ MEŠTROVIĆ(Croatia)
- Amra TALIĆ-ČIKMIŠ (Bosina and Herzegovina)
- Anatoliy ZAVDOVEEV (Ukraine)
- Andrej BAŠIĆ (Croatia)
- Damir JURIĆ (Croatia)
- Igor ĆULUM (Croatia)
- Igor GABRIĆ (Croatia)
- Ivana DUMANIĆ LABETIĆ (Croatia)
- Ivan PEKO (Croatia)
- Karla KUNAC (Croatia)
- Karla ANTUNOVIĆ (Croatia)
- Ladislav VRSALOVIĆ (Croatia)
- Liane ROLDO (Croatia)
- Marijana KALAJŽIĆ (Croatia)
- Marko MLADINEO (Croatia)
- Massimo ROGANTE (Italy)
- Nikolay STOIMENOV (Bulgaria)
- Nikša ČATIPOVIĆ (Croatia)
- Petar LJUMOVIĆ (Croatia)
- Slaven ŠITIĆ (Croatia)

PROGRAMME AND SCIENTIFIC COMMITTEE:

- Jure KROLO (Croatia) – President
- Nikša ČATIPOVIĆ (Croatia) – Vice President

- Branimir LELA (Croatia)
- Sonja JOZIĆ (Croatia)
- Dražen ŽIVKOVIĆ (Croatia)
- Dražen BAJIĆ (Croatia)
- Goran CUKOR (Croatia)
- Lidija ĆURKOVIĆ (Croatia)
- Ivan JANDRLIĆ (Croatia)
- Nikola GJELDUM (Croatia)
- Mirko GOJIĆ (Croatia)
- Krešimir GRILEC (Croatia)
- Senka GUDIĆ (Croatia)
- Fuad HADŽIKADUNIĆ (Bosnia and Herzegovina)
- Dario ILJKIĆ (Croatia)
- Zlatko JANKOSKI (Croatia)
- Michaela ŠTAMBORKSA (Slovakia)
- Kateryna KAMYSHNYKOVA (Slovakia)
- Zoran JURKOVIĆ (Croatia)
- Erol KAM (Turkey)
- Darko LANDEK (Croatia)
- Cândida MALÇA (Portugal)
- Dragan MARINKOVIĆ (Germany)
- Aleš NAGODE (Slovenia)
- Zoran PANDILOV (Macedonia)
- Mladen PERINIĆ (Croatia)
- Massimo ROGANTE (Italy)
- Liane ROLDO (Croatia)
- Nikolay STOIMENOV (Bulgaria)
- Jaroslav JERZ (Slovakia)
- Amra TALIĆ-ČIKMIŠ (Bosnia and Herzegovina)
- Matej VESENJAK (Slovenia)
- Ladislav VRSALOVIĆ (Croatia)
- Anatoliy ZAVDOVEEV (Ukraine)
- Łukasz GIERZ (Poland)
- Łukasz WARGUŁA (Poland)
- Mariola ROBAKOWSKA (Poland)
- Luka CELENT (United Kingdom)
- Vânia CALDAS de SOUSA (Brazil)
- Ivan PIVAC (Croatia)
- Željko PENGA (Croatia)
- Achim KAMPKER (Germany)
- Fabrizio FIORI (Italy)
- Paolo MENGUCCI (Italy)
- Heiner HEIMES (Germany)
- Hasan AVDUŠINOVIĆ (Bosnia and Herzegovina)
- Miroslav SAHUL (Czech Republic)

- Franjo KOZINA (Croatia)
- Špiro IVOŠEVIĆ (Crna Gora)
- Irena ŽMAK (Croatia)



Mechanical Technologies and Structural Materials MTSM2025

CONTENT

1. ***Keynote lecture: Jelena Čulić-Viskota***
Thermal challenges in semiconductor industry and potential solution space 1

2. ***Keynote lecture: Michaela Štamborská***
Numerical simulations and microstructural evolution of $Al_{0.35}CoCrFeNi$ high-entropy alloy under hot forging processes 3

3. ***Paul Adde and Quentin Dos Santos Silva***
Integrating virtual reality in drone education: a gateway to scientific exploration and skill development 5

4. ***Andrej Bašić, Ivan Peko and Ivan Jerković***
Integrative approach to evaluating the quality of 3D printed cultural artifacts: multicriteria analysis and human perception using the AHP method 11

5. ***Derzija Begic-Hajdarevic, Simon Klancnik, Maida Cohodar Husic, Kristijan Sket, Kenan Muhamedagic, Edin Begovic and Mirko Ficko***
Multi-objective optimization of process parameters in fiber laser cutting of aluminium alloy 21

6. ***Milena Biserova, Rosen Petrov, Nikolay Stoimenov, Mira Tzvetkova-Arsova and Margarita Tomova***
Accessible entertainment and socialization opportunities for visually impaired people: technologies, challenges, and innovations 31

7. ***Igor Ciganović, Zdenka Keran, Petar Piljek, Andrej Razumić and Davor Jurić***
Accuracy and efficiency optimization-mass scaling effects in ECAP process simulations 39

8. ***Malik Čabaravdić, Amer Sarajlić and Amra Talić-Čikmiš***
PLC-controlled manufacturing line with multi-robot integration and computer vision 49

9. ***Maida Čohodar Husić, Kenan Muhamedagić, Ahmet Čekić and Đerzija Begić-Hajdarević***
Research potential and development of a Simscape Multibody-based dynamic model of collaborative robot 61

10. ***Sabahudin Ekinović, Edin Begović, Adnan Mustafić and Mario Dragičević***
Experimental and mathematical modeling of surface integrity indicators during the turning of X5CrNi18-10 steel using an advanced MQLC system 71

11. ***Nikola Gjeldum, Boženko Bilić, Marko Mladineo, Marina Crnjac Žižić and Amanda Aljinović Meštrović***
Evaluation of the self-study modules developed in ExCurS project 81

12. ***Mirko Gojić, Stjepan Kožuh, Ivana Ivanić, Daniela Dumenčić, Ivica Garašić, Borut Kosec and Aleš Nagode***
Microstructural analysis of Cu-Al-Mn shape memory alloy before and after TIG welding 91

13. ***Mihael Holi***
Digital twin-enhanced virtual laboratories for advanced manufacturing education: a comparative analysis of development platforms 99

14. ***Aida Imamović, Mirsada Oruč, Milenko Rimac, Gorazd Kosec and Amra Talić-Čikmiš***
The cause of the precocious fracture of the samples during the dynamic strength test of the wear-resistant steel 105

15. ***Jaroslav Jerz and Jaroslav Kováčik***
High density aluminium foam based heat exchangers 115

16. ***Damir Jurić, Nikša Čatipović, Ivan Peko, Jure Krolo, Karla Antunović, Karla Kunac, Matej Kljajo, Angelo Oñate and Víctor Tuninetti***
Multi-objective optimization of thermally sprayed CrNiMo coatings on titanium substrates: influence of spray distance and layer count on mechanical properties using desirability analysis 123

17. ***Matej Kljajo, Ladislav Vrsalović, Senka Gudić, Nikša Čatipović, Ivan Peko, Ante Bilušić, Petar Ljumović and Danijel Šogorović***
Process errors and problems in adhesion of magnetron sputtered platinum coatings 139

18. ***Josip Kos, Luka Kurtalj, Maximilian Hercigonja, Vedran Starčević and Tomislav Hercigonja***
Practical examples of the correct selection of 3D measurement technology for modern production processes 147

19. ***Franjo Kozina, Zdenka Zovko Brodarac, Matea Kuprešak and Mitja Petrič***
Simulation of irradiation-induced damage in Al-Mg-Li alloys 159

20. ***Jure Krolo, Aleš Nagode, Matej Kljajo, Nikša Čatipović, Damir Jurić and Ivan Peko***
Tribological and microstructural characterization of thermal-sprayed Cr-Ni-Mo coatings on stainless steel 177

21. ***Elvis Krulčić, Sandro Doboviček, Duško Pavletić and Goran Cukor***
Integration of agile methods and Lean Six Sigma approach in improving the quality of manufacturing processes 189

22. ***Olga Kushnarova, Olena Berdnikova, Igor Alekseienko, Valeriy Pozniakov, Aleksandr Gaivoronskiy, Anatoliy Zavdoveev and Massimo Rogante***
Influence of surface high-frequency mechanical forging on the structure of welded joints of structural steel 197

23. ***Dario Kvrgić, Graciela Šterpin Valić, Tea Marohnić, Robert Basan and Goran Cukor***
Effect of cooling methods on the surface chemistry and corrosion performance of X2CrNiMo17-12-2 austenitic stainless steel 203

24. ***Francisko Lukša, Željko Domazet and Đorđe Dobrota***
Impact of caliber height reduction on roll fatigue life 217

25. ***Francisko Lukša, Željko Domazet, Đorđe Dobrota and Branko Lalić***
Failure analysis of scrap shear knives 231

26. ***Petar Ljumović, Petar Bronić, Ivana Radić Boršić and Ivan Rogan***
Production line of migrating corrosion inhibitors for the protection of steel reinforcement systems 241

27. ***Sven Maričić and Dario Iljkić***
Optimizing additive manufacturing processes for high-performance mechanical components using AI-driven parameter prediction and virtual reality simulation 251

28. ***Luka Mesek, Zdenka Zovko Brodarac, Mitja Petrič and Desimir Bobina***
Investigation of the quality of EN-GJS-400-15 ductile cast iron 259

29. ***Marko Mladineo, Pol Menou, Mate Buzov and Luka Celent***
Design of the reconfigurable workstation for collaborative robot Franka 277

30. ***Lyudmila Nyrkova, Svetlana Osadchuk, Larysa Goncharenko and Oleg Bratochkin***
Stress-corrosion cracking of X70 steel for main pipelines in different corrosivity environments at cathodic polarization 283

31. ***Rosen Petrov, Milena Biserova, Aleksander Vulkov and Nikolay Stoimenov***
Improving chairlift operations with safety measures, technological innovations, and efficiency optimization 295

32. ***Massimo Rogante and Luigi Arcangeli***
Feasibility study for damage analysis of a hip prosthesis made of Ti6Al7Nb alloy 301

33. ***Massimo Rogante***
Structural and operational dynamics of small-to-medium cast-iron foundries in Italy: a 2025 perspective 321

34. ***Anđela Rohtek, Nikša Čatipović, Željko Penga, Jure Penga, Mišo Jurčević and Petra Bagavac***
Characterization of bipolar plates for hydrogen fuel cells manufactured using additive manufacturing technology 337

35. ***Amra Talić-Čikmiš, Kenan Šabanović and Aida Imamović***
Comparison of the optimization results of a polyamide crane support obtained through numerical simulation and testing under operating conditions 353

36. ***Ladislav Vrsalović, Senka Gudić, Nediljka Vukojević Medvidović, Sandra Svilović and Mario Nikola Mužek***
Electrocoagulation and hybrid electrocoagulation for wastewater treatment: strength, challenges and future prospects 359

37. ***Olga Kushnarova, Olena Berdnikova, Tetyana Alekseienko, Svitlana Grigorenko, Valeriy Pozniakov, Aleksandr Gaivoronskiy, Anatoliy Zavdoveev and Massimo Rogante***
Structural features of welded joints of special-purpose steel with increasing number of fatigue load cycles 373

Thermal challenges in semiconductor industry and potential solution space

Jelena Čulić-Viskota[1]

1) Intel Corporation (Retired), 5000 W. Chandler Blvd, Chandler, Arizona

Corresponding author: jelena.culicviskota@gmail.com

ABSTRACT

The demand for semiconductor devices continues to accelerate, with estimates projecting the global transistor count to double from 1 trillion to 2 trillion by 2030. This growth has been enabled by continued transistor scaling and the adoption of advanced 3D packaging integration technologies, resulting in significantly increased transistor density. In addition to the increased computational power, this trend also leads to escalating thermal power densities, posing critical challenges for thermal management.

This keynote will explore the semiconductor packaging trends, with a particular focus on innovations in thermal interface materials (TIMs). TIMs play a pivotal role in reducing interfacial thermal resistance caused by surface roughness and entrapped air gaps, which impede efficient heat transfer. Key attributes of high-performance TIMs include high thermal conductivity, low thermal resistance, and mechanical compliance to surface topology. The selection of TIMs must address the specific thermal and mechanical requirements of each package type and use application.

This session will provide an overview of the current TIM landscape, highlight areas of active research, and discuss materials development to meet the performance and reliability targets set forth by semiconductor technology roadmaps.

Attendees will gain insights into future semiconductor industry directions, recent advancements in thermal materials, and key considerations for integrating TIMs in next-generation semiconductor packages.

BIOGRAPHY



Jelena Čulić - Viskota, holds a PhD in Chemical Engineering from California Institute of Technology in Pasadena, CA. She has over a decade of experience working at Intel Corporation Assembly and Test Research and Development Department, and is a recognized semiconductor materials, manufacturing processes and strategy expert. Jelena has international and multidisciplinary experience, having worked with industrialand academic partners in Asia, Europe and North America. Her research focuses on developing and testing materials that meet the ever-growing requirements of new generations of semiconductor devices, aiming to develop novel thermal interface materials and testing sockets.

- LinkedIn: https://www.linkedin.com/in/jelena-culic-viskota-ph-d-3096371b/
- Research Interest: Semiconductor materials used in assembly and testing manufacturing stages

Numerical simulations and microstructural evolution of $Al_{0.35}CoCrFeNi$ high-entropy alloy under hot forging processes

Michaela Štamborská[1]

1) Institute of Materials and Machine Mechanics, Slovak Academy of Sciences, Dúbravská cesta 9, 845 13 Bratislava, Slovak Republic, EU.

Corresponding author: michaela.stamborska@savba.sk

ABSTRACT

This study investigates the influence of different hot forging processes: one-step (F100) and two three-step (F30-60-40 and F30-60-80) processes on the microstructure and dynamic recrystallization behavior of the $Al_{0.35}CoCrFeNi$ high-entropy alloy. All forging processes preserved the single-phase face-centered cubic (FCC) structure of the alloy. Finite element analysis was used to simulate thermal and mechanical fields during forging and to predict the regions prone to dynamic recrystallization. The one-step hot forging process (F100) led to non-uniform microstructures with significant grain size variations (10–423 µm), resulting in low recrystallized area fractions and higher dispersion in mechanical properties. In contrast, the three-step hot forging process (F30-60-40) produced a uniform distribution of equiaxed dynamically recrystallized grains, with a median grain size of 64 ± 1 µm and a recrystallized fraction above 95% in the middle region of the sample. The more intensive three-step hot forging process (F30-60-80) resulted in a duplex grain structure, attributed to increased plastic strain and stress in the final forging step. Room temperature mechanical properties were evaluated after F100 and F30-60-40 hot forging process. Comparative analysis demonstrated that controlled multi-step forging enhances grain refinement and mechanical uniformity. The study highlights the importance of optimized gradual deformation for tailoring microstructure and achieving desirable mechanical performance in high-entropy alloys.

BIOGRAPHY



Dr. Michaela Štamborská has expertise in mechanics of novel advanced metallic materials designed and developed at the Institute of Materials and Machine Mechanics, Slovak Academy of Sciences. She works on the development of mathematical and simulation models, numerical modelling of heat transfer processes, deformation behaviour of materials, crack initiation and propagation and signal analysis of acoustic emission technique. She is a specialist in digital image correlation method. She has experience with hydrogenation, as evidenced by articles in which she investigated the effect of hydrogen on deformation behaviour. So far, she has published 20 articles in Current contents (CC) journals and 14 other articles indexed in Scopus. Her works have been cited 267 times in Scopus with H-index 10.

- LinkedIn: linkedin.com/in/michaela-štamborská-99145094
- Skype: Michaela6661

- Research Interest:
  - Advanced metallic materials and their mechanical behaviour
  - Numerical modeling of heat transfer, deformation processes, and crack initiation and propagation
  - Development of mathematical and simulation models
  - Application of DIC and AE in material testing and evaluation
  - Hydrogen embrittlement and its effect on deformation behaviour

Integrating virtual reality in drone education: a gateway to scientific exploration and skill development

Paul Adde[1] ***and Quentin Dos Santos Silva***[1]

1) Cesi Assat, Pôle Aéropolis, 1 Cr de l'Industrie, 64510 Assat, France/ Cesi Assat, Pôle Aéropolis, 1 Cr de l'Industrie, 64510 Assat, France

Corresponding author: paul.adde@viacesi.fr

Original scientific article

Abstract: Integrating virtual reality (VR) into drone training opens new pedagogical horizons by combining immersion, interactivity, and experiential learning. This synergy enables the simulation of complex missions in environments that are otherwise inaccessible, hazardous, or costly to reproduce. Drones are used at various educational levels, from beginner to advanced research, and across disciplines like engineering, computer science, and environmental studies. Their use supports hands-on learning, programming, data collection, and analysis and aligns with project-based approaches. Moreover, drones may act as assistants or mediators in collaborative scenarios. When combined with gamification, they boost motivation and learning skills. This fusion aligns with Education 4.0 dynamics, preparing users for the challenges of engineering education by blending innovation, interactivity, and pedagogy.

Keywords: *virtual reality; drone simulation; immersive learning; scientific training; godot engine*

1. Introduction

The development of virtual reality (VR) technologies has opened up new possibilities in engineering education, particularly in fields such as robotics, simulation, and unmanned aerial vehicles (UAVs). As educational institutions seek more engaging and safer training environments, immersive technologies have emerged as effective tools to bridge theoretical learning with hands-on practice. The use of VR allows students to engage with complex systems in a risk-free environment, increasing accessibility and flexibility while enhancing motivation and long-term knowledge retention [1, 2].

Drone training in particular presents unique challenges: flight operations involve expensive hardware, require open spaces, and carry risks of damage or injury. This is especially problematic for beginners or in academic settings where equipment availability is limited. Traditional training methods often fail to provide sufficient time or freedom for experimentation. VR-based simulators can address these issues by offering customizable, repeatable, and safe environments for learning basic to advanced drone control.

Studies have shown that VR supports experiential learning, improves skill acquisition, and enhances user engagement [1, 3, 4]. When combined with gamified elements, it can significantly boost learners' motivation, immersion, and practical understanding of physical phenomena [2]. These benefits align with the core principles of Education 4.0, which emphasize active learning, autonomy, and the integration of advanced technologies in the learning process.

The aim of this study is to present the design and implementation of a VR-based drone simulator developed using the open-source Godot engine. The simulator was created to support scientific and technical training by simulating realistic flight behavior in a virtual environment.

Research question:

Can a VR-based simulator provide a realistic, pedagogically effective, and accessible alternative for initial drone pilot training in engineering education?

2. Methodology

This research follows a design-based approach focused on the development and implementation of a functional prototype: a virtual reality drone simulator aimed at enhancing training experiences in engineering education. Rather than conducting empirical testing with participants at this stage, the study emphasizes the technical and pedagogical rationale behind the system’s construction.

2.1. Development tools and frameworks

The simulator was developed using Godot Engine (v4), an open-source, lightweight game engine chosen for its modular node-based architecture and its scripting language, GDScript, which enables rapid prototyping [10]. The simulator is structured around independent scenes that include the player controller, drone object, environment elements, and interaction logic.
Figure 1 shows the main scene hierarchy, where the *Player* node is structured with a *CharacterBody3D*, a *Camera3D*, and a *Head* node. This configuration supports free head movement and smooth first-person navigation, essential for immersive VR training.

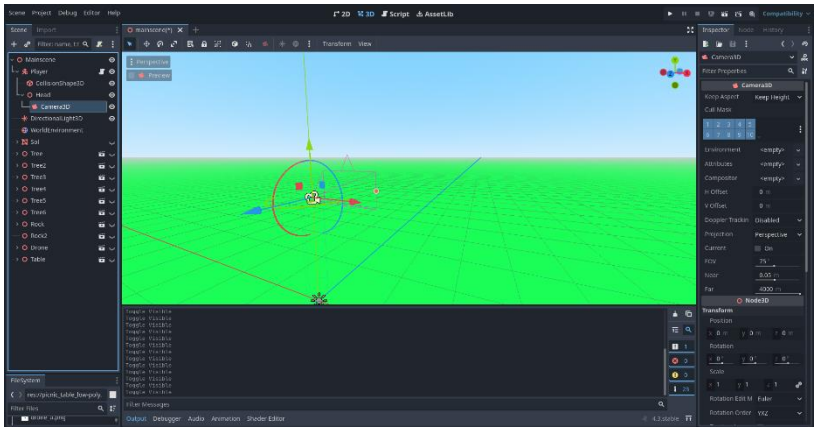


***Figure 1**: Main Scene Hierarchy*

Environment assets such as trees, rocks, and furniture were added to provide spatial context and enhance realism (Figure 2).

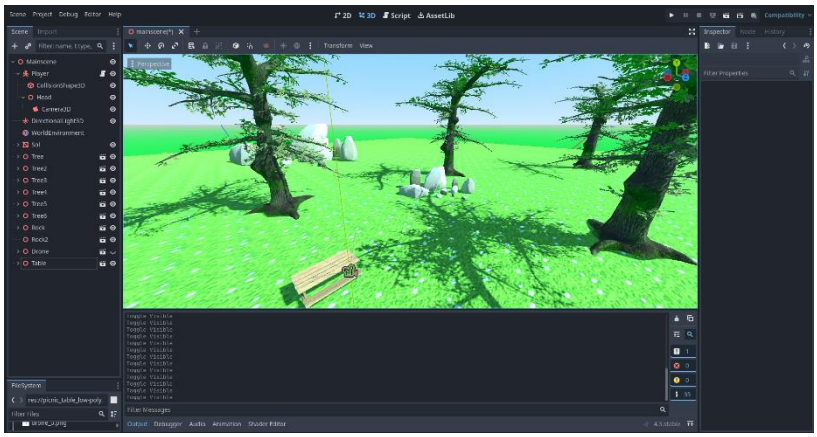


***Figure 2:** Environment with Assets*

A drone model is placed at the center of the scene (Figure 3), currently static but ready to support interactive behaviors.

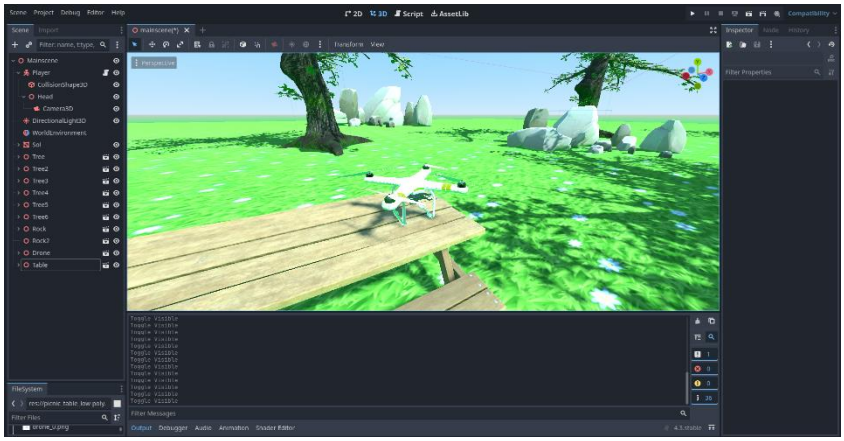


Figure 3: *Drone model integration*

2.2. Simulation design and parameters

The physical behavior of the drone and environment is simulated using built in Godot physics. The simulation includes:

- Gravity and inertia calculations
- Jump and movement logic
- Cursor locking and mouse input for camera control
- Basic aerodynamic response, such as wind influence

As shown in Figure 4, the player's script uses functions like *_physics_process()* and *_input()* to handle movement, gravity, and camera rotation. Constants for speed, jump velocity, and sensitivity ensure adaptable control for users of different skill levels.

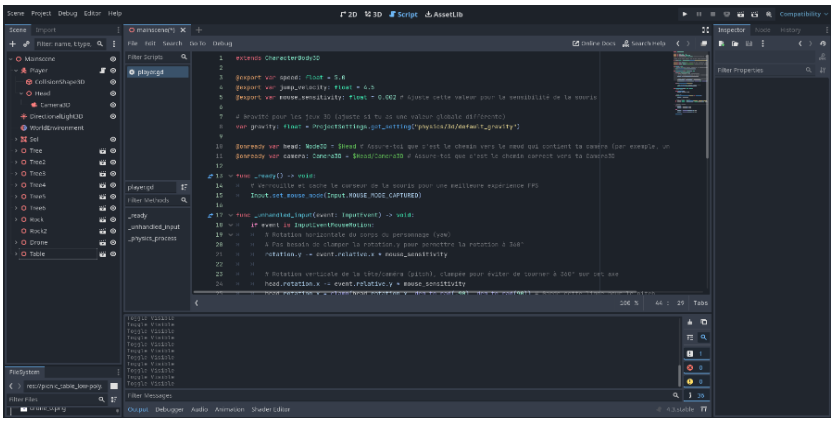


Figure 4: *GDScript player script*

Figure 5 displays the user interface and visual rendering of the VR simulation environment. The design aims to replicate core drone control mechanics while remaining accessible on mid-range hardware, thereby supporting a wide range of learners and institutions. The system also allows for future upgrades, such as real-time drone control, telemetry simulation, or integration with CAD-modeled drone components, as suggested by Maricic et al. [8].

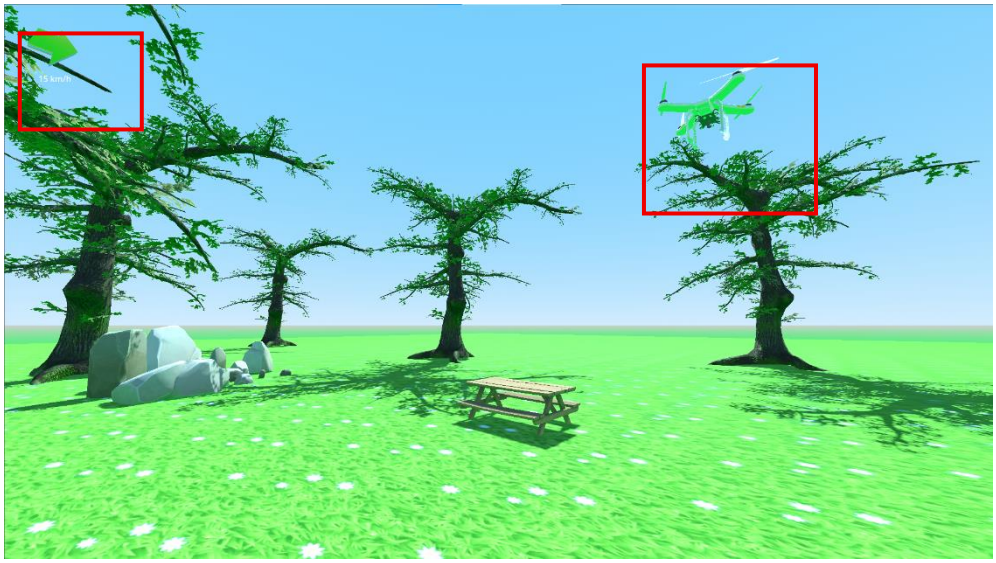


Figure 5: *VR interface the drone simulation*

3. Educational contributions and pedagogical relevance

Learning to pilot drones involves more than just technical coordination; it also requires spatial awareness, decision-making under constraints, and a solid understanding of flight mechanics. In traditional training, these skills are often limited by equipment availability, safety concerns, and lack of flexibility for repeated practice. Virtual reality offers a solution by creating a safe, immersive, and repeatable environment that fosters skill development and active engagement.

The simulator developed in this study enables learners to explore a realistic 3D environment, control a drone from a first-person perspective, and interact with simulated physical forces such as gravity and wind. These features help students intuitively understand the consequences of their actions, encouraging experiential learning.

According to Cardona-Reyes et al. [1], integrating gamification and VR in drone education increases motivation, focus, and autonomy. Maricic et al. [2] also highlight that combining VR with 3D modeling and interactive interfaces promotes creativity, problem-solving, and critical thinking in engineering students. Our approach supports these findings by encouraging trial-and-error learning, where students can experiment freely, make mistakes, and correct their strategies without real-world consequences. In terms of specific skill acquisition, the simulation helps develop:

- Spatial orientation and trajectory planning
- Understanding of basic aerodynamics
- Sensorimotor coordination using VR controls
- Technical autonomy through interaction with physical parameters

Furthermore, the simulator aligns well with project-based learning methodologies, which are central to Education 4.0 frameworks. It can be integrated into multidisciplinary curricula where students design, test, and evaluate drone missions within a simulated but technically consistent environment.

4. Technical limitations and constraints

While virtual reality offers substantial pedagogical benefits, several technical and practical limitations must be considered when developing and deploying a training simulator for drone education.

4.1. Hardware and performance constraints

Running a realistic simulation with physical interactions, 3D rendering, and dynamic environments requires relatively high computing power. Systems must maintain stable frame rates and low latency to avoid disrupting immersion and inducing discomfort [9]. This may limit the use of VR in institutions with constrained hardware resources or for learners accessing training from home environments.

4.2. Software and design limitations

On the software side, real-time simulation of complex environments (for example, large outdoor areas, weather systems) places heavy demands on performance optimization. Current engines, including Godot, have limitations in reproducing high-fidelity aerodynamic behaviors, especially under changing environmental variables like turbulence [8]. Simplified physics, while sufficient for pedagogical scenarios, may not fully replicate the nuances of real-world flight. Additionally, real-time user interaction with multiple autonomous agents (e.g., multi-drone coordination) is technically complex and not yet fully implemented in our prototype.

4.3. Pedagogical technical challenges

Despite its strengths, VR cannot replicate certain critical aspects of real-world drone training, such as:

- Emotional pressure or stress experienced during real operation
- Social coordination, especially in collaborative drone missions or field operations
- Long-term exposure effects, including visual fatigue, cybersickness, or cognitive overload during extended VR sessions [7]

These factors can influence user performance and may reduce the effectiveness of long training periods. They must be considered when designing curricula that incorporate immersive tools.

4.4. Economic and logistical barriers

The acquisition and maintenance of VR headsets, compatible PCs, and associated sensors represent a significant initial cost, particularly for small institutions or underfunded programs. Moreover, instructors must be trained not only in drone theory but also in VR system setup, troubleshooting, and classroom integration.

Despite these limitations, continuous technological improvements and growing accessibility of VR equipment are helping mitigate many of these constraints. As shown by Clay et al. [9], even in resource-constrained environments, carefully designed immersive training can still provide effective learning outcomes when well-integrated into educational strategies.

5. Insights from the implementation

The development of the VR drone simulator confirmed the relevance of open-source tools, such as Godot Engine, for educational simulation purposes. The modular scene architecture and physical scripting capabilities allowed for the rapid creation of an immersive, interactive environment tailored to drone training needs. While no formal user testing was conducted at this stage, the implemented features already align with several pedagogical goals. The simulator supports spatial navigation, physical reasoning, and user experimentation all key aspects of experiential learning. It also provides a flexible platform where new scenarios, interactive elements, or real drone models can be added for advanced use cases. Most importantly, the project demonstrates that even with limited resources, it is possible to create a realistic and safe training system that:

- Facilitates trial and error learning
- Encourages technical autonomy
- Enhances motivation and engagement through immersion and interactivity

This implementation validates the practical feasibility of integrating immersive learning into drone education, and provides a strong foundation for future evaluation, refinement, and classroom integration.

6. Conclusion

This study explored the development of a virtual reality simulator for drone education, with the goal of creating a safe, immersive, and pedagogically effective training tool. By using open-source technologies and a modular design approach, the system enables learners to engage with flight dynamics in an interactive environment while avoiding the risks and costs associated with physical drone training. The simulator supports essential skills such as spatial awareness, motor coordination,

and physical reasoning, all within a flexible framework compatible with project-based learning and Education 4.0 strategies. While no formal user study has yet been conducted, the prototype demonstrates strong potential as a scalable and accessible tool for engineering education. Answering our initial question, the results suggest that a VR-based simulator can indeed serve as a realistic and pedagogically valuable alternative for initial drone pilot training. Future work will focus on integrating more advanced drone behavior, collaborative missions, and experimental validation with students across different educational levels.

References

[1] Cardona-Reyes, H., Trujillo-Espinoza, C., Arevalo-Mercado, C., Muñoz-Arteaga, J., 2021. Training of Drone Pilots through Virtual Reality Environments under the Gamification Approach in a University Context. Interaction Design and Architecture(s), (49), 64–83. https://doi.org/10.55612/s-5002-049-004

[2] Maricic, S., Kovac, A., Peric, M., 2024. Innovative Technologies in Computer Education: Integration VR, CAD/CAM and 3D Modeling with Gamification. MIPRO 2024. https://doi.org/10.1109/MIPRO60963.2024.10569466

[3] Marron, T., Dungan, N., Mac Namee, B., O'Hagan, A. D., 2024. Virtual Reality & Pilot Training: Existing Technologies, Challenges & Opportunities. Journal of Aviation/Aerospace Education & Research, 33(1). DOI: https://doi.org/10.58940/2329-258X.1980

[4] Villada Castillo, J. F., Bohorquez Santiago, L., Martínez García, S., 2025. Optimization of Physics Learning Through Immersive Virtual Reality: A Study on the Efficacy of Serious Games. Applied Sciences, 15(6), 3405. https://doi.org/10.3390/app15063405

[5] Sakib, N., Chaspari, T., Changbum, A., Behzadan, A., 2020. An Experimental Study of Wearable Technology and Immersive Virtual Reality for Drone Operator Training.

[6] Paterson, J., 2019. Improving Usability, Efficiency, and Safety of UAV Path Planning through a Virtual Reality Interface.

[7] Van Damme, S., Sameri, J., Schwarzmann, S., Wei, Q., Trivisonno, R., De Turck, F., & Vega, M. T., 2024. Impact of latency on QOE, performance, and Collaboration in Interactive Multi-User Virtual Reality. Applied Sciences, 14(6), 2290. https://doi.org/10.3390/app14062290

[8] Maricic, S., Haber, I. M., Veljovic, I., Palunko, I., 2020. Implementation of Optimum Additive Technologies Design for Unmanned Aerial Vehicle Take-Off Weight Increase. EUREKA Physics And Engineering, 6, 50-60. https://doi.org/10.21303/2461-4262.2020.001514

[9] Clay, C. J., Budde, J. R., Hoang, A. Q., Gushchyan, A., 2024. An evaluation of the effectiveness of immersive virtual reality training in non-specialized medical procedures for caregivers and students : a brief literature review. Frontiers in Virtual Reality, 5. https://doi.org/10.3389/frvir.2024.1402093

[10] Salmela, T., 2022. Game development using the open-source Godot Game Engine. Thesis. https://urn.fi/URN:NBN:fi:amk-202205057482

Integrative approach to evaluating the quality of 3D printed cultural artifacts: multicriteria analysis and human perception using the AHP method

***Andrej Bašić*[1], *Ivan Peko*[2] *and Ivan Jerković*[3]**

1) University of Split, Faculty of Electrical Engineering, Mechanical Engineering and Naval Architecture, Ruđera Boškovića 32, 21000 Split, Croatia

2) University of Split, Faculty of Science, Ruđera Boškovića 33, 21000 Split, Croatia

3) Faculty of Forensic Sciences, University of Split, Ruđera Boškovića 33, 21000, Split, Croatia

Corresponding author: andrej@fesb.hr

Original scientific article

Abstract: 3D technology is reshaping how museums preserve, share, and interpret cultural heritage. Since many artifacts are fragile, difficult to access, or otherwise unavailable to the public, it is essential that 3D-printed replicas remain faithful representations of the original artifacts. Such high-quality reproductions can provide valuable sources for learning, public engagement, and heritage conservation while allowing more people to explore and connect with cultural artifacts through educational programs and interactive displays. This study provides a comprehensive evaluation of 3D-printed replicas of a mace excavated near Bribir, presumed to date from the 9th to 11th century. The original artifact is preserved in the Museum of Croatian Archaeological Monuments in Split (MHAS). The mace was scanned into a digital model with the 2020 EinScan Pro 2X structured light scanner and then reproduced into four variants by various 3D printing technologies. During the Museum Night 2025, organized as part of the celebration of the 1100th anniversary of the Croatian Kingdom, replicas of maces were presented to visitors at the Franciscan Museum in Tomislavgrad (BiH), and a structured survey was conducted to assess their fidelity and quality. The results provided direct insight into the acceptance of replicas in the context of a museum exhibition and into the way visitors experience 3D printed artifacts compared to the original. In this paper, the data collected through the visitor survey were analyzed using a mixed linear model to identify variables that significantly influence respondents' satisfaction with the 3D-printed models. In addition to the qualitative analysis, the Analytical Hierarchy Process (AHP) was employed as a multi-criteria decision-making method. The AHP was conducted based on survey ratings provided by museum visitors, which enabled the integration of human perception into a comprehensive assessment of 3D printed model quality. Based on a previous research with a 13th-century iron spur presented during Museum Night 2023, this study extends the application of 3D technologies in cultural heritage. The combined results provide guidelines for reproducing artifacts based on object type and replica purpose — exhibition, educational, or interpretive.

Keywords: *cultural heritage; 3D scanning; 3D printing; reverse engineering; human-centered approach; multi-criteria analysis; Analytic Hierarchy Process (AHP)*

1. Introduction

Over the decades of its development and application in various industries, 3D technology has become one of the key tools in the preservation and presentation of cultural heritage [1-4]. Its application is not only based on the creation of documentation, where a digital database provides the possibility of preserving and studying materials, but also offers new ways of interpretation, education, and interaction with museum content [4-6], especially throught the use of physical replicas. The application of 3D technology is even more significant in cases where original objects are fragile, rare, or inaccessible to the public [4, 5], as it provides the possibility of wider access while preserving the original. In such cases, replicas serve as a link between the protected artifacts and the audience, providing an opportunity to experience the shape, proportions, and details of the object firsthand [6,

7]. Therefore, the authenticity of printed replicas is essential for the presentation and preservation of cultural and scientific values, as it ensures fidelity to the form and details of the original. Starting from the assumption that the perception of the quality of 3D replicas depends on a combination of technical characteristics and the subjective impression of the observer [7], this research aims to examine how different 3D printing technologies affect visitor satisfaction. The goal is to offer guidelines for choosing optimal methods for creating replicas, adapted to their purpose, whether it is for museum exhibition, education, or interpretive work that conveys the use, meaning, and symbolism of objects within the museum context.

2. Scanning & Printing

The focus of this study is an iron mace provided by the Museum of Croatian Archaeological Monuments in Split. It is a valuable archaeological artefact that, according to the museum's curator, originates from the Bribir area and dates back to the 10th and 11th centuries. The significance of this mace as an artefact selected for the research lies in its unique and interesting texture. On one side, the surface of the mace is well preserved with minimal damage and decorative engravings are visible, while the other half of the mace is damaged and unpreserved, which could be attributed to the position and the influence of the medium in which it was found (Figure 1).



Figure 1. *Iron mace from 10th or 11th century, multiple side views*

Since it is a valuable artifact that is part of the museum's collection and permanent exhibition, its scanning was performed in situ on the premises of the Museum using a 3D scanner EinScan PRO 2X

[8]. Given that the artifact is small in size, its scanning was carried out on a rotating table, which enabled precise scanning since the scanned object is always located at the same distance from the scanner (Figure 2).

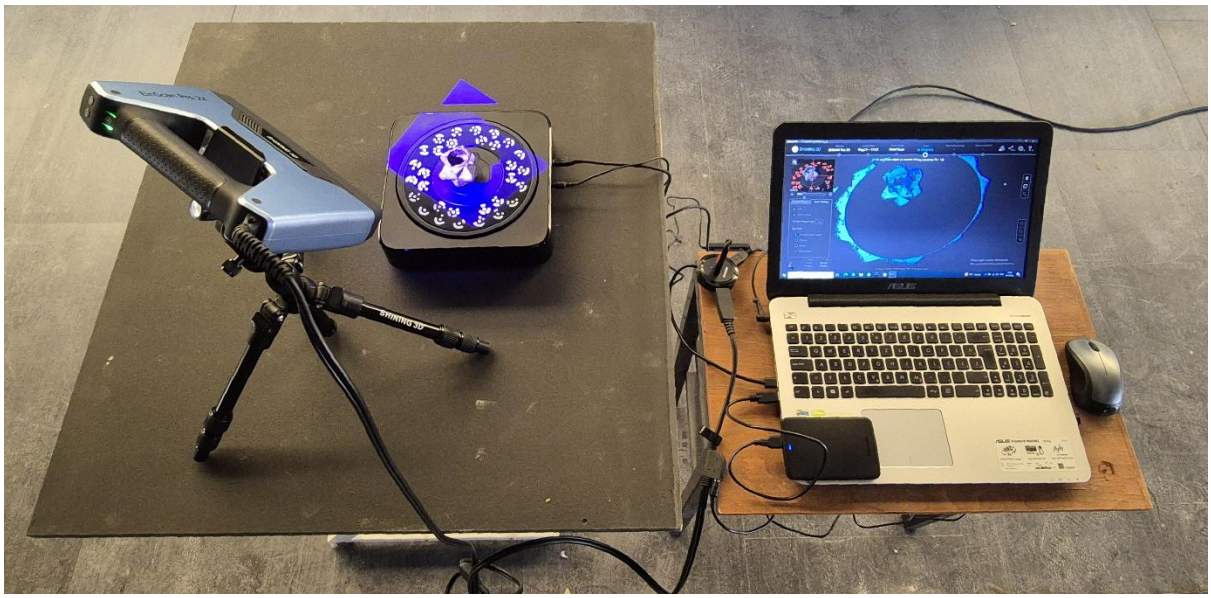


Figure 2. *Scanning process with EinScan PRO 2X 3D Scanner*

Upon completion of the scanning process, the scanned data was processed by scanner software that supports the 3D scanner in order to remove excess data, i.e. noise, recorded during the scanning process. The processed and prepared data was exported in the 3MF format, which stores more information than the STL format, which includes materials, colors, texture, as well as some other possible details of the scanned model, and is therefore a more comprehensive format for industrial 3D printing. [9]. The result of the scan is an accurate digital replica of the mace model, showing all the characteristics of the original artifact, consisting of 161,259 vertices and 322,256 faces (Figure 3). Since the previously mentioned steps resulted in a pure digital 3D model of the mace, there was no need for post-processing in one of the available programs such as Autodesk® Meshmixer™, MeshLab 2025.7 or any similar software, as was the case with the research conducted on the iron spur on Museum Night 2023. [7], but one could immediately proceed to the preparation of the model for 3D printing.

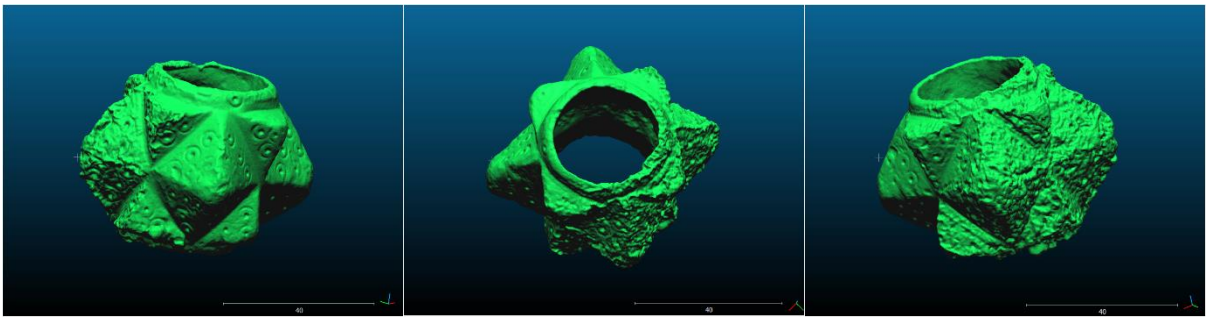


Figure 3. *Digital model of mace, multiple side views*

The model of mace was printed using four different printing technologies, in order to see which of these technologies would provide the most realistic appearance of the mace, given the printing settings and technical characteristics of the material used. For the FDM (Fused Deposition Modeling) printing process [10], the PLA Strongman™ C8 filament, manufactured by Azurefilm [11], was selected. This material had already demonstrate solid printing results in some previous cases, such as the printing an iron spur for research purposes at the Museum Night 2023 [7]. The Strongman™ filament is characterized by exceptional strength, toughness and durability, offering a robust option for

applications where mechanical resistance is important. In the MSLA (Masked Stereolithography Apparatus) process [12], Elegoo ABS-like resin V3.0 Pro [13] was used because of its great performance and suitability for making high-quality prints. This resin was selected for its scratch resistance, exceptional impact resistance, and its ability to minimize the risk of breakage due to potential drops or impacts. The final printing result is a model characterized by high dimensional accuracy, smooth surface finish, and preservation of fine details, without any distortion or loss of fine details. The third technology applied to print the mace replica was BJ (Binder Jetting) 3D printing technology [14], which creates objects by selectively applying a liquid binder to a thin layer of powdered material. In this case, a gypsum-based composite ZP150 [15], manufactured by Z Corporation, was used. A specialized polymer-based liquid was used as a binder for the particle material, which is precisely applied using inkjet heads, selectively binding the powder in the required areas, allowing layer-by-layer curing throughout the printing process. After the printing is complete, additional impregnation of the model is required to improve its strength and durability; otherwise, it may collapse during manipulation. The final printing technology was SLS (Selective Laser Sintering) [16, 17], known for its ability to produce strong, functional parts. This additive manufacturing (AM) technology uses a high-power laser to sinter small particles of polymer powder into a solid structure based on a 3D model. The material used for printing was PA12 (nylon 12) [17, 18], manufactured by Materiallise. This thermoplastic is well known for its excellent mechanical properties, including high strength, ductility, and chemical resistance, and is therefore suitable for the production of prototypes and end-use parts. for prototyping and manufacturing end-use parts. Figure 4 shows replicas of maces made using the aforementioned 3D printing technologies and materials, where differences in surface quality, detail precision, and the overall visual impression of the model are clearly visible.

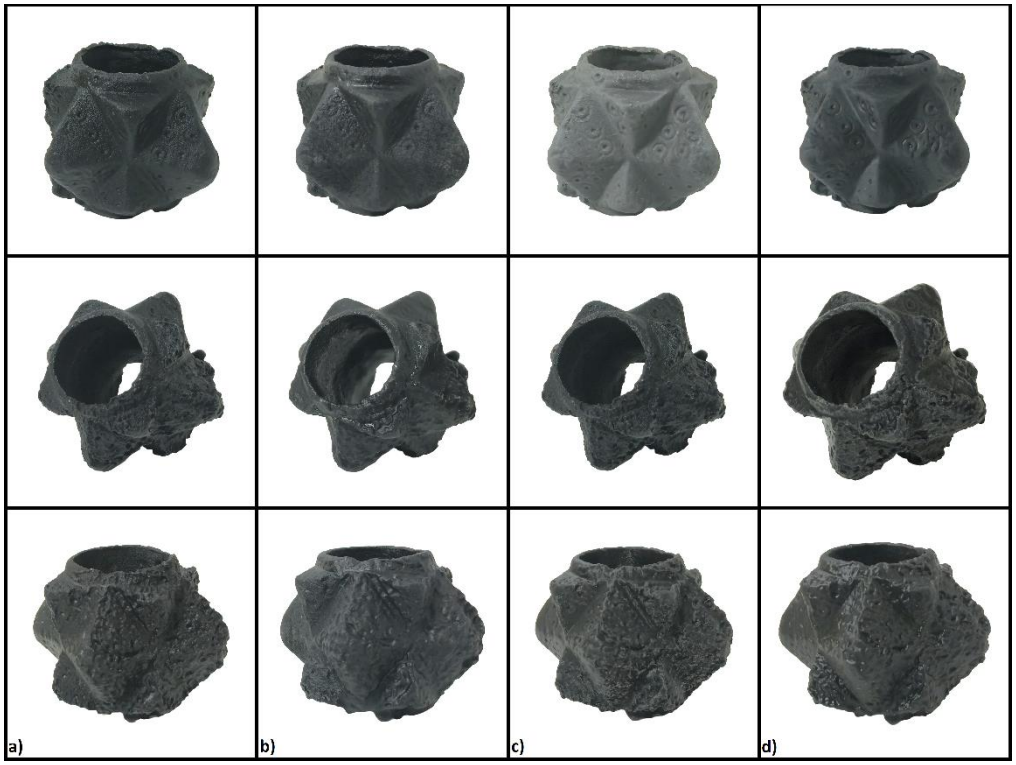


Figure 4. *From left to right the image shows finished models of 3D-printed maces with different materials: a) Materiallise PA12 b)* Z Corporation *ZP150 c*) Azurefilm PLA Strongman™ d) Elegoo ABS-like resin V3.0 Pro

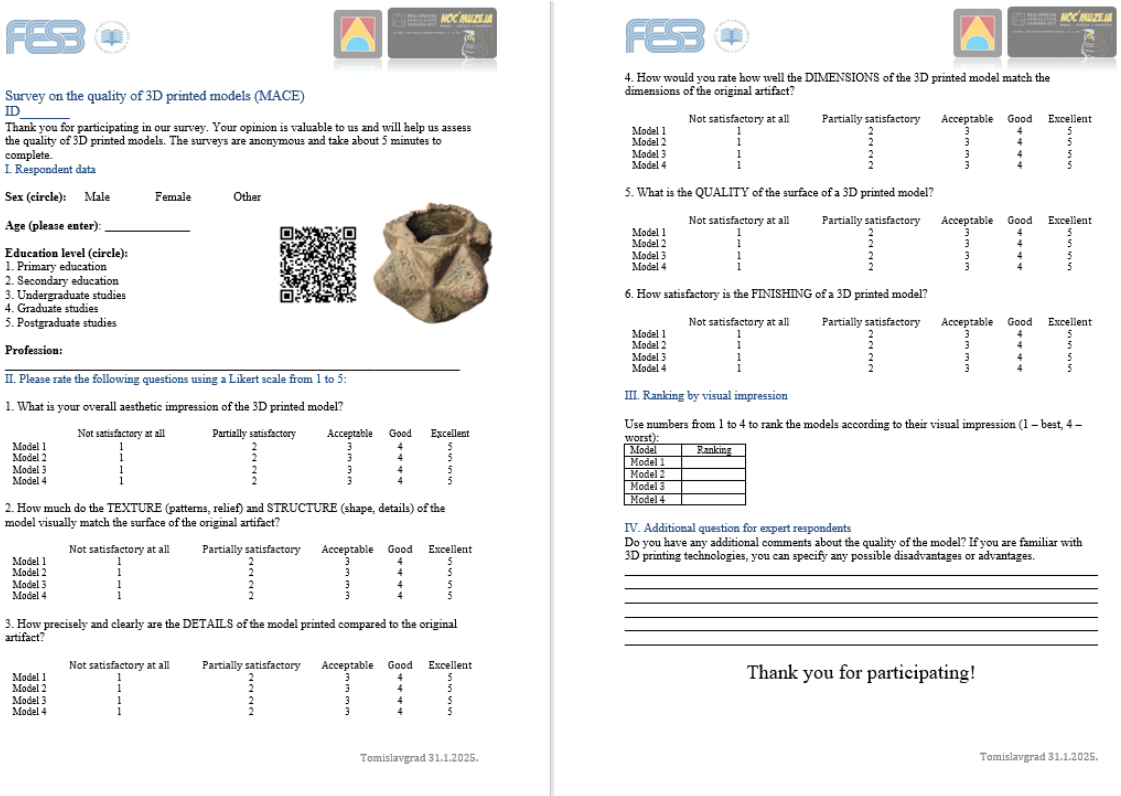
3. 3D Survey creation

After printing, the mace models were visually analyzed, documented with photographs, and numerically labeled for a structured survey (Figure 5). The survey was conducted on January 31, 2025, during the Night of Museums in cooperation with the Franciscan Museum Tomislavgrad (BiH), with

the support of the Museum of Croatian Archaeological Monuments from Split, Croatia. The survey collected demographic data, including gender, age, education level, and occupation, through seven evaluation questions. The questions addressed key indicators: detail precision, dimensional accuracy, surface quality, finish, texture, and structure, as well as the overall visual impression of the model (Figure 6). Respondents were asked to rate various aspects of the printed models on a Likert scale from 1 to 5. The purpose of the selected criteria was to provide a thorough assessment of the accuracy and quality of the 3D printed models in comparison to the original artifact that was placed in a display case next to them. The survey was conducted with a broad and diverse group of respondents, including cultural heritage experts, museum visitors, and technical experts. Feedback from this survey provided quantitative and qualitative data on the fidelity of 3D-printed replicas to the original artifact, providing a valuable basis for assessing the credibility and usability of 3D-printed replicas in a museum context.



Figure 5. *Mace replicas, form left to right: (1)SLS, (2) FDM, (3) MSLA, (4) BJ*



Survey on the quality of 3D printed models (MACE)

ID_____

Thank you for participating in our survey. Your opinion is valuable to us and will help us assess the quality of 3D printed models. The surveys are anonymous and take about 5 minutes to complete.

I. Respondent data

Sex (circle): Male Female Other

Age (please enter): _____

Education level (circle):
1. Primary education
2. Secondary education
3. Undergraduate studies
4. Graduate studies
5. Postgraduate studies

Profession:

_____

II. Please rate the following questions using a Likert scale from 1 to 5:

1. What is your overall aesthetic impression of the 3D printed model?

	Not satisfactory at all	Partially satisfactory	Acceptable	Good	Excellent
Model 1	1	2	3	4	5
Model 2	1	2	3	4	5
Model 3	1	2	3	4	5
Model 4	1	2	3	4	5

2. How much do the TEXTURE (patterns, relief) and STRUCTURE (shape, details) of the model visually match the surface of the original artifact?

	Not satisfactory at all	Partially satisfactory	Acceptable	Good	Excellent
Model 1	1	2	3	4	5
Model 2	1	2	3	4	5
Model 3	1	2	3	4	5
Model 4	1	2	3	4	5

3. How precisely and clearly are the DETAILS of the model printed compared to the original artifact?

	Not satisfactory at all	Partially satisfactory	Acceptable	Good	Excellent
Model 1	1	2	3	4	5
Model 2	1	2	3	4	5
Model 3	1	2	3	4	5
Model 4	1	2	3	4	5

Tomislavgrad 31.1.2025.

4. How would you rate how well the DIMENSIONS of the 3D printed model match the dimensions of the original artifact?

	Not satisfactory at all	Partially satisfactory	Acceptable	Good	Excellent
Model 1	1	2	3	4	5
Model 2	1	2	3	4	5
Model 3	1	2	3	4	5
Model 4	1	2	3	4	5

5. What is the QUALITY of the surface of a 3D printed model?

	Not satisfactory at all	Partially satisfactory	Acceptable	Good	Excellent
Model 1	1	2	3	4	5
Model 2	1	2	3	4	5
Model 3	1	2	3	4	5
Model 4	1	2	3	4	5

6. How satisfactory is the FINISHING of a 3D printed model?

	Not satisfactory at all	Partially satisfactory	Acceptable	Good	Excellent
Model 1	1	2	3	4	5
Model 2	1	2	3	4	5
Model 3	1	2	3	4	5
Model 4	1	2	3	4	5

III. Ranking by visual impression

Use numbers from 1 to 4 to rank the models according to their visual impression (1 – best, 4 – worst):

Model	Ranking
Model 1	
Model 2	
Model 3	
Model 4	

IV. Additional question for expert respondents

Do you have any additional comments about the quality of the model? If you are familiar with 3D printing technologies, you can specify any possible disadvantages or advantages.

_____

_____

_____

_____

_____

_____

Thank you for participating!

Tomislavgrad 31.1.2025.

Figure 6. *The featured image shows a survey designed to collect data on respondents and evaluate 3D-printed mace models*

4. AHP analysis

The Analytic Hierarchy Process (AHP), developed by Thomas L. Saaty, has become one of the most widely recognized approaches to multi-criteria decision-making. Its appeal lies in the fact that complex

problems, which often involve conflicting criteria, can be broken down into a clear hierarchical structure. This structured approach has been successfully applied in many different fields — from engineering and management to healthcare and, more recently, cultural heritage studies [19-21]. By enabling systematic pairwise comparisons, AHP makes it possible to transform subjective judgments into quantitative measures, providing both transparency and reproducibility in the decision-making process [22, 23].

In this study, the method was applied with the aim of selecting the most suitable additive manufacturing technique for producing models that reflect the expectations of museum visitors. As input information for the Analytic Hierarchy Process (AHP), visitor assessments obtained through a survey conducted in the museum were used. The survey respondents evaluated four different models produced by additive manufacturing, and their ratings served as the basis for the multi-criteria decision-making process. The decision problem was organized into three levels: the overall goal at the top, six evaluation criteria in the middle, and four alternative processes at the bottom (SLS, FDM, MSLA, and BJ) (Figure 7). The chosen criteria were: C1 - aesthetic impression, C2 - texture and structure, C3 - details accuracy, C4 - dimensions, C5 - surface quality, C6 - finishing.

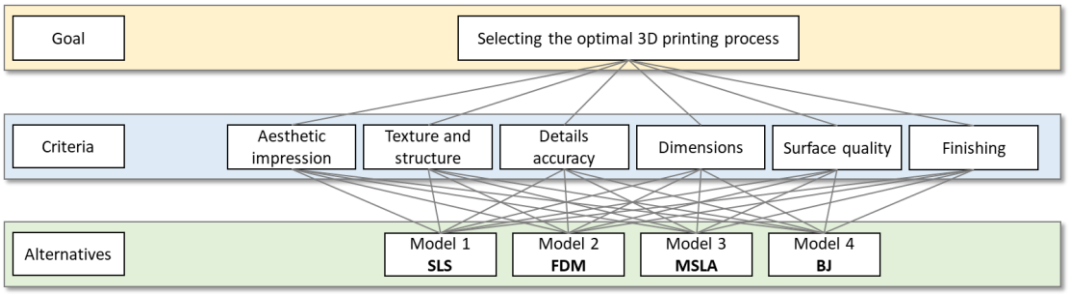


Figure 7. *Multicriteria decision making problem*

To establish the relative importance of these criteria, a pairwise comparison matrix was created (Table 1). The comparisons were carried out using Saaty’s fundamental scale, which assigns values from 1 to 9 (and their reciprocals). On this scale, the value 1 denotes equal importance of two criteria, 3 indicates a moderate preference, 5 a strong preference, 7 a very strong preference, and 9 an extreme preference. The reciprocal values express the opposite relationships. In this way, qualitative judgments can be expressed numerically in a consistent and systematic form.

Table 1. *Pairwise comparison matrix*

	Aesthetic impression	Texture and structure	Details accuracy	Dimensions	Surface quality	Finishing
Aesthetic impression	1	1/3	1/5	5	1	1
Texture and structure	3	1	1	5	1	3
Details accuracy	5	1	1	7	3	5
Dimensions	1/5	1/5	1/7	1	1/5	1/5
Surface quality	1	1	1/3	5	1	1
Finishing	1	1/3	1/5	5	1	1

From the pairwise comparison matrix, the weights of the criteria were calculated (Figure 8). As part of the procedure, the consistency ratio (CR) was also determined in order to verify whether the judgments were logically coherent. The obtained CR value of 0.05 confirmed that the matrix reached an acceptable level of consistency, meaning that the comparisons could be considered reliable (CR<0.1).

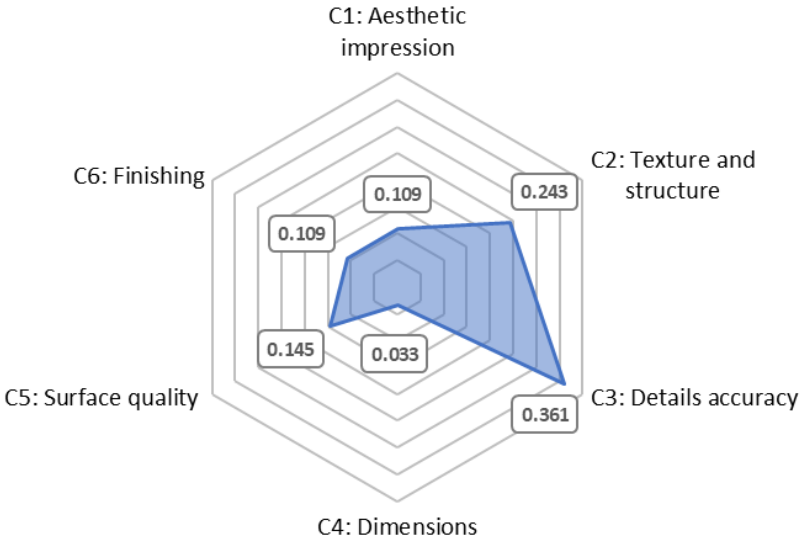


Figure 8. *Criteria weights*

After establishing the weights, the four additive manufacturing processes were assessed against each criterion individually (Figure 9a–f). These partial results were then synthesized to derive the overall priorities of the alternatives (Figure 10). The final outcome provided a clear ranking of the considered technologies, reflecting the preferences expressed by museum visitors. The results demonstrated that the most faithful replica of the archaeological artifact was obtained with Model 1, produced by the Selective Laser Sintering (SLS) process, which achieved the highest evaluations primarily due to its ability to reproduce fine details, dimensional stability, and surface quality. The second-ranked alternative was Model 2, manufactured using Fused Deposition Modeling (FDM), which, although more limited in terms of surface finishing and accuracy, provided a satisfactory overall appearance and robustness appreciated by the visitors. Model 3, obtained through Masked Stereolithography (MSLA), followed next; this process is capable of high-resolution printing but in this case was somewhat disadvantaged by the brittleness of the material and certain limitations in texture reproduction. Finally, Model 4, produced by the Binder Jetting (BJ) technology, was placed last, as visitors perceived it to have weaker surface quality and finishing compared to the other alternatives.
The outcome of the AHP procedure provided a clear and structured ranking of the additive manufacturing processes, offering a sound basis for the final choice. By organizing the evaluations of museum visitors within a hierarchical framework, the method made it possible to identify a solution that not only reflects the preferences of the audience but is also supported by a transparent decision-making process. The selected model, produced by the most suitable technology, can be regarded as a high-quality replica of archaeological artifacts displayed in the museum. In addition to faithfully reproducing the original objects, such replicas open up new possibilities for their use in education, interactive interpretation, and visitor engagement. They allow museums to share heritage in a safe and sustainable way, while at the same time protecting the integrity of the originals. In this sense, the study illustrates how combining a structured decision-making tool such as AHP with additive manufacturing technologies can serve both technical and cultural purposes, supporting not only process optimization but also new approaches in heritage presentation and museum practice.

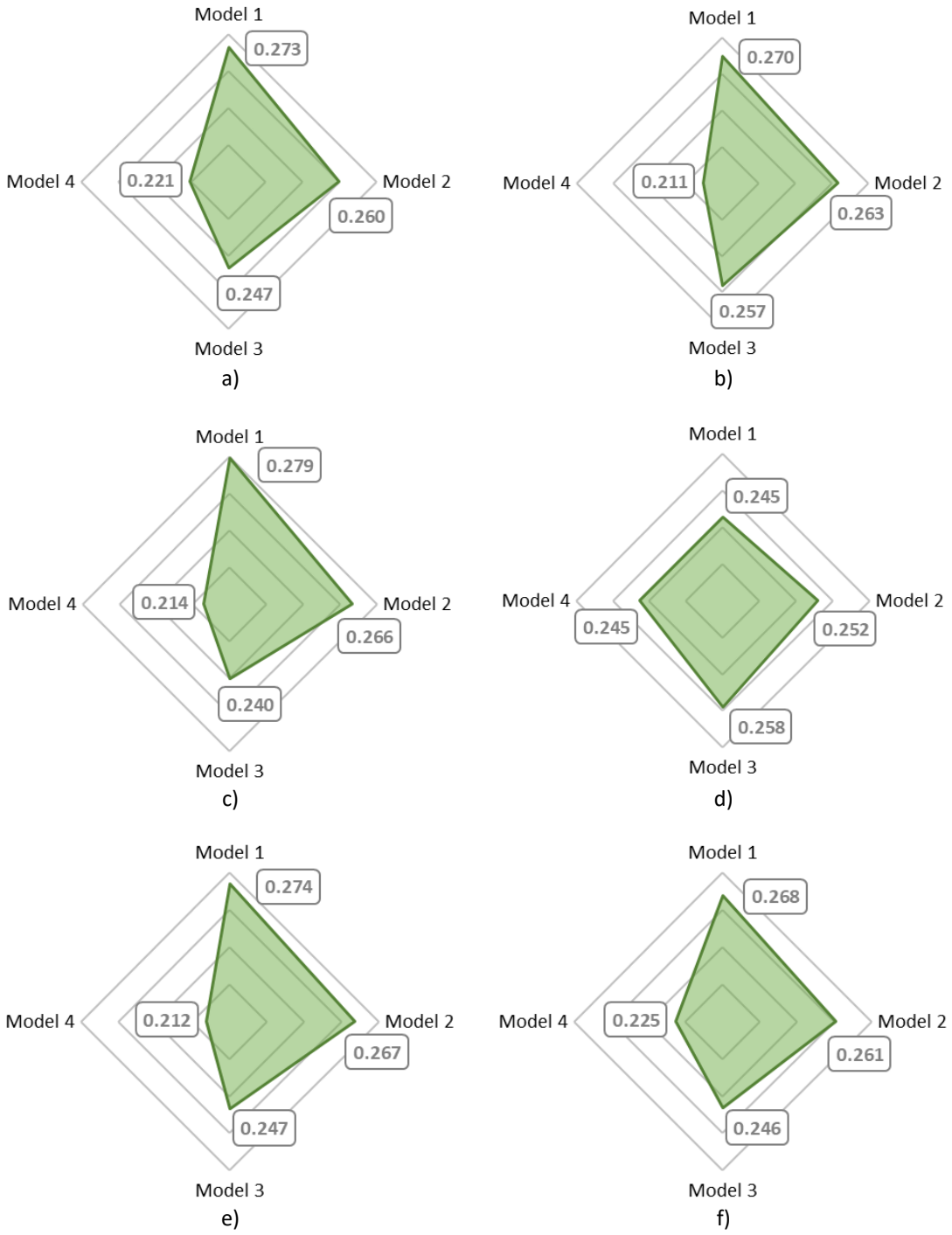


Figure 9. *Priorities of alternatives according to criteria: a) aesthetic impression, b) texture and structure, c) details accuracy, d) dimensions, e) surface quality, f) finishing*

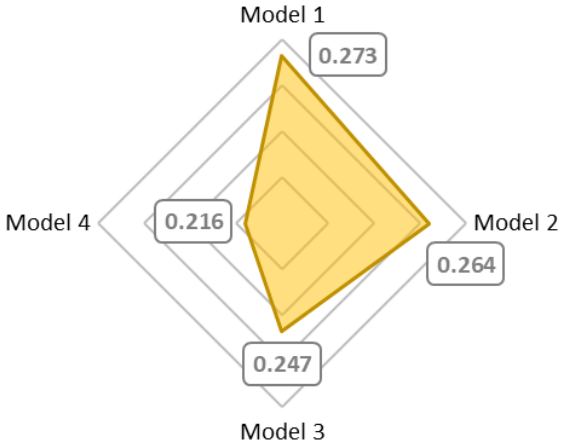


Figure 10. *Overall priorities of alternatives*

5. Conclusions

This research showed that the assessment of the quality of 3D printed replicas of cultural artifacts depends on the combination of technical features of the applied technology and the materials used, as well as on the experience of end users. The application of multi-criteria AHP analysis enabled the connection of technical data with user perception, which provided a more complete picture of the fidelity of printed replicas compared to the original artifacts. It was found that different technologies have specific advantages: for example, MSLA and SLS processes achieve greater precision in details and a more aesthetically impressive result, while other technologies are more suitable for educational or interactive purposes. This integrative approach has established the foundation for the development of guidelines that can be applied in museums and research institutions when choosing technology, depending on the purpose of the replica — whether for exhibition display, educational or interpretive activities. In addition to practical application, the results have also contributed to the development of evaluation methodology in the field of cultural heritage, as it has been shown that engineering approaches can be successfully combined with a humanistic perspective in the creation of credible and functional museological solutions.

Acknowledgments

The authors would like to thank the Museum of Croatian Archaeological Monuments in Split, particularly the director Miroslav Katić, and curator Deni Tojčić, for providing access to the artifact and for their assistance in setting up the survey stand during the 2025 Night of the Museum event at the Franciscan Museum Tomislavgrad, as a part of celebration of the 1100th anniversary of the Croatian Kingdom.

References:

[1] Balletti, C., & Ballarin, M., 2019. An application of integrated 3D technologies for replicas in cultural heritage. ISPRS International Journal of Geo-Information, 8(6), 285.

[2] Zhao, S., Hou, M., Hu, Y., Zhao, Q., 2018. Application of 3D model of cultural relics in virtual restoration. The International Archives of the Photogrammetry, Remote Sensing and Spatial Information Sciences, 42, 2401-2405.

[3] Adane, A., Chekole, A., Gedamu, G., 2019. Cultural heritage digitization: Challenges and opportunities. International Journal of Computer Applications, , 178.33: 1-5.

[4] Bašić, A., Mladineo, M., Jerković, I., 2023. Utilizing 3D scanning, optimization, and 3D printing for cultural heritage conservation. In 12th International Conference Mechanical Technologies and Structural Materials 2023 (MTSM 2023) (pp. 5-20).

[5] Wilson, P. F., Stott, J., Warnett, J. M., Attridge, A., Smith, M. P., Williams, M. A., 2017. Evaluation of touchable 3D-printed replicas in museums. Curator: The Museum Journal, 60(4), 445-465.

[6] Ballarin, M., Balletti, C., Vernier, P., 2018. Replicas in cultural heritage: 3D printing and the museum experience. The International Archives of the Photogrammetry, Remote Sensing and Spatial Information Sciences, 42, 55-62.

[7] Bašić, A., Peko, I., Jerković, I., 2024. Multi-criteria analysis of 3D-printing procedures in cultural heritage: a human-centered approach. In Proceedings of 13th International Conference Mechanical Technologies and Structural Materials 2024 (pp. 15-28). Split: Fakultet elektrotehnike, strojarstva i brodogradnje Sveučilišta u Splitu.

[8] https://www.einscan.com/handheld-3d-scanner/einscan-pro-2x-v2/ (accessed 22 September 2025).

[9] Iancu, C., 2018. About 3d printing file formats. Annals of'Constantin Brancusi'University of Targu-Jiu. Engineering Series/Analele Universităţii Constantin Brâncuşi din Târgu-Jiu. Seria Inginerie, (2).

[10] Sapkota, A., Ghimire, S. K., Adanur, S., 2024. A review on fused deposition modeling (FDM)-based additive manufacturing (AM) methods, materials and applications for flexible fabric structures. Journal of Industrial Textiles, 54, 15280837241282110.

[11] https://azurefilm.com/product/pla-strongman-filament-black/ (accessed 17 September 2025).

[12] Huang, J., Qin, Q., Wang, J., 2020. A review of stereolithography: Processes and systems. Processes, 8(9), 1138.

[13] https://eu.elegoo.com/collections/abs-like-resins/products/elegoo-abs-like-resin-v-3-0-pro/ (accessed 17 September 2025).

[14] Ziaee, M., Crane, N. B., 2019. Binder jetting: A review of process, materials, and methods. Additive Manufacturing, 28, 781-801.

[15] 3D Systems. 2010. ZP150 Powder [3D printing material]. United States. Available at: https://www.3dsystems.com.

[16] Song, Y., Ghafari, Y., Asefnejad, A., Toghraie, D., 2024. An overview of selective laser sintering 3D printing technology for biomedical and sports device applications: Processes, materials, and applications. Optics & Laser Technology, 171, 110459.

[17] Saffarzadeh, M., Gillispie, G. J.,Brown, P., 2016. Selective Laser Sintering (SLS) rapid protytping technology: A review of medical applications. In Proceedings of the 53rd Annual Rocky Mountain Bioengineering Symposium, RMBS 2016 and 53rd International ISA Biomedical Sciences Instrumentation Symposium (pp. 142-149). Denver, CO.

[18] https://www.materialise.com/en/industrial/3d-printing-materials/pa12-sls/ (accessed 17 September 2025).

[19] Schuhmann, D., Rupp, M., Merkel, M., & Harrison, D. K., 2022. Additive vs. conventional manufacturing of metal components: Selection of the manufacturing process using the AHP method. Processes, 10, 1617.

[20] Al Awadh, M., 2022. Utilizing multi-criteria decision making to evaluate the quality of healthcare services. Sustainability, 14, 12745.

[21] Fiore, P., Sicignano, E.,Donnarumma, G., 2020. An AHP-based methodology for the evaluation and choice of integrated interventions on historic buildings. Sustainability, 12, 5795.

[22] Peko, I., Bajić, D., Veža, I., 2015. Selection of additive manufacturing process using the AHP method. In Proceedings of 5th International Conference Mechanical Technologies and Structural Materials 2015 (pp. 119-129). Split: Fakultet elektrotehnike, strojarstva i brodogradnje Sveučilišta u Splitu.

[23] Peko, I., Gjeldum, N., Bilić, B., 2018. Application of AHP, Fuzzy AHP and PROMETHEE method in solving additive manufacturing process selection problem. Technical gazette, 25(2), 453-461.

Multi-objective optimization of process parameters in fiber laser cutting of aluminium alloy

***Derzija Begic-Hajdarevic*[1], *Simon Klancnik*[2], *Maida Cohodar Husic*[1], *Kristijan Sket*[2], *Kenan Muhamedagic*[1], *Edin Begovic*[3] *and Mirko Ficko*[2]**

1) University of Sarajevo, Faculty of Mechanical Engineering, Vilsonovo setaliste 9, 71 000 Sarajevo, Bosnia and Herzegovina

2) University of Maribor, Faculty of Mechanical Engineering, Smetanova 17, 2000 Maribor, Slovenia

3) University of Zenica, Faculty of Mechanical Engineering, Fakultetska 1,72000 Zenica, Bosnia and Herzegovina

Corresponding author: begic@mef.unsa.ba

Original scientific article

Abstract: The focus of this study was to investigate the effect of fibre laser cutting of aluminium alloy to optimize process parameters to achieve good cut quality. The input parameters for optimization were selected cutting speed and assist gas pressure. Kerf width, kerf taper angle and surface roughness were used as output parameters to evaluate the quality of laser cutting. ANOVA was applied to determine the most important process parameters, while the hybrid PSI-TOPSIS method was used for the multi-criteria optimization of process parameters. According to ANOVA results, it was observed that the cutting speed has the most significant impact on the cut quality characteristics, especially on the kerf taper angle and the kerf width with a contribution of 85.33% and 82.62%, respectively. The optimal combinations of process parameters obtained through optimization are cutting speed 11500 mm/min and assist gas pressure 6.5 bar.

Keywords: *fibre laser; cut quality; aluminium alloy; process parameters, multi-criteria optimization*

1. Introduction

Fibre laser cutting is non-conventional method that uses a focused laser beam to cut different materials, mainly metals. Laser cutting process is widely used in the automobile, solar, and other manufacturing industries due to its good cutting quality, high production efficiency, and wide range of applications [1], [2] and [3]. To take advantages offered by the laser cutting process, it is very important to carefully consider and select the process parameters. The selection of process parameters mainly depends on the workpiece material type, the thickness of the workpiece and the desired laser cutting performance related to quality and productivity [4], [5] and [6]. The fact that the optimal combination of process parameters is different for different laser cutting conditions. Therefore, determining the conditions of the laser cutting process for multi-objective optimization is of crucial importance. The preference selection index (PSI) method was applied in [4] for optimization of CO_2 laser cutting of stainless steel. Surface roughness, kerf width, material removal rate and heat affected zone were considered as optimization criteria. A hybrid method of grey relational analysis (GRA) and fuzzy logic was used [7] to optimize the kerf taper and heat affected zone during cutting aluminium alloy with a pulsed Nd:YAG laser. Results showed that the applied hybrid method can reduce the heat affected zone and kerf taper in laser cutting. A genetic algorithm combined with the RSM (response surface) method was used to investigate the influence of cutting speed, focal point location and nitrogen gas pressure on the surface roughness during cutting of SS 304 stainless steel, using a CO2 laser [8]. Machining parameters such as cutting speed, laser power and additive percentage on kerf taper angle, surface roughness and ovality percentage of glass microballon/epoxy syntactic foams were investigated and optimized [9]. The GRA method was used for optimization, and the obtained results were validated using MOORA method. Results showed that low power and high speed are favourable parameters for laser drilling in resin/glass microballon composites. TOPSIS –

entropy weight method was used to optimize cut perpendicularity, surface roughness and material removal material during cutting of mild steel with a fibre laser [10]. Liu et al. [11] developed a data augmentation-based artificial neural network model to achieve accurate prediction of heat affected zone and recast layer thicknesses during fibre laser cutting of sheet metal. Latin hypercube sampling and neural networks was used for optimizing fibre laser cutting of stainless steel [12]. Coati optimization algorithm was applied [13] to optimize a Decision Tree model by fine-tuning critical hyperparameters to enhance the accuracy prediction of models for kerf width and kerf taper, based on process parameters such as cutting speed, assist gas pressure, lamp current, pulse frequency and pulse width in laser cutting of basalt fibre reinforced polymer composites.
The aim of this study is to determine the optimal combination of process parameters during fibre laser cutting of 4 mm thick aluminium alloy using the modified PSI-TOPSIS method to jointly consider the kerf width, kerf taper angle, and surface roughness.

2. Experimental details

The laser cutting experiment was performed using BySmart Fiber 3015 laser cutting system with a nominal output power of 6 kW, Figure 1. Aluminium alloy, 4 mm thick, used as the workpiece material. Cutting speed and assist gas pressure were chosen as input parameters, and their corresponding levels are given in Table 1. Preliminary experiments were carried out to determine the range of input parameters to ensure that the sample was completely cut through without dross.

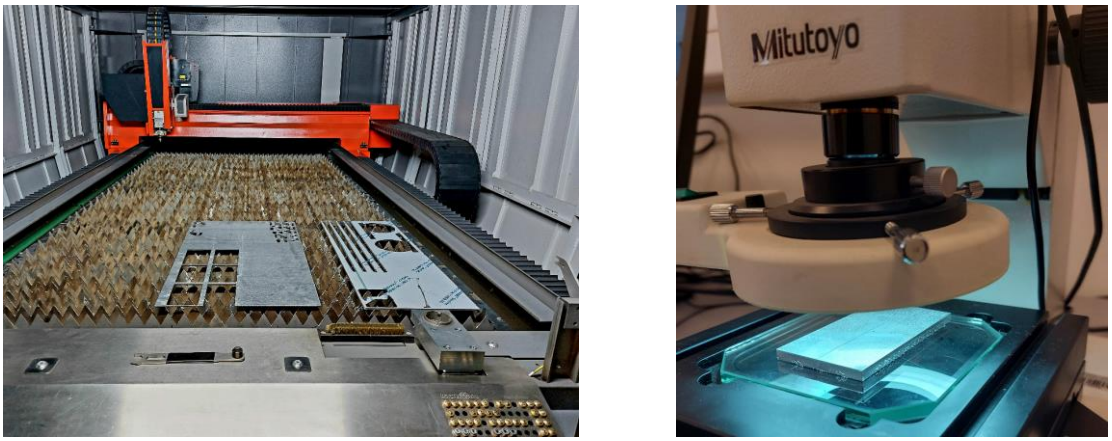


Figure 1. *Experimental laser cutting process (left) and measurement of kerf width (right)*

Table 1. *Laser cutting process parameters and their levels*

Parameter	Unit	Symbol	Level 1	Level 2	Level 3
Cutting Speed	mm/min	CS	11500	12000	12500
Assist Gas Pressure	bar	GP	6	6.5	7

The output responses considered in this study are kerf width, kerf taper angle, and surface roughness (Ra). A laser power of 6000 W, focal position of 2 mm and a nitrogen assist gas were selected to be constant throughout the experiment. Kerf widths are measured using a Mitutoya TM-505 optical microscope equipped by a camera DeltaPix, Figure 1. Five measurements were taken for the top and bottom kerf widths, and then the average value for both kerf widths were used to calculate the kerf taper angle value for each combination. The kerf taper angle was calculated using:

$$A = \tan^{-1}\left(\frac{K_b - K_t}{2t}\right) \quad (1)$$

where K_b is the bottom kref width, K_t is the top kerf width, and t is the sample thickness.

The mean surface roughness (Ra) was measured at five different places along the laser cut using a Mitutoyo SurfTest SJ-210 device, and then the average value was calculated. An optical profilometer Filmetrics Profilm3D was used to create the 3D surface cutting topography.
In this study, since there are two factors with three levels (cutting speed and assist gas pressure), the orthogonal array was selected as L9. Each combination of parameters and its experimental results are shown in Table 2.

Table 2. *Experimental design and results*

No.Exp.	Input parameters		Output responses		
	Cutting Speed (mm/min)	*Gas Pressure* (bar)	Kerf width (mm)	Kerf taper angle (^{o})	*Ra* (μm)
1	11500	6	0.374	0.28	3.13
2	11500	6.5	0.372	0.24	2.86
3	11500	7	0.371	0.27	3.09
4	12000	6	0.377	0.31	3.16
5	12000	6.5	0.371	0.34	3.20
6	12000	7	0.374	0.39	3.01
7	12500	6	0.440	0.81	3.03
8	12500	6.5	0.400	0.56	2.90
9	12500	7	0.414	0.58	2.95

3. Results and discussion

3.1. Effect of process parameters on quality characteristics

Figure 2 shows the effect of cutting speed and assist gas pressure on the kerf width. At lower cutting speeds (at a speed of 11500 mm/min) the assist gas pressure has no effect on the kerf width. As the cutting speed increases, the kerf width increases, especially at a low assist gas pressure of 6 bar and a cutting speed of 12500 mm/min. Also, it can be seen from Figure 3 that the kerf taper angle increases with the increase in cutting speed. The most unfavourable combination is the cutting speed of 12500 mm/min and the lowest assist gas pressure of 6 bar.

According to the results obtained by ANOVA analysis, Table 3, the most important process parameter for the kerf width is the cutting speed, with a percentage contribution of 82.62%. Also, the cutting speed was shown to be the most important process parameter for the kerf taper angle, with a percentage contribution of 85.33%. Based on the *p* value, the cutting speed is statistically significant for kerf width and kerf taper angle, while the assist gas pressure is statistically insignificant. However, cutting speed and assist gas pressure are not statistically significant for surface roughness.

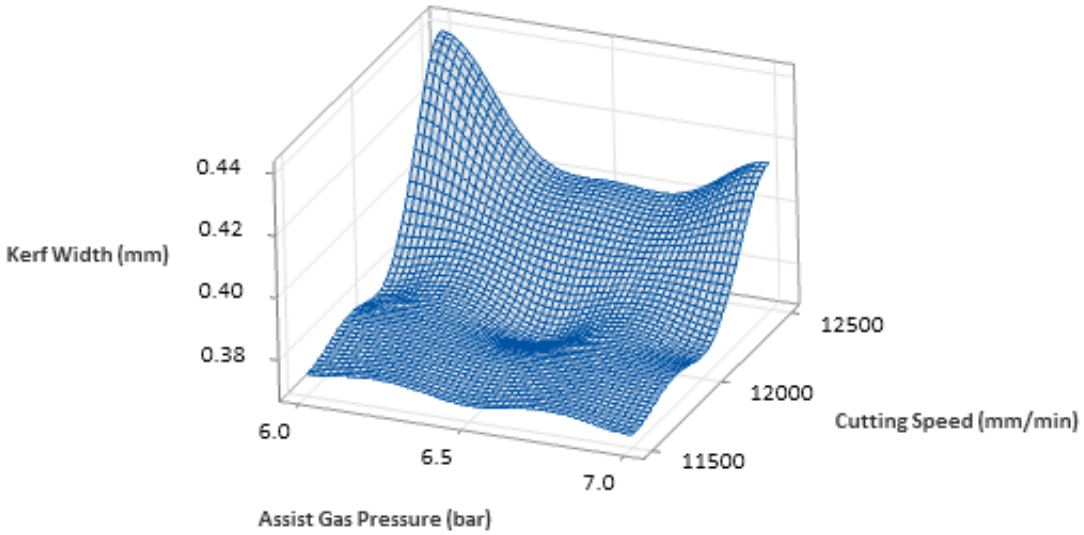


Figure 2. *Influence of process parameters on the kerf width*

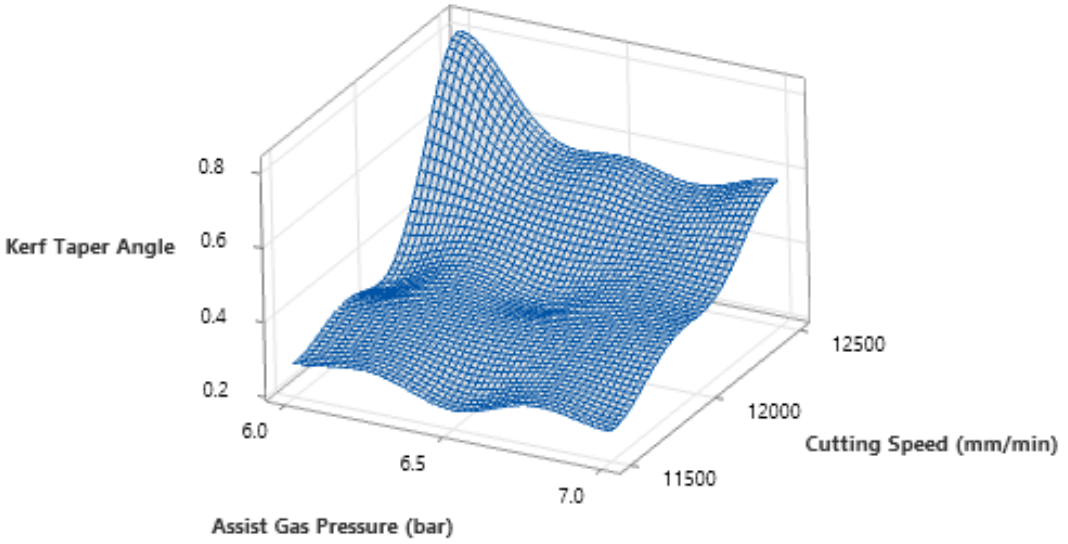


Figure 3. *Influence of process parameters on the kerf taper angle*

Table 3*. ANOVA results on kerf width, kerf taper angle and surface roughness*

Kerf width						
Source	DF	Adj SS	Adj MS	F-Value	P-Value	Contribution, %
CS	2	0.00402	0.00201	17.95	0.010	82.62
GP	2	0.0004	0.0002	1.78	0.281	8.18
Error	4	0.00045	0.00011			9.21
Kerf taper angle						
Source	DF	Adj SS	Adj MS	F-Value	P-Value	Contribution, %
CS	2	0.24847	0.12423	15.89	0.012	85.33
GP	2	0.01147	0.00573	0.73	0.535	3.94
Error	4	0.03127	0.00782			10.74

Surface roughness						
Source	DF	Adj SS	Adj MS	F-Value	P-Value	Contribution, %
CS	2	0.04047	0.02023	1.70	0.293	36.26
GP	2	0.0234	0.0117	0.98	0.450	20.97
Error	4	0.04773	0.01193			42.77

3.2. Optimization using modified PSI-TOSPSIS method

Optimization of process parameters in the fibre laser cutting of aluminium alloy was performed using the modified PSI-TOPSIS method described in detail in [14].

The normalized matrix for all three output responses was calculated as follows:

$$N_{ij} = \frac{D_{ij} - D_j^{\min}}{D_j^{\max} - D_j^{\min}} \tag{2}$$

where, D_{ij} is actual value of the *i*-th alternative for the *j*-th criterion. The weighted normalized matrix was calculated as follows:

$$W_{ij} = w_j \times N_{ij} \tag{3}$$

where, w_j is weight factor of the criterion.

Table 4 consists the values of the normalized matrix and the weighted normalized matrix.

Table 4. *N_{ij} matrix and W_{ij} matrix*

Exp.	N_{ij} matrix			W_{ij} matrix		
	Kerf width	Kerf taper angle	Ra	Kerf width	Kerf taper angle	Ra
1	0.0435	0.0702	0.7794	0.0059	0.0430	0.1956
2	0.0145	0.0000	0.0000	0.0020	0.0000	0.0000
3	0.0000	0.0526	0.6765	0.0000	0.0322	0.1698
4	0.0870	0.1228	0.8824	0.0119	0.0752	0.2214
5	0.0000	0.1754	1.0000	0.0000	0.1075	0.2510
6	0.0435	0.2632	0.4412	0.0059	0.1612	0.1107
7	1.0000	1.0000	0.5000	0.1363	0.6127	0.1255
8	0.4203	0.5614	0.1176	0.0573	0.3440	0.0295
9	0.6232	0.5965	0.2647	0.0850	0.3655	0.0664

The closeness coefficient for each criterion was calculated using:

$$C_i = \frac{\sqrt{\sum_{j=1}^{n}\left(W_{ij} - W_j^{-}\right)^2}}{\sqrt{\sum_{j=1}^{n}\left(W_{ij} - W_j^{+}\right)^2} + \sqrt{\sum_{j=1}^{n}\left(W_{ij} - W_j^{-}\right)^2}} \tag{4}$$

The positive ideal solution (W_j^+) and negative ideal solution (W_j^-) are calculated:

$$W_j^+ = \{(\max W_{ij} \text{ if } j \in LB), (\min W_{ij} \text{ if } j \in SB)\} \quad (5)$$

$$W_j^- = \{(\min W_{ij} \text{ if } j \in LB), (\max W_{ij} \text{ if } j \in SB)\} \quad (6)$$

where *LB* is affiliated to the larger is better and *SB* is affiliated to the smaller is better.
Table 5 contains the values of the closeness coefficient and the ranking order of the given alternatives. As shown in Table 5, alternative No. 2 is the best option, the value of the coefficient closeness is 0.9971. The kerf taper angle and surface roughness for alternative No. 2 are 0.24° and 2.86 μm, respectively, that is the smallest of any other sample, the kerf width is 0.372 mm. Alternative No. 7 is the last in ranking, with cutting speed of 12500 mm/min and assist gas pressure of 6 bar. From the main effects plot for mean C_i, as shown in Figure 4 and the response table, as shown in Table 6, the optimal process parameters are cutting speed at level 1 and assist gas pressure at level 2. So, the optimal combination of input parameters in laser cutting process of aluminium alloy regarding the considered outputs are 11500 mm/min cutting speed, and 6.5 bar assist gas pressure.

Table 5. *C_i and ranking*

No. Exp.	*Cutting Speed* (mm/min)	*Gas Pressure* (bar)	Closeness Coefficient	Rank
1	11500	6	0.7456	3
2	11500	6.5	0.9971	1
3	11500	7	0.7769	2
4	12000	6	0.7023	5
5	12000	6.5	0.6572	6
6	12000	7	0.7148	4
7	12500	6	0.1639	9
8	12500	6.5	0.5050	7
9	12500	7	0.4508	8

Table 6. *Optimal levels for input parameters*

Parameters	Levels			max. – min.	Rank	Optimal levels
	Level 1	Level 2	Level 3			
Cutting speed	0.8398	0.6914	0.3732	0.4666	1	Level 1 (11500 mm/min)
Assist gas pressure	0.5373	0.7198	0.6475	0.1825	2	Level 2 (6.5 bar)

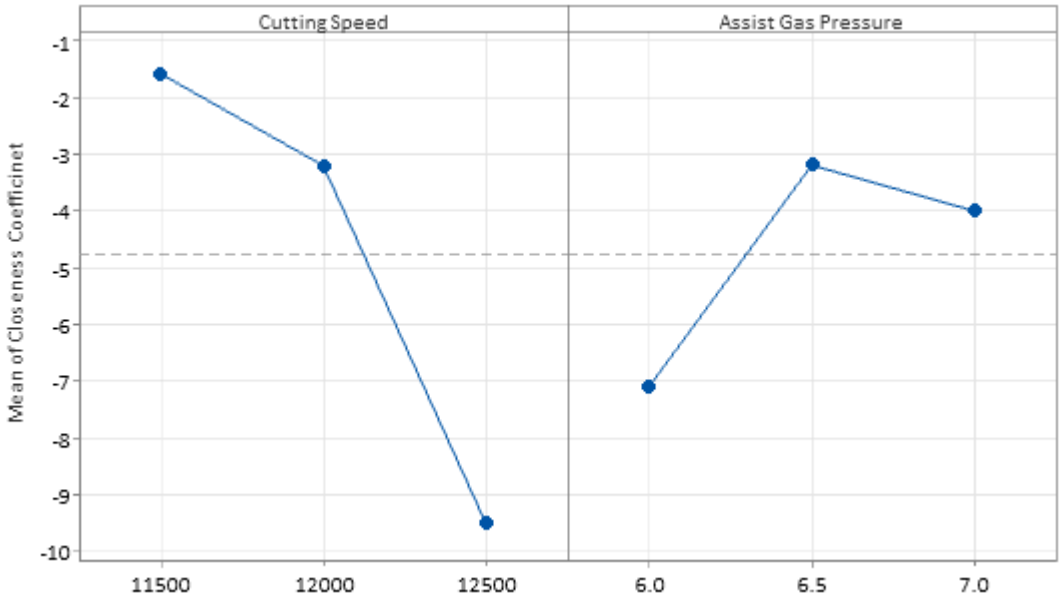


Figure 4. *Mean effects plot for mean Ci*

The 3D surface cutting topography of the first best (alternative No. 2) and last ranked (alternative No. 7) samples is shown in Figure 5 and Figure 6, respectively.

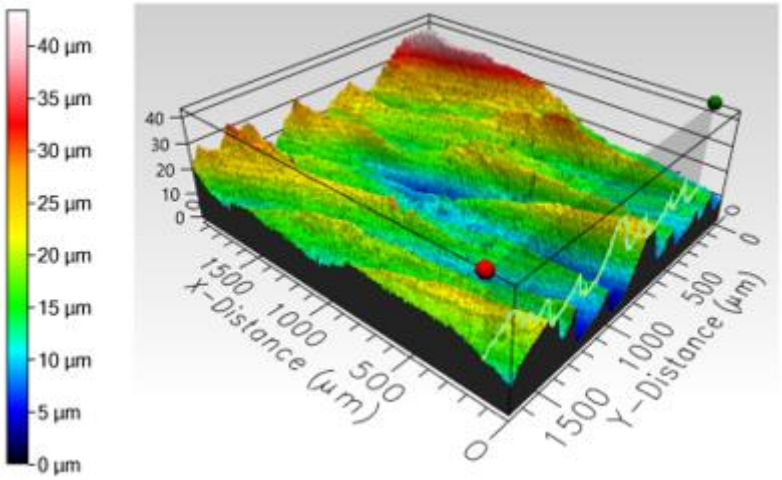


Figure 5. *The 3D surface cutting topography of first best sample*

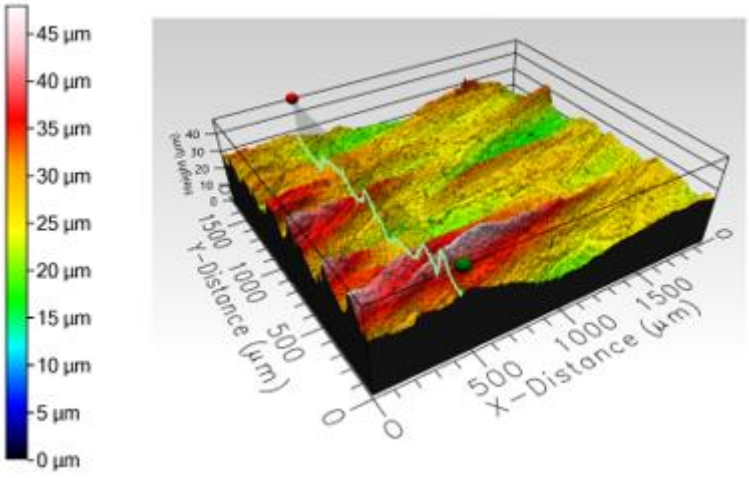


Figure 6. *The 3D surface cutting topography of last ranked sample*

4. Conclusion

In this study, the hybrid PSI-TOPSIS method was used to optimize the process parameters in fibre laser cutting. To achieve this, nine different combinations of input parameters such as cutting speed and assist gas pressure were used to cut 4 mm thick aluminium alloy. Kerf width, kerf taper angle and surface roughness were considered as indicators of the cut quality.

According to the multi-response optimization results, the optimal combination is a cutting speed of 11500 mm/min and an assist gas pressure of 6.5 bar. Based on the ANOVA analysis, it was found that the cutting speed has the most significant effect on the considered responses. Furthermore, the proposed method is computationally simple, understandable and can be applied to a different number of input and output responses.

Future research could include other process parameters, such as focus position, laser power, and material type, on the cut quality characteristics.

Acknowledgments

The authors acknowledge the financial support from the Slovenian Research Agency, Republic of Slovenia (research core funding No. P2-0157) and the Federal Ministry of Education and Science, Bosnia and Herzegovina (Projects: “Improving robot-human interaction during various robotic tasks” and “DigitalTrans-24/25”).

References

[1] Zhang, Y., Li, J., Yang, R., Liu, T., Yan, Y., 2019. Analysis of kerf quality on ultrafast laser cutting of anode material for lithium-ion battery. Optics and Lasers in Engineering 118, 14–21. https://doi.org/10.1016/j.optlaseng.2019.01.013

[2] Petousis, M., Ninikas, K., Vidakis, N., Mountakis, N., Kechagias, J.D., 2023. Multifunctional PLA/CNTs nanocomposites hybrid 3D printing integrating material extrusion and CO2 laser cutting. Journal of Manufacturing Processes 86, 237–252. https://doi.org/10.1016/j.jmapro.2022.12.060

[3] Yang, T., Li, K., Li, X., Li, J., Hu, C., Fan, X., Wang, R., Deng, A., 2025. Ultraviolet nanosecond laser-cutting mechanisms of flexible stainless steel-based Cu(In, Ga)Se2 solar cells. Solar Energy 296, 113603. https://doi.org/10.1016/j.solener.2025.113603

[4] Madić, M., Antucheviciene, J., Radovanović, M., Petković, D., 2017. Determination of laser cutting process conditions using the preference selection index method. Optics & Laser Technology 89, 214–220. https://doi.org/10.1016/j.optlastec.2016.10.005

[5] Turkkan, Y.A., Aslan, M., Tarkan, A., Aslan, Ö., Yuce, C., Yavuz, N., 2023. Multi-Objective Optimization of Fiber Laser Cutting of Stainless-Steel Plates Using Taguchi-Based Grey Relational Analysis. Metals 13, 132. https://doi.org/10.3390/met13010132

[6] Huang, S., Fu, Z., Liu, C., Li, J., 2023. Multi-objective optimization of fiber laser cutting quality characteristics of glass fiber reinforced plastic (GFRP) materials. Optics & Laser Technology 167, 109720. https://doi.org/10.1016/j.optlastec.2023.109720

[7] Joshi, P., Sharma, A., 2018. Simultaneous optimization of kerf taper and heat affected zone in Nd-YAG laser cutting of Al 6061-T6 sheet using hybrid approach of grey relational analysis and fuzzy logic. Precision Engineering 54, 302–313. https://doi.org/10.1016/j.precisioneng.2018.06.007

[8] Tura, A.D., Mamo, H.B., Desisa, D.G., 2021. Multi-objective optimization and analysis for laser beam cutting of stainless steel (SS304) using hybrid statistical tools GA-RSM. IOP Conf. Ser.: Mater. Sci. Eng. 1201, 012030. https://doi.org/10.1088/1757-899X/1201/1/012030

[9] Singh, S., Doddamani, M., Powar, S., 2023. Multi-objective optimization of machining parameter in laser drilling of glass microballoon/epoxy syntactic foams. Journal of Materials Research and Technology 23, 3869–3879. https://doi.org/10.1016/j.jmrt.2023.02.025

[10] Begic-Hajdarevic, D., Ćutuk, M., Kristijan, Š., Muhamedagic, K., Cohodar Husic, M., Ficko, M., 2024. Multi-response optimization of laser cutting parameters on mild steel using TOPSIS-entropy

weight method. 13th International Conference on Mechanical Technology and Structural Materials, MTSM 2024, Split

[11] Liu, Y., Yin, Y., Zhang, S., 2024. Multi-objective optimization of high-power fiber laser cutting process using data augmentation-based ANN-Adam model. Optical Fiber Technology 87, 103875. https://doi.org/10.1016/j.yofte.2024.103875

[12] Sket, K., Potocnik, D., Berus, L., Hernavs, J., Ficko, M., 2025. Optimizing laser cutting of stainless steel using latin hypercube sampling and neural networks. Optics & Laser Technology 182, 112220. https://doi.org/10.1016/j.optlastec.2024.112220

[13] Elsheikh, A.H., Ma, N., Essa, F.A., Khedr, M., Ibrahim, A.M.M., 2025. Kerf geometry prediction and optimization in laser cutting of basalt fiber reinforced polymer composites using decision tree and coati optimization algorithm. Results in Engineering 26, 105514. https://doi.org/10.1016/j.rineng.2025.105514

[14] Pasic, M., Marinkovic, D., Lukic, D., Begic-Hajdarevic, D., Zivkovic, A., Milosevic, M., Muhamedagic, K., 2024. Prediction and Optimization of Surface Roughness and Cutting Forces in Turning Process Using ANN, SHAP Analysis, and Hybrid MCDM Method. Applied Sciences 14, 11386. https://doi.org/10.3390/app142311386

Accessible entertainment and socialization opportunities for visually impaired people: technologies, challenges, and innovations

***Milena Biserova*[1], *Rosen Petrov*[1], *Nikolay Stoimenov*[1], *Mira Tzvetkova-Arsova*[2] *and Margarita Tomova*[2]**

1) Institute of Information and Communication Technologies at the Bulgarian Academy of Sciences, Sofia, Bulgaria

2) Dept. of Special Education, Faculty of Educational Studies and Arts, Sofia University "St. Kliment Ohridski" Sofia, Bulgaria

Corresponding author: nikistoimenow@gmail.com

Review article

Abstract: The aim of this article is to explore existing solutions and technologies that offer leisure opportunities for blind people, while also addressing the challenges that accompany this process, as well as the prospects for future innovations and opportunities to improve accessibility. The article aims to provide a clear overview of current solutions and to highlight the importance of developing new technologies and social approaches that can overcome barriers and create more enriched and accessible leisure opportunities for blind people. The barriers faced by the blind and visually impaired are examined, as are the challenges facing today's technologies and the opportunities for their implementation.

Keywords: *blind; visually impaired; social skills; leisure time; recreation; 3D printing; optimization*

1. Introduction

Leisure activities and the opportunity to participate in a variety of recreation activities are important aspects of the quality of life of every person, regardless of their physical or social limitations. For people with visual impairments, however, this freedom is often limited by various barriers, which can be both physical and social. Leisure time and recreation for these people not only represents a way of relaxation and entertainment, but also plays an important role in their social integration, personal development and strengthening of mental health. Recreation enhances people's emotional, physical and intellectual growth and development [1]. Recreation can be defined as "preferred pleasurable and enjoyable activity conducted during leisure time" [2, 3].

It is believed that socialization and social skills are probably the most strongly influenced by vision area of development [4, 5]. The lack of enough visual information or the full lack of it, negatively affects the social development since infancy [6]. Sacks and Page in 2017 [6] suggest the following three models to be taken into consideration when defining the term "social skills" – the trait model, based on the assumption of skillfullness in social behaviors, the component model, based on a number of observable learned behaviors, and the process model, based again on development of specific behaviors. As in all of these models vision plays critical role, it can be concluded, that social skills and socialization in general would not be as easy for visually impaired as for sighted children, students and adults. Research suggests that individuals with visual impairments—including both partial sight and total blindness, particularly those affected from an early age—often experience difficulties in directly perceiving social interactions. This limitation can result in reduced social engagement and challenges in maintaining relationships with family and the broader community. Such factors may negatively impact their personal development, potentially leading to social isolation and a decline in self-esteem [7].

According to the World Health Organization (WHO), at least 2.2 billion people have vision problems, of which 1 billion have vision impairments that can still be corrected. The WHO also states that 36%

of people with farsightedness have vision problems related to refractive errors, while 17% of people with vision problems due to cataracts have access to appropriate interventions [8].
One of the main factors that limit the leisure opportunities of people with sight loss is technology and resources, which are often not adapted to their needs. For example, in most cases, access to games or even ordinary objects in everyday life does not take into account the specific requirements of the users, making participation in these activities difficult or even impossible. Technologies that could help solve this problem are under development, but often face problems such as high costs, lack of accessibility or insufficient support from public and private initiatives.
Another important barrier is the social isolation that often accompanies these people. It is not only due to physical obstacles related to access to places and events, but also to a lack of understanding on the part of society about the needs and capabilities of people with disabilities. This makes it difficult for them to integrate into different social and cultural environments and limits their opportunities to benefit from the same forms of leisure that others have access to.
Despite these challenges, innovative solutions exist to overcome these barriers. For example, innovative technologies for adapting games and leisure activities, specialized audio applications, and other resources are beginning to make these experiences accessible to people with visual impairments. Training programs that focus on introducing new methods of providing opportunities, resources, or conditions that allow people with visual impairments to actively and fully engage in activities during their free time also play a crucial role in socialization and personal development.
Also, the approach to leisure activities for people with vision loss must include an awareness of the importance of this activity not only for their personal satisfaction, but also for the creation of a more equal community. Achieving this requires significant changes in both technology and public attitudes toward those with visual impairments.
The aim of the paper is to be reviewed the accessible entertainment and socialization spportunities for visually impaired people, the technologies, challenges, and innovations.

2. Entertainment, recreation and leisure opportunities for blind people

In time people with visual impairments have been having access to variety of classical recreation opportunies (either with or without using adaptations), such as:

- Sport – bicycling, gymnastics, running and walking, swimming and variety of water sports, skiing, bowling, fishing, goalball, dance, boccia etc.;
- Arts and crafts;
- Music, movies, reading and writing by using either Braille or large-print;
- Games – card games by using Braille or large-pring playing cards, board games such as chess, domino etc., computer games.

As technology advances, accessible forms of entertainment for individuals with blindness have gone through different stages. The solutions introduced start with basic adaptations and progress through innovations such as audio technologies, virtual platforms, and specialized games. Figure 1 illustrates these stages of development along a timeline that shows the main steps in the development of technology.
In spite of these significant advances, there are also various opportunities for meaningful leisure activities that combine enjoyment, personal development, and social integration. Even though the challenges that accompany the daily life of individuals with visual impairments, they have access to a range of activities that not only improve their quality of life but also facilitate their integration into society. Table 1 summarizes the main forms of entertainment for blind individuals, the relevant technologies that make them accessible, and examples that illustrate their application [9-20].



Figure 1. *Timeline illustrating the development of accessible forms of entertainment for people with visual impairments*

The board games leisure activities such as Checkers, Chess, Chinese checkers, Tic Tac Toe, Backgammon, Snakes & Ladders require specificity in their production for users with special needs. Creating single pieces, due to not so widespread demand, for production conditions is an extremely expensive process. The final price for consumers is unjustifiably expensive, which does not motivate to buy them. The use of today's technologies, in particular 3D printing, is a good alternative for creating single pieces and for lowering the prices. Before details are created, they need to be researched, starting with the software for creating the details (games), printing technology, method of creation and perception, including testing for tactile suitability [21-24]. Software solutions allow for preliminary research of products, especially when working with specialists in the field, where virtual models can be examined before 3D printing. Another possible optimization before printing process, can be implemented the regression modelling method [25, 26].
The use of online socialization is being worked extremely hard, with the EU having introduced strict rules and directives that regulate the online environment to be accessible to people with special needs and requirements [27, 28].

Table 1. *Main forms of entertainment and technologies for people with visual impairments*

Type of Leisure Activity	**Type of Technology/Service**	**Application/Advantages**	**Examples**
Music	Tactile musical instruments	Supports creative expression and develops musical skills	Tactile pianos, musical instruments with tactile feedback
Audiobooks	Audio technologies	Provides access to literature and encourages curiosity and learning	Audio versions of books, mobile apps for audiobooks, portable cameras for scanning texts such as Pearl®, and software such as speech synthesizers – JAWS, NVDA, Orca, SpeakUp etc.
Games	Board games adapted for the people with vision loss	Develops strategic thinking and socialization	Tactile chess and checkers, adapted video games

Virtual Platforms	Virtual reality (VR), mobile apps	Encourages socialization, participation in virtual events, education	VR games, social platforms like Second Life
Walking and Sports	GPS Technologies and apps	Supports independent navigation and mobility in outdoor environments	GPS apps with audio navigation for pedestrians, such as WeWalk cane, applications for phones: Lazarillo, Be My Eyes, Moovit, BlindSquare, DotWalker, the Bulgarian app Sofbus 24 etc.
Online Socialization	Specialized communication platforms	Helps build social connections and express emotions	Virtual meetings, chat platforms, and forums for people with sight loss

Many organizations supporting people with vision loss offer a range of accessible recreational resources. With appropriate adaptations and creativity, many activities can be made inclusive for individuals who are blind or have low vision. These may include reading books and magazines in accessible formats, playing adapted card or board games such as chess, engaging in cooking and crafts, exercising at home, gardening, listening to music, and enjoying radio, television, and Internet-based content [29].

3. Technological, social, and economic barriers for blind people in leisure time

Despite significant advances in technology and social initiatives that seek to provide access to various forms of entertainment and cultural experiences for blind people, there are still a number of challenges and limitations that hinder the full inclusion of these individuals in society. These obstacles include both technological, social and economic aspects.

Technological challenges:

One of the main challenges is the need to make technologies accessible to be used by blind people. Although screen readers and adaptive interfaces exist for various platforms, they are not always optimized or fully compatible with all applications or online services. This means that some popular social networks, games, and audio and video streaming platforms remain partially or completely inaccessible. For example, many applications and games do not offer an audio interface or tactile adaptations, which makes them difficult to use by blind users. Also, adapting existing products for the blind people, such as musical instruments or games, is accompanied by high costs that can be a barrier for many people. Specialized musical instruments, digital audio workstations (DAWs), music notation software, and other devices that are fully compatible with screen readers or offer tactile features are significantly more expensive than their traditional counterparts, which limits their access. As pointed out in some studies, screen readers are often not sufficient for the full use of digital audio workstations by blind musicians, necessitating the development of new solutions through haptic feedback and machine learning [30].

Social barriers:

Although advances in technology that facilitate communication and social contact, many blind people remain isolated due to the lack of sufficient opportunities for full social participation. Social integration remains a serious problem that cannot be fully overcome through virtual platforms and online clubs. Perceptions and stereotypes in society about people with visual impairments can also limit their activity and participation in cultural and social events. Even with progress in the integration of blind people into social life, public attitudes and the lack of a broader understanding of their needs continue to create barriers to their full inclusion.

Education and access to resources:
Another important obstacle is the need for adapted educational resources and specialized programs. Although there are music schools and training programs that offer opportunities for the blind people, not all of these programs are easily accessible or sufficiently adapted to their specific needs. For example, the lack of availability of Braille sheet music or tactile versions of texts and books can limit the ability of the users to actively participate in educational and recreational activities related to music, art, or literature. (Figure 2).

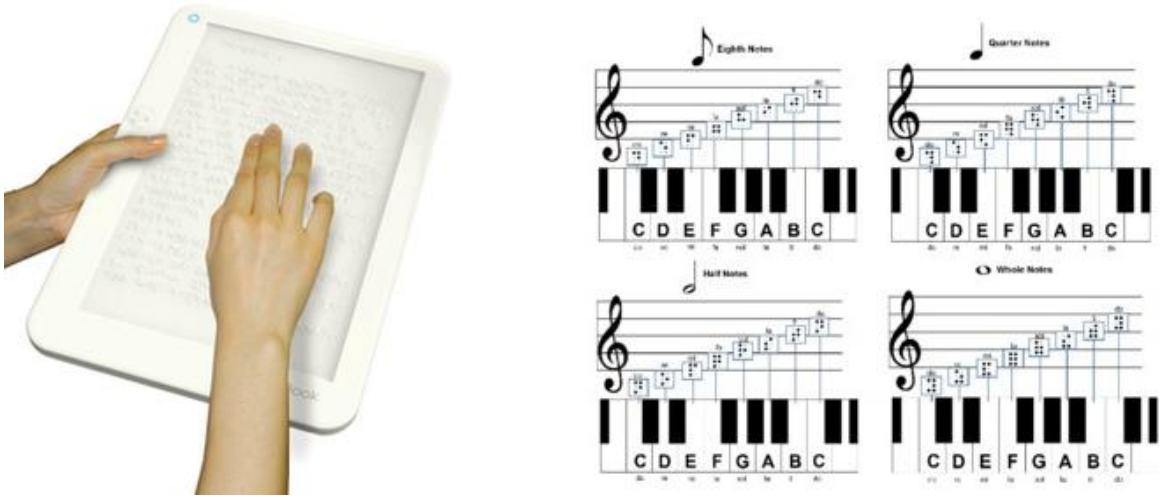


Figure 2. *Timeline illustrating the development of accessible forms of entertainment for people with visual impairments*

There is also a lack of professionally trained teachers to work with blind students in specialized areas such as music or computer science. Studies show that one of the main reasons for low literacy among people with visual impairments is the lack of trained Braille teachers and a shortage of adapted educational resources, especially in STEM education [31]. In a handbook [32], and in many more of this kind, direct teaching instructions and variety of adaptations are provided to be used for visually impaired pupils in different school subjects, incl. art and design, music, physical education etc., which can be seen also as a basis for leisure time activities and recreation options.

Economic constraints:
Economic barriers also play a role in limiting the leisure opportunities of blind people. Specialized devices and applications that can provide access to music, games, books, and other forms of entertainment are often expensive, making these technologies inaccessible to many blind people. While there are free alternatives, they often do not offer the same quality or variety of features found in paid versions. However, in times of high economic competition, many new technological solutions are developed and their prices are becoming more and more affordable – e.g. Orcam, Orbit player etc. which costs are dropping in time. In addition, as mentioned before, organizations supporting people with vision loss often offer accessible recreational resources.

Lack of standardization and compatibility:
Another problem is the lack of unified accessibility standards across many platforms and applications. Sometimes, different technologies are not compatible with each other, which creates additional difficulties in using devices and software. For example, some musical instruments and composition applications may not support the same audio or haptic technologies that are available in others, limiting the opportunities for blind musicians to take advantage of the full range of capabilities.

Regulations and policies:
Blind people also face inadequate support from the government and private institutions that can provide financial and institutional aid. Legislative initiatives to ensure the accessibility of products and services are lacking, and those that do exist are often not effectively implemented. This means that many technological solutions and social platforms, although available, are not adequately tailored to the specific needs of people with visual impairments or are not offered at affordable prices. Global data shows that over 2.2 billion people live with visual impairment, with a significant proportion of cases being preventable or untreated due to a lack of integrated eye care services and ineffective implementation of accessibility policies [33].
While there have been significant achievements in providing entertainment and socialization opportunities for blind people, challenges remain in improving accessibility, removing social and economic barriers, and building greater public understanding of the needs and potential of people with disabilities. Investments in innovation, compatibility between technologies, and the effective implementation of rights-oriented laws are key to improving the lives of blind people and achieving equality in their opportunities to participate in cultural and social activities.

4. Conclusion

In conclusion, providing accessible leisure opportunities for visually impaired people requires a combination of innovative technologies and inclusive social strategies. Technology and social initiatives play a key role in overcoming the barriers that blind people face in their free time and recreation. Music, audiobooks, walks, board and digital games, virtual social platforms and many more provide opportunities for entertainment and socialization and contribute to their personal and emotional development.
The availability of adapted resources—such as tactile musical instruments, audio interfaces, specialized applications, and online platforms and many others—significantly enhances the independence and inclusion of people with visual impairments in cultural and social life. However, serious challenges remain that require continuous improvement of technological solutions and the development of social approaches tailored to the needs of this community.
Educational programs, accessible services, and technological innovations will continue to be essential to ensuring equal access to all forms of cultural participation and entertainment. In the future, it is important to encourage the creation of solutions that support the social integration and personal growth of blind people.
True equality requires not only accessible technologies but also building a supportive environment through educational policies, public awareness, and inclusive initiatives. Only by combining innovation and societal commitment can we ensure the full participation of people with visual impairments and build a world in which everyone lives freely, without barriers and limitations. The 3D printing process may be a possible solution for overcoming some barriers and for offering new opportunities.

Acknowledgments

The research was carried out as part of the project No KP-06-H85/11 "Exploring 3D technologies to support the learning process and lives of the visually impaired", financed by the Bulgarian National Science Fund.

References

[1] Ross, D.B., Lotters, C.R., Glenn, B. 1998. An adaptive physical education program teaching golf to students with visual impairments, JVIB, 92, 684-686

[2] Lieberman, L.J., Ponchillia, P.E., Ponchillia, S.V. 2013. Physical Education and Sports for People with Visual Impairments and deafblindness: Foundations of Instruction, New York: AFB Press.

[3] McGregor, D., Farrenkopf, C. 2017. Recreation and Leisure. In: M. C. Hoolbrook, C. Kamei-Hannan, T. McCarthy (eds.). Foundations of Education, 3rd ed., Volume II: Instructional Strategies for Teaching Children and Uouths with Visual Impairments, New York: AFB Press, pps. 804-830

[4] Warren, D.H. 2000. Developmental Perspectives: Youth. In: B. Silverstone, M.A. Lamg, B.P. Rosenthal, E. L. Fste (eds.). The Lighthouse Handbook on Visual Impairment and Vision Rehabilitation, Volume 1, New York: Oxford University Press, pps. 325-338.

[5] Sacks, S. Z., Silberman, R. K. 2000. Social skills. In: A.J. |Koenig & M. C. Hoolbrook (eds.). Foundations of Education, 2nd ed., Volume II: Instructional Strategies for Teaching Children and Youths with Visual Impairments, New York: AFB Press, pps. 615-652.

[6] Sacks, S. Z., Page, B. 2017. Social skills. In: M. C. Hoolbrook, C. Kamei-Hannan, T. McCarthy (eds.). Foundations of Education, 3rd ed., Volume II: Instructional Strategies for Teaching Children and Youths with Visual Impairments, New York: AFB Press, pps. 753-803.

[7] Zoomax, Last accessed June 2025 https://www.zoomax.com/low-vision-information/the-benefits-of-socialization-for-visual-impairments/

[8] Manirajee, L., Hanis Shariff, S. Q., & Mohd Rashid, S. M. 2024. Assistive technology for visually impaired individuals: A systematic literature review (SLR). International Journal of Academic Research in Business and Social Sciences, 14(2), 20827. https://doi.org/10.6007/IJARBSS/v14-i2/20827

[9] Wang, Y., Zhang, Y., Zhang, J., & Li, Z. 2023. Inclusive harmonies: Co-creating accessible music experiences with deaf or blind advisors through interdisciplinary design workshop. IASDR 2023. https://doi.org/10.21606/iasdr.2023.264

[10] Dang, K., Korreshi, H., Iqbal, Y., & Lee, S. 2023. Opportunities for Accessible Virtual Reality Design for Immersive Musical Performances for Blind and Low-Vision People. SUI '23, October 13–15, 2023, Sydney, NSW, Australia. ACM. https://doi.org/10.1145/3607822.3614540

[11] Likhar, T., Khan, A., Parihar, B. S., Rakesh, N., Gulhane, M., & Agrawal, P. 2024. Integration of Computer Vision for Book Detection and Text-to-Speech Conversion Using API for Blind People. ICISCT '24, November 7–8, 2024, Seoul, Korea. IEEE. https://doi.org/10.1109/ICISCT64202.2024.10956795

[12] Shah Ahmad Shahrizal, A. Z., Rahmatullah, B., Ab Majid, M. H., Samuri, S. M., Hidayanto, A. N., Yas, Q. M., & Purnama, S. 2022. A systematic literature review on the use of podcasts in education among university students. AJTLHE, 14(1), 222-236. https://doi.org/10.17576/ajtlhe.1401.2022.10

[13] Chava, T., Srinivas, A. T., Sai, A. L., & Rachapudi, V. 2021. IoT based Smart Shoe for the Blind. ICICT '21, January 20–22, 2021, Coimbatore, India. IEEE. https://doi.org/10.1109/ICICT50816.2021.9358759

[14] Beingolea Garay, J. R., Zea-Vargas, M. A., Huallpa Muñoz, R., & Vilca, X. (2021). Assistive devices: Technology development for the visually impaired. Designs, 5(4), 75. https://doi.org/10.3390/designs5040075

[15] Bolesnikov, A., Kang, J., & Girouard, A. 2022. Understanding Tabletop Games Accessibility: Exploring Board and Card Gaming Experiences of People who are Blind and Low Vision. TEI '22, February 13, 2022. ACM. https://doi.org/10.1145/3490149.3501327

[16] Karim, S., Kang, J., & Girouard, A. 2023. Exploring Rulebook Accessibility and Companionship in Board Games via Voice-based Conversational Agent Alexa. DIS '23, July 10, 2023. ACM. https://doi.org/10.1145/3563657.3595970

[17] Gonçalves, D., Piçarra, M., Pais, P., Guerreiro, J., & Rodrigues, A. 2023. "My Zelda Cane": Strategies Used by Blind Players to Play Visual-Centric Digital Games. CHI '23, April 19, 2023. ACM. https://doi.org/10.1145/3544548.3580702

[18] Nair, V., Karp, J. L., Silverman, S., Kalra, M., Lehv, H., Jamil, F., & Smith, B. A. 2021. NavStick: Making Video Games Blind-Accessible via the Ability to Look Around. UIST '21, October 12, 2021. ACM. https://doi.org/10.1145/3472749.3474768

[19] Kim, K. M., & Lee, C. E. 2022. Digital Inclusion and Social Networks Among Adults with Disabilities in South Korea, Vulnerable People and Digital Inclusion (pp. 277–299)

[20] Singh, R. K., Sharma, H. D., Mitra, M., & Saraswat, B. K. 2024. Speech Oriented Multipurpose App for Visually Impaired People. ICICC '24: International Conference on Innovative Computing & Communication, August 23, 2024

[21] Piedra-Cascón, W., Krishnamurthy, V.R., Att, W. & Revilla-León, M. 2021. 3D printing parameters, supporting structures, slicing, and post-processing procedures of vat-polymerization additive manufacturing technologies: A narrative review. Journal of Dentistry, 109, pp. 103630. ISSN 0300-5712. DOI: 10.1016/j.jdent.2021.103630. [viewed 13 March 2025]. Available from: https://www.sciencedirect.com/science/article/pii/S0300571221000518.

[22] The Role of 3D Printing in Reducing Manufacturing Costs and Waste. [viewed 24 June 2025]. Available from: https://tavtechsolutions.com/resources/whitepapers/the-role-of-3d-printing-in-reducing-manufacturing-costs-and-waste/.

[23] Mitev V., Malakov I. 2024. Analysis of the quality of polymer parts for automatic assembly. AIP Conf. Proc. 21 February 3063 (1): 060012. https://doi.org/10.1063/5.0195873

[24] Dinev G., Malakov I., Dotsev D., CAD optimal design, documentation and automated assembly of mechanical product, Journal of Advanced Materials Research, Volume 463-464, Pages 1202 - 12052012 2012 2nd International Conference on Advanced Material Research, ICAMR 20127

[25] Svezhenov Y., Dimitrov L., Nikov A., 2025. Hybrid user experience design of virtual products based on swarm intelligence optimization. AIP Conf. Proc. 31 March 3182 (1): 070003. https://doi.org/10.1063/5.0246884

[26] Radoslavov A., Dimitrov L., Nikov A., 2025. Partial least squares regression modelling in user experience design of cheese packages. AIP Conf. Proc. 31 March 3182 (1): 070004. https://doi.org/10.1063/5.0246136

[27] Alexieva J., Tomov P., 2022. "The Role of Digital Content Accessibility in Decision Making," 2022 V International Conference on High Technology for Sustainable Development (HiTech), Sofia, Bulgaria, pp. 1-4, doi: 10.1109/HiTech56937.2022.10145540.

[28] Alexieva J., Tomov P., 2021. "Improving the Work Process for Checking Websites and Mobile Applications," 2021 IV International Conference on High Technology for Sustainable Development (HiTech), Sofia, Bulgaria, pp. 01-04, doi: 10.1109/HiTech53072.2021.9614217.

[29] Karpodini, C. 2023. Evaluating Haptic Technology in Accessibility of Digital Audio Workstations for Visually Impaired Creatives. ACM SIGACCESS Accessibility and Computing, Issue 135, Article No. 6, p. 1. https://doi.org/10.1145/3584732.3584738

[30] Vision loss - recreational activities Last accessed June 2025, https://www.betterhealth.vic.gov.au/health/conditionsandtreatments/vision-loss-recreational-activities#gardening

[31] Singh, P., Kapoor, I., & Goyal, A. 2023. Educational Software System For Teaching STEM To Visually Impaired People. Journal of Physics: Conference Series, **2570**(1), 012030. https://doi.org/10.1088/1742-6596/2570/1/012030

[32] Salisbury, R. (ed.) 2008. Teaching Pupils with Visual Impairments: A Guide to making school curriculum accessible, Routledge.

[33] World Health Organization. (2019). World report on vision. World Health Organization. https://www.who.int/publications-detail/world-report-on-vision

Accuracy and efficiency optimization-mass scaling effects in ECAP process simulations

***Igor Ciganović*[1], *Zdenka Keran*[1], *Petar Piljek*[1], *Andrej Razumić*[2] *and Davor Jurić*[1]**

1) University of Zagreb Faculty of Mechanical Engineering and Naval Architecture, Department of Technology, Ivana Lučića 5, 10000 Zagreb

2) Dr. Franjo Tuđman Defense and Security University, Department of Polytechnics, Ilica 256b, 10000 Zagreb, Croatia

Corresponding author: igor.ciganovic@fsb.unizg.hr

Original scientific article

Abstract: This paper investigates the optimization of Equal Channel Angular Pressing (ECAP) process simulations within Abaqus, focusing on computational efficiency. The approach involves systematic simplification of workpiece and tool geometries, combined with the application of varying mass scaling factors to accelerate explicit dynamic analyses. The influence of mass scaling on force-time responses is rigorously evaluated and visualized, while the induced numerical errors are assessed through detailed statistical analysis. The findings provide a framework for balancing simulation accuracy and computational cost in ECAP modeling.

Keywords: *ECAP; simulation; mass scaling; dynamic analysis*

1. Introduction

Metallic materials featuring fine-grained or ultrafine-grained (UFG) microstructures constitute a distinct class of engineering materials, recognized for their enhanced mechanical performance, particularly increased strength, improved toughness, and often superior resistance to fatigue and fracture. These properties stem from their specific microstructural features, primarily the reduced average grain size.([1], [2])

A key theoretical framework underpinning the relationship between microstructure and mechanical behavior is the Hall–Petch equation, which establishes that the yield strength of a material increases with decreasing grain size, expressed as [3]:

$$\sigma_y = \sigma_0 + \frac{k_y}{\sqrt{d}} \tag{1}$$

where is:

σ_y yield stress, d average grain size, σ_0 i d material-specific constants.

Among the most effective approaches to achieving UFG microstructures is the group of techniques known as Severe Plastic Deformation (SPD). These processes allow for the introduction of extremely large plastic strains while maintaining the external geometry of the specimen, an essential characteristic for industrial applicability. Within this group, Equal Channel Angular Pressing (ECAP) shown in Figure 1, is particularly prominent. ECAP involves pressing a metallic billet through a die composed of two channels with identical cross-sections that intersect at a prescribed angle, commonly 90° or 120°. As the material flows through the channel intersection, it undergoes intense shear deformation, resulting in plastic flow and progressive grain refinement. This process can be repeated

multiple times to accumulate strain and achieve a more homogeneous microstructure.([4], [5], [6], [7])

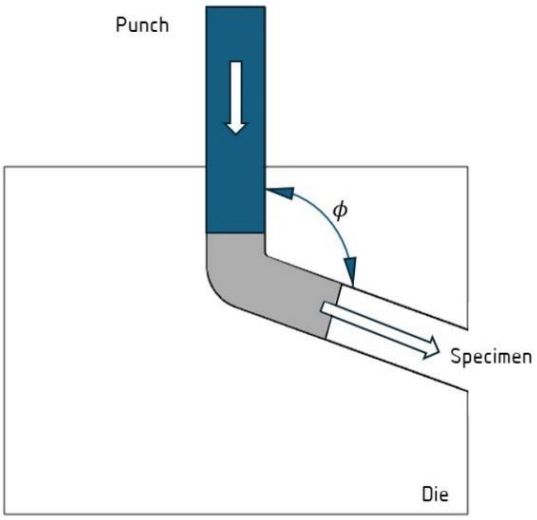


Figure 1. *ECAP parts*

Due to the complexity of deformation flow, frictional effects, contact interactions, and the nonlinear behavior of materials, ECAP poses significant challenges for experimental investigation. Consequently, computational simulations, particularly those based on the Finite Element Method (FEM) have become an indispensable tool for analyzing and optimizing this process. Abaqus, as one of the leading FEM software platforms, is frequently employed for ECAP simulations. Numerical modeling enables detailed analysis of plastic strain distribution, prediction of stress development, and evaluation of the influence of die geometry, friction, and pressing speed. Such simulations provide valuable insights into phenomena that are difficult to observe experimentally and contribute to reducing the need for time-consuming and costly physical testing ([1], [8], [9], [10], [11], [12]).

A review of the existing literature reveals that the optimization of ECAP simulation procedures has not been extensively addressed. Publications that discuss computational simulations related to the ECAP process generally lack detailed descriptions regarding the setup of the simulations, and they do not adequately explore issues related to the typically long computation times or potential methods for their reduction

The optimization is important for several reasons:

- Shorter simulation times enable faster iteration and process optimization, allowing a greater number of variants to be tested in a shorter period, which increases the overall efficiency of product development.
- Reducing simulation time directly contributes to lower costs, as fewer computational resources are required, and engineers can make decisions more quickly and allocate resources to other tasks.

The objective of this study is to reduce the simulation time while maintaining the simulation results within minimal deviation limits, in order to achieve simulation process optimization. ([12],[13])

2. Numerical Simulation Procedure – Method

A numerical simulation of the Equal Channel Angular Pressing (ECAP) process was performed using the explicit analysis method in Abaqus 2023. The simulation was run on an Acer Nitro 5 laptop equipped with an Intel Core i5/i7 processor, an RTX 3060/4050/4060 GPU, 16 GB of RAM, and 1 TB of SSD storage.

2.1. Rigid components

To reduce computational complexity while preserving the accuracy of the contact interaction, only the internal channel of the die was modeled, as it represents the functional surface relevant to the deformation process. The channel, inclined at an angle of 110°, was treated as a rigid body using shell geometry and discretized with R3D4 elements (four-node rigid shell elements) shown in Figure 2, which do not contain integration points or field output, which significantly reduces computational time. In this study, a die angle of 110° was selected, although the choice of angle is arbitrary. Since the primary objective is to optimize the process in reducing computational time, the same methodology would apply to any chosen angle.

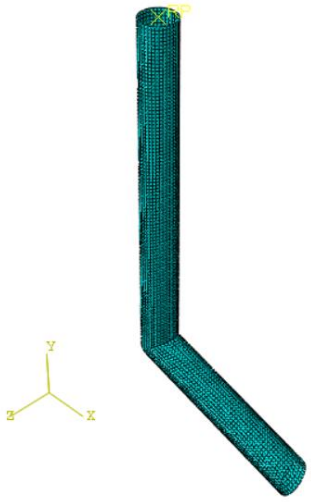


Figure 2. *Die channel after discretisation*

Similarly, the punch was also modeled as a rigid body, as its deformation is negligible compared to that of the workpiece. It was defined using the shell geometry as shown in Figure 3 and element type (R3D4), ensuring consistency in the definition of tool components.

For both the die and the punch, a reference point (RP) was assigned. In Abaqus, assigning a reference point to a rigid body is essential because it serves as the control node through which boundary conditions, prescribed motions (e.g., displacement or velocity), and reaction forces/moments are applied or extracted. The RP effectively governs the motion of the entire rigid body, which behaves as a single undeformable unit.[12]

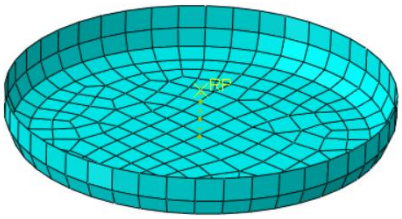


Figure 3. *Punch after discretisation*

2.2. Deformable component

The workpiece was modeled as a deformable cylindrical body, as shown in Figure 4, with dimensions of Ø10 mm × 80 mm and assigned the elastic properties corresponding to aluminum Al99.5. The material’s plastic behavior was characterized using a true stress–strain curve, the values of which are provided in Table 1. Finite element discretization was performed using C3D8R elements, which are

eight-node linear brick elements with reduced integration, offering an efficient balance between computational cost and accuracy for large deformation problems.



Figure 4. *Workpiece after discretization*

Table 1. *Plastic Flow Curve for Al99.5* [14]

Plastic Flow Stress, σ [MPa]	Logarithmic Strain, ε
55.16	0.00
103.43	0.20
124.11	0.40
137.90	0.60
151.69	0.80
179.27	1.00
193.06	1.20
206.85	1.40
234.43	1.60
262.01	1.80
275.80	2.00

2.3. Boundary conditions

Since the die remains stationary during the Equal Channel Angular Pressing (ECAP) process, an encastre boundary condition was applied to the reference point assigned to the channel geometry. This condition fully constrains all translational and rotational degrees of freedom, ensuring that the die does not move or rotate throughout the simulation. For the punch, all degrees of freedom at the reference point were constrained except in the Y-direction, which corresponds to the longitudinal axis of the channel. A prescribed displacement was applied in this direction to simulate the punch movement during the forming process.

2.4. Interaction

In the ECAP process, two primary contact interactions were defined: between the workpiece and the die, and between the punch and the workpiece. In both cases, a surface-to-surface contact formulation was employed, with the rigid components (die and punch) assigned as master surfaces and the deformable workpiece as the slave surface.

Contact behavior was defined using the penalty contact method, which provides a computationally efficient means of enforcing contact constraints by allowing small penetrations between surfaces. This approach is particularly well-suited for highly nonlinear problems involving large deformations, as it

offers improved numerical stability and significantly reduces simulation time compared to more strict contact enforcement methods, such as those based on Lagrange multipliers.[9]
Additionally, frictional behavior within the channel was modeled using a Coulomb friction coefficient of 0.1, representing realistic interface conditions between the workpiece and the die during severe plastic deformation.

2.5. Simulation Time and Output Data

In the Step module, the simulation time was set to 45 seconds, matching the actual duration of a single ECAP pass. This helped to capture the realistic time-dependent behavior of the process. Within the same module, output settings were configured to enable detailed post-processing. A field output was defined to include key result variables such as stress, strain, and equivalent plastic strain (PEEQ). In addition, a history output was specified to record the reaction force at the reference point of the punch, allowing the evaluation of forming loads over time during the simulation.

3. Results and discussion

The numerical simulation was conducted under 11 defined conditions. The initial condition was executed without mass scaling, while the remaining 10 conditions employed varying scale factors. The objective was to monitor the reduction in simulation time and evaluate the output results, specifically focusing on the force–time diagram corresponding to each simulation case. Particular attention was given to assessing the extent to which the use of mass scaling factors influenced computational efficiency, while potentially compromising the accuracy of the results and the physical fidelity of the observed behavior.
Figure 5 illustrates the variation of the force on the punch over time without using a mass scaling factor. According to the literature, the shape of the graph is similar [4], indicating that the simulation captures the expected physical behavior, thereby confirming the physical validity of the simulation. This curve will be referred to as the reference curve throughout the remainder of this study.

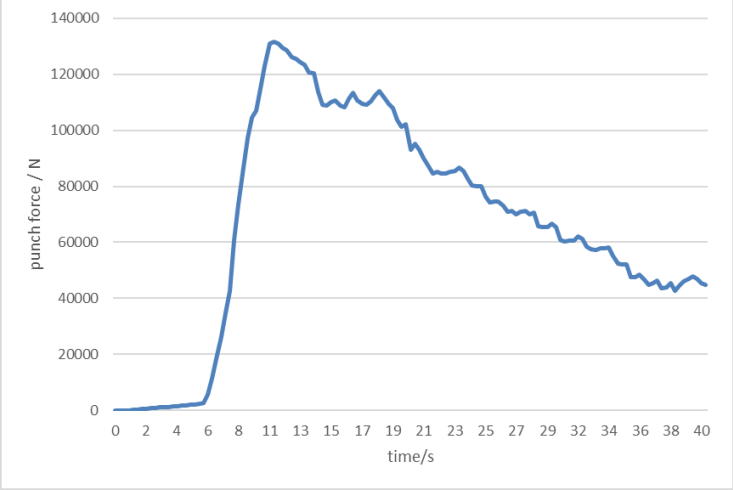


Figure 5. *Force-time graph without mass scaling factor*

After each simulation run, the total computation time was recorded. The application of mass scaling factors led to a progressive reduction in simulation time, as presented in Table 2. The scaling was limited to a factor of 100 000, beyond which the results deviated significantly from expected physical behavior, thus compromising the validity of the simulation.

Table 2. *Mass scaling impact on simulation time*

Mass scale factor	Simulation time [min]
No scale factor	4800
150	560
300	480
500	314
1000	348
5000	247
10000	131
25000	94
50000	65
75000	55
100000	26

Figure 6 illustrates the time-dependent punch force obtained from simulations performed with various mass scaling factors, including one simulation without mass scaling (denoted as "0"). The results show that the general shape of the force–time curve remains consistent across different scaling values, with a rapid increase in force up to approximately the 8th second, followed by a progressive decline. However, noticeable deviations in the peak force are observed in the case of a mass scaling factor of 150, while further discrepancies in the force decay phase become evident with a mass scaling factor of 300. The simulation without mass scaling serves as the reference case, providing a basis for evaluating the influence of different mass scaling factors on the simulation results.

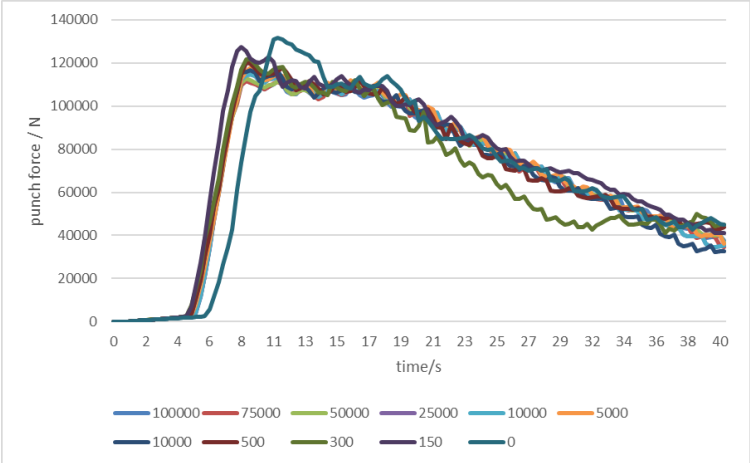


Figure 6. *Punch force over time for simulations conducted with and without mass scaling*

In order to provide a simpler representation of the relation between the scaled curves and the reference curve, a diagram (Figure 7.) was created, in which the scaled values are shown through their arithmetic mean. The red curve represents the averaged force values over time for all 10 mass scaling factor cases. Alongside it, the reference curve is shown to provide a clearer comparison. From Figure 7, it can be observed that the use of mass scaling factors does not significantly distort the physical behavior of the system, and the resulting deviations from the reference are minor.

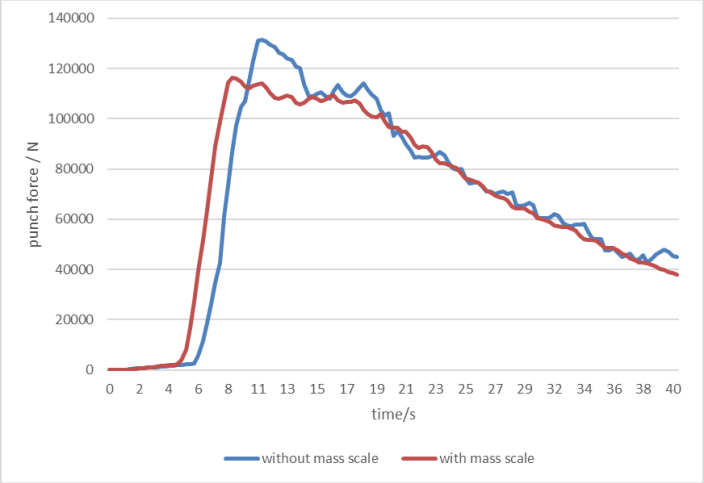


Figure 7. *Comparison of the results without mass scale and the arithmetic mean of scaled results*

4. Statistical analysis of the results of a numerical simulation

To assess whether variations in the scaling factor have a significant impact on the simulation results, an analysis of variance (ANOVA) was conducted. The resulting p-value of 0.953 indicates that there is no significant difference between the outputs of the simulations. Consequently, it can be concluded that the scaling factor does not significantly affect the physical behavior of the simulated process.

To determine whether there is a statistically significant difference in the percentage deviations from the nominal value at specific time points, an analysis of variance (ANOVA) was conducted. The resulting p-value of 0.000 indicates a statistically significant variation across different time points in the simulation. In other words, there exists a period within the simulation during which the deviations are significantly greater than in other intervals.

Figure 8 illustrates the percentage differences from the nominal simulation, accompanied by the corresponding 95% confidence intervals. It is evident from the figure that the most pronounced deviations occur between the 4th and 9th seconds. Between the 15th and 35th second, the difference between simulations with mass scaling and the simulation without mass scaling remains within 10% of the nominal value.

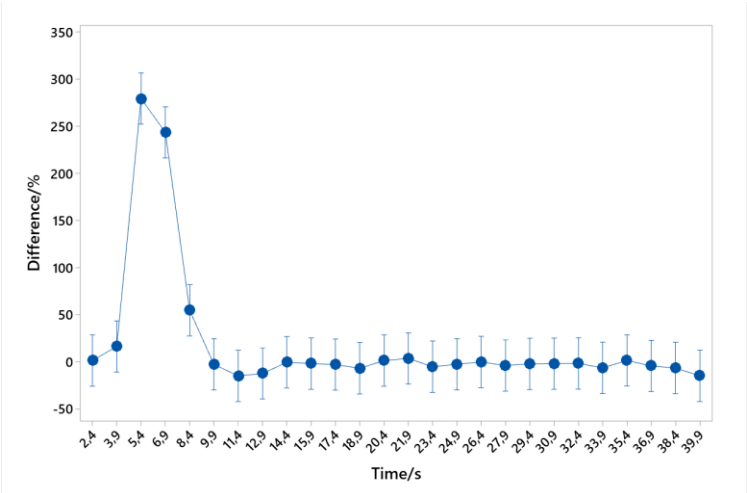


Figure 8*. Percentage deviations from the unscaled simulation with corresponding 95% confidence intervals across the simulation time*

5. Conclusion and recommendation for future work

Computational simulations can often be extremely time-consuming, sometimes requiring several hours, days, or even weeks for completion, especially in complex models. While upgrading to high-performance computing systems is one solution, it is often financially and logistically impractical. Alternative approaches within the simulation software itself may be employed to reduce computation time. One common method is increasing the mesh size, although this can compromise result accuracy and may not always yield significant time savings. Another effective strategy is the application of mass scaling.

In Abaqus, mass scaling is used in explicit analyses to artificially increase the mass of selected elements, thereby raising the critical time increment and accelerating the simulation. This is particularly useful when very small elements constrain the time step, drastically extending the simulation duration. When applied carefully, mass scaling significantly reduces run time with minimal impact on physical accuracy. The results of this study indicate that mass scaling led to a substantial reduction in simulation time, with only a minor and acceptable decrease in the accuracy of the physical output.

To further enhance the efficiency and accuracy of ECAP process simulations, future work should explore the use of alternative finite element software packages that offer different solver architectures, such as implicit solvers or hybrid explicit–implicit approaches. These may provide better stability and computational performance depending on the specific characteristics of the problem. In addition, the application of alternative element formulations, such as higher-order elements or reduced-integration elements, could improve the balance between accuracy and computational cost. Exploring the effects of time scaling techniques, especially in quasi-static simulations, may offer additional opportunities for reducing total run time, provided the physical validity of the results is preserved. Furthermore, future studies should leverage parallel computing capabilities by utilizing multi-core processors or high-performance computing (HPC) environments, which can significantly accelerate simulation time, particularly in large-scale or multi-pass ECAP models. Comparative studies between different solvers, mesh strategies, and hardware configurations would be beneficial in establishing optimal simulation workflows tailored to severe plastic deformation processes.

References

[1] Patil, B.V., 2016. 3D finite element simulation of equal channel angular pressing with different material models. J Emerg Technol Innov Res. Mar;3(3): JETIR1603005. Available from: https://www.jetir.org

[2] Mohammed, R.H., Shahab, AF, Rezaei, 2023. A. Effect of ECAP process on mechanical properties and microstructure of AA-6061 recycled chips. Eng Technol J. 41(7):924–939.

[3] Cui, L, Shao, S, Wang, H, Zhang, G, Zhao, Z, Zhao, C., 2022. Recent advances in the equal channel angular pressing of metallic materials. Processes. 10(10):2181. doi:10.3390/pr10112181

[4] Eskandarzade, M, Najafi Ershadi, M., 2021. Experimental and numerical investigation of the frictional forces in equal channel angular pressing. Uludağ Univ J Fac Eng.;26(1). doi:10.17482/uufmd.818759

[5] Djavanroodi, F., Ahmadian, H., Kookhan, K., Naseri, R., 2013. Ultrasonic assisted-ECAP. Ultrasonics. 53(6):1089–1096. doi:10.1016/j.ultras.2013.02.003

[6] Awang Sh’ri, D.N., Zahari, Z.S., Yamamoto, A., 2021. Effect of ECAP die angle on mechanical properties and biocompatibility of SS316L. Metals. 11(9):1513. doi:10.3390/met11091513

[7] Valiev, R.Z., Langdon, T.G., 2006. Principles of equal-channel angular pressing as a processing tool for grain refinement. Prog Mater Sci. Sep;51(7):881–981. doi:10.1016/j.pmatsci.2006.02.003

[8] Agwa, M.A., Ali, M.N., Al-Shorbagy, A.E., 2016. Optimum processing parameters for equal channel angular pressing. Mech Mater. Sep;100:1–11. doi:10.1016/j.mechmat.2016.06.003

[9] Dayal, A, Raj, K.H., Sharma, R.S., 2018. ECAP die design for minimising corner gap. Mater Today Proc. 5(1, Part 1):1686–90. doi:10.1016/j.matpr.2017.11.264

[10] Fadhil, A., et al. 2021. Design parameters for Equal-Channel Angular Pressing (ECAP) via numerical approach. J Phys Conf Ser. 1973:012103. doi:10.1088/1742-6596/1973/1/012103

[11] Ghazani, M.S., Moslemi, S., 2018. The effect of inner corner radius of ECAP die on strain distribution and damage accumulation in deformed sample. Trans Indian Inst Met. 71:135–42. doi:10.1007/s12666-017-1230-7

[12] Dassault Systèmes. ABAQUS 6.14 Documentation. 2014. Providence, RI: Dassault Systèmes Simulia Corp.

[13] Wongsa-Ngam, J., Noraphaiphipaksa, N., Kanchanomai, C., Langdon, T.G., 2021. Numerical investigation of plastic strain homogeneity during equal-channel angular pressing of a Cu-Zr alloy. Crystals. 11(12):1505. doi:10.3390/cryst11121505

[14] Doege, E., Meyer-Nolkemper, H., Saeed, I. 1986. Fliesskurvenatlas metallischer Werkstoffe. Hanser Verlag Meunchen Wien,

PLC-controlled manufacturing line with multi-robot integration and computer vision

***Malik Čabaravdić*[1], *Amer Sarajlić*[1] *and Amra Talić-Čikmiš*[1]**

1) University of Zenica 1, Fakultetska 1, 72000 Zenica, Bosnia and Herzegovina

Corresponding author: malik.cabaravdic@unze.ba

Original scientific article

Abstract: This paper presents a comprehensive simulation model for an intelligent manufacturing system featuring multi-robot coordination, computer vision integration, and Arduino-based Programmable Logic Controller (PLC) automation. The proposed system demonstrates a complete production cycle incorporating object recognition, robotic manipulation, additive manufacturing through 3D printing, CNC machining, and automated stacking operations. The simulation is developed using Arctos Studio Pro software, which provides advanced robotic simulation capabilities with real-time computer vision processing. The system integrates multiple robotic arms controlled through a unified Arduino-based PLC program that coordinates conveyor belt operations, camera-based object detection, and multi-stage manufacturing processes. This research contributes to the field of Computer Integrated Manufacturing (CIM) by demonstrating how modern simulation tools can bridge the gap between digital automation design and real-world implementation using affordable, open-source hardware platforms. The cost-effectiveness of Arduino-based implementation is demonstrated through comparative analysis with commercial PLC systems, showing significant cost advantages while maintaining industrial-grade functionality.

Keywords: *Computer Integrated Manufacturing; CIM; Robotic Simulation; Arduino PLC; Computer Vision*

1. Introduction to the Article

The evolution of manufacturing systems toward Industry 4.0 has emphasized the integration of cyber-physical systems, Internet of Things (IoT), and intelligent automation [1]. Modern manufacturing environments require flexible, adaptive systems capable of handling diverse production requirements while maintaining high efficiency and quality standards. Computer Integrated Manufacturing (CIM) represents the foundation for these advanced manufacturing paradigms, enabling seamless communication between different production components [2].

The integration of computer vision, robotic manipulation, and programmable logic control has become essential for creating intelligent manufacturing systems [3]. Unlike traditional fixed automation, modern manufacturing lines must adapt to varying product requirements, quality specifications, and production volumes. This flexibility is particularly important in the context of mass customization and small-batch production scenarios that characterize contemporary manufacturing trends.

Arduino-based control systems have emerged as a cost-effective and accessible platform for implementing industrial automation solutions [4]. The open-source nature of Arduino platforms, combined with their extensive ecosystem of sensors, actuators, and communication modules, makes them particularly suitable for educational and small-scale industrial applications. The ability to prototype and deploy control systems using Arduino Mega, Uno, or ESP32 platforms significantly reduces the barrier to entry for automation implementation.

This paper presents a simulation model developed using Arctos Studio Pro software that demonstrates a complete manufacturing line featuring multi-robot coordination, computer vision-guided operations, additive manufacturing, and CNC machining processes. The system is designed around an Arduino-based PLC architecture that can be directly implemented in real-world applications. The

simulation showcases how modern robotics simulation tools can serve as both educational platforms and practical design environments for industrial automation systems.
The manufacturing line integrates three robotic manipulators working in coordination to handle a complete production cycle: object recognition and 3D printing preparation, CNC machining operations, and final product stacking. Computer vision systems guide each stage of the process, demonstrating the practical application of Industry 4.0 technologies in manufacturing automation.

2. Literature Review and Related Work

Recent advances in manufacturing automation have focused on the integration of Industry 4.0 technologies with traditional manufacturing processes. The concept of digital twins and cyber-physical systems has gained significant attention in academic and industrial research [5]. Computer vision applications in manufacturing have evolved from simple presence detection to sophisticated quality control and adaptive process optimization [6].
Arduino-based industrial automation has been explored in various contexts, from simple sensor monitoring to complex multi-axis control systems [7]. The platform's accessibility and extensive community support have made it attractive for educational applications and small-scale industrial implementations. Multi-robot coordination in manufacturing environments presents unique challenges related to path planning, collision avoidance, and task synchronization [8].
Recent developments in AI-driven human-robot interaction, particularly in 3D-printed robotic systems using advanced AI models and ROS integration, show promising developments in intelligent manufacturing automation [14]. These advances demonstrate the potential for more sophisticated and adaptable manufacturing systems that can respond to changing production requirements.

3. Simulation Environment and System Architecture

The simulation was developed using Arctos Studio Pro, an advanced robotic simulation software that provides comprehensive tools for multi-robot programming, computer vision integration, and PLC-based automation control [9]. Unlike traditional factory simulation software, Arctos Studio Pro offers direct integration with physical hardware platforms, enabling seamless transition from simulation to real-world implementation.
Arctos Studio Pro provides several key advantages for manufacturing system simulation:

- Real-time physics simulation with collision detection
- Advanced computer vision processing with object recognition
- Multi-robot coordination and programming capabilities
- Direct Arduino integration for PLC implementation
- 3D printing and CNC machining simulation modules
- Python scripting for custom automation logic

The software's ability to interface directly with Arduino-based control systems makes it particularly valuable for educational institutions and small-scale manufacturing operations where cost-effectiveness and accessibility are important considerations.

3.1. Arduino-Based PLC Architecture

The control system is designed around Arduino microcontroller platforms, utilizing Arduino Uno for the main PLC functions and Arduino Mega 2560 for individual robot control. This distributed architecture choice provides several benefits:

- Cost-effective implementation compared to commercial PLC systems
- Open-source development environment with extensive community support
- Direct compatibility with a wide range of sensors and actuators
- Scalable architecture supporting Arduino Uno, Mega, and ESP32 platforms
- Real-time control capabilities suitable for industrial automation

The Arduino Uno serves as the main PLC controller for system coordination, while the Arduino Mega 2560 is dedicated to individual robot control due to its expanded I/O capabilities (54 digital pins, 16 analog inputs) and larger memory capacity (256KB flash memory), making it suitable for complex robotic motion control and sensor integration.

3.2. Cost-Benefit Analysis: Arduino vs. Commercial PLC Systems

A comparative analysis between Arduino-based and commercial PLC implementations reveals significant cost advantages for the proposed system. The following comparison demonstrates the economic benefits of using Arduino platforms:

Table 1. *Cost Comparison: Arduino vs. Commercial PLC Systems*

Component	Arduino	Siemens S7	Rockwell AB
Basic Controller	$25	$800	$1,200
Programming Software	Free	$2,500	$3,000
I/O Modules	$50	$400	$500
Communication	$20	$300	$400
Training Requirements	Low	High	High
Total Cost	$95	$4,000	$5,100

The Arduino-based system demonstrates approximately 98% cost reduction compared to commercial alternatives while maintaining comparable functionality for educational and small-scale manufacturing applications. However, commercial systems offer advantages in terms of industrial certification, extended temperature ranges, and comprehensive technical support.

3.3. System Overview

The simulated manufacturing line represents a fully automated production system incorporating object recognition, additive manufacturing, CNC machining, and automated material handling (Figure 1). The system demonstrates a complete production cycle where raw objects are processed through multiple manufacturing stages with full computer vision guidance and robotic manipulation.
The manufacturing line incorporates several Industry 4.0 principles:

- Cyber-physical systems integration through Arduino-based control
- Real-time data processing through computer vision systems
- Autonomous decision-making based on sensor feedback
- Digital twin simulation enabling virtual commissioning
- Modular system architecture supporting flexible reconfiguration

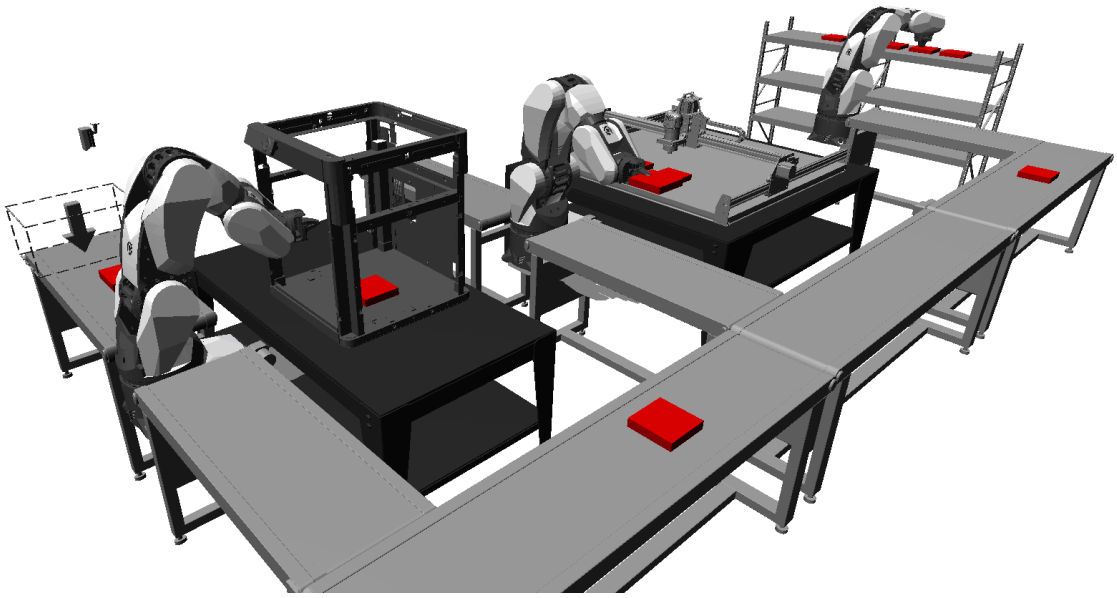


Figure 1. *Complete overview of the Arctos Studio Pro manufacturing simulation showing multi-robot coordination, conveyor systems, and manufacturing stations*

4. Manufacturing Process Flow and Stations

The manufacturing process begins with objects being introduced onto the first conveyor belt through an automated spawning mechanism. This represents real-world scenarios where parts arrive from upstream processes or material handling systems. The objects move along the conveyor at a controlled speed, allowing sufficient time for computer vision processing.

The first camera station employs advanced computer vision algorithms to identify and classify incoming objects based on shape, size, color, and orientation characteristics (Figure 2). The computer vision system utilizes machine learning algorithms to achieve robust object recognition under varying lighting conditions and object orientations.

The implementation leverages cost-effective web cameras combined with OpenCV for image processing [10] and YOLO (You Only Look Once) algorithms for real-time object detection and classification [11]. This approach provides industrial-grade performance while maintaining accessibility for educational and small-scale manufacturing applications.

The system can be trained to recognize specific part types, quality indicators, and orientation requirements, making it adaptable to different production scenarios. Additionally, the cameras serve a crucial role in quality control by detecting production defects during manufacturing processes. Parts that fail quality inspection are automatically identified and displaced from the main production line through a rejection mechanism, ensuring only conforming products continue through the manufacturing sequence.

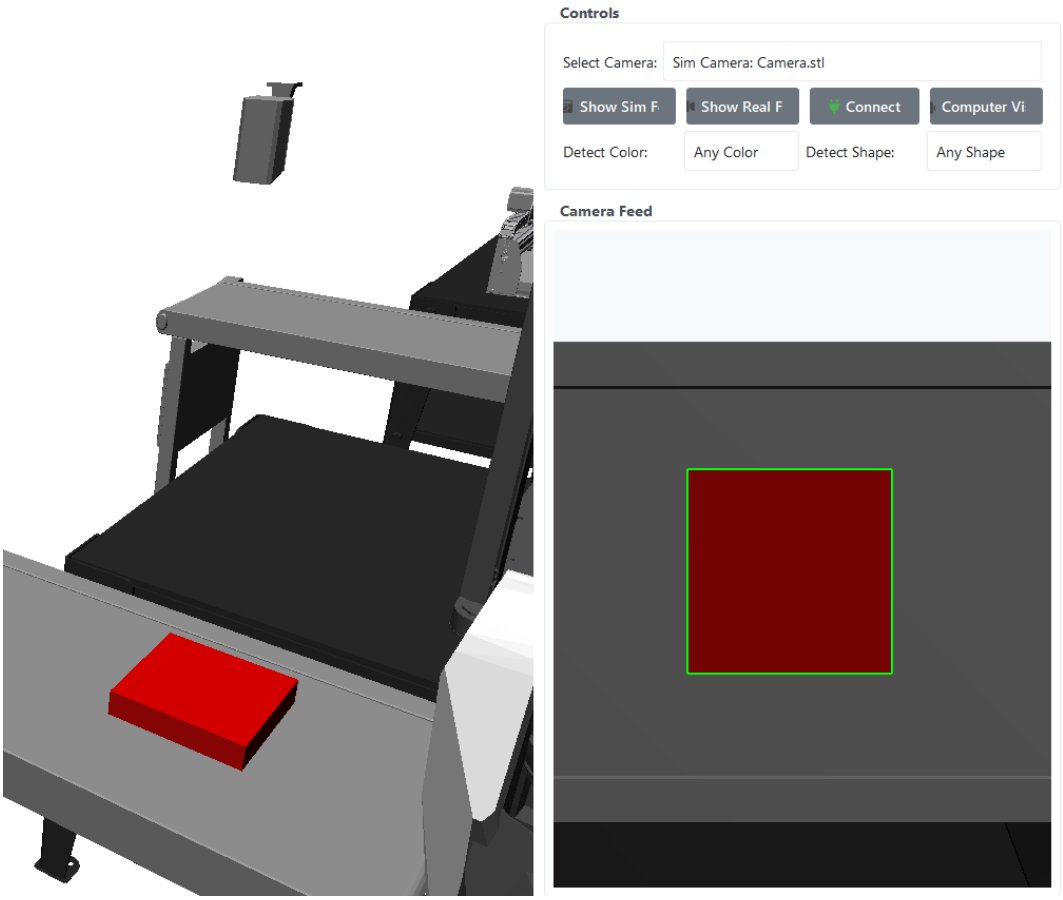


Figure 2. *Computer vision system performing real-time object recognition and classification on the conveyor belt*

4.1. First Robot: 3D Printing Operations

Upon successful object recognition, the first robotic manipulator receives coordinate data from the vision system and performs a precision pick-and-place operation. The robot retrieves the identified object from the conveyor and transports it to the 3D printing station for additive manufacturing operations.

The 3D printing process represents a modern manufacturing paradigm where additional features, protective coatings, or custom geometries are added to existing parts. This hybrid approach combines traditional manufacturing with additive processes, enabling mass customization and complex part geometries that would be difficult to achieve through conventional machining alone.

The Arduino-based control system monitors the 3D printing process through sensor feedback, ensuring proper material deposition and process completion. Temperature sensors, filament flow monitoring, and print bed leveling systems provide real-time feedback to maintain print quality and consistency.

4.2. Second Camera and CNC Preparation

After completion of the 3D printing process, a second computer vision system inspects the printed object to verify print quality and completion status. This quality control step ensures that only properly processed parts continue through the manufacturing line, maintaining overall system reliability and product quality.

The second robot receives the quality-verified object and transports it to the CNC machining station via another conveyor belt system. This intermediate conveyor provides buffering capacity and allows for process timing optimization, ensuring smooth material flow through the manufacturing line.

4.3. CNC Machining and Post-Processing

The CNC machining station performs precision subtractive manufacturing operations on the 3D printed objects. This combination of additive and subtractive processes enables the creation of complex parts with both organic geometries from 3D printing and precision features from CNC machining [12].

A third computer vision system monitors the CNC machining process and verifies completion status. The vision system performs dimensional verification and surface quality inspection to ensure machining specifications are met. Upon successful machining, the finished part is returned to the conveyor system for final handling operations.

4.4. Final Robot: Automated Stacking

The third robotic manipulator performs the final operation in the manufacturing line: automated stacking of completed parts onto storage racks. This robot utilizes advanced path planning algorithms to optimize stacking patterns and maximize storage efficiency.

The stacking operation demonstrates the importance of precise robot control and sensor feedback in maintaining system reliability. Position sensors and force feedback ensure proper part placement and prevent damage during handling operations.

5. Arduino-Based PLC Programming and Implementation

The control system is implemented using a modular Arduino-based PLC program that coordinates all manufacturing operations. The program architecture follows industrial automation best practices while leveraging the flexibility and accessibility of Arduino platforms.

The PLC program utilizes a visual programming approach that simplifies complex automation logic into easily understood function blocks (Figure 3). This approach makes the system accessible to users with varying levels of programming experience while maintaining the sophistication required for industrial applications.

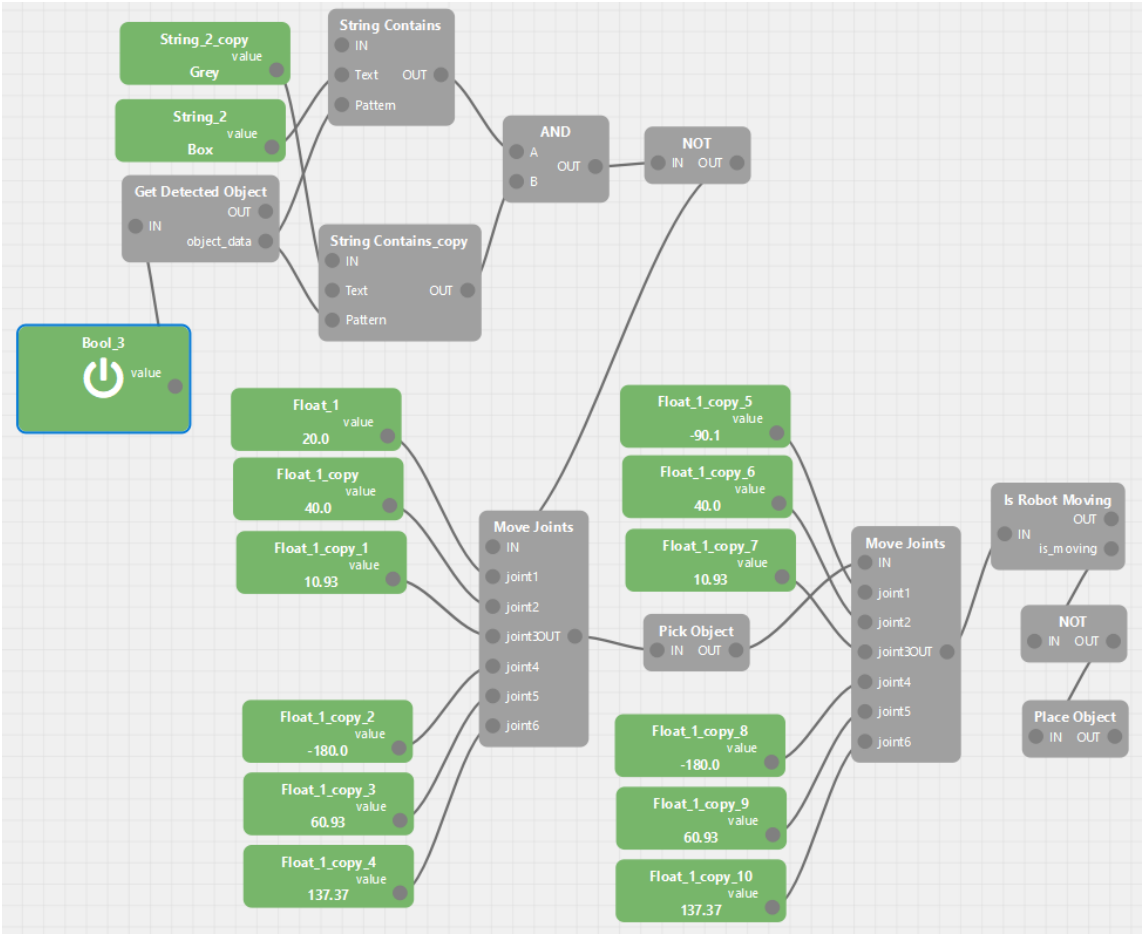


Figure 3. *Arduino-based PLC program structure showing the visual programming interface and logic blocks for manufacturing control*

5.1. Unified Control Logic for Multiple Robots

A key feature of the control system is the use of unified control logic for all three robotic manipulators. The same core program structure is used for each robot, with only coordinate parameters and timing values modified for specific applications. This approach provides several advantages:

- Reduced development time through code reuse
- Simplified maintenance and troubleshooting procedures
- Consistent behavior across all robotic systems
- Easier training and operator familiarization
- Simplified system expansion and reconfiguration

Each robot receives position coordinates and operational parameters from the central PLC system, but executes the same fundamental motion and control algorithms. This modular approach aligns with modern software engineering principles and industrial automation standards.

5.2. Arduino Hardware Implementation

The simulation demonstrates a control architecture that can be directly implemented using readily available Arduino hardware components (Figure 4). The system supports multiple Arduino platforms depending on application requirements and complexity.

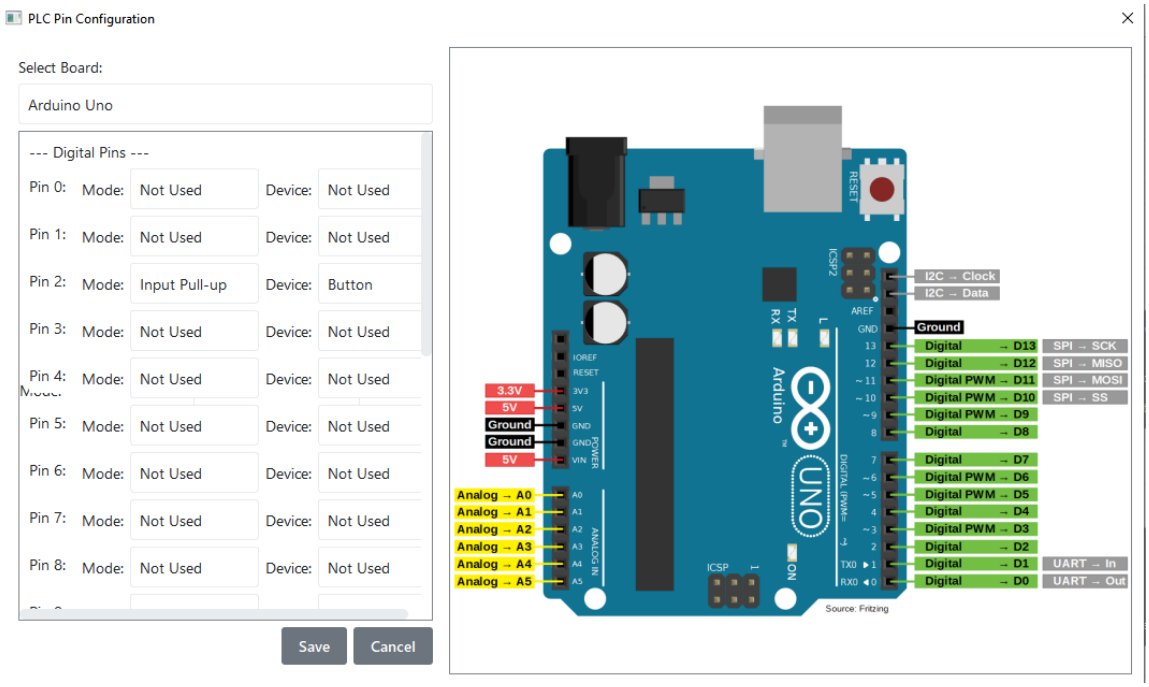


Figure 4. *Arduino Uno configuration showing PLC pin assignments and hardware connections for industrial automation implementation*

Arduino Mega 2560: Dedicated to individual robot control requiring extensive I/O capabilities. The Mega provides 54 digital I/O pins and 16 analog inputs, making it suitable for complex robotic motion control with multiple sensors and actuators.

Arduino Uno: Used for main PLC functions and system coordination in distributed control architectures where the central controller manages overall manufacturing flow.

ESP32: Ideal for applications requiring wireless communication, IoT integration, or advanced processing capabilities. The ESP32's dual-core processor and built-in WiFi/Bluetooth capabilities enable advanced Industry 4.0 features.

The Arduino-based implementation ensures that the simulated manufacturing system can be directly translated to physical hardware using cost-effective, open-source components. This approach significantly reduces the barrier to entry for implementing advanced manufacturing automation in educational and small-scale industrial environments.

5.3. Sensor Integration and Feedback Systems

The PLC program integrates multiple sensor types to provide comprehensive system monitoring and control:

- Vision sensors for object recognition and quality control
- Proximity sensors for object detection and positioning
- Encoder feedback for precise robot positioning
- Temperature sensors for 3D printing process monitoring
- Force sensors for collision detection and safety
- Limit switches for system boundaries and homing operations

The Arduino platform's extensive sensor ecosystem enables easy integration of additional monitoring and control capabilities as system requirements evolve [13]. Modern programmable logic controllers increasingly incorporate these diverse sensor types to achieve comprehensive system monitoring and intelligent automation [15].

6. Computer Vision Integration and Object Recognition

The integration of computer vision systems throughout the manufacturing line demonstrates the practical application of Industry 4.0 technologies in automation. Each vision station performs specific functions while contributing to overall system intelligence and adaptability.

The computer vision systems utilize advanced image processing algorithms to perform real-time object recognition, quality inspection, and process monitoring. The integration with Arduino-based control systems ensures rapid response times and seamless coordination between vision processing and robotic operations.

The integration demonstrates practical applications of computer vision algorithms in manufacturing automation [16], while the robotic coordination follows established principles from modern robotics handbooks [17]. Machine learning algorithms enable adaptive quality control that can learn from production data and improve detection accuracy over time.

6.1. Multi-Stage Quality Control and Defect Management

The three-camera system provides comprehensive quality control throughout the manufacturing process:

- Input inspection for incoming object classification and initial quality assessment
- Process monitoring during 3D printing operations for layer adhesion and dimensional accuracy
- Final quality verification after CNC machining for surface finish and dimensional conformance
- Automated defect detection using machine learning algorithms trained on common manufacturing defects

The system employs OpenCV image processing techniques combined with YOLO object detection algorithms to identify various types of manufacturing defects including surface imperfections, dimensional variations, incomplete processing, and material inconsistencies. When defects are detected, the control system automatically activates rejection mechanisms that displace non-conforming parts from the main production line.

This multi-stage approach ensures consistent product quality and enables early detection of process variations or defects, reducing waste and improving overall system efficiency. The automated quality control system maintains detailed logs of inspection results, defect rates, and process variations, providing valuable data for continuous improvement initiatives and process optimization.

7. Results and System Performance Analysis

The Arctos Studio Pro simulation demonstrates successful integration of multiple manufacturing processes under unified Arduino-based PLC control. Key performance indicators include:

- Cycle time optimization through coordinated robot operations
- High accuracy in computer vision-guided object handling
- Reliable process coordination between additive and subtractive manufacturing
- Effective quality control through multi-stage inspection
- Scalable architecture supporting system expansion

The simulation validates the feasibility of implementing complex manufacturing automation using accessible, cost-effective hardware platforms while maintaining industrial-grade performance and reliability.

7.1. Educational and Practical Applications

The simulation approach follows established principles of discrete-event system simulation [18], providing reliable modeling of complex manufacturing processes. The modular architecture supports incremental implementation of advanced manufacturing concepts, while artificial intelligence techniques enable adaptive decision-making in modern automation systems [19].

The simulation provides significant value for both educational and practical applications:

Educational Benefits:
- Hands-on experience with industrial automation concepts
- Understanding of multi-robot coordination principles
- Practical application of computer vision in manufacturing
- Experience with Arduino-based industrial control systems
- Integration of additive and subtractive manufacturing processes

Practical Implementation:
- Direct hardware implementation pathway using Arduino platforms
- Cost-effective automation solutions for small-scale manufacturing
- Rapid prototyping and system validation capabilities
- Modular architecture supporting incremental implementation
- Open-source foundation enabling customization and expansion

7.2. System Flexibility and Adaptability

The modular design of both the simulation and control architecture enables significant flexibility in system configuration and operation. The unified robot control logic allows for easy reconfiguration of manufacturing processes, while the Arduino-based hardware platform supports rapid modification and expansion of system capabilities.

This flexibility is particularly valuable in modern manufacturing environments where product mix changes, customization requirements, and process optimization drive the need for adaptable automation systems. The system can be easily reconfigured for different manufacturing scenarios including assembly operations, packaging systems, and material handling applications.

8. Conclusion

Future work will focus on physical implementation, advanced IoT integration [18], and machine learning algorithms for process optimization. The open-source foundation contributes to the democratization of advanced manufacturing technologies and represents a significant step toward accessible Industry 4.0 implementation.

This paper has presented a comprehensive simulation of an Arduino-based PLC-controlled manufacturing line featuring multi-robot coordination, computer vision integration, and hybrid additive/subtractive manufacturing processes. The use of Arctos Studio Pro simulation software demonstrates how modern simulation tools can bridge the gap between educational automation concepts and practical industrial implementation.

The key contributions include demonstration of unified control logic for multi-robot systems, integration of OpenCV and YOLO-based computer vision with defect detection and displacement capabilities, practical implementation using Arduino hardware, and web-based API integration for on-demand manufacturing services. The system enables remote production management and comprehensive quality control through cost-effective web cameras and open-source algorithms.

The Arduino-based control architecture ensures direct implementation using readily available components, making advanced manufacturing automation accessible to educational institutions and small-scale manufacturers. The integration of Arctos Studio API capabilities with automated quality control and paper sticker printing demonstrates the potential for fully automated manufacturing services with global remote monitoring capabilities.

References

[1] Lasi, H., Fettke, P., Kemper, H.G., Feld, T., Hoffmann, M., 2014. Industry 4.0. Business & Information Systems Engineering, 6 (4), 239-242.

[2] Rehg, J.A., Kraebber, H.W., 2005. Computer-Integrated Manufacturing, 3rd ed. Pearson Prentice Hall, Upper Saddle River, NJ.

[3] Groover, M.P., 2007. Automation, Production Systems, and Computer-Integrated Manufacturing, 3rd ed. Prentice Hall, Upper Saddle River, NJ.
[4] Banzi, M., Shiloh, M., 2014. Getting Started with Arduino: The Open Source Electronics Prototyping Platform, 3rd ed. Maker Media.
[5] Grieves, M., 2014. Digital twin: manufacturing excellence through virtual factory replication. Digital Manufacturing, 1 (1), 1-7.
[6] Newman, T.S., Jain, A.K., 2017. A survey of automated visual inspection. Computer Vision and Image Understanding, 61 (2), 231-262.
[7] Margolis, M., 2011. Arduino Cookbook: Recipes to Begin, Expand, and Enhance Your Projects, 2nd ed. O'Reilly Media.
[8] Korsah, G.A., Stentz, A., Dias, M.B., 2013. A comprehensive taxonomy for multi-robot task allocation. The International Journal of Robotics Research, 32 (12), 1495-1512.
[9] Arctos Robotics, 2024. Arctos Studio Pro Documentation. https://www.arctosrobotics.com/ (accessed 10 July 2025).
[10] Bradski, G., 2000. OpenCV Library. Dr. Dobb's Journal of Software Tools.
[11] Redmon, J., Divvala, S., Girshick, R., Farhadi, A., 2016. You Only Look Once: Unified, Real-Time Object Detection. Proceedings of the IEEE Conference on Computer Vision and Pattern Recognition, 779-788.
[12] Lynch, M., 2007. Computer Numerical Control for Machining. McGraw-Hill Education.
[13] Arduino LLC, 2023. Arduino Programming Reference. https://www.arduino.cc/reference/ (accessed 10 July 2025).
[14] Sarajlić, A., Banjanović-Mehmedović, L., 2025. AI-Driven Human-Robot Interaction for a 3D-Printed Robotic Arm Using Gemini AI and ROS. 2025 24th International Symposium INFOTEH-JAHORINA (INFOTEH), DOI: 10.1109/INFOTEH64129.2025.10959192.
[15] Bolton, W., 2015. Programmable Logic Controllers, 6th ed. Newnes.
[16] Szeliski, R., 2021. Computer Vision: Algorithms and Applications, 2nd ed. Springer.
[17] Siciliano, B., Khatib, O., 2016. Springer Handbook of Robotics, 2nd ed. Springer.
[18] Banks, J., Carson, J.S., Nelson, B.L., Nicol, D.M., 2014. Discrete-Event System Simulation, 5th ed. Pearson.
[19] Russell, S.J., Norvig, P., 2020. Artificial Intelligence: A Modern Approach, 4th ed. Pearson.

Research potential and development of a Simscape Multibody-based dynamic model of collaborative robot

***Maida Čohodar Husić*[1], *Kenan Muhamedagić*[1], *Ahmet Čekić*[1] *and Đerzija Begić-Hajdarević*[1]**

1) University of Sarajevo – Faculty of Mechanical Engineering, Vilsonovo setaliste 9, 71000 Sarajevo, Bosnia and Herzegovina

Corresponding author: cohodar@mef.unsa.ba

Original scientific article

Abstract: In the context of the European Commission's vision and strategic commitment to transform existing production in a way that makes it sustainable, smart, resilient, and human-centered, robots are taking on a new role in manufacturing. Instead of replacing human workers when performing work tasks, robots work in collaboration with them. Such application of robots creates numerous challenges that need to be answered. In this paper, the dynamic model of the UR5e collaborative robot is first automatically developed based on a step file in the Simscape/Multibody environment of MATLAB. Then such obtained dynamic model was upgraded. The necessary components and transformations were added to it. This paper investigates current trends and requirements imposed by Industry 5.0 and points to the research potential offered by the collaborative robot model developed in this way. In future work, it is planned to use the dynamic model as a research platform for motion analysis and optimization, development and testing of control algorithms, safety analysis, as an educational platform for learning kinematics, robot dynamics, planning work tasks. Finally, in future investigations, it will be used with RoboDK (using ROS2) and with the real UR5e robot, which opens numerous opportunities to optimize the processes cobots perform.

Keywords: *Collaborative robots; Dynamic model; Simscape Multibody; Forward kinematics*

1. Introduction

The rapid development of robotics has provided a significant place for robots in manufacturing, which are recognized as an effective response to the goals of Industry 4.0. Industry 4.0 places high demands on robotic systems. Robotic systems are becoming increasingly complex, equipped with numerous sensors that significantly improve their functionality and expand areas of their application.

As a technological advance and continuation of Industry 4.0, Industry 5.0 represents a shift towards a human-centered industrial model [1]. The production philosophy is changing, insisting on personalized production that has to be both flexible and efficient. Traditional programmed robots give way to collaborative robots, which are not aimed at replacing human workers at work, but at performing complex work tasks through interacting with them. Different models of collaborative robots are widely used today and are the subject of numerous researches. These are some of them: Universal Robot UR3 [2] and [3], UR5 [2], [4], [5], [6], [7], [8], [9] and [10], UR5e [9], [11], [12], [13] and [14], Franka Emika Panda [15], Kinova [16], ABB SWIFTI CRB 1100-4 [17], ABB CRB 15000 GoFa LBR14 [18], KUKA iiwa [19], myCobot [9] etc.

In order to the potential provided by cobots to be used in real production facilities, it is necessary to answer numerous security challenges that have been investigated in [20]. Safety, as a necessary requirement that must be met during human-robot interaction, is the focus of research in [12], where a comparison was made between UR5e and geared magnetorheological (MR) actuated cobot MR5.

There are numerous examples of robot applications, each of them causes new challenges for the cobot application. Assembly tasks form great challenges for their automation and robotization. Therefore, numerous studies have been conducted to address these challenges, [2] and [16]. The results of a comparison of assembly tasks performed using cobots UR3 and UR5 with manual assembly show the great potential of using cobots in medium-volume assembly tasks [2]. In [16] it is proposed a new

software tool to improve human-robot collaboration in a shared workspace when performing assembly tasks. Robot control during robotic writing, as well as the technology for processing written samples have been investigated in [5]. In order to achieve automatic quality control, the possibility of adapting older robotic arms and using them equipped with 3D scanners is explored in [21]. A new approach to path planning for an N-link robot based on torque feedback parameterization tested on the UR10 is proposed in [22]. Research and optimization of the energy consumption of the UR5e collaborative robot through the identification of the robot dynamics and electrical parameters is given in [14]. The cobot work efficiency during workpiece sorting is the subject of research in [7].

A new method for robot calibration based on a mathematical approach using the Jacobian matrix on the example of the cobot UR3 is presented in [3]. The research in [8] presents a method for testing the cobot’s parameters according to ISO 9283:2012, which is important when purchasing used cobots as well as when repairing them after damage during their work. In order to achieve greater precision, work [4] presented a methodology to detect deviations in joints.

In order to achieve greater flexibility, there is a need for more frequent reprogramming of cobots, and relevant methods of programming and controlling cobots currently used in industry were investigated in [23]. A comparison between the complexity of the task that the cobot should perform and the skills needed by the operator to program the cobot was made as well. The possibility of adapting cobot programming to non-experts is explored in [15]. Interactive control and programming of robot located on mobile platform based on Mixed Reality (MR) is analysed in [19]. Visualization, Augmented Reality (AR), Virtual Reality (VR) and Mixed Reality (MR) have opened up new perspectives for improving the work and performances of robots. In AR and MR, the actual robot cell is visible, but in AR the degree of immersion in the digital world is low or medium with limited interaction between the real and digital worlds, while in MR the degree of immersion in the digital world is high with full interaction between the real and digital worlds. To make production more flexible and reconfigurable in the context of Industry 5.0 requirements, the tools based on Augmented Reality could support human operators in many tasks such as assembly, inspection, reconfiguration, etc, that is pointed out in [24]. For educational purposes, virtual robotic platforms have been developed in [10] and [13]. In [10], a 3D virtual model UR5e is created that allows students to evaluate inverse kinematics and test different independent joint control models. An educational cloud platform focused on controlling virtual and real physical robots in subject of research in [13]. The research presented in [18] shows the potential of MR where the addition of virtual sensors can improve safety in robotic cells.

The Unified Robot Description Format (URDF), based on XML (eXtensible Markup Language) is one of the popular description formats for representation of the robot, its kinematics or dynamics, its joints, links, motors, etc., [25] and [26]. Approach for automatically generating URDF files from SolidWorks is proposed in [27]. The methodology for systematically developing a virtual 3D model of an articulated mechanism is proposed [28], where the model is developed as a DOM (the Document Object Model)-like tree during which the corresponding XML document is generated. Two different motion control modes for three cobots UR5, UR5e and my Cobot, based on MR, were successfully demonstrated in [9].

In a dynamic environment, modelling and simulation of robotic systems play a significant role and are emerging as a powerful tool in optimizing work and planning work tasks. Their implementation implies knowledge of the kinematics and dynamics of the robotic systems. Therefore, kinematic modelling is still the subject of numerous researches. Inverse kinematics with several motion control models is implemented in [10], the algorithm for calculating direct and inverse kinematics of the cobot UR5e was developed using MATLAB in [11].

In this work, a dynamic model of the mechanical part of the cobot UR5e was developed, based on its 3D CAD model given in the form of a step file. The validation of the developed model (its geometric and kinematic properties) was done on the basis of the achieved position and orientation of the end-effector for certain values of the joint variables. The obtained values were compared with the analytical solution of the forward kinematics, and with the values obtained by using the software RoboDK [29]. The paper is organized as follows: in the second part of the paper, a direct kinematic

model is presented. In the third part of the paper, the methodology of developing a dynamic model using a step file is explained on the example of the well-known UR5e robot. Validation of the results is the subject of the fourth section. The last part of the paper provides concluding considerations and presents ideas and recommendations for further research.

2. Forward kinematics

In this section, the forward kinematics of the robot manipulator UR5e is derived. The direct kinematics describes the pose of end-effector (tool, gripper or sensor) in function of joint variables. Taking into account the importance of the robot direct kinematics, it is presented in the numerous papers such as [6], [10], [11] and [30]. To develop the direct kinematic model in this paper, the robot manipulator UR5e is located to its *zero* pose, with all zero joint variables, Figure 1. Geometric parameters of manipulator are taken from [31] and [32]. The general procedure based on modified Denavit-Hartenberg (DH) convention [33] was used.

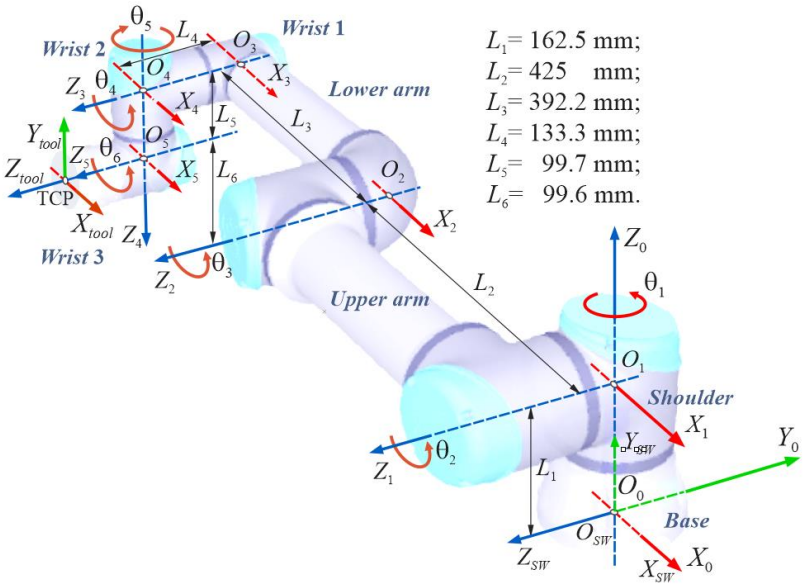


Figure 1. *Collaborative robot UR5e with attached coordinate frames*

Since the robot UR5e has six revolute joints or six degrees of freedom (DoF), a total of seven coordinate systems are set up, as shown in Figure 1. The first frame (Frame 0) is the base and it is unmovable. The last frame (Frame 6) is the tool frame attached to the end-effector (marked as $X_{tool}Y_{tool}Z_{tool}$ with the origin located at Tool Center Point - TCP). For the first coordinate system, the Denavit- Hartenberg procedure provides non-unique definition of its *x*-axis and the origin O_0 position. They were set up in a way that the base frame coincides with one, defined by the manufacturer Universal Robot. The same is done for the last coordinate system (the Frame 6), which is set up in a way that it coincides with the tool frame, also defined by Universal Robot.

The matrix of homogeneous transformation which defines the position and orientation between two neighbouring coordinate frames (Frame *i* regarding to Frame *i*-1 for *i* = 1, 2,..5, 6(or *tool*)) is given by [33]:

$$\mathbf{A}_i^{i-1} = \begin{bmatrix} c_{\theta_i} & -s_{\theta_i}c_{\alpha_i} & s_{\theta_i}s_{\alpha_i} & a_i c_{\theta_i} \\ s_{\theta_i} & c_{\theta_i}c_{\alpha_i} & -c_{\theta_i}s_{\alpha_i} & a_i s_{\theta_i} \\ 0 & s_{\alpha_i} & c_{\alpha_i} & d_i \\ 0 & 0 & 0 & 1 \end{bmatrix} \tag{1}$$

and it is in function of geometric parameters and joint variable (a_i, α_i, d_i and θ_i, where, if joint is revolute the joint variable is θ_i, and if joint is prismatic that is d_i). (In Eq.(1) it is denoted: c_θ=cos(θ) and s_θ=sin(θ).) More about this matrix and the meaning of its parameters can be found in [33].

The corresponding DH kinematic parameters are specified in Table 1.

Table 1. *The DH kinematic parameters for UR5e*

Link	a_i	α_i	d_i	θ_i
1	0	$\pi/2$	L_1	θ_1
2	- L_2	0	0	θ_2
3	- L_3	0	0	θ_3
4	0	$\pi/2$	L_4	θ_4
5	0	- $\pi/2$	L_5	θ_5
6	0	0	L_6	θ_6

The matrices which describe the position and orientation of two neighbouring coordinate systems $\mathbf{A}_1^0, \mathbf{A}_2^1, \mathbf{A}_3^2, \mathbf{A}_4^3, \mathbf{A}_5^4$ and $\mathbf{A}_{tool}^5$ are obtained by introducing the DH parameters from Table 1 in the DH matrix (Eq.1). Their successive multiplication, using the rules of addition of successive transformations, yields a matrix of homogeneous transformations that describes the position and orientation of the tool frame with respect to the base frame:

$$\mathbf{A}_{tool}^0 = \mathbf{A}_1^0 \cdot \mathbf{A}_2^1 \cdot \mathbf{A}_3^2 \cdot \mathbf{A}_4^3 \cdot \mathbf{A}_5^4 \cdot \mathbf{A}_{tool}^5 = \begin{bmatrix} \mathbf{R}_{tool}^0 & \mathbf{p}_{tool}^0 \\ \mathbf{0}^T & 1 \end{bmatrix} = \begin{bmatrix} r_{11} & r_{12} & r_{13} & p_x \\ r_{21} & r_{22} & r_{23} & p_y \\ r_{31} & r_{32} & r_{33} & p_z \\ 0 & 0 & 0 & 1 \end{bmatrix} \tag{2}$$

The coordinates of the origin of the tool frame - *TCP* with respect to the base frame are given by radius vector $\mathbf{p}_{tool}^0$ and represented by the first three elements of the fourth column of matrix (2). The orientation of the end-effector with regard to the base frame is defined by the rotation matrix $\mathbf{R}_{tool}^0$ with their nine elements. One way of minimal representation of orientation is by famous XYZ roll-pitch-yaw angles (angles of successive rotation α, β, γ about fixed axes) which can be extracted from rotation matrix $\mathbf{R}_{tool}^0$ as follows:

$$\begin{aligned} \alpha &= \operatorname{atan2}\left(\frac{r_{21}}{c_\beta}, \frac{r_{11}}{c_\beta}\right), \\ \beta &= \operatorname{atan2}\left(-r_{31}, \pm\sqrt{{r_{11}}^2 + {r_{21}}^2}\right), \\ \gamma &= \operatorname{atan2}\left(\frac{r_{32}}{c_\beta}, \frac{r_{33}}{c_\beta}\right). \end{aligned} \tag{3}$$

3. Dynamic modelling

In general, the automatic generation of a dynamic model of some mechanism, for example robot manipulator, in the Simscape Multibody environment, based on its 3D CAD model developed in Solid Works can be implemented in several steps:

1. develop an assembly in SolidWorks (SLDASM type) with fully and precisely defined constraints and mates between the parts of assembly,
2. export such a model (SLDASM type) from SolidWorks (using Simscape Multibody Link), in order to create a model in the form of an xml assembly, whereby a separate step file will be created for each part from which the assembly is formed,
3. import the xml file into MATLAB, in order to automatically generate the dynamic model of the mechanism in form of slx file. On this occasion, an m-file is created, with specified the geometric and material properties of the parts which the assembly consists of.

It is possible, and often desirable, to reorganize the structure of the generated model in order to be presented more systematically. It is possible to upgrade the model, for example, add dynamic motor models, develop control algorithms and the like. If in the first phase the constraints and mates

between parts of the assembly are not completely precisely defined, it is necessary to correct and update the model. Of course, a dynamic model can be developed directly using components from Simscape/Multibody library, but it requires much more time and is much more complex, especially when the structure of the mechanism whose model is being developed is complex. The procedure for gradually developing a dynamic model for the ABB IRB910 industrial robot is presented in [34].

3.1. Export assembly from Solid Works u form of xml

In this paper, the dynamic model of the cobot’s manipulator is automatically generated in the Simscape Multibody environment of MATLAB/Simulink. The 3D CAD model of the robotic manipulator UR5e in the form of a step file was downloaded from [35].

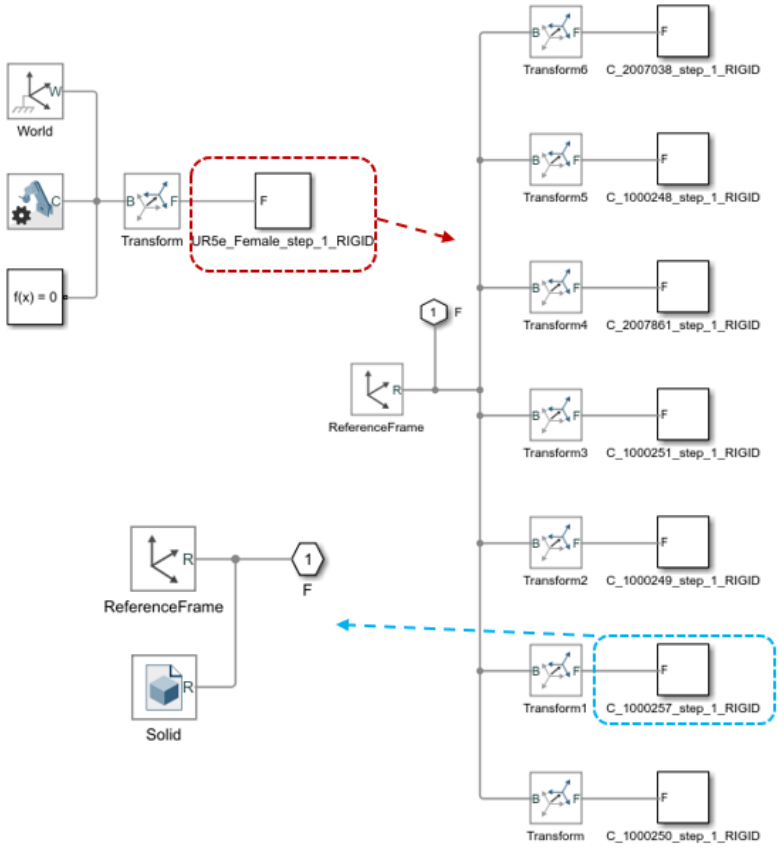


Figure 2. *The automatically generated manipulator dynamic model*

The step file is first loaded into Solid Works, with the "Import Multiple Bodies as Parts" option activated. In this way, the assembly is created in SolidWorks in the form of SDLASM. After that, it was exported and the manipulator model was generated in the form of an xml file. In the next step, by importing model if form of an xml file into MATLAB, the dynamic model of the manipulator was automatically created and, in this case, on several levels as shown in Figure 2.

At the first level (Figure 2 upper left), the *World* component defines the world coordinate system in which the assembly is created. It is the frame in which the 3D CAD model is developed in SolidWorks. It is marked with $X_{SW}Y_{SW}Z_{SW}$, and its position and orientation regarding to the base frame (defined by Universal Robot) are shown in Figure 1. The *UR5e_Female_step_1_RIGID* subsystem represents the manipulator model. The *Transform* component would enable the transformation from the World frame to another. However, during the automatic generation of this dynamic model, a *Transform* component was developed, but it had no function because it described neither translational nor rotational motion (as emphasized, the assembly is defined in the World frame $X_{SW}Y_{SW}Z_{SW}$ in SolidWorks). The structure of the *UR5e_Female_step_1_RIGID* subsystem at the next level of decomposition is shown in Figure 2 on the right. The figure shows that the assembly consists of seven

bodies that represent manipulator parts (Base, Shoulders, Upper Arm, Lower Arm, Wrist1, Wrist2 and Wrist3). Each body is added to the assembly with a previous transformation performed using the *Transform*(*i*) component, which allows the transformation of coordinates from the World frame $X_{SW}Y_{SW}Z_{SW}$ to the coordinate system in which the 3D part was originally developed. Each part could be developed in its own frame.

3.2. Upgrade of the automatically generated dynamic manipulator model

The first level of the upgraded model is shown in Figure 3. Since the assembly model (like as its 3D CAD model) was developed in the frame $X_{SW}Y_{SW}Z_{SW}$, and not in the base frame (see Figure 1), which was defined by the robot manufacturer Universal Robot, the *Transform* component (shown at the first level of the dynamic model from Figure 2, upper left) was updated to allow the transformation of coordinates from the base frame to the coordinate system $X_{SW}Y_{SW}Z_{SW}$. This updated *Transformer* component is renamed as X0Y0Z0->CFSW, Figure 3. After the update, the World frame from the first level of the upgraded dynamic model (Figure 3) becomes the base frame ($O_0X_0Y_0Z_0$, see Figure 1). Some visual changes were also made, e.g., the masks were added to some components to make the assembly more clearly visible. Two sensors, one to measure coordinates of TCP and second one to read the end-effector orientation, all with respect to the base frame and several output components to present simulation results were also added.

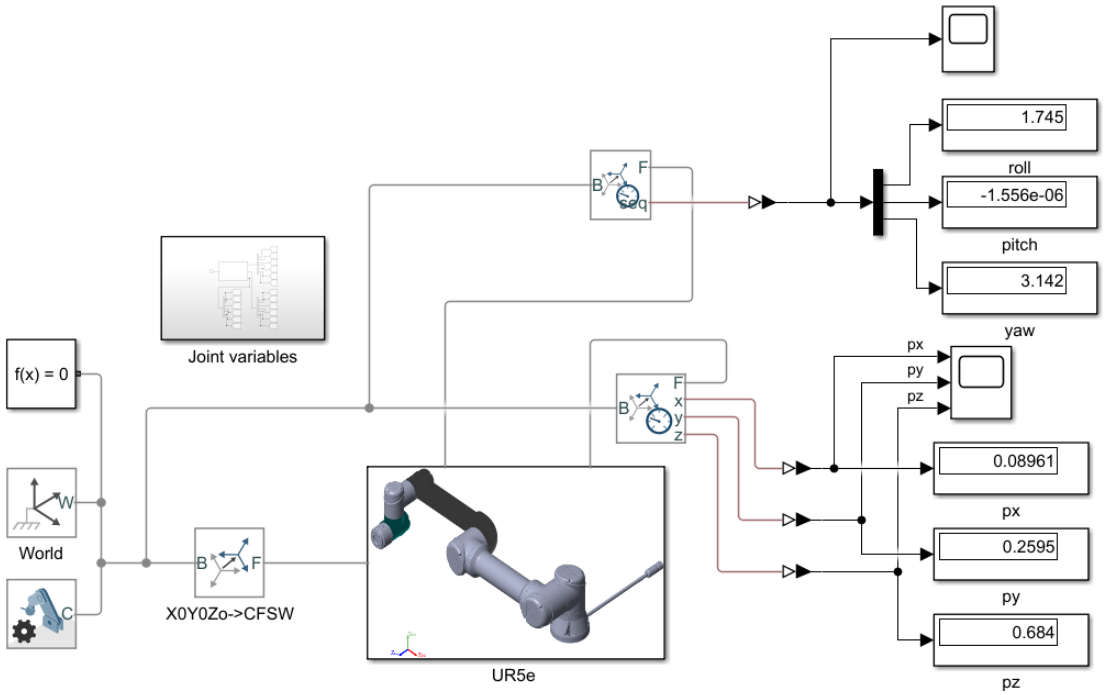


Figure 3. *The updated dynamic model of the cobot manipulator UR5e*

Structure of the subsystem *UR5e* at the following level of decomposition is shown in Figure 4 (right). Six subsystems were added representing six rotational joints, named *Base Joint*, *Shoulder Joint*, *Elbow Joint*, *Wrist Joint* 1, *Wrist Joint* 2, and *Wrist Joint* 3. Each subsystem has two *Transform* components and a *Joint* component representing the revolute joint. The structure of such a subsystem is shown in Figure 4 (left). Before each joint, one *Transform* component was added enabling the transformation of the coordinates from the frame $X_{SW}Y_{SW}Z_{SW}$ to the coordinate system of the i^{th} joint ($O_{i-1}X_{i-1}Y_{i-1}Z_{i-1}$ i=1,2,...6). Then, after the rotation around the axis of the i^{th} joint Z_{i-1}, another *Transform* component was added to enable the reverse transformation, this time from the frame of the i^{th} joint ($O_{i-1}X_{i-1}Y_{i-1}Z_{i-1}$ i=1,2,...6) into the frame $X_{SW}Y_{SW}Z_{SW}$, relative to which the pose of each body is defined.

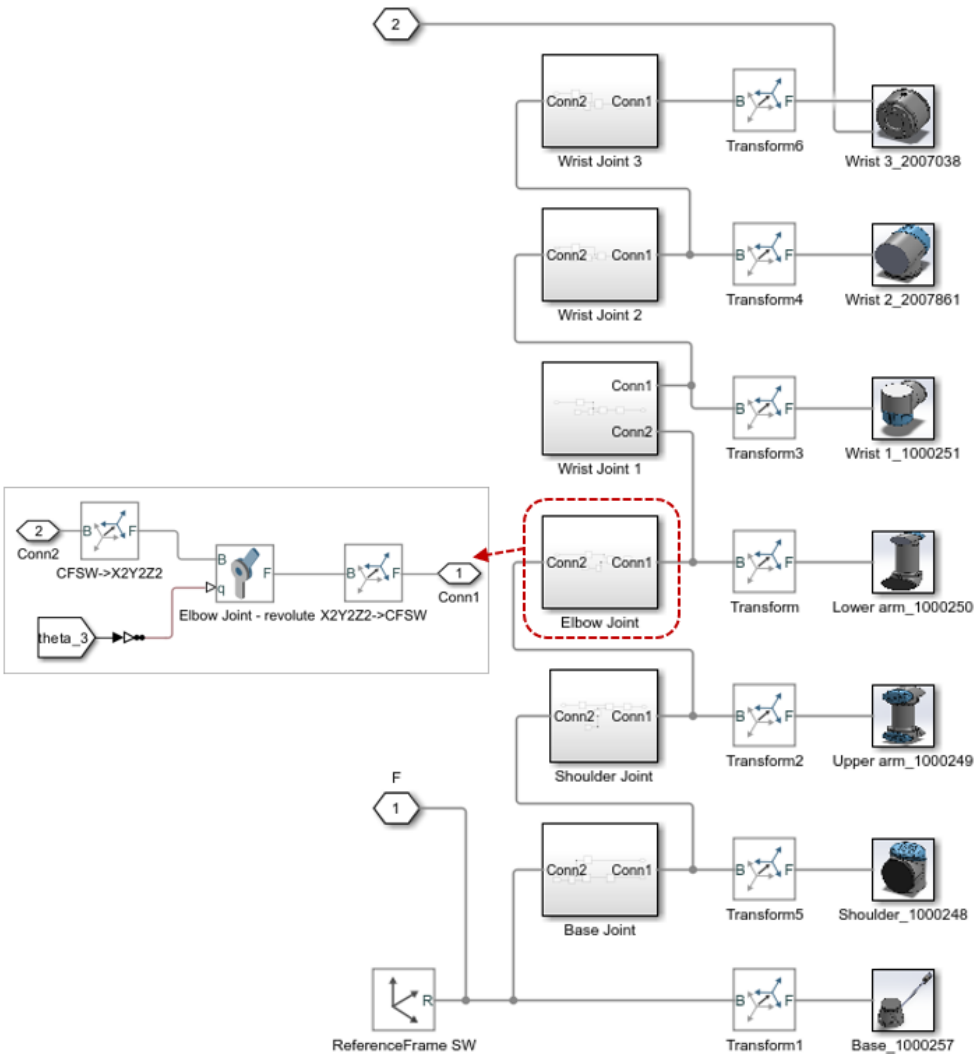


Figure 4. *The structure of subsystem UR5e of updated dynamic model*

4. Model verification

In order to validate the developed model, the robot's task was defined in the joint space using cubic polynomial. The trajectory is planned by the component *Polynomials trajectory* and defined by eight points. First, one pre-simulation (with zero rotation at each joint) was performed to check the values of TCP coordinates and the orientation of end-effector in zero pose of the robot. The resulting TCP coordinates and values of roll-pitch-yaw angles are presented in Table 2. After that, two simulations were carried out. In the first, the robot moved from *zero* to *Home* position. During the second simulation, the robot moves from *zero* to an arbitrary defined pose.

4.1. Motion from *Zero* to *Home* position

The robot needs to move from the *zero* position to its *Home* position for which the vector of joint variables is given by:

$$\mathbf{q} = [0 \quad -90^0 \quad -90^0 \quad 0 \quad 90^0 \quad 0]^T \tag{4}$$

Simulation was performed in such a way that values of rotation in Joint 2, Joint 3 and Joint 5 obtained values defined in Eq. (4) at the time of 10 s.

4.2. Motion from Zero to arbitrary pose

In the second case the robot moves from the *zero* position to an arbitrary pose for which the vector of joint variables is given by:

$$\mathbf{q} = [100^0 \quad -90^0 \quad -60^0 \quad 60^0 \quad -90^0 \quad 90^0]^T \tag{5}$$

Similar to the first simulation, now polynomial trajectory for each joint is set so that joint variables obtain values specified in Eq. (5) at 10 s. The values of TCP coordinates and roll-pitch-yaw angles relative to the base frame are presented in Table 2. These values can also be seen in Figure 3 (screenshot of the model in an arbitrary pose).

Table 2. *The simulation results*

	for *zero* pose: joint variables $\mathbf{q} = [\theta_1\ \theta_2\ \theta_3\ \theta_4\ \theta_5\ \theta_6]^T = [0\ 0\ 0\ 0\ 0\ 0]^T$					
	p_X [m]	p_Y [m]	p_Z [m]	*roll* [deg]	*pitch* [deg]	*yaw* [deg]
Simulation	-0.8172	-0.2329	0.0628	0	0	90
Analytical solution	-0.8172	-0.2329	0.0628	0	0	90
RoboDK	-0.81725	-0.2329	0.0628	0	0	90
	for *Home* pose: joint variables $\mathbf{q} = [\theta_1\ \theta_2\ \theta_3\ \theta_4\ \theta_5\ \theta_6]^T = [0\ -90\ -90\ 0\ 90\ 0]^T$					
	p_X [m]	p_Y [m]	p_Z [m]	*roll* [deg]	*pitch* [deg]	*yaw* [deg]
Simulation	0.4918	-0.1333	0.6872	-90	0	-90
Analytical solution	0.4918	-0.1333	0.6872	-90	0	-90
RoboDK	0.49185	-0.1333	0.6872	-90	0	-90
	for the *arbitrary* pose: joint variables $\mathbf{q} = [\theta_1\ \theta_2\ \theta_3\ \theta_4\ \theta_5\ \theta_6]^T = [100\ -90\ -60\ 60\ -90\ 90]^T$					
	p_X [m]	p_Y [m]	p_Z [m]	*roll* [deg]	*pitch* [deg]	*yaw* [deg]
Simulation	0.08961	0.2595	0.684	100 (1.745 rad)	0	180 (3.142 rad)
Analytical solution	0.0896	0.2595	0.684	100	0	180
RoboDK	0.0896	0.2596	0.684025	100	0	180

The resulting values from all simulations are presented in Table 2 together with analytical solutions of the forward kinematics, calculated using Equations (2) and (3). They are compared with ones obtained using software RoboDK, showing excellent agreement and confirming validity of the geometric and kinematic properties of the developed model and the direct kinematics as well.

5. Conclusion and future work

This paper describes the procedure for development a dynamic model of manipulator in the Simscape Multibody environment of MATLAB/Simulink. First, it has been automatically generated from a step file from Solid Works, and after that, it has been upgraded by MATLAB/Simulink. Performed simulations confirm validity of the model geometric and kinematic properties. Comparison of TCP coordinates and roll-pith-yaw angles that define the end-effector orientation, obtained by simulations with the analytical solution of direct kinematics and ones by using RoboDK, as well, shows excellent agreement.

Analysis of future research trends in the context of Industry 5.0 requirements confirms the potential of the developed dynamic model that can serve as a platform for future research in several directions. First, it is planned to upgrade the dynamic model with motor models and test the dynamic parameters. The resulting dynamic model will be used to plan and optimize the robot's motion (to reduce the time needed to perform work tasks, avoid collisions, etc.). Also, one of the research directions will be the development and testing of control algorithms (for example, hybrid control for the use of robots in the application of polishing, assembly, etc.). The developed model can also be used as an educational platform for learning forward and backward kinematics, dynamic modelling, testing control algorithms, etc.

Finally, one very promising direction of future work is connecting the model via ROS2 and RoboDK with the real robot to make the processes more flexible, human-robot interaction safer, programming more flexible. This means the implementation of the MR concept, which is considered one of the important technologies in Industry 5.0 to make production more flexible, human-centered and resilient, following EC directives.

Acknowledgments

This paper is part of a study within the framework of the project “Improving human-robot interaction in performing various tasks”, founded by the Federal Ministry of Education and Science of Bosnia and Herzegovina.

References

[1] European Commission: Directorate-General for Research and Innovation, Breque, M., De Nul, L. Petridis, A., 2021. Industry 5.0 – Towards a sustainable, human-centric and resilient European industry, Publications Office of the European Union, https://data.europa.eu/doi/10.2777/308407 (accessed 30. July 2025).

[2] Fast-Berglund, Å., Palmkvist, F., Nyqvist, P., Ekered, S., Åkerman, M., 2016. Evaluating Cobots for Final Assembly. Procedia CIRP 44, 175–180.

[3] Huczala, D., Oščádal, P., Spurný, T., Vysocký, A., Vocetka, M., Bobovský, Z., 2020. Camera-Based Method for Identification of the Layout of a Robotic Workcell. Applied Sciences 10, 7679.

[4] Galan-Uribe, E., Morales-Velazquez, L., Osornio-Rios, R.A., 2023. FPGA-Based Methodology for Detecting Positional Accuracy Degradation in Industrial Robots. Applied Sciences 13, 8493.

[5] Miatliuk, K., Wolniakowski, A., Diaz, M., Ferrer, M.A., Quintana, J.J., 2019. Universal robot employment to mimic human writing, 2019 20th International Carpathian Control Conference (ICCC). IEEE, Krakow-Wieliczka, Poland, pp. 1–5.

[6] Kebria, P. M., Al-wais, S., Abdi, H., & Nahavandi, S., 2016. Kinematic and dynamic modelling of UR5 manipulator. In 2016 IEEE International Conference on Systems, Man, and Cybernetics (SMC).

[7] Mu, L., Zhou, Y., Zhao, T., 2021. Cartesian space robot manipulator clamping movement in ROS simulation and experiment. Applied Mathematics and Nonlinear Sciences 6, 43–52.

[8] Semjon, J., Janos, R., Sukop, M., Tuleja, P., Hajduk, M., Jurus, O., Marcinko, P., Virgala, I., Vagas, M., 2020. Verification of the UR5 robot’s properties after a crash caused by a fall of a transferred load from a crane. International Journal of Advanced Robotic Systems 17.

[9] Chen, H., 2023. Motion Control of Interactive Robotic Arms Based on Mixed Reality Development, in: Proceedings of the 2023 6th International Conference on Robot Systems and Applications. ACM, Wuhan China, pp. 86–93.

[10] Arenas-Rosales, F., Martell-Chavez, F., Sanchez-Chavez, I.Y., Paredes-Orta, C.A., 2023. Virtual UR5 Robot for Online Learning of Inverse Kinematics and Independent Joint Control Validated with FSM Position Control. Robotics 12, 23.

[11] Figliolini, G., Lanni, C., Tomassi, L., 2025. Cobot Kinematic Model for Industrial Applications. Inventions 10, 37.

[12] Gingras, S., St-Jean, A., Plante, J.-S., 2025. Preliminary investigation of the design space of geared magnetorheological actuators for safer robotic manipulators. Front. Robot. AI 12, 1581651.

[13] Harrigan, S., Coleman, S., Kerr, D., Quinn, J., Lindsay, L., Madden, K., 2023. Cloud-based Learning for Robot Control, 2023 IEEE International Conference on Industrial Technology (ICIT), Orlando, FL, USA, pp. 1–4.

[14] Clochiatti, E., Scalera, L., Boscariol, P., Gasparetto, A., 2024. Electro-mechanical modeling and identification of the UR5 e-series robot. Robotica 42, 2430–2452.

[15] Ionescu, T.B., Schlund, S., 2019. A Participatory Programming Model for Democratizing Cobot Technology in Public and Industrial Fablabs. Procedia CIRP 81, 93–98.

[16] Pulikottil, T.B., Pellegrinelli, S., Pedrocchi, N., 2021. A software tool for human-robot shared-workspace collaboration with task precedence constraints. Robotics and Computer-Integrated Manufacturing 67, 102051.

[17] Cohodar Husic, M., Lemes, K., Muhamedagic, K., Cekic, A., Begic-Hajdarevic, D., 2024. Improving the performance of industrial production lines based on human-robot collaboration using 3D visualization techniques, Mechanical Technology and Structural Materials 2024, Split

[18] Maciá, N.S., Verdú, C.R., Schmidt, B., Holm, M., 2024. Toward safer Human-Robot collaboration in MR environment. Procedia CIRP 126, 200–205.

[19] Ostanin, M., Yagfarov, R., Klimchik, A., 2019. Interactive Robots Control Using Mixed Reality. IFAC-PapersOnLine 52, 695–700.

[20] Berx, N., Decré, W., Pintelon, L., 2022. Examining the Role of Safety in the Low Adoption Rate of Collaborative Robots. Procedia CIRP 106, 51–57.

[21] Sokovic, M., Bozic, D., Lukic, D., Milosevic, M., Sokac, M., Santosi, Z., 2025. Physical Adaptation of Articulated Robotic Arm into 3D Scanning System. Applied Sciences 15, 5377.

[22] McGovern, R., Athanasopoulos, N., McLoone, S., 2024. Safe Set-Based Trajectory Planning for Robotic Manipulators. IEEE Trans. Robot. 40, 3082–3096.

[23] George, P., Cheng, C.-T., Pang, T.Y., Neville, K., 2023. Task Complexity and the Skills Dilemma in the Programming and Control of Collaborative Robots for Manufacturing. Applied Sciences 13, 4635.

[24] Bavelos, A.C., Dimosthenopoulos, D., Togias, T., Kousi, N., Makris, S., 2022. Integrating AR based operator support features for reconfigurable production systems. Procedia CIRP 106, 276–281.

[25] URDF—Unified Robot Description Format, https://en.wikipedia.org/wiki/URDF (Accessed: 30. July 2025)

[26] Tola, D., Corke, P., 2024. Understanding URDF: A Dataset and Analysis. IEEE Robot. Autom. Lett. 9, 4479–4486.

[27] Feder, M., Giusti, A., Vidoni, R., 2022. An approach for automatic generation of the URDF file of modular robots from modules designed using SolidWorks. Procedia Computer Science 200, 858–864.

[28] Damic, V., Cohodar Husic, M., 2025. Three-Dimensional Visualization of Articulated Mechanisms: Coupling of Their Dynamic and Virtual Models Using the Example of Driving of the Omnidirectional Mobile Robot. Applied Sciences 15, 5179.

[29] The RoboDK software, https://web.robodk.com/web (accessed 30. July 2025).

[30] Williams II, R.L. 2024. Universal Robot URe-Series Cobot Kinematics & Dynamics, https://people.ohio.edu/williams/html/PDF/UniversalRobotKinematics.pdf (accessed 30. July 2025).

[31] Datasheets for UR5e (accessed 30. July 2025). https://www.universal-robots.com/media/1807465/ur5e_e-series_datasheets_web.pdf

[32] Universal robot – DH parameters for calculations of kinematics and dynamics, https://www.universal-robots.com/articles/ur/application-installation/dh-parameters-for-calculations-of-kinematics-and-dynamics/

[33] Siciliano, B., 2010. Robotics: Modelling, Planning and Control, Advanced Textbooks in Control and Signal Processing. Springer London, Limited, London.

[34] Cohodar Husic, M., Ficko, M., Begic-Hajdarevic, D., Persak, T., Cekic, A., Klancnik, S., 2023. An Approach to Dynamic Modelling of Industrial Robots Based on 3D CAD Technique, New Technologies, Development and Application VI, Lecture Notes in Networks and Systems. Springer Nature Switzerland, Cham, pp. 450–458.

[35] 3D CAD model of UR5e in form of step file (accessed 30. July 2025). https://www.universal-robots.com/download/mechanical-e-series/ur5eur7e/robot-step-file-ur5eur7e-e-series/

Experimental and mathematical modeling of surface integrity indicators during the turning of X5CrNi18-10 steel using an advanced MQLC system

***Sabahudin Ekinović*[1], *Edin Begović*[1], *Adnan Mustafić*[2] *and Mario Dragičević*[3]**

1) Faculty of Mechanical Engineering, University of Zenica, Fakultetska 1, Zenica, Bosnia and Herzegovina

2) Faculty of Mechanical Engineering, University of Tuzla, Urfeta Vejzagića 1, Tuzla, Bosnia and Herzegovina

3) Polymetrix AG, Switzerland

Corresponding author: adnan.mustafic@untz.ba

Original scientific article

Abstract: This paper presents a study on the mathematical modeling of surface integrity indicators during semi-dry turning of austenitic stainless steel X5CrNi18-10 (AISI 304), carried out with an advanced minimal quantity lubrication and cooling (MQLC) system. The experiments were performed under controlled laboratory conditions, varying cutting speed, feed rate, depth of cut, and aerosol flow rate according to a full factorial design. Several forms of regression models — linear, exponential, quadratic, and rational — were developed to predict the arithmetic average surface roughness (Ra), the average maximum profile height (Rz), and their ratio (Ra/Rz). The optimal models were selected based on the coefficient of determination, standard error, and analysis of standardized residuals. Among the investigated parameters, feed rate and aerosol quantity emerged as the most influential factors. The findings demonstrate that machining parameters and MQLC process variables can be reliably correlated with surface integrity indicators, offering valuable insights for controlling and optimizing the semi-dry turning process.

Keywords: *Surface Integrity; Semi-dry Machining; Minimal Quantity Lubrication and Cooling (MQLC); Mathematical Modeling*

1. Introduction

Sustainable machining in the manufacturing industry entails systematic changes in the type and quantity of resources used, methods of waste treatment, control of CO_2 emissions, and the overall volume of products produced. It is guided by regulations and sustainability-oriented frameworks, which emphasize the importance of compliance with environmental legislation in the transition toward sustainable production. In a broader context, sustainable manufacturing serves as a core component of sustainable development strategies within the machining sector, aiming to harmonize economic efficiency, environmental responsibility, and social welfare [1],[2]. The principal objective of machining processes is to produce high-quality components in minimal time. In this context, cutting fluids and machining parameters play a vital role. However, the use of conventional cutting fluids introduces serious concerns related to occupational health and environmental degradation. Consequently, the manufacturing industry is increasingly compelled to comply with stringent environmental and safety regulations [3]. It is well-documented that the costs associated with the use and disposal of conventional cutting fluids can be twice as high as the total machining costs. In the case of machining operations involving difficult-to-machine materials, these costs may rise significantly [4],[5]. Ammar et al. [6] conducted an analysis of sustainable machining technologies aimed at reducing the environmental impact associated with the use of conventional cutting fluids. In their study, various types of cutting fluids were examined, with a focus on their functional roles and advantages in machining. The results highlight the economic, environmental, and social aspects of green machining technologies, emphasizing their potential to contribute sustainable manufacturing.
Many researchers [7], [8] and [9] have confirmed that a key factor in ensuring the sustainable stability of the machining process lies in the appropriate selection of the type and quantity of cutting fluids

(CFs), as well as in the optimal combination of cutting parameters, cutting tools, and workpiece materials. Over the past decades, a number of advanced technologies have been developed to enhance the efficiency of machining processes while meeting sustainability criteria. These include cooling with compressed cold air (CCA), cryogenic cooling (CL) using various gases, high-pressure cooling (HPC), minimal quantity lubrication (MQL), combined minimal quantity lubrication and cooling (MQLC), and near-dry machining (NDM), among others. Ekinović et al. [10] conducted an investigation into the MQLC turning process of X5CrNi18-10 stainless steel, with the aim of identifying and selecting the most critical MQL parameters influencing the machinability of austenitic stainless steel. The results revealed that the most significant parameters for simultaneously reducing surface roughness and cutting forces were the oil and water flow rates, followed by the spray distance.

Dragicevic et al. [11] have investigated the influence of different MQLC parameters on the surface roughness and resultant cutting force during turning of St 50-2 steel. An experimental study was conducted to investigate the influence of key process parameters, specifically oil and water flow rates, on the cutting force F_{rez} and surface roughness Ra. The results have shown that oil flow parameter with 91.67% of contribution is more significant on the resultant cutting force than the water flow with 2.52% of contribution. In the case of surface roughness, it can be observed that the oil flow with 70.79% of contribution is more significant than the water flow with 6.66% of contribution. Kvrgić et al. [12] have investigated the influence of cutting parameters and cooling techniques on the corrosion resistance of AISI 316L austenitic stainless steel. The machining experiments were carried out using constant cutting speed (Vc), feed rate (f), and depth of cut (ap), while applying different cooling strategies: minimal quantity lubrication (MQL), minimal quantity lubrication combined with tube cooling (MQL-TC), and conventional emulsion cooling. The surface quality of AISI 316L stainless steel were quantified by Ra and Rz. The results have shown that the lowest roughness values, Ra = 0.4415 µm and Rz= 2.3950 µm, were achieved with the use of emulsion, suggesting that emulsion provides the finest surface finish. Machining with MQL Ra = 0.7425 µm and Rz= 3.9250 µm and the combination of MQL + Vortex cold compressed air Ra = 0.8417 µm and Rz= 4.0600 µm showed the higher roughness.

This paper presents a study on the mathematical modeling of surface integrity indicators during semi-dry turning of austenitic stainless steel X5CrNi18-10 (AISI 304), carried out with an advanced minimal quantity lubrication and cooling (MQLC) system.

2. Experimental setup

The experiments were performed on a conventional PA-501A Potisje lathe in the Laboratory for Metal Cutting (LORAM) at the University of Zenica. A commercial Iscar IC807 grade TiAlN + TiN-coated carbide insert (CNMG120408-WG) with a tool nose radius of 0.8 mm was selected for the turning tests. To minimize the influence of tool wear on the measured results, a fresh cutting edge was used for each experimental run. The workpiece material was a quenched and tempered X5CrNi18-10 (AISI 304) austenitic stainless steel. All machining tests were carried out on a bar with a diameter of 70 mm, separated into 15 mm long segments for each cutting test. The system used for aerosol formation in the MQLC technique was the JOOM (Jet Oil on Water Mist, OoW) manufactured by Daido Metal-Japan. The MQLC system type J-T2X-012-2K-T generates an aerosol in the form of water droplets coated with an oil film. This system allows independent adjustment of oil and tap water delivery rates in the ranges of 10–50 ml/h and 300–1800 ml/h, respectively. The aerosol, composed of tap water and a biodegradable MQL oil with a kinematic viscosity of 39 mm²/s (Castrol Hyspray V1066), was generated at a pressure of 2 bar and delivered into the cutting zone through a single nozzle positioned at an angle of approximately 30° relative to the rake face and at a distance of 30 mm from the tool. Figure 1 presents the experimental setup used in the turning tests.

For the purpose of quantitative measurement of the surface roughness indicators of the machined surface a mobile device of the Mitutoyo Surftest SJ-301 type was used in the laboratory at the Faculty of Mechanical Engineering in Tuzla. Before the measurement, the device was set for the planned measurement of parameters according to DIN 1990 (DIN EN ISO 4287: 1998) standard. The adopted

reference test length for all measurement tests was 4 mm for the selected profile filter lc = 0.8mm × 5. A total of five measurements were performed for each processed segment at different locations, and the arithmetic mean was adopted as a reference value for data processing. An example of roughness measurement and printed measurement report is shown in Figure 2.

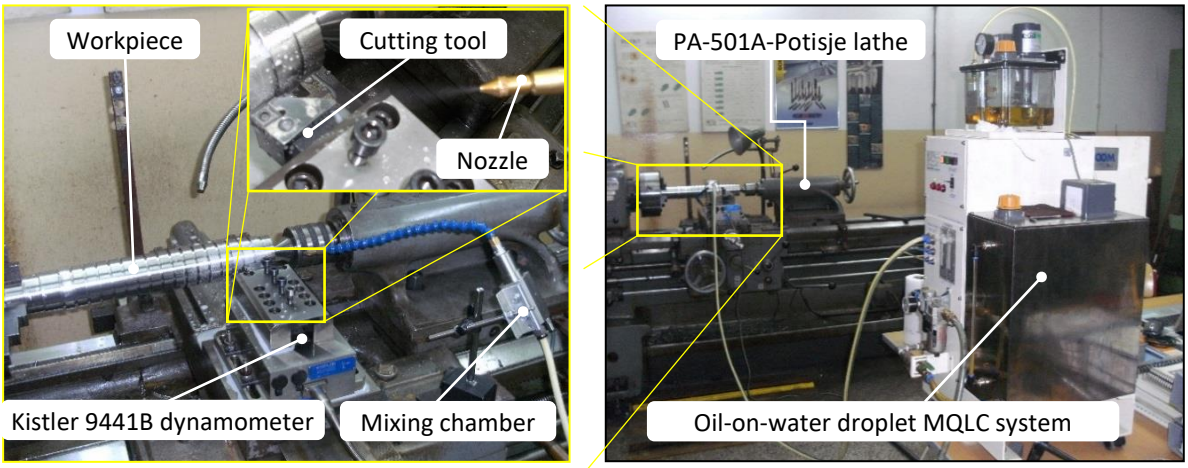


***Figure 1**. Experimental setup for the MQLC assisted turning test*

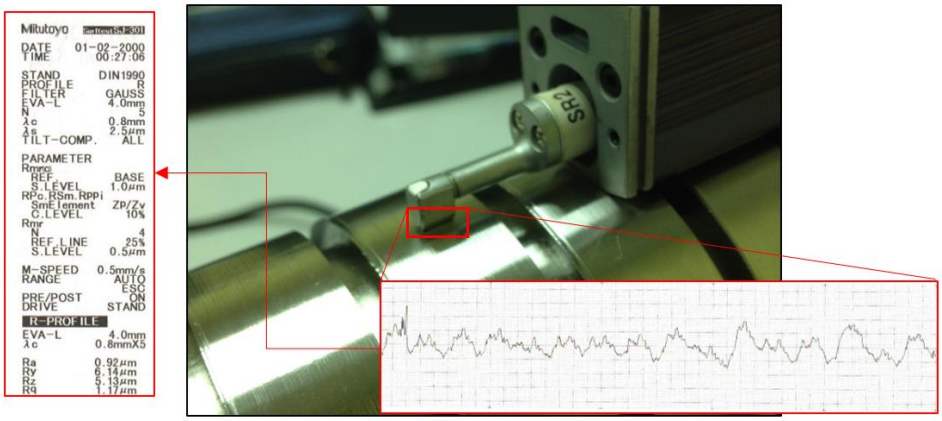


***Figure 2.** Surface roughness measurement of the treated surface using the Mitutoyo SJ-301*

The selected machining and MQLC parameters, cutting speed (Vc), feed rate (f), depth of cut (ap), and aerosol quantity (Q) were considered as input parameters. The values of process parameters were based on the recommendations of the cutting tool manufacturer and the preliminary experiments for the tested material. The cutting parameters and their levels are given in Table 1.

***Table 1.** Machining and MQLC parameters and their levels*

Parameter	Symbol	Notation	Units	Level values		
				-1	0	1
Cutting speed	A	Vc	m/min	57	108	159
Feed rate	B	f	mm/rev	0.04	0.196	0.357
Depth of cut	C	ap	mm	0.2	1	1.8
Aerosol flow rate	D	Q	ml/h	350	1080	1810

A full-factorial design with replication at the central point (2^k+n_0) was employed. The experimental design matrix, along with the measured results of the selected surface integrity indicators is

summarized in Table 2. To avoid systematic errors, all experiments were conducted in a randomized sequence.

Table 2. *Design matrix and measured data of responses*

Experiment number	Levels of cutting parameters				Measured data of responses		
	A	B	C	D	*Ra* (μm)	*Rz* (μm)	*Ra/Rz* (/)
1	-1	-1	-1	-1	0.390	2.416	0.161
2	1	-1	-1	-1	0.510	3.206	0.159
3	-1	1	-1	-1	0.883	4.716	0.187
4	1	1	-1	-1	1.230	6.286	0.195
5	-1	-1	1	-1	0.630	3.890	0.161
6	1	-1	1	-1	0.600	3.933	0.152
7	-1	1	1	-1	0.963	5.896	0.163
8	1	1	1	-1	1.080	6.170	0.175
9	-1	-1	-1	1	0.523	3.146	0.166
10	1	-1	-1	1	0.850	4.913	0.173
11	-1	1	-1	1	0.980	5.206	0.188
12	1	1	-1	1	1.743	7.276	0.239
13	-1	-1	1	1	0.650	3.573	0.181
14	1	-1	1	1	0.820	4.853	0.169
15	-1	1	1	1	1.436	7.056	0.203
16	1	1	1	1	1.860	7.690	0.242
17	0	0	0	0	0.946	4.900	0.193
18	0	0	0	0	0.910	5.310	0.171
19	0	0	0	0	1.030	5.390	0.191

3. Analysis of experimentally measured results

As previously mentioned, the surface roughness parameters were measured according to DIN 1990 (DIN EN ISO 4287: 1998) standard. A total of five measurements were performed for each processed segment at different locations, and the arithmetic mean was adopted as a reference value for data processing. Graphical interpretation of the measured roughness parameters is given in Figure 3.

Based on the presented influence of the varied parameters on the arithmetic mean deviation of the profile, it is evident that all varied factors exhibit direct proportionality. This observation is consistent with theoretical expectations as well as with experimental findings reported in other studies. Nevertheless, it is particularly interesting to examine the effect of the total amount of generated aerosol on the arithmetic mean deviation of the profile. It was found that a lower amount of generated aerosol resulted in improved performance with respect to all measured surface roughness indicators, and consequently, in the overall quality of the machined parts. Considering the capability of the

applied MQLC system to independently dose the quantities of oil and tap water, the minimal level of total generated aerosol (350 ml/h) in this study was obtained using 50 ml/h of biodegradable MQL oil and 300 ml/h of tap water. Conversely, the maximum total aerosol flow rate of 1810 ml/h was achieved with a ratio of 1800 ml/h of tap water to 10 ml/h of MQL oil. These observations indicate that a higher percentage of MQL oil in the generated aerosol leads to superior surface quality, whereas the opposite holds true for higher tap water content.

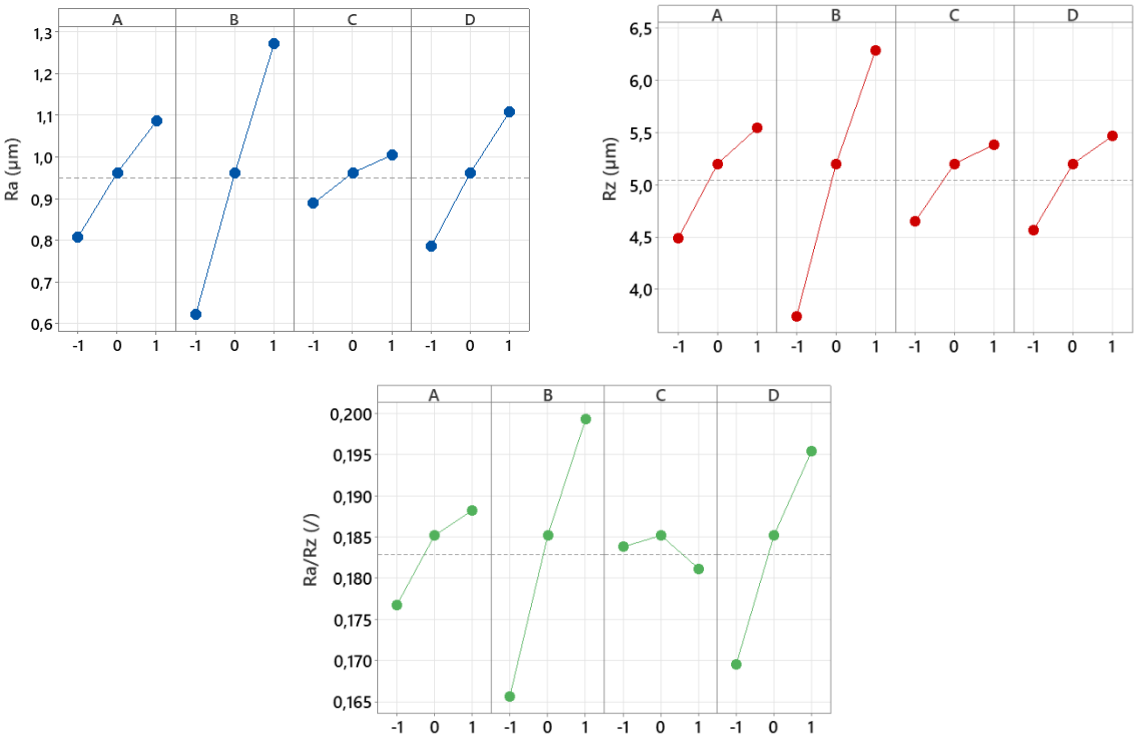


Figure 3. *Main effect plot for the measured data*

Regression analysis model the relationship between a dependent variable and one or more independent variables. The test results were employed to achieve the mathematical models by using first-order model. A first-order model can be expressed by equation (1):

$$y_M = b_0 + \sum_{i=1}^{k} b_i x_i + \sum_{1 \le i < m \le k} b_{im} x_i x_m + \sum_{1 \le i < m \le k} b_{imk} x_i x_m \, x_k \qquad (1)$$

where ''y_M'' is the corresponding response, and x_i are the values of the machining parameters. The term b_0, b_i, b_{im}, b_{imk} is the regression coefficient.

Analysis of variance (ANOVA) was conducted at a 95% confidence level to identify the parameters with a statistically significant influence on the measured response values. By eliminating all statistically insignificant interactions and performing a subsequent analysis, the results of the regression analysis for a simple linear model were obtained, including only statistically significant variables at the selected 5% significance level. Although the triple interaction (B × C × D) was statistically significant, it was excluded from the final model due to its low contribution of 1.68% to the total variation of the arithmetic mean deviation. The results of the ANOVA analysis, after the elimination of insignificant parameters are presented in Table 3.

Table 3. *ANOVA for Ra – linear regression function*

Source	DF	Adj SS	Adj MS	F-Value	P-Value
Regression	8	2.75431	0.34429	43.57	0.000
A	1	0.31304	0.31304	39.61	0.000
B	1	1.69130	1.69130	214.03	0.000
C	1	0.05406	0.05406	6.84	0.026
D	1	0.41474	0.41474	52.48	0.000
A*B	1	0.07076	0.07076	8.95	0.014
A*C	1	0.04796	0.04796	6.07	0.033
A*D	1	0.07981	0.07981	10.10	0.010
B*D	1	0.08266	0.08266	10.46	0.009
Error	10	0.07902	0.00790		
Lack-of-Fit	8	0.07144	0.00893	2.35	0.332
Pure Error	2	0.00758	0.00379		
Total	18	2.83333			

The mathematical models were also controlled through a numerical method by using the coefficient of determination R^2 adjusted coefficient of determination R^2adj, and predicted coefficient of determination R^2pred. Hence, the R^2 of the developed regression model is higher than 80%, in this case 97.21%. In the regression analysis, high R^2 with acceptable R^2_{pred} should be between 0.8 and 1 [13]. In this work, the R^2 value is high and very close to 1, which is desirable. Therefore, results from the coefficients of determination (R^2) indicate that mathematical models can be successfully applicable to predict the response. Each of the variables from the set of experimentally measured data (Table 2.) was related to the machining parameters and MQLC system parameters using multiple regression models, including linear, exponential, quadratic, and rational. The essence of the individual analysis of the experimentally measured data, alongside the formulation of regression equations, is also to obtain additional statistical indicators that provide insight into the significance of the variables and the adequacy of the models. The results of the regression analysis for *Ra* for a larger number of regression equations are presented in Table 4.

Table 4. *Multiple regression functions for Ra*

Response	Regression Function	Mathematical model and coefficients of determination
Ra	Linear	$Ra = 0.949 + 0.1399 \cdot A + 0.325 \cdot B + 0.058 \cdot C + 0.161 \cdot D + 0.0665 \cdot A \times B - 0.0548 \cdot A \times C + 0.07 \cdot A \times D + 0.072 \cdot B \times D$
		(R^2=97.21%; R^2_{adj}=94.98%; R^2_{pred}=87.17%)
Ra	Exponential	$Ra = e^{(-0.132+0.1386 \cdot A+0.354 \cdot B+0.0767 \cdot C+0.159 \cdot D-0.069 \cdot AC+0.0554 \cdot A \times D)}$
		(R^2=96.09%; R^2_{adj}=94.14%; R^2_{pred}=90.18%)
Ra	Quadratic	$Ra = (0.96 + 0.068 \cdot A + 0.167 \cdot B + 0.0325 \cdot C + 0.0783 \cdot D - 0.0303 \cdot A \times C + 0.031 \cdot A \times D)^2$
		(R^2=95.14%; R^2_{adj}=92.71%; R^2_{pred}=86.24%)
Ra	Rational	$Ra = \frac{1}{1.236 - 0.1635 \cdot A - 0.4305 \cdot B - 0.1214 \cdot C - 0.1884 \cdot D}$
		(R^2=86.33%; R^2_{adj}=82.43%; R^2_{pred}=74.25%)

In addition to the values of the coefficients of determination and the standard error, the criterion for selecting the best regression model should also consider the nature and range of the residual deviations as well as their conformity to normality, i.e., the linear distribution of the standardized residuals. The graphical representation of the residuals and standardized residuals relative to the regression, along with the conformity of the standardized residuals to a normal distribution for the arithmetic mean deviation of the profile, is shown in the diagrams in Figure 4. The nature and range of the standardized residuals, together with their linear distribution for the selected regressions of the arithmetic mean deviation of the profile, indicate a concentration around the central line, suggesting that all of the considered models can be regarded as adequate.

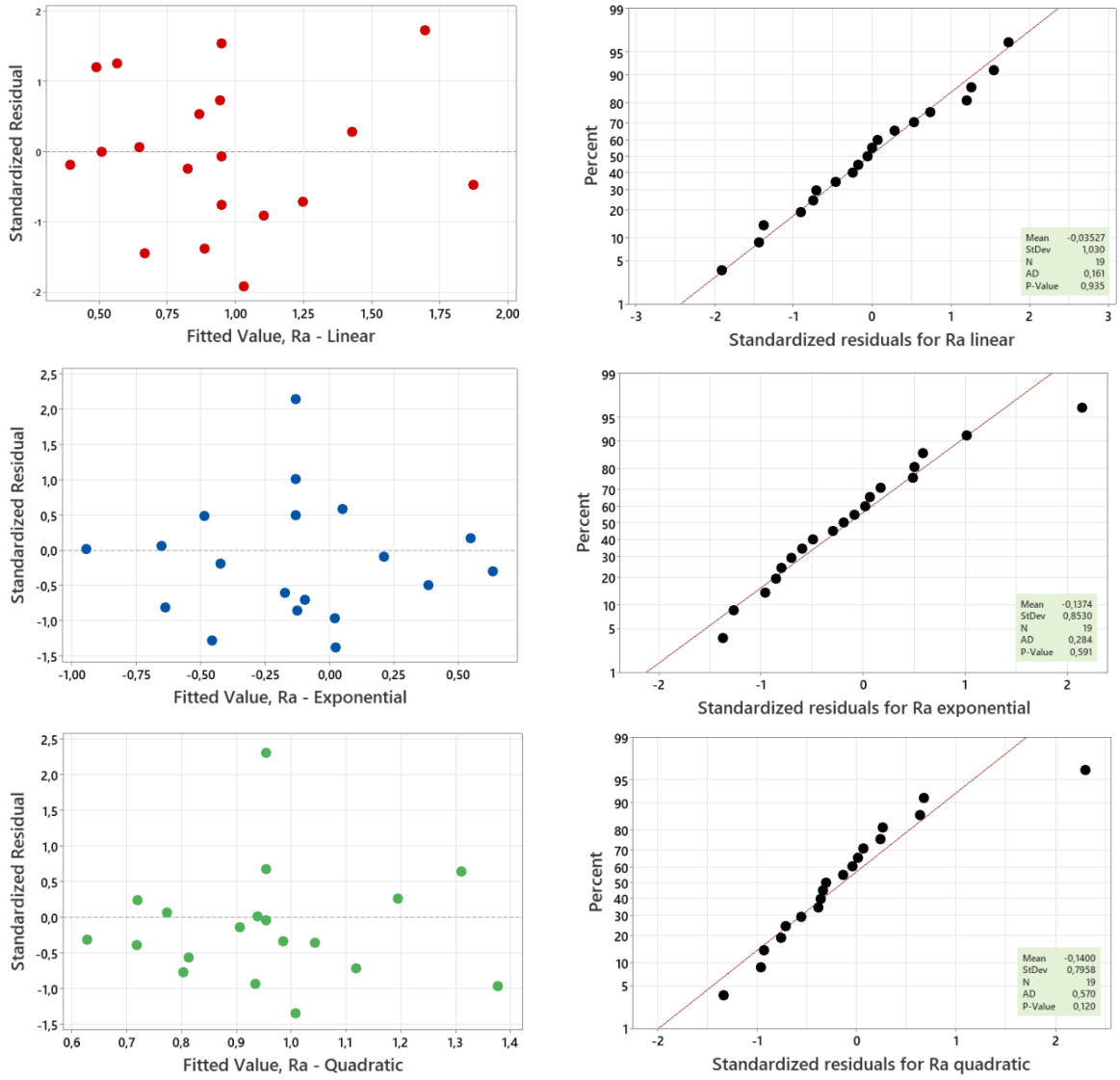


Figure 4. *Graphical interpretation of standardized residuals for different regression functions of Ra*

Considering all of the above, the linear regression model was selected as the most appropriate. This choice is supported on one hand by the high values of the coefficient of determination and the prediction coefficient of determination, and on the other hand by the most favorable results from the graphical interpretation of the residual deviations. Therefore, by summarizing all the presented statistical indicators regarding the significance of the regression coefficients and the adequacy of the formulated models, the following expression is proposed for a reliable estimation of the arithmetic mean deviation of the profile during minimal quantity lubrication and cooling (MQLC) machining of austenitic steels within the considered parameter variation range:

$$Ra = 0.949 + 0.1399 \cdot A + 0.325 \cdot B + 0.058 \cdot C + 0.161 \cdot D + 0.0665 \cdot A \times B - 0.0548 \cdot A \times C + 0.07 \cdot A \times D + 0.072 \cdot B \times D \quad (2)$$

In other words, by expressing Equation (2) in an alternative (decoded) form, it can also be represented as Equation (3):

$$Ra = 0.321 + 0.0005 \cdot Vc + 0.492 \cdot f + 0.2176 \cdot ap + 00.000108 \cdot Q + 0.00823 \cdot Vc \times f - 0001342 \cdot Vc \times ap + 0.00002 \cdot Vc \times Q + 0.000621 \cdot f \times Q \quad (3)$$

Based on the results of the regression analysis for Equation (3), the interaction between the machining regime parameters and the cooling and lubrication system parameter contributes a relatively small portion to the variation of the arithmetic mean deviation of the profile. Specifically, regardless of the presence of statistically significant interactions included in the regression model, the dominant influence on the experimentally measured variable arises from the partial effects, which account for a total of 87.29%. Among these, the largest contribution comes from the feed rate, representing 59,69%, which rightly positions it as the most dominant parameter not only for the arithmetic mean deviation of the profile but also for other surface roughness indicators. The second most influential factor is the quantity of generated mist, with a contribution of 14.64%, while the cutting speed and depth of cut are ranked third and fourth, respectively. As expected, the feed rate exerts the most dominant influence on the variation of the arithmetic mean deviation and should therefore be ranked as the primary contributing factor. Using a similar approach, regression analysis was performed for several different regression functions for the mean roughness depth parameter *Rz*. The results of the developed regression functions are presented in the Table 5:

Table 5. *Multiple regression functions for Rz*

Response	Regression Function	Mathematical model and coefficients of determination
Rz	Linear	$Rz = 5.043 + 0.527 \cdot A + 1.273 \cdot B + 0.368 \cdot C + 0.45 \cdot D - 0.248 \cdot A \times C + 0.192 \cdot A \times D$
		(R^2=96.8%; R^2_{adj}=95.20%; R^2_{pred}=91.30%)
Rz	Exponential	$Rz = e^{(1.575+0.112 \cdot A+0.265 \cdot B+0.085 \cdot C+0.0913 \cdot D-0.0564 \cdot A \times C)}$
		(R^2=93.81%; R^2_{adj}=91.42%; R^2_{pred}=86.31%)
Rz	Quadratic	$Rz = (2.22 + 0.1204 \cdot A + 0.2885 \cdot B + 0.087 \cdot C + 0.1 \cdot D - 0.0584 \cdot A \times C)^2$
		(R^2=95.18%; R^2_{adj}=93.32%; R^2_{pred}=89.18%)
Rz	Rational	$Rz = \frac{1}{0.217 - 0.026 \cdot A - 0.059 \cdot B - 0.022 \cdot C - 0.02 \cdot D}$
		(R^2=84.04%; R^2_{adj}=79.48%; R^2_{pred}=69.15%)

The parameter of mean roughness height is best described by a linear regression function, exhibiting a high coefficient of determination of R^2 = 96.8%. Therefore, for a reliable estimation of the mean roughness height within the considered range of machining regime parameters under the application of an advanced cooling and lubrication system, the following expression is proposed in Equation:

$$Rz = 1.153 + 0.011 \cdot Vc + 8.031 \cdot f + 1.117 \cdot ap + 0.00006 \cdot Q - 0.006 \cdot Vc \times a + 5 \cdot 10^{-6} \cdot Vc \times Q \quad (4)$$

The effects and behavior of the input variables on the mean roughness height show a complete correlation with the results for the arithmetic mean deviation of the profile.
However, it should be noted that one of the limitations of amplitude-based surface integrity parameters is that surfaces with different topographies can exhibit identical parameter values. In other words, determining these parameters alone does not provide complete information about the shape and size of the surface irregularities. For a more comprehensive analysis of the machined surface roughness, it is therefore necessary to consider additional supplementary indicators.
From the set of output variables, in addition to the amplitude-based roughness parameters (according to the DIN EN ISO 4287 standard), hybrid parameters were also selected, which specifically reflect the wear-related characteristics of the surface. Theoretically, the ratio of the arithmetic mean deviation of the profile to the mean roughness height (Ra/Rz) can be interpreted as a measure of the machined surface roughness, representing one manifestation of the cutting process as a function of the machining regime. The machining conditions, in interaction with auxiliary tools, govern “internal” phenomena such as forces, energy, vibrations, and wear. Therefore, the (Ra/Rz) ratio is considered as a supplementary indicator of surface integrity. Moreover, the numerical value of (Ra/Rz) provides insight into the surface profile shape, indicating either a pointed profile (Ra/Rz ≈ 0) or a flattened profile (Ra/Rz ≈ 1).
From the previously presented diagram on Figure 3., it is evident that all parameters exhibit a direct proportionality, except for the depth of cut. In terms of influence, the most significant factors are the feed rate, the aerosol quantity, the cutting speed, and, finally, the depth of cut.
Using a similar approach, regression analysis was performed for several different regression functions for the Ra/*Rz* ratio. It was found that this relationship is best described by a rational function, with coefficient of determination of R^2 = 81.52%, as represented by the Equation (5):

$$\frac{Ra}{Rz} = \frac{1}{6.397 + 0{,}0026 \cdot Vc - 0.31 \cdot f - 0.00049 \cdot Q - 0.0249 \cdot Vc \times f} \tag{5}$$

4. Conclusion

The experiment, model development, and subsequent analysis of the results come up with the following concluding remarks:

1. The factorial design and subsequent regression analysis demonstrated that all machining and MQLC system parameters exhibit a statistically significant influence on the surface roughness indicators. Among them, the feed rate and the aerosol quantity were identified as the dominant factors for Ra, with contributions of 65.64% and 13.22%, respectively.
2. Practically applicable regression models were developed for Ra, Rz, and Ra/Rz, exhibiting high coefficients of determination (R^2 = 97.21.%, R^2 = 96.8%, and R^2 = 81.52%, respectively). Ra and Rz were most accurately described by linear functions, whereas Ra/Rz was best represented by a rational function.
3. A higher proportion of MQL oil in the generated aerosol proved beneficial for improving surface quality. Under finishing conditions, the application of a minimal total aerosol flow rate (350 ml/h, composed of 50 ml/h MQL oil and 300 ml/h tap water) yielded favourable results compared to the maximum aerosol level (1810 ml/h, with 10 ml/h oil and 1800 ml/h tap water).In this regard, Ra and Rz are best described by a linear function, whereas the Ra/Rz ratio is most accurately represented by a rational function.
4. Overall, the findings confirm that the integration of optimized aerosol composition with minimal flow rates, combined with suitable machining regimes, can ensure reliable prediction and improvement of surface integrity in the semi-dry machining of austenitic steels.

References

[1] Tao, H., Niancong, L., Huazheng, X., Long, W., Yu, Z., Daigang, L., Yun, C., 2023. Progress and trend of minimal quantity lubrication (MQL): A comprehensive review, Journal of Cleaner Production, Volume 386, 135809.
[2] Gupta, K., 2020. A Review on Green Machining Techniques, Procedia Manufacturing, Volume 51, 2020, Pages 1730-1736.
[3] Donghui, L., Tao, Z., Tao, Z., Nan, Z., and Zhen, L., 2024. A comprehensive review of minimal quantity lubrication (MQL) machining technology and cutting performance, The International Journal of Advanced Manufacturing Technology, Volume 133, pages 2681–2707.
[4] Sk, M. A., Muhammad P. J., Rakurty, C.S., Nithin, R., Jianfeng, M., 2024. Cutting fluids in metal AM: A review of sustainability and efficiency, Journal of Manufacturing Processes, Volume 106, 24 November 2023, Pages 51-87.
[5] Shuoshuo, P.,Wenxiang, Z., Tianyang, Q., Weiliang, L., Pei, Y.,Li., Xibin, Wang. 2023. Effect of Cutting Fluid on Milled Surface Quality and Tool Life of Aluminum Alloy, Materials 2023, 16(6), 2198; https://doi.org/10.3390/ma16062198
[6] Ammar, E., Ali B.M., Amal, S., Hosam, F., Albraa, A. A., Abdullah, M. M., Walaa, A. E., Ahmed A. E. A., Ninshu, M., 2024. A review on sustainable machining: Technological advancements, health and safety considerations, and related environmental impacts, Results in Engineering, Volume 24, December 2024, 103042.
[7] Chin, K. G., Pay, J. L., Kin Y. L., Jiwang, Yan., 2024. Biodegradable cutting fluids for sustainable manufacturing: a review of machining mechanisms and performance, The International Journal of Advanced Manufacturing Technology, Volume 131, pp. 955–975.
[8] Javvadi, E. M., Nitin, A., Chetan, N., Naveen, K. G., Hari, K. C., 2025. Sustainable machining: enhancing performance with vegetable oil-based nano cutting fluids, Discover Materials, Volume 5, article number 63.
[9] Xiangcheng, L., Shujing, W., Dazhong, W., Yixin, Y., Qinglong, A., Changhe, L., 2024. Sustainable development of cutting fluids: The comprehensive review of vegetable oil, Journal of Cleaner Production, Volume 473, 143544.
[10] Ekinović, S., Begović, E., Mehmedović, M., Mustafić, A., 2018. Taguchi Based Screening Approach in the MQL Turning Process of X5CrNi18-10 Stainless Steel, Journal of Trends in the Development of Machinery and Associated Technology Vol. 21, No. 1, ISSN 2303-4009 (online), 5-8.
[11] Mario, D., Edin, B., Sabahudin, E., Ivan P., 2023. Multi-Response Optimization in MQLC Machining Process of Steel St50-2 Using Grey-Fuzzy Technique, Technical Gazette 30, ISSN 1330-3651 (Print), ISSN 1848-6339 (Online).
[12] Kvrgić, D., Šterpin Valić, G., Fonović, M., Cukor, G., 2024. Influence of cutting fluids on the corrosion resistance of X2CrNiMo17-12-2 austenitic stainless steel, 13 International Conference Mechanical Technologies and Structural Materials 2024 (MTSM 2024), pp. 251-263.
[13] Kuram, E., Tasci, E., Altan, AI., 2013. Investigating the effects of recycling number and injection parameters on the mechanical properties of glass-fibre reinforced nylon 6 using Taguchi method. Material Design 2013; Vol. 49: pp. 139– 150.

Evaluation of the self-study modules developed in ExCurS project

***Nikola Gjeldum*[1], *Boženko Bilić*[1], *Marko Mladineo*[1], *Marina Crnjac Žižić*[1] *and Amanda Aljinović Meštrović*[1]**

1) University of Split, Faculty of Electrical Engineering, Mechanical Engineering and Naval Architecture, R. Boskovica 32, 21000 Split, Croatia

Corresponding author: ngjeldum@fesb.hr

Original scientific article

Abstract: The Industry 4.0/5.0 era implies acquirement of new knowledge on digital, process improvement based on lean methodology technologies and digital transformation, sustainability and green approaches in the business. It represents significant effort for the enterprises to acquire all this knowledge, especially for small and medium-sized enterprises. Therefore, ExCurS project was initiated to bridge this knowledge gap by developing On-line platform with Self Assessment Tool, Concept of blended learning and Complementary resources. One of the most important aspects of this platform is more than 50 self-study modules that have been developed in the project. This paper uses scientific methodology of questionnaire to evaluate a dozen of self-study modules in a kind of validation process. Large sample of participants has been interviewed on the success rate of acquiring the knowledge of the self-study modules they've been learning. The results of analysis of 12 self-study modules are presented in this paper.

Keywords: *ExCurS project; Lean-green; SMEs; Digital transformation; Sustainability*

1. Introduction

Small and medium-sized enterprises (SMEs) are a key segment for economic growth and stability in most economies. This is underpinned by the fact that SMEs account for around 90% of global economic activity and 50-60% of total employment in the world [1]. In the modern business environment, these enterprises face two major challenges: firstly, the ever-increasing pressure to adapt to rapid digital transformation and secondly, the requirements to achieve the triple bottom line of sustainability, i.e. environmental, economic and social sustainability. In this context, with the European Green Deal and the EU Industrial Strategy, the European Union has set clear targets for environmental protection and the reduction of harmful gas emissions, as well as an accelerated transition to a circular economy with a focus on resource efficiency and digital resilience. These objectives have a direct impact on the activity of SMEs, which must adapt their processes to remain competitive and comply with the new environmental regulations that will be imposed on them in the future, considering that SMEs are responsible for 60-70% of hazardous emissions in the world [2], [3]. Although the COVID-19 pandemic has accelerated the transition to digital solutions and remote working [4], many companies are still only using information and communication technologies to support existing processes and are not taking full advantage of the digital environment.

The digital transformation of SMEs must be gradually integrated into the company and be multidimensional. This means that it requires a complete transformation of business processes, which should be based on the continuous improvement of technical, organizational and individual aspects and not only on the integration of suitable technologies or automation [5], [6], [7]. By combining advanced technologies and sustainability strategies, SMEs have the opportunity to increase their resilience, reduce waste and move towards circular and regenerative business models. In this sense, the digital and sustainable transformation of companies is no longer just an advantage, but also a strategic necessity for SMEs that want to grow and survive in a dynamic global environment [8], [9]. However, this transition is slowed down by numerous obstacles. Among the most common are limited financial resources leading to difficulties in investing in the infrastructure and technology required for

digital transformation, lack of strategic planning, shortage of skilled labour and lack of management willingness to innovate [10], [11]. One of the possible solutions that SMEs can use to respond to the above challenges is to adopt lean and green practices. Lean and green practices represent an operational strategy that enables companies to simultaneously achieve the desired economic goals and improve their sustainability performance [12], [13]. Lean tools focus on process optimization, waste reduction and value creation for the customer, while the green economy emphasizes the importance of efficient resource use, waste reduction and environmental responsibility. Together, these tools form a strategic platform through which digital tools are selected and implemented to achieve the desired goals, Figure 1. Digital transformation without lean-green compliance often leads to fragmented or short-term changes [14].

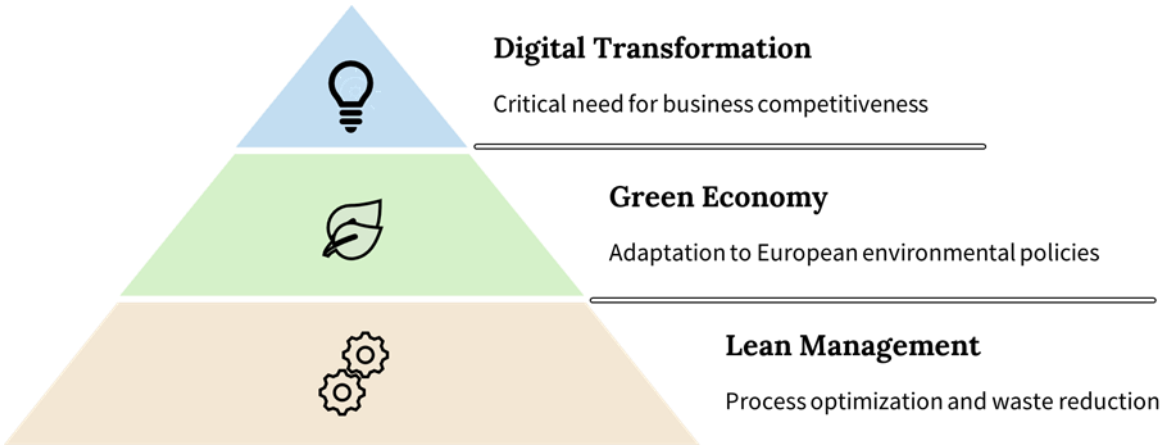


Figure 1. *Lean-green management skills as the basis for long-term digital transformation*

Due to the great diversity of SMEs and the specific challenges faced by each individual company, the need for a tailored approach to their digital transformation that is adapted to their unique characteristics, resources and individual needs has been recognised [9], [14]. Considering all these challenges and needs, it becomes clear that targeted tools and methodological approaches are crucial for a successful digital and sustainable transformation of SMEs. In response to these needs, An excellence-based curriculum to improve LEAN & GREEN management skills in SMEs, the ExCurS project, was launched in 2022.

The ExCurS project is oriented to the European SMEs and aimed to support companies through the development of an integrated digital platform based on self-assessment and flexible self-study modules. This platform will enable SMEs to identify transformation needs at an individual level and explore the opportunities of the green economy and digitalization.

2. ExCurS Project – short description

The ExCurS project [15] is an initiative funded by the Erasmus+ programme that aims to create a vocational training programme focusing on lean and green management skills for European SMEs. The expected duration of the project is 36 months and the implementation period is from 2022 to 2025. Six organisations from five different European countries and sectors are involved in the project. The project is coordinated by Gaia (Spain), the Knowledge and Technology Industries Association, which represents more than 304 companies from the ICT sector. The five partners come from the academic community: University of Reutlingen (Germany) and University of Split (Croatia) and from the business community: IBK Management Solutions (Germany), Irish Work Study Institute (Ireland) and Mindpedia (Romania). The diversity of the partners, including different work cultures, economic sectors, professional and scientific knowledge, and their international cooperation contribute to the creation of a comprehensive educational programme and open up the possibility of networking numerous companies in different European regions.

In order to achieve the project objectives, the project focuses on the development of a comprehensive digital and green transition tool, which includes three key intellectual outputs that will be developed sequentially during the project lifetime (Figure 2):

- Self-assessment tool,
- Concept of blended learning,
- Online platform.

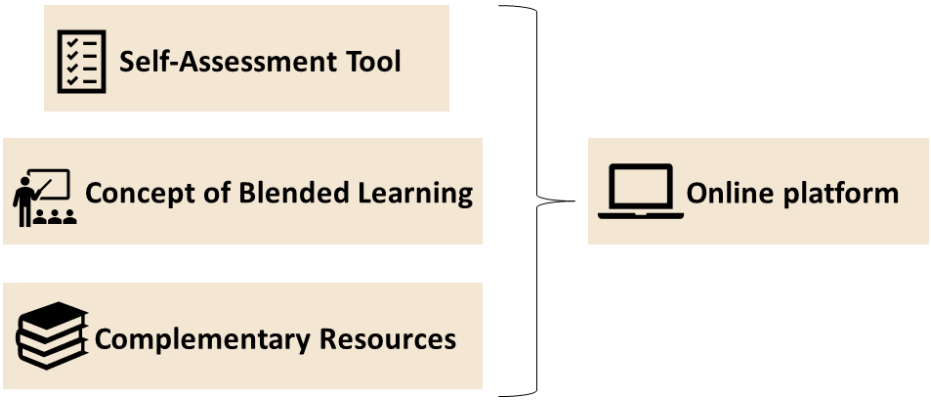


Figure 2. *Expected outcomes of the ExCurS project*

The Self Assessment Tool is a series of self-assessment tools developed on the basis of the EFQM 4.0 Excellence Model (European Foundation for Quality Management, EFQM). This tool was developed with the aim of enabling SMEs to recognise their own weaknesses and encourage them to independently identify opportunities for improvement in order to achieve digital transformation and environmental sustainability.

The Online platform is a validated digital environment that combines self-assessment tools, best practice examples and training content. It is available at regional, European, organisational and individual level. The platform is multilingual, easy to use, interactive and designed to support users in learning, analysing and implementing lean and green strategies in organisations.

The Concept of blended learning is a training concept aimed at managers and employees. It is based on the principles of learning through work, which develops professional, cognitive and digital skills.

These three intellectual outputs complement each other and form a logical and integrated system to promote the digital and green transformation of SMEs. The self-assessment tool serves as a starting point to lay the foundations, i.e. companies can identify their needs and weaknesses and determine which resources and modules are important to them. The online platform brings everything together and guides users to training courses that enable concrete skills development.

In addition to these main intellectual components, the project will also produce a number of Complementary resources that will further facilitate the application and customisation of the developed tools in real business and educational contexts. These resources include a library, a glossary, guidelines for trainers and other important documents.

In the long term, the ExCurS project makes a multidimensional contribution to the development of small and medium-sized enterprises, the improvement of education systems and the achievement of the objectives of the European Green Deal through four key levels of impact: organizational, educational, environmental and collaborative, Figure 3.

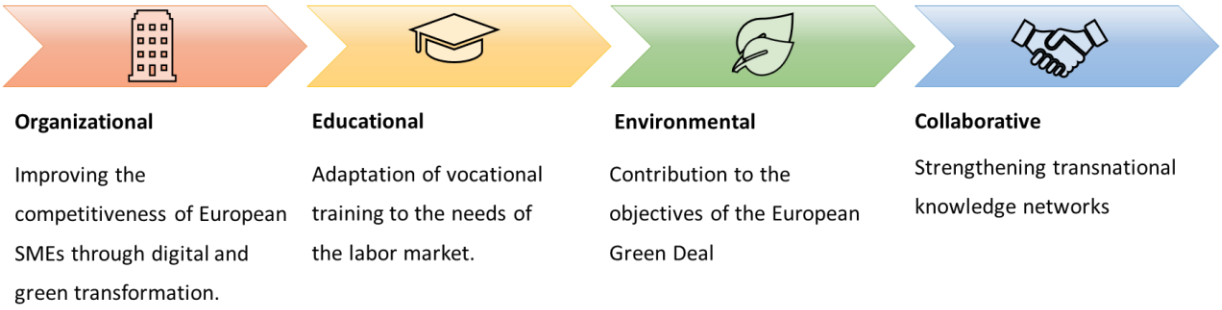


Figure 3. *Expected long-term results of the ExCurS project*

To ensure the effectiveness of these tools and their relevance to the real business environment, they have been developing and disseminating throughout the project, which consists of five work packages. However, one of the important aspects is the evaluation of the tools, especially the evaluation of the developed self-study modules (Figure 4). It is a kind of validation process for the self-study modules that can help further improvement of the modules.

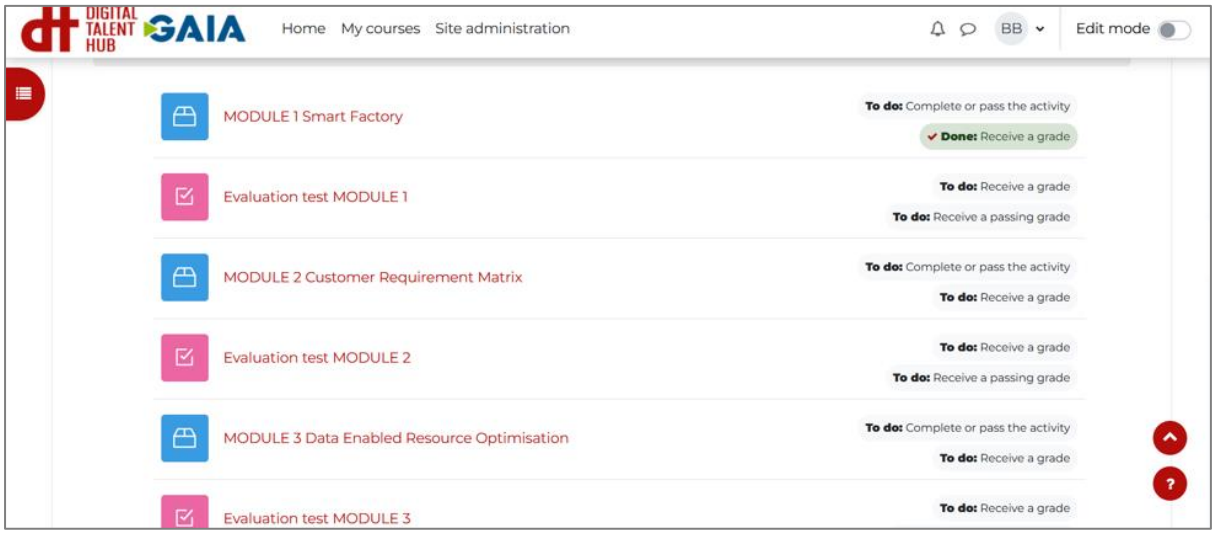


Figure 4*. On-line platform with self-study modules of ExCurS project*

3. Methodology

A dozen of ExCurS project's self-study modules have been selected for evaluation (Table 1). In total, 65 participants took part in evaluation process based on a questionnaire, so the large sample of answers was collected. The participants evaluated modules from the perspective of usage and relevance, and from perspective of the competence development.

The usage and relevance of self-study module was assessed through the following questions:

- How did you use the module?
- How helpful was the module for your understanding of the topic?
- How would you rate the module's practical relevance?
- How do you evaluate the learning format used?

On the other hand, the competence development was assessing how the self-study module helped participant to expand his/her knowledge on:

- Sustainability,
- Digitalization,
- Lean management.

Table 1. *ExCurS project's self-study modules evaluated in this analysis*

Module No.	**Module name**
Module 1	Connected Company / Smart Factory
Module 2	Customer Requirement Matrix (QFD)
Module 3	Data-enabled Resource Optimisation
Module 4	Digital Assistant Systems
Module 5	Digital Twin of the Facility
Module 6	KPI Analysis)
Module 7	Predictive Maintenance
Module 8	Process Identification and Mapping
Module 9	Benchmarking / Continuous Improvement
Module 10	Digital Human Resource Management
Module 11	EU-UN-ILO Policies
Module 12	Brainstorming

The participants were learning and using self-study modules in period from April to July 2025. After the period of self-study module learning, each participant answered the questionnaire to evaluate the modules that has been learning.

4. Results

As mentioned, 65 participants were evaluating 12 self-study modules (Table 1). The questionnaire consisted of four questions regarding the usage and relevance of self-study module, and three questions where participant needed to rate how much the module helped in their personal competence development.

The results show that most of the participants have been using self-study modules as "Supplementary material for lectures" (Figure 5), because the self-study modules were integrated into the curriculum of several courses in different studies at Faculty of Electrical Engineering, Mechanical Engineering and Naval Architecture.

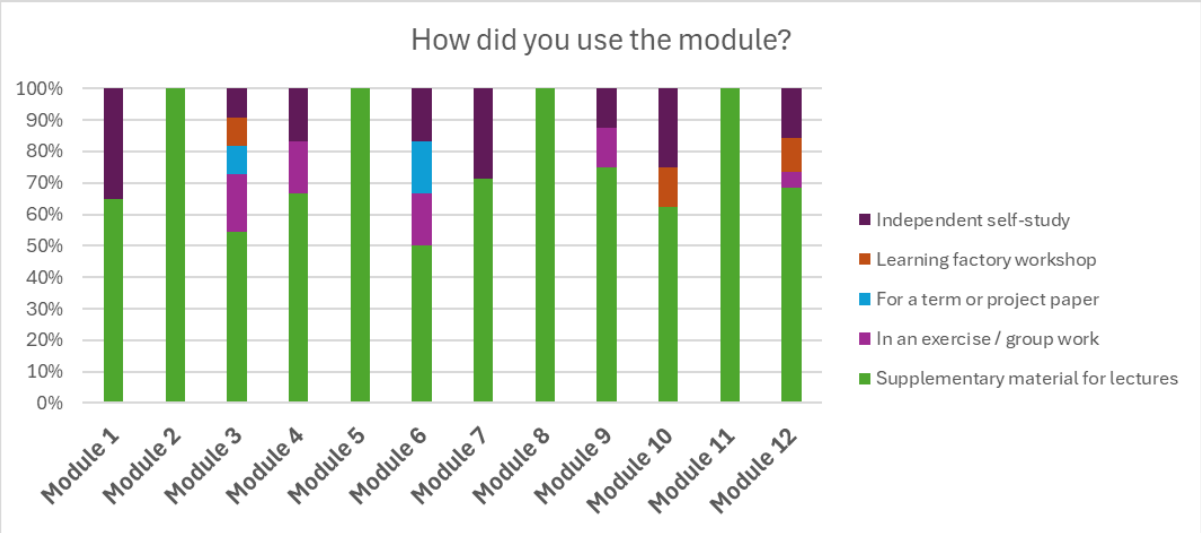


Figure 5. *Chart representing the usage of self-study module*

Regarding the understanding of the specific topic, the modules were mostly "Rather helpful" or "Very helpful" to better understand some specific topic, except Module 2 which was rated "Neutral" (Figure 6). And similar observation is regarding the module's practical relevance (Figure 7).

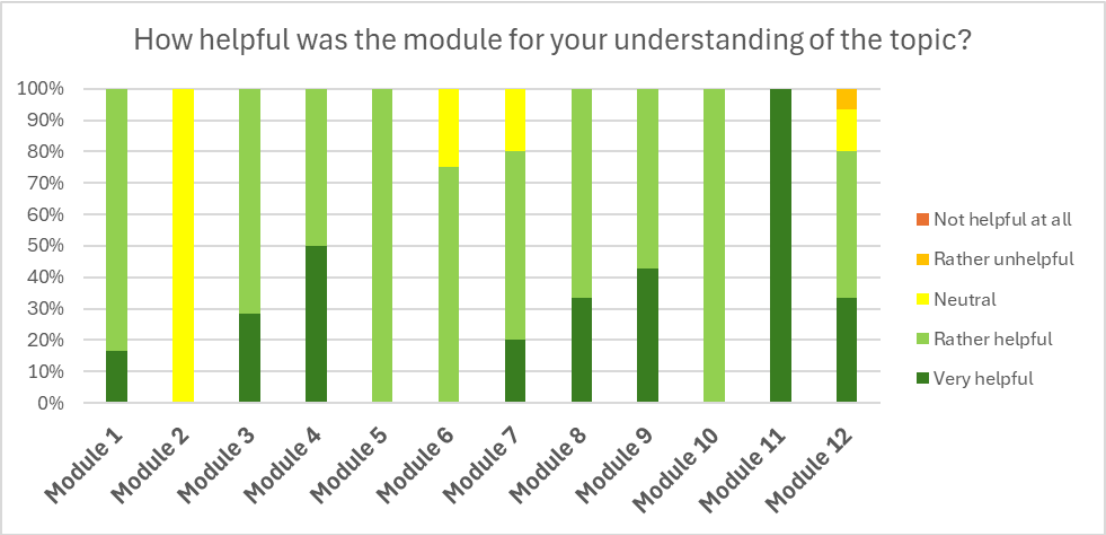


Figure 6. *Chart representing the understanding of self-study module*

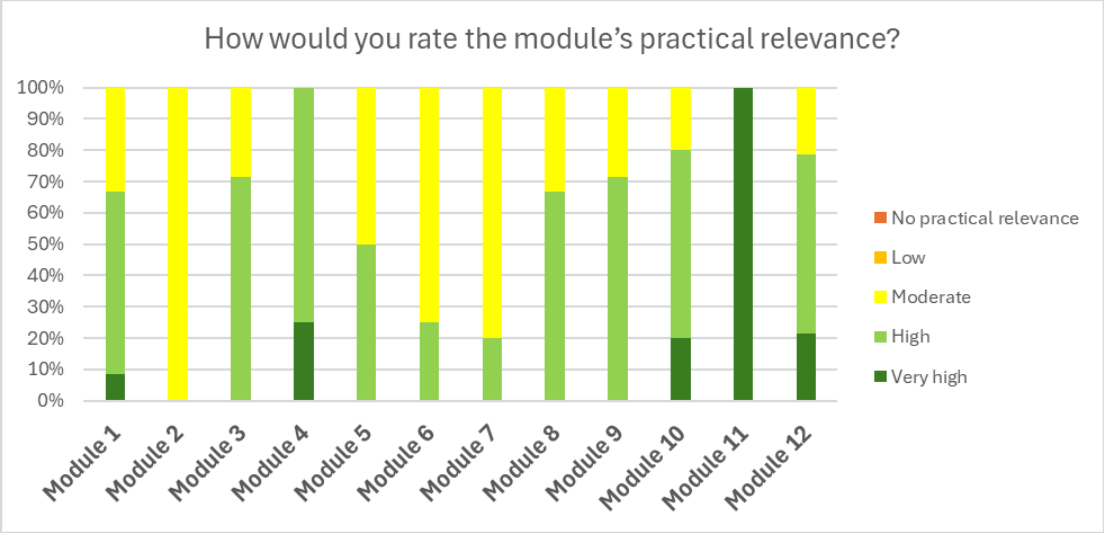


Figure 7. *Chart representing the practical relevance of self-study module*

Regarding the learning format used for the module, most of the participants rated module formats as "Rather suitable" or "Very suitable" (Figure 8).

The next, and the more important, part of the questionnaire was competence development, i.e. how the module helped participant to expand his/her knowledge on sustainability, digitalization and lean management. The participant rated each aspect (sustainability, digitalization and lean management) with a rate from 1 to 5, i.e. a scale from "1 = not at all" (module wasn't helpful) to "5 = very much" (module was very helpful). The rating of each aspect for each module is presented in Table 2.

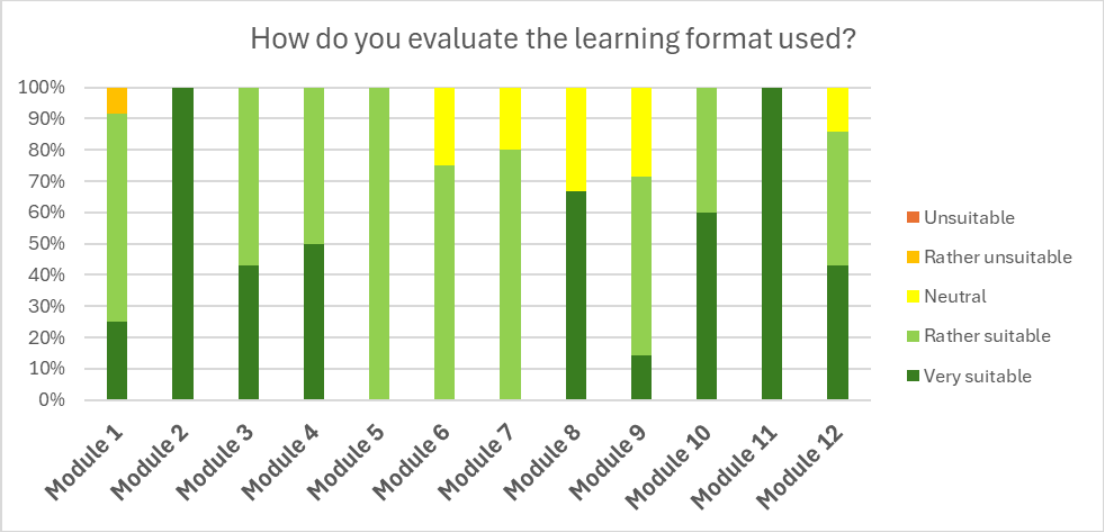


Figure 8. *Chart representing the evaluation of the learning format of self-study module*

Table 2. *Evaluation of the acquirement of knowledge through learning a self-study module (scale from 1 to 5; 1 = not at all; 5 = very much)*

Module No.	*1*	*2*	*3*	*4*	*5*	*6*	*7*	*8*	*9*	*10*	*11*	*12*
Sustainability	3.50	3.00	3.86	3.50	4.50	3.75	4.00	3.67	3.86	3.40	5.00	3.71
Digitalization	4.17	4.00	3.71	4.50	3.50	3.00	4.00	4.00	2.57	4.00	2.00	3.50
Lean management	3.08	3.00	3.57	3.25	4.00	3.00	3.40	4.00	3.57	3.40	3.00	3.93
Min	3.08	3.00	3.57	3.25	3.50	3.00	3.40	3.67	2.57	3.40	2.00	3.50
Average	3.58	3.33	3.71	3.75	4.00	3.25	3.80	3.89	3.33	3.60	3.33	3.71
Max	4.17	4.00	3.86	4.50	4.50	3.75	4.00	4.00	3.86	4.00	5.00	3.93

Table 2 shows the quite different ratings of modules regarding the extension of a knowledge sustainability, digitalization and lean management. In some cases, the module gained very low rating for one aspect, for example Module 11 "EU-UN-ILO Policies" was scored 2.00 for the digitalization. But it is a logical score, since it is a module about policies, and these policies really doesn't address digitalization issue, but mostly the sustainability issue which was rated 5.00.

From this and other examples, it can be concluded that ratings are quite realistic. However, it is important to look at some statistics, as well. Because it would be a strange thing that average rating of all three aspects for one module is below 3.00. It could be a signal that the module wasn't designed well, so it didn't transfer proper knowledge. But there is no such a module, all modules have average rating above 3.00 (Table 2). That fact is kind of validation of self-study modules, and the conclusion is that all 12 modules have been successfully validated.

Table 2 has been visualized in Figure 9 (Modules from 1 to 6) and Figure 10 (Modules from 7 to 12) by using radar chart with three axes: sustainability, digitalization and lean management. These charts demonstrate the difference between the self-study modules regarding sustainability, digitalization and lean management.

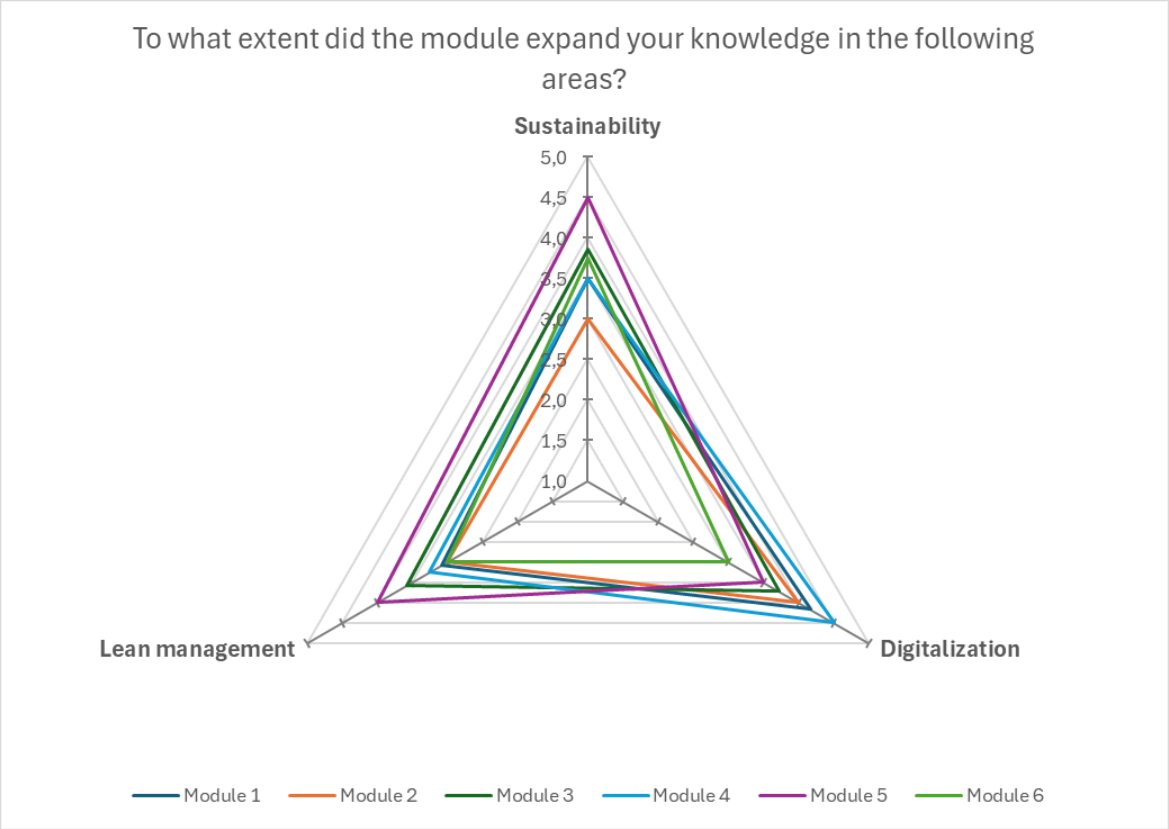


Figure 9. *Radar chart representing the acquiring of knowledge on sustainability, digitalization and lean management for each self-study modules 1-6*

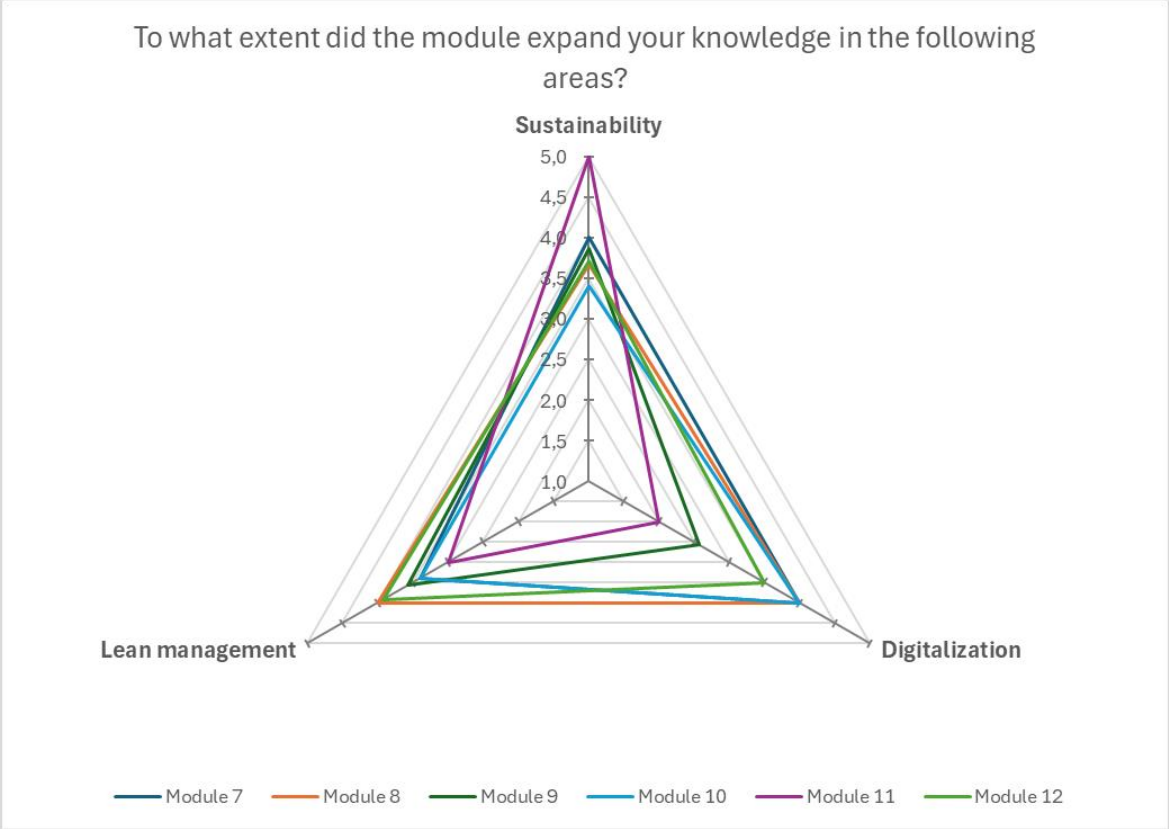


Figure 10. *Radar chart representing the acquiring of knowledge on sustainability, digitalization and lean management for each self-study modules 7-12*

5. Conclusions

The evaluation of 12 self-study modules developed in ExCurS project has been presented in this research. The evaluation was based on answers of 65 participants collected by using the questionnaire. Each participant was learning and using self-study modules for some period, after which he/she answered the questionnaire. The results gave insight into usage and relevance of each model, which can help further improvement of the module. The competence development evaluation was a kind of module validation, which showed that every module helped participant acquire above average knowledge on at least one out of three components: sustainability, digitalization, and lean management. So, it can be concluded that ExCurS project self-study modules have been successfully validated. The further research could be made with larger number of participants, and with some additional modules included.

Acknowledgments

This research was supported by the EU Erasmus+ “ExCurS” project [grant number 2022-1-ES01-KA220-VET-000086786].

References

[1] Das, M., Rangarajan, K., 2020. Impact of policy initiatives and collaborative synergy on sustainability and business growth of Indian SMEs. Indian Growth and Development Review, 13, 607-627.

[2] Parker, C.M., Redmond, J., Simpson, M., 2009. Review of Interventions to Encourage SMEs to Make Environmental Improvements. Environment and Planning C: Politics and Space, 27, 279-301.

[3] Luthra, S.D., Garg, D., Haleem, A.A., 2015. Critical success factors of green supply chain management for achieving sustainability in Indian automobile industry. Production, Planning & Control, 26, 339–362.

[4] Klein, V.B., Todesco, J.L., 2021. COVID-19 crisis and SMEs responses: The role of digital transformation. Knowledge and Process Management, 28, 117–133.

[5] Kahveci, E., 2025. Digital Transformation in SMEs: Enablers, Interconnections, and a Framework for Sustainable Competitive Advantage. Administrative Sciences, 15(3), 107.

[6] Nambisan, S., 2017. Digital entrepreneurship: Toward a digital technology perspective of entrepreneurship. Entrepreneurship Theory and Practice, 41, 1029–1055.

[7] Kosasih, W., Pujawan, I.N., Karningsih, P.D., 2023. Integrated Lean-Green Practices and Supply Chain Sustainability for Manufacturing SMEs: A Systematic Literature Review and Researc Agenda. Sustainability, 15, 12192.

[8] Han, H., Trimi, S., 2022. Towards a data science platform for improving SME collaboration through Industry 4.0 technologies. Technological Forecasting and Social Change 174, 121242.

[9] Omowole, B.M., Olufemi-Phillips, A.Q., Ofodile, O.C., Eyo-Udo, N.L., Ewim, S.E., 2024. Barriers and drivers of digital transformation in SMEs: A conceptual analysis. Internatinal Journal of Scholary Research in Science and Technology, 5(2), 19-36.

[10] Hanelt, A., Bohnsack, R., Marz, D. and Antunes Marante, C., 2021. A systematic review of the literature on digital transformation: Insights and implications for strategy and organizational change. Journal of management studies, 58(5), 1159-1197.

[11] Mittal, S., Khan, M.A., Romero, D. and Wuest, T., 2018. A critical review of smart manufacturing & Industry 4.0 maturity models: Implications for small and medium-sized enterprises (SMEs). Journal of manufacturing systems, 49, 194-214.

[12] Garza-Reyes, J.A., 2015. Lean and green–A systematic review of the state of the art literature. Journal of Cleaner Production, 102, 18–29.

[13] Queiroz, G.A., Alves Junior, P.N., Melo, I.C., 2022. Digitalization as an Enabler to SMEs Implementing Lean-Green? A Systematic Review through the TopicModelling Approach. Sustainability, 14, 14089.

[14] Mick, M.M.A.P., Kovaleski, J.L., Chiroli, D.M.d.G., 2024. Sustainable Digital Transformation Roadmaps for SMEs: A Systematic Literature Review. Sustainability, 16, 8551.

[15] ExCurS – An Excellence based Curriculum for the Improvement of LEAN & Green Management Skills in SME. https://www.excurs.eu/the-project/ (accessed 11 June 2025)

Microstructural analysis of Cu-Al-Mn shape memory alloy before and after TIG welding

***Mirko Gojić*[1,2], *Stjepan Kožuh*[1], *Ivana Ivanić*[1], *Daniela Dumenčić*[1], *Ivica Garašić*[3], *Borut Kosec*[4] *and Aleš Nagode*[4]**

1) University of Zagreb, Faculty of Metallurgy, Aleja narodnih heroja, 3, 44000, Sisak, Croatia

2) University North, Trg Dr. Žarka Dolinara, 1, 48000, Koprivnica, Croatia

3) University of Zagreb, Faculty of Mechanical Engineering and Naval Arcitecture, Ivana Lučića 5, 10000 Zagreb, Croatia

4) University of Ljubljana, Faculty of Natural Sciences and Engineering, Aškerčeva 12, 1000, Ljubljana, Slovenia

Corresponding author: gojic@simet.unizg.hr

Original scientific article

Abstract: Shape memory alloys (SMAs) have a wide range of applications (medical, automotive, seismic damping, mechanical coupling, actuator applications, etc.). For their wider use, welding techniques are becoming increasingly important to obtain complex shaped devices and other components. Therefore, in this work, 82.3% Cu-8.3% Al-9.4% Mn (in wt. %) shape memory alloy was investigated before and after tungsten inert gas (TIG) welding. The results of the optical microscopy (OM) and scanning electron microscopy (SEM) analyses showed that a martensite microstrucure is present in every part of welding joints, but with different grain size. The grain size into weld metal (WM) is finer due to the remelting of base metal (BM) and filler material, which has the same chamical composition. The results of the energy dispersive spectroscopy (EDS) analyses showed that the average chemical compositions of BM and heat affected zone (HAZ) are quite similar, while in WM the aluminium content is lower due to evaporation. Cracks and intermetallic phases in the weld joint did not occurred. The martensite microstructure is determined in the as-cast state, after heat treatment and after welding. In these alloys, the martensite structure is the basic prerequisite for the shape memory effect.

Keywords: *shape memory alloy; continuous casting; rolling; heat treatment; welding; martensite*

1. Introduction

Shape memory alloys (SMAs) are relatively new metallic materials that have the ability to return to a previously defined shape when treated appropriately. This is the result of a reversible diffusionaless phase transformation of martensite in the solid state. The most important are four characteristic temperature phase transformation: Ms-martensite start temperature, M_f-martensite finish temperature, A_s-austenite start temperature and A_f-austenite finish temperature. When the temperature is lowered from the high temperature austenitic phase, austenite begins to transform to twined martensite in the temperatures between M_s and M_f. Increasing of temperature from low temperature martensitic phase, the martensite transforms to austenite in the temperature range A_s-A_f. Thereby becomes to fully reversing to the parent phase (austenitic). The main types of these alloys are nitinol (Ni-Ti), Cu-based (Cu-Al-Ni, Cu-Al-Zn, Cu-Al-Be, Cu-Al-Mn etc.) and Fe-based alloys (Fe-Mn, Fe-Pt, Fe-Mn-Si, Fe-Co-Ni-Ti etc.) [1]. Among them Ni-Ti alloys are the most important.

These alloys are of interest for numerous commercial technical applications (medicine, automotive engineering, aerospace, seismic damping, mechanical coupling, applications for actuators, sensor technology etc.). Nitinol is an almost equiatomic alloy of nickel and titanium, which is the most widely used due to its unique properties (shape memory effect, pseudoelasticity, biocompatibility, resistance to corrosion etc.). However, they are very expensive. The main advantages of Cu-based alloys are their low price, their relatively simple manufacturing process and their high electrical and thermal

conductivity compared to other shape memory alloys. The Cu-Al-Ni and Cu-Al-Zn alloys are brittle and susceptible to intergranular fractures. Compared to other Cu-based SMAs, the Cu-Al-Mn shape memory alloy has a higher shape memory strain, greater resilience, better ductility and higher damping capacity. The reason for higher ductility of Cu-Al-Mn shape memory alloys can be linked to the reduction in the degree of order of the β parent phase. The addition of manganese to Cu-based SMAs stabilises the β base phase and improves ductility of the alloys. The addition of manganese increases the binding force between the individual atoms, which leads to an increased activation energy for diffusion and a reduced diffusion rate of the atom for reorganisation.

SMAs can be fabricated using different technologies (mould casting, melt spinning, powder metallurgy etc.). Continuous casting is one of many technologies for production of SMAs, as it offers a particular mechanism of competitive crystal growth and resulting cast products with favourable texture formation [2,3]. SMAs produced by casting are followed by plastic processing (rolling or drawing) including heat treatment.

The development of joining technologies of SMAs (mechanical joining, welding, soldering and adhesive bonding) is very important due to it allows the growth potential application of these alloys for other field applications. Mechanical joining of SMAs is a simple and a relatively easy, but it does not create continuous joint. During of soldering the base metals are not melted, but the high temperature oxidation, elemental segregation and grain growth decreases of original properties of SMAs. Adhesive bonding of SMAs is very limited due to adhesives (for example epoxies etc.) can be degraded in the different environments. Welding of SMAs can be performed by fusion or in the solid state. Welding of SMAs is a very complex phenomenon which is accompanied with a numerous challenge due to lower mechanical properties, change microstructure and temperature phase transformation, possibility the formation of intermetallic phases etc. Difficulties arise especially with excessive heat input and distorted shielding gas during welding. Among the SMAs, the Ni-Ti alloys are most commonly used for welding techniques (laser, electron beam, resistance welding, explosive welding, ultrasonic welding, friction welding etc.) [4-13]. There is a few references on welding of Cu-SMA alloys [14-16]. In this paper, for the first time in the Republic of Croatia, studies on welding of Cu-Al-Mn SMAs using tungsten inert gas (TIG) technique are presented.

2. Experiments

The Cu-Al-Mn alloy used in this study was produced by melting pure elements (99.9%Cu, 99.8%Mn, and 99.5%Al, wt. %) in a vacuum induction furnace under a protective argon atmosphere. Total mass of materials was 15 kg. First, the ingot (ϕ110 x 180 mm) was produced by graphite mould casting. The ingot was then remelted in the same furnace and cast in a continuously casting process. The continuous cast strand (8 mm diameter cylindrical bar) of the alloy was produced using the vertical continuous casting device connected to the vacuum induction furnace. The solid bars were produced directly from the 13.15 kg melt. The initial temperature of the melt was 1250 ^{o}C. Remelting was carried out in a vacuum (2-4) x 10^{-1} mbar. During casting, the pressure of the argon protective atmosphere was set to approximately 500 mbar. The casting speed was 290 mm/min.

After continuous casting the rods (diameter of 8 mm) were inserted in the chamber furnace at 900 ^{o}C and heated for 5 minutes. After that, rods are hot rolled in light section rolling mill up to strip width 14 mm and thickness of 1.75 mm. Heating time of rods/strips was 5 minutes until 5.4 mm, then 3 minutes for thickness from 3.5 to 1.75 mm. The number of hot rolling passes was seven. The hot rolled strips of thickness 1.75 mm were heated at 880 ^{o}C for 1 minute before cold rolling. Cold rolling of hot rolled strips was carried out by cold rolling mill. The number of cold rolling passes was ten. After cold rolling width strip was 14 mm and thickness was 1 mm. After hot and cold rolling, heat treatment of strips was performed in laboratory electro-resistance furnace. Solution annealing of samples was carried out at 900 °C for 30 minutes, followed by cooling in water.

The Cu-Al-Mn alloy was butt welded using the TIG process with 100 % Ar (flow rate of 10 l/minute) as shielding gas at following parameters: Current of 30 A and voltage of 13 V (Figure 1). The filler material was produced by cutting strips of 2x1x100 mm from the base material.

The microstructure of the samples was characterised by optical microscopy (OM) and scanning electron microscopy (SEM) with energy dispersive spectroscopy (EDS). The standard metallographic preparation included cutting of the samples, embedding of the samples in conductive resin, grinding as well as coarse and fine polishing. A solution of 2.5 mg $FeCl_3$, 48 ml methanol and 10 ml HCl was used as a reagent etching.

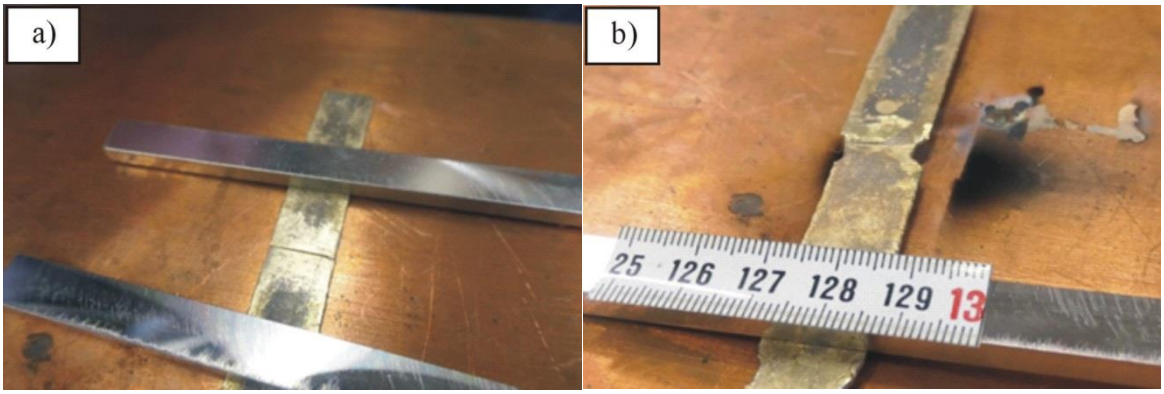


Figure 1. *Photos of the strips before welding (a) and butt-welded joint (b)*

3. Results and discussion

After continuous casting, the Cu-Al-Mn alloy has a martensitic microstructure with grain boundaries that can be clearly recognised by OM or SEM (Figure 2). The microstructure changes after rolling. Figure 3 shows the microstructure of the strip after cold rolling or after heat treatment. After cold rolling, all grain shapes show a greater or lesser degree of deformation due to cold working (Figure 3a). The overall impression is that the microstructure of the original casting state is intensely and inhomogeneously deformed in the direction of deformation during cold forming.

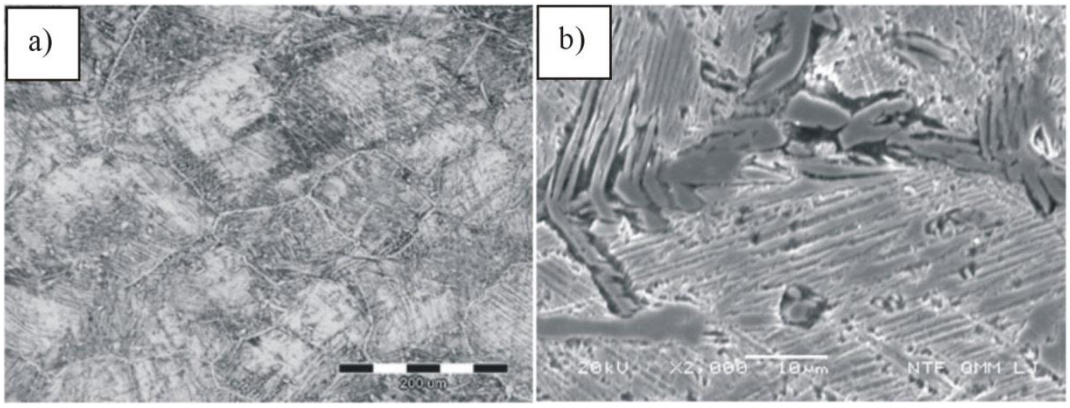


Figure 2. *OM (a) and SEM micrographs (b) of the Cu-Al-Mn alloy after continuous casting*

After heat treatment (900 °C and quenching in water) the samples at room temperature contain β_1' martensite and β parent phase (Figure 3b). By rapid cooling in water the alloy undergoes the ordering transitions $\beta(A2) \rightarrow \beta_2(B2) \rightarrow \beta_1(L2_1)$ and then martensite transformation $\beta_1(L2_1) \rightarrow \beta_1'$ occurs. During rapid cooling from the stable β-phase region the martensite phase occurs below the M_s-temperature. The micrographs contain grains and martensite plates (Figure 3b). The grains are clearly recognisable and the martensite plates have different orientations in the different grains. The martensite mainly forms as a needle-like shape. In some fields a V-shape martensite was observed. This is the typical self-adapting zig-zag martensite morphology that characterises the β´ martensite in SMAs. The parallel bands in the martensite can be considered as twin-like martensite.

Figure 4 shows optical micrographs of the basic metal (BM), heat affected zone (HAZ) and the weld metal (WM) at the same magnification. As can be seen, there are martensite microstructure in every

part of weld joint, but with different grain size. The grain size is larger in the HAZ due to the heat input during TIG welding. The grain size in the WM is finer due to the remelting of the BM and the filler metal, which has the same chemical composition. This is confirmed by SEM micrographs (Figures 5a-7a). The chemical composition in all parts of the welded joint is very homogeneous (Tables 1-3), which is confirmed by EDS spectra (Figures 5b-7b). The average chemical compositions of BM and HAZ are quite similar (BM=82.05Cu-8.52Al-9.43Mn; HAZ=81.81Cu-8.27Al-9.92 Mn, wt. %), while in WM the aluminium content is lower due to evaporation (82.45Cu-7.83Al-9.72Mn, wt. %). Cracks and intermetallic phase in the weld joint did not occur. Obviously, the cooling rate during solidification after welding was high enough to prevent the formation of other phases, unless it is transformation martensite. A uniform chemical composition and the use of welding filler material from base material probably contributed to this.

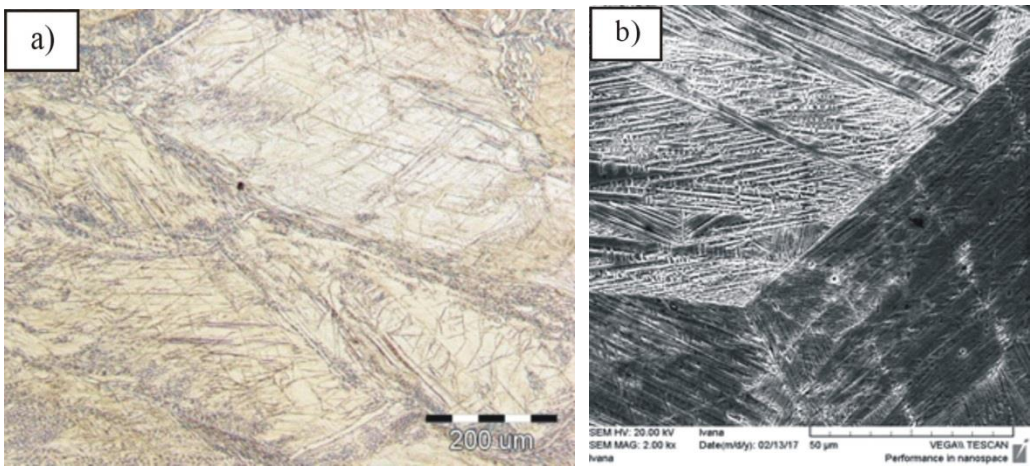


Figure 3. *OM (a) micrography of the strip after cold forming and SEM (b) micrography of the strip after heat treatment at 900 °C/30`/H_2O*

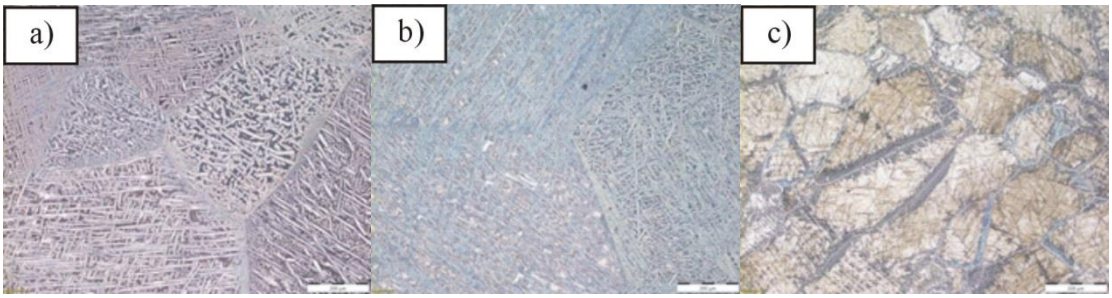


Figure 4. *OM micrographs of Cu-Al-Mn of basic metal (a), heat affected zone (b) and weld metal (c)*

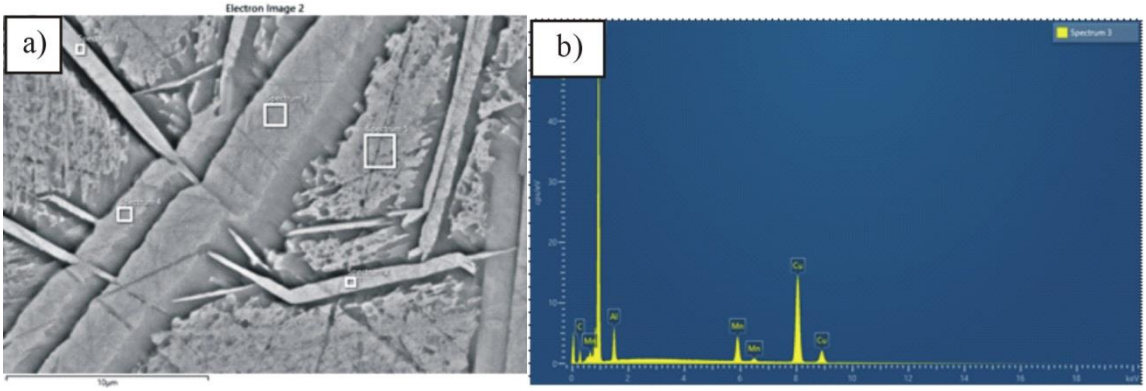


Figure 5. *SEM micrograph of Cu-Al-Mn of basic metal (a) and EDS analysis of spectrum 3 (b)*

Table 1. *The chemical composition of the Cu-Al-Mn SMA of the basic metal (positions of spectrum marked at the Figure 5), wt. %*

Spectrum label	Spectrum 1	Spectrum 2	Spectrum 3	Spectrum 4	Spectrum 5
Al	9.26	8.99	7.88	8.17	8.28
Mn	9.01	8.90	9.75	9.52	9.98
Cu	81.73	82.11	82.37	82.31	81.74
Total	100.00	100.00	100.00	100.00	100.00

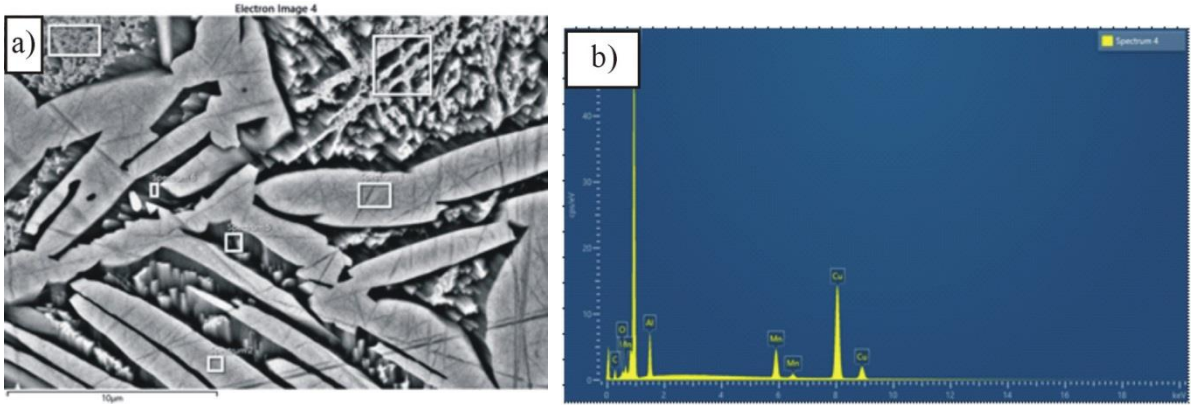


Figure 6. *SEM micrograph of Cu-Al-Mn of heat affected zone (a) and EDS analysis of spectrum 4 (b)*

Table 2. *The chemical composition of the Cu-Al-Mn SMA of the heat affected zone (positions of spectrum marked at the Figure 6), wt. %*

Spectrum label	Spectrum 1	Spectrum 2	Spectrum 2	Spectrum 4	Spectrum 5	Spectrum 6
Al	7.88	7.93	8.92	9.24	7.45	8.22
Mn	9.05	8.86	10.11	10.11	10.75	10.64
Cu	83.08	83.21	80.96	80.65	81.80	81.14
Total	100.00	100.00	100.00	100.00	100.00	100.00

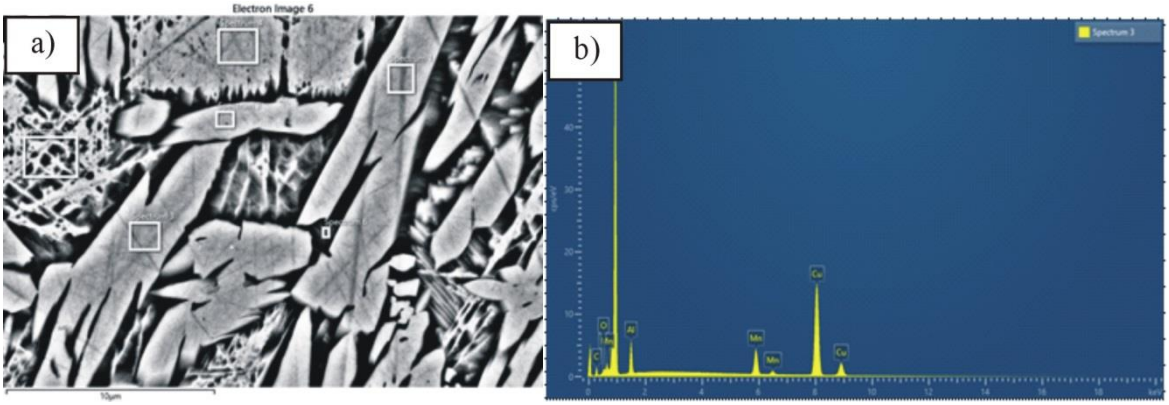


Figure 7. *SEM micrograph of the weld metal (a) and EDS analysis of spectrum 4 (b)*

Table 3. *The chemical composition of the Cu-Al-Mn SMA of the weld metal (positions of spectrum marked at the Figure 7), wt. %*

Spectrum label	Spectrum 1	Spectrum 2	Spectrum 3	Spectrum 4	Spectrum 5	Spectrum 6
Al	7.43	7.87	7.46	8.47	8.37	7.38
Mn	9.12	9.33	9.36	9.87	9.88	10.74
Cu	83.45	82.80	83.17	81.66	81.75	81.88
Total	100.00	100.00	100.00	100.00	100.00	100.00

4. Conclusion

After continuous casting, the Cu-Al-Mn shape memory alloy has a martensite microstructure. By hot rolling a strip with thickness of 1.75 mm was obtained, while by cold rolling a strip with thickness of 1 mm was produced. After cold rolling, the crystals are elongated in the rolling direction and the structure is martensite. After the rolling process, heat treatment was performed. Heat treatment was carried out by solution annealing at 900 °C held for 30 minutes and water quenched immediately after heating. Martensite β_1' is obtained by quenching in water, whereby the martensite plates have a different grain orientation.

The results of the OM and SEM analyses showed that a martensite microstrucure is present in every part of welding joints, but with different grain size. Grain size is larger in the HAZ due to the heat input during TIG welding. The grain size into WM is finer due to the remelting of BM and filler material, which has the same chamical composition. The average chemical compositions of BM and HAZ are quite similar, while in WM the aluminium content is lower due to evaporation. Cracks and intermetallic phase in the weld joint did not occurred.

In futher studies, the change in hardness in the weld, the effect of welding parameters on the mechanical properties, the possibility of welding this SMAs with other materials etc. must be analysed.

References

[1] Lexcellent, C., 2013. Shape-memory Alloys Handbook. John Wiley&Sons, New York.

[2] Gojić, M., Vrsalović, L., Kožuh, S., Kneissl, A., Anžel, I., Gudić, S., Kosec, B., Kliškić, M., 2011. Electrochemical and microstructural study of Cu-Al-Ni shape memory alloy. Journal of Alloys and Compounds, 509 (41) 9782-9790.

[3] Lojen, G., Gojić, M., Anžel, I., 2013. Continously cast Cu-Al-Ni shape memory alloy-Properties in as-cast condition. Journal of alloys and compounds, 580 (12) 497-505.

[4] Oliveira, J. P., Miranda, M., Braz Fernandes, F. M., 2017. Welding in Joining of NiTi Shape Memory Alloys: A Review. Progress in Materials Science, 88 (7) 412-466.
[5] Kramár, T., Tauer, J., Vondrouš, P., 2019. Welding of Nitinol by Selected Technologies. Acta Polytechnica, 59 (1) 42-50.

[6] Sari, N., Doğan, H., 2019. Microstructural Characterization of Welded hape Memory Alloys, Sheets. Shap. Celal Bayer University Journal of Science 15 (4) 415-421.
[7] Mehrpouya, M., Gisario, A., Barletta, M., Veniali, F., 2020. Investigation on the functionality of laser-welded NiTi to NiTiCu dhape memory wires. Journal of Inteligent Material Systems and Structure, 31 (9) 1171-1175.

[8] Wang, W., 2020. Shape Memory Characteristics in Welded SMA Alloys. Journal of Physics: Conference Series 1676, 012030. doi:10.1088/1742-6596/1676/1/012030.

[9] Viebranz, V. F., Hassel, T., Niendorf, T., Maier, H. J., 2022. Welding characteristics an microstructure of an industrially processed Fe-Mn-Al-Ni shape memory alloy joined by tungsten inert gas welding. Welding in the World, 66 (11) 2207–2216. doi:org/10.1007/s40194-022-01364-8.

[10] Bauer, A., Wiegand, M., Wicke, P., Sommer, N., Volmer, M., Böhm, S., Niendorf, T., 2023. Electron Beam Welding of Hot-Rolled Fe-Mn-Al-Ni Shape Memory Alloy Sheets. Shap. Mem. Superelascity, 56 (9) 364-376.

[11] Zhang, W., Ao., S., Oliveira, J. P., Zeng, Z., Luo, Z., 2018. Microstructural Characterization and Mecnaical Behaviour of NiTi Memory Alloys Ultrasonic Joings Using Cu Interlayer. Materials, (11) 1830. doi:103390/ma1110183.

[12] Ao., S. S., Zhang, W., Li, C. J., Oliveira, J. P., Zeng, Z., Luo, Z., 2021. Variable-parameter NiTi ultrasonic welding with Cu interlayer. Materials and Manufacturing Processes, 36 (5) 599-607.

[13] Kim, D., Kim, T., Ji, C., Ji, S., Lee, W., Kim, W., 2024. Microstructure and Shape Memory Properties of Gas Tungsten Arc Welded Fe-17Mn-5Si-10Cr-4Ni-(V,C) Shape Memory Alloy. Materials, (17) 4547. doi:org/103390/ma17184547.

[14] Oliveira, J. P., Panton, B., Zeng, Z., Omori, T., Zhou, Y., Miranda, R. M., Braz Fernandes, F. M., 2016. Laser welded superplastic Cu-Al-Mn shape memory alloy wires. Materials and Design 90, 122-128. doi: 10.1016/j.matdes.2015.10.125.

[15] De Albuquerque, A. A., Louche, H., De Oliveira, D.F., Brito, I.C.A., 2024. Rotary friction welding applied to Cu11.8Al0.45Be. Journal of Advanced Joining Processes (10) 100233. doi:org/101016/j.jajp.2024.100233.

[16] Gojić, M., Kožuh, S., Ivanić, I., Dumenčić, D., Kozina, F., Garašić, I., Juraga, I., Kosec, B., Nagode, A., 2025. Zavarivanje Cu-Al-Ni legure s prisjetljivosti oblika TIG postupkom, SBZ 2025, Slavonski Brod.

Digital twin-enhanced virtual laboratories for advanced manufacturing education: a comparative analysis of development platforms

Mihael Holi[1]

1) Juraj Dobrila University of Pula, Faculty of Engineering, Pula, Croatia

Corresponding author: mholi@student.unipu.hr

Review article

Abstract: Digital twin technology is transforming manufacturing education by creating interactive virtual laboratories that replicate industrial additive manufacturing environments. This study presents a comparative analysis of Unity and Godot game engines for developing educational digital twins of 3D printing systems, evaluating both proprietary and open-source platforms in terms of development workflow, system performance, and educational effectiveness. Virtual laboratories were created featuring multiple 3D printer models with contextual interaction panels, enabling students to explore complex manufacturing processes without equipment access barriers or safety risks. The comparative analysis reveals distinct advantages: Unity offers robust VR integration and industry-standard tools, while Godot provides lightweight, cost-effective development with Python-like scripting accessibility. Results demonstrate that digital twin-based virtual laboratories significantly enhance student engagement and understanding of advanced manufacturing processes, preparing future engineers for Industry 4.0 challenges while reducing institutional costs and safety concerns.

Keywords: *Digital twins; virtual laboratories; manufacturing education; additive manufacturing; educational technology; game engine comparison; industrial simulation; engineering pedagogy*

1. Introduction

Virtual reality (VR) is becoming a key tool in engineering education, especially in additive manufacturing (AM). It enables students to simulate complex 3D printing scenarios without relying on costly or hazardous equipment. Learners can explore machine components, internal geometries, and operational workflows that are often inaccessible in traditional settings. Recent developments in digital twins, AI-enhanced simulations, and game-based learning extend this potential by creating adaptive and personalised environments. These tools bridge the gap between theoretical knowledge and hands-on practice, preparing students for advanced manufacturing roles. Affordable CAE and VR solutions have already shown strong results in connecting theory with practical skills [1–4]. This paper presents the design and implementation of a fully interactive virtual laboratory using Unity and Godot—two widely used game engines, one proprietary and one open-source. The virtual lab includes several 3D printers arranged in a realistic environment for learning in mechanical engineering. When a user approaches a printer, a contextual interaction panel appears, displaying technical information and operational options specific to that device. This feature mimics real-world interaction with 3D printing hardware and reinforces experiential learning.

The primary objective is to evaluate and compare different approaches in Unity and Godot in terms of development workflow, usability, system performance, educational effectiveness, and adaptability for VR and mobile deployment. This comparison aims to help educators and developers select the most appropriate engine for building scalable, cost-efficient, and pedagogically sound VR applications in AM education for realistic scenarios in various areas of engineering. The virtual environment also lays the foundation for future extensions, such as multiplayer scenarios, remote collaboration, and AI-integrated tutoring systems [5].

2. Development and Evaluation Approach

To evaluate Unity and Godot for developing digital twin-based virtual laboratories in additive manufacturing education, we implemented two equivalent interactive simulations. Each digital twin lab recreated a workshop environment featuring three 3D printer models [4] for testing purposes in a mechanical engineering environment and contextual UI panels. Both were developed to support exploration, interaction, and system configuration tasks typically encountered in AM workflows. Artificial intelligence has shown strong potential to enhance additive manufacturing processes, particularly in areas like material selection and efficiency optimization [3].
The evaluation criteria included:

- Development workflow
- System performance
- VR/mobile adaptability
- Usability and educational effectiveness
- Cost and scalability

User observations, interaction logs, and comparative studies from peer-reviewed literature were integrated into the analysis. Quantitative data such as task accuracy, time, retention rates, and user satisfaction scores provided insight into each platform’s pedagogical utility.

Table 1. *Key Evaluation Dimensions*

Criteria	Unity	Godot
Development Workflow	C# scripting, modular prefab system	GDScript, node-based, Python-like logic
System Performance	High fidelity, requires stronger GPU	Lightweight, optimized for low-end hardware
VR/Mobile Adaptability	Mature XR pipelines (Meta, SteamVR)	Supports OpenXR, still developing
Usability	Powerful but steeper learning curve	Simplified, fast for beginners
Licensing/Cost	Proprietary, per-seat model	Fully open-source (MIT license)

3. Platform Implementation

3.1. Unity Engine

Figure 1 illustrates Unity's object-oriented structure, which leverages GameObjects and C# scripting to define behavior. Scenes were built using modular prefabs and enriched with physics, audio, and animation components. VR support was implemented using Meta XR plugins, allowing for immersive first-person navigation. Interaction logic was embedded into each printer's prefab using Unity's event system. Technical details and control panels activated when users approached a device, as shown in Figure 2. Users can configure print parameters and view animations simulating printer status.

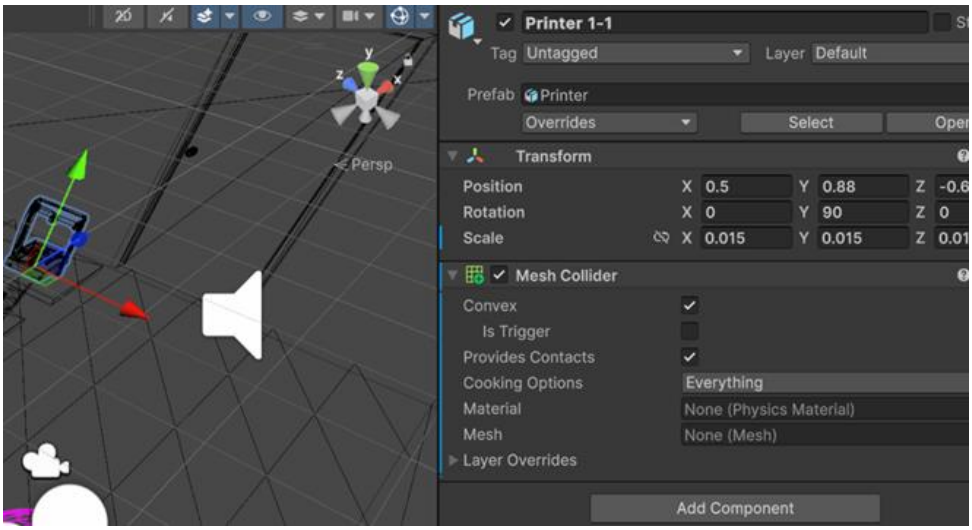


Figure 1. *Collider component on a GameObject in Unity.*

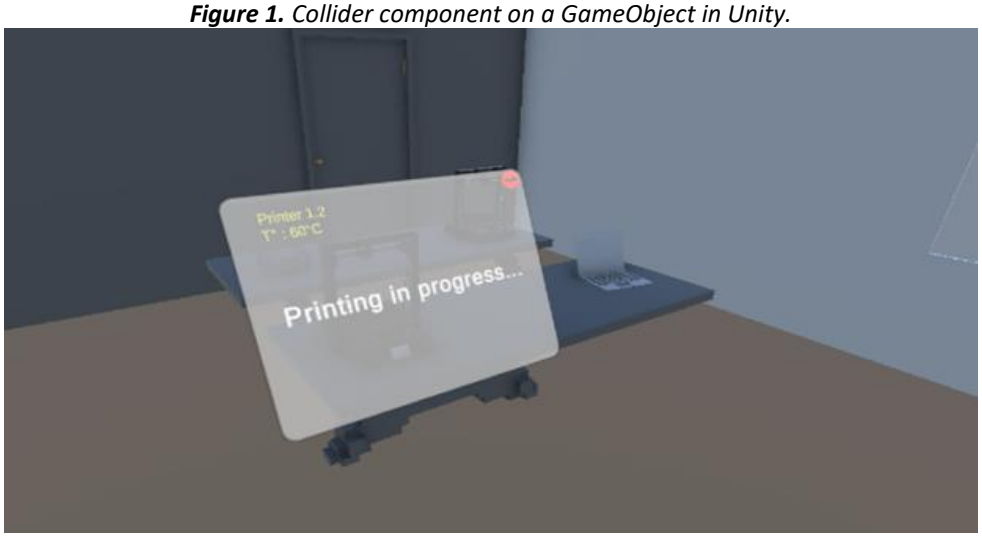


Figure 2. *UI 3D printer interface in Unity showing user interaction panel.*

Optimizations such as occlusion culling, GPU instancing, and baked lighting were applied to ensure high frame rates (90+ FPS) in VR environments.

3.2. Godot Engine

The Godot environment is structured around a node-based architecture and GDScript, a lightweight scripting language. Each 3D printer was implemented as a MeshInstance3D node, with Area3D and RayCast3D nodes used to define collision boundaries and interaction logic. When the user approached a printer and focused on it, a contextual control panel—built with CanvasLayer nodes—was displayed, as illustrated in Figures 3 and 4.

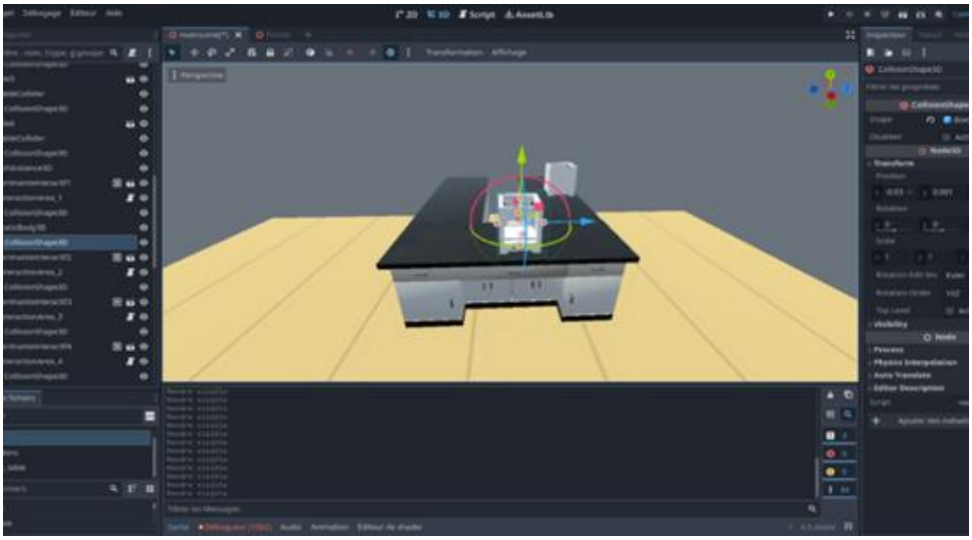


Figure 3. *Laboratory setup in Godot showing spatial arrangement of 3D printers.*

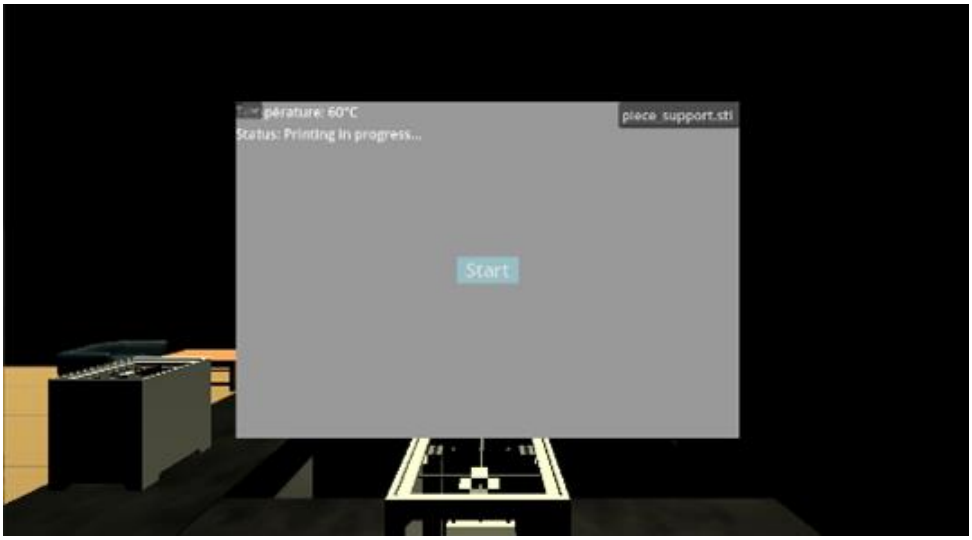


Figure 4. *Printer control interface in Godot, rendered using CanvasLayer nodes.*

The Godot VR setup is using the OpenXR plugin, allowing basic support for Meta Quest 2 headsets. Although less feature-rich when compared to Unity’s system, it enabled spatial navigation, gaze-based interaction, and low-latency feedback. The lightweight design allowed development and deployment on low-end hardware and mobile platforms. Code organization promoted modularity and rapid iteration.

4. Educational Evaluation and Student Impact

A review of literature from 2020 to 2025 confirms that virtual reality (VR) digital twin laboratories significantly enhance student outcomes across cognitive, affective, and behavioral learning domains [2–4]. These environments promote active engagement, support procedural understanding, and provide safe, repeatable scenarios for practicing complex skills. Studies indicate that VR’s immersive qualities lead to improved knowledge retention and more meaningful interaction with technical content.

Informal pilot testing with a group of five students indicated improved engagement and procedural understanding in both Unity and Godot environments. Tasks were generally completed faster in Unity due to its intuitive parameter controls and integration of XR interaction frameworks, a trend also observed in previous studies emphasizing Unity’s industrial-grade usability [6,10]. Godot, on the other hand, was praised for its clarity and ease of modifying simulation logic, which corresponds with

findings that highlight the advantages of open-source platforms in supporting rapid prototyping and pedagogical flexibility [7,9]. Although the pilot sample size was limited, these observations align with prior research reporting higher retention rates and stronger motivation when students use VR digital twin laboratories compared to conventional methods [2,10].

The results of the implemented Unity and Godot-based labs align with these findings. Unity’s high-fidelity simulation capabilities and support for extended reality (XR) enable intuitive parameter control, detailed process visualization, and integration with industry-standard hardware [6]. This makes it particularly effective for simulating advanced additive manufacturing workflows in near-realistic training settings. On the other hand, Godot’s open-source architecture and scriptable UI components provide flexibility for educators and students to rapidly prototype and modify simulation logic, which fosters deeper conceptual understanding and programming literacy [7].

Collaborative use cases further demonstrate the educational value of these platforms. Unity's support for multi-user digital twin environments has been shown to improve distributed teamwork, peer learning, and joint problem-solving in simulated industrial contexts [8]. Godot’s lightweight deployment and minimal hardware requirements enable broader accessibility, especially in institutions with limited financial or technical resources [9].

Both systems contribute positively to learning outcomes: Unity excels in realism and industrial fidelity, while Godot offers openness and ease of entry. Their complementary strengths mirror broader trends in educational technology, where adaptability and cost-efficiency remain central [10].

5. Conclusion

The presented research confirms that both Unity and Godot are effective platforms for developing digital twin-based virtual laboratories tailored to additive manufacturing education. Each engine exhibits distinct advantages that align with specific institutional needs and pedagogical goals. Unity proves particularly suitable for institutions seeking high-fidelity simulations and advanced extended reality (XR) features, making it ideal for industrial-level training that demands realistic process replication. Its advanced rendering pipeline and rich content ecosystem enable the creation of precise and complex virtual environments.

In contrast, Godot stands out as a lightweight, accessible, and open-source alternative, well-suited for educational settings with limited resources or a focus on fundamental programming skills. Its simplified architecture allows for rapid prototyping and iterative learning, supporting students in understanding core manufacturing principles through hands-on exploration.

A consistent body of literature and student feedback affirms that VR-based digital twins significantly enhance learning outcomes by boosting engagement, motivation, and retention. The immersive and interactive nature of these environments bridges the gap between theoretical knowledge and practical application—offering learners safe, repeatable, and cost-effective access to complex AM processes.

Ultimately, the choice between Unity and Godot should be informed by the specific educational context, infrastructure, and long-term curriculum objectives, ensuring strategic alignment between technological tools and institutional goals. Future work will integrate AI-driven adaptive feedback and cloud-based multi-user scenarios, extending scalability and personalization of digital twin education. Additionally, future studies will extend testing to larger student groups in order to strengthen empirical validation and provide broader insights into educational effectiveness.

Acknowledgments

Present research is financed in the framework of the project: "EduCalucemTech".

References

[1] Maričić, S., Krnjajić, Ž., Kršulja, M., Karabajić, D., 2025. Developing education: Incorporating computer-aided engineering simulations in existing learning environments. In Management, Tourism and Smart Technologies (ICMTT 2024), pp. 51–58. https://doi.org/10.1007/978-3-031-74825-7_6

[2] Norambuena, N., et al., 2025. Integrating digital twins of engineering labs into multi-user virtual reality environments. Applied Sciences, 15(7), 3819. https://doi.org/10.3390/app15073819

[3] Chiou, R. Y., Tseng, T. B., 2023. Implementing virtual reality project activities for enhancing student learning experience in robotics and automation. Proceedings of the 2023 ASEE Annual Conference & Exposition, Baltimore, Maryland. https://peer.asee.org/43563

[4] Maričić, S., Kršulja, M., Iljkić, D., Knežević, Z., 2024. An AI-driven approach for a comprehensive evaluation of 3D printed molds in aluminium casting. In Čatipović, N., Krolo, J., & Gjeldum, N. (Eds.), Proceedings of the 13th International Conference Mechanical Technologies and Structural Materials 2024 (pp. 273–280). Split: FESB, University of Split. https://www.croris.hr/crosbi/publikacija/prilog-skup/858849

[5] Ortiz, J. S., Quishpe, E. K., Sailema, G. X., Guamán, N. S., 2025. Digital twin-based active learning for industrial process control and supervision in Industry 4.0. *Sensors, 25*(7), 2076. https://doi.org/10.3390/s25072076

[6] Kong, X., et al., 2022. Work-in-progress: Developing an interactive, immersive, 360-degree virtual media for enhancing student learning in additive manufacturing. Proceedings of the ASEE Annual Conference & Exposition. https://doi.org/10.18260/1-2--41843

[7] Pandolfi, R. J., Donatelli, J. J., Todd, J., & Ushizima, D., 2025. ASCRIBE-XR: Virtual reality for visualization of scientific imagery. *arXiv*, arXiv:2507.03170. https://arxiv.org/abs/2507.03170

[8] Maričić, S., Mrša Haber, I., Radolović, D., & Veljović, I., 2019. The emerging role of new technologies in vocational education. *The Central European Journal of Engineering and Business Education*, *1*(1), 75–80. https://doi.org/10.2478/cplbu-2020-0009

[9] Santucci, F., Frenguelli, F., & De Angelis, A., 2021. An immersive open-source VR environment using Godot. In L. T. De Paolis & P. Bourdot (Eds.), *Augmented Reality, Virtual Reality, and Computer Graphics* (pp. 671–686). Springer. https://doi.org/10.1007/978-3-030-58820-5_56

[10] Zhang, J., et al., 2020. Developing a virtual reality module to improve the student learning experience in an additive manufacturing curriculum. Proceedings of the 2020 ASEE Virtual Annual Conference, Virtual Online. https://doi.org/10.18260/1-2--34420

The cause of the precocious fracture of the samples during the dynamic strength test of the wear-resistant steel

***Aida Imamović*[1], *Mirsada Oruč*[1], *Milenko Rimac*[1], *Gorazd Kosec*[2] *and Amra Talić-Čikmiš*[1]**

1) University of Zenica, Fakultetska 1, 72000 Zenica, Bosnia and Herzegovina

2) SIJ Acroni d.o.o. Slovenia, Jesenice, Slovenia

Corresponding author: aida.imamovic@unze.ba

Professional article

Abstract: Steel Sidur 450 (SIJ Acroni) belongs to the group of wear-resistant steels. It is a steel with high wear resistance, extreme hardness, strength and toughness. This makes it durable and suitable for use in the most difficult environments, where there is a risk of wear (abrasion) caused by contact with hard minerals and other abrasive materials. They are mainly used in the most important processes in the transport of soil and ores, in the cement industry, chemical industry, agriculture, asphalt bases, etc.

The Sidur steel group represents a range of steels that, with a selected chemical composition and heat treatment, guarantee the functionality of the steel with guaranteed toughness at low temperatures and a hardness in the range from 250 to 600 HB.

On products made of this steel, in addition to the usual mechanical and metallographic tests, tests are carried out in order to determine the dynamic strength. Since, in the tested samples made of Sidur 450 steel, the test tubes fracture occurred before the prescribed number of cycles, the cause of premature test tubes failure at the prescribed load was examined. After determining the cause of the appearance of micro-cracks on the surface of the test tubes that caused premature fracture, a new surface treatment procedure was started, after which tests were carried out that enabled the preparation of the Veler's curve and the determination of dynamic strength.

The paper shows the determination of dynamic strength, conducted tests on the surface of processed test tubes, fracture surface, microstructure, grain size, banding, hardness and microhardness on the transverse or longitudinal section of the test tubes in order to discover the cause of premature failure of the test tubes when determining the dynamic strength.

Keywords: *steel Sidur 450; fracture; metallography analysis; hardness; microhardness; fatigue testing*

1. Introduction

When determining the dynamic strength of hot-rolled sheets with a thickness of 20 mm, made of Sidur 450 steel, premature facture of some test tubes occurred during the test, where some test tubes withstood the expected number of cycles, which was the reason for the tests to be repeated. After the test, the test tubes were visually inspected and scratches caused by mechanical processing during the production of the test tubes were noticed on their surfaces. For this reason, a new series of additionally polished test tubes was made for testing dynamic durability. Since, during the testing of this series, the durability of one part of the test tube was again reduced, it was not possible to construct the Veler's curve and determine the dynamic strength. In order to determine the cause of this phenomenon, certain additional tests were carried out, in order to determine the reason for the occurrence of premature fracture during the test, on the basis of which certain changes could be made in the processing and polishing of the test tubes, and to perform a new test on the basis of which it could be constructed Veler's curve and determine the dynamic strength.

For the sake of comparison, additional tests were performed on the test tubes that withstood the specified load, and the test tubes that ruptured much earlier. The tests were carried out in the Metallographic and Mechanical Laboratories of the Institute "Kemal Kapetanović", University of Zenica.

The roughness test on the surface of the test pieces was not carried out because the test pieces were polished after the surface inspection. Also, additional tests are planned to analyze possible hard inclusions that are located near the surface and can be initial fracture sites. Non-metallic inclusions play a very important role in the properties of the material, and have a great influence on the processing and application of steel products. The origin and mechanical properties of non-metallic inclusions depend on the type of inclusions and their chemical composition [1, 2]. Hard inclusions are mainly oxides and carbides, nitrides, carbonitrides and are not allowed during dynamic loads. It is important to note that some microalloying or trace elements found in the technological process of production can form carbides, nitrides and more often carbonitrides if there is a sufficient amount of nitrogen in the solution [3,4]. In this work, metallographic tests were also used to examine the presence of inclusions near the surface and in places where cracks appeared during fatigue testing.

2. The main characteristic of steel Sidur 450

The first developed wear-resistant steel containing about 1.2% carbon and 12% manganese was made by Sir Robert Hadfield in 1882, after whom the steel was named Hadfield's steel, which is unique in that it possesses a combination of high toughness and elongation with high strengthening capacity, and good wear resistance. Because of this, such steel was quickly accepted as a very useful engineering metal material. In the meantime, numerous variations of the original manganese austenitic steel have been proposed, but completely new steels with similar characteristics have been developed [5]. Compared to manganese steels that had an initial austenite microstructure that transformed into cold-strengthened martensite in the process of cold deformation during exploitation, the microstructure design of the new steels has been completely changed, in which the initial martensitic microstructure was formed after hot processing and heat treatment. The ability of steel to resist material loss, i.e. wear, in the case of these steels, it can mostly be achieved by microstructures that are mainly formed due to a certain chemical composition, and are certainly in a high degree of interaction with the applied thermal treatments. Many new types of steel, resistant to abrasive wear, have mainly martensitic or softened martensitic structures. Martensite is a very hard microstructure, with very high strength and hardness, and therefore very good resistance to abrasive wear. The martensitic microstructure of wear-resistant (abrasion) steel can consist of or include several other phases, mainly bainite [6].

The SIDUR steel group represents a range of wear-resistant steels that have been specially developed for applications that require high wear resistance. Sidur steels with selected chemical composition and heat treatment guarantee the functionality of steel with guaranteed toughness at low temperatures and classified hardness in the range from 250 to 600 HB. Sidur steels are delivered in heat-treated condition - hardened and tempered, depending on quality and dimensions [7]. The unique combination of chemical composition and mechanical characteristics of Sidur 450 steel also improves deformability, bending, machining and welding properties. Sidur 450 steel is a material suitable for wide application in exploitation, where high resistance of material exposed to extreme wear during exploitation of particularly hard minerals and ores, in the cement industry, construction and agriculture is required [7,8].

The prescribed chemical composition for 20 mm thick hot-rolled plates made of Sidur 450 steel, for the hardened and tempered state, as well as C - equivalent and hardness, are given in Table 1 [9].

Table 1. *Chemical composition, C - equivalent and hardness of hot-rolled plates made of Sidur 450 steel [9]*

Steel	Chemical composition (Heat analysis in mas. %)									C_{ekv}	Hardness, HB
Sidur 450	C	Si	Mn	P	S	Cr	Ni	0,5	B		
	0.27	1.0	1.5	0.002	0.012	0.8	0.5	Mo	0.004	0.49	420-470

3. Experimental procedure

In order to determine the reason for the occurrence of premature fracture during the fatigue test, additional tests were performed, mainly focused on tests related to the surface of the test tubes. When testing the dynamic durability of these and other high-strength steels, it is very important that the tested test tubes do not have scratches on the surface, non-metallic inclusions and other inclusions near the surface, because fatigue fractures always start from the surface.

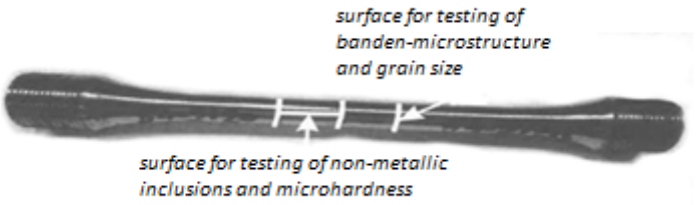
Possible causes of breakage or fracture due to material fatigue are by their nature visible and invisible. The visible causes of material fatigue are related to the concentration of stresses that arise as a result of technological errors, the invisible causes of material fatigue, as well as the onset of fracture, theoretically have no categorical explanations. However, regardless of the correctness of certain hypotheses, each fracture surface due to fatigue has its own characteristic appearance in relation to other types of fractures [8].

For additional tests for comparison, after the dynamic tests, samples were taken from one test tube that withstood a satisfactory number of cyclic stresses, marked as good (D), and two that did not withstand that load, marked as bad (L1 and L2).

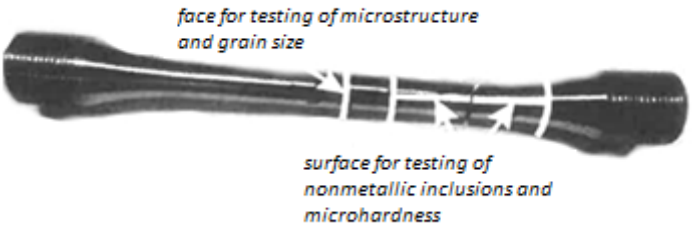
The following comparative identical tests were performed on the test tubes:

- Examining the surface and breakage of test tubes on a stereo microscope,
- Testing of hardness and microhardness,
- Microstructures on the longitudinal and transverse sections of the test tubes, in the unetched and etched state,
- Grain sizes according to ASTM E 112-13 and streakiness (banding) according to ASTM E 407-07.

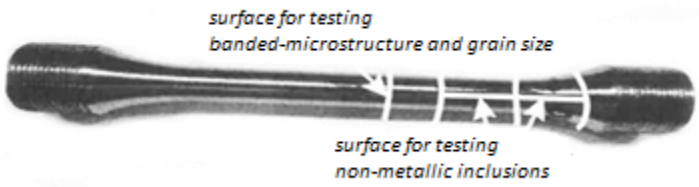
The places on the surface of the dynamically tested test tubes for the mentioned tests are shown in the images of the test tubes, Figure 1. Metallographic samples were taken on the transverse and longitudinal sections along with the fractures that occurred during the dynamic tests.



a)Test tube that has withstood cyclic loading - good D



b) Test tube that did not withstand cyclic loading - bad L1



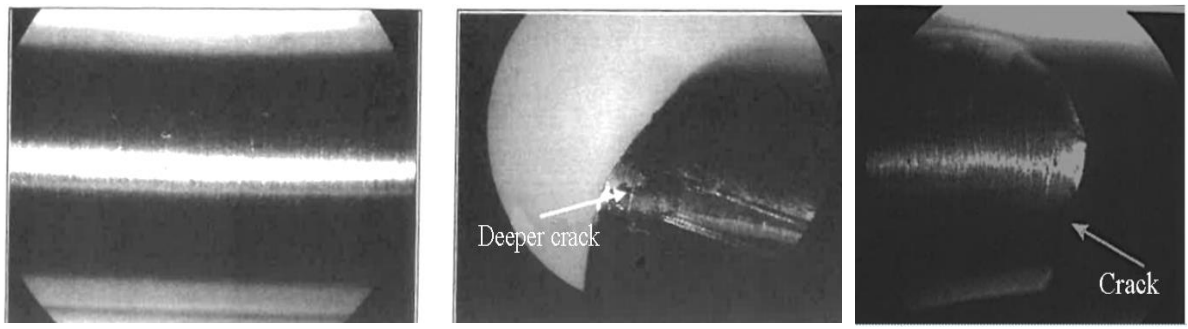
c) Test tube that did not withstand cyclic loading - bad L2

Figure 1. *Test tubes with marked sampling points for metallographic tests*

In the experimental work, the following tests were carried out in order to discover the cause of the premature fracture of the test tubes during the fatigue test: test of the test tube surface, testing of the fracture of the test tube, testing of hardness and microhardness of metallographic samples, testing of the microstructure, testing of the microstructure in characteristic places in order to determine the dynamic strength. All the mentioned tests were carried out in the laboratories of the Institute"Kemal Kapetanović", University of Zenica.

a) Examination of the test tube surface

Examination under a stereo microscope Tehnival 2 revealed damage up to 10 µm in size in the form of micro-cracks (scratches) on the surface of all three samples, which were not observed by visual examination before the dynamic strength test.Smaller micro-cracks were observed on the surface of good test tube D, and deeper ones on the surfaces of both bad test tubes L1 and L2.Micro-cracks are mostly located in unfavorable places and directed towards the radius at the transition from the thread to the body of the test tube, with a greater presence in bad test tubes L1 and L2, and their depth on the surface is generally up to 5 µm.Due to the fact that during the final polishing, an emulsion with a size of up to 3 µm was used, the micro-cracks formed in the mechanical processing could not be eliminated, and they were not visible with the usual control before testing.The appearance of micro-cracks (scratches) is shown on the images of the surface of the test tubes on a stereo microscope in Figure 2.



a) *b)* *c)*

Figure 2. *Microcracks(scratches) on test tube surfaces after dynamic testing (Increment:.1.1)*
a) Minor scratches on the surface of the good test tube D
b) Deeper scratches on the surface of the bad test tube L1
c) Deeper scratches on the surface of the bad test tube L2

b) Examination of tube breakage

The fracture surfaces of the test tubes after a certain number of cycles were observed on a stereo microscope and are shown in Figure 3. From the appearance of the fractures, it is evident that the initial places of the fracture move from the surface towards the middle of the test tube which is characteristic of fractures after fatigue testing [10].

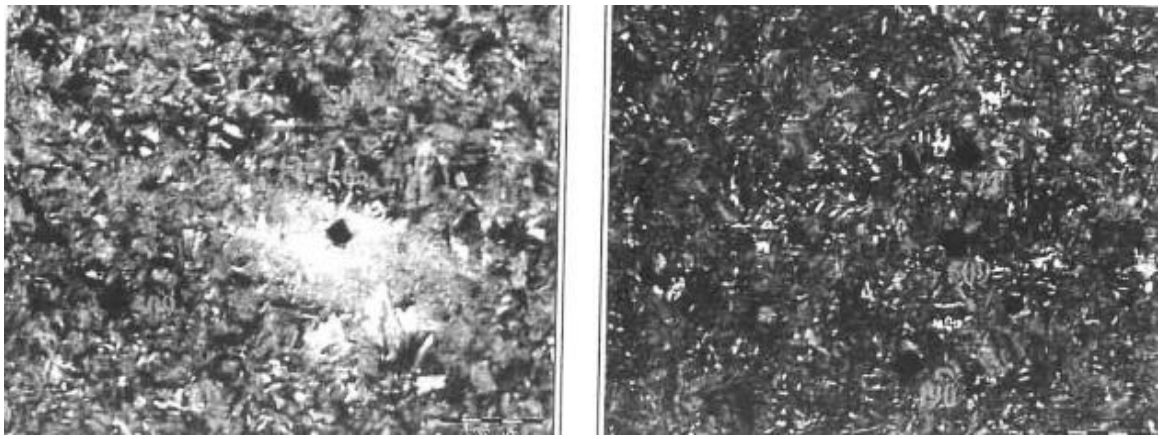


a) b) c)

Figure 3. *Appearance of fractures on dynamically tested test tubes (Increment:6x)*
a) Fracture on good test tube D
b) Fracture on bad test tube L1
c) Fracture on bad test tube L2

c) Testing of hardness and microhardness

The hardness was tested according to the BAS EN ISO 6507-1:2018 standard using the Vickers HV10 method [11].The mean hardness values for the test tubes are: for a good test tube D is 416 HV, and for a bad test tube L1 is 422 HV. In both test tubes, the results are close to the prescribed lower limit for Sidur 450 steel (Table 1). The HV0.2 microhardness test was performed on the cross-sections of the samples on the Zwick device under a load of 200 g and at a magnification of x400 according to BAS EN ISO 6507-1:2018. The test results were recorded directly at the test points shown on the microstructures of the good D and better L1 test tubes in Figure 4. The measured values range from a minimum of 471 HV0.2 to a maximum located of 593HV0.2 in the segregated zone inside the good test tube D.



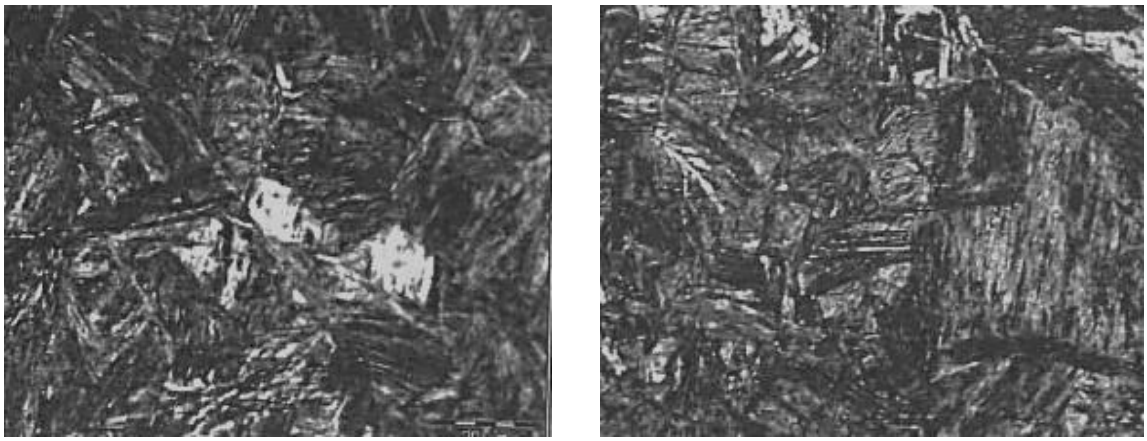
2% HNO_3 750x 2%HNO_3 750x

a) b)

Figure 4. *Microhardness HV0.2 in the microstructure of the sample of good D (a) and bad L1 test tube (b)*

d) Examination of the microstructure

Examination of the microstructure of the samples on the longitudinal and cross sections was carried out in the unetched and etched state under the microscope Olympus PMG3 and according to the standard ASTM E 407-07 [12].Characteristic microstructures at x750 magnification are shown in Figures 5. for the samples of good test tube D and bad test tube L1.The microstructure is softened marensite with partially residual austenite. No noticeable difference in microstructure was found between the samples in the good D and bad L1 tubes.On the longitudinal samples, there are noticeable segregations in which the presence of non-metallic inclusions was observed.



2% HNO_3 750x 2%HNO_3 750x

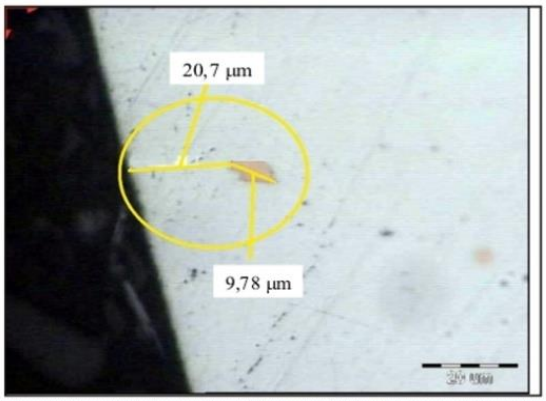
a) b)

Figure 5. *Microstructures of the softened martensite sample of good test tube D (a) and bad test tube L1 (b)*

The secondary grain size test was arranged according to the ASTM E 112-13 standard by the method of comparison with the standard scale (Plate I), [13]. All three samples have a homogeneous fine-grained microstructure, with an average grain size of 10.

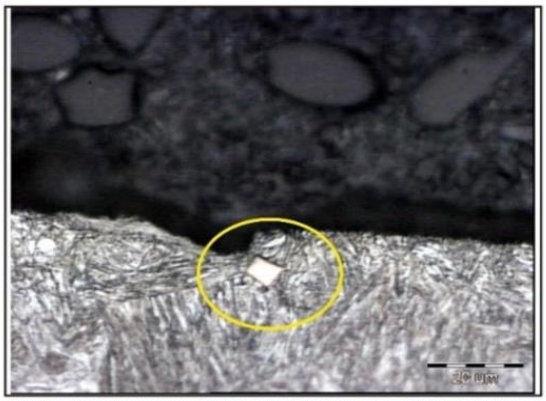
e) Examination of the microstructure in characteristic places

In addition to standard tests, characteristic places in the microstructure were also examined, especially along the edge of the surface of the samples, which may have an impact on the appearance of surface defects and micro-cracks (scratches), which are the initial places for the appearance and propagation of fractures.The tests were carried out on the transverse and longitudinal sections in the unetched and etched state. Characteristic micrographs are shown in Figure 6.a.b.



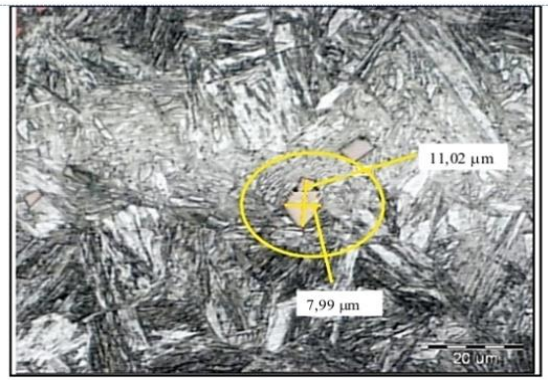
2%HNO_3 x 750

a) Ti (C,N) in the polished microstructure along the edge



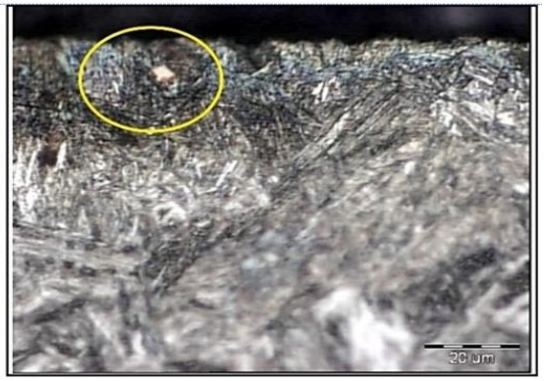
2%HNO_3 x 750

b) Ti(C,N) along the very edge and rough due to processing



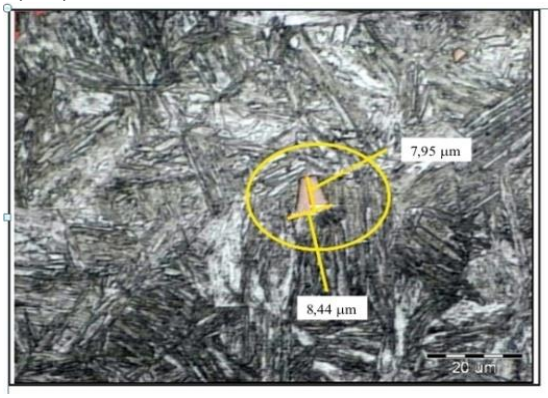
2%HNO_3 x 750

c) Ti(C,N) in the interior of the surface



2%HNO_3 x 750

d) Ti(C,N) along the edge of the surface



2%HNO_3 x 750

e) Ti(C,N) in the interior of the surface



2%HNO_3 x 750

f) Ti(C,N) in the interior of the surface

Figure 6. *Position and size of carbonitrideTi(C,N) on the cross section of the sample surface*

During tests on the entire surface of the cross-section, the presence of polygonal rough carbonitrides of titanium Ti(C,N) with a size of up to 11 µm was observed in all three samples. Titanium carbonitrides of different sizes are generally arranged in rows, and are found predominantly in segregated zones. The chemical composition of Sidur 450 steel does not prescribe the content of titanium, and its presence is related to the composition of the charge during the production of the tested Sidur 450 steel melt.

In Figure 6.a on the unetched surface of the sample of a good test tube, titanium carbonitride with a size of 11x9.78 µm was observed at a distance of 20.7 µm from the surface. On the same sample in an etched state, rough titanium carbonitride is shown next to the surface, near the damage caused by mechanical processing (Figure 6.b).On the bad test tubes, in Figure 6.c a series of titanium carbonitrides is shown, the largest of which measures 7.95x8.44 µm at a distance of 59.49 µm from the edge, and on the second bad test tube, next to the very edge of the diagonal surface, the size is 9.78 µm, and the other smaller size at a depth of 5 µm (Figure 5.d). The tests showed that coarse carbonitrides of titanium located along the very edge, or on the very surface of the sample, are associated with the formation and development of micro-cracks (scratches). In Figure 6.e, titanium carbonitrides are shown on sample D under a magnification of x750, in the central part, and in Figure 6.f, titanium carbonitride is shown in the central part of sample L1 with a measured distance from the edge of 59.49 µm. Examination of the type and type of inclusions was carried out using an optical microscope because their shape is characteristic and indicates this type of inclusion. Similar examinations were previously carried out using SEM, which confirmed that these inclusions were present [2, 14].

Controlling the formation of non-metallic inclusions and their characterization is fundamental in improving the properties of steel products, as well as designing new types of steel [15].

3.1. Testing of dynamic strength

Since the test results were not satisfactory due to the aforementioned defects such as microcracks and inclusions along the edge of the surface, a new series was tested of 10 test tubes was made, which were mechanically processed and polished according to standard technology, after which they were examined in detail on a stereo microscope in order to detect micro-cracks (scratches), and refinish by polishing. Before the dynamic strength test, a tensile test was performed on one test tube according to the standard BAS EN ISO 6892-1:2017–B table 1, which is necessary to set the parameters for the fatigue test [16]. The results of the tensile strength test together with the standard values are given in Table 2. The tensile characteristics of the 20 mm thick panels made of Sidur 450 steel are in accordance with the prescribed values.

Table 2. *Tensile characteristics of test tubes made of Sidur 450 steel [17]*

Steel Sidur 450	Yield stress $Rp_{0,2}$ MPa, min.	Tensile strength Rm, MPa, min.	Elongation A, %, min.
Prescribed	970	1350	10.0
Accomplished	987	1358	13.0

The dynamic strength test was performed on a HF pulsator at the Institute, and the results are shown in Table 3.

Table 3. *Test results for the purpose of determining dynamic strength*

Sample	$\sigma_{max,MPa}$	$\sigma_{min,MPa}$	$\sigma_{sr,\ MPa}$	$\sigma_{a,\ MPa}$	Number of cycles	Testing with:
1	930	0	465	465	50 700	Fracture
2	900	0	450	450	484 500	Fracture
3	870	0	435	435	824 300	Fracture
4	840	0	420	420	1 873 200	Fracture
5	810	0	405	405	1 749 900	Fracture
6	800	0	400	400	2 317 300	Without fracture
7	800	0	400	400	2 006 200	Fracture
8	780	0	390	390	2 333 400	Without fracture
9	780	0	390	390	4 105 000	Without fracture
10	780	0	390	390	2 225 300	Without fracture

Legend: σ_{max}-maximum dynamic load,σ_{min}-minimum dynamic load, σ_{sr}-average dynamic load, σa –amplitude dynamic load.

In the repeated testing, the number of test tubes that withstood the given load was reached, so based on the data listed in Table 2, the Veler's curve was constructed, shown in Figure 7. From the test data listed in Table 2, and based on that, the Veler's curve was constructed curves, the dynamic dynamic strength of Sidur 450 steel plates in the hardened and tempered state is 780 MPa.

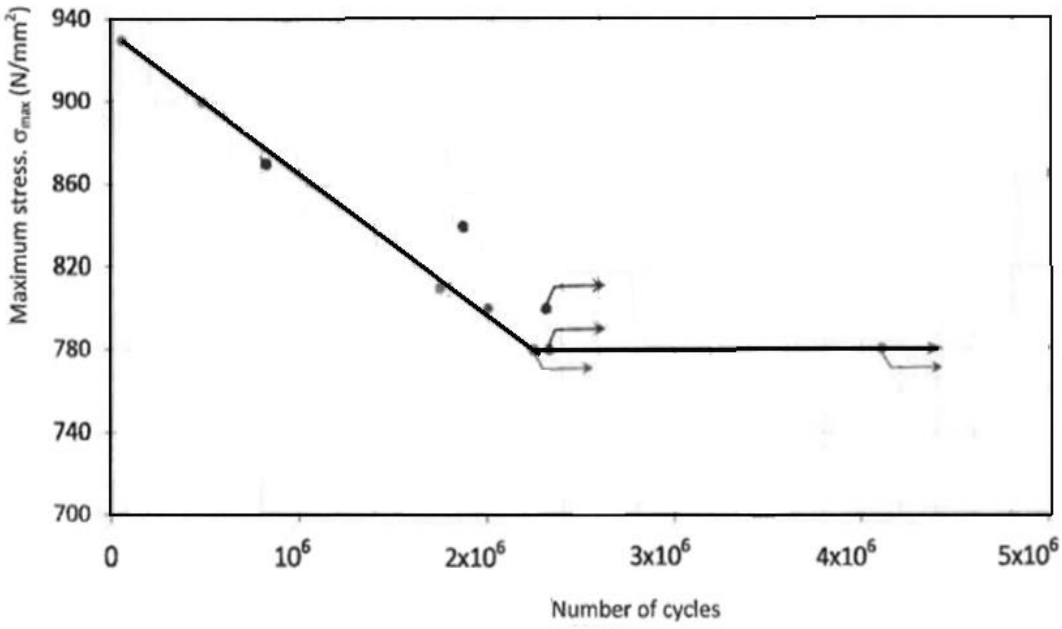


Figure 7. *Veler's curve for test tubes made of Sidur 450 steel in the quenched and tempered state*

4. Examination summary

Tests were carried out on the tested test tube samples in order to determine the cause of the impossibility of determining the dynamic strength due to premature breakage of individual test tubes made of Sidur 450 steel. During repeated dynamic tests, after special mechanical processing and fine polishing of the surface of the test tubes with fine granulation emulsions, a sufficient number of test tubes was obtained which withstood the specified load, and it was possible to construct the Veler's curve, and determine the dynamic strength of Sidur 450 steel plates in the hardened and tempered state in the amount of 780 MPa. In order to discover the cause of premature failure, additional tests of macro and micro hardness and metallographic tests of samples taken from test tubes that withstood the loads during the dynamic tests and test tubes that had premature fracture at the same loads were performed. Based on those tests, the following was concluded:

- The macro- and micro-hardness of all samples is within the range of the values achieved in Sidur 450 steel, with the fact that there are differences in hardness between segregated and non-segregated areas in the microstructure,
- In the microstructure of all tested samples, a softened partially banded martensitic structure is present, with residual austenite present in places, and the same grain size, and with a difference in microhardness between segregated and non-segregated areas,
- Examination under a stereo and optical microscope on the surface of the test tubes of all three samples revealed surface defects caused by mechanical processing and micro-cracks (scratches), which were not observed by visual inspection before the dynamic strength test,
- Micro-cracks (scratches) up to 11 μm in size are mostly located and directed towards the radius at the transition from the thread to the body of the test tube with penetration to a depth of 5 μm, and their presence is greater in test tubes marked as bad,
- In the softened martensite matrix, especially in the segregated zones, on the entire surface of all three samples, there are rough of coarse polygonal titanium carbonitrides up to 11 μm in size, although the titanium content in the Sidur 450 steel is not prescribed and it is assumed that they originate from the charge in the steel,
- Certain rough titanium carbonitrides are found next to, or on the very surface of the test tube, often in the immediate vicinity or even connected to the resulting micro-cracks (scratches).

5. Conclusion

Tests have established that there is a certain connection between the appearance of micro-cracks on the surface of the test tubes and the presence of rough titanium carbonitrides that are arranged in rows along the surface of the test tubes. This configuration and morphology of the microstructural constituents is present and approximately the same in all three test tube samples.

During the machining process, especially at the radii of the test pieces, it is assumed that some brittle angular titanium carbonitrides on the surface of the test pieces are excavated from the matrix. The initial sites for the formation of visible microcracks or scratches created at these sites are only observed under a microscope.

In order to continue the dynamic tests on Sidur 450 steel, it is necessary to inspect the surface of each manufactured test tube under a stereo microscope before testing in order to detect micro-cracks and other damages. In the event that loads and micro-cracks (scratches) are detected, the test tube needs to be finished with additional polishing, and the procedure must be repeated until re-examinations confirm that all surface defects and micro-cracks (scratches) have been completely eliminated.

References

[1] Imamović A., Sunulahpašić R., Oruč M., Kablar O., Mujagić D., 2021, The influence of continuous casting technology on the cleaness of carbon steel , Advanced Technologies and Materials, 46 (1)

[2] Gigović-Gekić A., Oruč M., Vitez I., Vujičić B., 2009, Analize and research of non-metallic inclusions for steel 100Cr6, Metalurgija/ Metallurgy, ISSN 0543.5846, 48 (1)

[3] Tong K., Sun H., Duan L., Zuo X., 2025, Influence of TiN inclusions and segregation bands on the mechanical properties and ballistic performance during ballistic impact tests in low-alloy high-strength steel, Sec. Structural Materials, (12)
https://www.frontiersin.org › fmats.2025.1545242 › full (accessed 28 June 2025)

[4] Liu D. , Wang Z., Liu J., Wang Z., Zuo X., 2022, Study of the Fracture Behavior of TiN and TiC Inclusions in NM550 Wear-Resistant Steel during the Tensile Process, Journals Metals 12 (2)

[5] Kožuh, S., 2010. Specijalni čelici-skripta, Metalurški fakultet, Sveučilište u

[6] Luksic 2020 Zavrsni Preddiplomski | PDF
https://www.scribd.com › document (accessed 10 June 2025)

[7] Vitez, I., Oruč, M., Sunulahpašić, R., 2006, Ispitivanje metalnih materijala, mehanička i tehnološka ispitivanja, FMM, Univerzitet u Zenici, BiH

[8] Oruč, M., Sunulahpašić, R., 2009, Lomovi i osnove mehanike loma, FMM, Univerzitet u Zenici, BiH

[9] sidur-450.pdf
https://www.hardsteel.com.ua › uploads › 2019/02 (accessed January 2025).

[10] Oruč, M., Sunulahpašić, R., Hadžalić, M., 2019, Lomovi metalnih dijelova /Fractures of metallic parts, MAŠINSTVO, ISSN 1512-5173, 3-4(16), 63-75.

[11] Standard BAS EN ISO 6507-1: 2018

[12] Standard ASTM E 407-07

[13] Standard ASTM E 112-13

[14] Lei J., Zhao D., Jiang Y., 2018, Research on the Solid Solution Behavior of Titanium Inclusion for the High Strength Tire Cord Steel , Journal of Surface Engineered Materials and Advanced Technology, 8 (3)

[15] Mujagić, D., Imamović, A., Oruč, M., Muhamedagić, S., 2018, Analysis of the type and chemical content of the inclusion on SEM of the stainless steel with and without the addition of Zr and Te, 4th International Conference “New Technologies NT-2018”, Sarajevo, B&H

[16] Standard BAS EN ISO 6892-1:2017–B

[17] HIGH-STRENGTH FINE-GRAINED WEAR RESISTANT ...Skupina SIJ
https://cms.sij.si › SIDUR-450-2023_Acroni (accessed January 2025).

High density aluminium foam based heat exchangers

***Jaroslav Jerz*[1] *and Jaroslav Kováčik*[1]**

1) Institute of Materials & Machine Mechanics, Slovak Academy of Sciences, Dúbravská cesta 9/6319, 845 13 Bratislava, Slovakia

Corresponding author: e-mail: ummsjerz@savba.sk

Professional article

Abstract: The energy costs can be significantly reduced by increasing the use of renewable energy converted primarily from solar radiation. In the case that solar energy is considered to be utilized in buildings, the mismatch between energy availability and energy demand must be solved by heat storage. This contribution describes the principles of latent heat accumulation and the possibility of using Phase Change Materials (PCMs) reinforced by cellular metallic skeleton as a very efficient heat storage media.

Available PCMs are used accordingly to match the respective application temperature ranges. This contribution focuses for PCMs of temperature range from 5 to 40°C, typically used for heating – cooling applications in buildings. High-density aluminum foam (with the density above 1.5 g/cm^3) can, in addition to its function as an efficient heat exchanger, also play a significant role as a building structural material. Building structures with the ability to accumulate heat therefore play an important role in future buildings, as they significantly reduce operating costs and maintain adequate thermal comfort during both winter and summer season.

The possibilities how properly to regulate the temperature fluctuations for achievement not only the heating of hot water, but also maintaining sufficient thermal comfort in the interiors of buildings throughout the year will be described within this contribution. Various PCMs will be thoroughly examined to use the storage and release of latent heat when they are changing between solid and liquid state. The investigation of their thermophysical behavior will allow soon much more effective use of PCMs with a favourable impact on the environment in building construction. The new types of ecological bio-PCMs with huge potential of use, especially in lightweight building structures, can very effectively replace the required thermal capacity of buildings and significantly reduce the CO_2 footprint of used structural components.

Keywords: *aluminium foams; heat exchangers; phase change materials; heat storage*

1. Introduction

Various ice storage systems can be used as an effective way to remove excess heat during the summer, as well as a heat source for heat pumps during the winter. In this contribution we propose to reduce energy consumption and the greenhouse gas emissions by installing systems that can repeatedly capture large amounts of latent heat during the phase transformation of various PCMs. Obviously, the most common optimal storage cycle requires freezing the water during late winter and when the air temperature drops below 0°C. Increasing the storage volume increases both storage efficiency and the amount of free cooling available during summer. For these reasons, economies of scale can make larger systems more competitive than smaller ones. The size of the storage and the level of thermal insulation affect the duration of the charging and discharging. Thermal insulation significantly improves seasonal efficiency and free cooling. However, high current investment costs and the seasonal variation in CO_2 intensity of electricity reduce the economic and environmental competitiveness of long-term ice storage systems, respectively.

The overarching concept of the proposed contribution is a novel, high-efficiency thermal energy storage (TES) system based on PCMs reinforced with high-density aluminium foam skeletons. These composite materials are designed to overcome key limitations of conventional PCMs – namely, their

low thermal conductivity and susceptibility to leakage – by embedding them into thermally conductive porous metallic frameworks.

The high-density aluminium foams (density ≥ 1.5 g/cm³) have been prepared using a powder metallurgical technique, enabling the formation of a uniform network of interconnected pores. These microstructures, including microcracks in pore walls, provide a continuous heat conduction path, significantly enhancing thermal transport within the impregnated Bio-PCMs. The result is an advanced composite capable of rapid heat absorption and release, while maintaining mechanical stability and structural integrity across multiple thermal cycles.

2. Aluminium foams for building structures

2.1. Thermal energy system description

Heating and cooling of residential and industrial buildings interiors in order to maintain sufficient thermal comfort throughout the year with conventional heating, ventilation, and air conditioning (HVAC) installations are energy intensive and thus expensive. To reduce the energy use and the emission of greenhouse gases by these installations, the building sector needs energy efficient solutions operating at the lowest possible cost. Underground thermal energy storage provides a technically and economically feasible alternative for current conventional technologies for heating and cooling. Ground source heat pumps are recognized as outstanding heating and cooling systems which have very low maintenance requirements and are environmentally attractive. Furthermore, the integration of thermal energy storage for space heating and cooling of buildings is becoming increasingly important due to the rising cost of fossil fuels, environmental concerns and the flexibility towards the electricity network. A significant potential exist currently for the reduction of the energy consumption by an aquifer thermal energy system (ATES) described in Figure 1 [1]. During cooling mode, groundwater is extracted from the cold well to cool down by air handling unit (AHU) the ventilation air in the building interior. The building's heat is subsequently injected into the warm well. During winter mode, groundwater is extracted from the warm well and injected in the cold well after delivering its heat to the secondary circuit. Groundwater extracted from the warm well which has been warmed up during summer mode can be eventually transferred to the evaporators of the heat pumps, causing the flow to cool down. The heat pumps increase the temperature level of the heat by which it becomes useful to warm up the ventilation air.

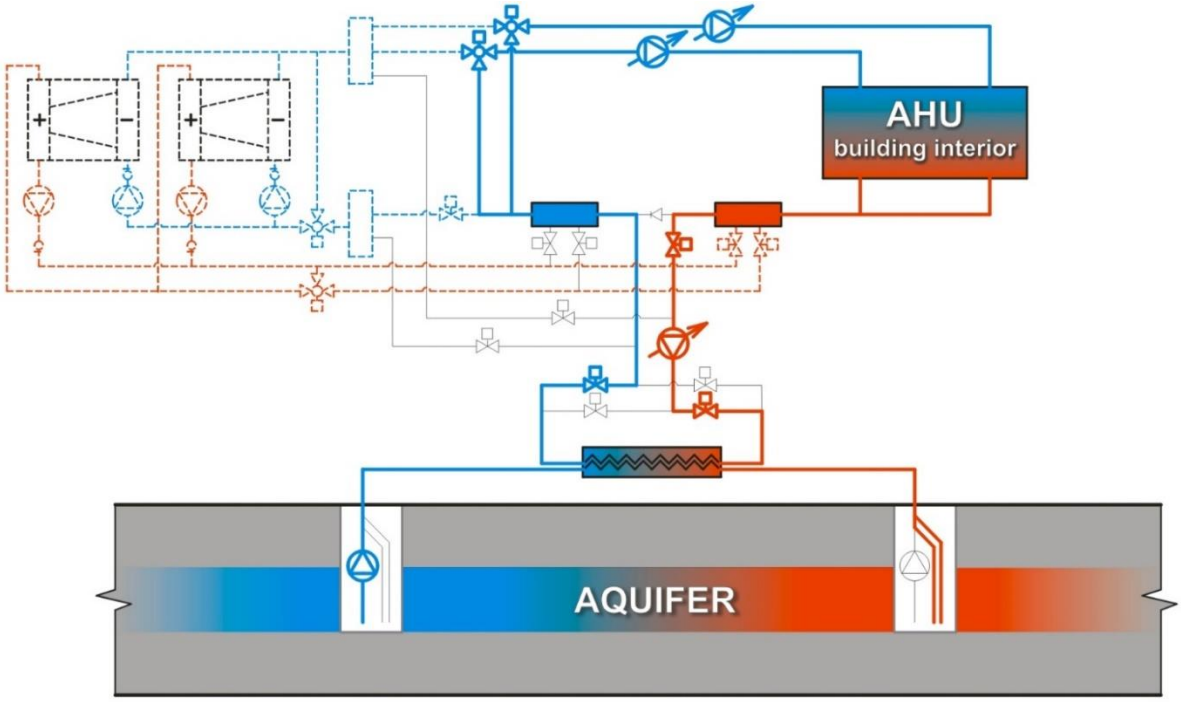


Figure 1. *Hydraulic scheme of the aquifer thermal energy system (ATES) in cooling mode*

The ATES conveniently consists of two wells at least 65 m deep and 100 m apart to prevent hydraulic and thermal interfaces. The cooling capacity of ATES can be at a groundwater flow rate of 100 m^3/hour can be approximately 1.2 MW. A major disadvantage of this system, which currently appears to be the best technical solution for ensuring sufficient thermal comfort in the interior of buildings with the efficient use of energy from renewable sources, is the relatively high investment costs. Moreover, an ATES project requires suitable hydrogeological conditions, as they have a strong influence on the system’s performance, as well as relatively high thermal loads and it must meet the regulatory requirements (the temperature of the injected water is not allowed to be above 25°C, thermal imbalance is not allowed between the hot and cold wells, etc.).

The thermal insulation of the building envelope has been recently considered as one of the best ways of improving the thermal performance and energy efficiency enhancement of the building. However, the conventional thermal insulation cannot be considered as the only system to achieve improved thermal performance in highly insulated buildings due to relatively high cost and diminishing energy benefits.

The researchers therefore aim to verify an alternative much more advantageous technical solution, shown in Figure 2, which requires the use of highly efficient heat exchangers with the possibility of repeatable storage of latent heat in the bio-material during its phase transformation between solid and liquid states. A seasonal cylindrical underground reservoir used for conditioning of the ventilation air in residential or industrial buildings with a diameter of 3.2 m and a depth of 20 – 30 m may be filled with snow and ice at the end of the winter season. A heat exchanger on the base of bio-PCMs reinforced with a metal foam skeleton, which is the subject of this contribution, is in this case located at the bottom of such an underground reservoir. It would bring significant savings in investment and operating costs for maintaining sufficient thermal comfort in the interiors of future residential and industrial buildings and building complexes.

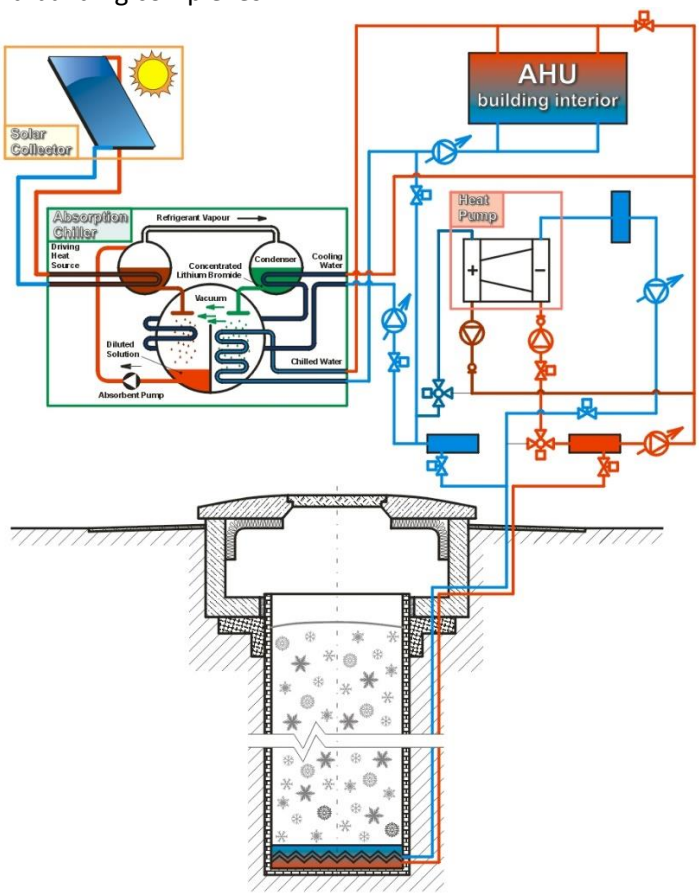


Figure 2. *Seasonal cold underground storage tank used for ventilation air conditioning in buildings with a PCMs-based heat exchanger reinforced with an aluminium foam skeleton placed at its bottom*

2.2. Thermal energy storage

Thermal energy storage (TES) allows the storage of heat so that it can be used later. The storage method is therefore reversible, i.e. capable of being charged as well as discharged repeatedly. Sensible heat storage is based on changing a material's temperature by changing its internal energy. Unlike PCM, it does not undergo any phase change during the storage process. The amount of energy stored, Q (kJ), is expressed by the following equation:

$$Q = \rho \cdot C_p \cdot V \cdot \Delta T \tag{1}$$

where ρ (kg/m^3) and V (m^3) is the density and volume of the storage material, respectively, C_p is specific heat over the temperature range of operation (kJ/kg·K), and ΔT is temperature range of the operation (K).

When a material changes phase from solid to liquid, it absorbs a large quantity of energy to break the intermolecular bonds. The uptake of this thermal energy, also known as latent heat, happens whilst the temperature of the material remains constant or within a very close temperature range i.e. isothermal (Figure 3). This process is reversible i.e. the phase change from liquid to solid in which the latent heat is released. A small volume change usually follows the melting/solidification at around 10%. The amount of the latent heat, ΔQ (kJ) stored is calculated from the differences of enthalpy between the two phases, ΔH and it can be expressed as follows:

$$\Delta Q = \Delta H = m \cdot \Delta h \tag{2}$$

where m is the mass of the storage material (kg) and Δh is the specific enthalpy (kJ/kg). Heat accumulation through sensible heat is also part of the process before and after the melting process.

PCMs undergo melting and solidification at a temperature within the operating range of the heat storage applications. They are able to store a large amount of energy in a small volume range, which remains at a constant temperature.

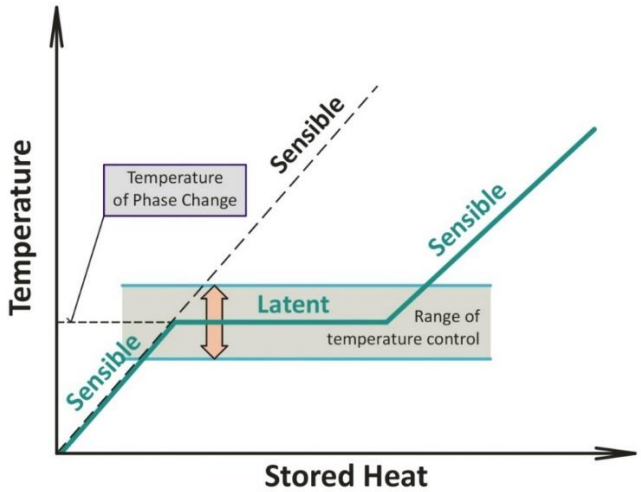


Figure 3. *The temperature-heat energy response of the PCMs [3]*

2.3. The role of aluminium foam in heat transfer

The low thermal conductivity of bio-based PCMs dramatically reduces the speed of the melting and solidification process and causes a wide temperature distribution within themselves. The thermal conductivity of coconut oil is approximately 0.21 W/(m·K) in the liquid state and 0.26 W/(m·K) in the solid state [4]. Impregnating of bio-based PCMs into a highly thermally conductive porous aluminium foam skeleton (Figure 4) significantly increases thermal conductivity and thus also affects the heat storage ability. The random distribution of the porous internal structure and relatively high open porosity (pores are interconnected by microcracks in pore walls) are used to enhance and accelerate

the phase change process without significant reduction of the heat storage capacity of bio-based PCMs.

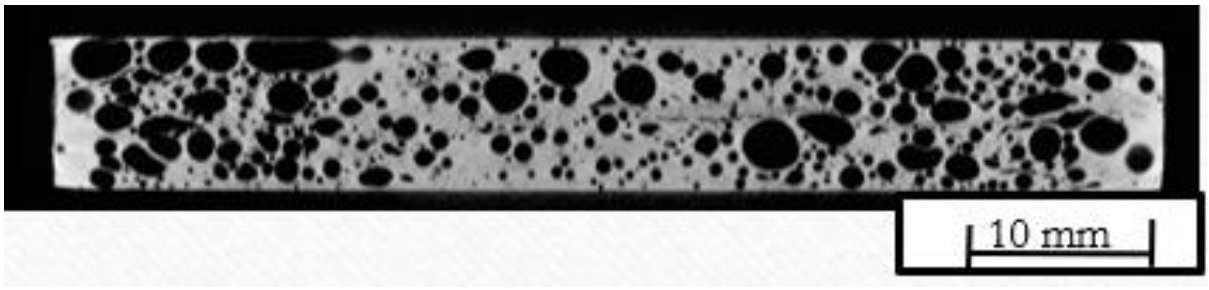


Figure 4. *X-ray tomography image of aluminium alloy Al-1050 (99.7% of Al) foam with 36.25% porosity (density: 1.72 g/cm^3). Foamable precursor was prepared powder metallurgically using 0.05 wt.% of TiH_2 as a foaming agent [3]*

A major original innovation, which is thoroughly explored in this contribution, is the use of an unusually efficient heat exchanger with thermal conductivity higher than approximately 100 W/(m·K), which has more than 30% of its volume impregnated with bio-based PCM, capable of repeatedly storing the latent heat of its phase transition between the solid and liquid states at a temperature of 23 – 28 °C.

The scientists involved in this research have all the technological know-how necessary to prepare a composite based on a bio-based PCMs reinforced with a highly conductive foamed aluminium skeleton. Moreover, they also have all the prerequisites for a thorough analysis of heat flows and thus the possibilities of using the investigated composite materials in various industrial applications, which allows a significant reduction in energy consumption compared to current technical solutions.

The system described in this contribution is an example demonstrating one of the possibilities of how the investigated bio-materials could significantly help increase the share of renewable energy sources and thus reduce energy consumption to maintain sufficient thermal comfort in building interiors without the need to increase the investment and operating costs of future buildings.

Conduction of heat through the solid aluminium pore walls, conduction through the gas phase in the pores, convection of the gas and radiation are the main mechanisms which may contribute to the thermal conductivity of an aluminium foam. A wide variety of models for the conduction mechanism, all of them proposed for closed-cell foams, has been considered recently. Nowadays it is the Ashby model one of the most accepted models described thermal conductivity of cellular solids similar to aluminum foam. According to this model overall conductivity of the foam is based on conduction through the combined gas and solid phase, λ_{gs} (W/m·K):

$$\lambda_{gs} = \zeta \cdot \lambda_s \cdot (\rho_f/\rho_s) = \zeta \cdot \lambda_s \cdot (1 - V_g) \quad (3)$$

where ρ_f and ρ_s are foam and solid density, respectively, λ_s is the conductivity of solid (aluminium), and V_g is the volume fraction of gas in the cellular material also named porosity. ζ is an efficiency factor which allows for the tortuous shape of the cell walls, which ranges between 1/3 and 2/3 [6]. Thermal conductivity of aluminium λ_s = 237 W/(m·K). It can be therefore expected, that overall conductivity of aluminium foam with the density ρ_f = 1.8 g/cm^3 can reach the value of λ_{gs} = 53 – 105 W/m·K (see Figure 5).

The emissivity of the surface of an aluminium foam (its effectiveness in emitting energy as thermal radiation) is almost always higher than that one of the bulk aluminium from which the foam is made of [7]. The foam will emit or absorb more thermal radiation than structural component made of bulk aluminium as the actual surface area of the foam is always at least slightly higher at equal outer dimensions. This property in combination with small specific heat per unit volume can be effectivelly utilized in structural applications where rapid heating or cooling by radiation is required.

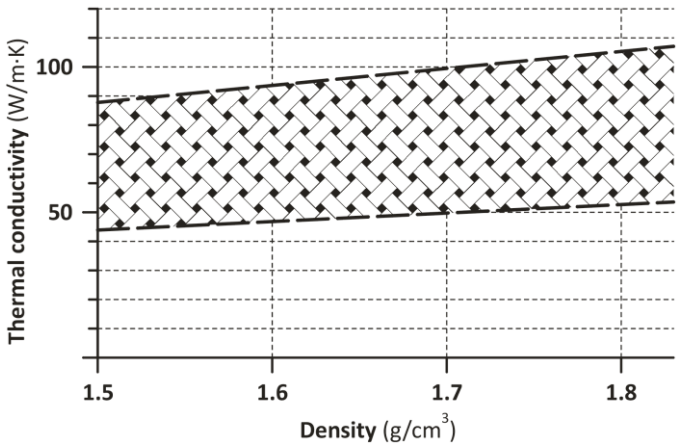


Figure 5. *The relationship between the thermal conductivity of aluminium foam and its density*

Although ceramic and polymer foams are used more for thermal insulation than for any other purpose, application of aluminium foams in this field is unlike because their thermal conductivity λ is about several orders of magnitude higher then polymers. However, higher thermal conductivity and diffusivity of aluminium foam can be successfully utilized not only in heat exchangers of building structures, but also in heat sinks for power electronics, air-cooled condenser towers and regenerators, etc. The main design principles for heat exchangers made from high density aluminium foams are:

- ✓ high thermal conductivity of aluminium foam based heat exchanger;
- ✓ turbulent flow of heat transfer fluid to enhance local heat transfer; and
- ✓ minimized low-pressure drop between fluid inlet and outlet.

The PCMs to be used in the design of aluminium based thermal storage systems should have desirable thermophysical, kinetic and chemical properties:

- ✓ melting temperature in the desired operating temperature range (to assure storage and extraction of heat in an application with a fixed temperature range);
- ✓ high latent heat of fusion per unit volume (to achieve high storage density compared to sensible storage);
- ✓ high specific heat to provide additional significant sensible heat storage;
- ✓ ability to impregnate in liquid state into porous aluminium foam with high thermal conductivity to assist the charging and discharging heat of the storage system;
- ✓ small volume change on phase transformation and small vapor pressure at operating temperature.

3. Conclusions

This contribution presents the possibility of using high-density aluminum foam in systems providing short-term heat accumulation in building structures. The heat exchangers based on the aluminium foam with the density above 1.5 g/cm^3 impregnated by PCMs can be successfully integrated into conventional heating, ventilation and air conditioning systems, solar collectors, hot water tanks, ventilation ducts, specific heat exchangers as well as also into packed bed reactors in the cemical process industry.

There have been several advantages for the storage collector system that can be achieved such as, reducing the thermal energy loss of the system, reducing the initial cost, reducing the space required for the system. The following conclusions can be drawn as follow:

- ✓ The incorporation of high density aluminium foam based heat exchangers into seasonal cold underground storage tank used for ventilation air conditioning in buildings was studied extensively whereas further investigations requires comparison of this system with state-of-the-art aquifer thermal energy system under various real weather conditions.

- ✓ Based on the experimental results obtained by investigation of the thermal behavior of PCMs embedded in high-density aluminum foam heat exchangers, their great potential significantly to reduce energy consumption to ensure sufficient thermal comfort and domestic hot water heating can be expected.
- ✓ An optimization tool at the early design stage is required for creative system design such as the storage dimension and suitable PCMs with specific melting point to get a good thermal behavior.

Acknowledgments

The financial support by the Slovak Grant Agency for Science under the contract VEGA 2/0102/25 (project: Aluminium foam reinforced bio-based phase change materials for latent heat storage) is gratefully acknowledged.

References

[1] Vonhoudt, D., Desmedt, J., Van Bael, J., Robeyn, N., Hoes, H., 2011. An aquifer thermal storage system in a Belgian hospital: Long-term experimental evaluation of energy and cost savings. In: Energy and Buildings, 43, pp. 3657-3665.
https://www.sciencedirect.com/science/article/pii/S0378778811004427

[2] Gopinathan, A., Jerz, J., Kováčik, J., Dvorák., T., 2021. Investigation of the relationship between morphology and thermal conductivity of powder metallurgically prepared aluminium foams. In: Materials, vol. 14, no. 3623, ISSN 1996-1944.

[3] Gopinathan, A., 2021. Composite panels with aluminium foam skeleton for heat storage, PhD Thesis, Trnava.

[4] Irsyad, M., Amrizal, A., Susila, M. D., Amrul, A., Fransisco, T. M., 2022. Heat transfer characteristics of coconut oil as phase change materials in freezing process. In: Int. Journal on Techn. and Phys. Problems of Engineering, vol. 14, iss. 50, no. 1, 29-33, ISSN 2077-3528.

[5] Gopinathan, A., Jerz, J., Kováčik, J., Sadeghi, B., Cavaliere, P., 2023. Implementation of T-history method to determine the thermophysical. In: Thermochimica Acta 723, 179485. doi.org/10.1016/j.tca.2023. 179485.

[6] Solórzano, E., Reglero, J. A., Rodríguez-Pérez, M. A., Lehmhus, D., Wichmann, M., de Saja, J. A., 2008. An experimental study on the thermal conductivity of aluminium foams by using the transient plane source method. In: International Journal of Heat and Mass Transfer, vol. 51, 6259–6267. doi.org/10.1016/j.ijheatmasstransfer.2007.11.062..

[7] Simancik, F., Kovacik, J., 2002. Chapter 5.3 - Electrical, Thermal, and Acoustic Properties of Cellular Metals, in: Handbook of Cellular Metals, Production, Processing, Applications, Edited by Degisher, H. P. and Kriszt, B., 215-242, Wiley-VCH Verlag GmbH & Co. KGaA, ISBN: 3-527-30339-1.

[8] Anuar Sharif, M. K., Al-Abidi, A. A., Mat, S., Sopian, K., Ruslan, M. H., 2015. Review of the application of phase change material for heating and domestic hot water systems. Renewable and Sustainable Energy Reviews 42, 557-568, doi.org/10.1016/j.rser.2014.09.034.

[9] Kahwaji, S., White, M. A., 2019. Edible Oils as Practical Phase Change Materials for Thermal Energy Storage. In: Appl. Sci. vol. 9, p. 1627; doi.org/10.3390/app9081627.

Multi-objective optimization of thermally sprayed CrNiMo coatings on titanium substrates: influence of spray distance and layer count on mechanical properties using desirability analysis

***Damir Jurić*[1], *Nikša Čatipović*[1], *Ivan Peko*[2], *Jure Krolo*[1], *Karla Antunović*[1], *Karla Kunac*[1], *Matej Kljajo*[3], *Angelo Oñate*[4] *and Víctor Tuninetti*[5]**

1) University of Split, Faculty of Electrical Engineering, Mechanical Engineering and Naval Architecture, Ruđera Boškovića 32, 21000 Split, Croatia

2) University of Split, Faculty of Science, Ruđera Boškovića 33, 21000 Split, Croatia

3) University of Mostar, Faculty of Mechanical Engineering, Computing and Electrical Engineering, Matice hrvatske bb, 88000 Mostar, Bosnia and Herzegovina

4) Department of Materials Engineering (DIMAT), Faculty of Engineering, Universidad de Concepción, Edmundo Larenas 315, Concepción 4070415, Chile

5) Department of Mechanical Engineering Universidad de La Frontera, Temuco 4811230, Chile

Corresponding author: djuric03@fesb.hr

Original scientific article

Abstract: This study investigates the mechanical properties of thermally sprayed coatings deposited on Ti6Al4V alloy substrates. A nickel-based powder with additions of Al and Mo was used as an interlayer, while the functional coating consisted of austenitic CrNiMo steel powder. The samples were preheated to 130°C prior to deposition, which was carried out using a flame spray gun. A Taguchi L6 orthogonal experimental design was employed with two variable parameters: spray distance (150 and 250 mm) and number of coating layers (1, 2, 3). The testing included measurements of macrohardness and surface coefficient of friction. The results showed that spray distance has a greater influence on the coating's mechanical properties compared to the number of layers. The optimal distance provided a good balance between thermal energy and particle velocity, resulting in better adhesion and more favorable coating microstructure. At shorter distances, negative effects such as overheating were observed, while larger distances led to poorer adhesion and reduced properties. On the other hand, increasing the number of layers gradually improved hardness, with the most pronounced effect seen when transitioning from one to two layers, after which the properties stabilized. . Multi-objective desirability analysis identifies optimal parameters, 250 mm spray distance with 1 layer for sprayed coatings and 3 layers for polished coatings, achieving a balance between minimized friction and maximized hardness. Regression models R^2 and ANOVA validate the findings, confirming spray distance as the dominant factor influencing coating performance. The results demonstrate that precise control of process parameters is crucial for enhancing coating quality and functionality. Although both factors affect the coating properties.

Keywords: *thermal spraying; Ti6Al4V; macohardness; spraying distance; number of layers; coefficient of friction*

1. Introduction

Thin film deposition technologies represent a key tool in modern materials engineering, with applications in industries such as aerospace, automotive, energy, and biomedical. These technologies enable modification of surface properties such as wear resistance, corrosion, high temperatures, or enhanced biocompatibility, often without compromising the mechanical stability of the underlying substrate [1]. Thermal spraying is one of the oldest surface engineering methods, with origins dating back to the early 20th century. The main advantages of thermal spraying include flexibility in material selection (metals, ceramics, carbides, polymers), the ability to deposit coatings of various thicknesses,

low thermal deformation of the substrate (the base material onto which the coating is applied), and relatively low costs compared to vacuum-based techniques such as Physical Vapor Deposition (PVD) and Chemical Vapor Deposition (CVD) [2–4]. A significant advantage of this method is the low thermal distortion of the substrate due to short contact time and the relatively low temperature of the substrate, thermal spraying allows the processing of temperature-sensitive materials without degrading their mechanical properties. Flame spraying, as one of the simplest and most cost-effective variants, is particularly notable in applications where large surfaces need to be processed quickly, such as in shipbuilding, the energy sector, or heavy machinery. Before spraying, the substrate must be properly prepared. The surface is cleaned and often roughened (e.g., by sandblasting) to increase coating adhesion, and in most cases, preheating is subsequently performed. Sandblasting or grinding enhances the interfacial reaction, resulting in increased adhesion [5]. Preheating primarily serves to reduce the temperature difference between the sprayed particles and the substrate, thereby improving the bonding of the deposited material. By varying process parameters such as surface roughness, preheating temperature, spray temperature and velocity, number of passes, and coating thickness, the characteristics of the deposited layer can be significantly influenced [6]. Compared to plasma or oxy-fuel systems, the velocity and temperature of deposited particles are considerably lower, approximately 150 m/s and 2000–3000 K, respectively [7–8]. Owing to the robustness of the coatings, which are relatively thick and mechanically stable, it is possible to test various mechanical properties and study the influence of spraying parameters on coating performance.

Arboleda et al. [9] investigated the influence of spray distance and the volumetric ratio of acetylene to oxygen (C_2H_2:O_2) on the microstructure and roughness of Al_2O_3–13%TiO_2 coatings deposited on an aluminium alloy substrate and showed that spray distance has a significant effect on coating thickness, with the thickest coatings obtained at a greater spray distance (140 mm). This can be attributed to greater particle deceleration and cooling, which consequently leads to reduced deformation upon impact and the formation of thicker lamellae. Mihoob et al. [10] focused on the optimisation of thermal spraying parameters (distance, number of passes, and gas pressure) when spraying Mo/ZrB_2 metal–matrix composite coatings. The primary goal was to achieve the highest possible Young’s modulus and hardness, as well as good surface formation without cracks and with minimal porosity, with spray distances of 20 cm, 25 cm, and 30 cm, number of passes of 12, 18, and 24, and gas pressures of 2 bar, 4 bar, and 6 bar. The shortest distance of 20 cm proved optimal for hardness. Particles spend less time in the air before impact, retaining relatively high temperature and velocity, which results in better droplet adhesion and lower porosity. While the longest distance (30 cm) resulted in the lowest hardness and Young’s modulus, the intermediate distance of 25 cm was optimal for Young’s modulus of elasticity. Although an increased number of passes should positively influence cohesion and porosity, an excessive number of layers can lead to the accumulation of internal stresses, weaker bonding between layers, or an increased likelihood of defects within a thicker layer. In the study, 24 passes were the less favourable option for both hardness and Young’s modulus. This suggests that the excessive thickness obtained with 24 passes did not improve the mechanical properties and may have even worsened them due to the aforementioned issues (stress accumulation, increased probability of defects within the layer). Although the method is essentially simple and does not require advanced technology, it is necessary to precisely optimise the parameters, as even small variations in parameters (spray distance, pressure, fuel ratio, etc.) can significantly affect the final results.

2. Experimental method

2.1. Material and test methods

In this study, the substrate used was Titanium Grade 5 (Ti6Al4V), one of the alpha–beta titanium alloys. The alloy consists of approximately 6% aluminium and 4% vanadium, with the remainder being titanium. Due to its mechanical and chemical properties, particularly its high strength-to-weight ratio and exceptional corrosion resistance, Ti6Al4V is widely used in the aerospace, chemical, and medical industries [11–12]. The alloy also exhibits high resistance to uniform, galvanic, crevice, and pitting corrosion, making it an almost ideal choice for applications in aggressive environments where other

metals degrade rapidly [13]. The test samples were cylindrical in shape, with a diameter of 12 mm and a length of 20 mm. Spraying is not feasible on thin samples (<10 mm) due to the high temperatures involved, which can result in delamination of the surface layer caused by the inability to dissipate heat from the sprayed surface.

The base (primer) powder used was CASTOLIN ULTRABOND 5100, a nickel-based metallic powder alloyed with aluminum and molybdenum (Ni-5Al-5Mo). This powder is known for its exceptionally high adhesion strength, making it recommended for use as an intermediate layer prior to the application of functional coatings. Coatings produced from this material demonstrate good corrosion resistance in contact with water, atmosphere, and alkaline media. The coating is micro-porous and can be further processed by grinding or machining. Its hardness ranges from 140 to 190 HV10, while tensile strength lies between 30 and 50 MPa [14].

For the final (functional) layer, Castolin RotoTec 19300 CE was used, a metallic powder based on austenitic CrNiMo steel, shown in Figure 1. This material provides good resistance to sliding wear in metal-to-metal contact, particularly under lubricated conditions. In addition to good machinability, it also exhibits high corrosion resistance and stability under operating conditions up to 450°C. The coating is heterogeneous and micro-porous, with a typical hardness of around 250 HV30. The powder grain size ranges from 38 to 125 µm, and the density is approximately 7.8 g/cm³. Typical applications include pistons, valve spindles, and components used in the chemical industry [15].

The coating deposition was carried out using a RotoTec 80 gas thermal spraying device, shown in Figure 2. Prior to the application of the functional layer, the cylindrical samples were cleaned with acetone, roughened with abrasive paper (grit 200), and preheated to 130 °C. This was followed by the gradual deposition of the base and final layers, with temperature being monitored during the process. The device parameters, including gas flow rate, rotation speed, and the amount of material deposited, were kept constant throughout all tests to ensure repeatability of results. Within the experimental design, a Taguchi L6 orthogonal array was used with two control variables: spraying distance (150 mm and 250 mm) and number of deposited layers (1, 2, and 3). This method enabled a systematic evaluation of the influence of individual parameters on the final mechanical properties of the coating, while minimising the number of experiments required. Figure 3. shows sprayed samples.



Figure 1. *Castolin RotoTec 19300 CE*



Figure 2. *RotoTec 80*



Figure 3. *Titanium samples after spraying*

3. Mechanical properies testing

3.1. Macrohardness

Macrohardness measurements were carried out on the bare (uncoated) titanium substrate, on the samples after coating deposition, and finally on the samples ground to the same height. In this way, it was possible to monitor hardness changes at each stage of the surface treatment process. Each sample was tested three times in each stage (after coating deposition and after grinding), while macrohardness on the uncoated titanium was measured once to obtain a reference value. The measurements were performed using a WOLPERT DIA TESTOR 2 RcS hardness tester. Table 1. shows the hadness results for polished and sprayed layer.

Table 1. *Average macrohardness of the sprayed and polished layer*

Sample	Spraying distance (mm)	Number of layers	Hardness of the polished layer (HV)	Hardness of the sprayed layer (HV)
1	150	3	120,3	180,0
2	150	2	119,3	157,3
3	150	1	180,3	266,3
4	250	3	200,7	206,7
5	250	2	148,3	176,3
6	250	1	230,3	250,3

3.2. Coefficient of fricition

The testing of the coefficient of friction and wear was conducted on the surfaces of six samples that had previously been sprayed and ground to the same level. The testing was carried out using a device Pin-On-disc tribometre, TRB^3(Anton Paar) [16].

Set parameters: Pin material: ruby
Linear speed: $1.95\ m/s$
Normal load: 15N

Before testing, the sample surfaces were cleaned with 70% ethanol to remove surface contaminants that could affect the results. Table 2. shows the averade coefficient of fricition for polished and sprayed layer.

Table 2. *Average coefficient of friction of the sprayed and polished layer*

Sample	Spraying distance (mm)	Number of layers	CoF sprayed	CoF polished
1	150	3	0,54	0,365
2	150	2	0,57	0,476
3	150	1	0,636	0,592
4	250	3	0,531	0,329
5	250	2	0,605	0,507
6	250	1	0,265	0,529

4. Multi-Objective Optimization

4.1. Regression Modelling and Response Surface Analysis

Multiple regression analysis was employed to quantify the influence of spray distance (**A**) and number of layers (**B**) on the measured responses: coefficient of friction (CoF) in the as-sprayed and polished states, and macrohardness in the as-sprayed and polished states. The regression models incorporated linear terms for **A** and **B**, a quadratic term for $\mathbf{B^2}$ to capture non-linear effects of layer count, and an interaction term (**A·B**) to account for coupled influences of spray distance and layer number. The general model form was expressed as:

$$Y = \beta_0 + \beta_1 A + \beta B + \beta_3 B^2 + \beta_4 AB \quad (1)$$

Predicted responses generated from the regression models were compared to experimental measurements to assess model adequacy. Although statistical analysis indicated that none of the models achieved significance at the 95% confidence level due to the limited experimental degrees of freedom, the fitted equations provided consistent engineering trends. Figure 4. and 5. shows the models for CoF indicated that increasing spray distance exerted a modest negative effect on friction values, whereas the number of layers displayed a non-linear influence, with the quadratic term suggesting the existence of an optimal layer count for friction reduction.

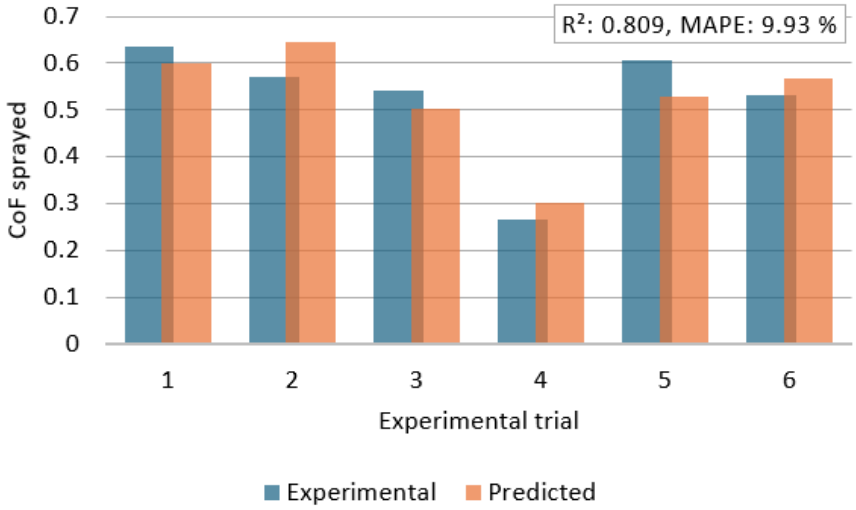


Figure 4. *Comparison experimental – regression model predicted responses, CoF sprayed*

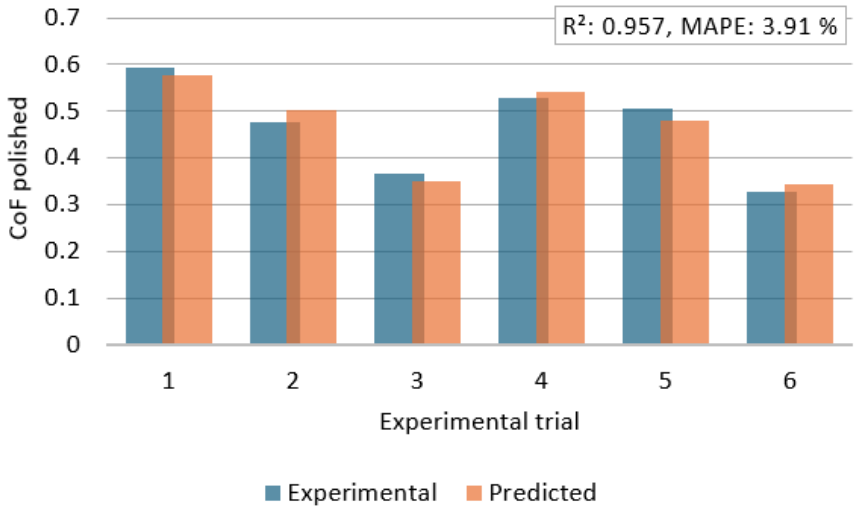


***Figure 5**. Comparison experimental – regression model predicted responses, CoF polished*

To visualise the parametric effects, three-dimensional response surface plots and corresponding two-dimensional contour plots were constructed for each response. Figure 6. and 7. show that in regard CoF, the response surfaces revealed broad valleys corresponding to optimal process regions, which shifted depending on the surface condition. In the as-sprayed state, minima in CoF were located toward moderate-to-high layer counts at extended spray distances, whereas in the polished state, the lowest CoF values were consistently associated with higher layer counts.

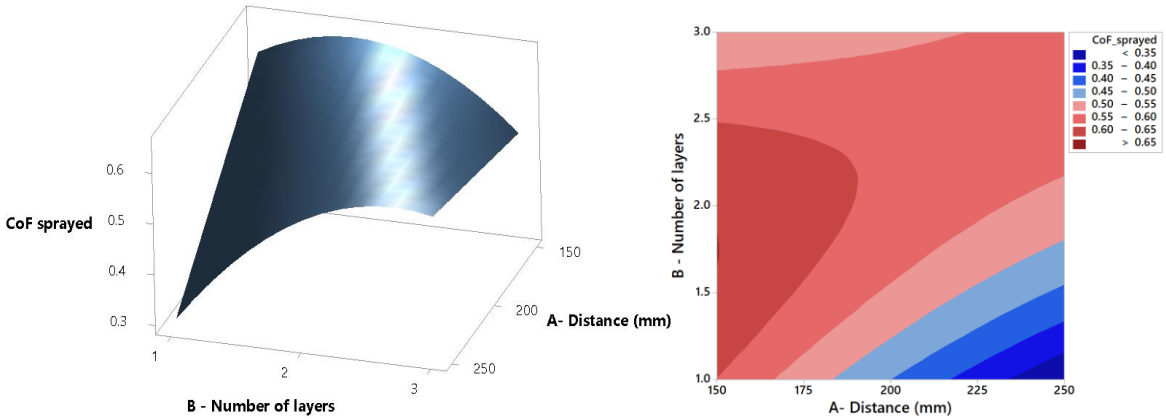


***Figure 6.** Response surface & contour plots, CoF sprayed*

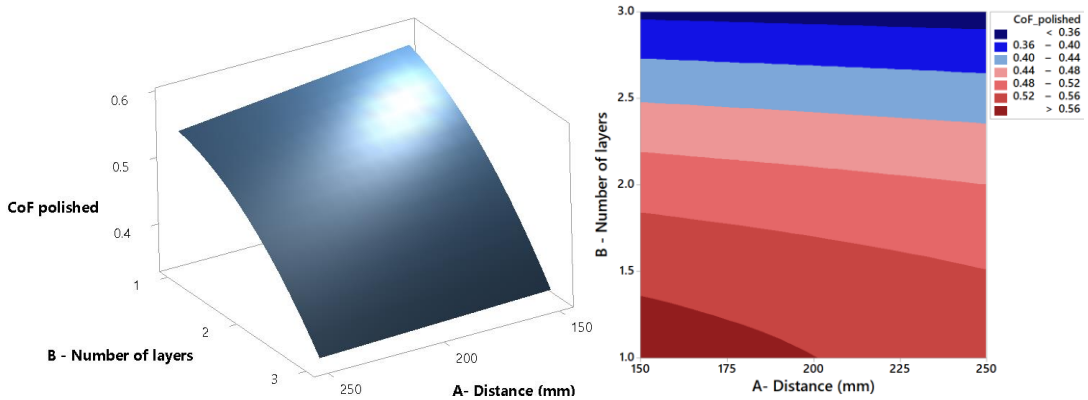


***Figure 7.** Response surface & contour plots, CoF polised*

For macrohardness, Figure 8. and 9. show that the number of layers exerted the strongest influence, particularly in the polished state, with both linear and quadratic coefficients contributing substantially to the prediction. Spray distance effects on hardness were less pronounced but in certain cases

indicated a slight hardness increase at greater distances, potentially linked to reduced thermal loading of the substrate.

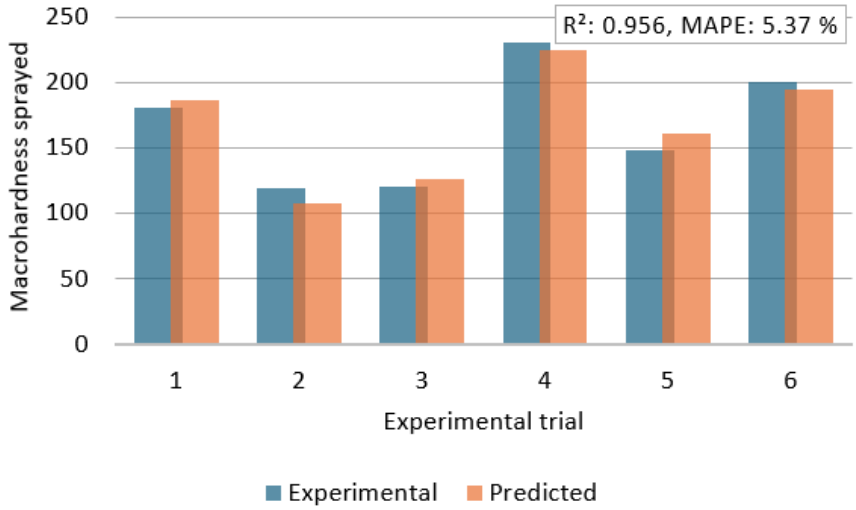


Figure 8. *Comparison experimental – regression model predicted responses, Macroardness sprayed*

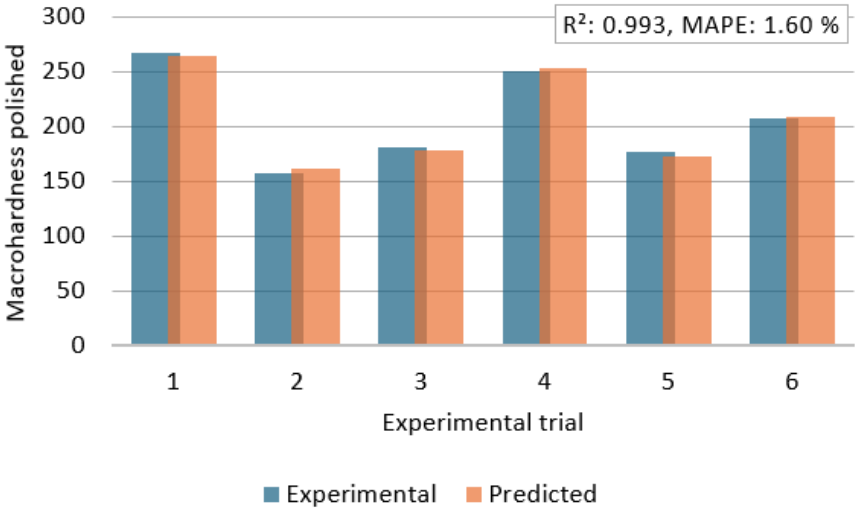


Figure 9. *Comparison experimental – regression model predicted responses, Macroardness polished*

Figure 10. and 11. show that macrohardness response surfaces exhibited distinct peaks at higher layer numbers, with relatively broad optimal zones indicating stable performance across a range of spray distances. Contour plots delineated these regions, enabling the identification of process windows that balance performance objectives and avoid regions where parameter changes yield negligible improvement.

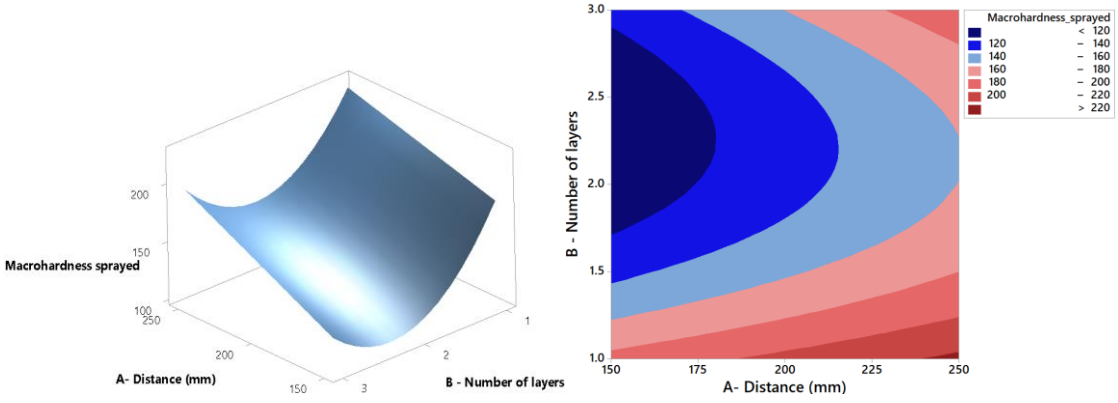


Figure 10. *Response surface & contour plots, Macroardness sprayed*

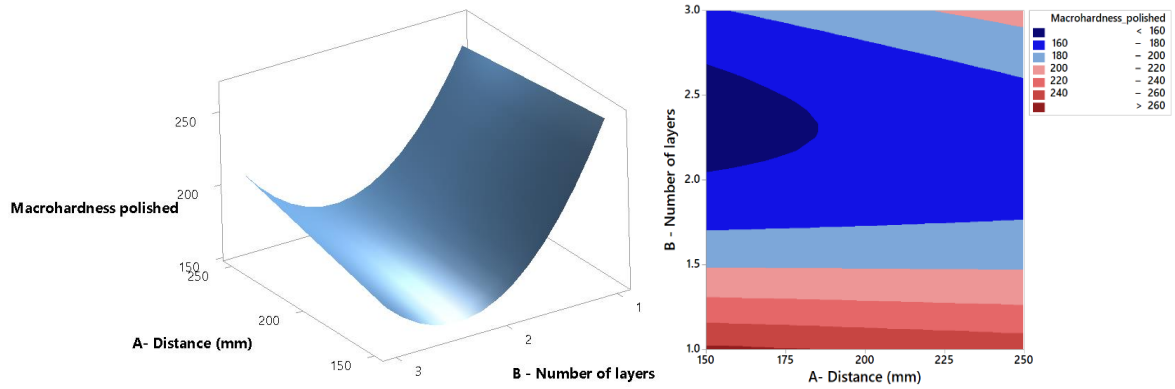


Figure 61. *Response surface & contour plots, Macroardness polished*

4.2. Analysis of Variance (ANOVA)

Analysis of variance was conducted for each regression model to assess the relative contributions of spray distance (**A**), number of layers (**B**), quadratic layer term (B^2) and the interaction term (**A·B**) to the total variation in each response. The ANOVA tables reported sums of squares, mean squares, F-values, and corresponding **p**-values. Due to the Taguchi L6 design and the resulting single degree of freedom for error, the statistical power was inherently limited, and none of the factor effects reached significance at the 95% confidence level. Nonetheless, the magnitude of the F-values and the relative contributions provided valuable insight into the physical behaviour of the system.

Table 3. and 4. shows that for the CoF models, the number of layers (**B**) consistently exhibited higher F-values than spray distance (**A**), indicating a greater influence on tribological performance. This was particularly evident in the polished state, where **B** and its quadratic term accounted for a substantial proportion of the explained variance. In the as-sprayed state, the interaction term (**A·B**) also contributed to the model, suggesting that the effect of spray distance on friction was modulated by the number of layers applied.

Table 3. *ANOVA for CoF sprayed*

Source	DF	Adj SS	Adj MS	F-Value	P-Value
Regression	4	0.07173	0.017933	1.06	0.613
A - Distance (mm)	1	0.048756	0.048756	2.89	0.339
B - Number of layers	1	0.000211	0.000211	0.01	0.929
B^2	1	0.011907	0.011907	0.71	0.555
AB	1	0.032761	0.032761	1.94	0.396
Error	1	0.016875	0.016875		
Total	5	0.088606			

Table 4. *ANOVA for CoF polished*

Source	DF	Adj SS	Adj MS	F-Value	P-Value
Regression	4	0.048435	0.012109	5.61	0.306
A - Distance (mm)	1	0.000529	0.000529	0.24	0.708
B - Number of layers	1	0.000018	0.000018	0.01	0.942
B^2	1	0.0019	0.0019	0.88	0.52
AB	1	0.000182	0.000182	0.08	0.82
Error	1	0.00216	0.00216		
Total	5	0.050595			

For macrohardness, Table 5. and 6. show the number of layers was again the dominant factor, with minimal contributions from spray distance. The quadratic term (B^2) was relevant for both surface conditions, implying diminishing hardness gains or slight declines beyond an optimal layer count.

Table 5. *ANOVA for Macrohardness sprayed*

Source	DF	Adj SS	Adj MS	F-Value	P-Value
Regression	4	9687.2	2421.8	5.54	0.307
A - Distance (mm)	1	110.7	110.7	0.25	0.703
B - Number of layers	1	3821.6	3821.6	8.75	0.208
B²	1	3214.4	3214.4	7.36	0.225
AB	1	231	231	0.53	0.6
Error	1	436.8	436.8		
Total	5	10124			

Table 6. *ANOVA for Macrohardness polished*

Source	DF	Adj SS	Adj MS	F-Value	P-Value
Regression	4	9469.23	2367.31	38.12	0.121
A - Distance (mm)	1	229.69	229.69	3.7	0.305
B - Number of layers	1	5960.87	5960.87	95.98	0.065
B²	1	4645.27	4645.27	74.79	0.073
AB	1	454.54	454.54	7.32	0.225
Error	1	62.11	62.11		
Total	5	9531.33			

Although the statistical significance of individual terms was constrained by the experimental design, the ANOVA results aligned with the physical mechanisms governing thermal spray deposition, where layer build-up directly affects coating density and cohesion, and spray distance influences splat morphology and oxidation behaviour. These observations supported the retention of all terms in the regression models for subsequent optimisation.

4.3. Desirability-Based Multi-Objective Optimisation

To identify parameter combinations that jointly optimise tribological and mechanical performance, a desirability function approach was implemented. In this method, each response variable was transformed into an individual desirability index ranging from 0 (completely undesirable) to 1 (fully desirable) according to the target objective—minimisation for CoF and maximisation for macrohardness. The individual desirabilities were then combined using a geometric mean to yield a composite desirability index for each set of process parameters. Table 7. shows multi-objective optimization problems settings

Optimisation was performed separately for the as-sprayed and polished surface conditions. Figure 12., 13., 14. and Table 8. show that for the as-sprayed state, the highest composite desirability (0.922) was achieved at a spray distance of 250 mm and a single coating layer, corresponding to a predicted CoF of 0.3025 and macrohardness of 224.27 HV. This result reflects the benefit of a thin, relatively smooth coating in reducing friction, while still maintaining sufficient hardness. In contrast, Figure 15., 16., 17. and Table 9. show that for the polished state, the optimal solution shifted to a spray distance of 250 mm and three layers, yielding a composite desirability of 0.671 with predicted values of CoF = 0.342 and macrohardness = 208.94 HV. In this case, the increased layer count provided greater coating integrity after grinding, preserving low friction and mechanical strenght.

Table 7. *Multi-objective optimization problems settings*

Multi-objective optimization problem	State	Objective functions	Goal
1	sprayed	coefficient of friction (CoF) macrohardness	*min* *max*
2	polished	coefficient of friction (CoF) macrohardness	*min* *max*

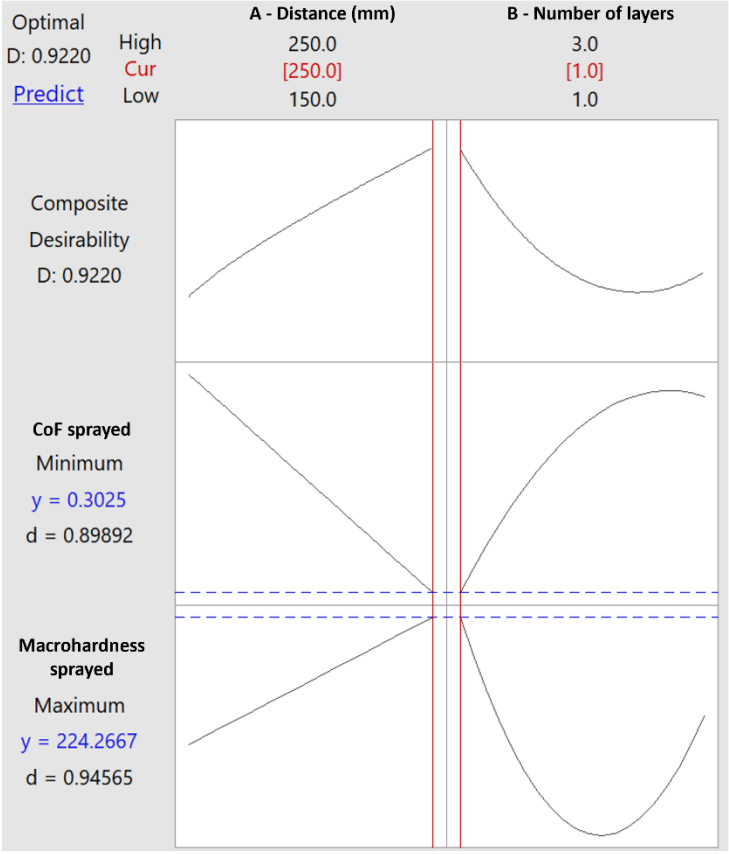


Figure 12. *Visualization of optimal solution for multi-objective optimization problem 1*

Table 8. *Optimal solution for multi-objective optimization problem 1*

Solution	A - Distance (mm)	B - Number of layers	CoF sprayed	Macrohardness sprayed	Composite Desirability
1	250	1	0.3025	224.267	0.921988

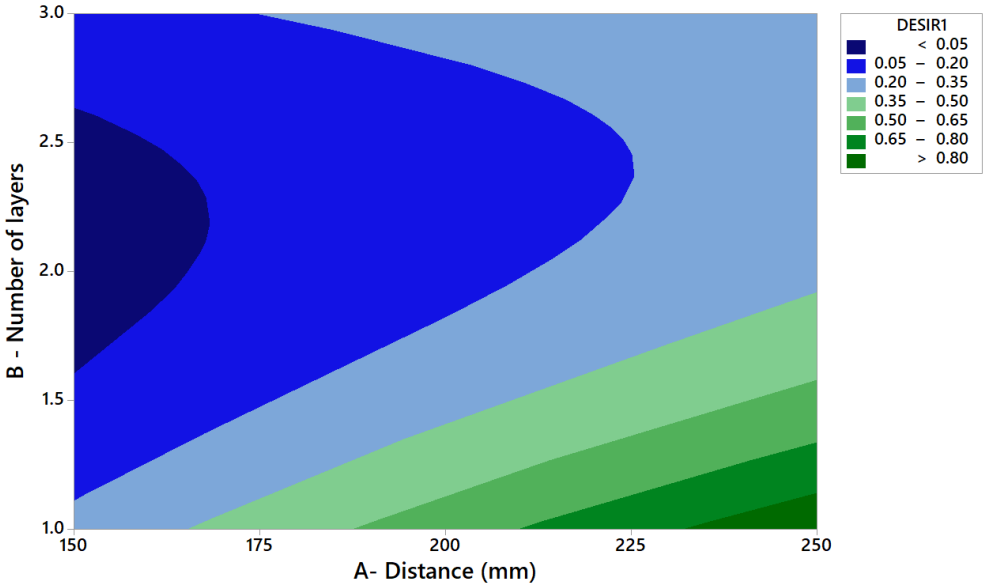


Figure 13. *Influence of process parameters on desirability distribution in multi-objective optimization problem 1*

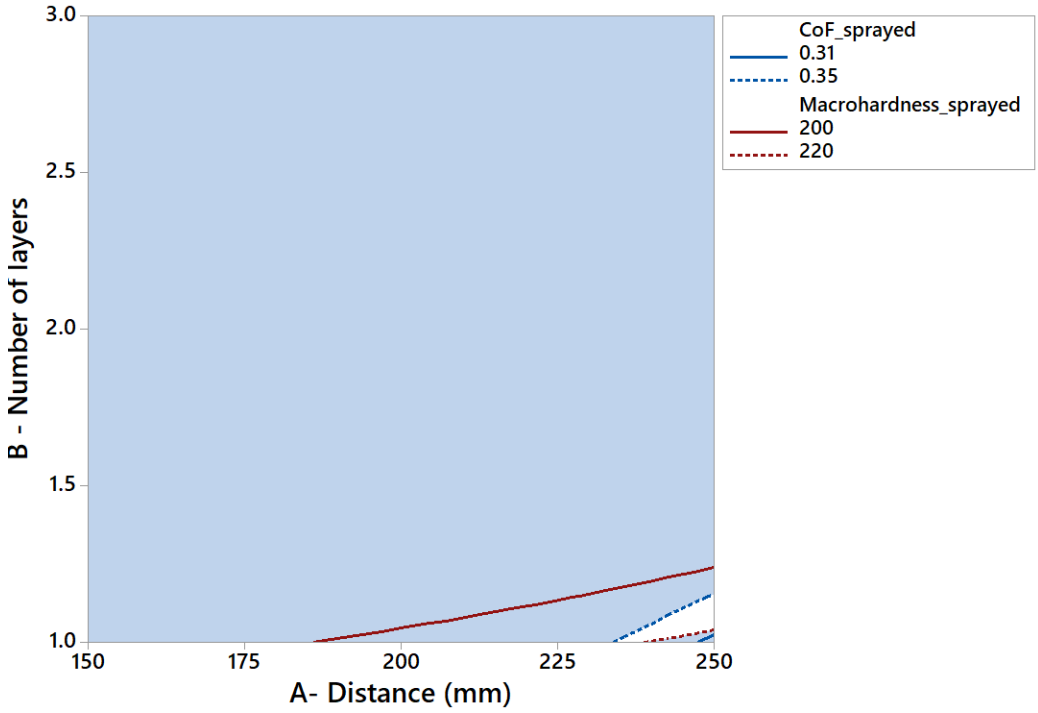


Figure 14. *Optimal processing area (white) for multi-objective optimization problem 1*

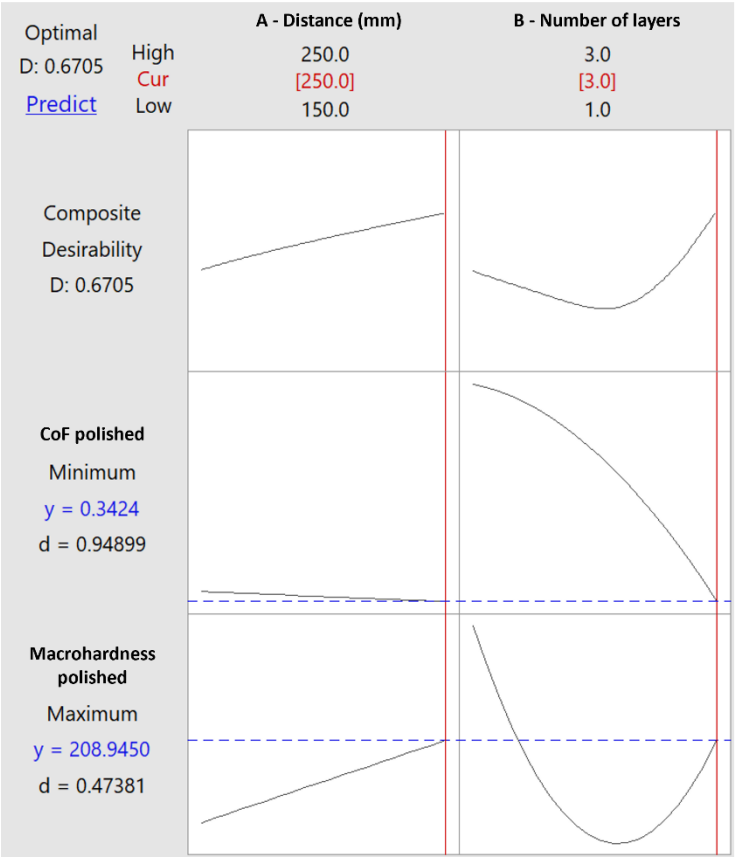


***Figure 15**. Visualization of optimal solution for multi-objective optimization problem 2*

***Table 8.** Optimal solution for multi-objective optimization problem 2*

Solution	A - Distance (mm)	B - Number of layers	CoF polished	Macrohardness polished	Composite Desirability
1	250	3	0.342417	208.945	0.670549

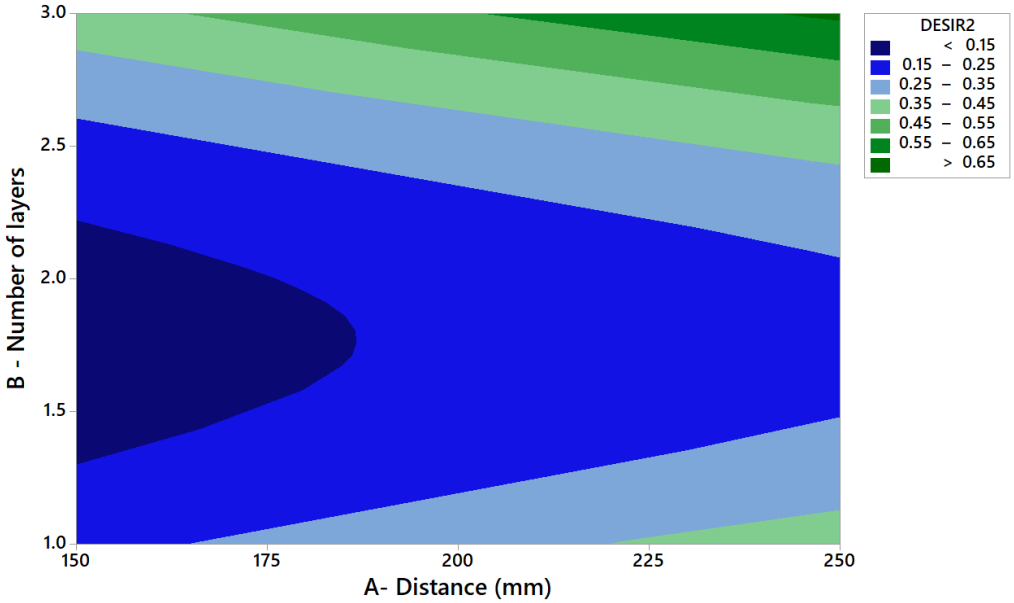


***Figure 16.** Influence of process parameters on desirability distribution in multi-objective optimization problem 2*

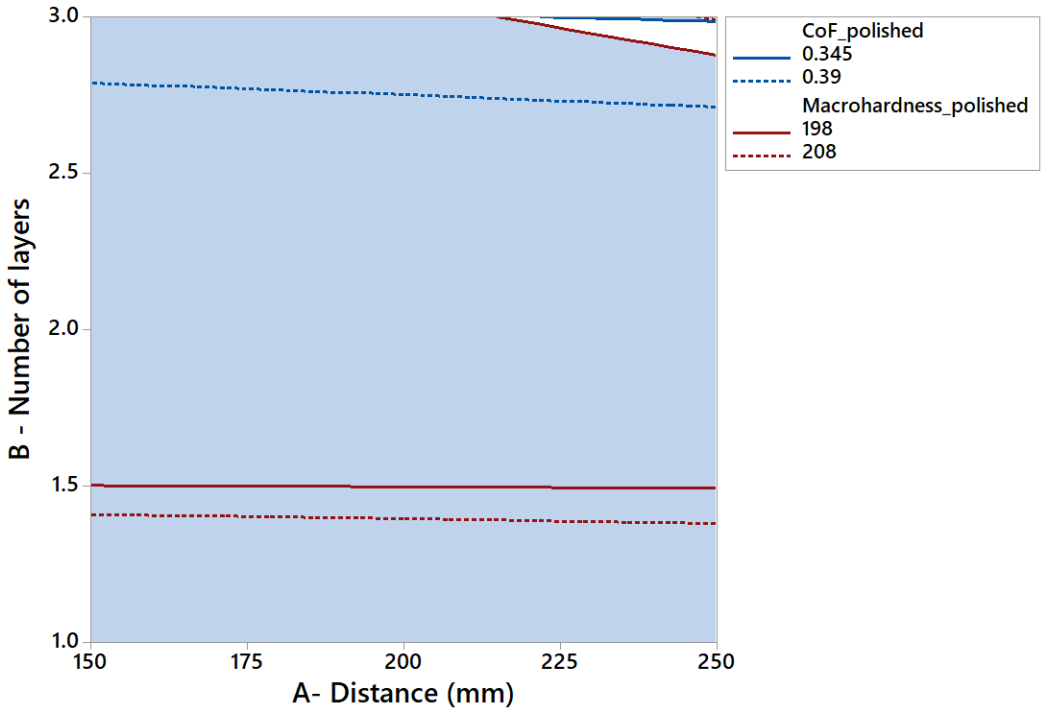


Figure 17. *Optimal processing area (white) for multi-objective optimization problem 2*

The desirability surfaces indicated that the optimal parameter region is dependent on the intended final condition of the coating. For components intended for service in the as-sprayed state, thinner coatings deposited at longer spray distances may be favoured. For applications requiring post-deposition finishing, thicker multi-layer coatings at similar spray distances are preferred to maintain performance. This outcome underscores the importance of integrating final surface condition into thermal spray process optimisation, rather than optimising solely on as-deposited properties.

5. Conclusion

This study investigates the effect of spray distance and number of layers on the mechanical properties of thermally sprayed CrNiMo steel coatings applied over a Ni-based interlayer on Ti6Al4V substrates. Coatings were deposited using a Taguchi L6 design at 150 and 250 mm with one, two, or three layers, and tested for macrohardness and friction coefficient. The results identify spray distance as the dominant factor, with optimal performance achieved at 250 mm for one-layer sprayed coatings and three-layer polished coatings.

- The influence of spraying distance shows that at a distance of 200 mm, the most stable and highest ground hardness was achieved, especially for samples with two layers, where the values were closest to the expected (≈266 HV).
- In contrast, at a distance of 150 mm, lower hardness values of the applied layer were recorded, except in the case of the sample with one layer, which showed unusually high hardness, potentially a result of the coating being penetrated during the measurement itself. Lower hardness values may be caused by overheating, oxidation, or excessive particle splattering during spraying [17-18].
- The distance of 250 mm showed the greatest range of results, suggesting reduced kinetic energy of the particles and weaker adhesion. Nevertheless, samples with one layer showed high hardness, which could be attributed to material concentration and lower porosity after grinding or to penetration of the layer itself, as in the case of sample 3.
- Influence of the number of layers shows different trends. Samples with one layer surprisingly achieved the highest hardness values in most cases. The first layer often bonds better to the

substrate, which can increase the overall hardness after processing. This can also be explained by the previously mentioned penetration of the applied layer during measurement.

- Samples with two layers, especially at the 200 mm distance, showed very stable and uniform results, making them the optimal choice in terms of repeatability and predictability.
- On the other hand, three layers did not necessarily result in higher hardness; in some cases, even lower values were recorded. Thickness itself can influence some measurements, but from a microstructural standpoint, each new layer is deposited onto previously cooled layers, so no significant difference was observed. Although an increased number of passes should positively affect cohesion and porosity, too many layers can lead to the accumulation of internal stresses [10].
- In the as-sprayed condition, shorter spray distances (150 mm) generally resulted in lower or more stable coefficients of friction, particularly when multiple layers were applied. This can be attributed to improved particle impact velocity and temperature at reduced stand-off distance. These conditions promote enhanced splat spreading and interlocking, resulting in reduced porosity through better particle packing and stronger mechanical interlocking with the substrate. However, excessive thermal input at short distances poses a risk of substrate overheating, especially for titanium alloys, potentially leading to interfacial oxidation or thermal degradation that may impair adhesion.
- At the longer spray distance of 250 mm, frictional behavior was more variable. Notably, the sample with one layer exhibited a significantly lower average coefficient of friction (0.265), which increased substantially after grinding. This suggests weak or incomplete coating coverage, likely due to particle cooling and deceleration in flight, which reduce deposition efficiency and bonding quality. The poorer adhesion and lower deposition temperature at this distance can also facilitate oxidation of the sprayed particles, further degrading coating cohesion.
- Increasing the number of layers improved coating performance in both spray conditions. Thicker coatings contributed to better surface continuity and higher resistance to mechanical disruption during wear. This effect was more pronounced after surface grinding, where multi-layer coatings maintained consistent friction values, indicating retained structural integrity.
- In contrast, thinner coatings, especially those applied at 250 mm, were more susceptible to damage or removal during grinding, exposing the substrate and increasing friction. Surface grinding reduced surface roughness and removed loosely bonded splats, generally lowering friction values for well-adhered coatings. However, in cases where the coating was too thin or poorly bonded, grinding may have compromised the coating, leading to increased friction. This was observed in samples with one layer, particularly at greater spray distances.

Acknowledgment

The authors express their sincere gratitude to Anton Paar Croatia for providing the Pin-on-Disc Tribometer TRB³, which was essential laboratory equipment for the completion of this work.

References

[1] Sakthinathan, S., Meenakshi, G. A., Vinothini, et al., 2025. A Review of Thin-Film Growth, Properties, Applications, and Future Prospects. Processes, 13(2), 587.

[2] Hardide Coatings: CVD vs Thermal Spray: Advantages and limitations for harsh environments, UK, http://blog.hardide.com/cvd-vs-thermal-spray, (accessed 16 June 2025).

[3] Amin, S., Panchal, H., 2016. A Review on Thermal Spray Coating Processes, International Journal of Current Trends in Engineering & Research (IJCTER), 2(4), 556-563.

[4] Vardavoulias, M.,2015. Industrial Thermal Spray Coatings for Tribological Applications: Influence of Nanostructure on Wear Properties, TURKEYTRIB’15, Greece.

[5] Kuroda, S., 2008. Control of Residual Stress in Thermal Spray Coatings by Substrate Preheating, Surface and Coatings Technology, Elsevier, 202(10), 2093–2097.

[6] Fauchais, P. L., Heberlein, J. V. R., Boulos, M. I., 2014. Thermal Spray Fundamentals: From Powder to Part, Springer Science & Business Media.

[7] Kuroda, S., Kawakita, J., Watanabe, M., 2016. Warm Spraying—A Novel Coating Process Based on High-Velocity Impact of Solid Particles, Nature Publishing Group, Scientific Reports, 6, 21864.

[8] Joshi, S., Nylen, P., 2019. Advanced Coatings by Thermal Spray Processes, Technologies, 7(4), 79.

[9] Arboleda, J. A., Serna, C. M., Cadavid, 2018. Effect of Flame Spray Deposition Parameters on The Microstructure of Al2O3-13% TiO2 Coatings Applied Onto 7075 Aluminum Alloy, Materials Research, 21(5).

[10] Mihoob, M. M., Albarody, T. M. B., Ahmad, F., 2023. Optimizing the Thermal Spray Parameters for Producing High-Performance Mo/ZrB2 Metal Matrix Composites Using the Taguchi Method, Coatings, 13(9), 1620.

[11] Ezugwu, E.O., Wang, Z.M., 1997. A Review on High-Speed Machining of Titanium Alloys, Journal of Materials Processing Technology, Vol. 68, pp. 262–274.

[12] R. B. Silva, 2006. Performance of different cutting tool materials in finish turning of Ti-6Al-4Valloy with high pressure coolant supply technology, UNIVERSIDADE FEDERAL DE UBERLÂNDIA FACULDADE DE ENGENHARIA MECÂNICA.

[13] Metals Piping: The crystal structure of titanium, https://www.metalspiping.com/the-crystal-structure-of-titanium.html, (accessed 29 June 2025).

[14] UltraBond® 51000, Saudi Arabia, https://www.talakeel.com/ultrabond-51000, (accessed 3 June 2025).

[15] RotoTec CoroResist 19300 metal powder, Austria, https://l1nq.com/TVoU2, (accessed 30 June 2025).

[16] Pin-on-disk tribometer: TRB³, Austria, https://sl1nk.com/OiOW6, (accessed 30 June 2025).

[17] Adrian P. M., 2012. Mechanical and durability testing of aerospace materials, Introduction to Aerospace Materials, Woodhead Publishing, 91-127

[18] Julia A Baimova, 2024. An Overview of Mechanical Properties of Diamond-like Phases under Tension, Nanomaterials.

Process errors and problems in adhesion of magnetron sputtered platinum coatings

***Matej Kljajo*[1], *Ladislav Vrsalović*[2], *Senka Gudić*[2], *Nikša Čatipović*[3], *Ivan Peko*[4], *Ante Bilušić*[4], *Petar Ljumović*[3] *and Danijel Šogorović*[1]**

1) University of Mostar, Faculty of Mechanical Engineering, Computing and Electrical Engineering, Matice hrvatske bb, 88000 Mostar, Bosnia and Herzegovina

2) University of Split, Faculty of Chemistry and Technology, Ruđera Boškovića 25, 21000 Split, Croatia

3) University of Split, Faculty of Electrical Engineering, Mechanical Engineering and Naval Architecture, Ruđera Boškovića 32, 21000 Split, Croatia

4) University of Split, Faculty of Science, Ruđera Boškovića 33, 21000 Split, Croatia

Corresponding author: matej.kljajo@fsre.sum.ba

Original scientific article

Abstract: Platinum coatings deposited by magnetron sputtering are valued for their unique properties, such as electrical conductivity, high catalytic activity, and corrosion resistance. However, achieving defect-free coatings with strong adhesion to the substrate is still a major challenge. In this study, platinum films were deposited on 316L stainless steel substrates using different DC sputtering parameters, such as sputtering current, vacuum, and deposition time, to determine their effects on coating quality and corrosion resistance. After coating deposition, the surface was analyzed using optical microscopy, and an SEM/EDS analysis was performed. Subsequently, the deposited samples were electrochemically tested to assess their corrosion behavior in 0.5 M NaCl solution. The results indicated that the coating did not affect the corrosion resistance of stainless steel. Namely, it was observed that the coating completely delaminated during the measurement, resulting from poor Pt adhesion to the steel surface. Poor adhesion of platinum can be caused by inadequate substrate preparation and the presence of internal stresses in the coating that occur under inadequate deposition conditions. Corrective measures, such as optimizing electrode preparation and adjusting deposition parameters, were identified to reduce delamination and enhance uniformity and stability in future coatings.

Keywords: *magnetron sputtering; platinum films; coatings; corrosion resistance*

1. Introduction

Reducing the use of precious metals is a critical goal in developing catalysts, catalyst layers, and other applications. To achieve this, various techniques focus on maximizing the surface area and generating active sites within the surface layer rather than throughout the bulk of the carrier material [1], [2] and [3]. Platinum is known for its superb catalyst properties [4], corrosion-resistant applications [5], sensors [6] etc. Due to the high cost of platinum, utilizing it in the form of thin films offers a cost-effective approach that preserves its advantageous properties while significantly reducing material expenditure [7]. Thin film technology enables industries to leverage platinum's exceptional performance characteristics without the substantial financial burden associated with its bulk usage. Magnetron sputtering, as a precise and efficient deposition technique, plays a pivotal role in minimizing material waste while ensuring high-quality film production [8], [9]. The thin-film deposition technique of magnetron sputtering, widely recognized and extensively applied in microsystem technology, is regarded as a viable alternative for catalyst preparation and electrode assembly. The process is highly reproducible and offers several advantages, including cost efficiency, scalability for industrial applications, and the ability to tailor coating properties for specific purposes [10]. Experimental findings indicate that the key properties of metal and metal oxide films produced via

magnetron sputtering, including catalyst properties, corrosion resistance, adhesion, surface morphology, and mechanical properties, are susceptible to the selected sputtering parameters. Variations in power, gas flow rate, chamber pressure, and deposition duration have been shown to influence the film's composition and above-mentioned characteristics substantially. While the electrocatalytic, optical, and anticorrosive properties of these films are increasingly investigated, there remains a need for systematic studies to optimize sputtering conditions, even for well-studied metals like platinum.

The presented study investigates the deposition of thin platinum films onto stainless steel substrates via DC magnetron sputtering, with process parameters varied to assess their influence on corrosion resistance. Stainless steel was selected as the substrate material due to its widespread industrial use, cost-effectiveness, and suitability for application in highly corrosive environments. However, its relatively low hardness, high friction coefficient, and poor wear resistance can contribute to accelerated material degradation [11]. These limitations can be addressed through surface engineering techniques, such as magnetron sputtering, which enable the enhancement of surface properties without compromising the bulk characteristics.

While stainless steel offers a unique combination of mechanical strength, corrosion resistance, and thermal stability, its direct compatibility with platinum has occasionally been called into question due to metallurgical differences between the two materials. This study aims to demonstrate that 316L stainless steel can effectively serve as a substrate for platinum coatings without the need for an intermediate interlayer, given that platinum is known to adhere well to various other substrate materials [12].

2. Experimental procedure

In this study, thin Pt-films were deposited on 316 stainless steel cylinders (Cr 16.80%, Ni 10.08%, Mo 2.04%, Mn 1.64%, Cu 0.35%, Si 0.35%, P 0.036%) using a Q150T ES Plus DC magnetron sputtering system (Figure 1).



Figure 1. *Magnetron sputtering device Quorum Q150 ES*

The cylinders were prepared by cutting a 316 stainless steel rod with a diameter of 6 mm into 8 cylindrical specimens. These specimens were soldered to insulated copper wires to ensure reliable electrical contact and then isolated with QPrep KEM 60 cold mounting resin, as shown in Figure 2. Eight different samples were prepared for coating, plus an extra sample, without coating, to serve as a reference. The exposed cylindrical bases were polished up to a 1200-grit finish, achieving a surface roughness of Sa = 0.1043 µm, as measured by a SOTO TT75 optical profilometer. Prior to deposition, the polished surfaces were cleaned with alcohol and dried using compressed air. The platinum coating was applied to the prepared surfaces, which subsequently served as the working electrode in contact with the electrolyte. The protective mass around the surface and the copper wire were covered with vacuum tape, and after deposition the tape is removed, to ensure that coating is only applied to the desired area.

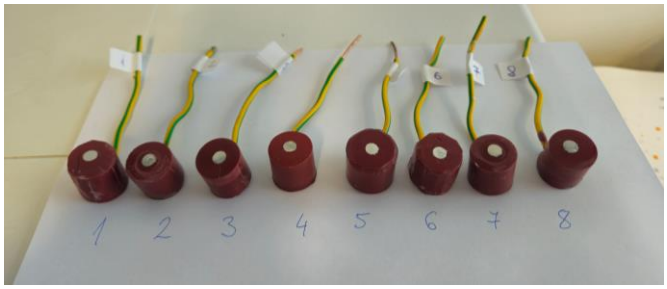


Figure 2. *Stainless steel electrodes coated with platinum*

The platinum target utilized in the sputtering system has a diameter of 50,8 mm and a purity of 99.99%. It is mounted on a copper holder and positioned at the top of the sputtering chamber. The chamber was evacuated to a base pressure of 0,0005 mbar, after which Ar gas (99.99%) was introduced at a constant flow rate to achieve various operating pressures, listed in Table 1.
The substrate-to-target distance was maintained at 45 mm, and the substrate holder was rotated at a constant speed to ensure uniform distribution of coating. Prior to deposition, the chamber was purged with Ar for 120 seconds to eliminate residual gases. Additionally, the target was precleaned for 120 seconds with 150 mA to remove surface contaminants.

Table 1. *Sputtering parameters*

No.	Current [mA]	Vacuum [mbar]	Deposition time [min]
1	50	0,005	2
2	50	0,005	12
3	50	0,015	2
4	50	0,015	12
5	70	0,005	2
6	70	0,005	12
7	70	0,015	2
8	70	0,015	12

JEOL JSM - 7610FPlus, field emission scanning electron microscope equipped with the Ultim Max 65 EDS detector from Oxford Instruments was used for investigation of Pt coating on two chosen samples. SEM/EDS analysis is shown on Figures 8. and 9.
Electrochemical measurements were performed in the electrochemical cell equipped with the platinum mesh counter-electrode and saturated calomel reference electrode, in a 0.5 M NaCl solution at T = 22 °C. The open circuit measurements (EOC) last 60 minutes by measuring the potential value every 30 seconds. Potentiodynamic polarization measurements were performed from -0.4 V vs. EOC to 0.8 V with the scan rate of 0.5 mV s^{-1}. After electrochemical measurements, the surfaces were investigated with the optical microscope.

3. Results and discussion

Prior to conducting electrochemical tests, the surfaces were examined using an optical microscope MXFMS-BD. Figure 3 shows the reference electrode, without coating, while Figures 4 - 7 show electrodes 1, 5, 6 and 8. As could be seen on images obtained from an optical microscope, some electrodes exhibited a wrinkled surface topography, indicating potential issues with film adhesion to the substrate (electrodes no. 2, 4, 6, and 8). In contrast, electrodes 1, 3, 5, and 7 showed no observable surface defects, suggesting successful coating adhesion.



Figure 3. *a) Reference electrode; optical microscope images at b) 50× and c) 100×*



Figure 4. *a) Coated electrode 1; optical microscope images at b) 50× and c) 100×*



Figure 5. *a) Coated electrode 5; optical microscope images at b) 50× and c) 100×*



Figure 6. *a) Coated electrode 6; optical microscope images at b) 50× and c) 100×*



Figure 7. *a) Coated electrode 8; optical microscope images at b) 50× and c) 100×*

SEM/EDS analysis was performed on samples 5 and 7, with the corresponding images presented in Figure 8 and Figure 9, respectively. Both samples were coated but exhibited distinct surface topographies, as previously observed in optical microscopy images.

Sample 5 displayed a smooth, wrinkle-free surface with flawless homogeneity and a platinum content exceeding 90%.
In contrast, sample 7 revealed slight imperfections in the coating, particularly in regions near surface creases. Elemental composition analysis of sample 7 showed variability, with platinum concentrations of 66.3% and 47.4% in specific areas. These regions of lower platinum content were closely associated with the creases in the coating texture, indicating that the observed compositional inconsistencies are likely attributable to imperfections in the coating morphology.

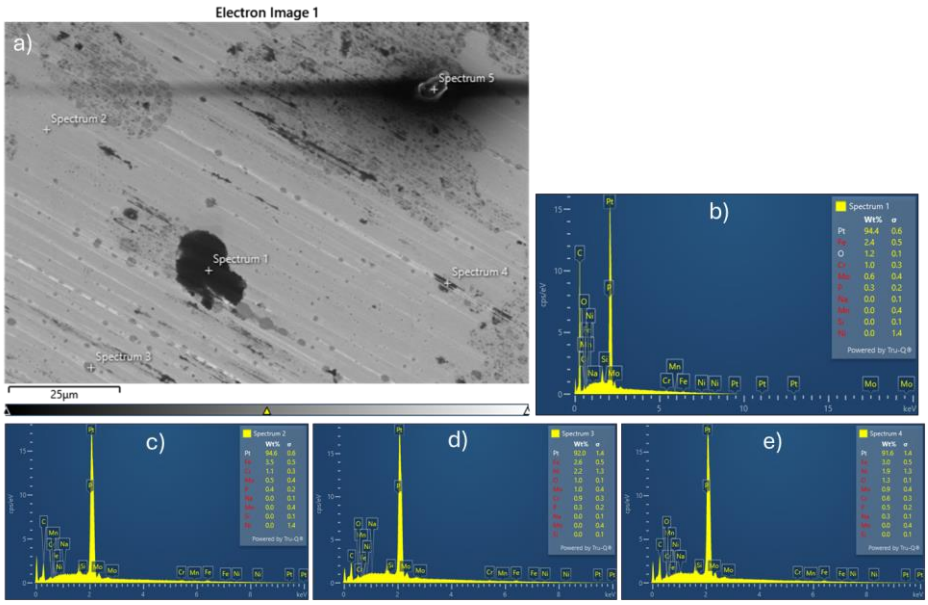


Figure 8. *SEM/EDS images of coated sample 5, a) points e.g. “spectrums” for EDS analysis, b) spectrum 1, c) spectrum 2, d) spectrum 3, e) spectrum 4*

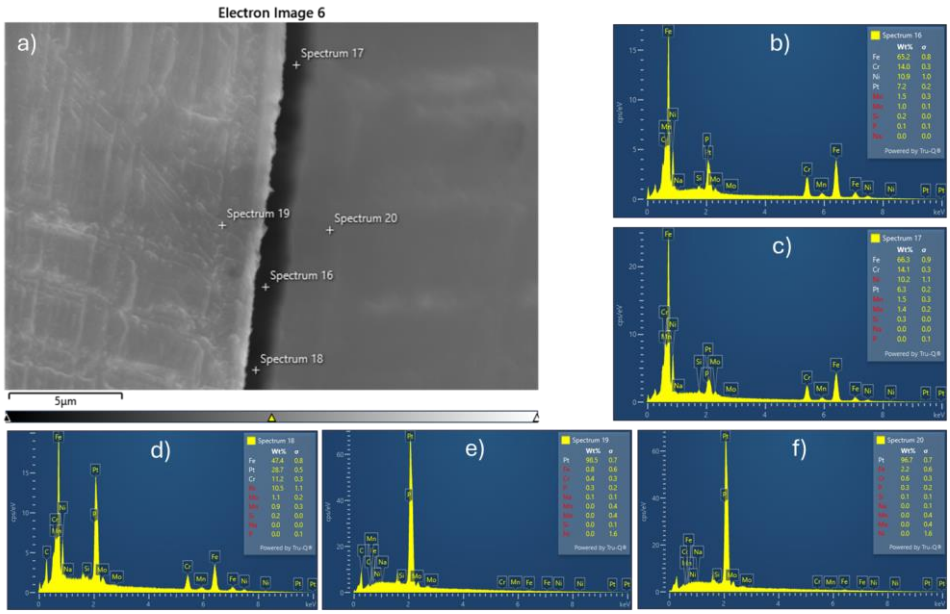


Figure 9. *SEM/EDS analysis of coated sample 7 a) points e.g. “spectrums” for EDS analysis, b) spectrum 16, c) spectrum 17, d) spectrum 18, e) spectrum 19, f) spectrum 20*

Results of the electrochemical measurements were shown on Figure 10 a) for the EOC measurements and b) for the potentiodynamic polarization measurements.
From Figure 10 a) it is evident that the starting potential of the coated samples has significantly higher values than that of the uncoated sample. However, the sharp drop in the EOC values at the beginning

of the measurements indicates that the contact between the AISI 316 steel surface and electrolyte is not prevented.

A similar conclusion can be drawn from polarization measurements (Figure 10 b) as the shape of the anodic part of the polarization curves is the same for all investigated samples. A steel substrate with a compact Pt coating should show minimal and unchanged values of anodic current density in the entire anodic potential range.

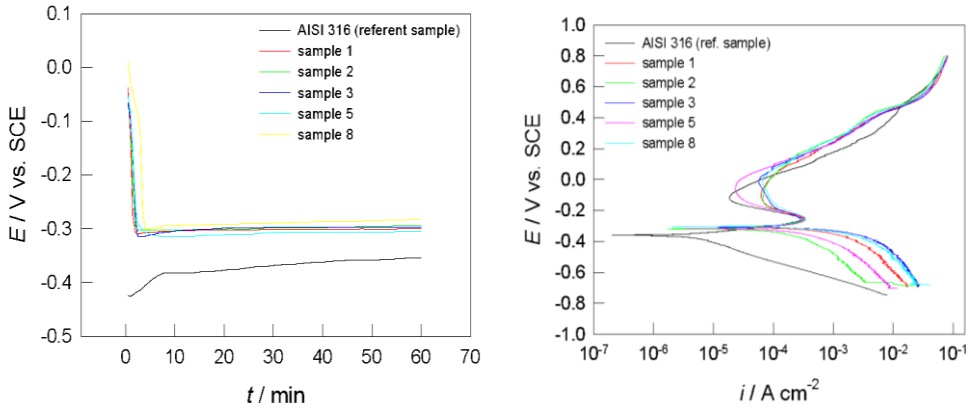


Figure 10. *a) EOC measurements for AISI 316 without and with Pt coating in 0.5 M NaCl solution, b) potentiodynamic polarization curves*

However, the anodic curves show an active-passive behavior characteristic of the polarization curves of stainless-steel samples exposed to NaCl solution [13], [14]. Namely, by changing the potential above the value of approx. 0 V, a significant increase in the anodic current density occurs, which indicates the breakdown of the oxide film and the occurrence of pitting corrosion, which was seen on optical microscopy images on all samples after polarization tests (Figure 11).



Figure 11. *Optical surface micrographs of AISI 316 after polarization measurements a) uncoated sample, b) sample 1 and c) sample 5 (magnification 50×)*

The platinum coating was completely removed for the AISI 316 sample surfaces during the corrosion investigation in NaCl solution. In Figure 11 b), only small fragments of Pt-coating can be seen on the surface after polarization measurements. Therefore, it can be concluded that all samples exhibit low adhesion between steel substrates and Pt-coatings. The low adhesion of platinum (Pt) coatings on stainless steel obtained by the magnetron sputtering method can be caused by various factors related to surface conditions, film properties, and process parameters [15], [16]. Additional investigations should be carried out to find the main reason for this phenomenon.

4. Conclusion

The paper presents unsuccessful attempts to form homogeneous and adherent platinum coating on AISI 316 stainless steel by magnetron sputtering methods with different sputtering parameters. Some electrodes exhibited a wrinkled surface coating topography, indicating potential issues with film adhesion on the substrate, while others showed no observable surface defects, suggesting successful coating adhesion. SEM/EDS analysis of smooth, wrinkle-free surface coating has shown coating

homogeneity with Pt content exceeding 90% in all investigated spots. In contrast, on the electrode with the wrinkled surface topography areas, low concentration of Pt (66.3% and 47.4%) was detected. These regions were closely associated with the crevices in the coating texture. Electrochemical measurements have shown similar behavior of the referent uncoated AISI 316 steel sample and coated samples (regardless of the quality of the coating), conformed to the low adhesion of platinum coating of the steel surfaces. Pitting corrosion was observed in all investigated surfaces. Although strong adhesion between platinum coatings and stainless steel substrates is achievable, it remains challenging and requires further investigation to clarify the direct relationships between deposition parameters, surface characteristics, and substrate preparation methods.

References

[1] Alekseeva, O. K., Mikhalev, A.I., Lutikova, E.K., Porembsky, V. I., Presnyakov, M. Y., Fateev, V. N., Shapir, B. L., & Grigoriev, S. A., 2018. Structural and Electrocatalytic Properties of Platinum and Platinum-Carbon Layers Obtained by Magnetron-Ion Sputtering, Catalysts, 8 (12), 665.

[2] Sui, S., Wang, X., Zhou, X., Su, Y., Riffat, S., and Liu, C., 2017. A comprehensive review of Pt electrocatalysts for the oxygen reduction reaction: Nanostructure, activity, mechanism and carbon support in PEM fuel cells, J. Mater. Chem. A, 5 (5), 1808–1825.

[3] Lebedeva, M.V., Yashtulov, N. A., Flid, V. R., 2016. Catalysts with platinum–palladium nanoparticles on polymer matrix supports, Kinet Catal, 57 (6), 847–852.

[4] Gatel, C., Snoeck, E., 2006. Comparative study of Pt, Au and Ag growth on Fe3O4(001) surface, Surface Science, 600 (13), 2650–2662.

[5]Bieberle-Hütter, A., Hertz, J.L., Tuller, H.L., 2008. Fabrication and electrochemical characterization of planar Pt–CGO microstructures, Acta Materialia, 56 (2),, 177–187.

[6] Hotovy, I., Huran, J., Siciliano, P., Capone, S., Spiess, L., Rehacek V., 2004. Enhancement of H2 sensing properties of NiO-based thin films with a Pt surface modification, Sensors and Actuators B: Chemical, 103 (1-2), 300–311.

[7] Kljajo, M., Peko., I., Čatipović, N., Bilušić, A., Ljumović, P., Krolo, J., Kunac, K., Periša, K., 2024. Multi-objective optimization of platinum deposition parameters on 316L stainless steel substrate in magnetron sputtering process, Proceedings of 13th International Conference Mechanical Technologies and Structural Materials 2024, 195–204.

[8] Mahan, J. E., 2000. Physical vapor deposition of thin films. New York, Wiley

[9] Wasa, K., Kanno, I., Kotera, H., 2021. Handbook of Sputter Deposition Technology, Elsevier

[10] Seshan, K., 2002. Handbook of Thin Film Deposition Techniques Principles, Methods, Equipment and Applications, CRC Press

[11] Wang, H., Lin, N., Nouri, M., Liu, Z., Yu, Y., Zeng, Q., Ma, G., Fan, J., Li, D., Wu, Y., 2023. Improvement in surface performance of stainless steel by nitride and carbon-based coatings prepared via physical vapor deposition for marine application, Journal of Materials Research and Technology, 27, 6021-6046.

[12] Alvisi, M., Galtieri, G., Giorgi, L., Giorgi, R., Serra,E., Signore, M.A., 2005. Sputter deposition of Pt nanoclusters and thin films on PEM fuel cell electrodes, Surface and Coatings Technology, 200 (5.6), 1325-1329.

[13] Kožuh, S., Vrsalović, L., Gojić, M., Gudić, S., Kosec, B. , 2016. Comparison of the corrosion behavior and surface morphology of NiTi alloy and stainless steels in sodium chloride solution, J. Min. Metall. Sect. B-Metall., 52 (1) 53-61.

[14] Klapper, H.S., Stevens, J., Wiese, G., 2013. Pitting corrosion of CrMn austenitic stainless steel in simulated drilling conditions-role of pH, temperature and chloride concentration, Corrosion, 69 (11) 1095-1102.

[15] Lattermann, M., Ehiasarian, A.P., Bohlmark, J., Persson, P.A.O., Helmersson, U., 2006. Investigation of high power impulse magnetron sputtering pretreated interfaces for adhesion enhancement of hard coatings on steel, Surf. Coat, 200 (1), 6495-6499.

[16] Tian, B., Vu, Q., Zhang, Z., Du, Z., Ren, W., Shi, P., Jiang, Z., 2018. Effect of magnetron sputtering parameters on adhesion properties on tungsten-rhenium thin film thermocouples, Ceramics International, 44 (1), 15-18.

Practical examples of the correct selection of 3D measurement technology for modern production processes

***Josip Kos*[1], *Luka Kurtalj*[1], *Maximilian Hercigonja*[1], *Vedran Starčević*[1] *and Tomislav Hercigonja*[1]**

1) Topomatika d.o.o., Industrijska ulica 3, Novaki, 10431 Sveta Nedelja , Croatia

Corresponding author: j.kos@topomatika.hr

Professional article

Abstract : Choosing a 3D measurement strategy is a crucial step in product quality control, and modern manufacturing processes require increasingly faster and more comprehensive measurements. In this context, modern advanced optical 3D measurement technologies and industrial computed tomography (CT) stand out as the best choice.
With more than two decades of experience in industrial 3D metrology, Topomatika d.o.o provides a solid foundation for reliable selection and application of these technologies, enabling high-quality control and reliable results in various production processes.
This paper provides an overview of practical examples for the proper selection of 3D measurement system technology, with characteristic examples from the production of polymer products, metal casting and the automotive industry, especially in the segment of new generation vehicles (NEV – New Energy Vehicles).
The article presents examples of 3D measurement results on data obtained using the ATOS and T-SCAN hawk 2 optical 3D measurement systems, and the ZEISS METROTOM industrial CT system. Data processing and creation of measurement reports were performed in the ZEISS INSPECT software package, which supports all of the aforementioned measurement technologies.

Keywords: *Industrial 3D digitization; 3D scanning; CT scanning; X-Ray; 3D metrology*

1. Introduction

By choosing the right 3D measurement technology, it is possible to significantly speed up the development of new products, optimize production processes and reduce the risk of scrap products.
At the outset, it is important to note that optical 3D measurement systems, as well as industrial CT systems, are actually industrial 3D digitizers (or 3D scanners) that first accurately 3D digitize the geometry of the product and digitally record it into the computer, Figure 1. This creates a digital copy or digital twin of the actual object on the computer, which is used for further work tasks.
A digital twin is recorded on the computer as a triangular mesh that describes in detail the shape of a 3D digitized object, and is most often saved in .STL format [1].

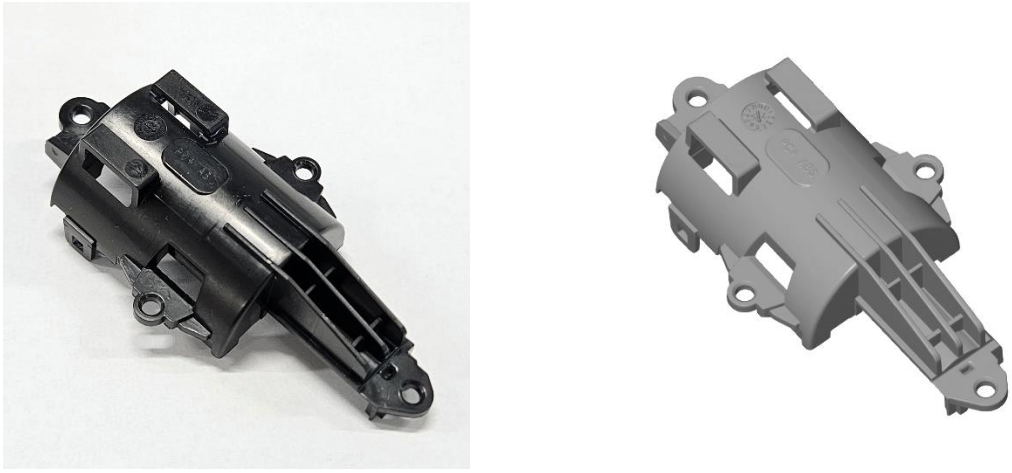


Figure 1. *The real product and its digital twin*

Characteristics of a triangular mesh in .STL format include:

- It is universally recognized, making it a reliable choice for exchanging digital twins or 3D models of various products.
- almost all user programs (such as GrabCAD , MakerBot CloudPrint ™, Cura, PrusaSlicer , etc.) use .STL files to prepare 3D print jobs
- Although .STL is great for 3D printing simple and complex shapes, it has limited capabilities in other areas such as colour, texture
- STL geometry is not parametric, so it is not possible to make significant changes to the 3D model

Compared to conventional methods, a 3D digitizer captures the entire surface of an object, not just individual points like tactile measurement technologies, Figure 2.

In general, since each 3D digitization process results in a digital record, it can be archived for quality assurance and monitoring purposes.

Processes of 3D digitization (3D scanning) are most often used by engineers, technicians, and designers of various fields for different purposes, the most common being [1]:

- dimensional analysis – very often in quality control processes when it is necessary to compare the geometry of the actual product and the digital 3D model according to which the product was made (reference polygonal mesh or CAD model)
- reverse engineering – for the digital reconstruction of an object for which no documentation exists (neither digital nor paper)
- digital manufacturing – for direct 3D printing based on the results obtained from 3D scanning

Since this paper provides an overview and guidelines for the proper selection of 3D measurement system technology for 3D measurement (dimensional analysis), it is necessary to have a certified metrology software package, such as the ZEISS INSPECT 3D software package available.

The 3D digitizers used for this work, together with the certified metrology software package ZEISS INSPECT, each form a 3D measurement system that guarantees reliability even in the most demanding metrology tasks of modern production.

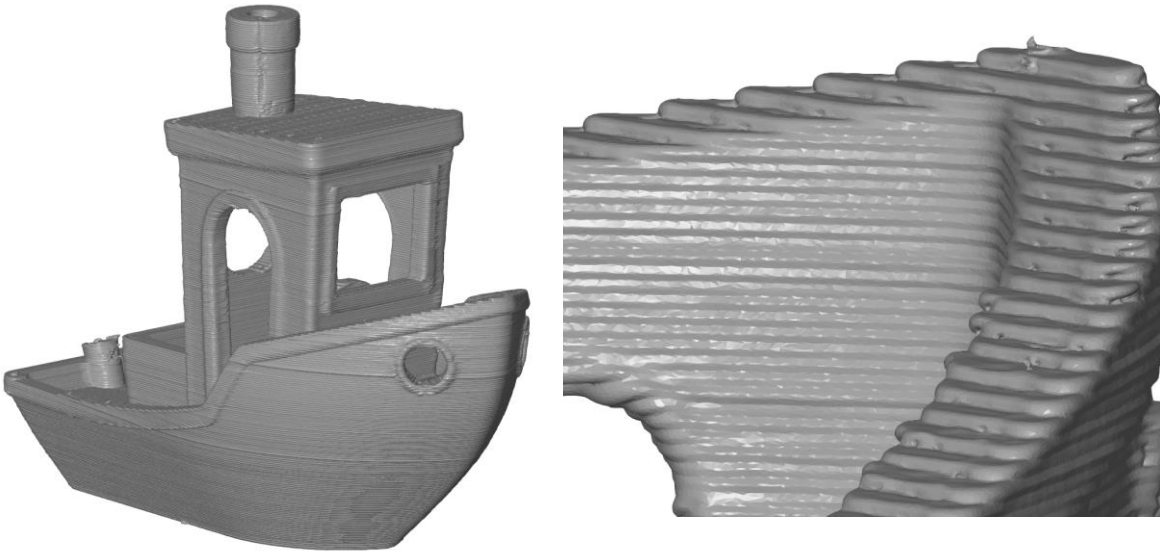


Figure 2. *Result of 3D digitization of a 3D-printed object – complete triangular mesh (left) and detail of a 0.2 mm 3D print layer (right)*

2. Optical 3D digitizers (3D scanners)

Today’s market offers 3D digitizers of varying quality and price ranges. This paper provides an overview and guidelines for the proper selection of two different metrology-grade optical 3D digitizers [5]:

- ATOS – a 3D digitizer that uses structured light for 3D digitization, Figure 3
- T-SCAN hawk 2 - which uses laser beams for 3D digitization, Figure 4



Figure 3. *ATOS 3D digitizer*



Figure 4. *T-SCAN hawk 2 3D digitizer*

In the 3D digitization process itself, reflected light from the surface of the 3D scanning object is digitized.

Advantages of optical 3D digitizers include:

- The ability to quickly capture a surface, and thereby the entire product
- high resolution when fine detail is required
- System mobility – 3D digitizers are generally easily portable and suitable for measurements in the lab or in the field

Limitations include:

- sensitivity to shiny, transparent, or dark surfaces, which can interfere with light reflection
  - When it is necessary to 3D measure glossy or transparent surfaces, a matte spray needs to be applied to the surface before 3D scanning to minimize reflectivity.
- inability to digitize the internal and optically invisible geometry of the object

2.1. ATOS – optical 3D digitizer

ATOS is an optical 3D digitizer or 3D scanner based on the principle of triangulation, and delivers metrology-grade precision even for the most demanding metrology tasks. It projects parallel line patterns onto the measurement object and captures them using two digital cameras. For each individual pixel in the cameras, the 3D scanner determines the three-dimensional coordinates of the corresponding point on the digitized real surface with high precision [5].

Working with the ATOS 3D scanner requires an industrial stand or a robot from which the real object is digitized in 3D. Depending on the size, quantity and requirements of the task, users will choose a manual ATOS configuration with a stand (Figure 5) or a robotized ATOS solution (ZEISS ScanBox robotic cell, Figure 6).



Figure 5. *ATOS 3D scanner on an industrial stand*

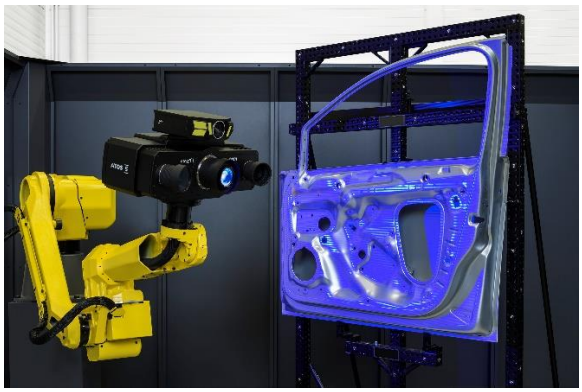


Figure 6. *ATOS 3D scanner on an industrial robot*

The ATOS 3D scanner is used for [3]:

- Precise 3D measurement in quality control processes of geometrically demanding products, such as injection molding or metal casting tools and their produced parts.
- Detailed analysis of product dimensions in industrial manufacturing.
- Detailed analysis of form and position tolerances of products in industrial manufacturing.

2.2. Examples of using the ATOS 3D measuring system

Optical ATOS 3D measurement systems have today become standard metrological solutions in industrial polymer production and metal casting [5].

Their advanced technology enables comprehensive, non-contact, and rapid inspection of product geometry throughout the entire production cycle – from development and tooling, prototyping, to serial production. Examples of typical plastic and metal products for 3D measurement with the ATOS system are shown in Figure 7 [5].

3D measurements performed with ATOS 3D digitizers are precise and fast, which enables comprehensive geometric analysis in individual stages of the production process for:

- Verifications of CNC machining of tools and molds
- Inspection of the geometry of cores, electrodes, and inserts of tools or molds
- Inspection of the geometry of pattern plates
- 3D measurements of castings
- 3D measurements of machined products

The measurement results are easy to read and most often displayed graphically in a color map.

Before the implementation of the ATOS system, the process of identifying the source of errors using a conventional approach was time-consuming and imprecise, accompanied by complicated reports usually in tabular form. When it comes to the application of optical measurement systems in polymer manufacturing, they are most often used to verify the quality of tool making and the polymer products themselves. In a typical project, the result of a 3D scan is compared with the original CAD geometry

to check if there are zones on the product with excess or insufficient material, or whether the product underwent deformation during cooling.
The results are clearly understandable, presented in a colour map over the entire surface or across specific cross-sections. Warm colours represent excess material or deformation in the positive direction of the surface, while cold colours indicate a lack of material or deformation in the negative direction relative to the surface, Figure 8 [3].



Figure 7. *3D digitization of polymers and castings with ATOS robotized solution – ATOS ScanBox*

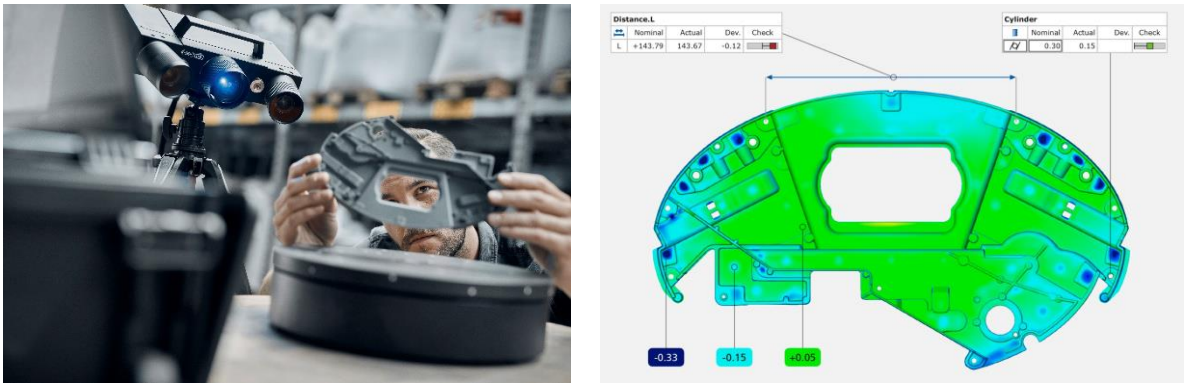


Figure 8. *The process of 3D digitization with manual ATOS and the display of deviations of the actual geometry from the CAD model in a color map*

With ATOS 3D digitizers, it is possible to digitize products ranging in size from just a few millimeters and up to much larger objects. The challenges in metal casting production are similar to those in polymer production, where deformation of the casting often occurs due to various influences in the manufacturing process. However, castings are commonly further machined after fabrication, so it is very important for that process to have a casting that contains enough material for machining. If a casting does not have sufficient material, there is no point in machining it.
For this reason, foundries use 3D digitizers precisely for measuring and inspecting a casting before machining (Figure 9).

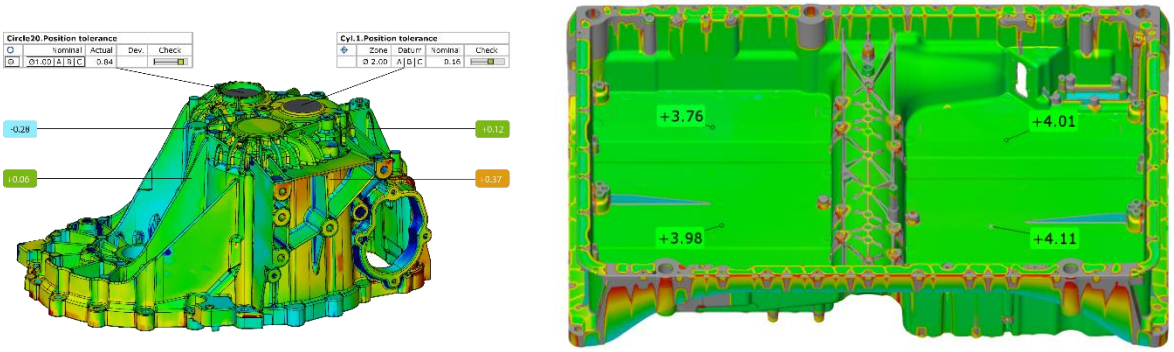


Figure 9. *Results of measurement of castings for various purposes;*
checking the machining allowance (left), checking the thickness of the casting wall (right)

Final dimensional inspection at the end of the production process is of course necessary, but in today’s industry the in-process (intermediate) control is extremely important as well. A detailed, double-sided 3D scan also enables analysis of wall thickness, Figure 9.

2.1. T-SCAN hawk 2 – optical 3D digitizer

T-SCAN hawk 2 is a portable 3D scanner of a new generation of lightweight laser 3D scanners, and it comes with metrology-grade accuracy and exceptional ease of use. This 3D scanner projects laser lines onto the object being measured, which are captured by two digital cameras. For the points on the laser line that the scanner’s cameras detect, the 3D scanner determines with high precision the three-dimensional coordinates of those points on the scanned surface.
The T-SCAN Hawk 2 is intuitive to use. 3D scanning is performed handheld by the operator and easily adapts to the operator’s hand movements, Figure 10.



Figure 10. *3D scanning using the ZEISS T-SCAN hawk 2 handheld 3D scanner*

Using the T-SCAN hawk 2 device, it is possible to 3D scan objects made of different materials and with different surface characteristics, providing highly precise and accurate 3D measurement results.
The ZEISS T-SCAN hawk 2 is used for:

- 3D measurement and inspection in quality control processes when a high degree of system mobility is required.
- Fast 3D digitization of large objects for the purposes of reverse engineering, for example in maintenance.
- Analysis of corrosion and damage in energy production, oil and gas industries (e.g. hydroelectric plants, thermal power plants, pipelines, etc.).
- 3D scanning of complexly shaped architectural and museum artifacts.

Because the T-SCAN hawk 2 handheld 3D digitizer is easily portable and robust, 3D digitization is effortlessly performed at the location of the object (for example, in industrial facilities, power plants, factory halls, etc.). In this way, the object does not need to be transported to a measurement laboratory, which is the usual requirement for many classical measurement methods.
One of ideal casting application of handheld 3D optical systems is in turbine reconstruction for Power Plants (Figure 11). To date, Pelton, Francis, and Kaplan turbines have been successfully digitized with the aim of determining their condition, inspecting their geometry, preparing for reconstruction, etc. By precisely measuring the flange of an existing turbine, the fabrication of new replacement parts was facilitated. Due to irregularities in the operation of several turbine assemblies, their complete geometries were also inspected. The use of modern 3D measurement methods contributed to a significant saving of time in planning and carrying out the refurbishment of multiple turbines, manufacturing replacement parts, and similar tasks [5].



Figure 11. *3D digitization in process (left) and the resulting 3D scan of a turbine flange in a hydroelectric power plant (right) using the T-SCAN hawk 2*

Other examples of using the handheld 3D digitizer include products (Figure 12) that also have complex geometries but fewer details, which are often digitized with ATOS 3D scanners.

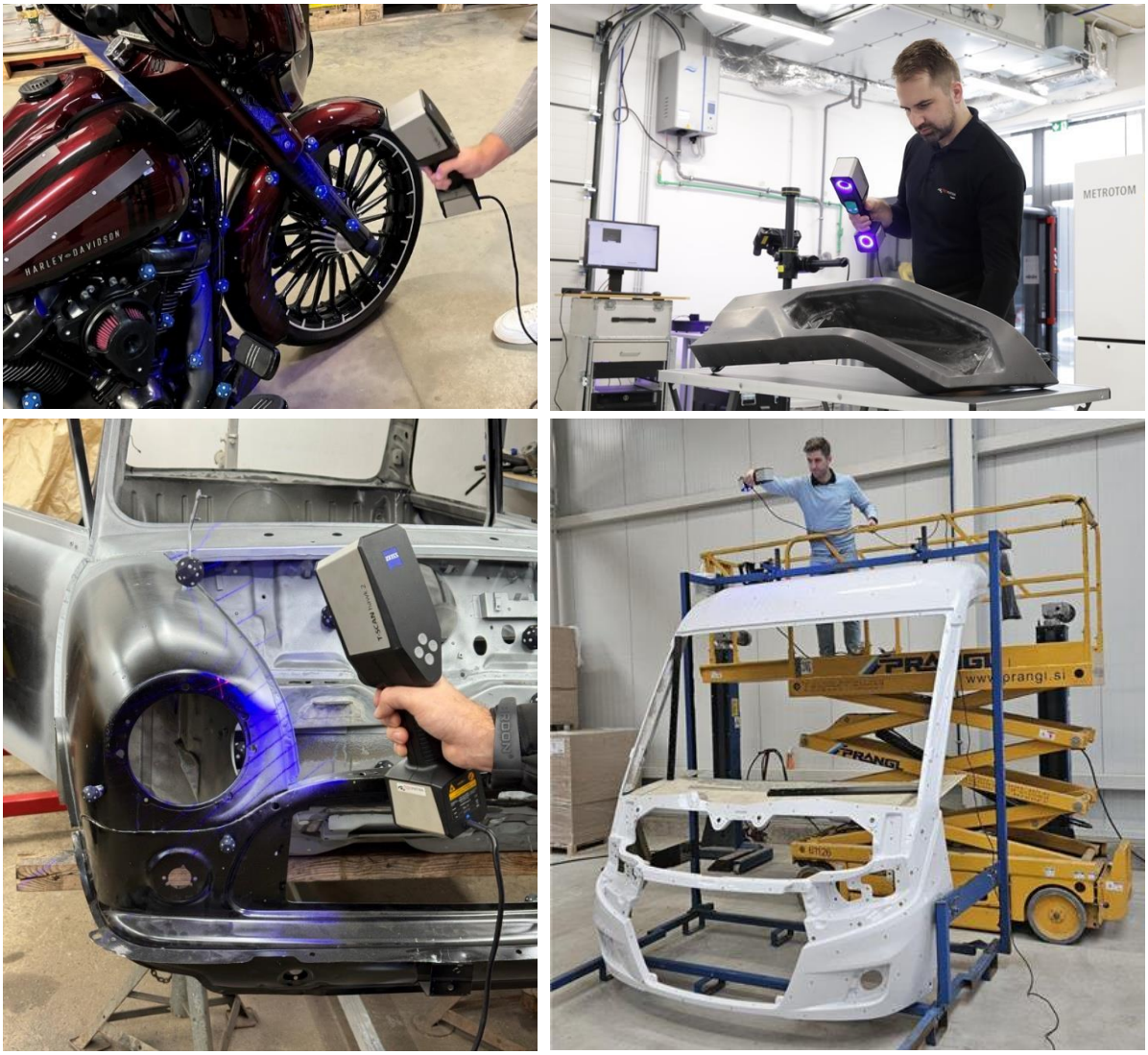


Figure 12 *. Examples of typical products for 3D digitization with optical 3D digitizers*

3. Industrial computed tomography (CT)

Industrial computed tomography, i.e. an industrial CT system (Figure 13), uses X-ray radiation to digitize the geometry of an object (Figure 14).
The object is irradiated from multiple angles, and the images (radiographic projections) are then reconstructed via software into a three-dimensional representation, providing a view of the object’s internal and external geometry [4].

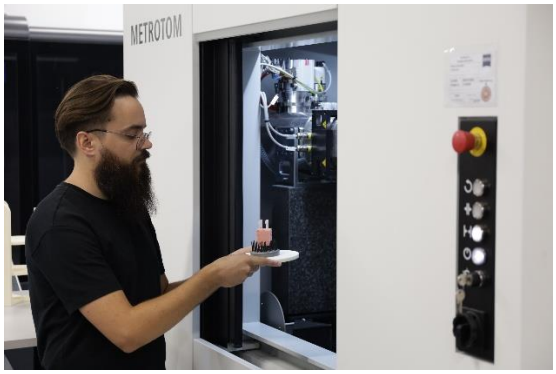


Figure 13. *Placing an object into the working space of the METROTOM 6 scout industrial CT system*

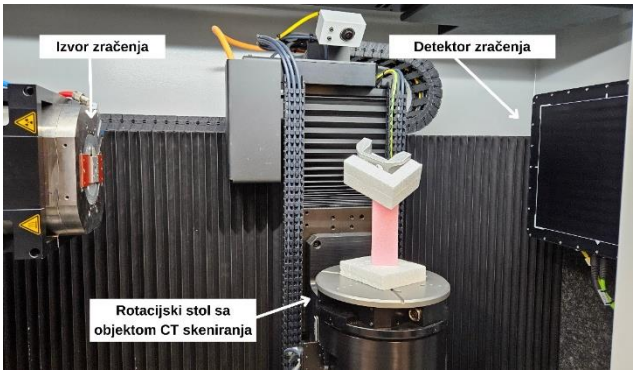


Figure 14. *Object ready for 3D digitization in the ZEISS METROTOM 6 scout industrial CT system*

The advantages of industrial CT technology include:

- Volumetric imaging, which enables digitization and analysis of an object’s internal structure, including cavities, cracks, porosity, or inclusions of other materials (Figure 15).
- High precision, which is suitable for complex parts with internal geometries, with the ability to perform high-resolution 3D digitization.
- Non-destructive analysis, which allows inspection of complex objects without cutting and of assemblies without disassembly (Figure 16).
- Simultaneous 3D digitization of multiple products at once (depending on the required resolution and the dimensions of the products).

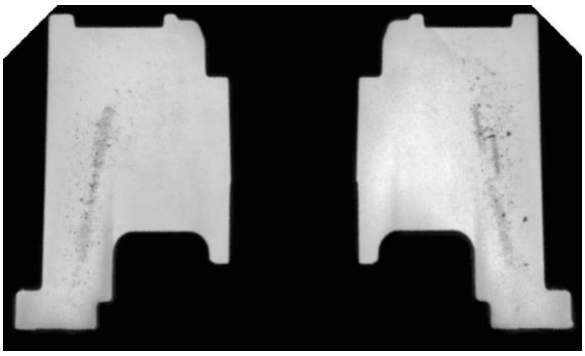


Figure 15. *2D view of casting porosity on a given cross-section*

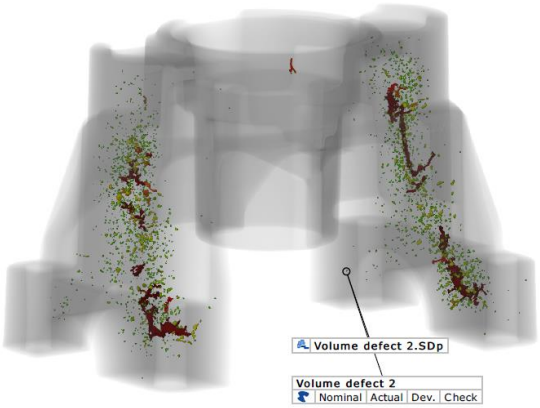


Figure 16. *3D view of casting porosity throughout the entire internal volume*

The disadvantages of industrial CT technology include:

- High equipment and maintenance costs.
- Limitations in object size and material density — dense metal parts require more powerful radiation sources.

3.1. Example of porosity analysis of aluminum castings

Computed tomography is an ideal tool for analyzing the porosity of castings in the automotive and aerospace industries, Figure 17.

Conventional methods of analysis involve cutting samples and evaluating them under a microscope, which destroys the product and creates additional unnecessary cost. After evaluation with CT technology, the product can still be sold or put into use.

CT porosity analysis is a quantitative method, meaning it is possible to automatically check whether the samples meet all the porosity tolerances specified for a given product. Some of the common indicators are:

- Volume of individual pores.
- Total porosity volume fraction (percentage of the part’s volume that is porous).
- Distance of a pore to the nearest outer surface.

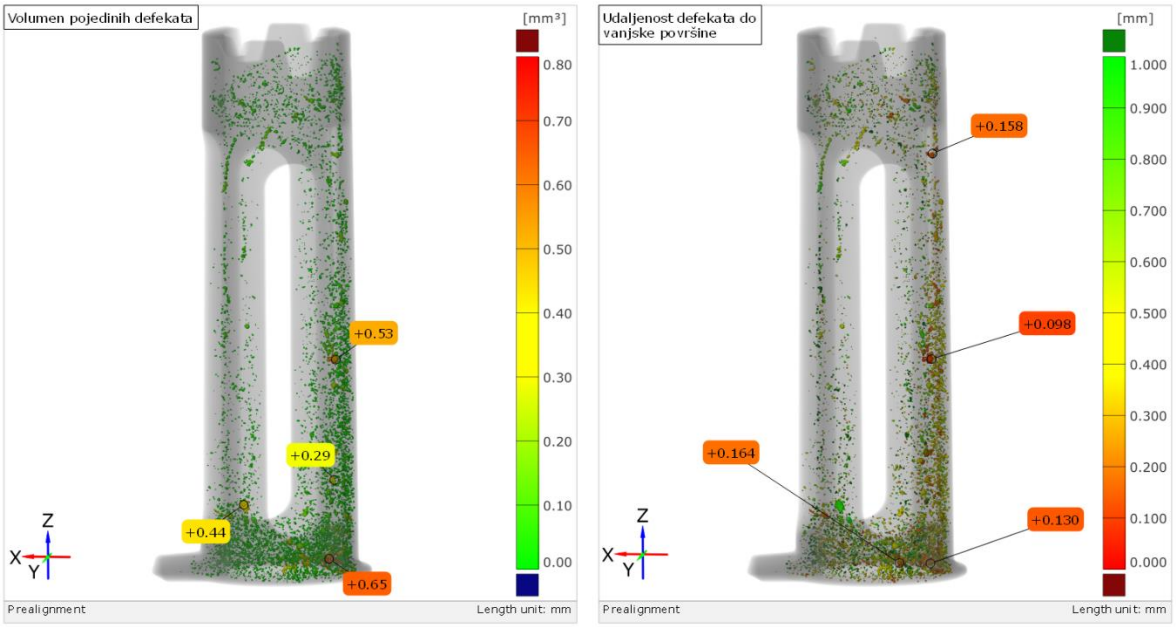


Figure 17. *Porosity analysis of aluminum castings*

3.2. Digitization and 3D measurement of a large number of small plastic samples

Disposable plastic in medicine is used to produce single-use medical products such as syringes, pipette tips (Figure 18), autoinjectors, and packaging. Its use enables the maintenance of sterility since each item is used only once, which significantly reduces the risk of infections.

In addition, plastic contributes to safety and hygiene in healthcare institutions by allowing clean and controlled contact with a patient or sample. Also, the manufacture of plastic medical products is relatively inexpensive, which reduces healthcare costs and allows for mass availability of such equipment.

However, to ensure the efficiency, reliability, and safety of disposable medical plastic products, quality control is required. By using CT technology, it is possible to digitize a large number of such samples in a single scan, and the actual measurement process only needs to be performed for one sample – all others are automatically recalculated. In the end, a measurement report is obtained for each sample, Figure 19, [6].

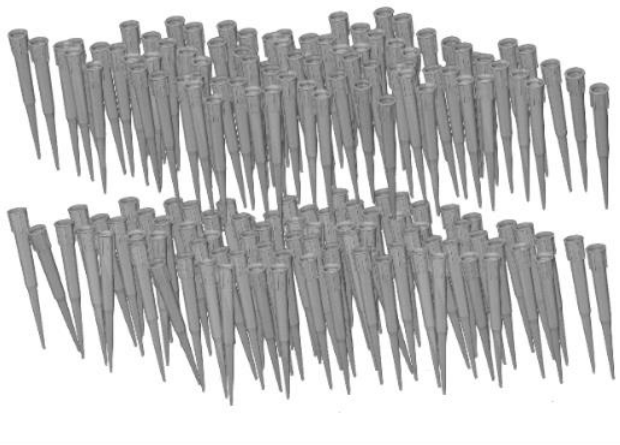


Figure 18. *Display of several 3D digitized pipette tips in a single scan*

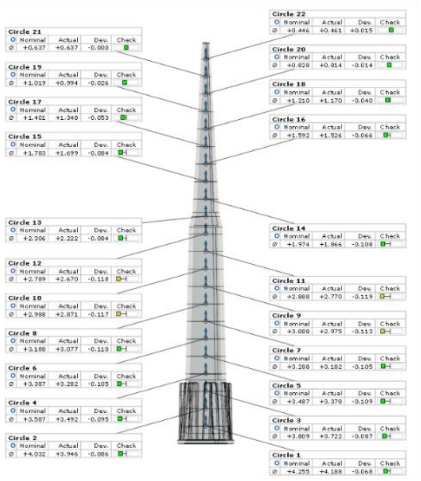


Figure 19. *Dimensional analysis of a pipette tip*

3.3. Example of quality control of battery cells

Furthermore, as mentioned earlier, CT technology is ideal for non-destructive analysis of internal geometries. Given the increasing emphasis on the use of electrical energy in the automotive industry – which implies the use of battery cells – this technology is increasingly establishing itself as one of the primary methods for quality control and development of battery modules, Figure 20, [2].

CT technology enables [2]:

- Non-destructive inspection of internal defects in battery cells (Figure 23), such as the detection of foreign particles (Figure 21), micro-cracks, delamination (Figure 22), and deformations within electrodes and separators.
- Measurement of geometries invisible to the naked eye, such as electrode bulging or misalignment (known as “overhang”), which significantly contributes to improving the safety and performance of lithium-ion cells in the automotive industry.
- Analysis of welds and joints in battery modules without disassembling the assembly, which greatly helps in drawing conclusions about their quality.
- Monitoring the degradation of cell interiors after cyclic charging and discharging.

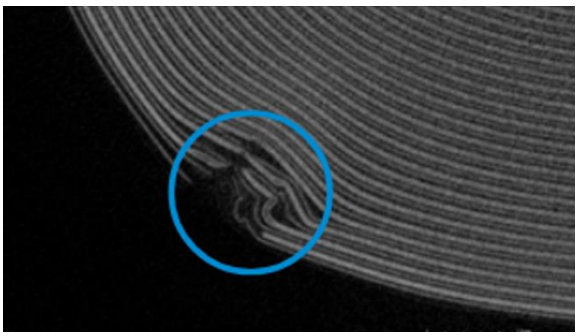


Figure 20. *Cracks and voids in the battery cell*

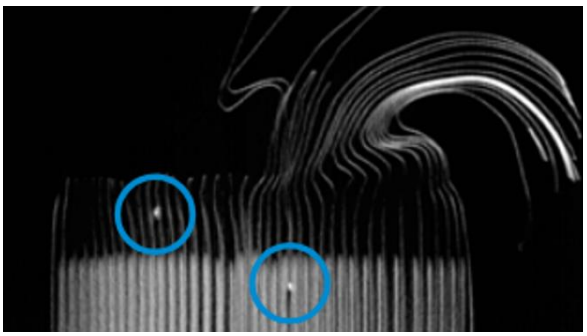


Figure 21. *Metal inclusions in a battery cell*

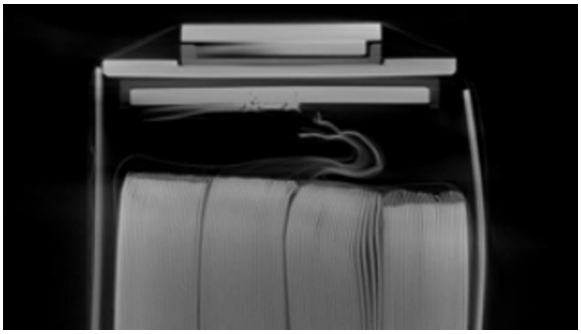


Figure 22. *Analysis of other components of a battery cell*

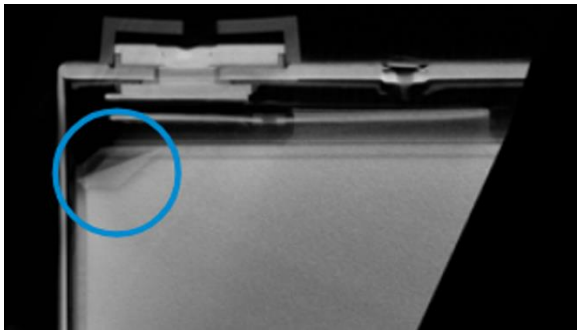


Figure 23. *Damage to a battery cell electrode*

4. Conclusion

Optical 3D measurement systems have today become standard metrological solutions in industrial polymer production and metal casting. Fast 3D digitalization of complete surface gives you possibilities for comprehensive dimensional analysis, especially for Geometric Dimensioning and Tolerancing, also known as GD&T.

Manual ATOS 3D systems are widely used for complex smaller, medium and big parts. When it is needed to measure larger quantities then you have to use standard ATOS robotized solution – ATOS ScanBox. Manual or robotized ATOS optical 3D systems are standardized solutions and systems can be installed in the laboratory or production hall.

T-SCAN hawk 2 is a portable 3D scanner of a new generation of lightweight laser 3D scanners which is used for midsized and bigger parts with complex geometry, but without small details. Main advantage of handheld 3D scanner is using it when is needed a high degree of system mobility for 3D measurement and inspection.

Industrial computed tomography, also known as an industrial CT system, is used when performing dimensional analysis and internal inspection of one or more small to midsized parts in various industries. The main advantage of a CT system is the ability to do dimensional analysis with non-destructive inspection on the same digital twin. An additional benefit is 3D digitizing of a large number of small plastic samples for very similar time as it is needed for one part.

References

[1] Pilipović, A., Godec , A., Kos, J., 2024. Additive manufacturing and 3D digitalization, Regional Competence Center in Vocational Education in Mechanical Engineering – Industry 4.0 (SSŠ VG), Velika Gorica

[2] Peričić, E., Perković, A., Kurtalj, L., Kos, J., Drvar, N., Hercigonja, T. 2025. Evaluation of battery cells and modules in the automotive industry using CT technology , IRT FORUM 2025, Portorož, Slovenia

[3] Karič , D. 2021. Optical measurement in serial production, IRT FORUM 2021, Portorož, Slovenia

[4] Čatipović , N., Sršen, F., Vukšić , I., Jurčević, A., Kos, J., Kurtalj, L., Krolo, L., Kunac, K., Periša, K. , Bošković, P., Peko, I., Ljumović, P. , Bašić, A. 2024. Possibility of using CT imaging and 3D scanning for the purpose of advanced analysis of archaeological artifacts , MTSM 2024, Split, Croatia

[5] Examples of use. https://www.topomatika.hr (accessed 13 May 2025).

[6] ZEISS X-Ray Series . Make the invisible visible . https://www.zeiss.com/metrology/en/systems/x-ray.html (accessed 20 May 2025).

Simulation of irradiation-induced damage in Al-Mg-Li alloys

***Franjo Kozina*[1], *Zdenka Zovko Brodarac*[1], *Matea Kuprešak*[1] *and Mitja Petrič*[2]**

1) University of Zagreb Faculty of Metallurgy, Aleja narodnih heroja 3, 44000 Sisak, Croatia

2) University of Ljubljana Faculty of Natural Sciences and Engineering, Lepi pot 11, 1000 Ljubljana, Slovenia

Corresponding author: fkozin@simet.hr

Original scientific article

Abstract: The reliability, sustainability and performance of components used in modern space and nuclear technology depend on the development of structural materials that can withstand extreme conditions. In this study, radiation-induced damage in Al-Mg-Li alloys is investigated using stopping and range of ions in matter (SRIM) and transport of ions in matter (TRIM) simulations to evaluate the mechanisms of stopping power and microstructural evolution under helium ion exposure. The results show that ionisation dominates over the entire energy range from 10.0 keV to 10.0 MeV. The SRIM simulations showed a transition from displacement to electronic interactions around ion energy of 52.0 keV and confirmed that electronic interactions dominate at higher energies The TRIM results also confirmed that the displacement damage occurs at low energies, while deeper penetration with minimal structural effects is expected at higher ion energies.

Keywords: *Al-Mg-Li alloys; chemical composition; density; ion-solid interaction simulations; irradiation damage; microstructure evolution; irradiation parameters*

1. Introduction

The reliability, sustainability and efficiency of next-generation nuclear reactors [1] depend on the development of advanced structural materials [2] and [3]. The operating conditions for the materials used in nuclear technology are determined by the reactor design and the function of the component. While the materials in the primary circuit of a nuclear reactor are exposed to high temperatures and chemically aggressive coolants, the operating conditions in the secondary circuit are generally characterised by lower temperatures, thermal and mechanical loads [4] and [5]. Although similar operating conditions are also encountered in other advanced engineering applications, the consideration of their combined and synergistic effect on material degradation is a challenge characteristic of nuclear engineering [6]. When selecting suitable materials for this type of application, the radiation effect must also be considered as a critical operating condition [6] and [7]. In addition to displacement damage, ionization and transmutation caused by the penetration of energetic particles into the material volume [8], irradiation can also cause the formation of unstable nuclei or radiological activation [9]. This increases the complexity and cost of material decommissioning, increases the amount of hazardous waste and reduces the recycling potential [6], [10] and [11].

1.1. Irradiation damage

Irradiation damage is caused by the transfer of energy from an ion particle to the target material. When an energetic particle with the starting energy (*E*) crosses the distance (*dx*) in a solid target material, these interactions lead to a loss of energy (*dE*). The stopping power (*dE/dx*) is defined by Equation 1 [12]:

$$\frac{dE}{dx} = \left(\frac{dE}{dx}\right)_d + \left(\frac{dE}{dx}\right)_e + \left(\frac{dE}{dx}\right)_n \quad (1)$$

Equation 1 indicates the stopping power due to three types of interactions: elastic collisions producing displacements damage (d), inelastic interactions or ionization between the bombarding particle and the electrons in the solid (e), and a nuclear reaction (n).
Displacement damage usually begins with the elastic collision of an energetic particle with a lattice atom, referred to as the primary knock-on atom (PKA). When the energy conditions are met [13], the lattice atom is displaced from its initial position into the interstitial space, creating a Frenkel pair or a large number of defects known as a displacement cascade (Figure 1). The unit of displacement per atom (dpa) is the preferred fundamental measure of the material's response to irradiation-induced displacement. It is accepted for a variety of particle types, including heavy ions, protons, electrons and neutrons [14]. Radiation damage, quantified as 1 dpa, means that each atom has been displaced from its lattice site on average once [15]. Whether a subcascade or a cascade occurs depends on the mass of the energetic particle, the recoil energy and the density of the material [16] and [17]. In the centre of the cascade, a temporarily diluted region is formed, which is surrounded by a densified region. After the cascade, the densified region becomes a region with interstitial defects (Figure 1, dynamic crowdion) and a diluted region typically becomes a region with vacancy defects (Figure 1, core of a small cascade) [18].

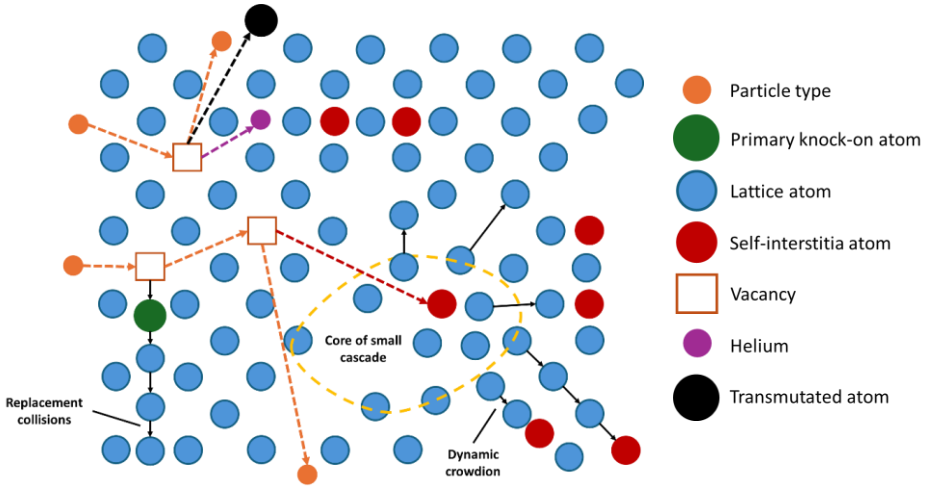


***Figure 1**. Schematic illustration of irradiation damage [16]*

The flowchart illustrating the effects of irradiation on atomic displacement is shown in Figure 2. Each displaced atom forms a Frenkel pair consisting of a vacancy and a self-interstitial atom (SIA) (Figure 1). The changes in the microchemistry and microstructure of the irradiated materials result from the production, migration, aggregation and annihilation of Frenkel pairs (Figure 2) [19].

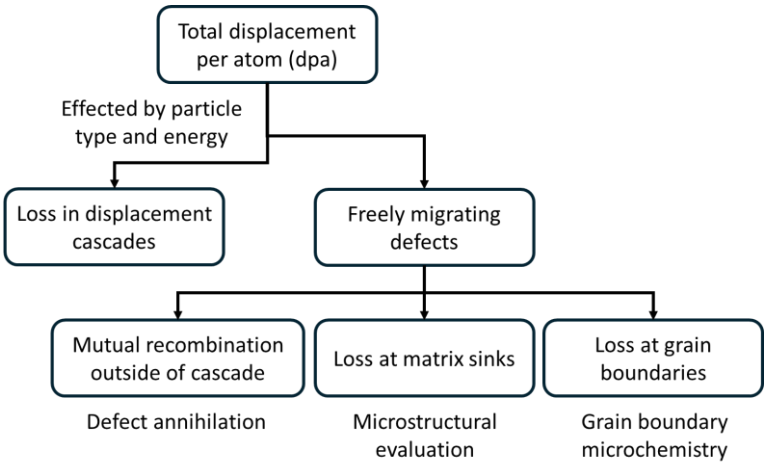


***Figure 2.** Flowchart of the atomic displacement caused by the cascade event and the subsequent changes in the microstructure and microchemistry induced by the irradiation [19]*

The microstructure evolution and the microchemical changes induced by irradiation depend on the irradiated material and the irradiation parameters such as temperature, particle type, dose and rate [19] and [20]. The microstructure evolution is controlled by the redistribution of vacancies and SIA leading to the formation of clusters, dislocation loops and voids (Figure 3). The microchemical changes are controlled by the migration of Frenkel pairs to the grain boundaries, leading to localised changes in chemistry (Figure 2, Figure 3) [19]. On the other hand, recombination and clustering refer to the mechanisms that reduce the number of defects generated in a displacement cascade (Figure 3). Irradiation-induced vacancies and interstitials can spontaneously recombine and become annihilated. The loss of both types of defects can occur in unbiased, biassed and variably biassed sinks. Voids, incoherent precipitates and grain boundaries are considered unbiased sinks that trap both types of defects. Since dislocations preferentially trap interstitial defects, they are regarded as biassed sinks. Variably biassed sinks such as impurity atoms and coherent precipitates act as recombination centres stopping the free movement of the defect until it is annihilated [18]. Although recombination does not necessarily lead to a reduction in the total number of defects, it can alter their mobility and thus affect their impact on material properties. Alternatively, defects can cluster together and form large structures such as vacancy clusters or interstitial loops (Figure 3) [21], [22] and [23].

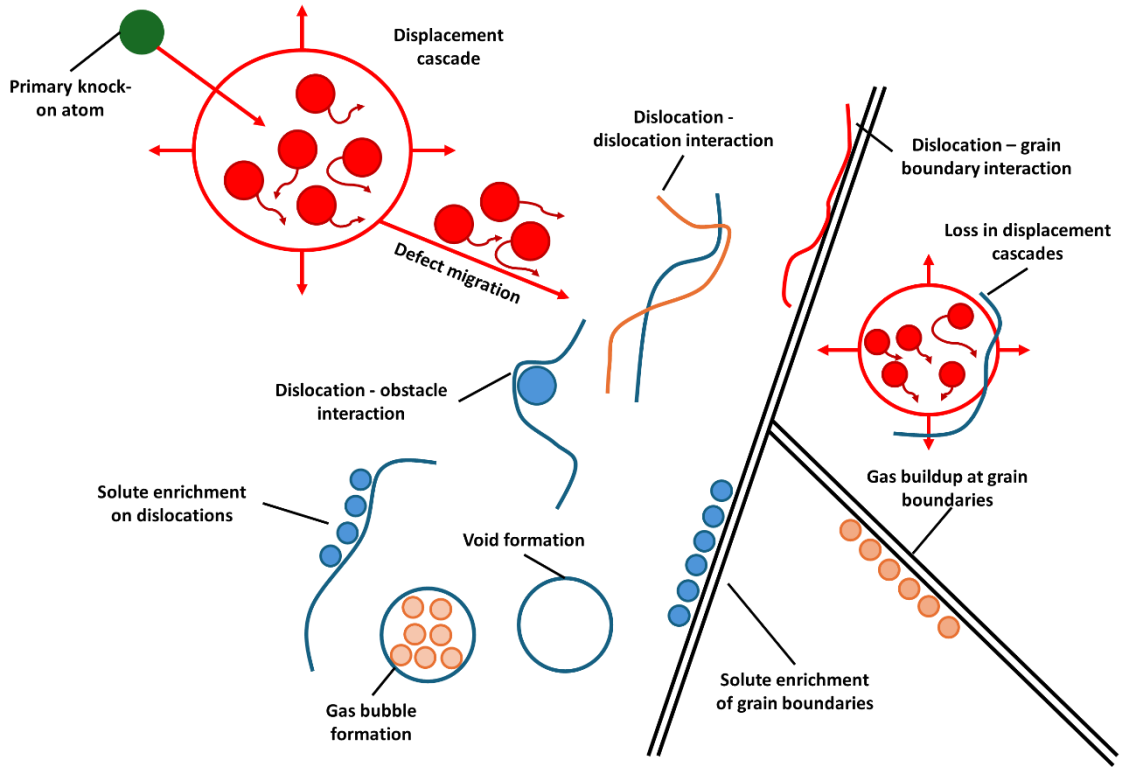


Figure 3. *Schematic representation of the microstructure evolution and the changes in the microchemistry induced by irradiaton damage [13] and [19]*

While causing displacement damage, an energetic particle can also interact with the nucleus of a target atom. This interaction triggers a nuclear reaction that changes the mass and/or charge of the nucleus *[13]*. Transmutation reactions require a large energy transfer and are most commonly associated with neutron irradiation. Long-term irradiation under these conditions can lead to a change in the chemical composition of the target and the formation of charged particles such as hydrogen or helium (Figure 1, Figure 3) [24]. Transmutation can cause radiological activation by creating unstable nuclei that emit radiation when they decay. Even after radiation exposure ends, these unstable nuclei may remain radioactive exceeding the safe hand-on limits over a long period of time [25]. Besides neutron interactions, the spallation reactions triggered by the high-energy proton bombardment of a heavy metal target can produce a wide range of isotopes and light metals [24] and [26].

If the energy of the bombarding particle is below the threshold required to displace atoms from the lattice *[13]*, inelastic collisions leading to electron excitation or ionisation become the dominant interaction. In this process, energy is transferred to bound electrons, which are brought to higher energy levels or completely ejected, leading to the formation of atomic ions. This mechanism is ineffective in metals, as the high density of free electrons quickly neutralises the local charge and prevents permanent structural damage [27].

1.2. The evolution of irradiated microstructure

Irradiation can cause eight major changes in a functional properties of metals by altering its microstructure. These changes include irradiation-induced amorphization, radiation-induced hardening, reduced thermal and electrical conductivity, changes in mechanical properties or corrosion resistance, dimensional instability, and high-temperature embrittlement [28], [29] and [30]. Table 1 summarizes how different types of irradiation damage are linked to changes in the material's microstructure.

Table 1. *The effects of the different types of irradiation damage on microstructure and functional properties* [31]

Effect	Consequence in material	Type of degradation in component
Displacement damage	Formation of point defect clusters and dislocation loops	Hardening, embrittlement
Segregation	Diffusion of different elements to grain boundaries	Embrittlement, grain boundary cracking
Phase formation	Formation or dissolution of phase, amorphization [28]	Embrittlement, softening
Swelling	Increase in volume due to defect clustering and void	Local deformation, residual stress
Creep	Irreversable deformation	Deformation, reduction in creep life
Helium formation and diffusion	Dimensional instabilities [28], void formation	Embrittlement, loss of stress required life and creep ductility

At low temperatures, where the movement of SIAs or SIA clusters is limited, a transition from the crystalline to the amorphous phase can occur. The amorphous phase transition can be directly related to the displacement cascade or the accumulation of point defects and disorder process.The critical temperature for amorphization increases with the increase in PKA and the mass of bombarding particles [32]. Hardening can occur when radiation causes the appearance of dense sessile defect clusters that impede the free movement of dislocations (Figure 1). This type of matrix hardening is usually accompanied by a decrease in elongation and fracture toughness [28]. The changes in thermal and electrical conductivity of pure metals can be caused by electron scattering from point defects or clusters and transmutations of target atomic nuclei [28] and [33]. At intermediate temperatures, where the Frenkel pairs have good mobility, segregation of the solutes to the unbiased sinks can occur (Figure 3). Localised bulking of the matrix with solute elements can lead to the phase precipitation. The segregation and precipitation associated with irradiation can lead to embrittlement of the matrix or the grain boundaries, increase the susceptibility to localized corrosion or stress corrosion cracking and influence the void swelling behaviour [18] and [28]. The increase in void size, irradiation growth and creep are dimensional instabilities associated with the anisotropic growth in polycrystalline materials, causing a decrease in strength as well as the nucleation and propagation of cracks along the grain boundaries. Irradiation creep occurs due to the absorption of point defects at biased sinks that are oriented relative to the applied stress [18]. High-temperature embrittlement is caused by a nuclear reactions and the formation of helium. This transmutation leads to the transition of grain boundary bubbles into voids (Figure 1 and Figure 3), breakaway growth, cavity coalescence and intergranular fracture. Helium embrittlement requires tensile stress during high-temperature irradiation. Otherwise, the resulting helium bubbles remain distributed in the material [28] and [34]. The evolution of microstructure under irradiation is a complex, multi-scale process governed by difect production,

migration, aggregation and annihilation. These structural changes influence the degradation of functional properties and the overall performance of materials in irradiation environments. A deeper understanding of how irradiation parameters influence microstructure evolution is needed for predicting materials behaviour and ensuring long-term stability in nuclear systems [35] and [36].

1.3. The influence of the irradiation parameters on microstructure evolution

Differences in PKA energy produce significant changes in the primary damage state and affect microstructural evolution during irradiation. Irradiation with low-energy PKAs produces isolated Frenkel pairs and submicroscopic defect clusters. In contrast, high-energy PKAs generate dense displacement cascades, form stable defect clusters, accelerate microstructural evolution and long-term damage accumulation [35]. The type of energetic particle significantly influences the nature and extent of microstructural evolution during irradiation. Light ions, such as helium or hydrogen, primarily produce displacement damage and can also lead to gas bubble formation due to absorption. Heavier particles like neutrons or heavy ions create more complex collision cascades, resulting in higher defect densities, defect clustering, and localized amorphization [15] and [35]. The microstructural development induced by irradiation is determined by the thermal mobility and/or stability of the associated defects. The early experimental studies measuring the electrical resistance of isohronally annealed metals irradiated near absolute zero [35] have identified five stages of defect recovery. Stage I is associated with the recombination of Frenkel pairs formed at the same displacement event and with the long-range recombination of defects from different displacement events. While stage II involves the migration of small SIA clusters, stage III corresponds to the vacancy movement onset. Stage IV involves the movement of void clusters and impurities. Stage V corresponds to the thermal dissociation of sessile vacancy clusters [28]. At low temperatures, below Stage I, the defects do not migrate. However, new displacement events can lead to the annihilation of the defects created earlier during irradiation. At low temperatures between the Stages I and III, the SIA and SIA clusters have sufficient mobility to migrate and form dislocation loops and vacancy clusters. Increasing the temperature to the medium temperature regime, between Stages III and V, increases the complexity of defect cluster development and its dependence on the lattice type. In materials with face-centered cubic lattice (fcc), the evolution of the microstructure is related to the mobility of vacancies and interstitial loops while in the metals with body-centered cubic lattice (bcc), in addition to the aforementioned defects, changes in the voids can also be observed [28], [18] and [37]. Microstructural defects that occur during irradiation at high temperatures above recovery Stage V include dislocation loops, network dislocations and voids. The main difference with respect to the lower temperature irradiation is the occurrence of dimensional instability in most materials. Irradiation at high temperatures (near or above the 0.5 melting point) usually results in only minor microstructural changes due to the strong influence of thermodynamic equilibrium processes, unless significant amounts of hydrogen and helium atoms are generated. This nuclear reaction leads to the formation of voids inside the grains and along the grain boundaries [28] and [38]. Molecular dynamics (MD) simulations of the primary damage in the displacement cascade [39] and experimental studies on defect accumulation have shown that defect production is highest for hexagonal close-packed materials (hcp), intermediate for bcc metals and lowest for fcc metals. This suggests that the anisotropic nature of the hcp lattice may inhibit defect recombination in the displacement cascade. Moreover, the average cluster size generated by the displacement cascade is larger in fcc metals than in bcc metals. Defect accumulation in the form of void swelling is significantly lower in bcc metals than in fcc and hcp metals [28]. Materials with a low atomic weight exhibit a spatially more diffused displacement cascade as a consequence of decreasing electronic stopping power with decreasing atomic weight (Equation 1). There is no universal relationship between atomic weight and irradiation-induced microstructural evolution or overall defect production [40]. As irradiation parameters, solute segregation and precipitation refer to the solute atoms added during alloying and to impurities resulting from nuclear reactions. There are three general categories of precipitation associated with radiation-induced segregation processes: radiation-induced precipitation, which includes the formation of non-equilibrium phases and dissolution during post-irradiation anneling, radiation-

enhanced precipitation, which relates to the formation of stable phases, and irradiation-modified precipitation, which leads to the precipitation of phases with altered chemical composition. Recent studies have also shown the irradiation-retarded precipitation due to the increase in phase precipitation temperatures [28].
The aim of this study is to simulate the interaction of helium ions with an aluminum–magnesium–lithium (Al–Mg–Li) alloy using the stopping and range of ions in matter (SRIM) and transport of ions in matter (TRIM) simulation tools. These simulations provide insight into primary damage formation and energy deposition profiles within the solid target material. The resulting data represent the first step in assessing the radiation resistance of this lightweight alloy and will be used as input parameters for future experimental validation. Considering the alloy's use in space technology, where resistance to solar energetic particles is critical, and its potential application in nuclear engineering, it is important to understand the possible microstructural changes caused by irradiation.

2. Materials and methods

The aluminum-magnesium-lithium alloy was synthesised in an induction melting furnace under a protective atmosphere of argon (Ar). The sample was produced by casting in a permanent mould in an open atmosphere. The chemical composition and the density of the alloy are listed in Table 2.

Table 2. *Chemical composition and density of the synthesised Al-Mg-Li alloy* [41]

Unit of measurement	Chemical composition			Li/Mg	Density, g/cm$_3$
	Al	Mg	Li		
wt.%	97.46	0.38	2.16	5.68	2.49
at.%	91.7	0.4	7.9		

In the hypoeutectic alloys microstructure development begins with the solidification of the α_{Al} dendritic network. The further microstructure development occurs according to the high Li/Mg ratio, which implies the solidification of the metastable Al_3Li (δ') phase. In the subsequent solidification sequence, this phase will serve as a nucleation site for AlLi (δ) phase. However, the thermodynamic calculation of the solidification sequence and the results of the extensive microstructural characterisation indicated a much more complex microstructure development comprehending additional formation of Al_2LiMg (T) and Al_8Mg_5 (β) phases [41], [42], [43], [44], [45] and [46].
The schematic representation of the SRIM and TRIM simulations with indicated input and output parametars is given in Figure 4. The simulation of the interactions of energetic particles with the Al-Mg-Li alloys was calculated using the SRIM simulation tool. This simulation tool consists of a set of programmes that calculate the stopping and ragne of energetic particles into the solid target material using a quantum mechanical treatment [47] and [48]. Helium is often used in experimental ion implementation studies for the simulation of radiation effects in light alloys. As alpha particles, helium nuclei constitute a significant proportion of galactic cosmic radiation and are therefore suitable for assessing radiation damage in aerospace materials. In nuclear technology, helium is also a by-product of nuclear reactions in modern reactor systems. The obtained results will provide a useful basis for evaluating the radiation tolerance of Al-Mg-Li alloys under such conditions. Its high atomic mass (4.003 u), its ability to cause displacement damage and to be absorbed in the crystal lattice provide a realistic insight into the degradation mechanisms to be expected in space environments [49] and [50]. The kinetic energy of the helium ions ranged from 10.0 keV to 10.0 MeV allowed a comprehensive investigation of ion penetration depth, stopping power (dE/dx) and damage profile over a broad energy spectrum. The stopping power results were expressed in keV/µm. This is a common and widely used unit that relates directly to the energy loss per distance travelled in the material. The use of this unit enables a direct interpretation of the depth-dependent energy dissipation and is particularly suitable for the experimental verification of the simulation results. The input parameters for the solid target material included the chemical composition of the alloy, defined in atomic per cent, and the density of the material (Table 2). These parameters were required for accurate modelling of the

target's atomic structure and the interaction cross-section. The simulation results were used to calculate the dependence of the displacement and electronic stopping on ion energy and the dependence of the ion range on the ion energy. The results of the longitudinal straggling were added as error bars together with the ion range to gain insight into the width of the distribution.

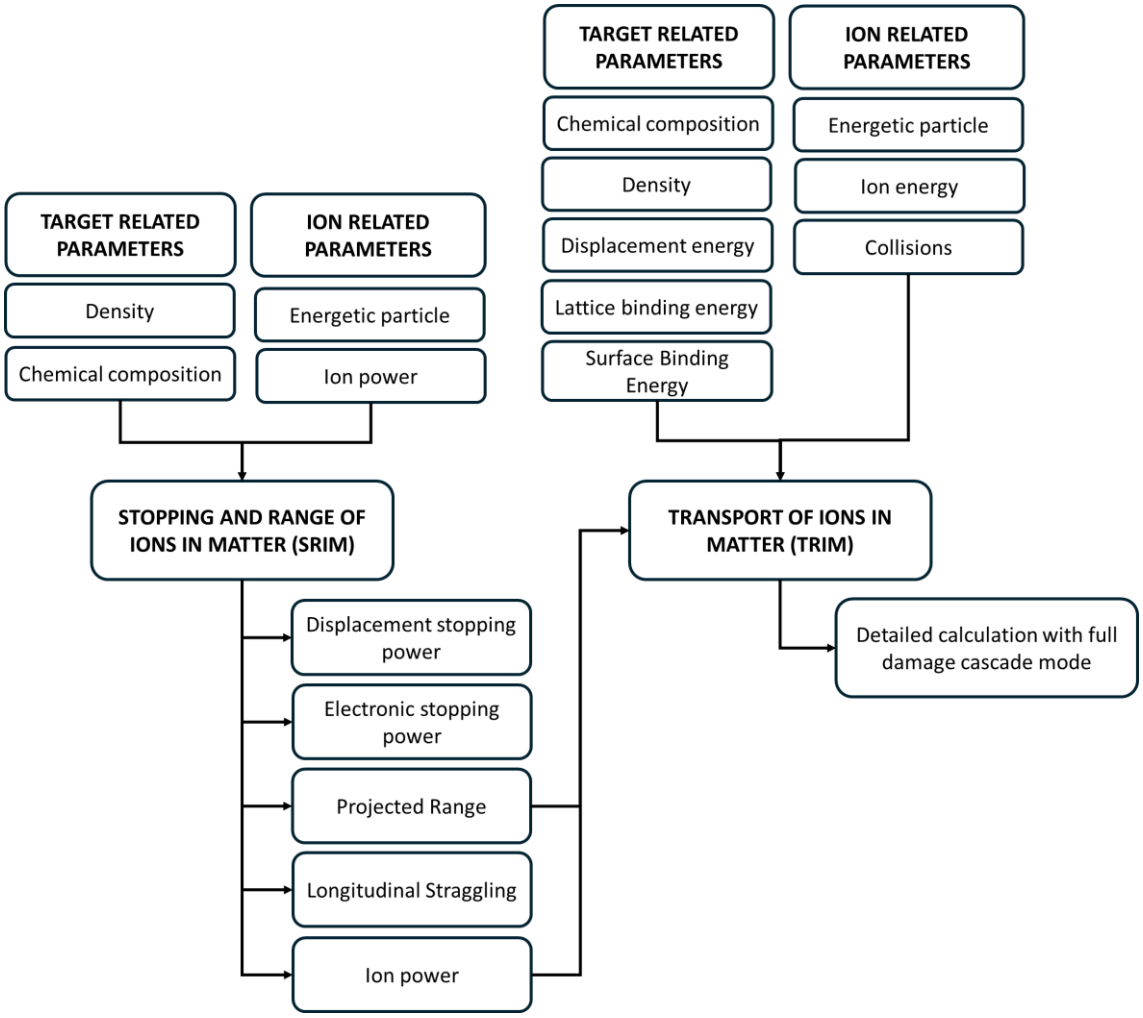


Figure 4. *Schematic representation of the microstructure evolution and the changes in the microchemistry induced by irradiaton damage*

The TRIM model was used to perform detailed Monte Carlo simulations of the ion interaction with the Al-Mg-Li alloy. In addition to the chemical composition and density (Table 2), which were already defined in the SRIM setup, the displacement energy, lattice binding energy and surface binding energy for each element in the target were also specified (Table 3). These parameters are available in the simulation database. The simulations were performed in a monolayer collision setting using the detailed calculation with full damage cascade mode, which allows accurate modelling of the collision events and damage production mechanisms.

Table 3. *The additional parameters for each element in the solid target material for the TRIM simulation*

Parameter	Al	Mg	Li
Displacement energy, eV	25.0	25.0	23.0
Lattice binding energy, kJ/mol	3.0	3.0	3.0
Surface Binding Energy, eV	3.36	1.54	1.63

The parameters for ion energy and depth ranges were selected based on the results of the SRIM simulation. A total of 10,000 ion collisions were simulated to ensure the statistical reliability of the ion

recoil distribution, the total damage event, the energy transfer to recoil, the ion range and the ionisation loss calculations.
Overall, the combination of SRIM and TRIM simulation results enabled a characterisation of the alloy's radiation sensitivity and its performance in the space and nuclear radiation environment. In addition, the results obtained can serve as a reliable basis for planning targeted experimental measurements and validating the predicted damage.

3. Results and discussion

Figure 5 presents the results of the SRIM simulation, which shows the dependence of the displacement and electronic stopping power in the Al-Mg-Li alloy.

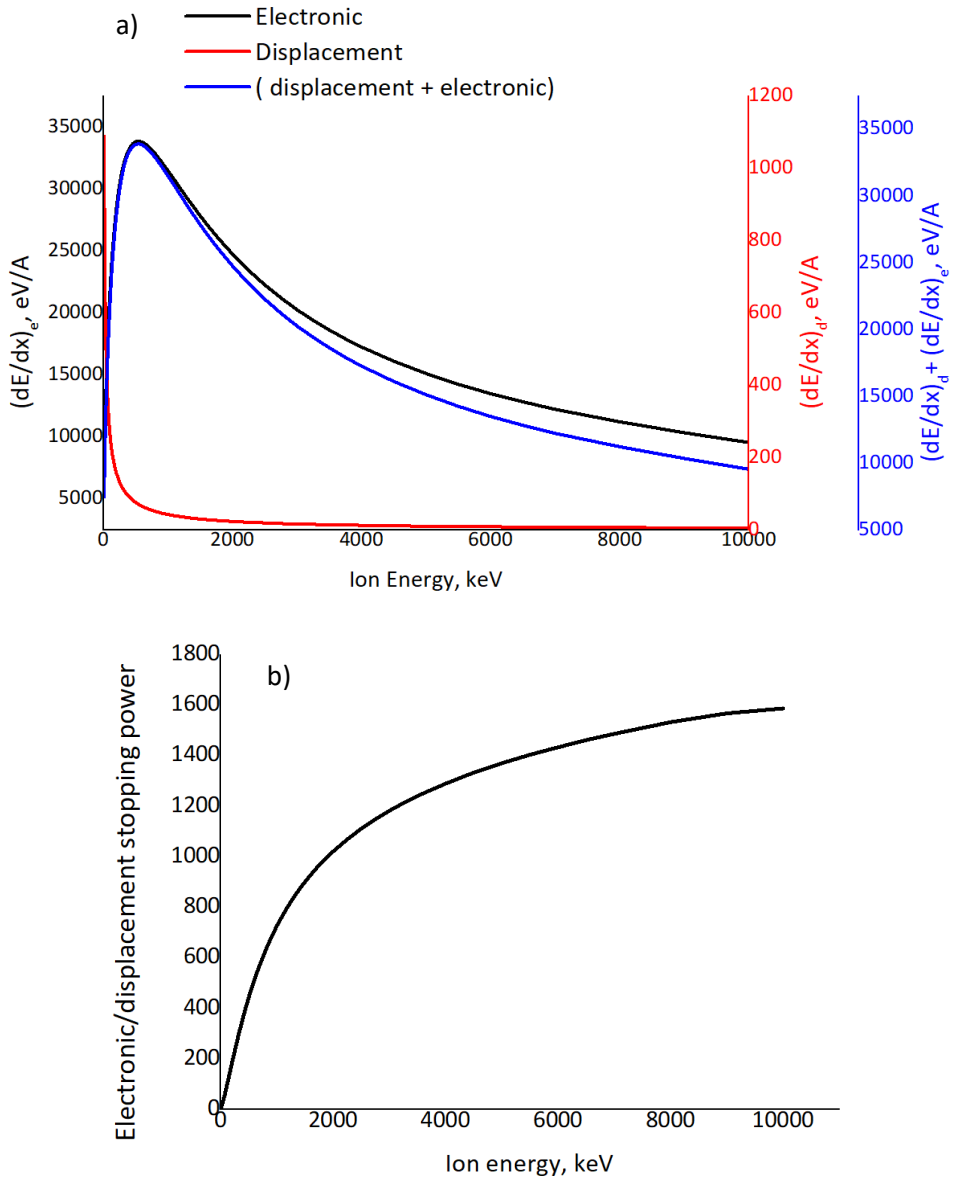


Figure 5. *The results of the SRIM simulation, shown as: a) dependence of displacement and electronic stopping on ion energy, b) dependence of electronic/displacement stopping power as a function of ion energy*

The stopping power curves (Figure 5 a) reveal the energy-dependent interaction mechanisms between helium ions and the Al-Mg-Li alloy. The maximum displacement stopping power is observed at 1,088.00 keV/Å at an ion energy of 10.0 keV. These results indicate that elastic collisions with the target nuclei dominate at low energies and primarily lead to atomic displacement and defect

formation. A transition point occurs at 402.7 keV/Å at 55.0 keV ion energy, where the contributions of displacement and electronic stopping are approximately equal, marking a shift from displacement to ionisation damage. At higher energies, electronic stopping becomes dominant and reaches a Bragg peak at 540.0 keV ion energy with a value of 33,840.0 keV/Å. This corresponds to intense inelastic interactions with the electronic cloud of the target, leading to ionisation and electronic excitation rather than displacement damage. Furthermore, the electronic to displacement stopping ratio (Figure 5 b) remains greater than one for the entire ion energy range (from $(dE/dx)_e/(dE/dx)_d$ = 5.9 for 10.0 keV to $(dE/dx)_e/(dE/dx)_d$ = 1,586.7 for 10.0 MeV), confirming that ionisation effects are consistently more pronounced than direct elastic collisions, even at lower ion energies. Analysis of the stopping power shows that the Al-Mg-Li alloy is most susceptible to displacement damage at low helium ion energies. At higher energies (> 100.0 keV), improved radiation tolerance due to lower atomic displacements is expected. Figure 6 shows the dependence of ion range on ion energy.

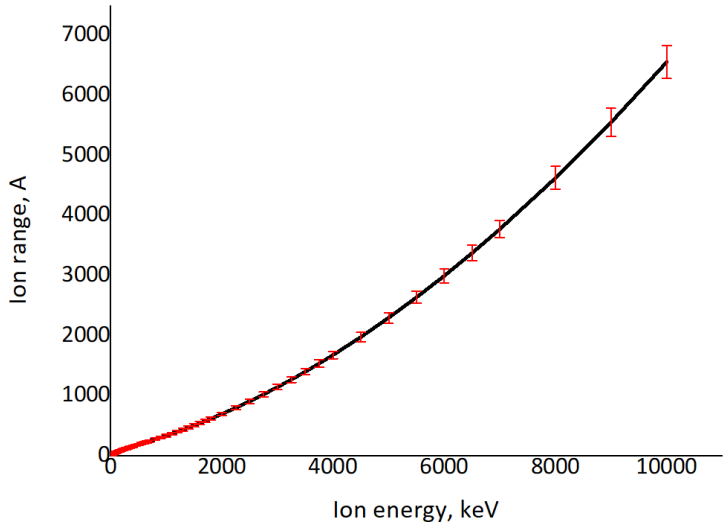


Figure 6. *The dependence of the projected range on the helium ion energy*

The ion range curve shows an almost exponential increase in penetration depth with the increase in helium ion energy (Figure 6). This trend is to be expected as ions with higher energy have sufficient kinetic energy to penetrate deeper into the material. The accompanying longitudinal straggling, shown by the error bars, also increases with ion energy (from initial ±5.0 Å at 10.0 keV to ±275.0 Å at 10.0 MeV) and indicates a broader distribution of ion penetration depth (Figure 6). This increasing scattering reflects the stochastic nature of ion interactions within the material. While the average projected range increases with energy, the straggle becomes more pronounced. This behaviour is crucial for understanding and predicting the depth profile of the radiation-induced effects in the Al-Mg-Li alloy.

Since the SRIM simulation results indicate that the excitation or ionisation of electrons is a dominant interaction mechanism over the entire range of simulated helium ion energies, a TRIM analysis was performed to gain additional insight into the resulting damaging events. Additional parameters, the energy of the helium ion and a projected range are given in Table 4.

Table 4. *The additional parameters for the TRIM simulation obtained after analysing the SRIM simulation curves (Figure 5 a and Figure 6)*

Area,eV/Å	Ion energy, keV	Projected range, Å
$(dE/dx)_d$	10.0	30.0
$(dE/dx)_e$	540.0	250.0

The ion energies and corresponding projected ranges were selected based on the regions identified by the SRIM simulation, where either displacement stopping (Table 4, $(dE/dx)_d$) or electronic stopping (Table 4, $(dE/dx)_e$) is dominant.
The Figure 7 represents a graphical output from the TRIM simulation illustrating the progression of helium ions and collisions with target atoms. Individual data points represent each interaction event (10,000 collisions).

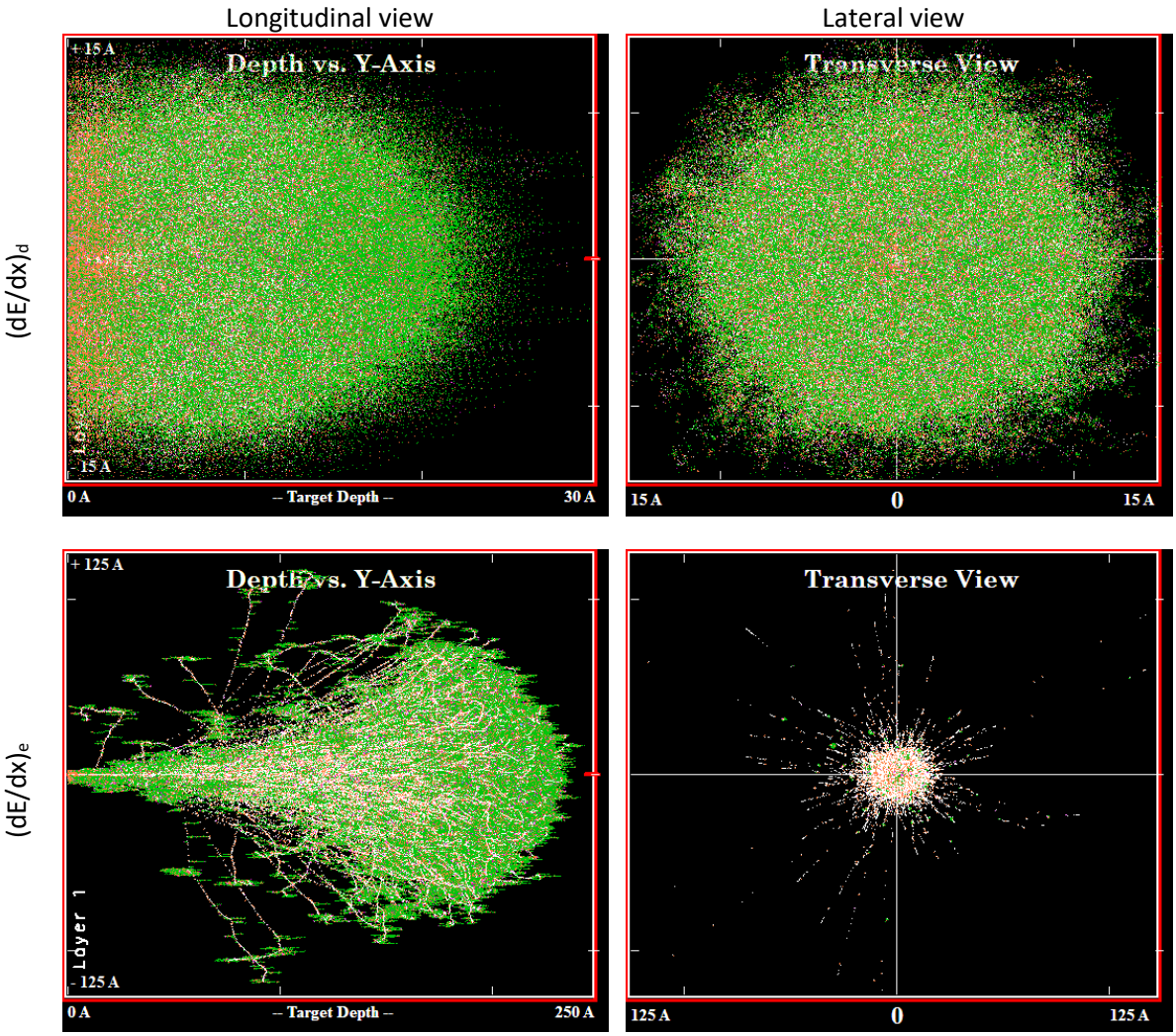


Figure 7. *Graphical output of TRIM simulation showing individual collisions between ion and target atom*

The longitudinal and lateral views show the trajectories of the helium ions and the subsequent collision cascades within the target material. Under conditions where displacement stopping is a dominant type of interaction, the cascade is dense and located close to the surface (Figure 7, $(dE/dx)_d$, target depth ≈30.0 Å). The collisions near the alloy surface indicate intense elastic interactions between ions and target nuclei. These interactions are responsible for the formation of primary knock-on atoms and displacement events. In contrast, the ions in the electronic stopping regime penetrate deeper into the material and experience less direct displacement collisions (Figure 7, $(dE/dx)_e \approx 250.0$ Å). The green markers in the diagrams indicate that the aluminium atoms are most involved in the collision sequences (Figure 7).
Combined TRIM results showing ion range distribution and ionization profile within the Al-Mg-Li alloy are given in Figure 8. The diagrams illustrate the correlation between straggle and electronic excitation stopping power. The ion range distribution during the displacement stopping peaks at about 10 10^6 atoms/cm^2 at a depth of ≈10.0 Å, pointing to the limited penetration and a high collision probability (Figure 8, ion range, $(dE/dx)_d$).This is confirmed by the higher amount of recoils simulated for this

interaction (Figure 8, $(dE/dx)_d$, recoils ≈420.0 eV/ Å). In contrast, the ion distribution in electronic stopping (Figure 8, ion ranges, $(dE/dx)_e$) extends to a depth of ≈250.0 Å into the material, resulting in a less elastic scattering. The ionisation profiles confirm that electronic stopping leads to ionisation (Figure 8, ionization, $(dE/dx)_e$) with minimum recoils of ≈250.0 eV/ Å at a depth of 200.0 Å.

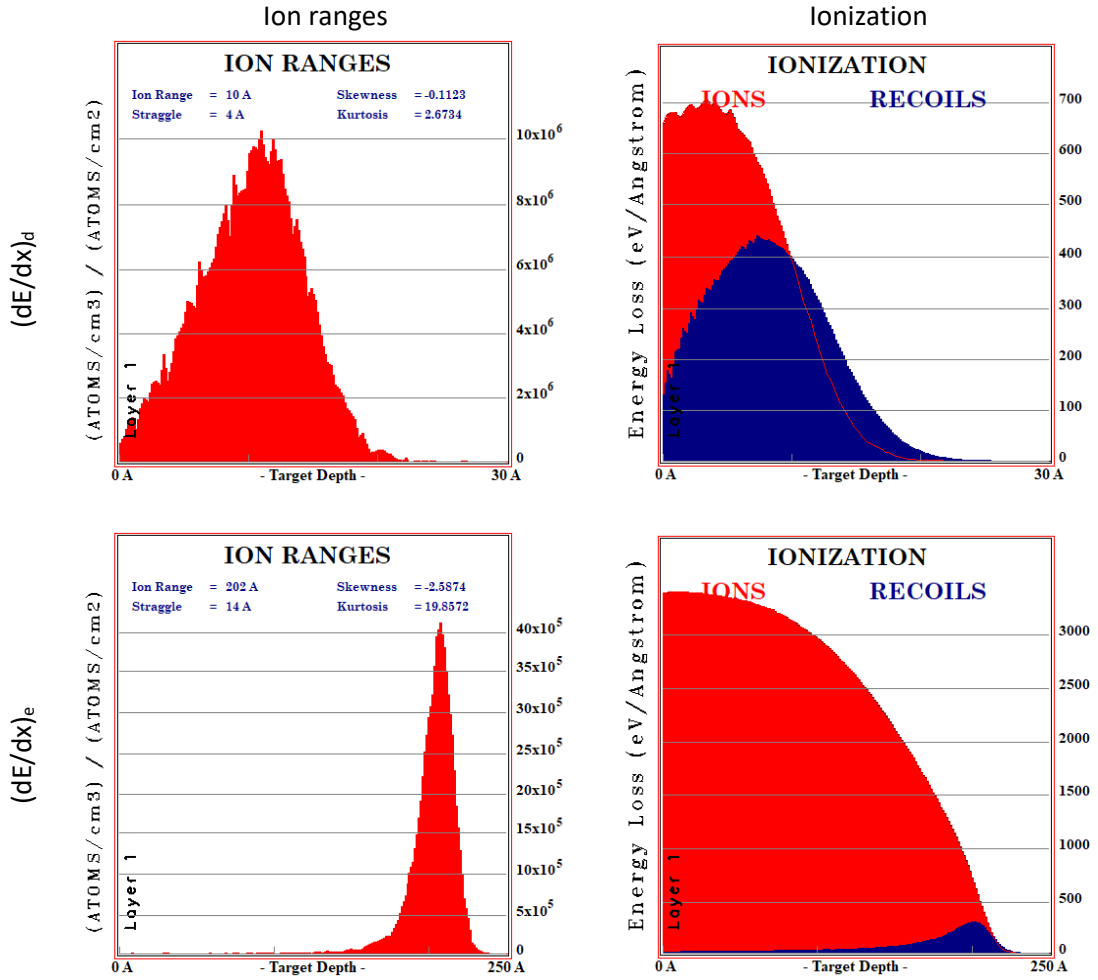


Figure 8. *The TRIM simulation results showing ion range distribution and ionization profile within the Al-Mg-Li alloy*

The ion range distribution under displacement stopping shows a shorter average range (Figure 8, ion range = 10.0 Å) and lower straggle (Figure 8, straggle = 4.0 Å), indicating that most ions are stopped within a narrow and shallow region due to frequent elastic collisions with target nuclei. The skewness is relatively low (Figure 8, skewness = 0.1), pointing to a more symmetric distribution of ion stopping depths. In contrast, the electronic stopping regime displays a longer ion range (Figure 8, ion range = 202.0 Å) and higher straggle (Figure 8, straggle = 14.0 Å), consistent with deeper and more varied ion penetration driven by inelastic interactions with electrons. The increased kurtosis (Figure 8, kurtosis = 19.8) in the electronic regime suggests a sharper peak around the middle range. Despite the deeper penetration, most ions stop within a well-defined depth interval.

The TRIM simulation of overall target displacement, vacancies and replacement collisions as well as the target vacancies for Al, Mg and Li are given in Figure 9. The results show that during displacement stopping (Figure 9, $(dE/dx)_d$) the number of displacement events is significantly higher and is concentrated near the exposed surface (Figure 9, $(dE/dx)_d$, ≈12.0 displacements per helium ion within a 1 Å-thick layer at a target depth of 8.0 Å). During electronic stopping interactions, the displacement damage is comparatively small (Figure 9, $(dE/dx)_e$, ≈8.0 displacements per helium ion within a 1 Å-thick layer at a target depth of 200.0 Å). These simulation results indicate that the ionisation

interactions are not sufficient to cause a significant atomic displacement. The elemental breakdown of the target vacancies reveals that Al atoms experience the most displacement damage (Figure 9, $(dE/dx)_d$, ≈12.0 displacements per helium ion within a 1 Å-thick layer at a target depth of 8.0 Å, $(dE/dx)_e$, ≈3.5 displacements per helium ion within a 1 Å-thick layer at a target depth of 200.0 Å), which is consistent with the higher atomic number of Al and its higher proportion in the alloy. Magnesium and Li have a lower number of vacancies. The low atomic mass of Li can also lead to increased mobility or sputtering effects.

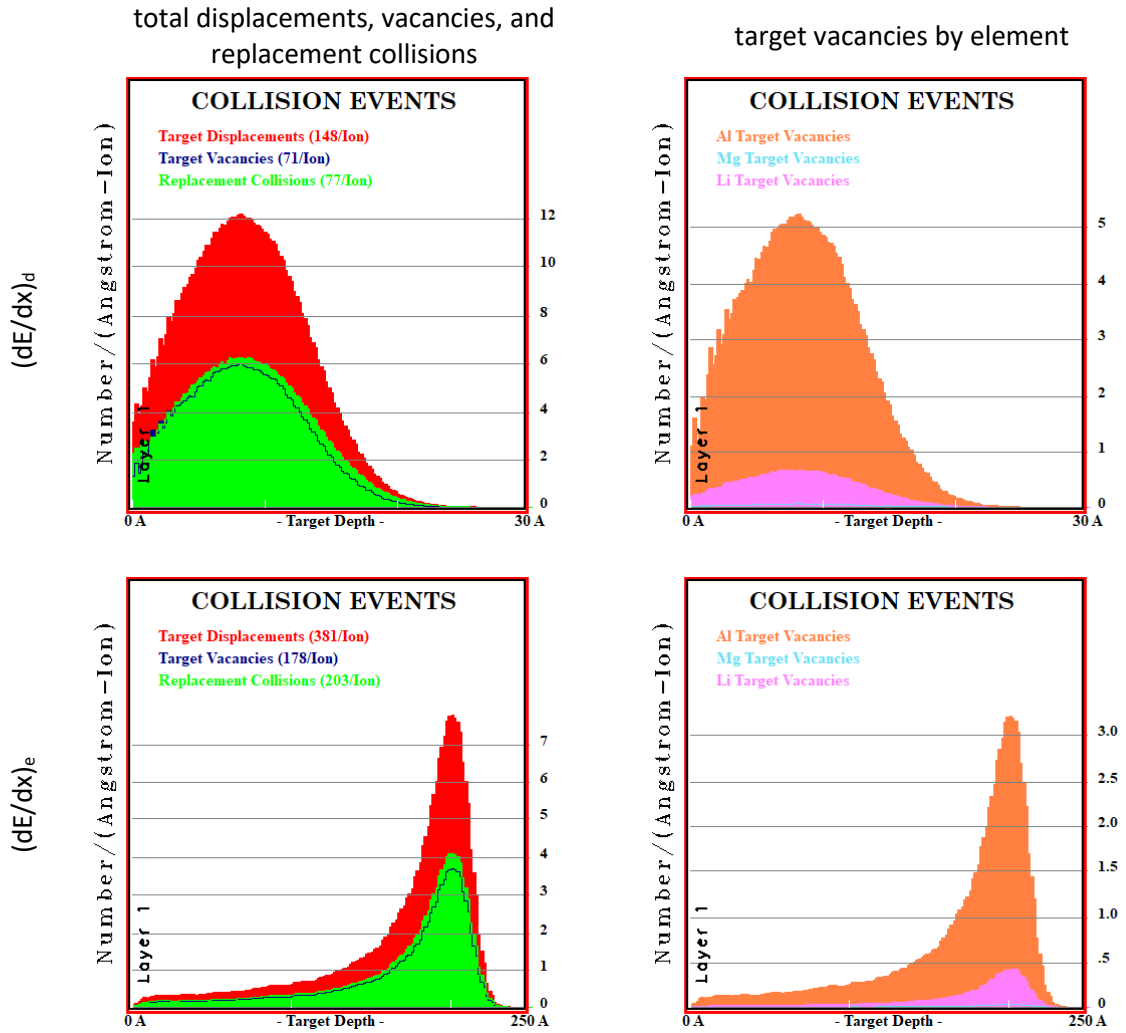
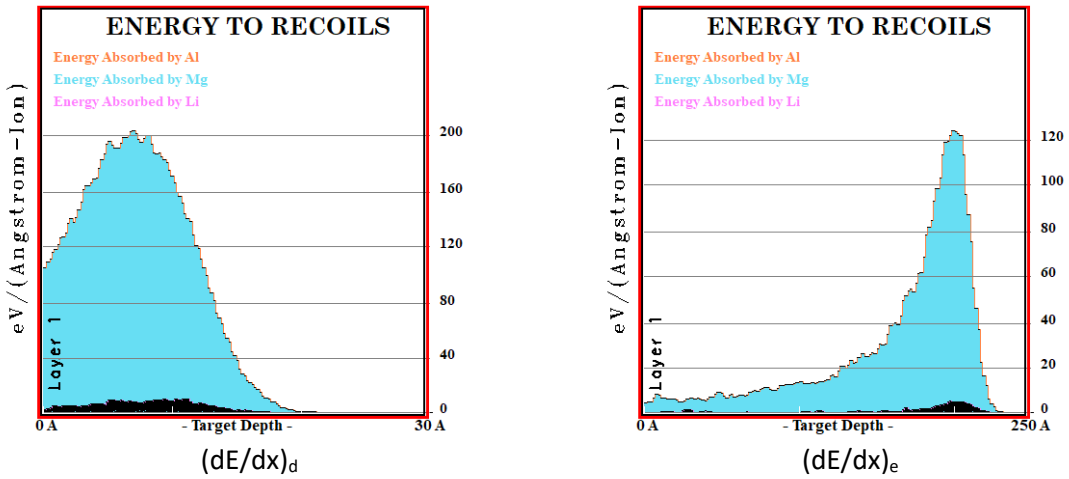


Figure 9. *TRIM simulation results illustrating a total displacements, vacancies, and replacement collisions and target vacancies by element*

To further assess the energy transferred directly to the lattice during ion collisions, the energy-to-recoil profile was analyzed (Figure 10). This diagram provides a quantitative measure of the energy responsible for atomic displacements and complements the vacancy and damage distribution results. Under the dislacement stopping condition (Figure 10, $(dE/dx)_d$), the energy recoil profile shows a sharp peak at ≈8.0 Å corresponding to concentrated displacement events near the surface. In contrast, the energy transfer profile under the electronic stopping condition (Figure 10, $(dE/dx)_e$) is flatter and significantly lower. Although the ions still penetrate to the depth of ≈200.0 Å, the amount of energy transferred directly to the target atoms is minimal. This observation complements the data on vacancy distribution (Figure 9) and supports the assumption that significant structural damage only occurs when displacement stopping interactions dominate. It is assumed that magnesium absorbs most of the recoil energy due to its average atomic mass. Figure 10 shows that for $(dE/dx)_d$, Mg atoms absorb approximately 200.0 eV per helium ion within a 1 Å-thick layer at a target depth of ≈8.0 Å, while for

$(dE/dx)_e$, Mg atoms absorb approximately 120.0 eV per helium ion within a 1 Å-thick layer at ≈200.0 Å depth.



$(dE/dx)_d$ $(dE/dx)_e$

Figure 10. *Energy transferred from He ions to the recoil atoms in the Al-Mg-Li alloy as a function of depth*

The TRIM simulation diagrams provide a comprehensive representation of helium ion interactions in the Al-Mg-Li alloy, distinguishing between displacement and electronic stopping power. Under displacement stopping, the diagrams indicate concentrated structural effects near the surface. In contrast, electronic stopping is associated with deeper ion penetration and limited atomic displacement, accompanied by low recoil energy transfer.

The TRIM results are in good agreement with the SRIM simulation, which identifies ionisation as the dominant interaction mechanism over the entire energy range. While TRIM highlights significant atomic displacements only at lower energies, its ionisation and recoil profiles agree well with the prediction of SRIM. Together, the two simulations confirm that structural damage is concentrated at low ion energies.

The results of both simulations show good agreement with the data available in the literature regarding the contribution of displacement [16] and [18] and electronic interactions [27] to microstructural evolution [28], [29] and [30]. In addition, the literature data confirm the behaviour of individual atoms, especially Al and Mg, in elastic and inelastic interactions [40].

4. Conclusions

The aim of this study was to investigate the interaction mechanisms and radiation-induced damage in the Al-Mg-Li alloy under helium ion irradiation. The simulations stopping and range of ions in matter (SRIM) and transport of ions in matter (TRIM) were used to characterise both energy loss processes and structural effects. The most important findings from the SRIM and TRIM simulations:

- The SRIM results showed that ionisation is the dominant interaction mechanism over the entire energy range of helium ions (10.0 keV - 10.0 MeV).
- It was found that the displacement stopping power dominates at low energies (up to 55.0 keV, with a maximum value of 1,088.00 keV/Å at an ion energy of 10.0 keV), leading to displacement damage near the surface.
- At higher ion energies (above 55.0 keV, reaching a Bragg peak of 33,840.0 keV/Å at 540.0 keV ion energy), electronic stopping contributes to ionisation without significant atomic displacements.
- The TRIM simulations confirmed that with displacement stopping power the displacement damage is localised and pronounced, while with electronic stopping power only minimal structural damage occurs.
- The ion range and ionisation profiles in TRIM correlate well with the SRIM predictions and confirm deeper penetration and increased ionisation at higher energies.

- The distribution of vacancies and energy transferred to the recoil atoms supports the dominance of elastic collisions in the low energy regime.
- The TRIM results indicate that magnesium absorbs the highest recoil energy, probably due to its average atomic mass and its position within the alloy.

Therefore, the simulation results indicate that the Al-Mg-Li alloy has a favourable radiation tolerance at higher ion energies where ionisation interactions are anticipated. This indicates its potential applicability in space and nuclear technology, particularly in high radiation environments where deep structural damage must be minimised.

Future research will focus on extending the current results by performing additional simulations at lower helium ion energies and by using heavier ion bombardment to extend the range of irradiation conditions. The knowledge gained from the SRIM and TRIM analyses will be used to design targeted irradiation experiments and characterise the behaviour of the alloy under different irradiation conditions. Furthermore, the results in combination with the data available in the literature will serve as a basis for a possible optimisation of the chemical composition of the alloy in order to improve its resistance to irradiation and enable its application in space and nuclear technology.

Acknowledgments

The investigation was performed within the research topic “Design and Characterization of Innovative Engineering Alloys,” Code: FPI-124-ZZB funded by the University of Zagreb within the Framework of Financial Support of Research, and Education and Infrastructural scientific projects: Center for Foundry Technology, Code: KK.01.1.1.02.0020 and VIRTULAB — Integrated Laboratory for Primary and Secondary Raw Materials, Code: KK.01.1.1.02.0022 funded by the European Regional Development Fund, Operational Programme Competitiveness and Cohesion 2014–2020.

References

[1] Kiegiel, K., Stańczyk, W.A., Ogiegło, J.M., 2025. The Future of Nuclear Energy: Key Chemical Aspects of Systems for Developing Generation III+, Generation IV, and Small Modular Reactors. Energies, 18 (3), 622.

[2] Igunma, T.O., Aderamo, A.T., Chukwuemeka, H., 2024. Advanced corrosion-resistant materials for enhanced nuclear fuel performance: A conceptual review of innovations in fuel cladding against molten salt degradation. Open Access Research Journal of Engineering and Technology, 7 (2), 56.

[3] Soni, S., 2025. Technologies for Enhancing the Safety of Next-Generation Nuclear Reactors. International Journal of Scientific Engineering and Science, 9 (3), 149–153.

[4] Bagheri, S., Khalafi, H., Bahrami, A.A., 2024. An Optimal Radiation Shield Design of a Small Modular Nuclear Power Reactor by Genetic Algorithm. Nuclear Technology, 211 (5), 940–952.

[5] Ji, Y., Hao, L., Wang, J., Han, E.H., Ke, W., 2024. Four-point method in evaluating the corrosion rate of secondary circuit structural materials in nuclear power plant. Anti-corrosion Methods and Materials, 1, (October), 82–92.

[6] Moschetti, M., Burr, P., Obbard, E., Kruzic, J.J., Hosemann, P., Gludovatz, B., 2022. Design considerations for high entropy alloys in advanced nuclear applications. Journal of Nuclear Materials, 567, 1–30, 2022.

[7] Pickering, E.J., Carruthers, A.W., Barron, P.J., Middleburgh, S.C., Armstrong, D.E.J., Gandy, A.S., 2021. High-entropy alloys for advanced nuclear applications. Entropy, 23, (1), 1–28.

[8] Féron, D., 2012. Nuclear Corrosion Science and Engineering, Woodhead publishing, Oxford.

[9] Little, E.A., 2006. Development of radiation resistant materials for advanced nuclear power plant. Journal of Materials Science and Technology, 22 (5), 491–518.

[10] Wang, D., Zhang, J., Chen, H., Wang, T., 2025. A study on in-situ characterization technology development for clearance verification of radioactive waste for nuclear decommissioning. Annals of Nuclear Energy, 211 (February) 110945.

[11] Clayton, R., Kirk, J., Banford, A., Stamford, L., 2024. A review of radioactive waste processing and disposal from a life cycle environmental perspective, Clean Technologies and Environmental Policy, 27 (2) 665–682.

[12] El Marsi, M., Elmaddahi, Z., Fechtal, I., Dezairi, A., 2022. Simulation study of stopping power and damage profiles of H/He plasma irradiation in tungsten and its alloys for fusion power plant. Journal of Radioanalytical and Nuclear Chemistry, 331 (9), 3795–3806.

[13] Nordlund, K., J. Zinkle, S., E. Sand, A., Granberg, F., Averback, R.S., Stoller, R.E., Suzudo, L., Malerba, T., Banhart, F., Weber, W.J., Willaime, F., Dudarev, S.L., Simeone,D., 2018. Primary radiation damage: A review of current understanding and models. Journal of Nuclear Materials, 512, 450–479.

[14] ASTM E521-96(2009), 2009. Standard Practice for Neutron Radiation Damage Simulation by Charged-Particle. Annual Book of ASTM Standards, 12.02, 1–21.

[15] Zinkle, S.J., Was, G.S., 2012. Materials challenges in nuclear energy. Acta Materialia, 61 (3), 735–758.

[16] Knaster, J., Moeslang, A., Muroga, T., 2016. Materials research for fusion. Nature Physics, 12 (5), 424–434.

[17] Das, S., 2019. Recent advances in characterising irradiation damage in tungsten for fusion power. SN Applied Sciences, 1 (12).

[18] Hoffelner, W., 2012. Materials for Nuclear Plants: From Safe Design to Residual Life Assessments. Springer London, London.

[19] Bruemmer, S.M., Simonen, E.P., Scott, M.P., Andresen, P.L., Was, G.S., Nelson, J.L., 1999. Radiation-induced material changes and susceptibility to intergranular failure of light-water-reactor core internals. Journal of Nuclear Materials, 274 (3), 299–314.

[20] Karpov, S.O., Azarenkov, M.O., Tolstolutska, G.D., 2024. Hardening Behavior of Nuclear Structural Materials Under Ion Irradiation,. Problems of atomic science and technology, 2024 (4), 3–19.

[21] Zinkle, S.J., Singh, B.N., 1993. Analysis of displacement damage and defect production under cascade damage conditions. Journal of Nuclear Materials, 199 (3), 173–191.

[22] Roy, A., Nandipati, G., Casella, A.M., Senor, D.J., Devanathan, R., Soulami, A., 2025. A review of displacement cascade simulations using molecular dynamics emphasizing interatomic potentials for TPBAR components. npj Materials Degradation, 9 (1).

[23] Tianzhou, Y., Huan, Y., Yingwei, W., Jing, Z., Junmei, W., Mingjun, W., Wenxi, T., Su, S. Q.,2021. Primary radiation damage characteristics in displacement cascades of FeCrAl alloys,. Journal of Nuclear Materials, 549 (June), 152909.

[24] Vladimirov, P., Bouffard, S., 2008. Displacement damage and transmutations in metals under neutron and proton irradiation. Comptes Rendus Physique, 9 (3–4), 303–322.

[25] Golovin, N.P., Lukasevich, I.B., Lopatkin, A.V., 2025. Analysis of criteria for transmutation as an effective method for removing hazardous radioactive waste. AT Energy, 137 (3) 206–213.

[26] Anderson, I.C., Andreani, C., Carpenter, J.M., Festa, G., Gorini, G., Loong, C.K., Senesi, R., 2016. Research opportunities with compact accelerator-driven neutron sources. Physics Reports, 654 (13), 1–58.

[27] Bates, D.R., Kingston, A.E., Mcwhirter, Recombination between electrons and atomic ions, I. Optically thin plasmas,. Proc. R. Soc. London. Ser. A. Math. Phys. Sci., vol. 267, no. 1330, pp. 297–312, 1962, doi: 10.1098/rspa.1962.0101.

[28] Zinkle, S.J., 2012, Comprehensive nuclear materials, Elsevier.

[29] Frydrych, K., 2023., Modelling Irradiation Effects in Metallic Materials Using the Crystal Plasticity Theory — A Review. Crystals, 13 (5) 1–20.

[30] Coarse, M.P., Zimina, M., Fedorikov, A., Harcuba, P., 2022. Influence of Neutron Irradiation on Microstructure and Mechanical Properties of Coarse- and Ultrafine-Grained Titanium Grade 2 . Materials, 12 (12) 2108.

[31] Wnuk, M.P., 2015. Toughening and instability phenomena in quantized fracture process: Euclidean and fractal cracks. Springer, Cham.

[32] Trachenko, K., 2004. Understanding resistance to amorphization by radiation damage. Journal of Physics: Condensed Matter, 16 (49).

[33] Zhang, Y., Osetsky, Y.N., Weber, W.J., 2022. Tunable Chemical Disorder in Concentrated Alloys: Defect Physics and Radiation Performance. Chemical Reviews, 122 (1) 789–829.

[34] G.S. Was, C.-B. Bahn, J. Busby, B. Cui, D. Farkas, M. Gussev, M. Rigen He, J. Hesterberg, Z. Jiao, D. Johnson, W. Kuang, M. McMurtrey, I. Robertson, A. Sinjlawi, M. Song, K. Stephenson, K. Sun, S. Swaminathan, M. Wang, E. How irradiation promotes intergranular stress corrosion crack initiation. Progress in Materials Science, 143 (February) 101255.

[35] Was, G.S., Fundamentals of Radiation Materials Science, Springer New York, New York.

[36] Chen, D., He, X., Chu, G., 2021. An overview : multiscale simulation in understanding the radiation damage accumulation of reactor materials. *SIMULATION,* 97 (10), 659–675.

[37] Kiritani, M., 1994. Microstructure evolution during irradiation. Journal of Nuclear Materials, 219 (October) 220–264.

[38] Liu, W., Ji, Y., Tan, P., Zang, H., He, C., Yun, D., Zhang, C., Yang, Z., 2016. Irradiation Induced Microstructure Evolution in Nanostructured Materials: A Review. Materials, 9 (2) 105.

[39] Antoshchenkova, E., Luneville, L., Simeone, D., Stoller, R.E., Hayoun, M., 2015. Fragmentation of displacement cascades into subcascades: A molecular dynamics study. Journal of Nuclear Materials, 458, 168–175.

[40] Kurudirek, M., 2016. Effective atomic number, energy loss and radiation damage studies in some materials commonly used in nuclear applications for heavy charged particles such as H, C, Mg, Fe, Te, Pb and U. Radiation Physics and Chemistry, 122, 15–23.

[41] Kozina, F., 2024. Solidification and characterization of aluminum-magnesium-lithium alloy. University of Zagreb, Faculty of Metallurgy, Sisak.

[42] Kozina, F., Zovko Brodarac, Z., Petrič, M., 2018. Influence of solution hardening on microstructure and mechanical properties of Al-2.5Mg-0.7Li alloy. 73rd World Foundry Congress (WFO), Krakow, Poland.

[43] Kozina, F., Zovko Brodarac, Z., Petrič, M., Šetina Batič, B., 2025. Degradation Susceptibility of Al-2.18Mg-1.92Li Alloy in Severe Environmental Conditions. Materials (Basel), 18 (9) 1–23.

[44] Kozina, F., Zovko Brodarac, Z., Petrič, M., 2016. Microstructural evaluation of Al-2.5wt.%Mg-0.7wt.%Li in as cast condition, 16th IFC, Opatija, Croatia.

[45] Kozina, F., Zovko Brodarac, Z., Brajčinović, S., Petrič, M., 2021. Determination of Al-2.18Mg-1.92Li alloy’s microstructure degradation in corrosive environment. Crystals, 11 (4), 338.

[46] Kozina, F., Zovko Brodarac, Z., Petrič, M., Penko, A., 2020. The influence of iron impurities on the compression behaviour of Al-2.24Mg-2.09Li alloy. *Journal of Mining and Metallurgy, Section B: Metallurgy*, 56 (3), 425–433.

[47] Biersack, J.P., Ziegler, J.F., 1982. Ion Implantation Techniques. Springer Series in Electrophysics, Berlin.

[48] Ziegler, J.F., 1980. Handbook of Stopping Cross-Sections of Energetic Ions in All Elements, Pergamon Pr Oxford.

[49] Yu, H.Z., 2022. Additive friction stir deposition of metallic materials: Process, structure and properties. Materials & Design, 234, 112356.

[50] Luoni, F., Weber, U., Lang, A.K., Westermayer, M., Horst, F., Baricco, M., Bocchini, L., Giraudo, M., Santin, G., Schuy, C., Durante, M., Boscolo, D., 2025. Dose build-up of high-energy ^{1}H and ^{4}He ions in standard, innovative and in situ shielding materials for space radiation: measurements and simulations. Radiation Research, 203 (3), 163–174.

Tribological and microstructural characterization of thermal-sprayed Cr-Ni-Mo coatings on stainless steel

***Jure Krolo*[1], *Aleš Nagode*[2], *Matej Kljajo*[3], *Nikša Čatipović*[1], *Damir Jurić*[1] *and Ivan Peko*[4]**

1) University of Split, Faculty of Electrical Engineering, Mechanical Engineering and Naval Architecture, 7 Ruđera Boškovića 32, 21000 Split, Croatia

2) University of Ljubljana, Faculty of Natural Sciences and Engineering, Aškerčeva 12, 1000 Ljubljana, Slovenia

3) University of Mostar, Faculty of Mechanical Engineering, Computing and Electrical Engineering, Matice Hrvatske bb, 88000 Mostar, Bosnia and Herzegovina

4) University of Split, Faculty of Science, Ruđera Boškovića 33, 21000 Split, Croatia

Corresponding author: jkrolo@fesb.hr

Original scientific article

Abstract: The main aim of this research is to determine the morphology, metallurgical appearance, and tribological behaviour of a flame-sprayed coating applied as a thermal spray technique on a stainless steel substrate. Thermal sprayed coating was based on CrNiMo powder, usually used to increase corrosion resistance, but also to reduce the friction coefficient in lubricated conditions. Due to the heterogeneously dispersed metal powder particles and residual porosity friction force was increased for thermal-sprayed specimens for used forces of 5 N, 10 N, and 15 N compared with the stainless steel substrate. 3D profilometry characterization of the tested specimens after friction testing was also performed to evaluate the actual wear that occurred on the tested specimens. It was clear that wear occurred on thermal-sprayed specimens is significantly higher, probably due to the relatively high porosity.

Keywords: *thermal spray; CrNiMo coating; friction force; metallography; 3D profilometry*

1. Introduction

Thermal spray coatings are widely employed in industrial applications to enhance surface properties such as good resistance to metallic sliding friction, lubricated wear resistance, corrosion protection, and thermal insulation. Thermal spraying is now extensively used in industrial applications to provide resistance to corrosion, both in aqueous conditions and at high temperatures, and to wear in a wide range of environments. Sometimes, the coating is exposed to simultaneous wear and corrosion (tribo-corrosion), possibly with synergistic interactions [1]. Thermal spraying is a coating process in which fine particles of metallic or non-metallic materials, in a molten or semi-molten state, are deposited, involving both mass and heat transfer. During thermal spraying, the molten or partially molten particles do not melt the substrate material upon contact but only heat the surface of the workpiece. Therefore, this process does not alter the microstructure or chemical composition of the substrate being coated. Thermal spraying offers a number of advantages, one of which is the ability to tailor the coating properties for each specific application. Additionally, a wide range of coating materials can be applied using this method. It is always important to keep in mind the goal of thermal spraying, as it must meet requirements such as adhesion, coating thickness, surface roughness, corrosion resistance, hardness, chemical composition, internal stresses, and more. Thermal spray technology helps to sustain our way of life by reducing energy consumption, providing environmental benefits, supporting human comfort, and reducing material waste. Applications already experiencing such growth include industrial gas turbines, biomedical devices, electronics and semiconductors, automotive and alternative energy (electrical generation, heating, and transportation) [2]. To ensure the thermal spraying process is as effective as possible, factors such as the condition of the workpiece, surface cleanliness, surface roughness, workpiece temperature, and others must be controlled. Among the

variety of materials used for thermal spraying, chromium-nickel-molybdenum (CrNiMo) alloys have attracted significant attention due to their excellent mechanical strength, good resistance to metallic sliding friction in lubricated conditions, corrosion protection, and suitability for operating temperature up to 450 °C [3]. When applied onto substrates like as unalloyed, low-alloy and high-alloy steels and the corresponding cast steel grades, CrNiMo coatings can significantly extend component lifespan in harsh environments, pistons and valve stems, components from chemical plants and chemical machinery [3]. Understanding the tribological performance and surface characteristics of these coatings is crucial for optimizing their application in demanding conditions such as aerospace, marine, and energy sectors. Friction behavior directly impacts energy efficiency and wear rate in mechanical systems. Therefore, comprehensive characterization—including microstructural analysis, hardness testing, and friction measurement—is essential for evaluating the coating's performance. Bolelli G. et al. (2007) studied microstructural and tribological comparison of HVOF (High-Velocity Oxygen Fuel) sprayed Co- and Ni-based coatings in as-sprayed and heat-treated conditions. As-sprayed coatings are mostly amorphous with low hardness and toughness. Heat treatment at 600 °C improves hardness and elasticity by forming fine intermetallic crystals. Wear behavior, tested by ball-on-disk against 100Cr6 steel and alumina, showed higher brittleness and crack susceptibility in Ni-based coatings. In the as-sprayed state, both coatings suffered wear loss due to low hardness and toughness, with Co-based showing more adhesive wear against steel and less abrasive wear against alumina, opposite to the Ni-based alloy. After heat treatment, wear against steel was significantly reduced for both coatings, though abrasive wear persisted against alumina [4]. Milanti A. et al. (2014) studied the microstructural details and tribological performances of Fe-based coatings (Fe-Cr-Ni-B-C and Fe-Cr-Ni-B-Mo-C) manufactured by the High Velocity Oxygen Fuel (HVOF) thermal spray process are evaluated. They found that coatings had a high density with negligible porosity and low oxide content for HVOF Fe-based coatings. Particle melting and rapid solidification resulted in a metastable austenitic phase with precipitates of mixed carbides and borides of chromium and iron which lead to remarkably high nano hardness. Tribological performances were evaluated by means of the ball-on-disk dry sliding wear test, the rubber-wheel dry particle abrasion test, and the cavitation erosion wear test. Dry sliding wear resistance of HVOF-sprayed Fe-based metal alloy coatings could not compare with that of a cermet material (WC-CoCr), their sliding wear rate was reported to be lower than that of conventional HVOF-sprayed Ni-based metal alloy coatings. Fe-based coatings showed a lower abrasion wear rate compared to a Ni-based reference coating [5]. Lin Tzu-Jing et al. (2021) studied the mechanical properties and corrosion behavior of the Fe-based amorphous alloy coatings on stainless steel substrate using high velocity oxygen fuel spraying. The coatings exhibited a mixed amorphous and amorphous/crystalline structure with micro-holes and micro-cracks visible in SEM images. The coatings demonstrated an average hardness of approximately 1024 HV. Scratch tests showed a critical load (LC2) of 46.0 N. The corrosion polarization curve shows that Fe-based amorphous alloy coating has better corrosion resistance in seawater than of in 3.5 wt% NaCl solution. The cold and hot alternating salt spray corrosion test and the high-speed water flow erosion test showed rust on the surface, but the weight loss was only 0.152 g [6]. Wood J.K.R in his study examines the tribological and corrosion behavior of thermally sprayed WC-Co-based coatings. It finds that erosion, abrasion, and sliding wear resistance are strongly influenced by microstructure, coating composition, and deposition method. Anisotropic microstructures and surface defects (voids, splat boundaries) pro. mote crack initiation during erosion. Optimizing HVOF parameters improves erosion resistance by over 50%. Slurry erosion is more angle-dependent at low energies. Abrasion resistance is comparable to sintered cermets, with wear–corrosion synergy influenced by passivation and phase removal. Sliding wear resistance is high, with wear mainly due to carbide ejection and influenced by oxides on binder phases [7]. Guo H. et al studied structural and tribological properties. of HVOF-sprayed CoMoCrSi alloy coatings before and after 800 °C-annealed treatment. A study showed that the heat treatment at 800 °C significantly improved the microstructure, mechanical, and tribological properties of HVOF-sprayed CoMoCrSi coatings. Compared to the initial state, microhardness increased by 13.3% and adhesive strength by 12.5% after annealing. A compact oxide layer (Cr_2O_3, Co_3O_4, MoO_3, and $CoMoO_4$)

formed on the surface, contributing to higher hardness and improved wear resistance. The annealed coatings exhibited lower friction coefficients and reduced wear rates across a wide temperature range, making them suitable for applications requiring high wear resistance [8]. Another study carried out by Tang L. et al. (2020) showed that enhanced mechanical and tribological properties of Co-based alloy coatings can be achieved by annealing treatment. The wear resistance of plasma-sprayed CoMoCrSi alloy coatings was enhanced more than 45 times by annealing treatment. Results show that the mechanical properties and wear resistance were significantly improved with the increment of annealing temperature, where surface analyses suggested that the good tribological properties were mainly attributed to the elimination of defects and the dense Cr_2O_3-riched lubricating film [9]. Lin C.M. et al (2016) utilized a hybrid AI approach combining the Taguchi design method, artificial neural networks (ANN), and genetic algorithms (GA) was used to optimize APS (Atmospheric Plasma Spraying) parameters for CoMoCrSi coatings on Ti-6Al-4V substrates. The Taguchi method provided an initial solution, which was further refined by ANN and GA, reducing coating porosity from 8.5% to 5.6%. The optimized coatings demonstrated low porosity, high hardness, and strong thermal stability [10]. Lanzutti A. et al. (2013) compared thermal spray coatings (NiCr, WC-CoCr, and NiCr+Cr_2O_3) and electrodeposited Ni/SiC composites with micro- and nano-sized particles. All coatings were analysed for microstructure, mechanical, and tribological properties under ball-on-disk tests at room temperature and 300 °C. WC-CoCr coatings showed the highest wear resistance due to their hard WC particles and tough CoCr matrix. Ni/nano-SiC coatings exhibited comparable wear resistance, attributed to grain refinement and nano-particle reinforcement. Wear mechanisms included tribooxidation and third-body abrasion, with thermal spray coatings more prone to material detachment due to porosity [11].

This study focuses on the analysis of the morphology, metallurgical characteristics, and tribological behavior of thermal-sprayed CrNiMo coatings applied to AISI 316 stainless steel substrates. The aim is to investigate the relationship between the coating's microstructure and its tribological behavior, providing insights into its suitability for high-performance engineering applications, but also to propose possible improvements in the technological process.

2. Experimental procedure

For thermal spray with gas flame Rototec 80 spray gun was used. Proposed parameters by the manufacturer are oxygen pressure of 4 bar and acetylene pressure of 0.7 bar to obtain an appropriate mixture. Specimens of the stainless steel AISI 316 were ground, degreased in acetone and afterwards preheated to approximately 100°C before thermal spray. Temperature was measured using a Testo 868 thermal camera. Thermal spray was performed at a distance of 200 mm in a duration of a few seconds to achieve satisfactory coating thickness. The thermal spray coating was applied in layers. The first, a base layer, consisted of a metal powder based on a NiAlMo alloy. This powder offers excellent corrosion resistance to water, weathering, and alkaline environments. It also provides high resistance to adhesion and erosion, as well as good performance under metallic sliding friction, both lubricated and unlubricated conditions. The second layer was made from a metal powder based on an austenitic CrNiMo steel. The chemical composition of the substrate and the reference specimen, and also CrNiMo coating, is given in Table 1.

Table 1. *Chemical composition of the AISI 316 stainless steel and CrNiMo coating(%wt.)*

AISI 316	**Fe%**	**Cr%**	**Ni%**	**Mo%**	**Mn%**	**Co%**	**Cu%**
	68.10	16.71	10.02	2.02	1.56	0.38	0.48
CrNiMo coating	**Fe%**	**Cr%**	**Ni%**	**Mo%**	**Mn%**	**Si%**	**W%**
	67.67	17.72	14.26	2.37	/	0.92	0.02

The second layer should exhibit good resistance to lubricated metallic sliding friction and corrosion. It is suitable for operating temperatures up to 450 °C and is machinable. The second layer were sprayed in three phases to achieve the desired thickness. Between each pass specimen temperature was

measured to approximately 100°C to prevent overheating and delamination, which was one of the main problems during the process.

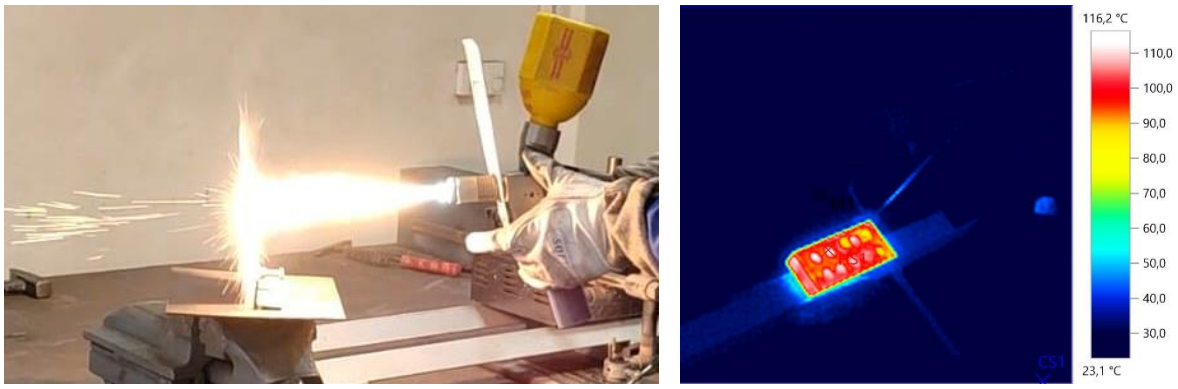


Figure 1. *a) thermal spray process b) temperature measurement*

After thermal spray for metallographic examination and friction testing, thermal-sprayed and reference specimens were mounted using Struers epoxy resin for metallographic testing. Metallographic preparation, including grinding and polishing, was carried out using a Struers Labopol-Z system. The specimens were ground using 1200 grit paper, followed by a four-stage polishing process, culminating in final polishing with 0.03 µm colloidal silica suspension. Grinding was done on thermal-sprayed specimens until a metal gloss surface appearance was achieved, however, with visible porosity. Tribology testing was performed on the instrument TRB3 pin-on-disk tribometer. The testing mode in this case was linear. Nominal load was 15 N, 10 N, and 5 N for both the reference stainless steel and thermal sprayed specimens. The stop condition for testing was 200 cycles. The system operated frequency of 1.00 Hz. The static partner was made of ruby as the substrate. It had a dimension of 6.00 mm and featured a ball-shaped geometry. Scanning electron microscopy (SEM) combined with energy-dispersive X-ray spectroscopy (EDS) was used for microstructural characterization of the coatings. The analyses were performed using a Thermo Scientific Quattro S field emission scanning electron microscope (FEG-SEM, Hillsboro, OR, USA) equipped with an Ultim Max 65 SSD EDS detector from Oxford Instruments and operated via the Aztec software platform (Abingdon, UK). The accelerating voltage during EDS analysis was set to 20 kV.

3. Results and discussion

3.1. Metallographic characterization

Figure 2 shows microstructure of coatings obtained by digital microscope. On the figure 2 the heterogeneous microstructure with different intermetallic phases is visible. Some of the metal powder retained its circular shape and the other is in a deformed state. The mostly irregular and deformed shapes of the phases indicated that the metal powder during the gas flame thermal spray process is in a soft state and that deformation and adhesion on the substrate surface are performed successfully. The sizes of different phases vary from about 10 microns to 100 microns. There is also visible microporosity, with different sizes from 100 µm up to 200 µm. Based on the microstructure observation with SEM-BSE four different microstructural phases are distinguished which are analysed with EDS.

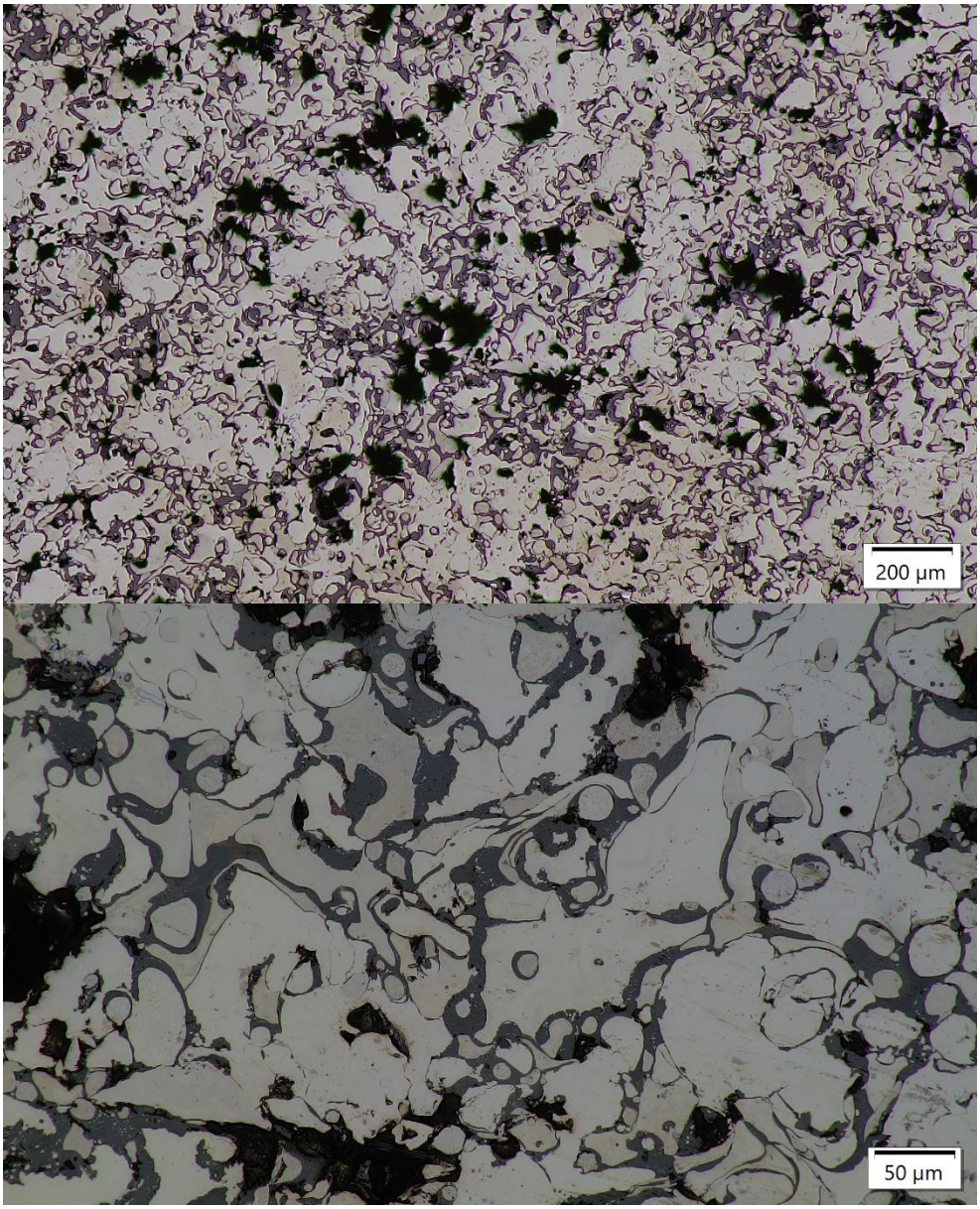


Figure 2. *Optical microscopy image of the surface appearance of the thermal sprayed specimens: a) lower magnification, b) higher magnification*

Namely, Figure 3. shows a backscattered electron image (BSE) of the microstructure of coating accompanied with sites of EDS analyses. The backscattered electron (BSE) image reveals compositional contrast based on atomic number (Z-contrast). In such images, brighter phases correspond to regions enriched with elements of higher atomic number, whereas darker areas indicate the presence of elements with lower atomic number.

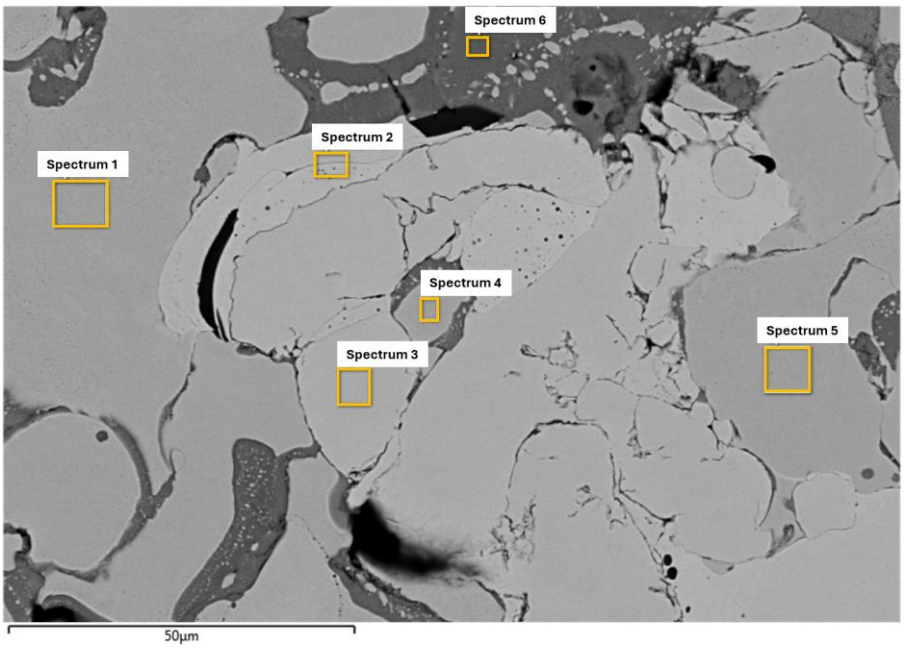


Figure 3. *SEM-BSE image of the microstructure of CrNiMo coating with selected points for EDS chemical analysis*

Figures 4 present four characteristic EDS spectra, with the corresponding chemical composition values summarized in Table 1. *According to results in Table 2, spectrum 1 corresponds to a phase consisting of 69.62 % of Fe, 8.99 %Cr, 17.79 %Ni and 3.06 %Mo. On the other hand, spectrum 2 and 3 had more than 85% Ni and 5 % of the Mo and had a white appearance on Figure 3. Somewhat darker grey phases are analysed with spectrum 4 and 5 and they indicate a similar composition to spectrum 1. Dark grey areas are analysed with spectrum 6 and it indicates that it is Cr-rich phase composed of more than 60% of Cr, 35% of Fe and 2% of Si. A more detailed analysis is given at higher magnification.*

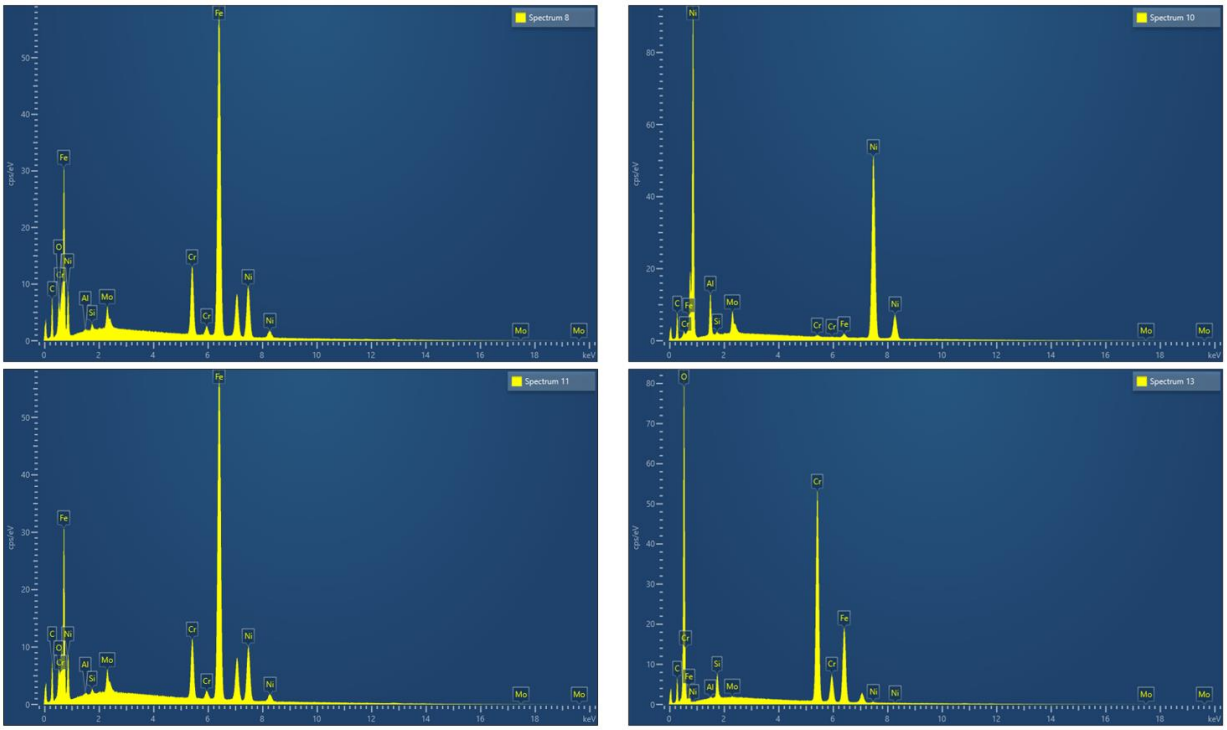


Figure 4. *EDS spectra of four different phases in the microstructure*

In table 2 are the results of the EDS chemical analysis for selected areas. According to the results, there is a quite significant heterogeneous structure of the thermal sprayed coating with three characteristic appearances at given magnification.

Table 2. *Chemical composition analysis for different material phases*

Spectrum Label	***Spectrum 1***	***Spectrum 2***	***Spectrum 3***	***Spectrum 4***	***Spectrum 5***	***Spectrum 6***
Al	0.12	2.17	6.14	0.12	0.13	0.15
Si	0.42	0.29	0.27	0.31	0.46	2.81
Cr	8.99	0.58	0.33	7.73	10.46	60.56
Fe	69.62	1.13	0.93	69.69	69.44	35.67
Ni	17.79	89.74	86.88	18.92	16.44	0.55
Mo	3.06	6.08	5.46	3.23	3.06	0.26
Total	100.00	100.00	100.00	100.00	100.00	100.00

Figure 5 shows a section of the coating microstructure along with EDS maps illustrating the elemental distribution across the analysed area. In the figure, there are quite clearly distinguished heterogeneous chemical compositions and morphologies of the thermal-sprayed layer and their distribution. EDS mapping revealed overlapping signals of Cr and O, as well as Cr, Si, and O, indicating the formation of chromium oxide (Cr_2O_3) and mixed Cr–Si oxides, most likely in the form of Cr_2O_3 and SiO_2 or their composite structures. Formation of Cr_2O_3 is responsible for corrosion resistance, among others.

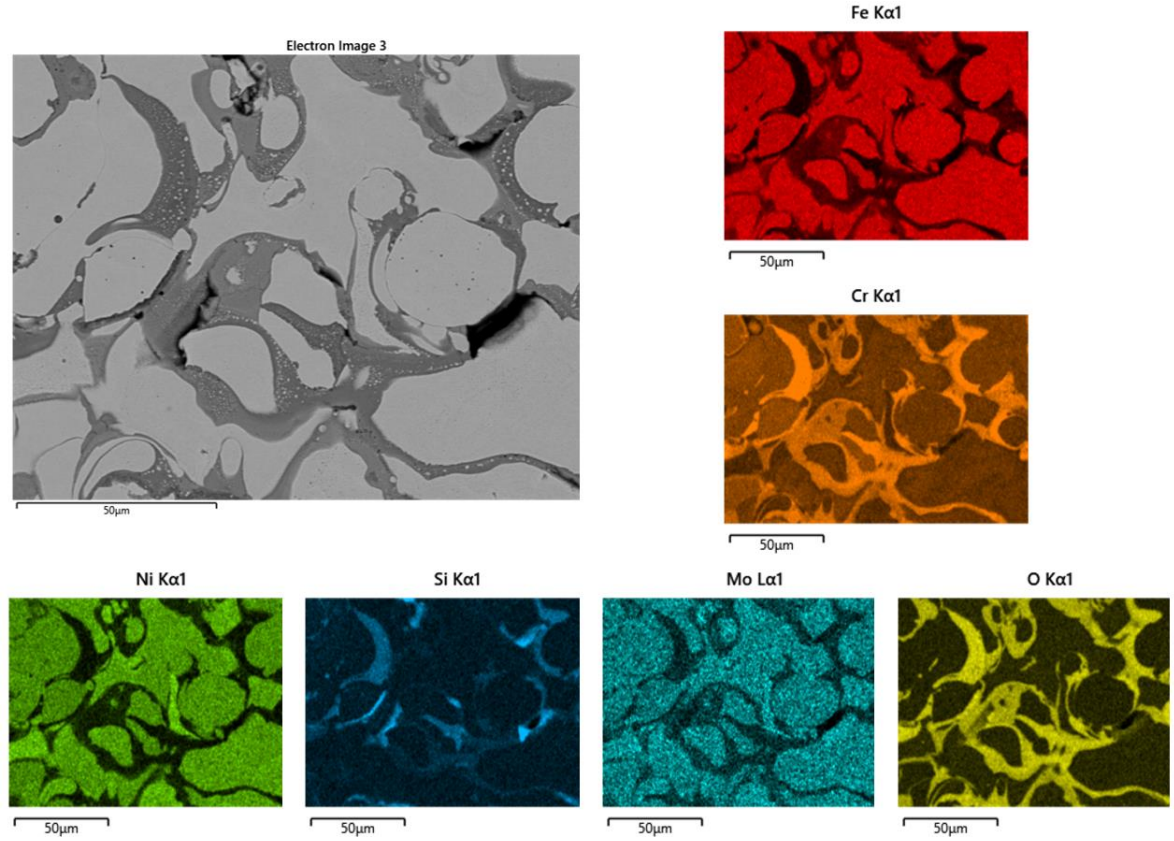


Figure 5. *SEM-BEI with EDS elemental maps*

The figure 6 shows a detail of the microstructure with Cr_2O_3 and Cr_2O_3/SiO_2 at higher magnification, accompanied by EDS maps indicating the elemental distribution. Within these oxide regions, rounded Fe-rich particles were observed, indicating the presence of iron-based inclusions embedded in the oxide matrix. The spherical Fe-rich particles observed within the oxide matrix likely originated from incomplete oxidation of the feedstock particles during thermal spraying. High processing temperatures and exposure to air promote surface oxidation, primarily of Cr and Si, due to their higher

affinity for oxygen compared to Fe. This preferential oxidation is thermodynamically driven by the lower Gibbs free energy of formation of Cr and Si oxides relative to iron oxides. As a result, the inner regions of some particles remained Fe-rich and were subsequently encapsulated within the growing Cr–Si–O oxide structures during rapid solidification. Light grey appearance, FeNiMo phases are formed around dark grey FeCrSi phases, which are also reacted with oxygen. FeCrSi-type phases are known for their high hardness, which makes them effective at resisting micro-cutting and abrasive wear. These hard phases act as reinforcements, making them particularly beneficial in abrasive or erosive environments. Phases such as Cr_2O_3, SiO_2, $FeCr_2O_4$, or FeCrSi are chemically stable and hard, contributing to improved wear resistance, especially under high-temperature or corrosive conditions. On the other hand, FeCrSi intermetallic and oxides, while hard, are often very brittle. If these phases are large or poorly bonded to the surrounding matrix, they may crack or spall under mechanical stress or impact, potentially reducing wear resistance in those regions. A lack of strong bonding between hard phases and the softer metal matrix can result in phase pull-out, microcracking, or interfacial wear, ultimately degrading the coating’s overall wear resistance.

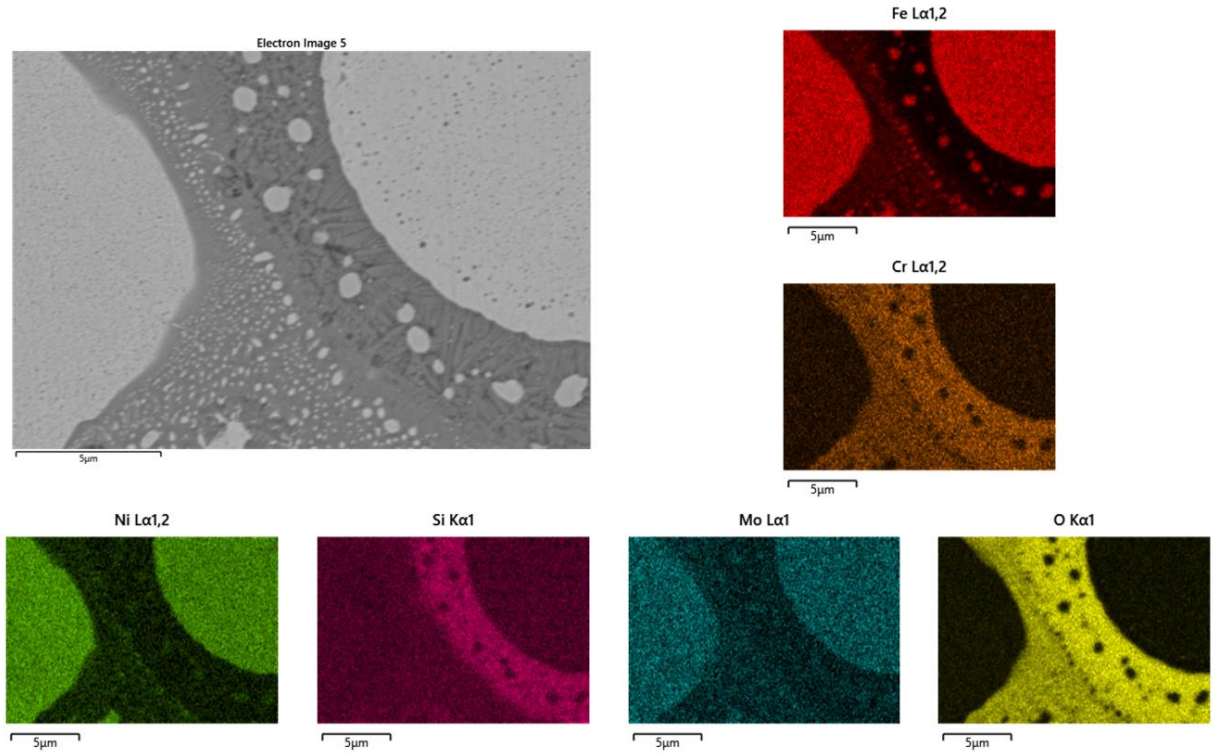


Figure 6. *SEM-BEI with EDS elemental maps*

3.2. Pin-on-disk testing

Figure 7 shows the friction force measurement for three different normal loads and both the reference stainless steel specimen and the thermal-sprayed specimens. It is visible that there is a significant reduction in friction force with a reduction of normal load from 15 N to 10 N and finally 5 N. It is visible that for reference specimens, values of the friction forces are reduced compared with thermal-sprayed specimens for all loads. In the next section, 3D topography analysis of the material wear is performed and analysed.

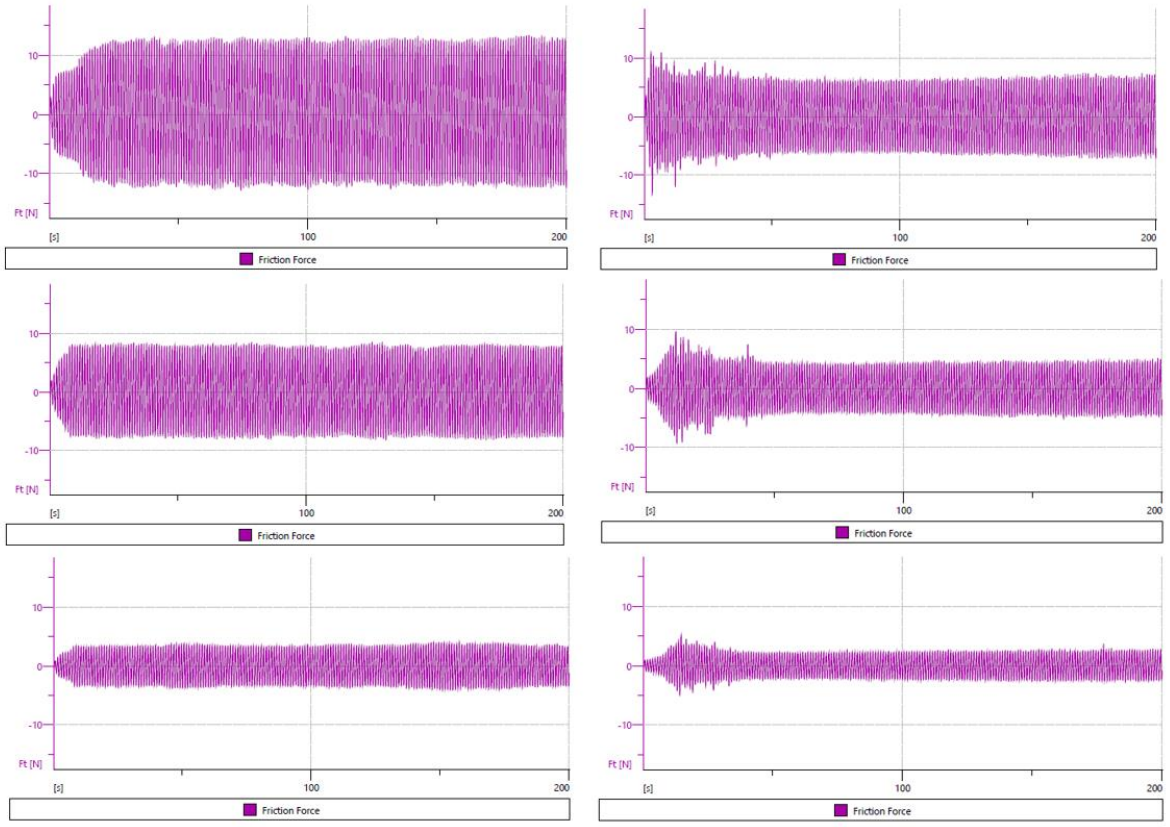


Figure 7. *Friction force testing results on TRB3 pin-on-disk tribometer: a) thermal sprayed specimen, b) reference specimen (for figure from top to bottom, normal loads used are 15 N, 10 N, and 5 N)*

3.3. 3D profilometry analysis

In this section analysis of the 3D topography of the tested samples is performed utilizing white light interferometry 3D profilometer. Figure 8. Shows significantly different wear depth after pin-on-disk testing for 5 N and for: a) reference specimens of the stainless steel and b) thermal sprayed specimens. Despite similar chemical composition, wear depth for thermal-sprayed specimens is about 32 microns, while for reference, stainless steel is only about 5 microns. The width of the testing groove for the stainless steel specimen was about 400 microns, and for the thermal sprayed specimen, about 780 microns, which indicated a significantly higher wear rate.

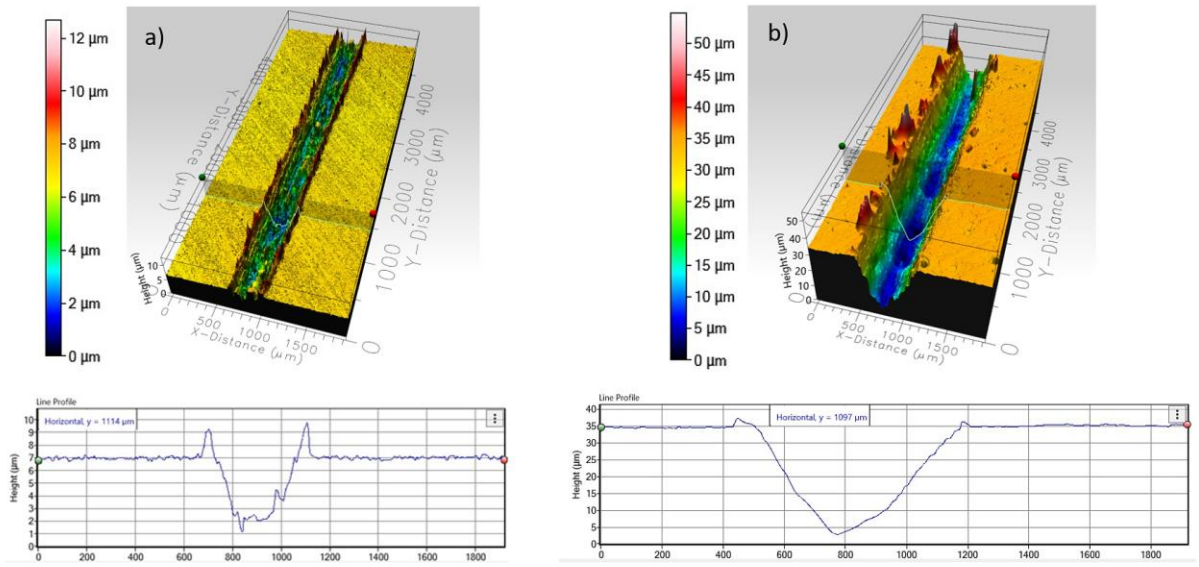


Figure 8. *3D profilometry stitched scan for 5 N testing on TRB3 pin-on-disk tribometer: a) reference specimen, b) thermal sprayed specimen*

Figure 9 shows 3D topography and wear width and depth after pin-on-disk testing for 10 N normal load and for: a) reference specimens of the stainless steel and b) thermal sprayed specimens. Normal load increased wear depth and width for reference specimens to approximately 8-10 microns and 500 microns, respectively. However, for thermal-sprayed specimens, wear depth and width were approximately 70 microns and 1200 microns, respectively. This suggests that thermal-sprayed coating, due to the heterogeneous and porous microstructure, is significantly influenced by the normal load increment, with significantly less tribological resistance to dry lubrication pin-on-disk wear testing.

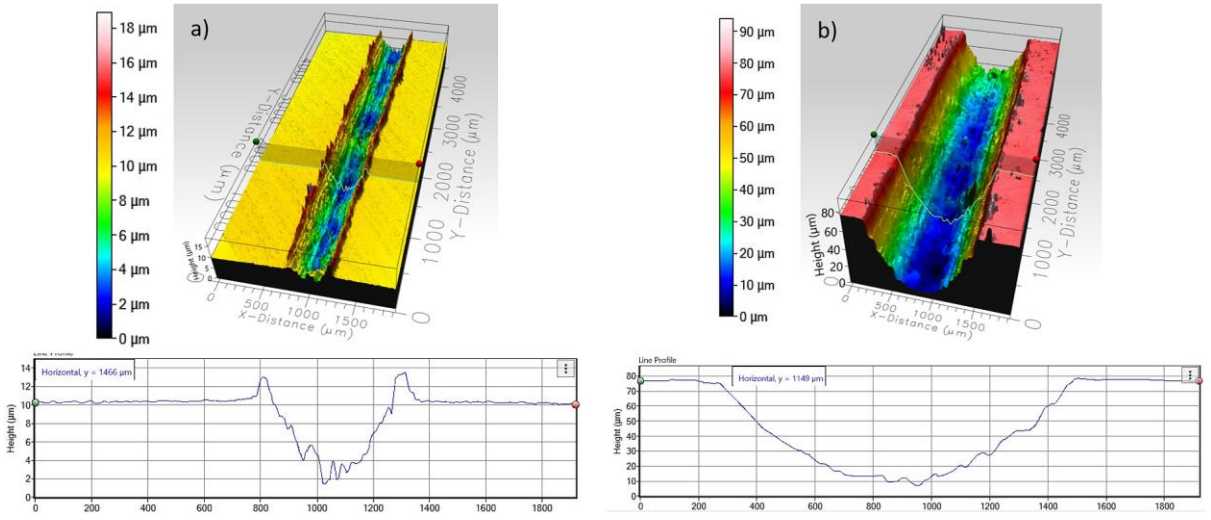


Figure 9. *3D profilometry stitched scan for 10 N testing on TRB3 pin-on-disk tribometer: a) reference specimen, b) thermal sprayed specimen*

Finally, Figure 10 shows 3D topography and wear width and depth after pin-on-disk testing for 15 N normal load and for: a) reference specimens of the stainless steel and b) thermal sprayed specimens. Normal load once again increased wear depth for reference specimens to approximately 600 microns. However, wear depth remained similar to that with a 10 N load. For thermal-sprayed specimens, wear depth and width remained similar to those for a 10 N normal load.

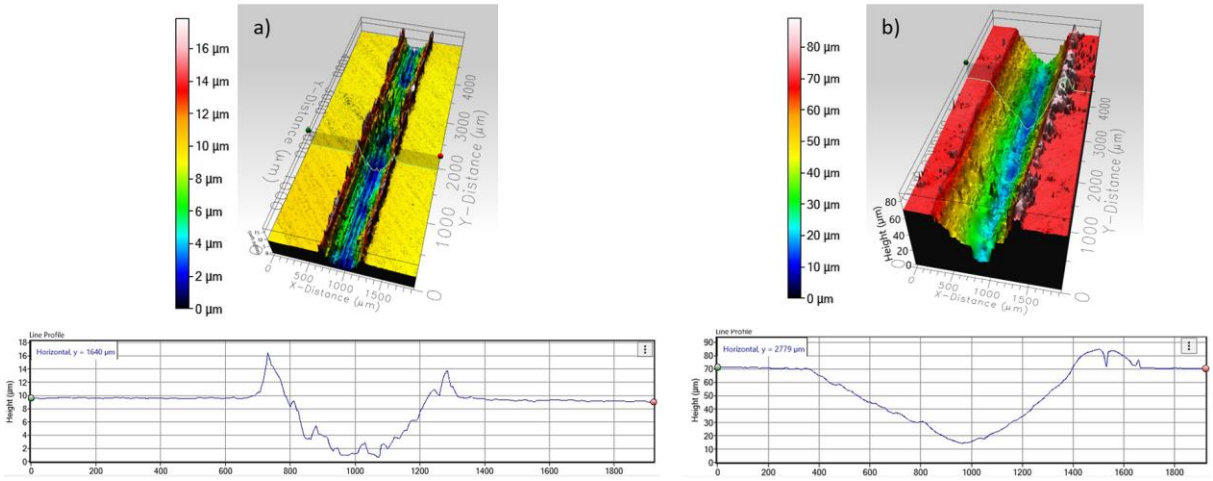


Figure 10. *3D profilometry stitched scan for 15 N testing on TRB3 pin-on-disk tribometer: a) reference specimen, b) thermal sprayed specimen*

3D topography analysis and wear depth and width analysis are shown in Figures 8 to 10 clearly indicating that wear tracks are significantly bigger for thermal-sprayed specimens compared to reference stainless steel specimens. Normal load during test increment for 5 N to 10 N had a bigger impact on wear depth and width changes than normal load increment from 10 N to 15 N, for both types of specimens.

4. Conclusions

According to the microstructural analysis presented in this study, the CrNiMo coating produced by thermal spraying with a gas flame gun and metal powder exhibits a heterogeneous and porous microstructure. This significantly affects its tribological behavior, as the friction force observed for the thermal-sprayed specimens was notably higher than that of the reference stainless steel specimens. Increasing the applied normal load from 5 N to 10 N and 15 N resulted in a corresponding increase in friction force for both specimen types.

Furthermore, 3D profilometry analysis of the wear tracks after pin-on-disk linear testing revealed that the thermal-sprayed specimens experienced considerably more wear than the reference specimens. For the stainless steel specimens, the depth of the wear tracks ranged from 5 µm to 10 µm as the load increased, while for the thermal-sprayed specimens, the depth increased from 30 µm to as much as 60–70 µm. Similarly, the width of the wear tracks ranged from 400 µm to 600 µm for the stainless steel and from 780 µm up to 1200 µm for the thermal-sprayed specimens, depending on the applied load. In conclusion, the thermal-sprayed coatings exhibited significantly higher wear compared to the stainless steel substrate, probably due to their heterogeneous and porous microstructure.

These findings underscore the critical importance of minimizing porosity within thermal-sprayed coatings and quality process implementation to enhance their wear resistance. Porosity, combined with the presence of brittle Cr_2O_3 and SiO_2 oxide phases, serves as a preferential site for crack initiation and spallation under mechanical loading, thereby compromising the coating’s tribological performance. To address these limitations, post-deposition treatments such as controlled heat treatments can be employed to densify the coating microstructure and induce the formation of stable oxide phases that contribute to improved wear resistance, albeit with a potential trade-off in corrosion resistance. Alternatively, the utilization of advanced thermal spray techniques, including High-Velocity Oxy-Fuel (HVOF) and plasma spraying, offers a viable pathway to achieve coatings with enhanced structural cohesion, reduced porosity, and superior tribological properties, thereby extending their service life under demanding operational conditions.

References

[1] Roy, M., Davim, J.P., 2015, Thermal Sprayed Coatings and their Tribological Performances. IGI Global.

[2] Tucker, R.C. et al., 2013, Thermal Spray Technology. ASM International.

[3] Website: ‘https://doi.org/10.1016/j.triboint.2020.106265’., acessed 04.07.2025.

[4] Bolelli, G. et al., 2007, Microstructural and tribological comparison of HVOF-sprayed and post-treated M-Mo-Cr-Si (M = Co, Ni) alloy coatings. Wear, 263 (7-12 SPEC. ISS.), p. 1397–1416.

[5] Milanti, A. et al., 2014, Microstructural characteristics and tribological behavior of HVOF-sprayed novel Fe-based alloy coatings. Coatings, 4 (1), p. 98–120.

[6] Lin, T.J. et al., 2021, The study of mechanical properties and corrosion behavior of the Fe-based amorphous alloy coatings using high velocity oxygen fuel spraying. Journal of Alloys and Compounds, 867, p. 159132.

[7] Wood, R.J.K., 2010, Tribology of thermal sprayed WC-Co coatings. International Journal of Refractory Metals and Hard Materials, 28 (1), p. 82–94.

[8] Guo, H. et al., 2022, Microstructures, mechanical properties and tribological behaviors of HVOF-sprayed CoMoCrSi alloy coatings before and after 800 °C-annealed treatment. Journal of Alloys and Compounds, 909 (July), p. 2022–2024.

[9] Tang, L. et al., 2020, Significantly enhanced mechanical and tribological properties of Co-based alloy coatings by annealing treatment. Tribology International, 146 (February), p. 106265.

[10] Lin, C.M. et al., 2016, Measurement and optimization of atmospheric plasma sprayed CoMoCrSi coatings parameters on Ti-6Al-4V substrates affecting microstructural and properties using hybrid abductor induction mechanism. Measurement: Journal of the International Measurement Confederation, 94, p. 157–167.

[11] Lanzutti, A. et al., 2013, Tribological behavior of thermal spray coatings, deposited by HVOF and APS techniques, and composite electrodeposits Ni/SiC at both room temperature and 300 °C. Tribology in Industry, 35 (2), p. 113–122.

Integration of agile methods and Lean Six Sigma approach in improving the quality of manufacturing processes

***Elvis Krulčić*[1], *Sandro Dobovičeк*[1], *Duško Pavletić*[1] *and Goran Cukor*[1]**

1) University of Rijeka – Faculty of Engineering, Vukovarska 58, 51000 Rijeka, Croatia

Corresponding author: elvis.krulcic@uniri.hr

Professional article

Abstract: Managing complex manufacturing systems requires a structured yet flexible approach to continuously improve quality and efficiency. This paper explores the integration of agile methods, in particular Scrum and Kanban, into a hybrid project management framework that combines the strengths of traditional (waterfall) approaches with the adaptability of agile practises. In addition, the Lean Six Sigma methodology is incorporated as a systematic framework for identifying and eliminating process deviations, waste and variation to achieve high levels of process stability and product quality. The focus is on managing projects where objectives are not fully defined at the outset and require iterative planning and execution. The combination of agile practises and Six Sigma tools such as the DMAIC cycle, cause-and-effect analysis and statistical process control enables greater transparency of workflows, faster detection of process deviations and more effective implementation of corrective actions. A case study from the automotive industry illustrates how this integrated approach can lead to measurable improvements in product quality and production efficiency, while reducing waste and improving operational excellence.

Keywords: *agile methods; Scrum; Kanban; Six Sigma; DMAIC; LSS; quality improvement; project management; continuous improvement*

1. Introduction

Industrial companies today are faced with increasingly demanding customer requirements on the one hand and rapid global changes on the other, leading to significant fluctuations in production volumes and delivery times. To successfully meet these challenges, companies must align their processes and organisational structures to accelerate all business activities. This process requires fast and adaptive decision making in operations, that must simultaneously meet market and customer demands and improve production processes to reduce total cost of ownership. Modern industrial organisations are increasingly integrating established improvement methodologies into their business processes, such as Six Sigma (SS) and Lean Production (LP), and in many cases a combined approach known as Lean Six Sigma (LSS) [1]. These methods are comprehensive and strategic initiatives that lead to significant long-term improvements in industrial processes. Given the dynamic and rapidly changing global market environment, it is necessary to accelerate these improvement processes. For timely and effective decision-making, it is essential to integrate elements of agile methods into business processes. The integration of agile frameworks such as Scrum and Kanban into an already established LSS environment can lead to similar or even equivalent improvements in a much shorter time frame [2]. This article deals with the integration of well-known agile methods into existing quality improvement programmes in the context of industrial production of automotive components.

2. Main features of LSS and agile methods in industrial practise

2.1. LSS methodology

Lean Six Sigma (LSS) is an integrated methodology for continuous process improvement that combines the principles of Lean Production (LP) and the statistical quality control of Six Sigma (SS). In industry, LSS is used to achieve optimum efficiency, reduce waste, minimise process variability and significantly

improve the quality of products or services. The main characteristics of LSS in industry include: a strong focus on eliminating waste, reducing process variability, customer orientation, the use of structured methods, interdisciplinary teamwork, management support and a culture of continuous improvement. Typical results of implementing LSS in industry are higher productivity and profitability, lower operating costs and lead times, higher customer satisfaction and a reduction in defects and complaints [3], [4]. The use of LSS as a method of continuous improvement has also become established in various service sectors, such as healthcare and education [5].

Despite the proven effectiveness of LSS in increasing productivity, quality and operational performance, its implementation is not without its challenges. The implementation of the LSS methodology requires significant organisational resources, including time, financial investment and qualified personnel. The complexity of the methodology, especially the use of statistical tools and the DMAIC structure, is often an obstacle for small and medium-sized enterprises [1]. In dynamic industrial environments characterised by rapid technological change and changing market demands, the rigidity of the LSS framework can further limit its effectiveness. Standardised approaches and long analysis cycles are often not flexible enough to meet the requirements of modern business environments [6].

2.2. Agile methods

Agile methods, originally developed in the context of software development, are increasingly used in industrial and organisational systems that strive for continuous improvement. Their main strength lies in their iterative approach, rapid feedback cycles and ability to respond quickly to change. Thanks to this flexibility, organisations can better adapt to changes in the environment and to changing customer requirements, thereby increasing their efficiency and innovative strength [7]. The benefits of agile methods in the context of continuous improvement include increased transparency, more frequent communication within the team, faster problem identification and greater involvement of end users. This approach usually leads to higher product quality, better customer satisfaction, better project control, lower risk, greater team member commitment and better project predictability [8].

However, agile methods are not without their challenges. Potential disadvantages of agile project management include poor resource management, minimal and inaccurate documentation, the development of overly complex products, unclear definitions of project completion and difficulties in measuring outcomes [8]. In complex production environments or highly regulated environments where stability and predictability are critical, agile approaches can lead to inconsistencies and integration issues. In addition, the lack of formal documentation and reliance on team dynamics can hinder long-term knowledge management and process scalability [9]. The introduction of agile approaches also requires a change in organisational culture, which is often met with resistance and a lack of understanding in traditional structures. Therefore, the successful application of agile methods in continuous improvement initiatives requires careful adaptation to the organisational context, supported by a clear strategy and commitment from all levels of management. The most commonly used agile methods in industrial practise are Scrum and Kanban.

2.2.1. Scrum method

With Scrum, project activities are restarted at regular intervals. It is based on the premise that a complete project plan cannot be fully known in advance. Instead, the project is developed, planned and iterated step by step [10]. Scrum is one of the most commonly used agile methods and is based on the concept of Sprints. Sprints are time-limited events with a fixed duration, usually lasting up to one month or less. The widespread use of Scrum can be attributed to the simplicity of its principles and the flexibility of its application to different project types and in different organisational contexts. According to Schwaber and Sutherland, Scrum comprises important artefacts that can be divided into three main groups, which represent the core components of the methodology:

- the Product Backlog (a comprehensive list of all tasks and activities to be completed),
- the Sprint Backlog (a selection of user stories, tasks and corrections to be realised during a particular Sprint), and
- the Increment (a usable and potentially deliverable product or result) [11].

Scrum uses cross-functional teams made up of experts who collectively have all the skills and knowledge required to fulfil the defined tasks. The Scrum execution, steps shown in Figure 1, consist of five main activities: the initial planning meeting, the Sprint planning, the actual Sprint, the daily Scrum and the Sprint review and Retrospective. Each new Sprint begins immediately after the end of the previous Sprint, and it is recommended that all Sprints have a consistent duration throughout the product development cycle. Within each Sprint, all tasks and events necessary to achieve the Sprint goal are carried out.

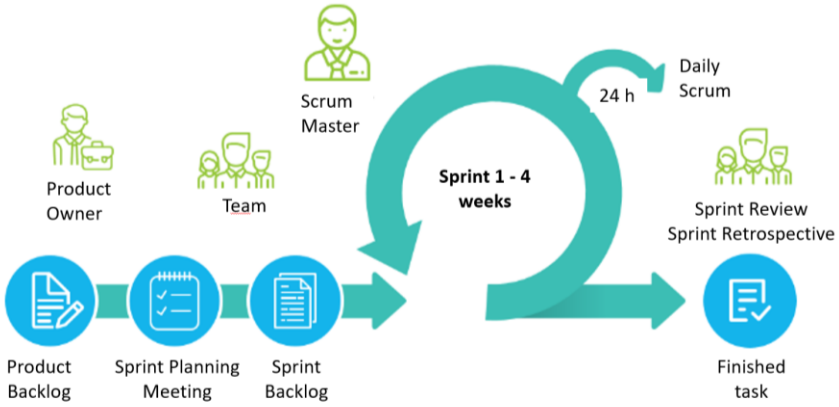


Figure 1. *Steps of Scrum execution*

2.2.2. Kanban method

The term Kanban originally comes from Japan and is closely associated with the concept of just-in-time production (JIT). In practise, Kanban is usually implemented using a visual board, the Kanban board, which is divided into columns representing the different phases of a workflow or project. An example of a Kanban board can be found in Figure 2. The Kanban method emphasises communication and transparency so that all team members are constantly informed about the current development phase and the project status can be tracked in real time. It is primarily focussed on the skills of the team and is particularly suitable for processes with small, incremental changes.

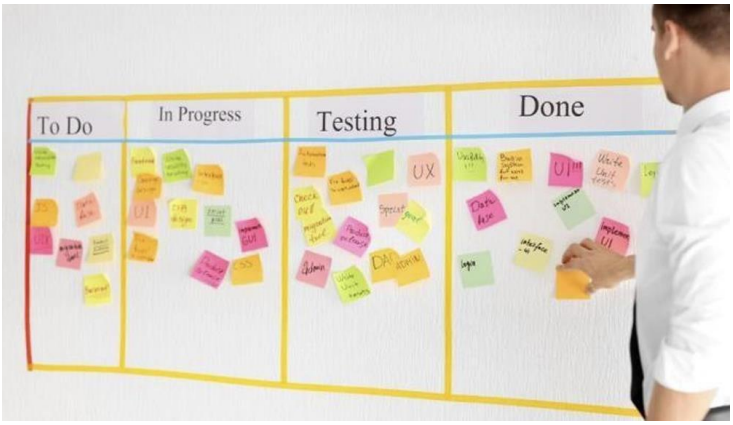


Figure 2. *Practical example of a Kanban board in industrial production [1]*

Unlike prescriptive frameworks, Kanban does not prescribe a specific process or structure. Similar to Scrum, it promotes self-organisation through a pull-based workflow — each team member "pulls" tasks when they are ready to take them on. Kanban is based on four basic principles and six core practises [12]. Work tasks are visualised as cards on a Kanban board, often organised in columns that reflect different stages of the process. A typical Kanban board contains the following columns: To Do, In progress, Developed, Testing (checking), and Done. The board can also be expanded to include additional sections such as Ideas, Backlog, Specifications, Integration or Delivery. This visual representation improves transparency by showing the flow of work while increasing team

accountability. Once one task is completed, the team can move on to the next, ensuring a continuous and flexible workflow. This development process provides planning flexibility, clear goals and real-time visibility of task progress, supporting continuous improvement in project delivery.

3. Integration of agile methods into existing quality improvement projects

An existing improvement programme called Factory Performance Improvement (FPI) was introduced in the investigated automotive parts manufacturing plant, specifically for the machining of castings. This programme was designed as a long-term and comprehensive initiative to increase competitiveness. The FPI programme is based on Lean Six Sigma (LSS) and applies the well-known Six Sigma DMAIC approach [14] to achieve improvements in two key performance indicators (KPIs). However, no sufficiently rapid progress was achieved. The targeted KPIs were Overall Equipment Effectiveness (OEE) and overall quality levels, the latter including customer complaints and internal defect rates. While OEE can be seen as an internal metric that allows for a certain tolerance in the speed of improvement, the quality indicators have a direct impact on customer satisfaction – compromise is not an option here. An initiative was therefore launched to accelerate improvement activities by incorporating agile methods to achieve faster results. Elements of agile project management were added to the existing FPI programme, including new roles and organisational changes, as described in a previous paper by the authors [2].
The standard schedule for the introduction of Scrum and the improvement team Sprints within the FPI is shown in Figure 3.

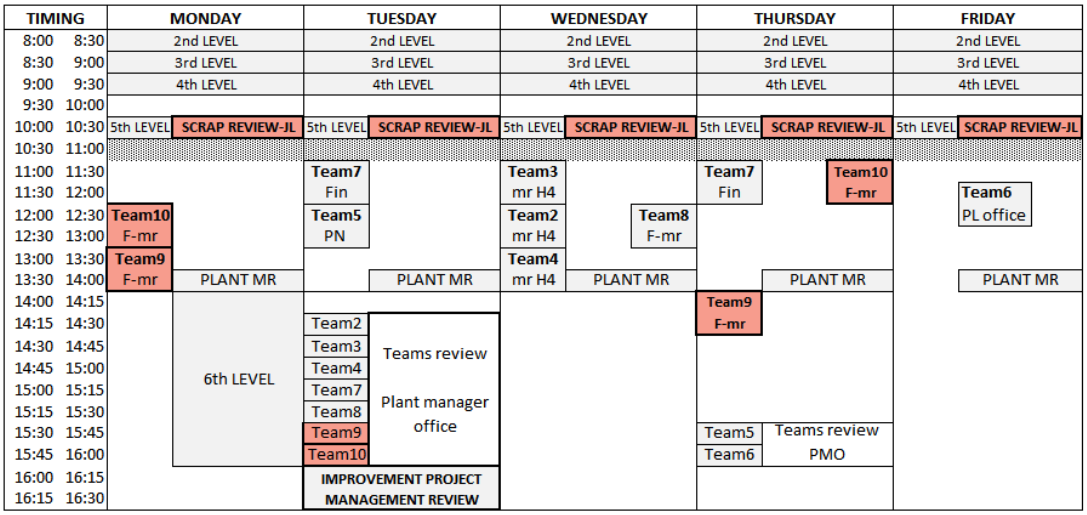


Figure 3. *Standard schedule for daily stand-up meetings and Scrum improvement projects results overview [1]*

The Sprint review includes weekly and monthly KPI reports on: Machining and casting scrap trends (measured in ppm — parts per million), Pareto charts on defects, ppm per customer and supplier, status of corrective actions related to complaints and results of internal product and process audits. The members of Team 9 and Team 10 meet weekly to review and update the status of existing tasks and to define new work tasks. These meetings are limited to a maximum duration of 45 minutes. In addition, the plant manager, together with the team leaders, conducts a weekly meeting to monitor the progress of the improvement programme and to identify and eliminate potential bottlenecks that could hinder the timely implementation of the planned improvement activities. This meeting usually lasts 15 minutes. Daily stand-up meetings are a combination of Daily Scrum and Kanban practises where the quality results of the previous working day are reviewed. Various quality indicators are analysed on several levels, including

- Machining and casting scrap (ppm),
- Customer complaints,
- Supplier complaints,

– Results of 100% inspections,
– and escalation of significant deviations.

These meetings take place in a specific production area equipped with Kanban boards and standardised forms to track quality indicators, (Figure 4). Each meeting lasts up to 30 minutes and includes review of performance results, identification of issues and coordination of team composition, location and follow-up schedule to resolve identified issues.

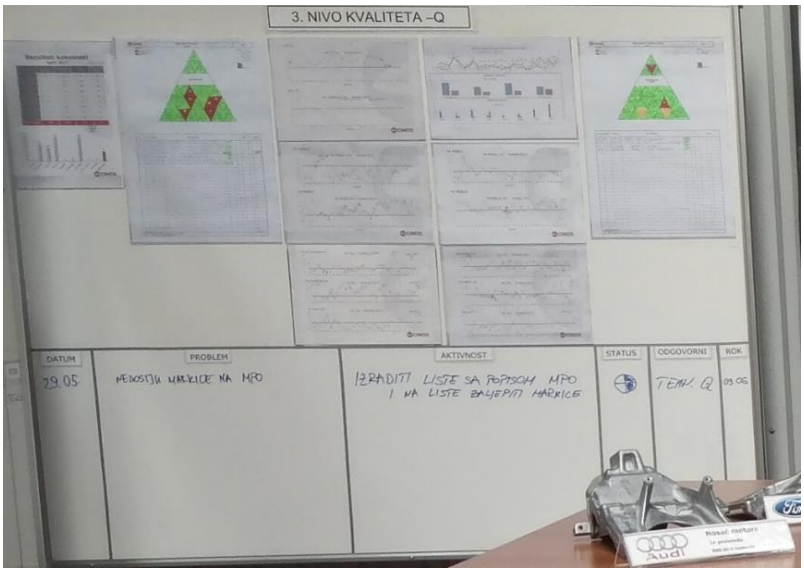


Figure 4. *Kanban board for monitoring quality indicators during production stand-up meetings*

As the planned results for quality improvement in die casting production (HPDC) could not be achieved, additional measures were introduced for this production area. The original Team 1, which was responsible for improving the quality of the 10 lowest-performing products, was reorganised into Teams 9 and 10, each of which received additional resources. The frequency of weekly Scrum reviews was increased from once a week to twice a week. An external HPDC expert was hired to define and monitor technical improvements within the HPDC process with the aim of improving quality. Internal quality control was introduced during the machining phase of the castings. In cases where non-conforming castings were detected, internal complaints were addressed to the foundry. In addition, radiographers (RTG) were assigned to each production shift in the HPDC process with the task of checking the structural integrity of the castings from each production batch. A typical HPDC casting cell and the RTG device used to check the integrity of the castings are shown in Figure 5.



Figure 5. *View of the HPDC casting cell and the X-ray machine with CT unit*

This approach enables the monitoring of die casting parameters that affect the quality of the castings and supports preventative measures — if deviations are detected, the casting process is stopped

immediately. Production is only resumed once corrections have been made to the die-casting parameters and the integrity of the castings has been reconfirmed.
This significant organisational change to quality control within the HPDC production process has resulted in a measurable reduction in defective products, particularly those affected by unacceptable porosity on machined surfaces.

4. Achieved improvement result

The consistent application of the agile approach as part of the existing Factory Performance Improvement (FPI) programme led to the expected improvement results for all planned activities. Figure 6 illustrates a strong positive trend and the achievement of the target in the reduction of customer complaints, with the number of complaints falling significantly within one year.
The main contribution to this result can be seen in the reduction of defective products in the die-casting process (HPDC), which significantly reduced the risk of defective parts occurring in the subsequent machining process. This improvement was achieved by introducing additional monitoring of the quality of the structural integrity of the casting within the HPDC process. In the event of deviations, the process was halted and production only resumed once the quality of the castings had been confirmed.

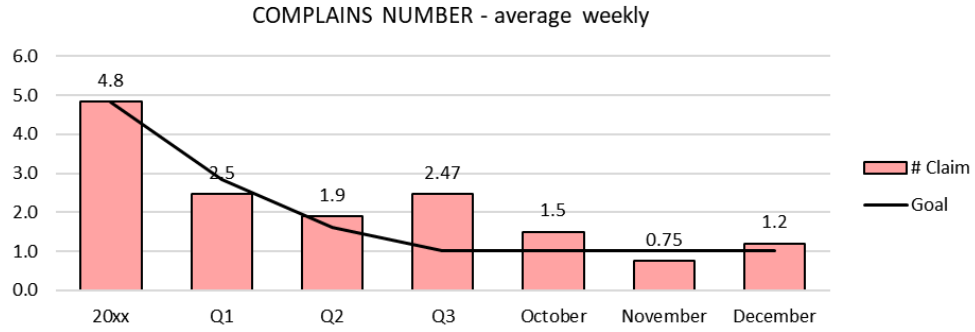


Figure 6. *Overview of Customer complaint trends*

A second important contribution was made by additional regular training sessions, in which important data on customer complaints — such as their consequences and associated costs — were communicated to improve the effectiveness of quality control for all employees involved in HPDC production and machining of castings.
The overview of the overall trends in non-compliance shown in Figure 7 does not show the desired continuous progress in improving results, apart from the initial increase in performance improvement. The reason for this is the significant impact of a large number of process series of new products with a high proportion of non-compliant parts. To ensure an objective measurement of FPI results, additional monitoring of non-conformance trends has been introduced for the selected TOP10 items to be improved.

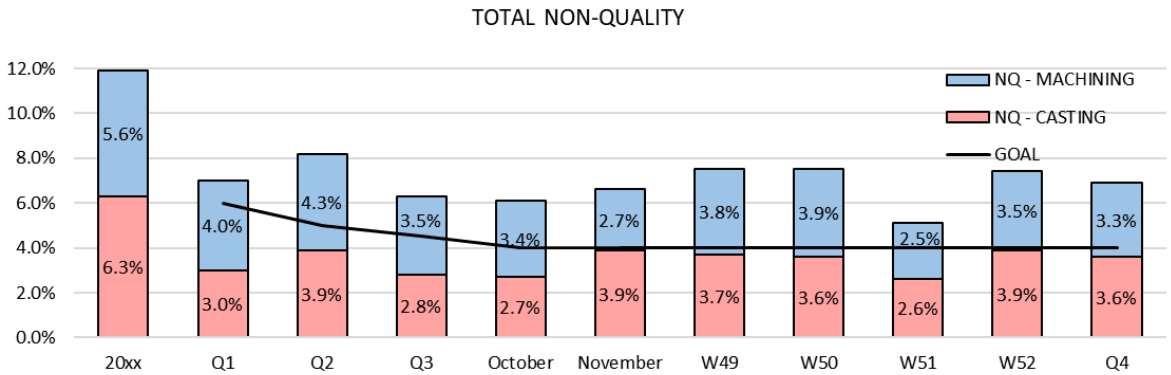


Figure 7. Overview of the overall trends in non-conformity results

The results of the corrective measures are shown in Figure 8. After an initial temporary improvement in the first quarter of the year, there was a significant deterioration in results in the following quarter. This was the result of the introduction of internal complaint activities between machining and casting as well as increased monitoring of the casting production process. Although the trend in internal non-conformity results was very unfavourable, the corrective measures proved to be effective, which was reflected in a simultaneous decline in customer complaints.

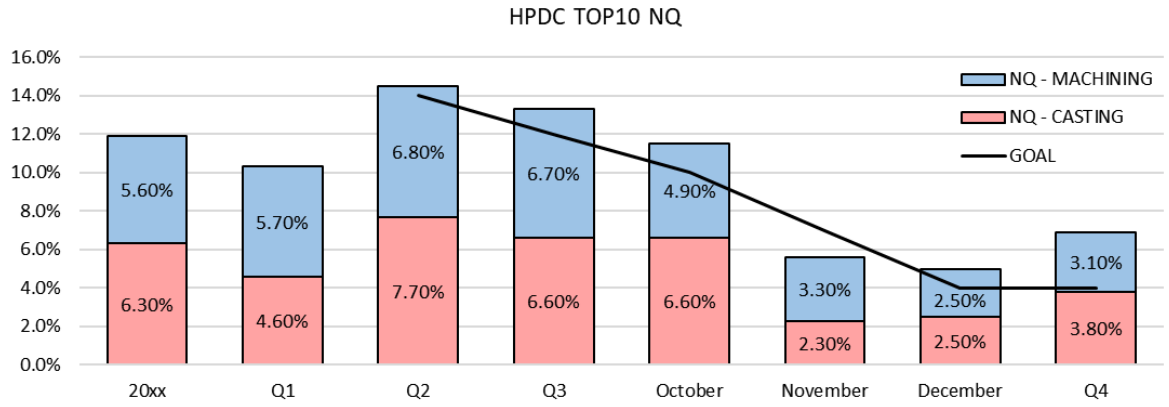


Figure 8. *Overview of non-conformity trends for the TOP10 products*

The consistent and rigorous implementation of the defined agile approach in conjunction with a changed organisational structure for monitoring the production process in the HPDC and the machining of castings meant that the positive trend in non-conformity results continued throughout the year. Although the results achieved by the end of the reporting period did not quite reach the targets originally set, significant progress was made compared to the period prior to the introduction of the changes described in the FPI.

5. Conclusions

Thanks to the introduction of agile management elements into the existing Lean Six Sigma (LSS) improvement projects, further significant progress was made in improving non-quality-related performance indicators. The combination of agile and LSS management principles together with additional changes in the quality control processes within production led to measurable and significant performance improvements with long-term benefits. The average number of complaints was significantly reduced from 4.8 to 1.2 per week. Nonconformance results in HPDC production also improved significantly – from 11.9% to 5.0% overall, with targets increasingly met or exceeded. The biggest benefit was the restoration of customer confidence, resulting in a significant reduction in complaints and improved delivery performance. This has led to numerous nominations for the manufacture of new products. The defined approach to improvement projects has become a standardised part of the company's operations, accompanied by improved communication and motivation among team members and other employees due to the clear and tangible benefits in various areas of the company.

Although the introduction of Agile Lean Six Sigma, offers significant benefits, it must be carefully adapted to the specific context of the company, taking into account the limitations of the methodology, organisational capabilities, knowledge levels and cultural factors. Only such a context-sensitive approach allows the full potential of the methodology to be realised without compromising the dynamics and flexibility of the system.

In summary, the feasibility of this approach depends on the involvement of all organisational levels within a top-down framework, with managers taking an active and substantive role in the implementation of the methodology, rather than limiting their contribution to declaratory approval.

Acknowledgments
This work was fully supported by the University of Rijeka (contract no. uniri-iskusni-tehnic-23-260 and uniri-iskusni-tehnic-23-255).

References

[1] Antony, J., Snee, R., Hoerl, R., 2017. Lean Six Sigma: Yesterday, Today and Tomorrow. International Journal of Quality and Reliability Management, 34, 1073–1093, doi:10.1108/IJQRM-03-2016-0035.

[2] Krulčić, E., Doboviček, S., Pavletić, D., Čabrijan, I., 2024. The Role of Hybrid Program Management in Driving Continuous Improvements on the Factory Floor, MTSM2024 Split.

[3] Olanrewaju, F., Chima Uzorh, A., Nnanna, I., 2019. Lean Six Sigma Methodology and Its Application in the Manufacturing Industry – A Review. American Journal of Mechanical and Industrial Engineering, 4, 40, doi:10.11648/j.ajmie.20190403.11.

[4] Olutade, O., Adeyinka, A.M., Durodola, O., 2023. Exploring Lean Six Sigma: A Comprehensive Review of Methodology and Its Role in Business Improvement. International Journal of Multidisciplinary Research and Growth Evaluation, 4, 939–947, doi:10.54660/.ijmrge.2023.4.6.939-947.

[5] Patel, A.S., Patel, K.M., 2020. Critical Review of Literature on Lean Six Sigma Methodology. International Journal of Lean Six Sigma, 12, 627–674.

[6] Bhat, S., Gijo, E. V., Jnanesh, N.A., 2014. Application of Lean Six Sigma Methodology in the Registration Process of a Hospital. International Journal of Productivity and Performance Management, 63, 613–643, doi:10.1108/IJPPM-11-2013-0191.

[7] Vanzant Stern, T., 2020. Lean and Agile Project Management; How to Make Any Project Better, Faster, and More Cost Effective, 2nd., Routledge, Taylor&Francis Group, New York, 2020, ISBN 978-0-429-34341-4.

[8] Sharma, S., Sarkar, D., Gupta, D., 2021. Agile Processes and Methodologies: A Conceptual Study. International Journal on Computer Science and Engineering, 4, 892–898.

[9] Conforto, E.C., Salum, F., Amaral, D.C., Da Silva, S.L., De Almeida, L.F.M., 2014. Can Agile Project Management Be Adopted by Industries Other than Software Development? Project Management Journal, 45, 21–34, doi:10.1002/pmj.21410.

[10] Watt, Adrienne. 2014. Project Management, 2nd ed., BCcampus, BC Open Textbook Project, ISBN 9781774200124.

[11] Schwaber, K., Sutherland, J. 2020. Scrum-Guide-Croatian.Pdf Available online: https://scrumguides.org/docs/scrumguide/v2020/2020-Scrum-Guide-Croatian.pdf (accessed on 5 July 2025).

[12] Kuster, J., Bachmann, C., HUbman, M., Lippmann, R., Schneider, P., 2023. Management for Professionals Project-Management Handbook Agile-Traditional-Hybrid, 2nd., Springer, 2023.

[13] Agarwal, S., Agarwal, A., 2020. Uses, Advantages and Opportunities of Kanban Methods in Mechanical Engineering and Product Manufacturing. International Journal of Scientific and Research Publications (IJSRP), 10, p9704, doi:10.29322/ijsrp.10.01.2020.p9704.

[14] Soković, M., Pavletić, D., Krulčić, E., 2006. Six Sigma Process Improvements in Automotive Parts Production. Journal of Achievements in Materials and Manufacturing Engineering, 19(1), 96-102.

Influence of surface high-frequency mechanical forging on the structure of welded joints of structural steel

***Olga Kushnarova*[1], *Olena Berdnikova*[1], *Igor Alekseienko*[1], *Valeriy Pozniakov*[1], *Aleksandr Gaivoronskiy*[1], *Anatoliy Zavdoveev*[1] *and Massimo Rogante*[2]**

1) Paton Electric Welding Institute of NAS of Ukraine, K.Malevicha 11, 03150 Kiev, Ukraine,

2) Rogante Engineering Office, Contrada San Michele n.61, 62012 Civitanova Marche, Italy,

Corresponding author: avzavdoveev@gmail.com

Original scientific article

Abstract: The paper considers the structural features of the welded joint metal of low-alloy structural (building) steel S420NL, obtained by arc welding using flux-cored wire Filarc PZ 6114S. Welding was carried out without preliminary heating in a protective gas environment with subsequent use of high-frequency mechanical forging along the joint line. The microstructure in the welded joint metal after welding with and without high-frequency mechanical forging (HFMF) of the surface was studied using microscopy methods. Experimental data on microhardness and grain structure, which are formed in the welded joint metal under the influence of HFMF, were obtained. Comparative analysis of the structural parameters of the welded joint metal has been made. It was proven that the surface treatment method using HFMF provides a general refinement of the structure with an increase in microhardness both in the fusion line zone of the welded joint and in the metal of the heat-affected zone. Such a structure will provide an increase in strength and prevent brittle fracture of the structural steel metal under operating load conditions. The use of HFMF for processing welded surfaces of joints reduces the likelihood of cracks and increases their strength.

Keywords: structural steel, welded joint, high-frequency mechanical forging (HFMF), heat-affected zone, microstructure, ferrite, pearlite, microhardness.

1. Introduction

Many operational characteristics of metal products, such as fatigue strength, hardness, tendency to crack formation, destruction, friction, wear and corrosion, significantly depend on the structural-phase and physicochemical state of the surface layers of the material. Often, the failure begins with the formation of surface cracks. Their formation depends on the structural state of both the uppermost and deeper surface layers of the material [1-6]. In recent years, new approaches to material processing by various methods have been used to increase the service life of mechanisms and machines [7–14]. Promising treatments of materials include energy fields [15–17], electric spark hydraulic shock [18], high-frequency forging [19, 20], ultrasound methods [21], electromagnetic processing [22, 23], and methods based on intense plastic deformations [4].

In mechanical engineering, as well as in bridge building and construction, the development of technologies for strengthening the surface of metal structure parts and welded joints is a priority task. Such technologies include: mechanical forging of deposited metal during welding, post-weld ultrasonic impact treatment of the weld surface and heat-affected zone (HAZ) of welded joints, shot blasting, vibration treatment of structures, etc. [24 – 28]. One of the promising methods for increasing the strength and reducing cracking of metal is high-frequency mechanical forging (HFMF) of the surface and welded joints. This approach was developed at the E.A. Paton Electric Welding Institute of the National Academy of Sciences of Ukraine and is used for different grades of steel [28, 29]. In the processing zone, the surface layer of the metal is strengthened and residual stresses are relieved. The technology of surface plastic deformation of welded joints HFMF has a number of advantages: high productivity and cost-effectiveness; compactness of equipment; processing in any spatial position; use both in production and on operational structures.

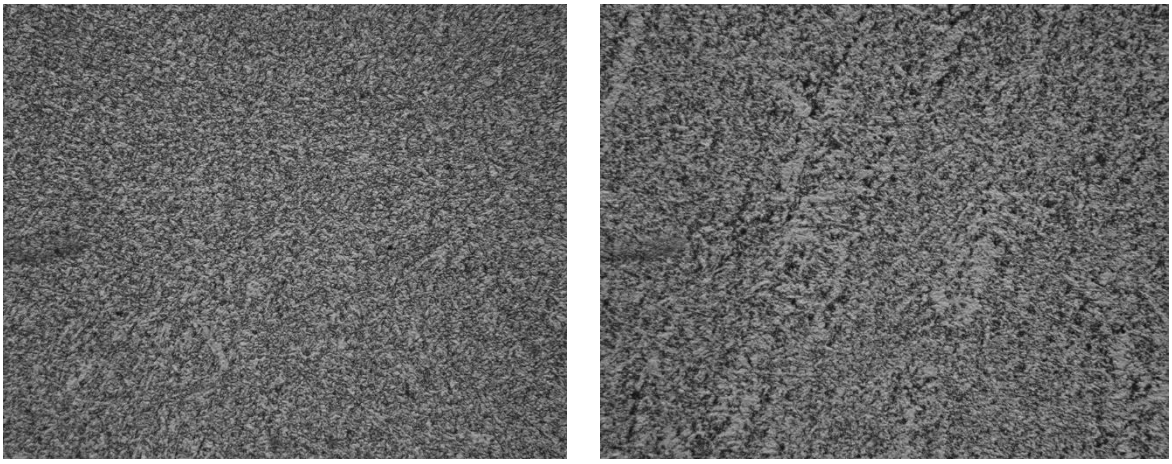
The aim of the work was to study structural changes in the metal of a welded joint of low-alloy structural (building) steel S420NL, obtained using flux-cored wire Filarc PZ 6114S after welding and high-frequency mechanical forging along the joint line. To achieve this goal, it is necessary to: obtain welded joints of steel S420NL using the arc welding method; carry out surface treatment of the welded joint using the HFMF method; examine the microstructure of the obtained welded joints in the weld metal and heat-affected zone, measure microhardness; conduct a comparative analysis of structural changes in the metal of welded joints after welding using high-frequency mechanical forging (HFMF) of the surface and without HFMF (initial state).

2. Materials and research methods

The article presents the results of studying the structural features of welded joints of low-alloy structural (building) steel grade S420NL (0.2% C; 0.6% Si; 1.0-1.7% Mn; 0.05% Nb; 0.2% V; 0.02% Al; 0.03% Ti; 0.03% Ti; 0.1% Mo; 0.55% Cu; The flux-cored wire Filarc PZ 6114S (0.04-0.08% C; 0.3-0.5% Si; 1.1-1.5% Mn; 0.25-0.5% Ni; 0.03% S; 0.025% P) was used for welding. The welded joints were studied after welding, both before (initial state) and after using high-frequency mechanical forging (HFMF) of the surface along the joint line. Arc welding was carried out without preliminary heating in the environment of protective gases Ar + CO2 in the modes I=180A; U=25-26B; V=18 m/hour. After welding, the HFMF was performed according to the proven technology with the parameters of the static load (tool compression) C=150-200H, with the frequency and amplitude of the converter oscillations of 27 kHz and a=15 μm and the longitudinal feed rate of the deforming tool V=25 mm/s. Only a narrow section of the metal of the connection line with the molding after forging a smooth groove 3-4 mm wide and up to 1.0 mm deep was subject to processing. The structure was studied using light microscopy (Versamet-2, Neophot-32 microscopes). Microhardness (HV) was measured on a LECO M-400 microhardness tester with a load of 100 g

3. Results and discussion

Using light microscopy methods, it was established that the structure of welded seams of structural steel S420NL in the initial state (without HFM) is ferrite-pearlite (FP) with a microhardness of HV= 1470-2210 MPa, Figure 1.



(a) (b)

Figure 1. *Microstructure of the weld metal of the welded joint of S420NL steel in the initial state (without HFMP), obtained using the Filarc PZ 6114S flux-cored wire (magnification ×500).*

A bainitic (B) structure is formed in the HAZ metal, Figure 2. From the fusion line, when approaching the base metal, the structure becomes ferritic-pearlite. The grain size decreases from Dп = 50-200 μm to Dп = 5...30 μm when moving from the overheating section (I section of the HAZ) to the recrystallization section (IV section of the HAZ). In this case, HV decreases from 1800-1940 MPa to

1760-1870 MPa. The structure in the base metal is ferritic-pearlite with grain sizes 10-40 µm and HV = 1600...2360 MPa.

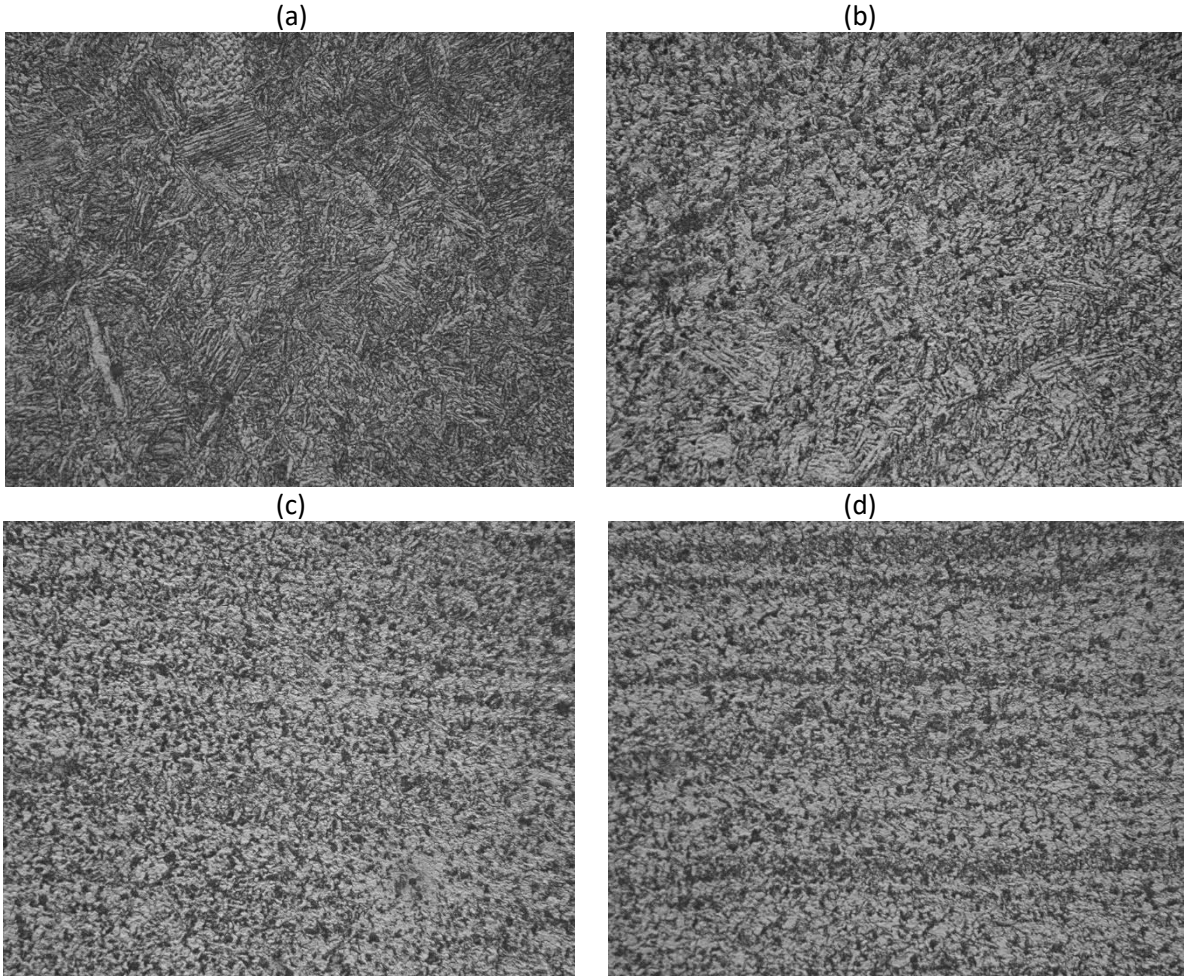


Figure 2. *Microstructure of the metal of the HAZ sections of the welded joint of S420NL steel in the initial state (without HFMP) with the Filarc PZ 6114S flux-cored wire: a – and HAZ (large grain); b – II HAZ (normalization); c – III HAZ (incomplete recrystallization); d – IV HAZ (recrystallization), (magnification ×500).*

In the weld zone, after HFMF the structure is ferrite-pearlite (FP) with an increase in microhardness by an average of 1.2 times (up to HV = 1930-2620 MPa). In the HAZ, a decrease in the size of the bainitic structure is observed compared to the initial state by an average of 1.2 times to Dп = 40-180 µm (I area) and Dп = 5-30 µm (IV area). Microhardness increases by 1.3 times to HV = 2450-3090 MPa and to HV = 2360 MPa, respectively.

After HFMP of the welded joint along the fusion line, the area where the surface treatment was performed visually looks like a groove, Figure 3. This groove appears both in the direction of the weld and in the HAZ. It was found that the structure refinement occurs at a depth of up to 125 µm from the sample surface in the weld metal up to Dп = 50 ... 100 µm, and in the HAZ - up to Dп = 15 ... 100 µm (I section) and 5 ... 20 (IV section). Moreover, after HFMP in the area of the treated surface, in the weld zone there is an increase in microhardness compared to the initial state - by 1.3 times to HV = 2540 - 2850 MPa, and in the HAZ - by 1.7 times to HV = 2360 - 3360 MPa.

Compared to the initial state, the grain size in the HAZ decreases on average by 1.2 times with an increase in microhardness by 1.3 times. After HFMF, along the joint line the structure is refined (graine size are significantly decreased) up to a depth of 125 µm from the sample surface in the weld metal, and in the HAZ by 1.8 times, with an increase in microhardness by 1.3 times in the weld zone, and by 1.2 times in the HAZ. Graine refinement of the structure in the surface layers of the welded joint will

increase strength, prevent cracking and brittle fracture of the structural steel metal under loading in operating conditions.

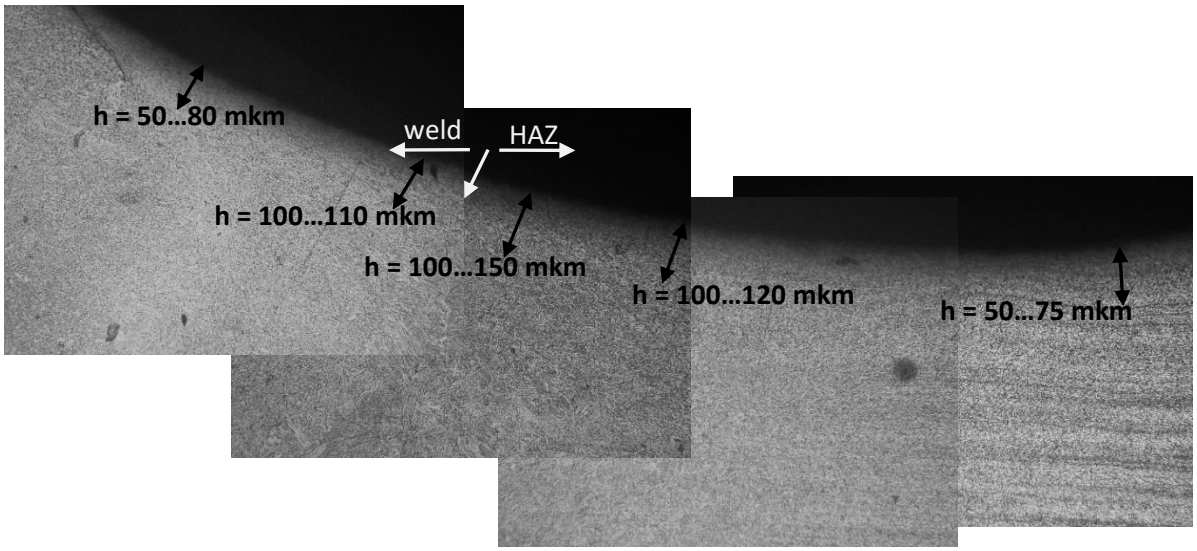


Figure 3. *Microstructure of the surface in the fusion line zone after HFMP of a welded joint of S420NL steel (magnification× 200).*

4. Conclusion

The use of high-frequency mechanical forging (HFMF) after welding low-alloy structural (building) steel S420NL using the Filarc PZ 6114S flux-cored wire contributes to the overall refinement of the structure in the surface layer of the welded joint. Compared to the initial state the grain size in the heat-affected zone (HAZ) decreases by an average of 1.2 times with an increase in microhardness by 1.3. After surface treatment by the HFMF method, a 125 μm thick layer is formed perpendicular to the fusion line with refinement of the structure in the weld metal (by 1.2 times) and HAZ (by 1.8 times) and an increase in microhardness compared to the initial state (by an average of 1.5 times). Dispersion of the structure in the surface layers of the welded joint will provide an increase in strength and prevent brittle fracture of the structural steel metal under operating load conditions, reducing the likelihood of cracks.

References

[1] Paton, B., 2000. Modern trends toward increase in strength and life of welded structures, The Paton Welding Journal, 9(10), 2-7.

[2] Trufnyakov, V., 1990. Strength of welded joints under alternating loads, Naukova Dumka, 256. p.

[3] Lobanov , L. M., Kondratenko, I. P. , Mikhalskyi, V. M. et.al., 2020. Electrotechnical Complex for Electrodynamic Processing of Welded Joints, Technical Electrodynamics, 6, 1–3.

[4] Sydorenko, S.I., Vasyliev, M.O., Voloshko, S.M. 2018. Surface engineering: methods of strengthening metal surfaces by intensive plastic deformation, Materials science: achievements and prospects, 393-413.

[5] Berdnikova, O., Kushnarova, O., Bernatskyi, A., Polovetskyi, Y., Kostin, V., and Khokhlov, M., 2021. Structure features of surface layers in structural steel after laser-plasma alloying with 48(WC-W2C)+48Cr+4Al powder, IEEE 11th International Conference Nanomaterials: Applications & Properties (NAP), 01-04.

[6] Khokhlova, J., Khokhlov, M., Tunik, A., Ishchenko, A., 2014. Nanoindentation of micro weld formed through thin nanolayered filler, Solid Mechanics and Its Applications Open source preview, 203, pp. 251–262,

[7] Imbirovych, N., Boyarska, I., Povstyanoy, O., Kurzydłowski, K., Homon, S., Kulakovskyi, L., 2023. Modification of oxide coatings synthesized on zirconium alloy by the method of plasma electrolytic oxidation, AIP Conference Proceedings, 2949, 020011.

[8] Dolgov, M., Zubrets'ka, N., Buketov, A., & Stukhlyak, P., 2021. Use of the method of mathematical experiment planning for evaluating adhesive strength of protective coatings modified by energy fields, Strength of Materials, 44 (1), 81–86.

[9] Qin, Sh., Zhang, X., 2022. Ultrafast regulation of nano-scale matrix defects using electrical property discrepancies to delay material embrittlement, Journal of Materials Science and Technology, 119, 25 – 3620.

[10] Mao, D., Xie, Y., Meng, X., Ma, X., Zhang, Z., Sun, X., Wan, L., Volodymyr, K., Huang, Y., 2024. Strength-ductility materials by engineering a coherent interface at incoherent precipitates, Materials Horizons, 11, 3408-3419.

[11] Kushnarova, O., Berdnikova, O., Tyurin, Y., Kolisnichenko, O., Alekseienko T., and Titkov , Y., 2023. Peculiarities of the Surface Structure of High-Speed Steel After Pulse-Plasma Treatment, IEEE 13th International Conference Nanomaterials: Applications & Properties (NAP), IMT07-1-IMT07-4 .

[12] Zhang, D., Liu, Y., Yin, Y., 2016. Preparation of plasma cladding gradient wear-resistant layer and study on its impact fatigue properties, J. Thermal Spray Technol, 25, 535–545.

[13] Grigorenko, G., Adeeva, L., Tunik, A., Korzhik, V., Karpets, M., 2020. Plasma Arc Coatings Produced from Powder-Cored Wires with Steel Sheaths, Powder Metallurgy and Metal Ceramics, 59(5-6), 318–329

[14] Berdnikova O., Kushnarova O., Bernatskyi A., Alekseenko T., Polovetskyi Y., Khokhlov M., 2020. Structure Peculiarities of the Surface Layers of Structural Steel under Laser Alloying, Proceedings of the 2020 IEEE 10th International Conference on "Nanomaterials: Applications and Properties", NAP , 9309615.

[15] Zhang, J., Liu, Ji., Zhang, X., et al, 2021. Effect of High Density Current Pulses on Microstructure and Mechanical Properties of Dual-Phase Wrought Superalloy, Acta Metallurgica Sinica, 34,1635 – 1644.

[16] Diao, A., Wang, J., Yang, Y., 2022. Jingdong Fatigue Damage Recovery of 20 Carbon Steel under Pulsed Current, Special Casting and Nonferrous, 42, 318 - 322.

[17] Guo, J., Wang, X., Dai, W., 2015. Microstructure evolution in metals induced by high density electric current pulses, Materials Science and Technology (United Kingdom), 31 (13a) 1545-1554.

[18] Totosko, O., Levytskyi, V., Stukhlyak, P., et al., 2020. Investigation of electrospark hydraulic shock influence on adhesive-cohesion characteristics of epoxy coatings. Functional materials. 27 (4), 60-766.

[19] Knysh V., Solovej S., Nyrkova, L., and Miryanin, V., 2018. Influence of corrosion damage on cyclic life of butt welded joints strengthened by high-frequency mechanical peening, The Paton Welding Journal, 2, 14-18.

[20] Stukhlyak P., Holotenko O., Zolotyi R., Mykytyshyn A., 2021. Investigation of superhigh-frequency treatment influence on structuring of epoxy composites by infrared- and electron paramagnetic resonance spectroscopy analyses. Functional Materials, 28 (2), 394 – 402.

[21] Chykhira I., Stukhlyak P., Mytnyk M., Kartashov V., 2021. Investigation of epoxycomposites linking kinetics during ultrasonic treatment, Functional Materials, 282021, 84 – 89.

[22] Razmyshlyaev, O., Maksimov, S., Berdnikova, O., Prilipko, O., Kushnarova O., 2023. Structure of low-alloy steel welded joints under action of an external electromagnetic field, Materials Science, 58 (7), 616–620

[23] Stukhlyak, P., Holotenko, O., Dobrotvor, I., et al., 2015.Investigation of the Adhesive Strength and Residual Stresses in Epoxy Composites Modified by Microwave Electromagnetic Treatment. Mater Sci, 51, 208–212 .

[24] Pysmennyi A.S., Pentegov I.V., Kislitsyn V.M., Stemkovsky E.P., Sheikovskiy D.A., 2012. Brazing welding with forging of the weld metal during its crystallization , Automatic welding, 11, 41-45.

[25] Lashchenko G., Demchenko. Yu., 2008. Energy-saving technologies for post-welding processing of metal structures, 168 p.

[26] Poznyakov, V., Babich, A., et al., 2017. The influence of low-temperature tempering and shock treatment on the durability of welded joints of steel grades 71 and HB 500 MOD when making LBT, Mechanics and Mechanical Engineering, 1, 247-253.

[27] Knysh, V., Solovey, V., Kiryan, V., Nyrkova, L., 2017. Application of high-frequency forging to improve the performance characteristics of butt welded joints in temperate climates, Automatic welding, 4, 15-20.

[28] Kushnarova, O., Berdnikova, O., Alekseienko, T., et.al., 2024. Features of the metal welded joints structure in special purpose steel under high-frequency mechanical peening International conference “Mechanical Technologies and Structural Materials 2024” Split, Croatia, 19 - 20 September 2024, pp. 245-250.

[29] Knysh, V., Solovej S., Nyrkova L., Miryanin V., 2018. Influence of corrosion damage on cyclic life of butt welded joints strengthened by high-frequency mechanical peening, The Paton Welding Journal, 2, 14-18.

Effect of cooling methods on the surface chemistry and corrosion performance of X2CrNiMo17-12-2 austenitic stainless steel

***Dario Kvrgić*[1], *Graciela Šterpin Valić*[1], *Tea Marohnić*[1], *Robert Basan*[1] *and Goran Cukor*[1]**

1) University of Rijeka, Faculty of Engineering,Vukovarska 58, 51000 Rijeka, Croatia

Corresponding author: graciela.sterpin@riteh.uniri.hr

Original scientific article

Abstract: This study continues previous research on the corrosion behavior of machined X2CrNiMo17-12-2 (AISI 316L) stainless steel by incorporating additional surface characterization techniques. The samples were prepared using four different cooling strategies: no cooling, conventional emulsion, minimum quantity lubrication (MQL), and MQL combined with vortex tube cooling. These methods were selected with an emphasis on sustainability, aiming to reduce the environmental impact commonly associated with conventional mineral oil-based fluids. Corrosion behavior was evaluated in 3.5% NaCl solution using open circuit potential (OCP), linear polarization resistance (LPR), and potentiodynamic polarization (PDP) measurements. The results demonstrated that the applied cooling method significantly affects corrosion resistance, with MQL-based techniques providing the most favorable electrochemical parameters and dry machining resulting in the poorest performance. To better understand the mechanisms behind these differences, surface chemical composition was analyzed using energy-dispersive X-ray spectroscopy (EDS) before and after corrosion testing. Additionally, scanning electron microscopy (SEM) was employed to assess surface morphology. This integrated approach highlights the critical role of machining-induced surface chemistry in localized corrosion behavior and confirms the potential of MQL based techniques as both effective and environmentally responsible cooling alternatives.

Keywords: *X2CrNiMo17-12-2; vortex tube cooling; MQL; corrosion performance; energy-dispersive X-ray spectroscopy (EDS); scanning electron microscopy (SEM)*

1. Introduction

In recent decades, the use of stainless steels has expanded significantly, driven by their corrosion resistance, mechanical reliability, and versatility across critical sectors such as construction, transportation, and biomedical applications [1,2]. They belong to the group of difficult-to-cut materials where two main problems can occur: short cutting tool life and bad machined surface quality which can be improved by the recommended abundant watering of the cutting zone with a conventional metalworking fluid which must provide cooling whose effect improve tool life and lubrication whose effect reduces tool wear [3]. Conventional mineral oil-based metalworking fluids are harmful to the environment and human health, and they bring significant additional costs into production. For this reason, they are recognized as the main unsustainable element of the machining process [4], and alternative cooling and lubrication techniques are increasingly being developed to strengthen the green transition, which includes protection of the environment and worker health.

Austenitic stainless steel X2CrNiMo17-12-2 (AISI 316L) is a low-carbon, austenitic chromium-nickel-molybdenum steel. It is resistant to intercrystalline corrosion when welded but not resistant to sea water. High chromium and molybdenum contents are key to resistance to pitting corrosion in chloride environments [1].

This study continues previous research on the corrosion behavior of machined X2CrNiMo17-12-2 stainless steel by incorporating additional surface characterization techniques [5]. Corrosion behavior was evaluated in 3.5% NaCl solution using open circuit potential (OCP), linear polarization resistance (LPR), and potentiodynamic polarization (PDP) measurements for the samples prepared in four different cooling strategies: no cooling, conventional emulsion, minimum quantity lubrication (MQL),

and MQL combined with vortex tube cooling. These methods were selected with an emphasis on sustainability, aiming to reduce the environmental impact commonly associated with conventional mineral oil-based fluids. The need to view the use of metalworking fluids from the perspective of significantly reducing environmental burden and risks to human health represents a major challenge for scientists in their search for better solutions that will not threaten the future, or sustainability, of machining. The results demonstrated that the applied cooling method significantly affects corrosion resistance, with MQL based techniques providing the most favorable electrochemical parameters and dry machining resulting in the poorest performance [5]. To better understand the mechanisms behind these differences, surface chemical composition and surface morphology was analyzed using SEM/EDS technique before and after corrosion exposure for the samples prepared in mentioned cooling strategies. For corrosion resistance, the highest possible chromium (Cr) content is generally desirable, along with the lowest possible carbon (C) content, which forms harmful chromium carbide with chromium [5]. Also important is the highest possible oxygen (O) content, which forms a passive film with chromium and helps it self-repair after machining [2].

Vortex tube cooling uses compressed air to create a cold air stream, and is considered the cleanest and most environmentally and health-friendly cooling method. MQL delivers a minimum amount of vegetable oil (consumption in ml/h) to the cutting zone for metalworking in the form of an aerosol instead of the conventional circulating flood systems in metalworking. In combination with vortex tube cooling, it shows significant potential in reducing environmental impact and improving process sustainability [7].

The following literature review is important for understanding microstructural changes and the influence of surface conditions on the shape and development of pits and the behavior of passive films.

Matula et al. [8] shows how local chromium-depletion along grain boundaries in 316L steel can cause intergranular corrosion. This confirms the importance of microlocal distribution of alloying elements in corrosion resistance. Although it deals with a different type of corrosion (intergranular), it is useful for theorizing that local changes in composition can promote selective attack, which can be transferred to our analysis of the edges and bottoms of corrosion pits. Šterpin Valić at al. [7] investigates the effect of MQL and vortex tube cooling on the surface quality when turning of martensitic stainless steel. It is relevant because it confirms that the condition of the surface after machining can influence the later corrosion behavior. Although it does not deal with 316L steel or analyze the chemical changes, it does well support the previous statement that microstructure and treatment before exposure to corrosion play a key role. Burstein & Pistorius [9] is a study showing that smooth surfaces have a lower frequency but higher stability of pitting corrosion. It provides an experimental basis for why, even on the polished 316L samples in our work, the development of clearly defined corrosion holes still occurs. It does not deal with chemical analysis, but is important for understanding the influence of surface conditions on the shape and development of pies. A study by DelVecchio et al. [10] on AM 316L steel shows that microsegregation of Cr and Mo leads to local corrosion. It helps to interpret that local depletions of passivation elements increase the tendency to pitting. Although they deal with an additive material, which is different from our machined 316L, their observations about the role of local chemistry in selective corrosion are very applicable to our EDS analysis in and around corrosion pits. Wang et al. [11] work shows that surface treatment affects the development of passive layer and corrosion resistance of 316L steel under high temperature conditions. Although the medium (simulated PWR water) is different, the study confirms that microstructural changes and surface condition significantly determine the behavior of the passive film. This supports our idea that the surface and edges of corrosion pits may have different chemical compositions as a result of local passivation or dissolution. Zhang et al. [12] showed using EDS analysis that inside and on the edge of corrosion holes on 304 steel there are increased amounts of sulfur and manganese, which indicates the role of MnS inclusions in pit initiation. This can be directly compared to our analysis of the chemical composition of the edge and bottom of holes on 316L steel. It varies by alloy and cooling medium, but the approach and mechanism help to interpret the role of surface

heterogeneities in the development of localized corrosion. Cukor et al. [13] concluded that cooling with cooled compressed air by vortex tube does not negatively affect corrosion resistance in turning of martensitic stainless steel. As far as corrosion resistance is concerned, the highest possible chromium (Cr) content and the lowest possible carbon (C) content are desirable. SEM/EDS analysis results showed that in the case of vortex tube cooling, the treated surface had a higher chromium content and a significantly lower carbon content.
The aim of this review is to provide a comprehensive understanding of how these cooling methods affect corrosion resistance and the chemical composition of the machined surface of austenitic stainless steel X2CrNiMo17-12-2.

2. Materials and methods

2.1. Materials

The austenitic stainless steel X2CrNiMo17-12-2 (AISI 316L) was selected as the test material. Rods Ø80 × 530 mm were used for the research. The length for longitudinal turning was 460 mm. CNC lathe TU 360 Prvomajska, Seco cutting inserts DNMG 150608-MF 4 grade TM3501 and Seco holder DDJNL 2525M15-M were used for turning.
All samples made of austenitic stainless steel X2CrNiMo17-12-2 required for SEM and EDS analysis were machined with the same cutting parameters, except for the cooling where four methods were applied: no cooling, emulsion, MQL and MQL + vortex. The turning process was carried out with constant cutting parameters: cutting speed (v_c= 60 m/min), feed rate (f = 0.22 mm/rev), and depth of cut (a_p= 1.3 mm).
INA BU 7 emulsifying concentrate for metalworking was used to prepare the emulsion. For MQL machining, an external SKF VectoLub system with a VE1B unit was available, which was supplied with oil from an integrated tank. The biodegradable oil LUB 200 from SKF was used for lubrication, specially adapted for use with all types of MQL systems. The chemical composition includes a mixture of triglycerides of natural origin and refined rapeseed oil. The EXAIR counter-flow vortex tube (VC), model 3825, is connected to the MQL unit in one system, the so-called Integrated MQL/VC system.

2.2. Methods

In order to gain an insight into the state and chemical composition of the sample surfaces, before and after testing the corrosion resistance in a 3.5% NaCl solution at a temperature of 25 °C, scanning electron microscopy (SEM) was used in combination with energy-resolving/dispersive X-ray spectroscopy (EDS). SEM/EDS analysis of the sample surfaces was performed in the Scanning Electron Microscopy Laboratory of the Faculty of Physics, University of Rijeka. SEM scanning electron microscope JSM-7800F, Jeol and energy-dispersive X-ray detector X-MaxN80, Oxford Instruments were used for EDS analysis of the elemental composition of the sample.

3. Results and discussion

The surface chemical composition of X2CrNiMo17-12-2 stainless steel samples subjected to various cooling methods during machining was examined using energy-dispersive spectroscopy (EDS). The aim of the analysis was to identify changes in the mass fractions (wt.%) of key alloying and contaminant elements, in order to assess how each processing method influenced the initial surface reactivity and the material’s subsequent corrosion resistance [14]. The analysis was conducted in two phases: before and after corrosion testing. After corrosion exposure, three characteristic surface zones were identified: the surface, the pit edge, and the pit bottom [15]. The collected data were statistically correlated with electrochemical measurements to determine the relationship between local chemical composition and the mechanisms of passive film formation and breakdown [8,11].
In this context, corrosion testing refers to a sequence of non-destructive (*OCP*, *Rp*) and destructive (E_{corr}, i_{corr}, corrosion rate) electrochemical procedures, which ultimately altered the surface condition

[16]. In addition to EDS, scanning electron microscopy (SEM) was employed to investigate surface morphology both before and after corrosion exposure.

3.1. Surface chemical composition before corrosion

Prior to corrosion testing, EDS analysis of the surface layer showed that the cooling method applied during machining significantly affected the distribution of chemical elements [14]. While the iron (Fe) content was dominant and relatively uniform across all samples (ranging from 61.7 to 62.8 wt.%), notable differences were observed in the concentrations of chromium (Cr), nickel (Ni), oxygen (O), and carbon (C), depending on the specific cooling methods employed, Table 1.

Table 1. *Surface chemical composition of X2CrNiMo17-12-2 stainless steel samples in pre-corrosion testing*

Cooling Medium	Fe (wt.%)	C (wt.%)	Cr (wt.%)	Ni (wt.%)	O (wt.%)	Mn (wt.%)	Mo (wt.%)	Si (wt.%)	S (wt.%)	Ca (wt.%)	Al (wt.%)
Base material without cooling	62.78	5.36	15.12	12.02	0.78	1.18	1.02	0.30	0.04	0.04	0
Emulsion	62.10	6.14	14.70	11.90	1.42	1.28	1.76	0.26	0	0.02	0.02
MQL	62.76	14.94	14.26	9.28	1.58	1.36	1.10	0.30	0.08	0.10	0.02
MQL + vortex	61.70	8.94	14.36	9.66	1.58	1.24	1.00	0.28	0	0	0

Samples processed without cooling exhibited the highest chromium (15.12 wt.%) and nickel (12.02 wt.%) content. This may suggest the retention of alloying elements in the surface layer due to the absence of flushing and dispersion during machining [14]. At the same time, these samples also showed the lowest oxygen content (0.78 wt.%), indicating limited oxide formation and weaker initial surface passivation [17].

For methods involving lubrication, particularly MQL, a sharp increase in carbon content was observed (14.94 wt.%), which is attributed to the adsorption of organic components from the lubricant [14]. The emulsion and MQL + vortex method showed moderate carbon values (6.14 and 8.94 wt.%, respectively), indicating partial contamination, but also possibly more effective removal of surface residues.

Oxygen content was higher in all cooling methods compared to samples without cooling. The highest oxygen levels were found in the MQL and MQL + vortex conditions (1.58 wt.%), which may reflect an increased degree of surface oxidation driven by thermal and chemical interactions with the cooling medium [14, 17]. The elevated presence of oxygen suggests the formation of oxides.

Molybdenum and manganese showed slightly elevated concentrations in the samples cooled by the emulsion and MQL methods, although the differences among methods were moderate. Trace amounts of sulfur, calcium, and aluminum did not display a consistent trend, which suggests possible contamination from the surrounding environment or from the cooling medium itself [15].

3.2. Surface chemical composition after corrosion

Following corrosion exposure in a 3.5% sodium chloride solution, localized surface degradation occurred, resulting in the formation of corrosion pits. EDS analysis was performed to determine changes in surface chemical composition caused by the direct influence of electrochemical processes. The analysis covered three characteristic zones: the surface without visible damage, the edge of the corrosion pits, and the pit bottom. This approach allowed for a detailed investigation of the local redistribution of alloying elements and the potential loss of protective components depending on spatial location [14,16].

3.2.1. Surface zone

After corrosion testing, EDS analysis of the surface revealed changes in the content of key elements depending on the applied cooling method. In general, surface homogeneity was reduced compared

to the condition before corrosion [9,15]. Surface chemical composition of stainless steel samples after corrosion on the surface zone is shown in the Table 2.

Table 2. *Surface chemical composition of stainless steel samples in post-corrosion testing – surface zone*

Cooling Medium	Fe (wt.%)	C (wt.%)	Cr (wt.%)	Ni (wt.%)	O (wt.%)	Mn (wt.%)	Mo (wt.%)	Si (wt.%)	S (wt.%)	Cl (wt.%)	Na (wt.%)
Base material without cooling	64.67	12.83	15.30	11.83	1.40	1.70	1.17	0.27	0.00	0.00	0.00
Emulsion	63.80	8.24	15.44	11.48	1.42	1.82	1.82	0.30	0.00	0.08	0.12
MQL	64.00	13.57	12.10	10.43	1.80	1.57	0.83	0.30	0.00	0.00	0.00
MQL + vortex	64.08	3.74	15.24	12.56	0.80	1.48	1.30	0.28	0.04	0.00	0.00

The most notable differences were observed in the content of chromium, nickel, molybdenum, and carbon. In samples processed with the MQL method, the lowest values of chromium (12.10 wt.%) and nickel (10.43 wt.%) were recorded. In contrast, the emulsion and MQL + vortex methods preserved slightly higher concentrations of these alloying elements. Notably, the nickel content in MQL + vortex samples even increased compared to the pre-corrosion state, which may indicate heterogeneous redistribution during electrochemical attack and possible local enrichment effects [9].

The carbon content remained elevated in the MQL method (13.57 wt.%), confirming the persistence of surface contamination from lubricant residues [14]. On the other hand, in the MQL + vortex method, the carbon level significantly decreased (3.74 wt.%), which may suggest partial removal of organic residues due to the turbulent airflow [9,14].

Oxygen levels increased in most samples, particularly in those processed using the MQL method (1.80 wt.%), suggesting the formation of oxide products after exposure to the solution [17]. Molybdenum content was highest in the emulsion-treated samples (1.82 wt.%), which may contribute to better preservation of the passive layer under these conditions [18].

3.2.2. Pit edge zone

The boundary of the corrosion pits represents a transition zone between the intact surface and the severely degraded pit bottom. EDS analysis of this region revealed intermediate values for both alloying elements and contaminants, Table 3, highlighting a gradual redistribution of elements due to localized electrochemical activity [15,18].

Table 3. *Surface chemical composition of stainless steel samples in post-corrosion testing – pit edge zone*

Cooling Medium	Fe (wt.%)	C (wt.%)	Cr (wt.%)	Ni (wt.%)	O (wt.%)	Mn (wt.%)	Mo (wt.%)	Si (wt.%)	S (wt.%)
Base material without cooling	60.25	9.63	18.58	11.03	1.48	2.10	0.90	0.20	0.18
Emulsion	65.28	2.79	17.76	7.43	1.00	2.39	0.50	0.22	0.13
MQL	63.57	10.60	16.43	11.45	2.52	2.27	0.97	0.25	0.00
MQL + vortex	55.80	11.28	15.78	10.60	2.75	1.95	1.30	0.25	0.18

Chromium and nickel values at the pit edge were, in most cases, comparable or slightly higher than on the surface, indicating partial retention of passivating elements despite local corrosion activity. For instance, the base material without cooling exhibited Cr = 18.58 wt.% and Ni = 11.03 wt.%, cromium notably higher than surface values, suggesting possible enrichment by selective dissolution [17]. In contrast, the emulsion-treated sample showed reduced values (Cr = 17.76 wt.%, Ni = 7.43 wt.%), which may indicate a more advanced loss of passivation in this zone [18].

Carbon content remained elevated across all samples, especially in MQL (10.60 wt.%) and MQL + vortex (11.28 wt.%), consistent with residual lubricant presence and partially oxidized degradation products [14,19]. The base material without cooling also exhibited elevated carbon levels (9.63 wt.%),

which may be attributed to the absence of flushing during machining, allowing thermal accumulation and adsorption of organic residues. These conditions can promote surface instability and hinder the removal of contaminant layers, resulting in persistent carbonaceous deposits at the pit edge [13,14,19].

Oxygen content increased compared to the surface zone, ranging from 1.00 to 2.75 wt.%, with the highest values recorded in MQL (2.52 wt.%) and MQL + vortex (2.75 wt.%). This trend reflects active oxide formation at the onset of passive film breakdown [17]. The progressive increase in oxygen content from surface to pit edge and further to pit bottom correlates with the degree of electrochemical activity and loss of surface protection [15].

The pit edge zone thus acts as an electrochemically unstable interface, where early signs of localized corrosion and passive film degradation are clearly detectable. Its intermediate composition reflects the combined influence of the machining process and the spatial progression of corrosion [17,18].

3.2.3. Pit bottom zone

At the bottom of the pit, the chemical composition showed the most pronounced deviations, reflecting the intensity of localized degradation caused by corrosion attack, Table 4.

Table 4. *Surface chemical composition of stainless steel samples in post-corrosion testing – pit bottom zone*

Cooling Medium	Fe (wt.%)	C (wt.%)	Cr (wt.%)	Ni (wt.%)	O (wt.%)	Mn (wt.%)	Mo (wt.%)	Si (wt.%)	S (wt.%)	Cl (wt.%)
Base material without cooling	55.13	11.83	14.03	7.20	0.60	1.27	0.67	0.37	0.00	0.20
Emulsion	65.95	1.25	15.85	10.15	0.35	1.70	1.55	0.25	0.00	0.10
MQL	61.60	8.27	14.53	9.40	1.87	1.53	0.90	0.37	0.00	0.17
MQL + vortex	0.78	51.34	0.28	0.00	24.22	0.00	0.00	0.02	1.26	1.54

Compared to the pit edge and the undamaged surface, this zone was characterized by a significant reduction in passivating elements and an increase in corrosion-related degradation products. These trends indicate the collapse of the protective film and the loss of electrochemical control at the pit bottom [17,18].

The iron content was most reduced in the MQL + vortex condition, falling to 0.78 wt.%, which is unrealistically low and likely reflects analytical artefacts due to severe pitting or poor signal quality in deep cavities. In contrast, emulsion-treated samples retained high Fe content (65.95 wt.%), indicating a more preserved metallic matrix.

Chromium levels dropped most in the MQL + vortex sample (0.28 wt.%), while more stable concentrations were observed in the emulsion (15.85 wt.%) and MQL (14.53 wt.%) samples. Nickel was fully depleted (0.00 wt.%) in the MQL + vortex condition, and strongly reduced in the no-cooling sample (7.20 wt.%), confirming significant loss of corrosion-resistant alloying elements [17,18].

The oxygen content sharply increased in the MQL + vortex condition (24.22 wt.%), reflecting intense oxide formation and accumulation of corrosion products. Carbon levels also peaked in the same condition (51.34 wt.%), far exceeding all other samples, including the no-cooling sample (11.83 wt.%), suggesting massive contamination with organic residues or analytical interference from non-metallic deposits [14,18]. In contrast, the emulsion-treated sample showed minimal carbon (1.25 wt.%), consistent with lower contamination and more stable surface chemistry.

Among alloying elements, molybdenum was best preserved in the emulsion-treated sample (1.55 wt.%), supporting its role in localized corrosion resistance [18]. Manganese and silicon remained within moderate and consistent ranges across most conditions, except for complete Mn loss in MQL + vortex, further pointing to measurement unreliability in extreme pit environments.

Chloride and sulfur were detected only in trace amounts, but the highest chloride content (1.54 wt.%) and sulfur (1.26 wt.%) were found in the MQL + vortex sample, likely reflecting local electrolyte entrapment and the presence of aggressive anions [9].

These findings confirm that the pit bottom represents the most chemically altered region, marked by severe depletion of key alloying elements and accumulation of oxides, organic residues, and aggressive anions. In the MQL + vortex condition, the original metallic surface appears fully replaced by corrosion products and lubricant remnants. Due to this extreme degradation, the EDS quantification in this zone may be significantly affected by analytical distortion and should therefore be interpreted with caution.

3.3. Correlation between surface chemistry and electrochemical parameters

The electrochemical parameters considered in this analysis include open circuit potential (*OCP*), polarization resistance (*Rp*), corrosion current density (i_{corr}), corrosion potential (E_{corr}), and corrosion rate. These parameters were previously measured and interpreted in an earlier study [5], and are now summarized in a single reference Table 5.

Table 5. *Measured electrochemical values for X2CrNiMo17-12-2 stainless steel depending on applied cooling method*

Cooling Medium	Open circuit potential, *OCP* (V)	Polarization resistance, *Rp* (kΩ)	Corrosion current density, i_{corr} (μA)	Corrosion potential, E_{corr} (mV)	Corr. Rate, (mmpy*10^{-3})
Base material without cooling	-0.0818	17.29	0.883	34.66	90.95
Emulsion	-0.0438	25.49	1.784	-29.15	41.72
MQL	-0.0750	11.26	1.445	-57.86	33.73
MQL + vortex	-0.0266	24.98	1.388	-19.33	33.66

OCP and *Rp* were obtained through non-destructive methods. The remaining values, including i_{corr}, E_{corr}, and corrosion rate, were determined using potentiodynamic polarization [17], which involves destructive testing. The current section focuses on the quantitative relationship between these electrochemical indicators and the surface chemical composition measured by EDS. The correlation analysis is carried out separately for the pre-corrosion and post-corrosion conditions, providing insight into how local chemistry influences both the stability of the passive layer and the progression of surface degradation.

The correlation analysis was conducted using the Pearson correlation coefficient [11]. Positive correlation values ($r > 0$) indicate that higher concentrations of a given element are associated with increased electrochemical parameter values, whereas negative values ($r < 0$) suggest an inverse relationship. Correlation strength is interpreted as follows: weak ($|r| < 0.5$), moderate ($0.5 \leq |r| < 0.8$), and strong ($|r| \geq 0.8$). This framework enables the identification of elements that contribute to improved passivation or, conversely, promote degradation [8,9].

3.3.1. Correlation between surface composition before corrosion and *OCP* and *Rp*

To investigate the influence of initial surface chemistry on corrosion resistance, Pearson correlation coefficients were calculated between the weight fractions of surface elements before corrosion and two key electrochemical parameters: open circuit potential (*OCP*) and polarization resistance (*Rp*) [14]. The obtained values provide insight into the contribution of each element to the stability or degradation of the passive film formed on X2CrNiMo17-12-2 stainless steel.

A visual representation of these relationships is provided in the heat map of Figure 1 with Pearson correlation coefficients, which further confirms the observed trends and clearly separates elements with positive and negative contributions to early-stage passivation.

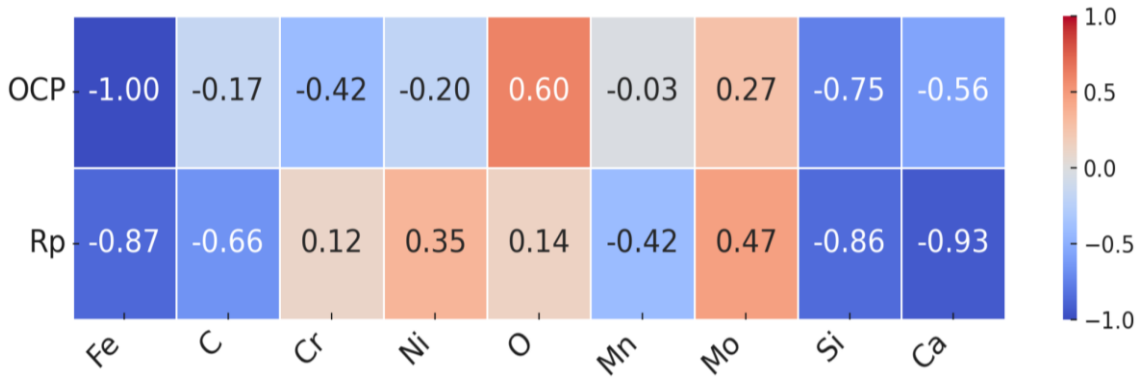


Figure 1. *Correlation between surface chemical composition before corrosion and electrochemical parameters (OCP and Rp) for X2CrNiMo17-12-2 stainless steel*

The results showed a strong negative correlation between iron and both *OCP* (r = –0.87) and *Rp* (r = –0.91), indicating that higher Fe content at the surface is associated with more active corrosion potentials and reduced resistance. This trend is consistent with previous findings suggesting that surface enrichment with base metal, often due to surface finishing or corrosion-induced segregation, can undermine passivation [9,15].

A similar negative relationship was found for silicon, which correlated negatively with both *OCP* (r = –0.75) and *Rp* (r = –0.86). Calcium followed the same pattern, showing a clear negative correlation with *OCP* (r = –0.56) and a particularly strong one with *Rp* (r = –0.93). As both elements are considered surface contaminants, their presence likely interferes with the formation of a stable passive film.

In contrast, positive correlations were observed for elements that support passivation. Molybdenum showed the strongest effect, correlating positively with *OCP* (r = 0.60) and *Rp* (r = 0.47). Chromium and nickel also exhibited favorable trends, with nickel positively correlated with *Rp* (r = 0.35), suggesting a contribution to corrosion resistance. Oxygen, as an indicator of oxide layer presence, showed a positive correlation with *OCP* (r = 0.60), reinforcing the link between surface oxidation and improved electrochemical stability.

Carbon showed a negative correlation with *Rp* (r = −0.66), which can be interpreted as an effect of surface contamination by organic residues (especially in the case of the sampel cooled with the MQL method), as well as a quantification effect where high carbon content reduces the relative shares of other elements. While some measurement artifacts cannot be excluded, the fact that samples with higher carbon consistently exhibit lower Rp values supports the functional relevance of this correlation.

3.3.2. Correlation between surface composition after corrosion and destructive electrochemical parameters

To further investigate the link between local changes in chemical composition and the severity of corrosion degradation, Pearson correlation analysis was conducted between the after corrosion weight fractions of surface elements and destructive electrochemical parameters, Figure 2. These include corrosion potentia (E_{corr}), corrosion current density (i_{corr}), and corrosion rate. The analysis focused on the pit edge zone, which was identified as the most representative region for quantifying the relationship between local chemical composition and electrochemical response, due to its intermediate position between passive and actively corroded areas [17,18]. Corresponding electrochemical values are presented in the Table 5.

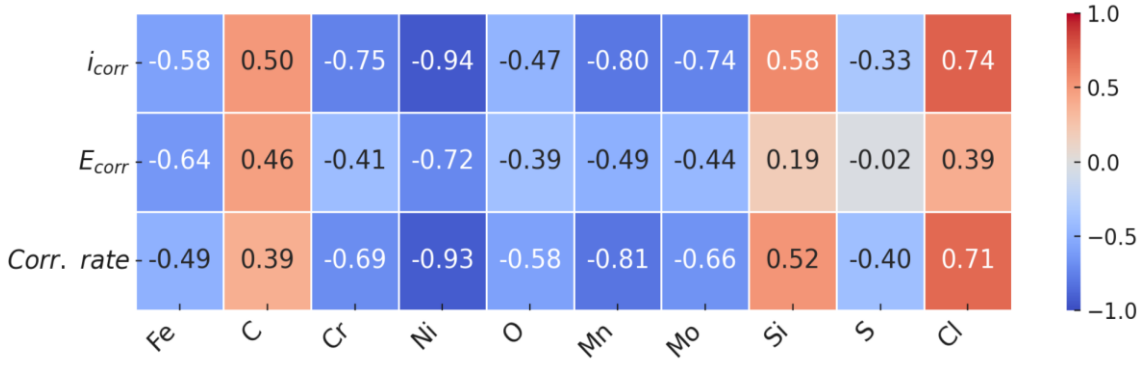


Figure 2. *Correlation between surface chemical composition after corrosion and destructive parameters for X2CrNiMo17-12-2 stainless steel*

Nickel exhibited the strongest negative correlation with all destructive parameters: i_{corr} (r = –0.94) and corrosion rate (r = –0.93). These results confirm that the depletion of nickel from the surface layer has a direct impact on passive film destabilization and increases the material's reactivity. Samples with the lowest nickel content showed the most intense degradation, highlighting its critical role in localized resistance to electrochemical activation [15].

Chromium displayed a similar trend, with correlation coefficients of –0.75 for i_{corr} and –0.69 for corrosion rate, reinforcing its essential function in maintaining a continuous and stable passive layer. This is consistent with previous observations of chromium depletion leading to increased susceptibility to intergranular and localized corrosion [8].

Although present in lower concentrations, molybdenum also showed consistent negative correlations (i_{corr}: r = –0.74; corrosion rate: r = –0.66), in line with its known role in suppressing localized corrosion, particularly in chloride-containing environments [18].

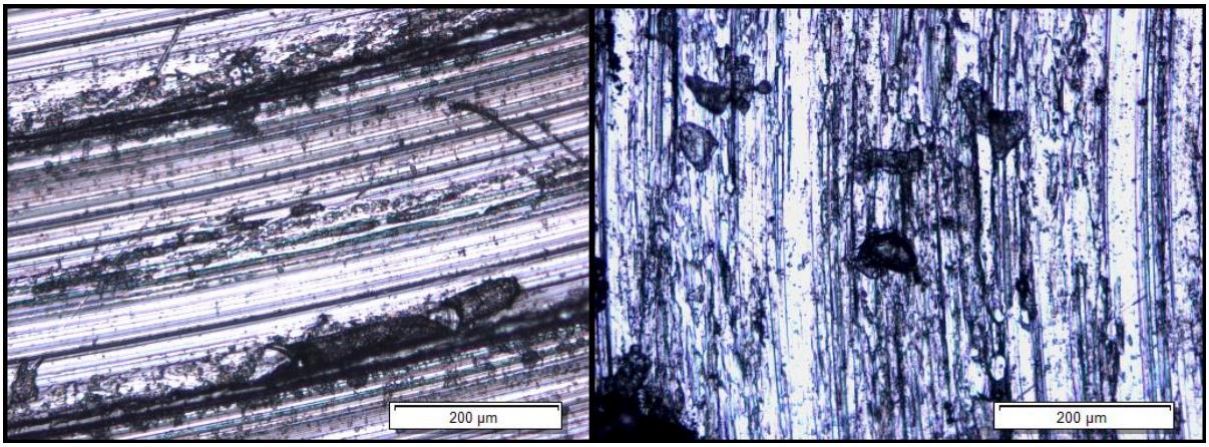
Iron also demonstrated negative correlations (i_{corr}: r = –0.58; corrosion rate: r = –0.49), but these values should be interpreted with caution. Since iron constitutes the bulk of the alloy, its relative increase after corrosion generally reflects the loss of alloying elements, rather than indicating any inherent protective contribution [9].

In contrast, carbon displayed positive correlations with both i_{corr} (r = 0.50) and corrosion rate (r = 0.39). This behavior may result from adsorbed organic residues or accumulation of degradation byproducts that fail to protect the surface and may act as local initiation sites for corrosion. Alternatively, high carbon content may obscure the presence of passivating elements, further weakening the protective character of the surface film. Such carbon enrichment was particularly noticeable in samples processed using MQL, likely due to lubricant residues [7,13].

Other elements, such as sulfur and silicon, showed weaker but still positive correlations, suggesting their possible role in destabilizing passivity or, at the very least, a lack of protective functionality under aggressive conditions [11].

3.4. SEM analysis

In our previous work, optical microscopy at a magnification of 10x was used to examine the X2CrNiMo17-12-2 steel surface before and after corrosion testing, Figure 3. The pre-corrosion surface, while marked by the characteristic grooves and ridges from the machining process, showed no signs of corrosion. After the corrosion testing, the optical images revealed the formation of localized pits, highlighting the difference between the original machined texture and the new corrosion sites. This pattern was consistently observed across all samples, regardless of the cooling method used, confirming that the formation of pits and the changes in surface texture were uniform across different conditions [5].



a) b)

Figure 3. *Optical microscopy images of the samples before (a) and after (b) the corrosion measurements, captured with 10x magnification*

In this analysis, we utilized scanning electron microscopy (SEM) to examine the surface morphology of X2CrNiMo17-12-2 stainless steel samples both before and after corrosion testing. The post-corrosion surface was further divided into three specific zones: the surface, which remained relatively inactive; the pit edge, where corrosion activity increased; and the pit bottom, which showed the most pronounced corrosion effects.

For the SEM analysis, we selected representative images from the emulsion-treated samples, as they best illustrate the observed patterns, Figures 4 - 7. These images include both the surface morphology and the corresponding EDS data, allowing us to directly compare the visual and chemical changes. Before corrosion, the surface morphology and composition appear uniform, with a machined texture, Figure 4.

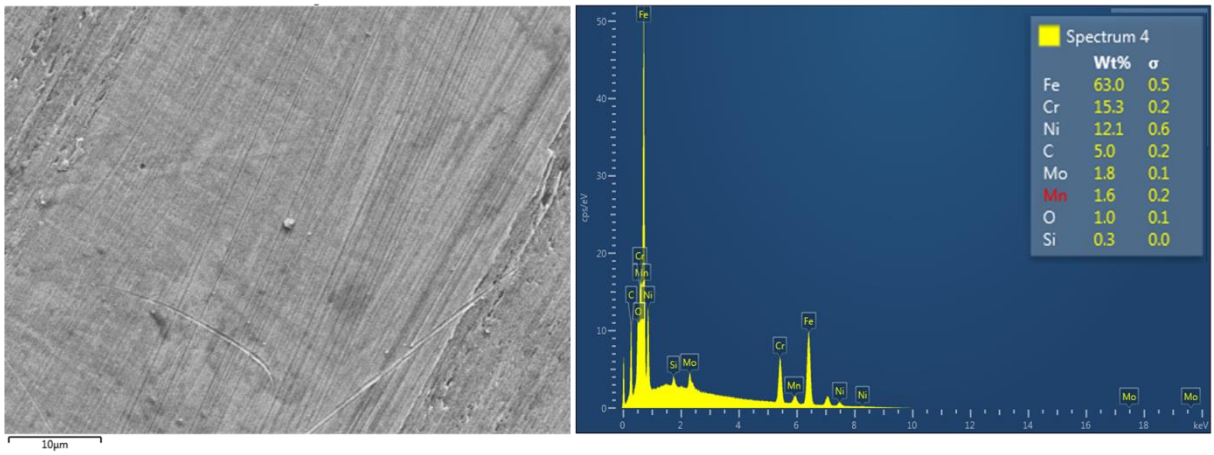


Figure 4. *SEM image and corresponding EDS analysis of the X2CrNiMo17-12-2 stainless steel pre-corrosion surface*

When examining the post-corrosion surface, the SEM images reveal that the surface appears almost identical to its pre-corrosion state. There are no visible signs of widespread damage, aside from the lines resulting from the initial mechanical machining process, Figure 5. In terms of chemical composition, the surface remains nearly identical, with only minimal changes. The only noticeable difference is observed in the samples that used organic lubricants, where an increased carbon content was detected.

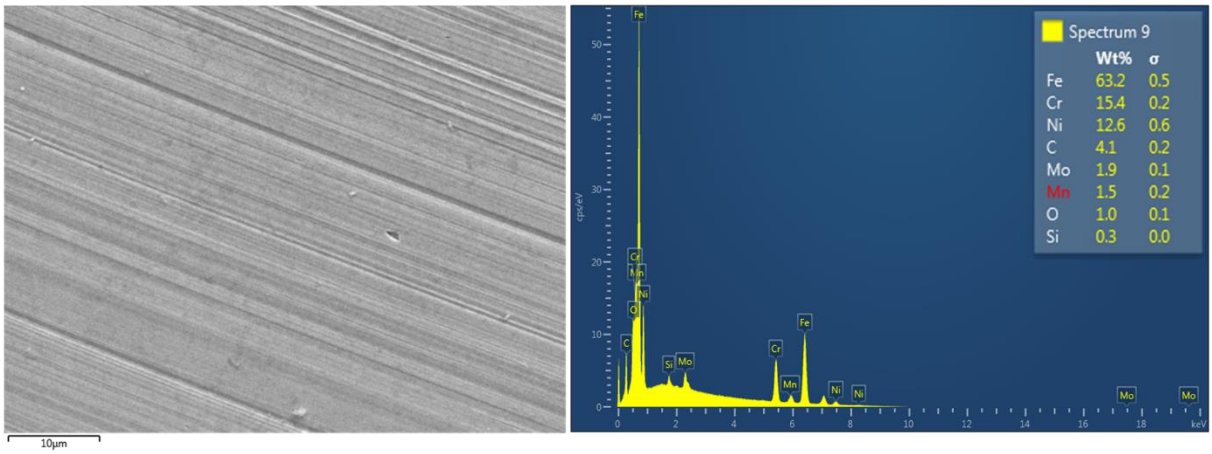


Figure 5. *SEM image and corresponding EDS analysis of the post-corrosion surface zone of X2CrNiMo17-12-2 stainless steel*

The SEM images of the pit edge clearly reveal a distinct visual boundary between the relatively intact surface and the onset of localized degradation, almost like a sharp edge marking the drop into a pit, Figure 6. This morphological transition reflects the breakdown of the passive layer at that point. The texture becomes visibly rougher and less defined, indicating that corrosion has started to progress.

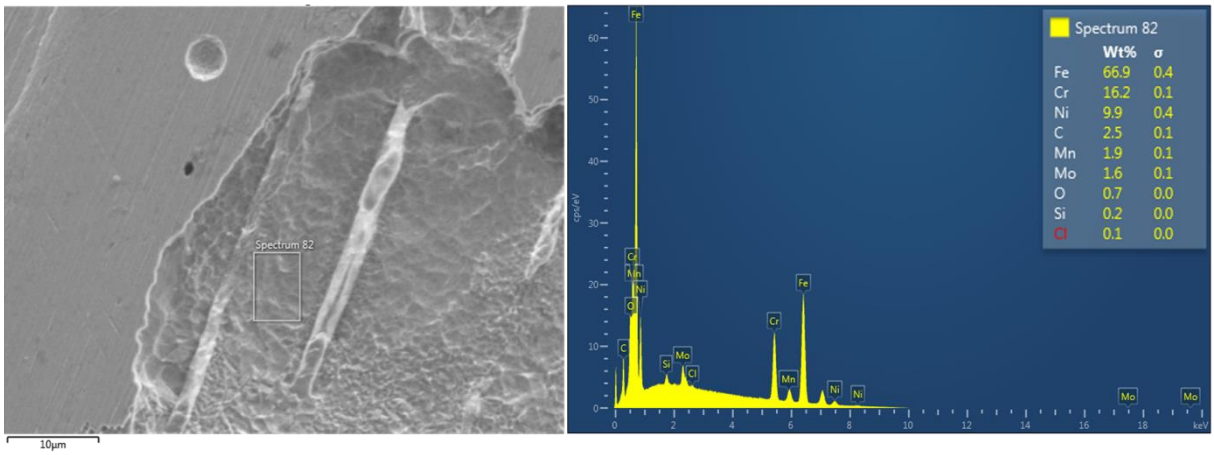


Figure 6. *SEM image and corresponding EDS analysis of the pit edge zone on X2CrNiMo17-12-2 stainless steel post-corrosion testing*

This visual boundary is supported by EDS analysis, which shows an increased iron content and a simultaneous reduction in oxygen at the pit edge. At the same time, the levels of chromium and nickel remain comparable to those on the general surface. This suggests that while early corrosion processes have initiated, the passive film is only partially degraded. The continued presence of key passivating elements contributes to a certain degree of residual protection, which limits the spread of corrosion and helps maintain its localized character in this region [15,18].

The SEM images of the pit bottom reveal the most severe morphological changes observed across all examined zones, Figure 7. The surface in this area appears highly irregular, with pronounced roughness and a complete loss of the original machining pattern. This degraded texture is a clear indication of advanced material dissolution.

EDS analysis supports these findings. Significant reductions in, nickel, molybdenum, and oxygen content were observed. Notably, chromium and manganese were the only alloying elements that increased in relative content, with chromium showing the most pronounced enrichment. This likely

reflects the preferential dissolution of more reactive elements, leaving behind residues of more corrosion-resistant species [8,18].

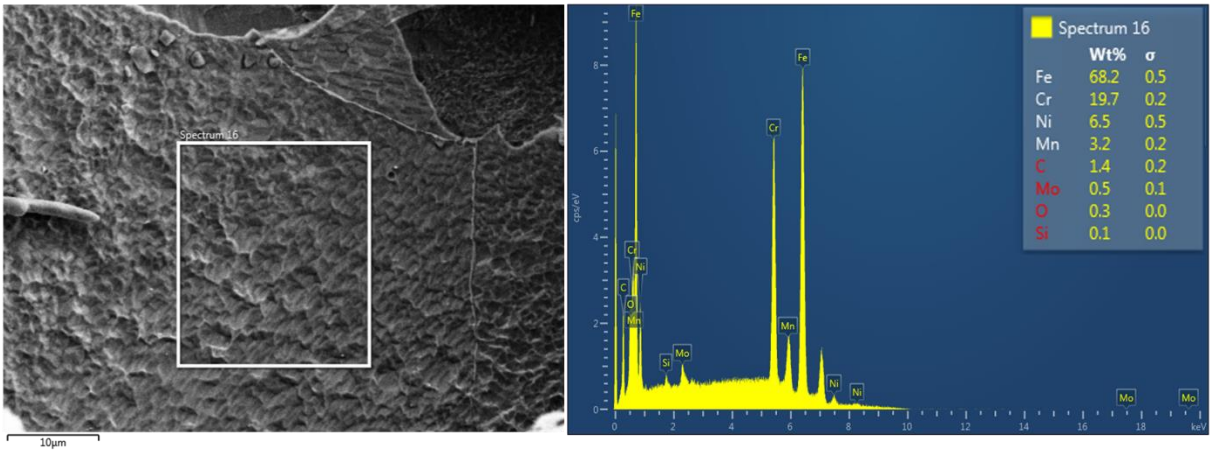


Figure 7. *SEM image and corresponding EDS analysis of the pit bottom on X2CrNiMo17-12-2 stainless steel post-corrosion testing*

Corrosion at the pit bottom is not confined but widespread within the entire zone, indicating complete loss of passivation and unrestricted corrosion progression [17,18].

4. Conclusion

This study confirmed that machining-induced surface chemistry has a decisive influence on the corrosion behavior of X2CrNiMo17-12-2 stainless steel. EDS analysis revealed that both the applied cooling method and subsequent exposure to a chloride-containing environment significantly altered the distribution of alloying and contaminant elements. Localized corrosion consistently developed in the form of pits, with measurable differences in chemical composition between the undamaged surface, the pit edge, and the pit bottom. SEM imaging reinforced these distinctions by clearly visualizing the morphological transition across zones and confirming the increasing severity of degradation from surface to pit interior [14,15].

The applied cooling method significantly influenced both the elemental composition and the electrochemical behavior of the machined surfaces. Emulsion-treated samples retained higher concentrations of chromium, nickel, and molybdenum. Key elements for the formation and stability of the passive film correspondingly exhibited more positive open circuit potentials, higher polarization resistance, and lower corrosion rates. In contrast, machining without cooling and MQL led to increased surface contamination with carbon and a marked depletion of passivating elements, which coincided with more negative potentials and elevated corrosion activity [4,14]. However, the MQL + vortex method achieved the lowest overall corrosion rate among all tested conditions [5], while simultaneously reducing surface carbon and promoting oxygen enrichment, indicating effective surface passivation. Despite these advantages, its performance at the pit bottom raised concerns, as EDS analysis revealed extreme deviations in elemental composition, including unrealistically low iron and nickel values and abnormally high carbon and oxygen levels [14]. These findings may reflect analytical artifacts caused by intense localized corrosion or topographical effects.

Correlation analysis confirmed that higher concentrations of Cr, Ni, Mo, and O are associated with better corrosion resistance, while enrichment in C and Fe correlates with passive film breakdown and increased electrochemical reactivity. Among the analyzed zones, the pit edge proved most reliable for interpreting localized degradation processes, capturing both the onset of corrosion and redistribution of critical elements [11,14].

In conclusion, the MQL + vortex method demonstrated the lowest overall corrosion rate [5] and clear environmental advantages, indicating strong potential for enhancing corrosion performance through

improved surface passivation. However, its behavior in severely corroded regions showed pronounced local deviations in chemical composition [14]. In contrast, emulsion cooling provided the most uniform and chemically stable surface across all zones, with consistent retention of protective elements and reliable electrochemical indicators. Together, these findings suggest that while MQL + vortex represents a promising and sustainable alternative, emulsion remains the most predictable and balanced option under the tested conditions. Further surface-sensitive investigations are recommended to better understand localized effects and support the refinement of cooling strategies in stainless steel machining.

Acknowledgments

This work has been partially supported by University of Rijeka, grant number uniri-mladi-technic-23-26 and grant number uniri-iskusni-tehnic-23-293.

References

[1] SreeMetaliks. A Comprehensive Guide to 316L Stainless Steel: The Differences, Properties, and Benefits.

[2] Rede, V., 2017. Nehrđajući čelici. Sveučilište u Zagrebu, FSB, Zagreb

[3] British Stainless Steel Association (BSSA). General principles of machining stainless steels.

https://bssa.org.uk/bssa_articles/general-principles-of-machining-stainless-steels/ (accessed 10 June 2025).

[4] Kopac, J., Pusavec, F., 2009. Concepts of Sustainable Machining Processes. 13th International Research/Expert Conference ”Trends in the Development of Machinery and Associated Technology” TMT 2009, Hammamet, Tunisia

https://sreemetaliks.com/blog/a-comprehensive-guide-to-316l-stainless-steel-the-differences-properties-and-benefits (accessed 10 June 2025).

[5] Kvrgić, D., Šterpin Valić, G., Fonović, M., Cukor, G., 2024. Influence of cutting fluids on the corrosion resistance of X2CrNiMo17-12-2 austenitic stainless steel, Proceedings of 13th International Conference Mechanical Technologies and Structural Materials 2024, MTSM 2024, FESB Split

[6] EN 10088-1:2014 (CEN): Stainless steels – Part 1: List of stainless steels.

[7] Šterpin Valić, G., Kostadin, T., Cukor, G., Fabić, M., 2023. Sustainable Machining MQL Technique Combined with the Vortex Tube Cooling When Turning Martensitic Stainless Steel X20Cr13, Machines 2023, 11(3), 336.

[8] Matula, M., Hyspecka, L., Svoboda, M., Vodarek, V., Dagbert, C., Galland, J., Stonawska, Z., Tuma, L. 2001. Intergranular corrosion of AISI 316L steel. Materials Characterization, 46 (2-3), 203-210.

[9] Burstein, G. T., Pistorius, P. C., 1995. Surface Roughness and the Metastable Pitting of Stainless Steel in Chloride Solutions. CORROSION, 51 (5), 380–385.

[10] DelVecchio, E., Liu, T., Chang, Y., Nie, Y., Eslami, M., Charpagne, M. A., 2024. Metastable cellular structures govern localized corrosion damage development in additive manufactured stainless steel. npj Materials Degradation, 8, 45.

[11] Wang, S., Hu, Y., Fang, K., Zhang, W., Wang, X., 2017. Effect of surface machining on the corrosion behaviour of 316 austenitic stainless steel in simulated PWR water. Corrosion Science, 126, 104-120.

[12] Zhang, H., Huang, W., Wei, H., Chen, Z., Cao, J., Tang, Y., Zhao, X., Zuo, Y., 2022. Effect of HAc on the Metastable Pitting Corrosion of 304 SS in NaCl Solution. Materials, 15, 3618.

[13] Cukor, G., Šterpin-Valić, G., Kostadin, T., Fabić, M., 2019. Sustainable Turning of Martensitic Stainless Steel. Transactions of FAMENA, 43 (3).

[14] Brinksmeier, E.; Meyer, D.; Huesmann-Cordes, A. G.; Herrmann, C. Metalworking Fluids—Mechanisms and Performance. CIRP Ann. 2015, 64, 605–628. https://doi.org/10.1016/j.cirp.2015.05.003

[15] Clark, R.N.; Chan, C.M.; Walters, W.S.; Engelberg, D.; Williams, G. Intergranular and Pitting Corrosion in Sensitized and Unsensitized 20Cr–25Ni–Nb Austenitic Stainless Steel. Corrosion 2021, 77, 552–563. https://doi.org/10.5006/3725

[16] Grandy, L.; Yassine, S. R.; Lacasse, R.; Mauzeroll, J. Selective Initiation of Corrosion Pits in Stainless Steel Using Scanning Electrochemical Cell Microscopy. Anal. Chem. 2024, 96, 7394–7400. https://doi.org/10.1021/acs.analchem.3c04637

[17] Sedriks, A.J. Corrosion of Stainless Steels, 2nd ed.; Wiley: New York, NY, USA, 1996; pp. 242–244.

[18] Sun Q, Xie F, Zhang Y, Wang D, Wu M. Stability of passive film and pitting susceptibility of 316L stainless steel in the aggressive oilfield environment containing Cl^-–CO_2–O_2. Electrochim Acta. 2024;499:144709. https://doi.org/10.1016/j.electacta.2024.144709

[19] Zhang, H.; Huang, W.; Wei, H.; Chen, Z.; Cao, J.; Tang, Y.; Zhao, X.; Zuo, Y. Effect of HAc on the Metastable Pitting Corrosion of 304 SS in NaCl Solution. Materials 2022, 15, 3618. https://doi.org/10.3390/ma15103618

Impact of caliber height reduction on roll fatigue life

***Francisko Lukša*[1], *Željko Domazet*[2] *and Đorđe Dobrota*[1]**

1) Pomorski fakultet Split, Ruđera Boškovića 37, Split, Croatia

2) Fakultet Elektrotehnike, Strojartva i Brodogradnje, Ruđera Boškovića 32, Split, Croatia

Corresponding author: fluksa1@pfst.hr

Original scientific article

Abstract: Profile rolls in rolling mills shape metal by reducing cross-sectional area and elongating its length. The dimensions of each caliber are chosen within technological limits. During the rolling process, significant forces act on the calibrated rolls, potentially leading to rotational bending fatigue in the roll necks and grooves. This study examines how reducing caliber height affects rolling forces and the corresponding roll fatigue life.

The fatigue life of the rolls in an eight-pass, three-roll mill was estimated using local stresses determined by finite element analysis. Three critical areas were identified: the roll neck, box caliber, and square caliber. Caliber height was adjusted in the first five passes based on technological parameters to assess its impact on fatigue life. As a result of this calibration change, the service life of the roll neck and box caliber may be extended by 40%. Meanwhile, for pass groove 7a, identified as the most susceptible to fatigue failure among the analyzed grooves, the service life of the associated caliber can be extended by more than 300%.

Keywords: *calibrated rolls; calibre height; rolling forces; local stress; fatigue life*

1. Introduction

Profile or calibrated rolls are used in the rolling mill process to shape metal workpieces by reducing their cross-sectional area while simultaneously elongating their length. These rolls have grooves on their working surfaces, and the grooves in two rolls placed one above the other form the calibers. The design and arrangement of these grooves are crucial, as they determine the final shape and dimensions of the rolled product. A standard arrangement of these grooves is shown in Figure 1, and the rolling schedule and parameters are presented in Table 1 [1].

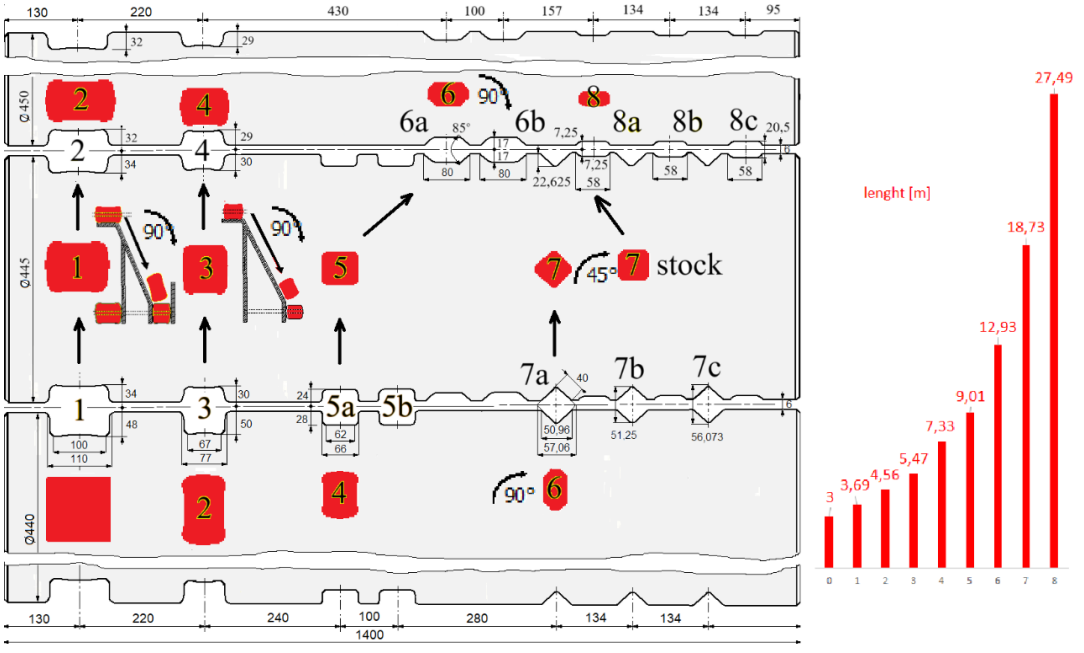


Figure 1. *Arrangement of the grooves*

***Table 1**. Rolling passes*

Pass No.		1	2	3	4	5	6	7	8
Pass shape		box	box	box	box	box	oval	square	oval
Pass size [mm]		100x82	100x66	67x80	67x59	66x52	80x34	40	58x20
Cross-section [mm^2]	9850	8015	6474	5398	4032	3280	2286	1578	1075
Width [mm]	100	104	108	71	76	65	82,5	53,5	60,5
Height before pass h_0 [mm]		100,0	82,0	108,0	80,0	76,0	52,0	82,5	40,0
Height after pass h_1 [mm]		82,0	66,0	80,0	59,0	52,0	34,0	51,0	20,5
Absolute draught Δh [mm]		18,0	16,0	28,0	21,0	24,0	18,0	31,5	19,5
Absolute reduction [mm^2]		1835	1541	1076	1366	752	994	708	503
Elongation coefficient		1,23	1,24	1,20	1,34	1,23	1,43	1,45	1,47
Working diameter [mm]		372,5	393,5	372,5	398,5	396,5	419,5	397,25	433
Roll speed [rpm]		120	120	120	120	120	120	120	120
Stock length [m]	3	3,69	4,56	5,47	7,33	9,01	12,93	18,73	27,49
Arc-contact projected length [mm]		57,84	56,10	72,08	64,68	68,97	61,44	79,10	64,97
Projected area of contact [mm2]		5900	5947	4938	4754	4276	4531	3461	3265
Rolling speed [ms-1]		2,33	2,62	2,42	2,77	2,55	2,78	2,7	2,89
Rolling time [s]		1,58	1,74	2,26	2,65	3,53	4,65	6,92	9,52
Pause [s]		3	3	3	3	3	3	3	3
Roll speed [rpm]		120	120	120	120	120	120	120	120

At the beginning of the rolling sequence, the first billet passes through eight passes. As the length of the rolled piece increases with each caliber pass, the rolling time also increases, as shown in Table 1 and illustrated in Figure 2.

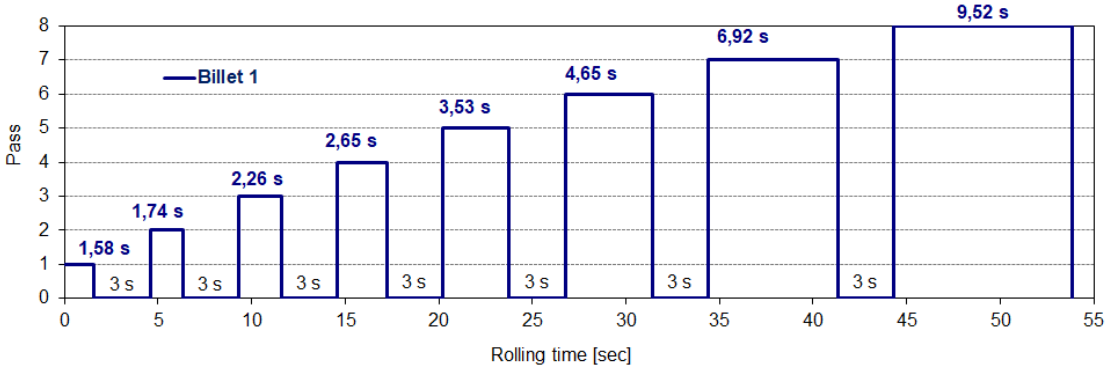


***Figure 2**. Rolling of first billet*

Rolling was typically performed with two billets, though three were used in some instances. Figure 3 illustrates the rolling process with three billets. The second billet begins its first pass at 20.23 seconds, simultaneously with the first billet in its fifth pass. The third billet begins rolling at approximately 52 seconds.

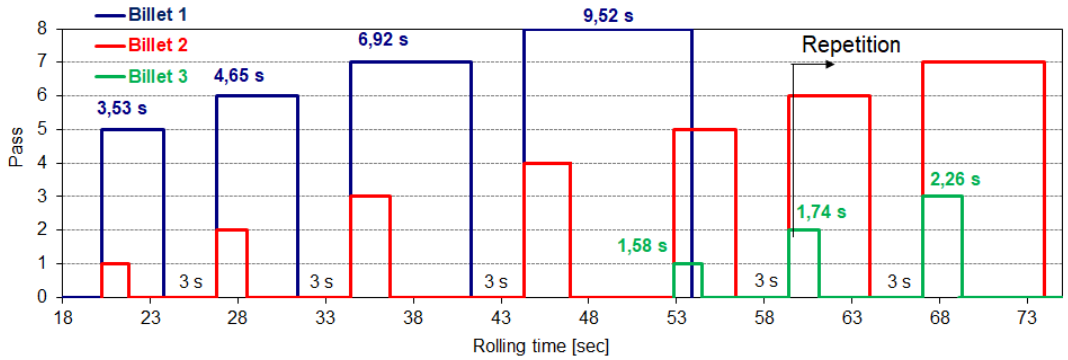


***Figure 3**. Rolling with two and three billets*

2. Rolling forces

During the rolling process, due to the reduction in stock height from h_0 to h_1 within the calibers, (Figure 1), the profile rolls are subjected to significant forces generated in each caliber. These forces can lead to rotational bending fatigue in both the roll necks and the grooves, as illustrated in Figure 4.

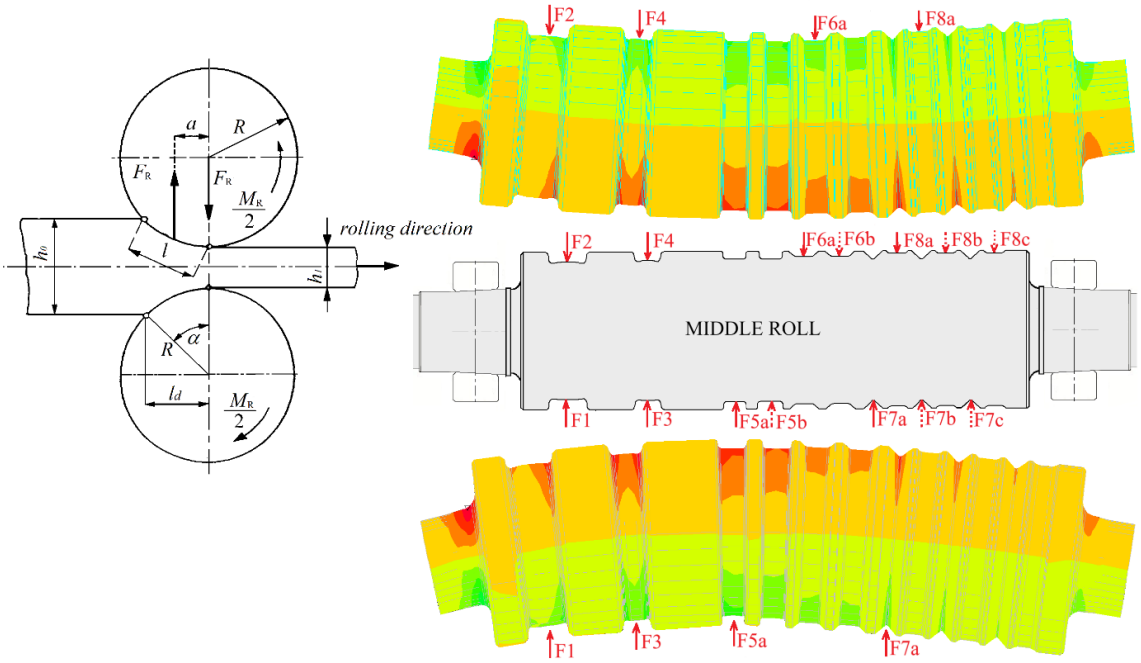


Figure 4. *Forces on upper, middle and lower roll*

Expressions for calculating rolling forces F_v [kN] can be found in [2] in which it is expressed as:

$$F_v = p_{sr} \cdot A \tag{1}$$

where A [mm^2] is the horizontal projection of the contact surface between the metal material and the rolls, and p_{sr} [MPa] is the mean specific pressure of the deformed metal surface on the rolls.
The contact surface of the metal with the rollers represents the surface of a trapezoid and is calculated from the expression:

$$A = \frac{b_0+b_1}{2} \cdot l_d \ , \tag{2}$$

where are:
b_0 – width of the workpiece *before pass*, b_1 - width of the workpiece *after pass* and
l_d – length of the deformation zone.

The length l_d (Figure 4) is calculated using the following expression:

$$l_d = \sqrt{R\Delta h} \tag{3}$$

where Δh is the difference between the height of the workpiece before the pass, h_0 [mm], and the height of the workpiece after the pass, h_1 [mm].

$$\Delta h = h_0 - h_1. \tag{4}$$

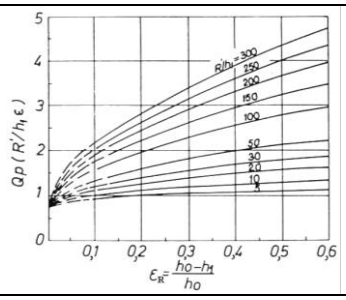
In case of a larger difference in the diameters of the rolls, the length of the deformation zone - l_d according to the literature [2] is calculated from the expression:

$$l_d = \sqrt{\frac{2R_1R_2}{R_1+R_2}\Delta h}, \tag{5}$$

where R_1 and R_2 are the radii of the rolls.

Table 2 presents several fundamental formulas for calculating the average specific pressure p_{sr} exerted by the deformed metal surface on the rolls during hot rolling, as provided in [2].

Table 2. *Basic expressions of Tselikov, Korolev, Sims, and Siebel*

Tselikov	$p_{sr}{}^{Tsel} = k \cdot \frac{2h_N}{\Delta h(\delta-1)}\left[\left(\frac{h_N}{h_1}\right)^{\delta} - 1\right]$ $h_N = h_1\left[\frac{1+\sqrt{1+(\delta^2-1)\left(\frac{h_0}{h_1}\right)}}{\delta+1}\right]^{\frac{1}{\delta}}$ $\delta = \frac{2f \cdot l_d}{\Delta h}$	k = 1 ÷ 1.155 k_f, k_f - experimental plastic yield stress $f = a_e$ (1,05 - 0,0005t) a_e=0,8 -factor of roll material t - temperature [°C] $h_{sr} = (h_0 + h_1)/2$	$p_{sr} = p_{sr}{}^{Tsel} \cdot n_k \cdot n_{vz}$ n_k – influence of caliber n_k=1,1÷1,2 for box shape n_k=1,2÷1,3 for romb and oval shape $n_{vz} = \sqrt[4]{\frac{h_{sr}}{l_d}}$ - influence of external zone
Korolev	$p_{sr}{}^{Kor} = k \cdot (1 + \frac{f}{2} \cdot \frac{l_d}{h_{sr}})$	k = 1 ÷ 1.155 k_f, k_f - experimental plastic yield stress $f = a_e$ (1,05 - 0,0005t) a_e=0,8 -factor of roll material t - temperature [°C] $h_{sr} = (h_0 + h_1)/2$	$p_{sr} = p_{sr}{}^{Kor} \cdot n_k \cdot n_{vz}$ n_k – influence of caliber n_k=1,1÷1,2 for box shape n_k=1,2÷1,3 for romb and oval shape $n_{vz} = \sqrt[4]{\frac{h_{sr}}{l_d}}$ - influence of external zone
SIms	$p_{sr}{}^{Sim} = k \cdot b_m \cdot \sqrt{R\Delta h} \cdot Q_P$	k = 1 ÷ 1.155 k_f, k_f - experimental plastic yield stress b_m – average width	
Siebel	$p_{sr}{}^{Sib} = k_f \cdot n_k \cdot C_{v/D}$	k_f - experimental plastic yield stress n_k – influence of caliber n_k=1,1÷1,2 for box shape n_k=1,2÷1,3 for romb and oval shape	$C_{v/D}$ v [m/s] | 1÷2 | 2÷5 | 5÷10 | 10÷20 | 20÷50 $C_{v/D}$ | 1 | 1,1 | 1,2 | 1,35 | 1,5

The rolling forces calculated using the approaches of Tselikov, Korolev, Sims, and Siebel align well with experimental data for the first six passes and the eighth pass [3], as confirmed by the diagrams in Figure 5 and the data in Table 3.

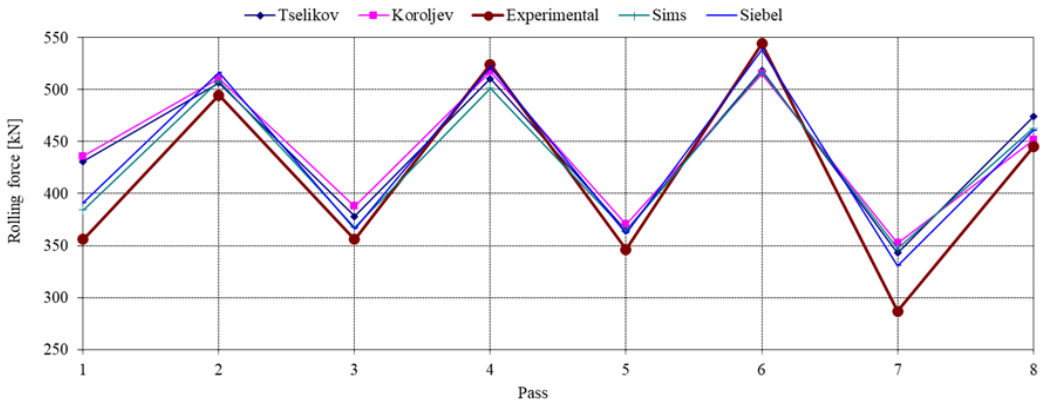


Figure 5. *Calculated and measured rolling forces*

Table 3. *Calculated and measured rolling forces*

Pass	No.1	No.2	No.3	No.4	No.5	No.6	No.7	No.7
Experimental [kN]	356,1	494,6	356,1	524,2	346,2	544,0	286,8	445,1
Tselikov F_{Tsel} [kN]	430,7	506,3	377,9	510,3	364,2	518,4	342,8	473,7
Koroljev F_{Kor} [kN]	436,0	510,5	387,8	517,2	370,4	515,2	352,3	451,6
Sims F_{Sim} [kN]	384,0	508,1	367,7	501,2	363,5	517,0	347,1	462,5
Siebel F_{Sib}[kN]	391,2	516,2	366,1	521,7	361,9	538,1	330,6	460,5

In the box and oval passes, the contact surface between the rolls and the workpiece is well-defined, resulting in a shape that closely resembles the desired flat profile. In contrast, during the seventh pass, the square cross-section causes uneven deformation of the workpiece, leading to significant pressure variations on the rolls and increased frictional forces along the sides of the caliber.
The deviations between the forces calculated using the approaches of Tselikov, Korolev, Sims, and Siebel and the experimentally determined values are presented in Table 4.

Table 4. *Deviations of computationally determined forces from experimentally determined forces*

Pass	No.1	No.2	No.3	No.4	No.5	No.6	No.7	No.8
Tselikov F_{Tsel}	21,0%	2,4%	6,1%	-2,6%	5,2%	-4,7%	19,5%	6,4%
Koroljev F_{Kor}	22,4%	3,2%	8,9%	-1,3%	7,0%	-5,3%	22,8%	1,5%
Sims F_{Sim}	7,8%	2,7%	3,3%	-4,4%	5,0%	-5,0%	21,0%	3,9%
Siebel F_{Sib}	9,9%	4,4%	2,8%	-0,5%	4,5%	-1,1%	15,3%	3,5%

3. Local stresses

The finite element method was applied to evaluate the stress distribution in critical regions, using experimental force data listed in Table 3. The linear-elastic model, shown in Figure 6, consists of 3D solid elements with eight nodes and three degrees of freedom for translation. It is constrained at both ends along its axis, with forces applied at the nodes. Figure 6 presents the rolling forces acting during Passes 1 and 2.

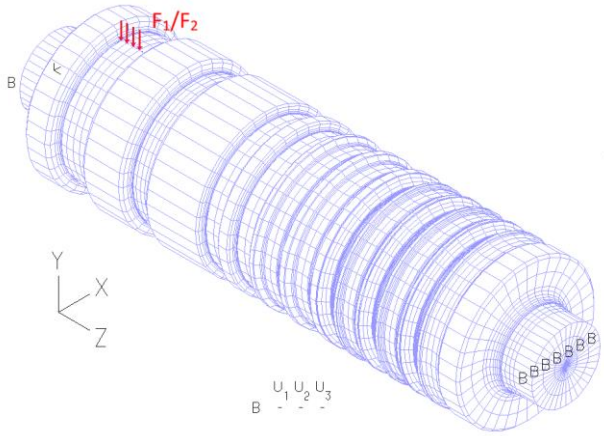


Figure 6. *Numerical model*

The study involved a comprehensive numerical analysis of 28 loading conditions defined by the rolling schedule, Table 5. Finite element method (FEM) simulations identified critical stress concentration areas on the roll: the neck, groove 3–4, and groove 7a. The stress concentration factors observed in these regions align well with values reported in the literature [4,5]. The maximum stresses on the middle roll appear at the neck near Pass 1, as well as at Passes 3–4 and 7a, corresponding to rolling in Passes 4 and 8a, and Passes 2 and 6a, respectively, as illustrated in Figure 7.

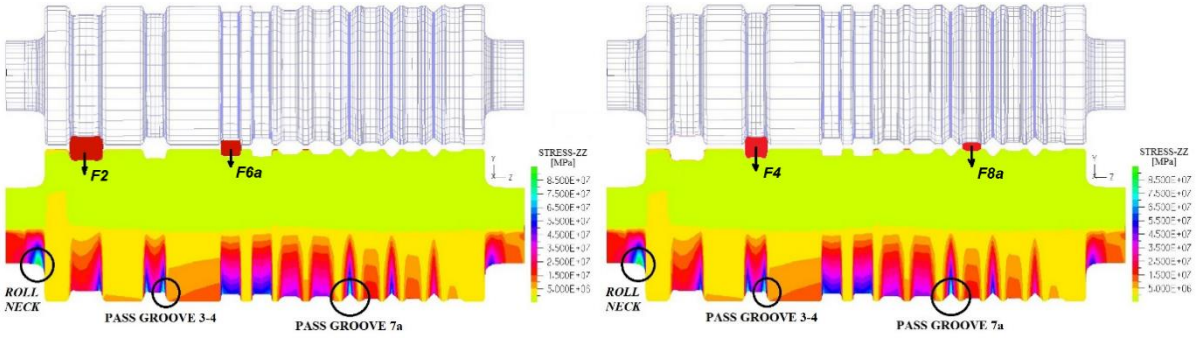


Figure 7. *Local stresses on the middle roll*

Table 5. *Local stresses at the roll neck and in the groove passes 3-4 and 7a*

Local stresses [MPa]				Local stresses [MPa]			
Force	Roll neck	Pass groove 3-4	Pass groove 7a	Forces acting together	Roll neck	Pass groove 3-4	Pass groove 7a
F_1 = *356,1* kN	41,4	25	12	$F_1 + F_{5a}$	68,8	64	46
F_2 = 494,6 kN	57,4	34	17	$F_1 + F_{5b}$	66	60	51
F_3 = *356,1* kN	36	43	23	$F_1 + F_{6a}$	91,8	83	85
F_4 = *524,2* kN	53	63	33	$F_1 + F_{6b}$	87	76	90
F_{5a} = *346,2* kN	27	39,6	33	$F_3 + F_{7a}$	49	61,8	62
F_{5b} = *346,2* kN	25	35	38,5	$F_3 + F_{7b}$	46	57,2	56
F_{6a} = *544* kN	34	49	67,8	$F_3 + F_{7c}$	43	52,6	46
F_{6b} = *544* kN	30	42	73	$F_4 + F_{8a}$	71	88.9	90
F_{7a} = *286,8* kN	13	19	38,5	$F_4 + F_{8b}$	66	81,7	77
F_{7b} = *286,8* kN	10	14	32	$F_4 + F_{8c}$	61	74,6	61
F_{7c} = *286,8* kN	6,9	9,7	22	$F_1 + F_{5a} + F_{8a}$	50,2	38	9,5
F_{8a} = *445,1* kN	18	26	56	$F_1 + F_{5a} + F_{8b}$	55,3	45	7,2
F_{8b} = *445,1* kN	13	19	43	$F_1 + F_{5b} + F_{8b}$	52,3	31	8,8
F_{8c} = *445,1* kN	8,1	11	26	$F_1 + F_{5b} + F_{8c}$	57,4	48	25

3.1. Stress spectrum

Numerically determined local stresses at three critical sections (Table 4), together with the rolling time schedule (Table 1), were applied to define the stress spectrum at these locations—first for a single billet, and then for 4,000 rolling tons, representing the wear limit before remachining. Figure 8 shows the stress spectra at the roll neck, in grooves 3 and 4, and in groove 7a. The SN curve of the material is taken from the literature [6].

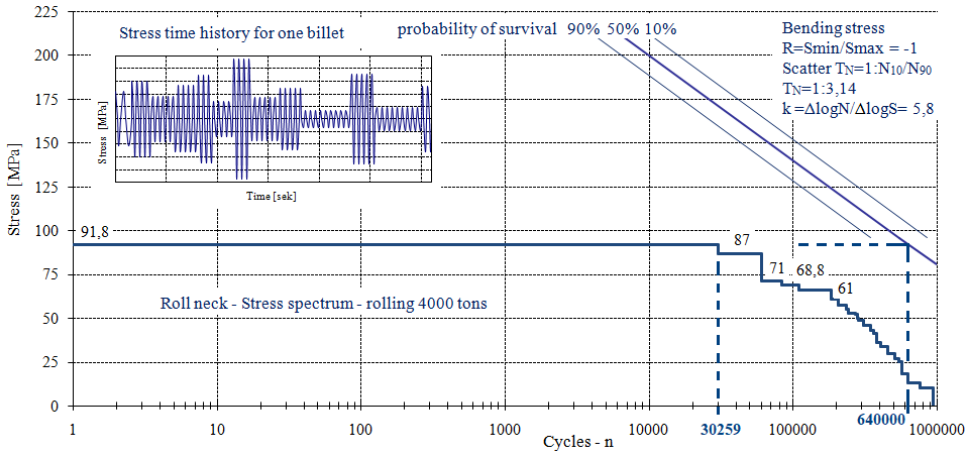


Figure 8.a *Stress spectra on roll neck*

From Table 5, it is evident that the stress on the roll neck reaches 91.8 MPa during rolling in the 2nd and 6th calibers. Over 4,000 tons rolled, the roll neck undergoes 30,256 cycles at this stress level, as shown in Figure 8.a. The material's fatigue limit indicates that it can withstand up to 640,000 cycles at 91.8 MPa without failure. Therefore, the ratio of the fatigue limit to the actual number of cycles is approximately 21.

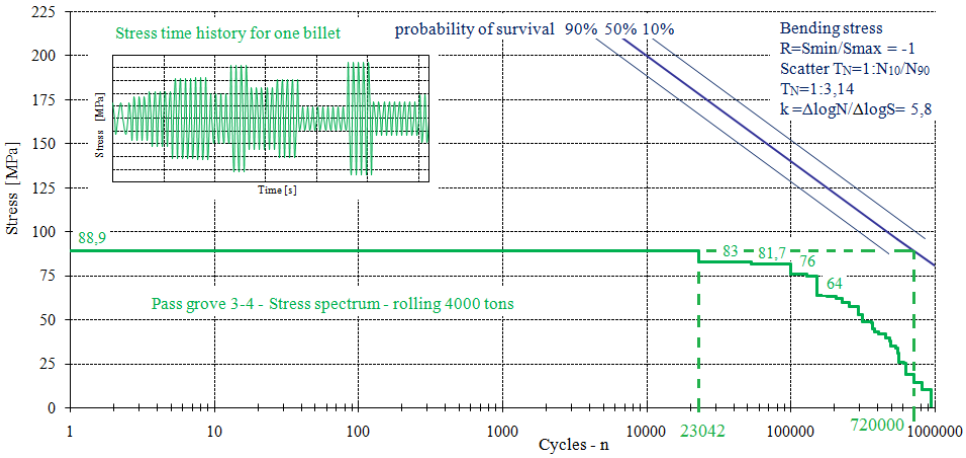


Figure 8.b *Stress spectra on pass groove 3-4*

Similarly, at pass groove 3-4, the maximum stress reaches 88.9 MPa during rolling at calibers 4 and 8. After rolling 4.000 tons, pass groove 3-4 undergoes 23,042 cycles at this stress level, as illustrated in Figure 8.b. Given that the fatigue limit at 88.9 MPa is 720,000 cycles, the resulting ratio is approximately 31, indicating a greater fatigue life margin compared to the roll neck.

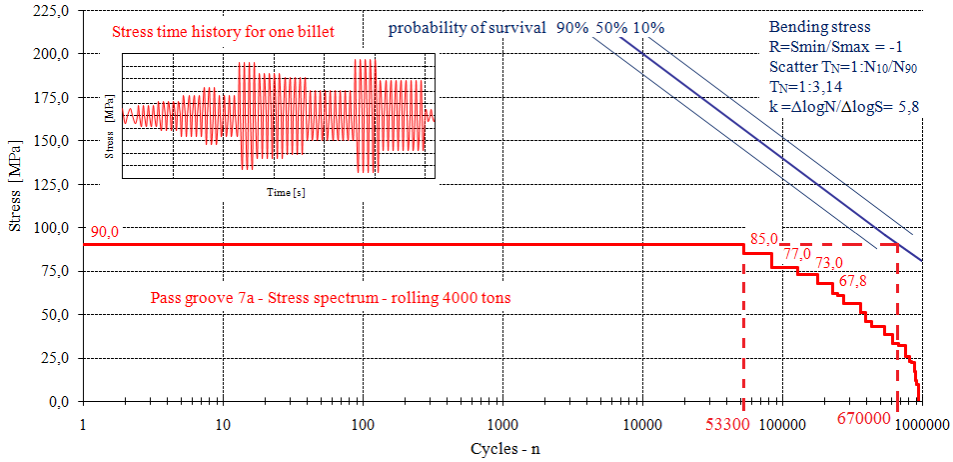


Figure 8.c *Stress spectra on pass groove 7a*

In the case of pass groove 7a, the maximum stress reaches 90 MPa during rolling at calibers 4 and 8a, as well as calibers 2 and 6b. At this stress level, pass groove 7a undergoes 53.300 cycles for 4.000 tons rolled, as shown in Figure 8.c. With a fatigue limit of 700.000 cycles at 90 MPa, the corresponding ratio is approximately 13, indicating that pass groove 7a is the most sensitive to fatigue failure among the analyzed grooves.

4. Caliber height reduction change

By changing the height of the selected caliber, the corresponding draught (reduction height) also changes, while the overall layout of the caliber remains unchanged. The allowable draught is limited by the maximum angle of contact. The maximum allowable draught can be determined using expression [2]:

$$\Delta h_{\max} = D \cdot (1 - \frac{1}{\sqrt{1 + tg^2 \alpha_{\max}}}) \quad (1)$$

where *D* is diameter [mm] of the work roll in contact and α is contact angle in degrees, Figure 4.

The draught is taken as $\Delta h = h_0 - h_1 \leq (0.8–0.9) \cdot \Delta h_{max}$ [2].

According to Z.& R. Wusatowski [2], the friction coefficient and contact angle depend on the rolling speed, Figure 9.

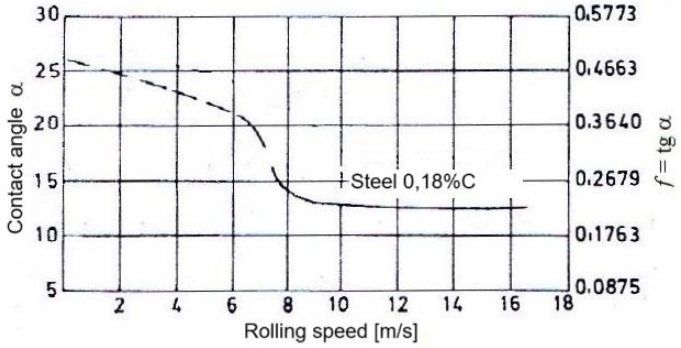


Figure 9. *Variation of angle of contact with rolling speed in grooved rolls, Z.i R.Wusatowski, [2]*

From the diagram in Figure 7, the maximum contact angle α_{max} for the rolling speeds in the selected caliber can be determined. Table 6 shows the maximum allowable draught for the calibers, determined according to expression (1).

Table 6. *Maximum allowable draught for the calibers*

Calibar number	1	2	3	4	5	6	7	8
Rolling speed [ms^{-1}]	2,33	2,62	2,42	2,77	2,55	2,78	2,7	2,89
Maximum contact angle – α_{max}	24	24	24	23,5	24	23,5	23,5	23
$tg\alpha_{max}$	0,445	0,445	0,445	0,434	0,445	0,434	0,434	0,424
Δh_{max} [mm]	32,3	34	32,3	32,9	34,4	34,7	32,8	34,4

The force magnitudes observed in calibers 2, 4, 6, and 8 are significantly higher than those in calibers 1, 3, 5, and 7 (Figure 5). The maximum stresses appear during rolling in calibers 2 and 6, as well as in calibers 4 and 8 (Table 3). To reduce the forces in calibers 2, 4, 6, and 8, a change in draught was implemented. The resulting change in caliber heights is shown in Figure 10, and the updated calibration is presented in Table 7.

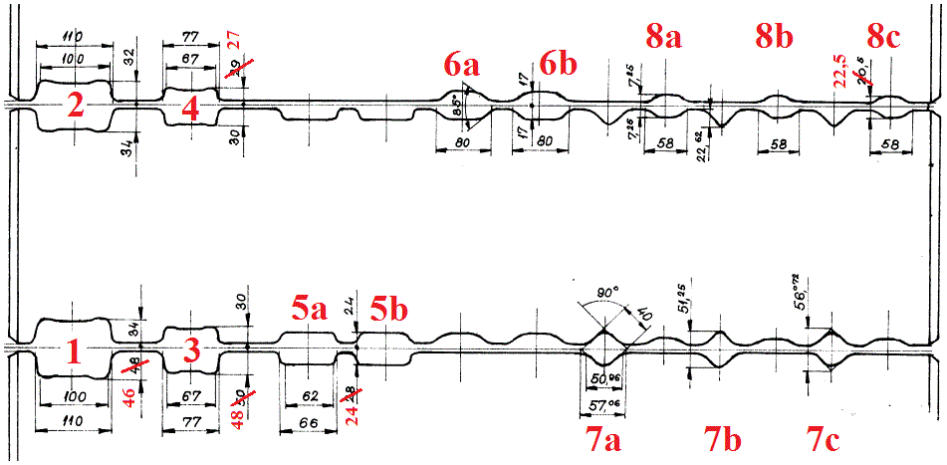


Figure 10. *Caliber height changes*

***Table 7**. Changes in rolling passes*

Pass No.		1	2	3	4	5	6	7	8
Pass shape		box	box	box	box	box	oval	square	oval
Pass size [mm]		100x82	100x66	67x80	67x59	66x52	80x34	40	58x20
Cross-section [mm^2]	9850	8015	6474	5398	4032	3280	2286	1578	1075
Width [mm]	100	104	108	71	76	65	82,5	53,5	60,5
Height before pass h_0 [mm]		100	82	108	80	76	52	82,5	40
Height before pass h_0 [mm]-modified		100	80	108	78	76	48	82,5	40
Height after pass h_1 [mm]		82	66	80	59	52	34	51	20,5
Height after pass h_1 [mm]-modified		80	66	78	61	48	34	51	22,5
Absolute draught Δh [mm]		18,0	16,0	28,0	21,0	24,0	18,0	31,5	19,5
Absolute draught Δh [mm]-modified		20	14	30	17	28	14	31,5	17,5
Absolute reduction [mm^2]		1835	1541	1076	1366	752	994	708	503
Absolute reduction [mm^2]-modified		2055	1321	1230	1366	854	738	708	403
Elongation coefficient		1,23	1,24	1,20	1,34	1,23	1,43	1,45	1,47
Elongation coefficient-modified		1,26	1,20	1,23	1,35	1,28	1,32	1,45	1,34
Stock length [m]	3	3,69	4,56	5,47	7,33	9,01	12,93	18,73	27,49
Stock length [m]-modified	3	3,79	4,56	5,64	7,62	9,77	12,93	18,73	25,15
Arc-contact projected length [mm]		57,84	56,10	72,08	64,68	68,97	61,44	79,10	64,97
Arc-contact p. length [mm]-modified		61,15	52,48	74,73	58,20	74,64	54,19	79,10	61,55
Projected area of contact [mm2]		**5900**	**5947**	**4938**	**4754**	**4276**	**4531**	**3461**	**3265**
P. area of contact [mm2]-modified		**6237**	**5563**	**5119**	**4754**	**4553**	**3996**	**3461**	**3093**
Coeficient of area contact change		**1,06**	**0,94**	**1,04**	**1,00**	**1,06**	**0,88**	**1,00**	**0,95**
Rolling speed [ms-1]		2,33	2,62	2,42	2,77	2,55	2,78	2,7	2,89
Rolling speed [ms-1]- after change		2,35	2,47	2,35	2,50	2,50	2,63	2,49	2,72
Rolling time [s]		1,58	1,74	2,26	2,65	3,53	4,65	6,92	9,52
Rolling time [s] - after change		1,54	1,74	2,20	2,55	3,27	4,65	6,92	10,41
Pause [s]		3	3	3	3	3	3	3	3

It can be seen from Figure 8 and Table 7 that the caliber height changes were made, namely:
- on the 1st caliber, the height of the lower part of the caliber was changed from 48 mm to 46 mm,
- on the 3rd caliber, the height of the lower part of the caliber was changed from 50 mm to 48 mm,
- on the 4th caliber, the height of the upper part of the caliber was changed from 29 mm to 27 mm,
- on the 5th caliber, the height of the lower part of the caliber was changed from 28 mm to 24 mm,
- no change was made on the 7th caliber, because to increase the force on the 7th caliber, the height reduction should be increased, which is very high, and
- on the 8th caliber, the height of the lower and upper part of the caliber was increased by 1 mm.

In the calculations of rolling forces for the modified calibration, the expressions of Tselikov, Korolev, Sims and Siebel were used under the same technological conditions. The plastic yield stresses for each caliber were determined as in the basic calculation according to the experimentally determined data of A.A. Dinnik [7], shown in the diagram in Figure 11.

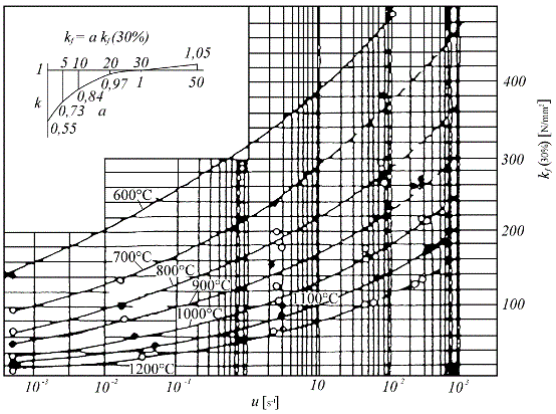


***Figure 11.** Plastic yield stress of low carbon steel St3 as a function of temperature and strain rate, according to A.A. Dinnik [7]*

Figure 9 shows the dependence of the plastic yield stress on temperature and strain rate for low-carbon structural steel St3, according to GOST, with the following chemical composition: 0.14–0.22% C, 0.05–0.17% Si, 0.40–0.65% Mn, ≤ 0.050% S, ≤ 0.045% P, ≤ 0.30% Cu, and ≤ 0.30% optional impurities. The diagram was obtained at a 30% reduction. The same figure also provides a correction coefficient for other reductions, which should be used to multiply the yield stress values read from the diagram. A comparison of rolling forces calculated according to Tselikov, Korolev, Sims, and Siebel for basic and modified caliber heights is presented in Table 8.

***Table 8**. Rolling forces acc. Tselikov, Korolev, Sims, and Siebel for basic and modified caliber heights*

Pass	No.1	No.2	No.3	No.4	No.5	No.6	No.7	No.7
Tselikov F_{Tsel} [kN]	430,7	506,3	377,9	510,3	364,2	518,4	342,8	473,7
Tselikov F_{Tsel} [kN]- after change	458,0	498,5	388,7	492,5	396,6	480,0	342,8	456,4
Coefficient of change - Tse	**1,06**	**0,93**	**1,03**	**0,91**	**1,09**	**0,88**	**1,00**	**0,91**
Koroljev F_{Kor} [kN]	436,0	510,5	387,8	517,2	370,4	515,2	352,3	451,6
Koroljev F_{Kor} [kN] – after change	464,8	501,5	400,2	496,6	405,7	475,2	352,3	438,4
Coefficient of change - Kor	**1,07**	**0,93**	**1,03**	**0,91**	**1,10**	**0,87**	**1,00**	**0,92**
Sims F_{Sim} [kN]	384,0	508,1	367,7	501,2	363,5	517,0	347,1	462,5
Sims F_{Sim} [kN] – after change	406,5	502,2	381,7	475,6	401,6	484,5	347,1	460,1
Coefficient of change - Sims	**1,06**	**0,94**	**1,04**	**0,90**	**1,10**	**0,89**	**1,00**	**0,94**
Siebel F_{Sib}[kN]	391,2	516,2	366,1	521,7	361,9	538,1	330,6	460,5
Siebel F_{Sib}[kN] – after change	414,1	510,3	380,1	495,1	399,8	504,3	330,6	458,1
Coefficient of change - Siebel	**1,06**	**0,94**	**1,04**	**0,90**	**1,10**	**0,89**	**1,00**	**0,94**
Average coef. of force change	**1,06**	**0,93**	**1,03**	**0,91**	**1,10**	**0,88**	**1,00**	**0,93**

As can be seen from Table 8, the coefficient of force change due to the change in the caliber heights is uniform and deviates slightly from the mean coefficient, so that the mean coefficient can be used to calculate the rolling forces after the caliber heights modification, shown in Table 9 and Figure 12.

***Table 9.** Comparison of measured rolling forces and calculated rolling forces after* caliber heights calibration

Pass	No.1	No.2	No.3	No.4	No.5	No.6	No.7	No.7
Experimental [kN]	356,1	494,6	356,1	524,2	346,2	544,0	286,8	445,1
Calculated forces after the calibration modification [kN]	**378,0**	**462,4**	**368,3**	**475,0**	**380,3**	**479,9**	**286,8**	**413,7**

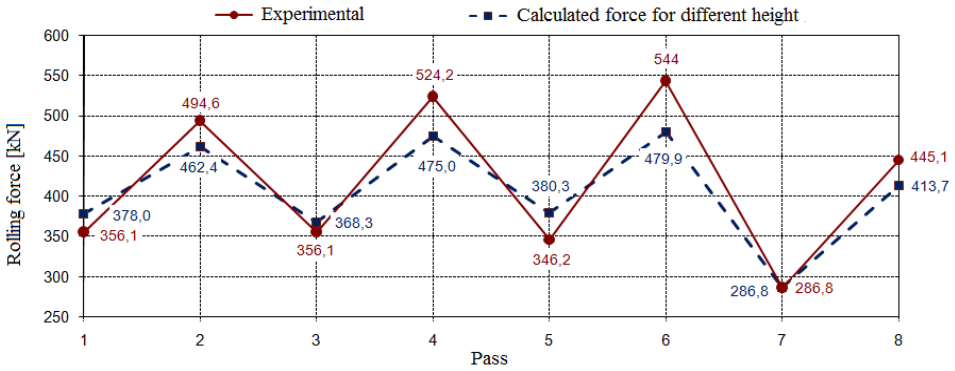


***Figure 12.** Comparison of measured rolling forces and calculated rolling forces after* caliber heights calibration

It is evident from Figure 10 that changes in the caliber height have a significant effect on the magnitude of the rolling force. Specifically, the rolling forces in passes 1, 3, and 5 increased, while those in passes 2, 4, 6, and 8 decreased. The rolling force in pass 7 remained unchanged.
From expression (1), it is evident that the rolling force depends on both the pressure component and the contact surface between the roll and the rolled piece. Table 10 clearly shows that the variation in contact area due to changes in calibre height has a significant impact on the rolling force.

Table 10. *Comparison of rolling forces for the basic and modified* caliber heights

Pass No.	1	2	3	4	5	6	7	8
Coeficient of area contact change	1,06	0,94	1,04	1,00	1,06	0,88	1,00	0,95
Average coeficient of force change	1,06	0,93	1,03	0,91	1,10	0,88	1,00	0,93

4.1. Stress spectrum

A numerical analysis of local stresses was performed for the modified caliber heights, and the results are presented in Table 11.

Table 11. *Local stresses on the roll neck, pass groove 3-4, and pass groove 7a for modified caliber heights [MPa]*

Local stresses [MPa]				Local stresses [MPa]			
Force	Roll neck	Pass groove 3-4	Pass groove 7a	Forces acting together	Roll neck	Pass groove 3-4	Pass groove 7a
F_1 = 378 kN	43	26	13	$F_1 + F_{5a}$	74	70	50
F_2 = 462,4 kN	53	32	16	$F_1 + F_{5b}$	71	65	56
F_3 = 368,3 kN	37	44	22	$F_1 + F_{6a}$	83,6	75	75
F_4 = 475 kN	48	57	28	$F_1 + F_{6b}$	80	69	83
F_{5a} = 380 kN	29,7	43,6	36	$F_3 + F_{7a}$	50	63	57
F_{5b} = 380 kN	27,5	38,5	42	$F_3 + F_{7b}$	47	58	52
F_{6a} = 480 kN	30	43	59,7	$F_3 + F_{7c}$	44	54	42
F_{6b} = 480 kN	26	37	64	$F_4 + F_{8a}$	65	81	82,6
F_{7a} = 287 kN	13	19	38,5	$F_4 + F_{8b}$	60	74,7	65
F_{7b} = 287 kN	10	14	32	$F_4 + F_{8c}$	56	68	51
F_{7c} = 287 kN	7	9,7	22	$F_1 + F_{5a} + F_{8a}$	56,7	46	1,3
F_{8a} = 413 kN	18	26	56	$F_1 + F_{5a} + F_{8b}$	61,4	52	14
F_{8b} = 413 kN	13	19	43	$F_1 + F_{5b} + F_{8b}$	58	47	20
F_{8c} = 413 kN	8	11	26	$F_1 + F_{5b} + F_{8c}$	63	54	32

Comparison of the stresses in Table 5 and Table 11 shows that changes in calibration also caused changes in the maximum local stresses on the roll neck, caliber 3–4, and caliber 7a. The stress spectra were obtained in the same way as the basic stress spectra shown in Figure 8. A comparison of the stress spectra for the basic and modified caliber heights are presented in Figure 13a for the roll neck, Figure 13b for pass groove 3–4, and Figure 13c for pass groove 7a.

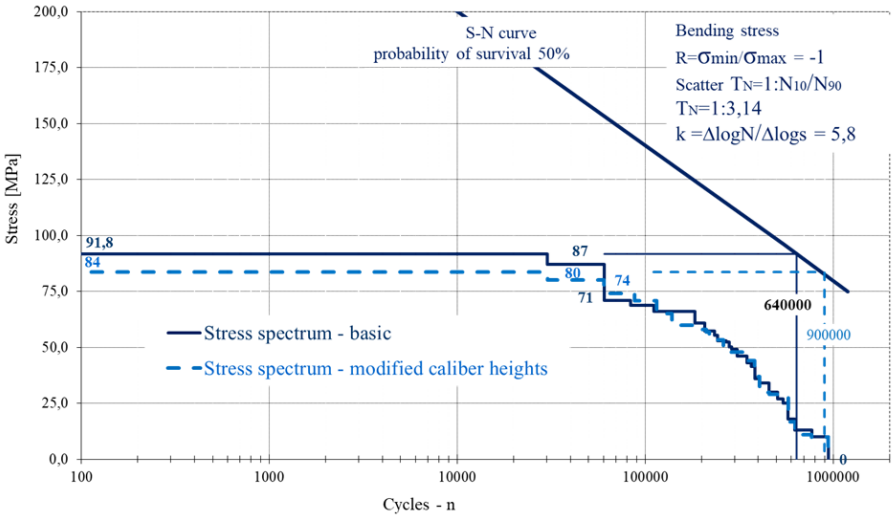


Figure 13.a *Stress spectra on roll neck*

Figure 13a illustrates that reducing the caliber height decreases the maximum stress on the roll neck by 9% (from 91.8 MPa to 83.6 MPa). The maximum number of cycles that can be reached at maximum stress increases from 640.000 to 900.000, which shows a possible extension of the service life by 40%.

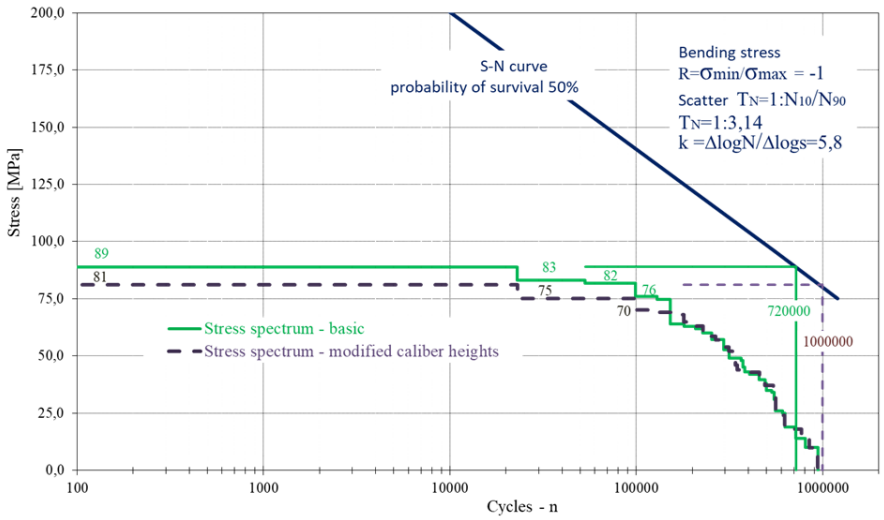


Figure 13.b *Stress spectra on pass groove 3-4*

Figure 13b illustrates that reducing the caliber height decreases the maximum stress in caliber 3–4 by 9% (from 89 MPa to 81 MPa). Additionally, the number of cycles that can be sustained at the maximum stress level increases from 720.000 to 1.000.000, representing a potential 40% extension in service life

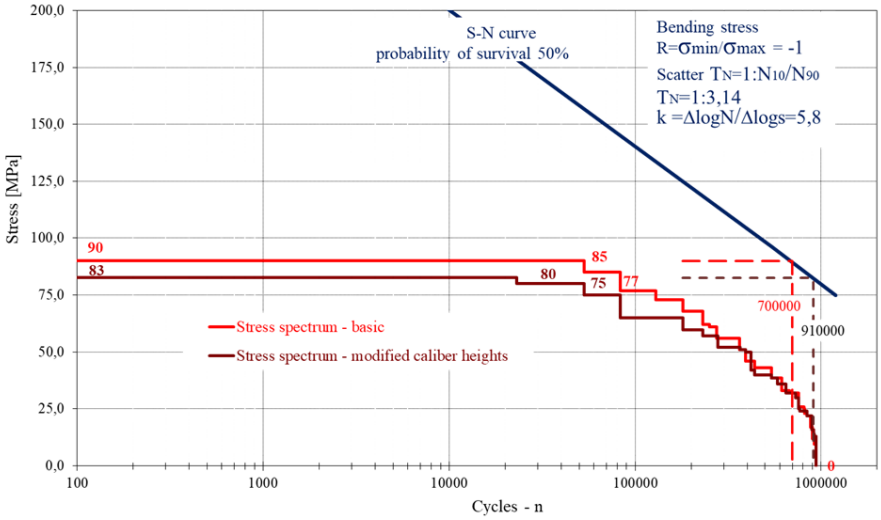


Figure 13.c *Stress spectra on pass groove 7a*

As seen in Figure 13c, reducing the caliber height decreases the maximum stress in caliber 7a by 8%, and the number of cycles at which this stress occurs drops from 53.300 to 23.042. Meanwhile, the limiting number of cycles at the maximum stress level increases from 700.000 to 910.000.

5. Concluding remarks

Numerical analysis showed that the maximum local stresses occurred at three critical locations: the roll neck, box caliber, and square caliber. A stress spectrum was determined for each of these areas. Further analysis revealed that pass groove 7a was the most susceptible to fatigue failure among the analyzed grooves.

It was evident that the force magnitudes in calibers 2, 4, 6, and 8 were significantly higher than those in calibers 1, 3, 5, and 7, resulting in higher stresses. Based on this observation, the caliber height was adjusted in the first five passes according to technological parameters to reduce local stresses at critical locations.

As a result of this calibration change, the service life of the roll neck and box caliber may be extended by 40%.

Meanwhile, for pass groove 7a—the most sensitive to fatigue failure among the analyzed grooves—for the basic calibration, the ratio of the limiting number of cycles at maximum stress to the number of cycles at which maximum stress occurs is approximately 700.000 ÷ 53.300 ≈ 13.With the modified calibre heights and the corresponding new calibration, this ratio increases to approximately 910.000 ÷ 23.042 ≈ 39.5. As a result of this calibration change, the service life at calibre 7a can be increased by over 300%.

The goal of this work was to increase fatigue life by adjusting the heights of the calibers, which was successfully demonstrated. Additionally, it is not clearly visible, but reducing the higher force magnitudes also decreases wear in the most heavily loaded calibers.

These results highlight the substantial impact of caliber height reduction on rolling performance. To optimize roll fatigue life and enhance operational efficiency, such analyses should be incorporated into the roll design process.

References

[1] Designs and technological rules "Steelworks Split", Split

[2] Čaušević, M., 1983. Obrada metala valjanjem, Veselin Masleša; Sarajevo

[3] Domazet, Ž., Lukša, F., 2005. Experimental determination of the rolling force on the rolls with grooves, Proceedings of the 22-nd Symposium "DANUBIA-ADRIA" on Experimental Methods in Solid Mechanics, Parma

[4] Pilkey,W.D., Pilkey,D.F., 2008. Stress concentration factors, 3rd ed., Hoboken, John Wiley & Sons, New York

[5] Heibach, E., 1989. Betriebfestigkeit, VDI Verlag Gmbh, Düseldorf

[6] Domazet, Ž., Lukša, F., Bugarin, M., 2014. Fatigue Strength of the Rolls with Grooves, Applied Mechanics and Materials, 459, 330-334.

[7] Dinnik, A.A., 1961. Obrabotka metallov davleniem, Sbornik, Vypusk 34., Moskva, Metallurgizdat, Moskva

Failure analysis of scrap shear knives

***Francisko Lukša*[1], *Željko Domazet*[2], *Đorđe Dobrota*[1] *and Branko Lalić*[1]**

1) Pomorski fakultet Split, Ruđera Boškovića 37, Split, Croatia

2) Fakultet Elektrotehnike, Strojartva i Brodogradnje, Ruđera Boškovića 32, Split, Croatia

Corresponding author: fluksa1@pfst.hr

Original scientific article

Abstract: This paper presents a failure analysis of scrap shear knives. A set of six knives, each with four blades, fractured during normal operation over the course of two weeks, during which ambient temperatures ranged between 0 °C and −10 °C. Spectral analysis of the fractured knife samples showed a 1.9% increase in carbon content and an absence of nickel, compared to the standard material typically used, which contains 0.46% carbon and 3.8–4.3% nickel. Further investigation revealed that the supplier had replaced the standard tool steel X45NiCrMo4 with X210Cr12. Analysis of the influence of carbon and nickel on toughness showed that increased carbon content reduces notch toughness at low temperatures, while nickel improves it. Based of that it is concluded that tool steel X45NiCrMo4 is more suitable for low-temperature applications, as confirmed by Charpy V-notch testing.

Keywords: *failure analysis; knife fracture, low temperature, tool steel; toughness*

1. Introduction

This article investigates the causes of blade fracture in a very short period of time on outdoor scrap metal shears. A set of six knives, each with four blades, had been in service for just two weeks and were performing regular cutting operations on scrap steel. During this period, ambient temperatures ranged between 0°C and −10°C. The fracture caused a production halt, resulting in significant downtime and a financial loss due to machine repairs, employee safety checks, and the disposal of damaged materials.

The investigation begins with a description of the machine, the location where the fracture occurred, and the blade design. Common knife damage is then described in terms of plastic deformation and the fracture surface appearance on broken knives. The investigation continues with a technical inspection of the equipment to identify the potential cause of the overload. Then, the chemical composition of both plastically deformed blades and broken blades was analyzed using a quantometer and compared with the DIN Standard [1]. A comparison of the chemical composition of X45NiCrMo4 steel and the material from the broken knives, as determined by quantometer analysis, showed that the broken knives were made from X210Cr12 steel. Since X210Cr12 steel is also a tool steel with similar properties as the required X45NiCrMo4 steel, an analysis of their chemical compositions and individual elements was performed. A comparison of the chemical composition of X45NiCrMo4 and X210Cr12 steels shows that X210Cr12 has an increased carbon content, while X45NiCrMo4 has a significant nickel content of about 4%, which has a decisive influence on toughness at low temperatures. This fact was confirmed experimentally using Charpy V-notch impact testing in the laboratory of the Shipbuilding Industry Split.

This case study aims to analyze the cause of the fracture and propose solutions to prevent similar incidents in the future.

2. Fracture location the blade design

In electric arc furnace steelmaking, the process begins with the selection and preparation of scrap metal. In the scrapyard outside the building, a stationary inclined scrap shear of the guillotine type

(Figure 1) was used to cut large pieces of scrap metal to the required size for charging into the electric arc furnace.

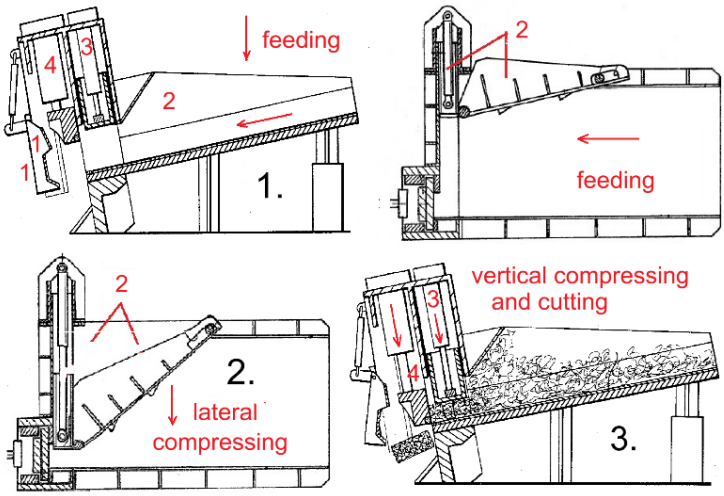


Figure 1. *Shema of stationary inclined scrap shear guillotine type*

The machine was gravity-fed from the top with randomly sized ferrous scrap metal. The scrap metal is conveyed downward by gravity and compacted under its own weight. The trough is inclined at an angle of 30° and has a substantially rectangular cross-section, with its longer side oriented horizontally. The trough walls include an inclined bottom surface on which the material slides, one side wall and horizontal piston reinforced with cross ribs.

As shown in Figure 2 and 3, there are four hydraulic cylinders for all the movements: one for stopper (1), one for the horizontal piston (not visible in Figure 3), one for vertical piston (3), and one for the guillotine. The first stopper (1) closed the cutting window at the bottom of the trough, while the horizontal piston, together with wall (2), compressed the metal scrap laterally. The vertical piston (3) then compressed the metal scrap from the top. Finally, the guillotine (4) cut the metal scrap. When all parts moved to their starting positions, the cut metal scrap fell through the cutting window.

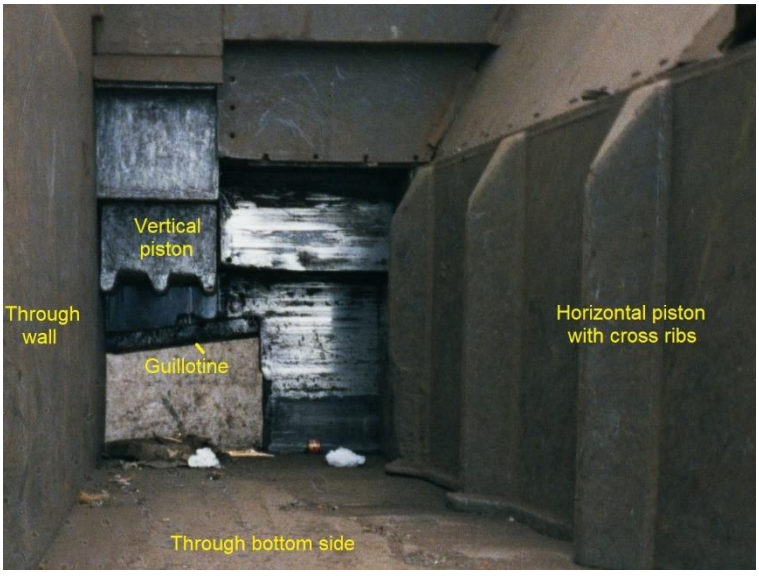


Figure 2. *Feeding trough*

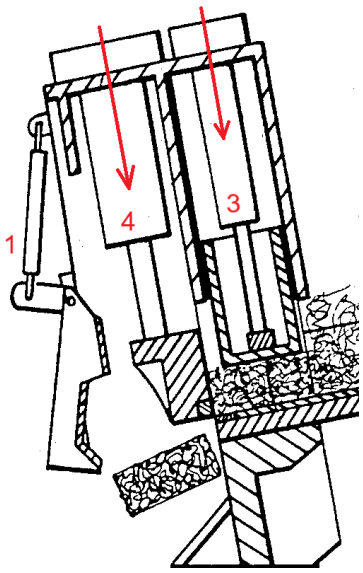


Figure 3. *Metal cutting*

One set of knives consists of six identical knives: three installed on the lower support as lower knives, and three installed on the guillotine as upper knives, as shown in Figure 4.

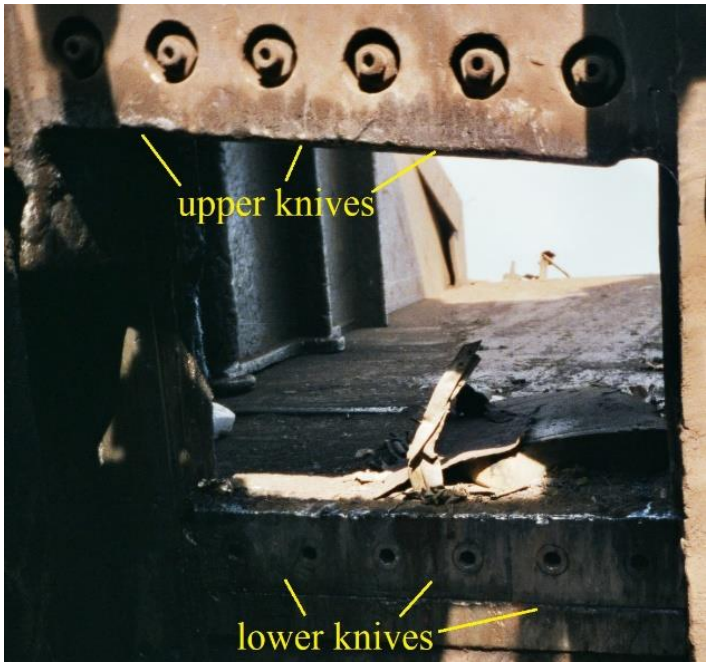


Figure 4. *Knives in working position*

Each knife consists of four blades. The dimensions of one knife are as follows: length 304 mm, thickness 80 mm, and height 160 mm, as shown in Figure 5. The service life of a complete set of knives exceeded three months. The cross-section of the knife is a symmetrical rectangle with sharp edges at a 90° angle, allowing all four corners to be used for cutting.

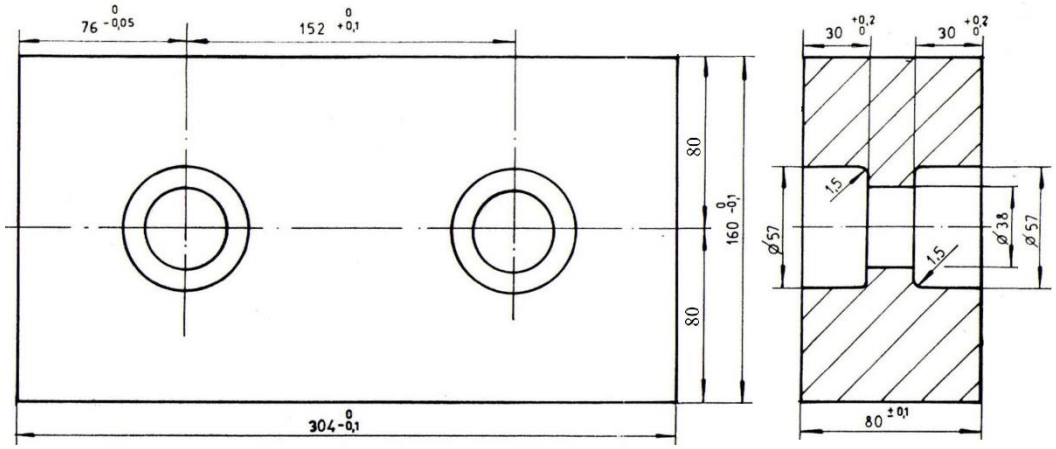


Figure 5. *Knife dimensions*

3. Plastic deformation of the knifes

The scrap shear was in service for several years with periodic maintenance. Blade durability was monitored during production. The durability of each blade typically ranged between 30 and 40 days, depending on the type of scrap used. Common blade damages included plastic deformation after the normal service life, as shown in Figure 6.

There can be several different sizes of plastic deformation on a single blade, as shown in positions 1, 2, and 3 in Fig. 6. These deformations were caused by cutting hard and tough materials. Although the scrap was sorted, some hard and tough materials would occasionally make it through, especially during night time operations. Despite this, no breakage occurred during the entire service period.



Figure 6. *Plastic deformation of knives from X45NiCrMo4*

4. Brittle fracture of the knives

One set of six knives failed during normal operation over a two-weeks period in winter, when 5 and 7 days. An example of one of the fractured knives is shown ambient temperatures ranged between 0 °C and -10 °C. The service life of each blade was between in Figure 7.



Figure 7. *Brittle fracture of the knifes*

As seen in Figure 5, the fracture surface has a bright, granular appearance, which is characteristic of brittle fracture. The crack initiated at the surface (point 1) and propagated rapidly through region 2, leading to the final fracture at point 3. The fracture spread across one part of the knife between the two edges, while in the other part, the edges remain undeformed, further indicating that the fracture occurred in a very short time.

5. Load investigation

An investigation into the possible cause of the overload began with a technical inspection of the equipment. The technical inspection confirmed that the guiding plates, which serve to guide the movable set of knives, were not worn, and that the blade clearance between the movable and fixed sets of knives was within normal limits (see Figure 8).

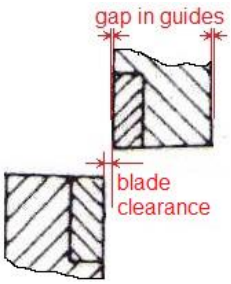


Figure 8. *Blade clearance*

The conclusion drawn was that there was no contact between the blades. It was also verified that all mechanical parts of the shear were in excellent condition, and there was no indication to suggest that the load on the knives should exceed the regular operating level.
The hydraulic pressure of the entire system was set to the required 250 bars. Furthermore, the inspection of the scrap material already cut by the shear revealed that it consisted of the usual materials, with no additional foreign materials that could have caused damage to the blades.
In summary, the technical inspection showed that there was no evidence of an unusual overload on the knives, and the load was within regular limits.

6. Material characterization

The first step in checking whether the knife material matches the design requirements is to verify its chemical composition using a quantometer in the factory laboratory. For analysis, it is sufficient to cut a knife sample with a diameter of 20mm. If the measured chemical composition matches the design specification, the next step is to proceed with hardness and structure testing. If the composition does not match the specification, the actual material must be identified.

6.1. Material from knives with plastically deformed blades according to design requirements

The standard material used for the knives was tool steel X45NiCrMo4, in accordance with the German DIN standard (Deutsches Institut für Normung) [1]. This is cold work tool steel with hardness on the surface after heat treatment 53-58 HRc, with high toughness, high impact strength and compressive strength. The chemical composition of this material, as specified by the standard, is presented in the first row of Table 1. The chemical composition of the material from the knives with plastically deformed blades was analysed using a quantometer, and the results are presented in the second row of Table 1.

Table 1. *Chemical composition of X45NiCrMo4 steel and the material from knives with plastically deformed blades, analysed using a quantometer*

Element	C [%]	Si [%]	Mn [%]	Cr [%]	Mo [%]	Ni [%]	W [%]	S [%]	P [%]
X45NiCrMo4 according to standard [1]	0,4-0,5	0,15-0,3	0,3-0,5	1,2-1,5	0,15-0,35	3,8-4,3	0,5	max 0,035	max 0,035
Knife material tested by quantometer	0,46	0,15	0,38	1,22	0,22	4,04	0,04	0,009	0,018

A comparison of the two materials shows that the chemical composition of the knife material matches that of X45NiCrMo4 steel as specified in the standard. Hardness measurements on the knife surface indicated a value of 56 HRC.

6.2. Chemical composition of the material in the broken knives

Additionally, the chemical composition of the material from the broken knives was analysed using a quantometer and is presented in Table 2.

Table 2. *Chemical composition of the material of the broken knifes checked by quantometer*

Element	C [%]	Si [%]	Mn [%]	Cr [%]	V [%]	S [%]
Material of broken knives tested by quantometer	1,9	0,35	0,33	12,2	0,15	0,005

A comparison of the chemical composition of X45NiCrMo4 steel and the material from the broken knives, as determined by quantometer analysis, clearly shows that the two materials are different. The broken knives were manufactured from a steel that does not correspond to the X45NiCrMo4 specification.

The next step was to identify the material from which the broken knives were manufactured. According to the chemical composition obtained by quantometer analysis, the material used for the broken knives corresponds to X210Cr12 steel as defined by the DIN standard [1]. This was later confirmed by the knife supplier following the warranty claim. The chemical composition of this material is shown in Table 3.

Table 3. *Chemical composition of steel X210Cr12 [1]*

Element	C [%]	Si [%]	Mn [%]	Cr [%]	V [%]	S [%]	P [%]
X210Cr12 Standard	2	0,3	0,3	12	0,1		

The certified material X210Cr12 is a high-carbon, high-chromium cold work tool steel, characterized by a blade surface hardness of 64–66 HRC after heat treatment, with very high wear resistance and moderate toughness. Hardness measurement on the surface of X210Cr12 steel showed a value of 63 HRC.

6.3. Practical experience with X210Cr12 in application

The steel X210Cr12 was used for the knives of a cold shear (Figure 9, [2]). During operation, the material showed good performance and durability at ambient temperatures ranging from 20 °C to 40 °C.

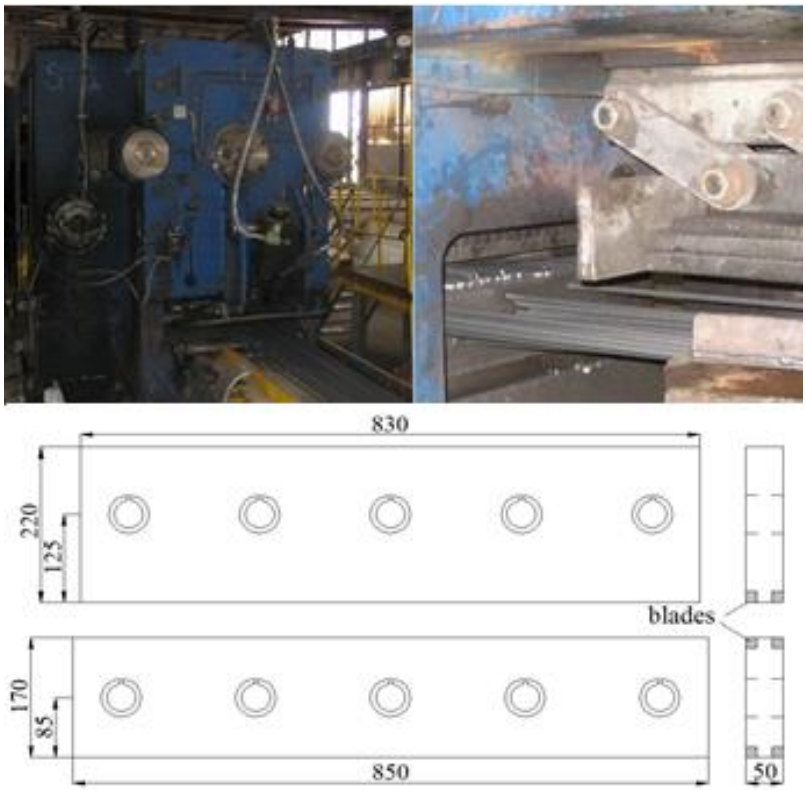


Figure 9. *Cold shear*

Cold shears are cutting machines with parallel knives, designed to cut chilled ribbed bars made of structural steel to the desired length. The cross-section of the lower knife is a symmetrical rectangle with sharp 90° edges, allowing all four corners to be used for cutting. The upper knife has an asymmetrical height profile and is designed to use only two of its sharp edges for cutting.
A comparison of the working conditions between the two shears shows that the knives were used outdoors at ambient temperatures ranging from 0 °C to −10 °C, while the knives of the cold shear were operated indoors at temperatures between 20 °C and 40 °C. The hardness and toughness of the cut materials were similar in both cases.

6.4. Difference in chemical composition between steels X45NiCrMo4 and X210Cr12

Table 4 presents the differences in chemical composition between X45NiCrMo4 and X210Cr12 steels.

Table 4. *Difference in chemical composition between X45NiCrMo4 and X210Cr12*

Element	C [%]	Cr [%]	Ni [%]
X45NiCrMo4	0,46	1,22	3,8-4,3
X210Cr12	1,9	12,2	-

A comparison of the chemical composition of X45NiCrMo4 and X210Cr12 steels shows that X210Cr12 contains approximately four times more carbon and ten times more chromium than X45NiCrMo4, while it contains no nickel. In contrast, X45NiCrMo4 has a significant nickel content of about 4%.

5.5. Influence of carbon, chromium and nickel on oughness

Influence of carbon content on toughness at different temperature is shown in Fig.10.

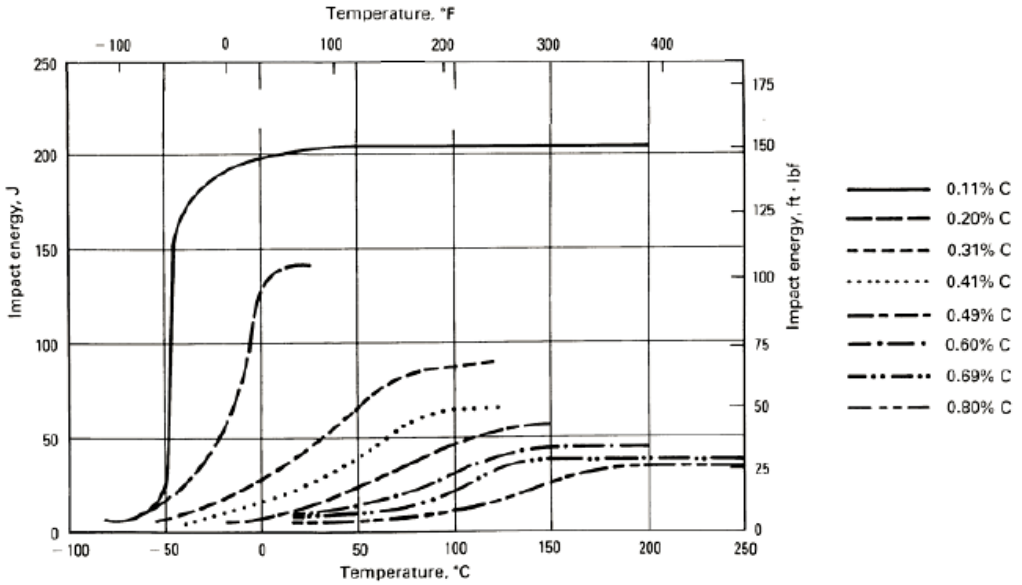


Figure 10. *Variation in Charpy V-notched impact energy by temperature for normalized plain carbon steel of varying carbon contents [3,4]*

The curves in Figure 10 indicate that increasing the carbon content results in reduced notch toughness at low temperatures.
Chromium slightly increases the transition temperature. For the steels with more than 0,9%, it is very difficult to achieve the microstructure and mechanical properties typical of plain carbon steels. Therefore, the test results are not comparable.
The influence of nickel content on toughness at different temperatures is shown in Figure 11. As illustrated, nickel is effective in improving the notch toughness of steel, particularly at low temperatures. A high nickel content reduces the upper-shelf fracture energy, but the values remain acceptable for most applications.

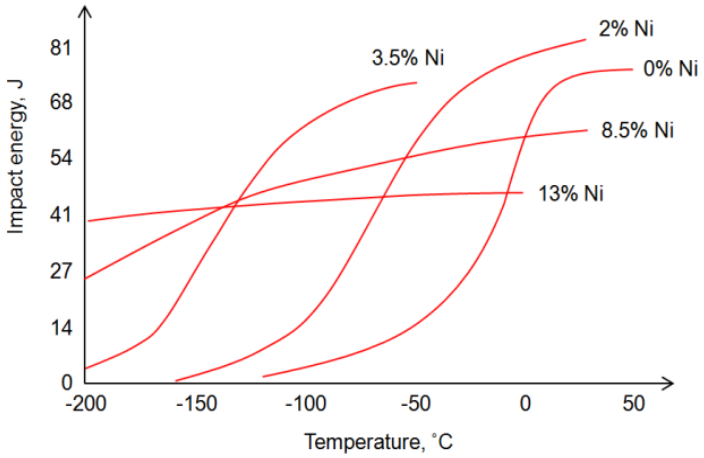


***Figure 11**. Effect of nickel on low-temperature embrittlement of low-carbon steels [4,5]*

7. Difference in toughness between X45NiCrMo4 and X210Cr12

The previous chapter showed the effects of carbon and nickel on the toughness of carbon steel at low temperatures. In general, increasing carbon content reduces the toughness of carbon steel at low temperatures, while increasing nickel content improves it.

Since the knives are made of tool steels X45NiCrMo4 and X210Cr12, the toughness of both materials was experimentally determined in the laboratory of the Shipbuilding Industry Split to obtain more accurate data. The test specimens of the materials (four for each material), made by the supplier, are shown in Figure 12, while the laboratory test results are presented in Figure 13. The toughness of the materials was evaluated using Charpy V-notch impact testing, performed at various temperatures to assess their behaviour under low-temperature conditions.

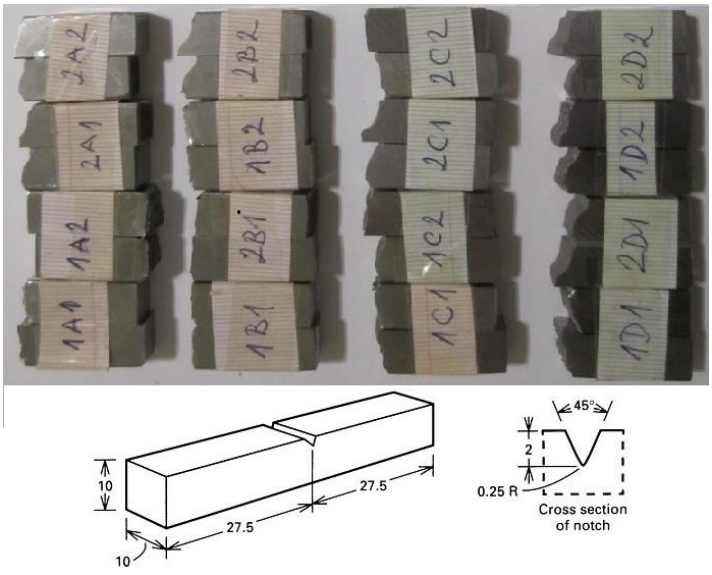


***Figure 12.** Shape and dimensions of the specimens [7]*

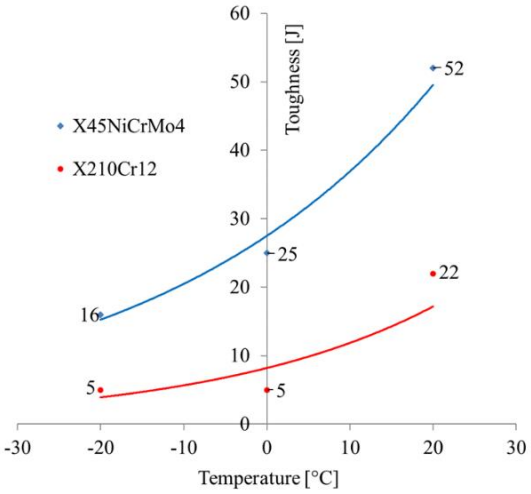


Figure 13. *Toughness of tool steels X45NiCrMo4 and X210Cr12 [7]*

Figure 13 clearly shows that steel X45NiCrMo4 has much better toughness, while steel X210Cr12 is more sensitive for operating at low temperatures which was the cause of blades fractures. Following the post-failure investigation, production continued with knives manufactured from X45NiCrMo4 steel. Monitoring during production showed that the duration of a single blade was consistent with the pre-failure period, between 30 and 40 days.
Finally, tool steel X45NiCrMo4 was confirmed as more adequate for operating at low temperatures.

8. Conclusions

The analysis has shown that two tool steels, although used for the same purpose, may have significantly different properties when they are used at low temperatures, which can significantly effect on their service life and increase total costs of production.
The comparison of the chemical composition of tool steels X45NiCrMo4 and X210Cr12 revealed significant differences in carbon, chromium, and nickel content. The study showed that these elements have a significant impact on toughness. Tool steel X45NiCrMo4 is more suitable for operation at low temperatures, as confirmed by Charpy V-notch testing.

References

[1] Deutsches Institut für Normung. DIN 17200. 1987 (DIN, Berlin)

[2] Lukša, F.; Domazet, Ž., Bugarin, M., Krstulović-Opara, L., 2018. Comparison of knife fabricated from tool steel by heat treatment and knife fabricated from structural steel by hard surface welding. Proceedings of the Second International Conference on Advanced Materials, Mechanics and Manufacturing (A3M’2018), Hammamet, Tunisia

[3] ASM Handbook Vol.01, Properties and Selection: Irons, Steels and High-Performance Alloys. 1991. ASM International USA

[4] **Burns, K.W.**, **Pickering**, **F.B.**, 1964. Deformation and fracture of ferrite-pearlite structures. Journal of the Iron and Steel Institute. Vol.202

[5] Kah, P., Layus, P., Martikainen J.,2015. Influence of alloying elements on the low-temperature properties of steel. Proceedings of the Twenty-fifth International Offshore and Polar Engineering (ISOPE), At Kona, Hawaii Big Island, USA

[6] Freitag, D.R., McFadden, T.T., 1997. Introduction to Cold Regions Engineering. American Society of Civil Engineers

[7] Domazet, Ž., Lukša, F., Bagavac. P., 2018. Toughness tests of tool steel for work at low temperature. Proceedings of the 35-nd "DANUBIA-ADRIA" Symposium on Advances in Experimental Mechanics, Sinaia, Romania

Production line of migrating corrosion inhibitors for the protection of steel reinforcement systems

***Petar Ljumović*[1], *Petar Bronić*[2], *Ivana Radić Boršić*[3] *and Ivan Rogan*[3]**

1) University of Split, Faculty of Electrical Engineering, Mechanical Engineering and Naval Architecture, Ruđera Boškovića 32, 21000 Split, Croatia

2) University of Split, University Department of Professional Studies, Kopilica 5, 21000 Split, Croatia

3) CorteCros Ltd., Nova Ves 57, 10000 Zagreb, Croatia

Corresponding author: petarlj@fesb.hr

Professional article

Abstract: This paper provides an introduction to the technology of migrating corrosion inhibitors (MCIs). The chemical background of how these special corrosion inhibitors work under real conditions is presented. In addition, the applications of migrating corrosion inhibitors are presented, in particular the application examples in the construction industry and in civil engineering. An overview is given of the production process of migrating corrosion inhibitors, which is carried out in special industrial plant. Laboratory testing of the quality parameters of the end product through the company's established quality control system is discussed. Finally, application guidelines for the end product under operating conditions are given.

Keywords: *Corrosion; Inhibitors; Migrating corrosion inhibitors; Steel reinforcement protection*

1. Introduction

The mechanical properties of concrete, such as tensile strength and elasticity, play an important role in the load-bearing capacity and integrity of the structure. Reinforced concrete is often used as a building material because of its high load-bearing capacity and durability. However, when exposed to various environmental influences such as water, moisture, salt and certain chemical substances, corrosion of the reinforcement in the concrete structure can occur. Corrosion of the reinforcement is a serious problem that can lead to a reduction in the load-bearing capacity of the concrete, deterioration of the structure and a reduction in the service life of the steel elements (Figure 1). To solve this problem, various protection techniques have been developed (cathodic protection, nano coatings, corrosion inhibitors, etc.), of which migrating corrosion inhibitors (MCIs) are attracting great attention due to the research and development of their field of application followed by their wide range of uses and implementation prospects [1].



Figure 1. *Examples of severe structural damage induced by corrosion of steel reinforcement elements [2]*

There is currently a total length of more than 1234 kilometres of bridges over 100 m in Europe. A considerable number of these bridges, which were built after 1945, have a life expectancy of 50 to 100 years. Research carried out in 2001, as part of the BRIME project, shows that highway bridges in France, Germany and the U.K. are damaged in 39% of cases, with corrosion being the main cause. The year 2018 has brought challenges for the maintenance of European bridges, especially after the

dramatic collapse of the bridge in Genoa, Italy. This incident underlined the need to improve knowledge of natural events such as earthquakes and wind loads and to improve the maintenance of structures, especially with regard to reinforced concrete and advanced bridge design methods. Most Member States of the European Union have had to invest significantly in solving maintenance problems to ensure the long-term usability and safety of bridges [3].

2. The technology behind MCI

By definition, inhibitors are substances that hinder the corrosion process and therefore result in a decrease of the dissolution rate of the steel. The application of corrosion inhibitors in reinforced concrete is possible by the addition to mixing water or by application on the surface of the concrete structure. Addition to the mixing water does not require any additional working steps and allows a simple handling of the inhibitor, unless it affects the properties of the cement paste adversely. Application from the concrete surface could be a promising technique to protect already existing structures or increase the lifetime of structures that already show corrosion attack [4].
The application of the inhibitor on the concrete surface requires the diffusion of the substance to the rebar where it has to reach a sufficiently high concentration to protect steel against corrosion or reduce the rate of the ongoing corrosion process [4]. Corrosion attacks can be caused by chloride ions from de-icing salts penetrating to the steel, which result in pitting corrosion of the passive steel or by reaction of the alkaline pore solution with carbon dioxide (CO_2), which results in a pH drop and the depassivation of the steel. Besides coating the rebar and the hydrophobic treatment of the concrete surface, the use of corrosion inhibitors is of increasing interest [4].

2.1. Chemical background

Migrating corrosion inhibitors have a special ability to migrate through concrete and form a passive layer on the surface of the reinforcement bars (Figure 2). Once exposed to corrosive agents, like water or chlorine, this type of inhibitor reacts with the surface of the reinforcement elements and forms a protective layer which prevents or slows down a chemical reaction. This particular mechanism enables a long-term protection of rebars and extends the life expectancy of reinforced concrete structures (Figure 3). MCIs are based on amine technology (amine alcohols and amine carboxylates). They are classified as mixed inhibitors, meaning they affect both anodic and cathodic portions of a corrosion cell. MCI is applied in many forms including as a concrete admixture or a topical treatment [5].

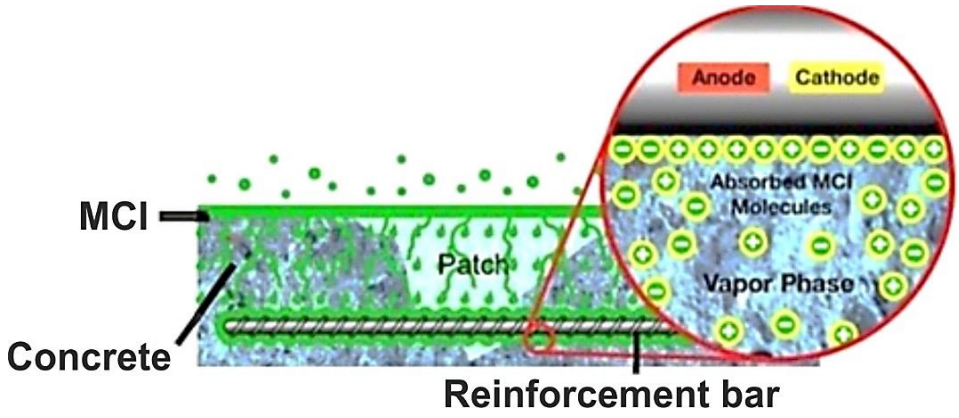


Figure 2. *The example of migrating corrosion inhibitor adhering to steel reinforcement bar [3]*

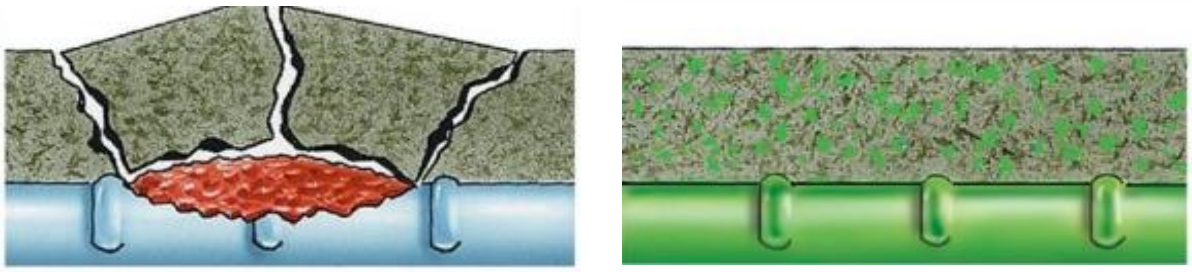


Figure 3. *Steel reinforcement bar corrosion without (left) and with the use of MCI (right) [3]*

It moves as a liquid through the concrete matrix via capillary action and migrates in a vapor phase throughout the concrete pore structure. When MCI comes in contact with embedded metals, it has an ionic attraction to it and forms a protective molecular layer. This film prevents corrosive elements from further reacting with the reinforcement and also reduces existing corrosion rates, greatly extending concrete service life [5].

2.2. Application examples

One of the most significant examples of migrating corrosion inhibitors technology implementation in Croatia is Pelješac bridge, (Figure 4). A great attention was directed on ensuring great durability of the bridge in order to prolong its lifecycle to more than 130 years. With the use of different technology approaches, in the form of additional anticorrosive coatings and cathodic protection for the steel pilot components, protective concrete coatings with the width between 65 and 85 mm on all concrete components, were introduced. Furthermore, in order to additionally improve the stability and corrosion resistance, the inner structure of concrete near sea level was strengthened by the use of stainless steel.

To protect all concrete surfaces, a special silane coating was applied, which serves as corrosion protection for the reinforcement elements and penetrates deep into concrete structure. It is important to emphasize that this coating must remain colourless in order to preserve the natural appearance of the bridge [3].



Figure 4. *Construction of Pelješac bridge, Croatia [6]*

Product used for bridge protection was MCI® - 2018 from Cortec Corporation. MCI® - 2018/MCI® - 2018 V/O is a 100 % silane water-repellent containing time-proven migrating corrosion inhibitors system. MCI® - 2018 penetrates deep into concrete providing corrosion protection to reinforcing steel

from carbonation, chlorides, and other contaminants. MCI® - 2018 V/O is formulated for easier application on vertical and overhead surfaces [7].
Modifications available for MCI® - 2018 and MCI® - 2018 V/O include incorporation of fugitive dye (MCI® - 2018 FD, MCI® - 2018 V/O FD), incorporation of a UV tracer (MCI® - 2018 UV) and the ability to add permanent stains [7].
Another example of the use of migrating corrosion inhibitors is the water tower in Vukovar, Croatia (Figure 5). In 2016, the initiative to renew the water tower was launched, which was completed in October 2020. In this case, MCI® - 2020 V/O was used for all concrete surfaces with reinforcing bars. MCI products were also used as concrete admixtures: MCI CorrVerter® (primer coating applied directly to corroded rebar), MCI Corshield® (to all exposed rebar) and MCI Architectural Coating® (for all concrete parts of the structure) [3].



***Figure 5**. Corroded steel elements before reconstruction of water tower in Vukovar, Croatia [3]*

MCI® - 2020 was also used in reparation and protection of jetty bearing blocks damaged from corrosion induced by seawater, particularly in the tidal zones. The location was Puerto de Bilbao (Vizcaya), Spain (Figure 6). MCI was used and applied by surface spraying method [3].



***Figure 6.** Corroded steel elements before reconstruction – Puerto de Bilbao, Spain [3]*

Cortec's MCI Coating for Rebar NT® is yet another migrating corrosion inhibitor product. It was used for rebar protection as well, and the application was conducted by direct spraying. It was used for the new control tower protection project at the Barcelona airport, Spain [3].
More examples of successful implementation of MICs can be found in:

- Wells Fargo - reinforced concrete garage construction: protected with MCI® – 2005 NS (214), California, USA;
- Pentagon – all outer walls reconstruction: MCI® - 2020 V/O (046), Virginia, USA;
- De Pere Waste Water Treatment Plant: MCI® - 2020, - 2023, - 2038 (219), Wisconsin, USA;

and in numerous other structural projects worldwide [8].

3. MCIs production line

CorteCros Ltd., stands for a migrating corrosion inhibitors (MCIs) leading producer in Europe, with its headquarters currently located in Zagreb, Nova Ves 57, and central production-distribution plant located in Kaštel Sućurac, Croatia. CorteCros Ltd. is founded in 1998, as a result of partnership

investment from Cortec Corporation, Minnesota, USA, and Crosco, Oil Service Ltd., member of INA Group. Due to the act of acquisition in 2016, CorteCros Ltd. becomes a part of Cortec Corporation ownership in total, therefore accompanying a new strategy of full resource business. Cortec Corporation, one of the global leaders in migrating corrosion inhibitors production, distributes its products in more than 90 countries worldwide. CorteCros Ltd. is now one of the leading companies at domestic and international market, providing corrosion protection services and technology. The company also provides technical support for Cortec products and services in all industrial fields, especially in industries such as the military and the oil and gas production and processing industry, in which CorteCros Ltd. has extensive experience [9].

As a part of its production plant in Kaštel Sućurac, CorteCros Ltd. owns a customs warehouse as well, which serves as a main distribution centre for Cortec products and also for the products from Bionetix International Company from Canada, which is engaged in producing microbial and enzyme based biological products, and is also owned by Cortec Corporation [9].

Production process starts with receiving customer’s Order Form as a job order sheet document, in which the necessary amount of the product is specified, as well as the exact number of MCI litres or containers to be produced. It is important to note that specific production formulas from Order Forms are considered business secret therefore were unavailable for more detailed insight.

After Order Form is defined, warehouse manager starts raw material preparation (Figure 7), whether liquid or powdered components are considered. The raw material is delivered to the production plant by the use of specialised cargo vehicle. The powdered components are added manually, while the liquids are added into tanks with the help of pneumatic membrane pumps (Figure 8).



***Figure 7**. CorteCros raw material warehouse*



***Figure 8**. Pneumatic membrane pumps for adding raw material components into tanks*

There are four important tanks in production plant; two 1000 litres capacity (Figure 9), for viscous oil-based liquids and two tanks with 9000 and 3000 litres capacity (Figure 10), for water-based liquids. Every amount of chemicals, additives and raw materials are monitored and calculated through mass percentage according to pre-defined calculations. Every tank is equipped with frontally positioned label device for accurate monitoring of added components.



Figure 9. *1000 litres tanks for oil-based liquids*



Figure 10*. 3000 litre tank for water-based liquids*

The production plant is also equipped with a heating chamber (Figure 11). Heating the raw materials is mandatory in order to obtain a homogeneous mixture enriched with additives. The raw material containers are carefully placed in the heating chambers overnight until the correct temperature is reached. In this way, the mixture is prepared for the morning production cycle and allows optimal chemical reactivity. The heating chambers play a key role in achieving a high quality and consistency of the product.



Figure 11. *Raw material heating chamber*

Due to the many chemical vapours and dusts generated during the production process, the plant is provided with a ventilation system that plays a key role in maintaining a safe and healthy working environment. The ventilation is activated during each production cycle to ensure sustainable working conditions. The system enables the successful removal of harmful gases, fumes and dusts, minimising the risk of workers being exposed to substances that are hazardous to their health. In addition, binding safety standards are set. Workers are required to wear protective gloves, masks and overalls throughout the entire production process to avoid any kind of health risk.

After all the raw materials and chemicals have been added to the tank, the mixing process follows to finalize homogeneity. Once the desired chemical composition and quality has been achieved, the product is prepared for packaging. A filling machine is used to fill containers (Figure 12), which is set to the required product quantity. The filling machine uses the density of the product to calculate the exact amount of product that will fit into each 19-litre container (package). For example, if the density

of the product is 0.8 units, the filling machine automatically calculates the appropriate amount of product and fills a 19-litre container with it.



Figure 12. *Container filler machine*

A special filling gun is used to fill the containers, that works with the aid of a diaphragm or membrane pump. Once the containers are filled with the product, they are carefully placed on the pallets and wrapped in cellophane to ensure their stability. These procedures release the products for further distribution.

A very important step in the production process is the quality control of the end product. For this purpose, a specialized laboratory with precise equipment is set up inside the factory.

The process of end product control begins when a 0.5 litre sample is subjected to a thorough analysis. The first step of the analysis consists of placing the sample in a water bath at a certain temperature (Figure 13). It is important to emphasise that the temperature varies depending on the type of analysis performed. For example, for the viscosity test, the temperature is set at 23 °C, while for the density test, a temperature of 20 °C is selected. Once the temperature of the sample has been determined, a detailed analysis is carried out according to pre-established procedures to determine the appearance, colour, density, amount of non-volatile matter and viscosity (Figures 14 and 15). The laboratory technicians use these parameters to assess the quality of the product. Each product has its own specific properties and quality requirements that must be matched to make the product acceptable for further use and distribution. Quality control is a key factor in the production process of migrating corrosion inhibitors and thus ensures the consistency and reliability of the product. The results of the analyses carried out give the company the assurance that all products meet the highest quality and safety standards before they leave the production line.

All products are registered under the EU REACH Regulation to ensure a high level of protection of human health and the environment from harmful substances.

The respective production line is organised, audited and certified according to globally recognised ISO framework. That includes ISO 9001 standard for Quality Management Systems (QMS) and ISO 14001 standard for Environmental Management Systems (EMS), which relates specifically to the management and mitigation of environmental risks such as pollution and resource depletion.



Figure 13. *Water bath for sample testing*



Figure 14*. Salt chamber for operating conditions simulation*



Figure 15*. Measuring equipment for density, colour and viscosity testing*

After the end product has successfully passed all stages of quality control, the Report (Quality Control Specification Listing) is created. The Report contains detailed data on all aspects of the production process, including the quantity of material used with its identification number, the total quantity of units produced and information on any waste materials or inconsistencies with the standards.
Once the Report has been completed, the end product is ready to be filled into containers, which are then stored (Figure 16), and delivered to the customer. This step signifies the end of the production line therefore product preparation for distribution.



***Figure 16**. End product warehouse*

Finally, before the product leaves the plant, the Certificate (Certificate of Analysis) is issued. This document accompanies the product throughout the entire delivery process to the customer and serves as a guarantee of the product's quality.

4. Conclusions

Migrating corrosion inhibitors can be applied in different ways in order to protect reinforced concrete structure from corrosion. Most common application methods are listed below.

- Inhibitor adding into concrete mixture: corrosion inhibitors are added directly to the concrete mix during the production process. The inhibitors are mixed with cement, sand, aggregates and water to distribute evenly throughout the concrete structure. Over time, the inhibitors migrate through the concrete and form a protective layer on the surface of the reinforcement, preventing contact between the reinforcement and corrosive substances.
- Inhibitor surface coating: after the concrete has hardened, the surface of the reinforced concrete structure is given a special coating containing corrosion inhibitors. These coatings are applied to the surface and form a protective layer that prevents moisture and corrosive ions from penetrating the reinforcement material.
- Inhibitor injection: this method involves the injection of a liquid inhibitor or the injection of an inhibitor in the form of a paste directly into the concrete structure. The injection is usually carried out in damaged or corrosion-infected areas. Injected inhibitors can penetrate deep into the concrete and form a protective layer around the reinforcement structure.
- Subsequent adding into microstructure: special migration inhibitors can be subsequently introduced into the concrete structure. This is usually done by injecting the liquid containing the inhibitors into small openings and microchannels in the concrete structure. The inhibitors are then gradually released and spread throughout the structure, ensuring protection at a microscopic level.

- Special fibre or additive implementation: in some cases, migration inhibitors can be introduced into the concrete as special fibres or additives. These fibres or additives contain chemical substances that migrate to the reinforcement surfaces and thus form a protective layer.

The matrix surfaces should be free of standing water, impurities, dust, oils, greases, solidifying agents and other contaminants. In addition, MCI®- 2018 can be applied to wet surfaces, for example, although dry surfaces are better suited to achieve maximum matrix penetration. Application can be carried out using air dispensers, rollers or brushes. The dispensers should be equipped with hoses and seals that are resistant to solvents.

References

[1] Bronić P., 2023. Properties of migrating corrosion inhibitors and their application in construction engineering, University of Split, University Department of Professional Studies, Split

[2] Serdar M., 2022. How safe is Croatian infrastructure? Sveučilište u Zagrebu, Građevinski fakultet

[3] Lipošćak I., 2021. Migrirajući inhibitori korozije – strategije, rješenja i iskustva s primjerima u zaštiti i sanaciji AB konstrukcija od korozije, Cortec Corporation, Zagreb

[4] Elsener B., Büchler M., Stalder F., and Böhni H., 1999. Migrating Corrosion Inhibitor Blend for Reinforced Concrete: Part 1 - Prevention of Corrosion, Corrosion Vol. 55 No. 12, 1155-1163

[5] Cortec Middle East, MCI for concrete, MCI Technology, https://cortec-me.com/mci-technology/ (accessed 5 March, 2025.)

[6] Lazzari. G., 2021. Cortec’s MCI® Technology Was Chosen to Protect One of The Largest European Bridges, International Paint & Coating Magazine, https://www.ipcm.it/en/post/cortecs-mci-protect-one-of-the-largest-european-bridges.aspx (accessed 10 March 2025.)

[7] MCI, pdf catalogue, https://www.cortecvci.com/Publications/PDS/MCI-2018_MCI_2018VO.pdf, (accessed 10 March, 2025.)

[8] MCI - Migrirajući inhibitori korozije za dugotrajnost betona, Cortec Corporation, pdf catalogue, 2004.

[9] https://cortecros.com/about-us/ (accessed 10 March, 2025.)

Optimizing additive manufacturing processes for high-performance mechanical components using AI-driven parameter prediction and virtual reality simulation

***Sven Maričić*[1,2] *and Dario Iljkić*[3]**

1) Juraj Dobrila University of Pula, Faculty of Engineering, Negrijeva 6, 52100 Pula, Croatia

2) University of Rijeka, Faculty of Medicine, Centre for biomodeling and innovations in medicine, Br. Branchetta 20, 51000 Rijeka, Croatia

3) University of Rijeka, Faculty of Engineering, Vukovarska 58, 51000 Rijeka, Croatia

Corresponding author: smaricic@unipu.hr

Original scientific article

Abstract: This study examines the advantages of Virtual Reality (VR) training in mechanical engineering literature and its capacity for transforming education. Virtual reality training enhances precision and productivity by delivering comprehensive visual and auditory information in immersive environments, hence reducing reliance on expert oversight and face-to-face instruction. It also facilitates virtual prototyping and testing, significantly reducing demand for physical prototypes. This conserves significant time, labour, and materials required for multiple physical model updates. Manufacturers may additionally perform virtual analyses and optimise processes, industrial configurations, and equipment positioning. This eliminates potential errors and interruptions by detecting inefficiencies, bottlenecks, and potential failure points prior to the implementation of physical modifications. This approach integrates also with digital twin technology to utilise virtual equipment inspection and predictive maintenance. By simulating stress scenarios and analysing utilisation patterns, manufacturers may proactively schedule maintenance, hence potentially reducing downtime and repair expenses.

Keywords: *virtual reality; additive manufacturing; virtual prototyping; mechanical engineering*

1. Introduction

Additive manufacturing (AM) has revolutionized the production of complex geometries and high-performance components, enabling designs that are unachievable through conventional methods. This transformative ability makes it possible to make complex, customised, light parts that work better in many fields, such as engineering in general, aircraft, automotive, healthcare, and more [1, 2, 3]. Advanced computational methods are needed to optimise these processes for mechanical characteristics and structural integrity in a complicated multi-parameter space. Complexity makes it difficult to forecast and regulate final material properties, requiring advanced process parameter selection and validation methods. Artificial intelligence (AI) and machine learning approaches are becoming essential tools for addressing these challenges through predictive modelling and optimisation of process parameters. This is especially clear in industries like industrial automation, medical and renewable energy systems that need real-time data analysis and adaptive control. AI-driven methods greatly improve the efficiency and lifespan of these systems [1, 4]. This study reviews the research on AI-driven integration parameter prediction with virtual reality simulation to improve additive manufacturing processes for high-performance mechanical components. Integration of these parameters should speed up process development by reducing iterative testing cycles and identifying optimal material formulations and processing conditions. This method efficiently identifies optimal material compositions and processing parameters, significantly reducing the time and resources required compared to conventional trial-and-error approaches [5, 6]. The increasing sophistication of additive manufacturing necessitates the development of robust predictive models that can accurately

forecast material behaviour under various processing conditions [7]. AI, particularly machine learning algorithms, holds significant potential in predicting material properties [4-7]. This approach helps solve additive manufacturing's specific problems, such as how surface roughness affects fatigue behaviour, that can be predicted with traditional materials [8, 9]. Research advancing towards utilising Virtual Reality (VR) simulations to address specific challenges in AM. The main problems are modeling new material properties and predicting structural weaknesses in 3D-printed parts. One of particular interest area of research is the possibility for 3D printing with less-explored materials, such as 20MnCr5 steel, to ascertain its mechanical properties.

2. Data and methods

2.1. Including and excluding criteria of research

In order to narrow the research scope, following elements presented in Table 1 have been used to collect and organise data from different scientific databases. This systematic procedure ensures methodological clarity.

Table 1. *Inclusion and exclusion criteria*

Criteria	Inclusion	Exclusion
Author Selection	20 unique author-year citations identified directly from research articles.	Duplicate citations or auto-citation combination.
Categorization	Five different categories derived from the primary research themes: "Fundamental AM Challenges & Traditional Limitations", "AI for Process Optimization & Prediction", "Digital Twins & VR Simulation in AM", "AI for Advanced Materials & Inverse Design", and "Synergistic Integration & Broader Impact".	Categories that didn't directly supported by the main criteria.
Contribution Description	A brief summary sentence for each author's contribution, based on the context of their citation in the provided text.	Information not directly stated or inferable; overly detailed or lengthy explanations.

The criteria for inclusion and exclusion, outlined in Table 1, were established to ensure accuracy in the method and sample homogeneity. They clarify the criteria for selecting authors and their contributions, ensuring that only information directly relevant to the subject of research is included. This methodology eliminates additional information, hence improving the accuracy and validity of the evaluation and analysis.

2.2. Methodology

The study implements a clear keyword-focused approach and begins with an initial pool of 60 resources. To extract the most relevant information, it uses keywords like "Virtual Reality", "Additive manufacturing," "AI-driven Parameter Prediction," and "New technologies". The preliminary phase of this systematic literature review entailed outlining the study's objectives, which directed the following selection procedure. Following a comprehensive review of scientific resources, 20 main contributors were identified. These fundamental sources enable a thorough synthesis of the connection and effects of principal domains—new technologies, artificial intelligence, virtual reality —on the technological advancement of additive manufacturing.

1. Evaluating how technological development affects the manufacturing industry. AM Challenges, Engineering Material Limitations. Examining how Virtual Reality is changing mechanical engineering education and manufacturing processes is the main goal.

2. Examining how organisational activities relate to the wider ethical and environmental effects of technology. Examining the advantages that AI and VR integration into engineering practices is the main goal of this objective.

3. Evaluating the integration of educational components and operational effectiveness. Evaluating the impact of VR-based training on operational procedures is the main objective. VR Simulation in AM AI/ML for Advanced Materials. By offering immersive learning environments that reduce the need for expert supervision and tangible training materials, this evaluation gauges gains in workflow efficiency, accuracy, and error reduction.

4. Suggested Future Research Goals: Examining how the adoption of advanced manufacturing technologies is impacted by workforce upskilling. Understanding how VR training environments support workforce upskilling for mechanical engineering tasks is the aim of this objective. Without the risks or expenses of training on real equipment, the emphasis is on examining how well immersive simulations can improve employee skills, especially in areas like equipment inspection, process analysis, and predictive maintenance.

5. Assessing the return on investment (ROI) and economic feasibility of deploying smart factory technologies. Doing a cost-benefit analysis of implementing applied technologies in engineering and manufacturing is the main goal of this objective. It will evaluate the financial benefits of eliminating the need for physical prototypes, using virtual analysis to minimise production disruptions, and using VR-assisted predictive maintenance to reduce repair costs.

3. Results

The literature review presented in Table 2 gives a detailed picture of how VR and AI are changing mechanical engineering, from educational institutions to market implementation. An analysis of the academic articles chosen for this study reveals an increasing trend toward combining new technologies to overcome the limitations of older methodologies. These articles, referenced as [10-31], were selected based on the criteria presented in Table 1. This convergence is particularly significant in fields like additive manufacturing, where artificial intelligence and machine learning can assist in helping to solve complex problems. These technologies can be used to more accurately predict material behavior and improve quality control for high-performance mechanical components. A common theme in the research is that VR can improve industrial accuracy, productivity, and sustainability by creating dedicated, risk-free spaces for virtual prototyping, process optimisation, and predictive maintenance.

Table 2. *Results of included study findings, detailed literature overview [10– 31]*

No.	Author(s) and Publication year	Description	Scope*
1	Strojny, 2023 [10]; Suryawinata & Mariana, 2022 [11]	Explained that VR enhances industrial precision and productivity by delivering comprehensive visual and auditory information in immersive settings. Stated that VR can simulate environmental conditions to assess a design's behavior before it's built.	1
2	Peruzzini et al., 2009 [12]	States that VR is a transformative technology in mechanical engineering education and practice, offering key advantages over traditional methods.	1, 3

No.	Author(s) and Publication year	Description	Scope*
3	Ciccone et al., 2023 [13]; Klenam et al., 2025 [14]	These studies demonstrate the detailed and multi-parameter nature of traditional and additive manufacturing, emphasising the difficulties of material prediction and the limitations of trial-and-error methods.	3, 4
4	Xie et al., 2021 [15]; Kanade & Duffy, 2022 [16]; Renganayagalu et al., 2021 [17]	Notes that VR simulations enable self-directed learning and skill acquisition, reducing the need for direct expert supervision. Its adaptability helps accelerate practical skills and that AI integration creates intelligent tutoring systems. VR training improves learning outcomes and skill retention for complex tasks due to its superior engagement over conventional methods.	3, 4
5	Win et al., 2021[18]	Describes how virtual prototyping significantly saves time and materials by decreasing the need for physical models.	5, 2
6	Din et al., 2024 [19]	Highlights that virtual analysis helps optimize industrial processes and layouts, identifying potential errors and bottlenecks before real implementation.	1, 5
7	Pedram et al., 2021 [20]	Details how VR, with digital twin technology, enables virtual inspections and predictive maintenance to reduce equipment downtime and repair costs.	4, 5
8	Abbas et al., 2021 [21]; Maulana & Purnomo, 2021 [22]; Marougkas et al., 2023 [23]	Mentions that VR provides flexible and adaptive training experiences that are tailored to the learner's progress and skill needs. Contended that active engagement in VR boosts student motivation and learning outcomes by being more interactive and stimulating than traditional methods.	2, 3
9	Grajewski et al., 2015 [24]; Jin et al., 2020 [25]	Explains that VR allows for product recyclability evaluations during the design phase to optimize for future disassembly and material recycling. This is particularly crucial in additive manufacturing, where AI and machine learning can address complex challenges such as surface quality defects and in-situ anomaly detection	2
10	Upadhyay & Khandelwal, 2018 [26]	Concludes that VR revolutionizes engineering by providing an efficient, safe, and engaging platform for skill development and process optimization.	1, 3, 4
11	Su et al., 2025 [27]; Suhag, 2025 [28]; Crogman et al., 2025 [29]	Asserts that integrating AI with immersive systems enhances student engagement in engineering education through personalized, self-paced learning. Suggests that VR improves student engagement and motivation, which are critical for effective knowledge transfer and retention in educational settings. Noted that VR's experiential learning approach aligns with modern engineering curricula that reinforce theory with practical application.	3

No.	Author(s) and Publication year	Description	Scope*
12	Lastrucci et al., 2025 [30]; Ziyatdinova & Bezrukov, 2021 [31];	Noted that AI and VR integration allows for the creation of realistic, risk-free training modules for highly complex procedures. Pointed out that VR allows for repeated practice in a safe environment, which is a major pedagogical advance for refining skills in high-stakes fields. Immersive VR lets students interact with complicated concepts and virtual prototypes, improving knowledge and practical abilities. VR's participatory learning model improves theory and problem-solving. It also improves soft skills like communication and collaboration, preparing engineers for teams.	2, 3, 4

*Five objectives from paragraph 2.2. Methodology

The study also shows that new technologies have a big effect on engineering education. Combining them, learning activities are becoming more interactive and personalised, which keeps students interested, speeds up the acquisition of practical skills, and helps them remember what they've learnt. Implementation of this approach, although promising, presents several obstacles. The increased expenses and specialised hardware prerequisites for advanced virtual reality systems may restrict their accessibility, especially for smaller research laboratories and businesses. The computational demands of complex AI models and multi-physics simulations pose considerable challenges, necessitating extensive processing power and perhaps constraining the framework's real-time applicability.

4. Conclusion

This research shows a significant scientific trend: integrating AI-driven parameter prediction with virtual reality simulation to improve additive manufacturing for high-performance mechanical components. Presented framework provides a thorough solution for improving complex additive manufacturing processes, shifting from traditional empirical approaches to a data-driven model. Described transition reduces development cycles and considerably enhances product quality. Integrated visualisation and interactive training tools enable the multimodal approach to be presented as a useful tool for advanced manufacturing research, which can enhance the accurate production of components with specified mechanical properties and functions. The integration of AI and VR can significantly enhance not only materials discovery but also process optimisation. This promising approach, however, encounters substantial challenges. The elevated expense of specialised VR equipment and the substantial processing demands of complex AI models may restrict its accessibility for broader adoption and scalability. Future research will focus on enhancing AI models with multi-physics simulations to improve predictive accuracy and integrating haptic feedback into VR environments to make virtual training more practical. These advancements aim to overcome current limitations, such as high costs and intensive processing, making the technology more accessible for wider adoption and scaling. Beside that, the integration of haptic feedback into the VR environment will also be investigated to improve the practicality of virtual training and operational interactions in additive manufacturing processes.

Acknowledgments

This research was supported by *EduCalucemTech* project.

References

[1] Bello, S. A., Wada, I., Ige, O. B., Chianumba, E. C., Adebayo, S. A., 2024. AI-driven predictive maintenance and optimization of renewable energy systems for enhanced operational efficiency and longevity. International Journal of Science and Research Archive, 13(1), 2823. https://doi.org/10.30574/ijsra.2024.13.1.1992

[2] Bubeník, P., Rakyta, M., Buzalka, M., Biňasová, V., Kovaríková, Z., 2025. Optimization of Business Processes Using Artificial Intelligence. Electronics, 14(11), 2105. https://doi.org/10.3390/electronics14112105

[3] Górski, F., Łabudzki, R., Żukowska, M., Sanfilippo, F., Ottestad, M., Zelenay, M., Băilă, D.-I., Pacurar, R., 2023. Experimental Evaluation of Extended Reality Technologies in the Development of Individualized Three-Dimensionally Printed Upper Limb Prostheses. Appl. Sci., 13, 8035. https://doi.org/10.3390/app13148035

[4] Erps, T., Foshey, M., Luković, M. K., Shou, W., Goetzke, H. H., Dietsch, H., Stoll, K., von Vacano, B., Matusik, W., 2021. Accelerated discovery of 3D printing materials using data-driven multiobjective optimization. Science Advances, 7(42) https://doi.org/10.1126/sciadv.abf7435

[5] Onyelowe, K. C., Hanandeh, S., Ulloa, N., Barba-Veras, R., Moghal, A. A. B., Ebid, A. M., Arunachalam, K. P., & Rehman, A. U., 2025. Developing machine learning frameworks to predict mechanical properties of ultra-high performance concrete mixed with various industrial byproducts. Scientific Reports, 15(1), 24791. https://doi.org/10.1038/s41598-025-08780-y

[6] Onukwuli S., K., Okpala C., C., Udu C., E., 2025. The Role of Additive Manufacturing in Advancing Lean Production System, International Journal of Latest Technology in Engineering, Management & Applied Science (IJLTEMAS), vol. 14(3), pages 179-188. https://doi.org/10.51583/IJLTEMAS.2025.140300022

[7] Zhou, L., Miller, J., Vezza, J., Mayster, M., Raffay, M., Justice, Q., Tamimi, Z. A., Hansotte, G., Sunkara, L. D., & Bernat, J., 2024. Additive Manufacturing: A Comprehensive Review. Sensors, 24(9), 2668. Multidisciplinary Digital Publishing Institute. https://doi.org/10.3390/s24092668

[8] Fonović, M., Kvrgić, D., Liverić, L., Kavre Piltaver, I., 2025. Impact of KNO3-Based Salt Nitriding Treatment on the Microstructure and Corrosion Resistance of Steel 20MnCr5. Materials, 18(8), 1857. https://doi.org/10.3390/ma18081857

[9] Maričić, S., Kršulja, M., Iljkić, D., Knežević, Z., 2024. An AI-Driven Approach for a Comprehensive Evaluation of 3D Printed Molds in Aluminium Casting, Considering Material, Speed, Precision, Modeling Time, and Costs // Proceedings of 13th International Conference Mechanical Technologies and Structural Materials 2024 / Čatipović, Nikša; Krolo, Jure; Gjeldum, Nikola (ur.). Split: Fakultet elektrotehnike, strojarstva i brodogradnje Sveučilišta u Splitu. str. 273-280

[10] Strojny, P., & Dużmańska-Misiarczyk, N., 2023. Measuring the effectiveness of virtual training: A systematic review. Computers & Education X Reality, 2, 100006. Elsevier BV. https://doi.org/10.1016/j.cexr.2022.100006

[11] Suryawinata, B. A., Mariana, Y., 2022. The Role of Virtual Reality in Green Building Design. IOP Conference Series Earth and Environmental Science, 998(1), 12037. https://doi.org/10.1088/1755-1315/998/1/012037

[12] Peruzzini, M., Mengoni, M., Germani, M., 2009. Evaluating the Impact of Virtual Reality on Mechanical Design Education. 107. https://doi.org/10.1115/winvr2009-722

[13] Ciccone, F., Bacciaglia, A., Ceruti, A., 2023. Optimization with artificial intelligence in additive manufacturing: a systematic review. J Braz. Soc. Mech. Sci. Eng. 45, 303. https://doi.org/10.1007/s40430-023-04200-2

[14] Klenam, D., Mcbagonluri, F. Asumadu, T., Osafo, S., Bodunrin, M., Agyepong, L., Osei, E., Mornah, D., Soboyejo, W.O., 2025. Additive manufacturing: shaping the future of the manufacturing industry – overview of trends, challenges and opportunities. Applications in Engineering Science. 22. 100224. 10.1016/j.apples.2025.100224.

[15] Xie, B., Liu, H., Alghofaili, R., Zhang, Y., Jiang, Y., Lobo, F. D., Li, C., Li, W., Huang, H., Akdere, M., Mousas, C., Yu, L.-F., 2021. A Review on Virtual Reality Skill Training Applications. Frontiers in Virtual Reality, 2. Frontiers Media. https://doi.org/10.3389/frvir.2021.645153

[16] Kanade, S. G., & Duffy, V. G., 2022. Use of Virtual Reality for Safety Training: A Systematic Review. Lecture Notes in Computer Science, 364. Springer Science+Business Media. https://doi.org/10.1007/978-3-031-06018-2_25

[17] Renganayagalu, S. K., Mallam, S., Nazir, S., 2021. Effectiveness of VR Head Mounted Displays in Professional Training: A Systematic Review. Technology Knowledge and Learning, 26(4), 999. Springer Science+Business Media. https://doi.org/10.1007/s10758-020-09489-9

[18] Win, L. L., Aziz, F. A., Hairuddin, A. A., Abdullah, L. N., Yap, H. J., Saito, H., Hisham, S., 2021. Visual effects creation to improve user performance in fully immersive virtual environment of automobile engine assembly. IOP Conference Series Materials Science and Engineering, 1109(1), 12038. https://doi.org/10.1088/1757-899x/1109/1/012038

[19] Din, Z. U., Mohammadi, P., Sherman, R., 2024. A systematic review and analysis of the viability of virtual reality (VR) in construction work and education. Cornell University. https://doi.org/10.48550/arxiv.2408.01450

[20] Pedram, S., Skarbez, R., Palmisano, S., Farrelly, M. C., Perez, P., 2021. Lessons Learned From Immersive and Desktop VR Training of Mines Rescuers. Frontiers in Virtual Reality, 2. https://doi.org/10.3389/frvir.2021.627333

[21] Abbas, Y., Martinetti, A., Nizamis, K., Spoolder, S., Dongen, L., 2021. Ready, trainer … one*! discovering the entanglement of adaptive learning with virtual reality in industrial training: a case study. Interactive Learning Environments, 31(6), 3698. https://doi.org/10.1080/10494820.2021.1940215

[22] Maulana, F. I., Purnomo, A., 2021. Development of Virtual Reality Application to Increase Student Learning Motivation with Interactive Learning in Vocational Education. IOP Conference Series Materials Science and Engineering, 1071(1), 12019. https://doi.org/10.1088/1757-899x/1071/1/012019

[23] Marougkas, A., Troussas, C., Krouska, A., Sgouropoulou, C., 2023. Virtual Reality in Education: A Review of Learning Theories, Approaches and Methodologies for the Last Decade. Electronics, 12(13), 2832. Multidisciplinary Digital Publishing Institute. https://doi.org/10.3390/electronics12132832

[24] Grajewski, D., Diakun, J., Wichniarek, R., Dostatni, E., Buń, P., Górski, F., Karwasz, A., 2015. Improving the Skills and Knowledge of Future Designers in the Field of Ecodesign Using Virtual Reality Technologies. Procedia Computer Science, 75, 348. https://doi.org/10.1016/j.procs.2015.12.257

[25] Jin, Z., Zhang, Z., Demir, K., Gu, G. X., 2020. Machine Learning for Advanced Additive Manufacturing. Matter, 3(5), 1541. https://doi.org/10.1016/j.matt.2020.08.023

[26] Upadhyay, A. K., Khandelwal, K., 2018. Virtual reality: adding immersive dimension to sales training. Human Resource Management International Digest, 26(4), 42. https://doi.org/10.1108/hrmid-01-2018-0014

[27] Su, M., Ma, L., Zhang, D., Yunusa-Kaltungo, A., Cheung, C., 2025. Exploring Benefits and Concerns of Incorporating Digital Tools into Engineering Education. European Journal of Education and Pedagogy, 6(1), 45. https://doi.org/10.24018/ejedu.2025.6.1.909

[28] Suhag, N., 2025. The Impact of Virtual Reality on Student Engagement in Higher Education. https://doi.org/10.2139/ssrn.5016008

[29] Crogman, H. T., Cano, V. D., Pacheco, E., Sonawane, R., Boroon, R., 2025. Virtual Reality, Augmented Reality, and Mixed Reality in Experiential Learning: Transforming Educational Paradigms. Education Sciences, 15(3), 303. https://doi.org/10.3390/educsci15030303

[30] Lastrucci, A., Iosca, N., Wandael, Y., Barra, A., Lepri, G., Forini, N., Ricci, R., Miele, V., Giansanti, D., 2025. AI and Interventional Radiology: A Narrative Review of Reviews on Opportunities, Challenges, and Future Directions. Diagnostics, 15(7), 893. Multidisciplinary Digital Publishing Institute. https://doi.org/10.3390/diagnostics15070893

[31] Ziyatdinova, J., Bezrukov, A., 2021. Virtual Reality for Developing Intercultural Communication Skills of Engineering Students. In Advances in intelligent systems and computing (p. 621). Springer Nature. https://doi.org/10.1007/978-3-030-68198-2_57

Investigation of the quality of EN-GJS-400-15 ductile cast iron

***Luka Mesek*[1], *Zdenka Zovko Brodarac*[1], *Mitja Petrič*[2] *and Desimir Bobinac*[3]**

1) University of Zagreb Faculty of Metallurgy, Aleja narodnih heroja 3, 44 000 Sisak, Croatia

2) University of Ljubljana Faculty of Natural Sciences and Engineering, Department of Materials and Metallurgy, Aškarčeva cesta 12, 1000 Ljubljana, Slovenia

3) Ferro-Preis d.o.o., dr. Tome Bratkovića 2, 40 000, Čakovec, Croatia

Corresponding author: lmesek@simet.hr

Original scientific article

Abstract: This study presents a comprehensive investigation of the microstructural, thermodynamic, chemical and mechanical properties of EN-GJS-400-15 ductile cast iron. A series of cast samples were analysed using thermal analysis (ATAS MetStar), metallographic analysis and mechanical properties analysis to evaluate the influence of processing parameters on material performance. The study showed that individual control of chemical composition is not sufficient to guarantee compliance with EN 1563:2018. Instead, an integrated approach is required that includes carbon equivalent (CEL), the effect of inoculation and nodulation, recalescence (R), cooling rates, and consequently ferrite/pearlite ratio and graphite morphology. While most of the values of the samples met the requirements of EN 1563:2018, only a subset did not fulfil the required mechanical properties due to microstructural degradation. In this work, a statistical analysis of the influence of the chemical composition, CEL, and thermodynamic parameters of the casting process on the final mechanical properties of the castings was carried out. The statistical analysis of obtained results underline the crucial role of combined control of chemistry, thermodynamic behaviour and microstructure features in ensuring reliable ductile iron quality.

Keywords: *EN-GJS-400-15; spheroidal graphite; chemical composition; thermal analysis; mechanical properties; microstructure; statistical analysis.*

1. Introduction

The metallurgical properties of ductile cast iron are a focus of research due to its wide range of industrial applications and its mechanical properties, which are similar to those of (some) steels. Compared to cast steel, ductile cast iron has many technical and manufacturing advantages. The advantages are particularly evident in the automotive industry and a variety of industrial applications [1], [2], [3]. Various factors such as melt treatment, cooling rates and alloy composition have a significant influence on the thermodynamic and mechanical properties of cast iron [4], [5]. Ductile cast iron is a ferrous alloy with the main alloying element carbon (C) which forms spheroidal graphite nodules while content of other alloying elements (e.g. silicon (Si), magnesium (Mg), manganese (Mn)) controls its morphology and shape [6]. In general, the carbon content is between 3-4% and the silicon content between 2-3%, which ensures the eutectic solidification temperature of 1165 °C. The amount of carbon remaining depends on the cooling and solidification rate, the inoculation practise and the presence of alloying elements that promote either the formation of graphite [7], [8]. The microstructure of ductile cast iron is characterised by spheroidal (nodular) graphite distributed in a ferrite-pearlite matrix. In EN-GJS-400-15 alloy recommended ferrite/pearlite ratio is 80/20 ([%]) [9]. The morphology and quantity of graphite have a significant influence on the properties of ductile cast iron. Graphite nodules with high roundness and small diameter can improve the mechanical properties of castings [10], [11]. Increasing the number of nodules reduces carbide precipitation by providing more nucleation sites for carbon diffusion, which stabilises graphite formation. This leads to a more homogeneous ferrite/pearlite matrix with less brittle phases, which improves the elongation and toughness of the material [12]. An increased number of nodules and their uniform distribution

lead to a rounder eutectic grain profile, which favours the fluidity of the melt, and thus reduces the tendency of ductile cast iron to shrink [13].The morphology, quantity and shape of the graphite nodules depend primarily on the cooling rate, the temperature of the surrounding sections, the casting temperature, the initial temperature of the mould and the moulding material [10], [11]. A higher cooling rate leads to an increased number of graphite nodules and a reduction in their size, accompanied by a higher ferrite content therefore lower pearlite content. The standard microstructure of EN-GJS-400-15 ductile cast iron typically consists of a predominant ferritic matrix (≥80%) with a minimal pearlite content [9]. This microstructure ensures a balanced combination of mechanical properties [10], [11]. In contrast to cast iron, where graphite precipitates in the form of lamellae, the main advantage of nodular cast iron lies in its spheroidal graphite morphology. This morphology reduces the internal stresses in the matrix and contributes to a higher hardness. A predominantly ferritic matrix ensures a relatively high ductility with an elongation of 15% [10], [11].
The chemical composition, melt treatment and the solidification conditions influence the development of the microstructure, which in turn determines important mechanical properties such as tensile strength and hardness. The role of alloying elements in ductile cast iron varies, as such each element influences the material in its own specific way. The correct balance of alloying elements must be carefully controlled. The most important ability of alloying elements is to promote the formation of a graphite phase and to stabilise the phase. Alloying elements are categorised into elements that encourage austenite, ferrite, carbides and nitrides formation [14], [15].

- Graphite-forming elements: silicon (Si), cobalt (Co), aluminium (Al) and nickel (Ni).
- Carbide-forming elements: chromium (Cr), titanium (Ti), tungsten (W), vanadium (V), manganese (Mn), and molybdenum (Mo).
- Austenite stabilising elements: manganese (Mn), cobalt (Co), nickel (Ni) and copper (Cu).
- Ferrite stabilising elements: silicon (Si), chromium (Cr), tungsten (W), vanadium (V), molybdenum (Mo)].

According to the literature, elements such as Mg, Si, Mn, Ni, Mo, Cu, Ti, V, Nb, Cr and others are typical alloying elements used in the production of ductile cast iron. The literature shows following:

- Magnesium (Mg) is the most important nodulising agent in ductile cast iron, as it plays a decisive role in the transformation of the graphite morphology from lamellar to spheroidal. This modification is achieved by adding magnesium-based alloys - usually in the form of ferrosilicon master alloys - to the base melt. Due to its high affinity for oxygen and sulphur, magnesium forms stable oxides and sulphides which promote the nucleation and growth of graphite nodules [15]. The residual magnesium content is in general between 0.02 and 0.06%. A strict additon of Mg is critical in order to ensure the reaction of spheroidization of graphite resulted with targeted amount of residual Mg content. However, a content of less than 0.03% leads to poor nodule formation and impaired mechanical properties. On the other hand, too high Mg content can promote the formation of carbides and inclusions. The phenomenon of the Mg fade effect can be counteracted by lowering the temperature. The solidification of ductile cast iron starts with the growth of austenite from liquid melt [16], [17].
- The silicon (Si) content is usually between 2-3%, it strongly promotes graphitisation and ferrite formation in ductile cast iron; it has a certain effect in preventing grain enlargement. Silicon increases stability, yield strength and wear resistance. Solid solution strengthening begins to take effect in ferritic ductile cast iron at contents above approx. 3% Si, but only up to approx. 4.3% Si, after which the mechanical properties decrease [18], [19], [20].
- The manganese (Mn) content is in general between 0.1 and 0.3%. It acts as a pearlite stabiliser and promotes the formation of carbides. This element is known for forming free cementite in the metallic matrix which is an udisirable phase in ductile cast iron [21]. In this content range Mn improves mechanical properties such as hardness and wear resistance by inducing the formation of carbides [21], [22], [23].

- The sulphur (S) content in ductile cast iron must be carefully controlled. During the nodularization process, a large number of nuclei are formed to precipitate the graphite. They are magnesium, calcium and cerium sulphides which are covered by thin layer of magnesium silicate. These particles will not yet serve as a growth site for graphite due to non coherent crystalline structure. However, the silicates formed have the same hexagonal crystalline structure as the graphite, so that they serve as effective nucleation sites for the growth of graphite nodules [24]. While a low sulphur content is generally desirable to prevent excessive magnesium consumption and the formation of deleterious phases, too low sulphur content can lead to inadequate heterogeneous nucleation sites. MgS particles, when properly controlled, act as effective nucleation substrates for spheroidal graphite. Consequently, the optimum sulphur content for a balance between melt cleanliness and nucleation efficiency is typically in the range of 0.008–0.015% [24], [25].
- Nickel is the most commonly used alloying element because it reduces the stability of the primary carbides and at the same time refines the pearlite, thus increasing the strength of the ductile cast iron [26]. It is mainly added to lower the temperature of the critical points and behaves similarly to Mn. The addition of Ni also improves the hardness [14].
- Molibdenium acts primarily as a carbide-promoting element. It is also assumed that Mo is dissolved in the ferrite matrix and serves as a strength-enhancing element. Its addition increases the yield and tensile strength [27], [28].
- Copper acts as a pearlite stabiliser in ductile cast iron, promoting a higher pearlite content and refining the interlamellar spacing, thereby increasing tensile strength and hardness at the expense of lower elongation and notched bar impact strength [29], [30].
- Titanium has grain-refining properties, it acts as inoculation modifier. Titanium promotes graphite nucleation and refines nodule size by increasing undercooling during solidification. According to the literature, in thin walled castings Ti addition slightly reduces ferrite fraction [31], [32]. Tensile strength slightly increases with addition of Ti up to 0.09%. Increasing the Ti content causes a decrease in tensile strenght and elongation in thin-walled iron casting.
- Chromium is a commonly used alloying element that promotes pearlitic transformation through the decomposition of carbides, which significantly increases tensile strength and hardness. However, increased amounts of Cr can lead to cooling effects, promote intercellular carbide mixing and greatly reduce elongation. Careful control of the amount of Cr is therefore necessary [33], [34].
- Phosphorus, even in traces, segregates strongly during solidification and forms low-melting phosphorus eutectics at the graphite nodule boundaries. The phosporus eutectics combine with iron and form Fe_3P. This phase is hard and brittle. It also leads to reduced mechanical properties as well as to the increase of brittle-ductile temperature transition and porosity. Maintaining the P content below 0.06% is standard practice, as exceeding 0.07% leads to a sharp drop in elongation and impact strength [35], [36], [37], [38].
- Aluminium, even in trace amounts (0.005-0.02%), is a beneficial inoculant in ductile cast iron. Aluminium forms complex silicate inoculants that promote graphite nucleation, resulting in a refined nodule count and improved mechanical properties without promoting porosity [39]. At higher concentrations (0.1-0.5%), aluminium promotes ferrite stabilisation at the expense of pearlite, which improves oxidation resistance at elevated temperatures and fatigue strength, although excessive Al content (more than 0.02%) can adversely affect castability and graphite morphology [40].
- Calcium is usually added in combination with Mg in a total amount of 0.01-0.03%. It acts as a strong graphite inoculant by forming compounds with Si and O in the melt. It improves the heterogeneous nucleation sites and increases the number of nodules, especially in castings with a thin cross-section [41].

In recent years, extensive research has been carried out on ductile cast iron [8], [13], [14], [17], [19], [20], [22], [29], [40], both on the theory of transformation and on the properties of the material. Most of the research has been focused on potential advances in the mechanical properties of ductile cast iron [8], [14], [19], [22], [28], [29], [31], [38], [40], [41]. This involves the thermodynamic and thermomechanical stability of the microstructure, the influence of alloying constituents on the mechanical properties, the influence of heat treatment and the influence of alloying constituents on the microstructure and the state of residual stress. The aim of this study was to investigate the influence of process temperatures, chemical composition and microstructure on the mechanical properties and overall quality of the ductile cast iron EN-GJS-400-15.
The quality and reliability of EN-GJS-400-15 ductile cast iron cannot be predicted by a single parameter. The chemical composition and thermodynamic behaviour determine the microstructural development of the casting, which in turn determines the final mechanical properties. If all parameters are in line with the standard, the result is a high-performance material suitable for the automotive industry and a wide range of industrial applications. Any deviation triggers cascading changes in the observed parameters, which are ultimately reflected in the final mechanical properties. Therefore, the comprehensive impact and mutual intereaction of the chemical composition, CEL, and thermodynamic parameters of the casting process on the final mechanical properties of the castings were analysed.

2. Materials and methods

The experiment was carried out under industrial conditions. The casting process was carried out in self-hardening sand moulds (furan resin bonded molding sand) at different temperatures. The samples differed in chemical composition and were treated with various additives (inoculants, carburisers, etc). The composition of the charge material for the melt and its range are listed in Table 1.

***Table 1**. Charge material composition*

Material	Pig iron	Steel	Recycled material	FeSi	Scrap	Additions
Range / [%]	50-60	10-30	15-25	0.8-1.2	3-10	Around 3%

Main addition for the melt modification si FeSiMg alloy. Besides Fe the content of other elements is as follows: Si 44-48%, Mg 5-6%, Ca 0.4-0.6%, Al 0.8-1-2% and lanthanum (La) 0.25-0.40%. In addition, a coating agent was used for the noduliser, which is also based on Fe. The content of other elements is as follows: Si 46-50%, Ba 0.75-1.25%, Ca 0.75-1.25% and Al 0.75-1.25%.
In accordance with standard EN 1563:2018 [9], the values for required chemical composition and mechanical properties are given in Table 2 and Table 3.

***Table 2**. Required chemical composition according to EN 1563:2018 [9]*

Material	C	Si	Mg	Mn	P	S	Cu	Al
Range / [%]	3.4-3.8	2.3-3.1	<0.07	0.1–0.3	<0.10	<0.02	-	-

***Table 3.** Required mechanical properties according to EN 1563:2018 [9]*

Material designation according to EN 1563:2018	Tensile strength, R_m / [N/mm^2]	Elongation, (A_{50}) / [%], min	Brinel hardness, HBW
EN-GJS-400-15	350-400	15	135-280

The temperature of the melt during pouring was measured with a Heraeus Electro-Nite Digitemp device, while the thermodynamic effects of the solidification process were monitored and controlled with the ATAS MetStar system, version 10.4.2.
The chemical composition of the alloys was determined using an ARC iSpark 8860/1016 optical emission spectrometer. For metallographic analysis, the samples were analised in polished and etched

condition. The samples were etched in 4 % Nital solution (4 mL of nitric acid in 96 mL of alcohol) for 10 s. The polished state was used for graphite analysis while the etched state enables the interpretation of the microstructure of the metal matrix. The microstructural analysis was then performed using an AmScope optical microscope equipped with an AmScope MU500 digital camera. The mechanical tests included an analysis of the tensile strength, which was carried out on a Wolpert U20 universal testing machine. The Brinell hardness of the samples was measured using a Nexus 3200 hardness tester.

3. Results and discussion

The investigation of the quality of ductile cast iron of grade EN-GJS-400-15 was analysed according to the data set. The data set consists from thermal parameters, chemical composition, microstructure features and mechanical properties such as elongation, hardness and tensile strength.

An overview of all thermal parameters is shown in Table 4. Thermal analysis provides an essential insight into the significant temperatures of phase changes and transformations of ductile cast iron by tracking the temperature changes during cooling, solidification and phase transformations [43], [44], [45]. The main thermal parameters used in this study are:

- pouring temperature (T_p),
- liquidus temperature (T_L). The value range is 1130.0-1145.0 °C [45],
- eutectic transformation start temperature (T_{ES}) - the temperature at which eutectic solidification begins and which marks the start of graphite and austenite formation [43], [44]. The value range is 1141.6-1154.1 °C [45],
- transformation temperature in the solid-state (T_S) - the point at which solidification is complete and the last liquid phase disappears [43], [44]. The value range is 1080.0-1150.0 °C [45],
- cooling rate at start of eutectic transformation (dT/dtT_{ES}) – indicates the rate of temperature decrease at the beginning of eutectic crystallisation. Higher values indicate rapid cooling, which can hinder proper graphite formation and increase the risk of carbide precipitation [43], [44]. The value range is: -2-0 [45],
- eutectic solidification energy (S_1) – represents the amount of thermal energy released during the eutectic reaction and is often interpreted as the area under the cooling curve in this interval. Higher values generally indicate a more stable and uniform graphite formation process [43], [44]. The value range is: 0-21.3 [45],
- minimum temperature before recrystallisation (T_{Elow}) and maximum temperature during recrystallisation (T_{Ehigh}) define the thermal window in which recrystallisation takes place and reflect nucleation activity and graphite expansion [43], [44]. The value range for T_{Elow} is 1130.9-1140.9 °C [45], while the value range for T_{Ehigh} is 1130.0-1150.8 °C [45],
- process stability index (R) – calculated as the difference between T_{Ehigh} and T_{Elow} - recalesence. This value quantifies the thermal fluctuations during eutectic solidification. Lower R values indicate stable thermal conditions, while higher values may be associated with inconsistent nucleation or an increased risk of porosity [43], [44]. The value range is: 2-6 [45].
- cooling rate at solid-state transformation (dT/dtT_S) – reflects the rate of temperature drop at the end of solidification. Excessive cooling rates in this phase can lead to microstructural inhomogeneities and the formation of undesirable phases [43], [44]. The value range is: -4.0--2.5 [45].

Table 4. *Overview of the temperature parameters for obtained casting samples*

Sample	T_p / [°C]	T_{ES} / [°C]	T_S / [°C]	dT/dtT_{ES}	S_1	T_{Elow} / [°C]	T_{Ehigh} / [°C]	R / [°C]	dT/dtT_S
1	1428	1140.1	1098.5	-0.08	0	1140.1	1142.3	2.20	-2.35
2	1401	1144.7	1092.1	-0.02	0	1144.7	1146.9	2.20	-3.09
3	1390	1134.0	1091.3	-0.05	0	1134.0	1141.8	7.80	-2.61

Sample	T_p / [°C]	T_{ES} / [°C]	T_S / [°C]	dT/dT_{ES}	S_1	T_{Elow} / [°C]	T_{Ehigh} / [°C]	R / [°C]	dT/dT_S
4	1399	1131.9	1091.1	-0.10	0	1131.9	1141.4	9.50	-2.44
5	1419	1139.3	1097.6	-0.09	0	1139.3	1143.8	4.50	-2.60
6	1423	1144.8	1096.3	-0.20	20.5	1143.2	1145.2	2.00	-2.97
7	1402	1141.4	1090.8	-0.19	27.7	1141.4	1138.5	0.50	-2.62

The thermal analysis of the ductile cast iron samples revealed differences in the eutectic transformation behaviour and in the process stability, which were primarily influenced by the pouring temperature and the cooling dynamics. Samples 1, 2 and 5 are thermodinamically stable, but their S_1 value is 0, indicating insufficient energy for eutectic transformation and a high risk of carbide and degenerate graphite nodule formation [43], [45]. Samples 3 and 4 have low T_{ES} values, excessively high recalesecence as well as S_1 values of 0, indicating insufficient energy for eutectic transformation and a high risk of carbide and degenerate graphite nodule formation [43], [45]. The parameters of the thermal analysis of sample 6 show a high-quality model of the melt, a thermodynamically stable sample characterised by a higher T_{ES}, recalescence of R=2.0 °C and S_1=20.5. The thermal analysis of sample 7 shows very high S_1 value, all other parameters are within acceptable range [45].
The chemical composition of the individual batches is listed in Table 5. Together with the chemical composition, the carbon equivalent (CEL) is also given in the table. The carbon equivalent is calculated according to the following equation [46], [47]:

$$CEL = \%C + \frac{\%Si}{4} + \frac{\%P}{2} \quad (1)$$

Table 5. *Chemical composition of collected casting samples*

Sample	C / [%]	Si / [%]	Mg / [%]	Mn / [%]	P / [%]	S / [%]	Cu / [%]	Al / [%]	CEL
1	3.727	2.725	0.045	0.264	0.032	0.013	0.040	0.012	4.420
2	3.660	2.910	0.051	0.209	0.025	0.010	0.036	0.018	4.400
3	3.600	2.690	0.046	0.202	0.023	0.012	0.033	0.011	4.280
4	3.830	2.670	0.041	0.155	0.022	0.010	0.017	0.009	4.510
5	3.780	2.937	0.045	0.227	0.026	0.013	0.021	0.009	4.530
6	3.660	2.588	0.038	0.178	0.026	0.012	0.027	0.008	4.320
7	3.697	2.758	0.055	0.161	0.025	0.011	0.094	0.014	4.400

The chemical composition of the analysed samples complies with the standard EN 1563:2018 [9] for the ductile cast iron grade EN-GJS-400-15. The chemical composition of all analysed samples is within the range specified in EN 1563:2018 [9]. The CEL determines the composition of the alloy. A CEL value of 4.25-4.30 indicates an alloy with an eutectic composition for the pearlite-ferrite matrix. Values above CEL 4.25-4.30 indicate an alloy with a hypereutectic composition, while alloys below the value of CEL 4.25-4.30 indicate an alloy with a hypoeutectic composition [48], [49]. The controlled residual Mg content supports proper graphite nodularity, while a low P and S content contribute to material quality. This is the main reason for the strict control of the content of these elements.
Table 6 shows a microstructural features analysis of the grade EN-GJS-400-15 ductile cast iron. The key parameters include the ferrite/pearlite ratio, graphite nodularity, graphite size and type as well as graphitisation factors (GRF1 and GRF2) and acicularity level. Acicularity level (ACEL) measures the extent of needle-like microstructures, commonly associated with pearlitic phases which can influence the hardness of ductile cast iron. Primary graphitisation factor (GRF1) refers to primary graphitisation which relates to the number and activity of nucleation sites during the initial stage of eutectic crystallization. The GRF1 targeted range value is: 51-110 [45]. High GRF1 values indicate an adequate presence of nodulizing elements (e.g. Mg, Al, Ce) and a large number of active nucleation centers therefore ensuring a uniform distribution of grapite and well-developed spheroidal graphite structure.

Low GRF1 values suggest insufficient nodulizer content or degradation and a lack of active nucelation centers, potentially leading to compromised mechanical properties and increased porosity. Secondary graphitisation factor (GRF2) corresponds to secondary graphitisation occuring in the later stages of eutectic crystallization, relating to the growth and shape of graphite nodules. GRF 2 targeted range value is: 40-80 [45]. High GRF2 values signify favorable conditions for nodule growth, producing rounded and compact nodules with good control of cooling rates and chemical composition of the melt. On the contrary, low GRF2 values indicate rapid cooling, interrupted nodule growth, and the presence of incompletely formed or irregular graphite nodules. Improvement of GRF1 and GRF2 can be achieved by the addition of ferrosilicon and nodulisers, strict temperature control (T_{ES}, T_S), controlled cooling rates (dT/dtT_{ES}, dT/dtT_S) and melt treatment. Together these parameters provide comprehensive insight into the quality of the ductile cast iron microstructure and its expected mechanical properties.

Table 6. *Overview of microstructure parameters for the EN-GJS-400-15 samples*

Sample	Ferrite fraction/ [%]	Pearlite fraction/ [%]	Nodularity/ [%]	Graphite size	Graphite type	(GRF1)	(GRF2)	Acicularity level
1	98	2	95	(4).5.6.7.	V.VI	63	80	4.30
2	98	2	90	4.5.6.7.	V.VI	88	50	4.26
3	99	1	90	4.5.6.7.	V.VI	75	67	4.36
4	99	1	90	4.5.6.7.	V.VI	78	73	4.38
5	98	2	90	4.5.6.7.	V.VI	90	64	4.31
6	99	1	95	4.5.6.7.	V.VI	70	47	4.25
7	99	1	95	4.5.6.7.	V.VI	78	64	4.29

The microstructural analysis of the ductile cast iron samples grade EN-GJS-400-15 shows a predominantly ferritic matrix with minimal pearlite content in accordance with the recommendations of EN 1563:2018 [9] and the literature [50], [51]. High nodularity values (≥90%) confirm effective nodulation of the graphite, resulting in a spheroidal graphite morphology – type VI [9]. However, in addition to type VI, the presence of type V - chunky graphite, a degenerative graphite morphology was determined. In general this type of graphite forms at low dT/dtT_{ES}, dT/dtT_S or Mg fade effect [52], [53]. According to ISO/TR 945-4:2020 [54] and the literature [52], [53] chunky graphite leads to reduced mechanical properties and promotes the formation of brittle fractures. The size of graphite particles was determined in accordance with ISO 945-1:2019 [55] and is given as graphite size class (4-7). The different graphite size classes ranges are as follows: Class 4 (0.12-0.25 mm), Class 5 (0.06-0.12 mm), Class 6 (0.03-0.06 mm), and Class 7 (0.015-0.03 mm). The graphite size distribution and the graphitisation factors (GRF1 and GRF2) indicate a well-developed microstructure, while low acicularity levels suggest minimal presence of undesirable phases. Overall, the microstructure analysis shows the distribution of graphite nodules disposition and their type, which could influence the mechanical properties.

Figures 1 and 2 shows metallography images in the polished and etched condition for the selected samples 6 and 7, respectively. Figures 1a and 1b show samples with an R-value in the target range of 2-6 °C [43], [45]. These samples exhibit a stable eutectic reaction, good graphite nodularity and a ferrite/pearlite ratio (80/20 [%]) [9], [50], [51].

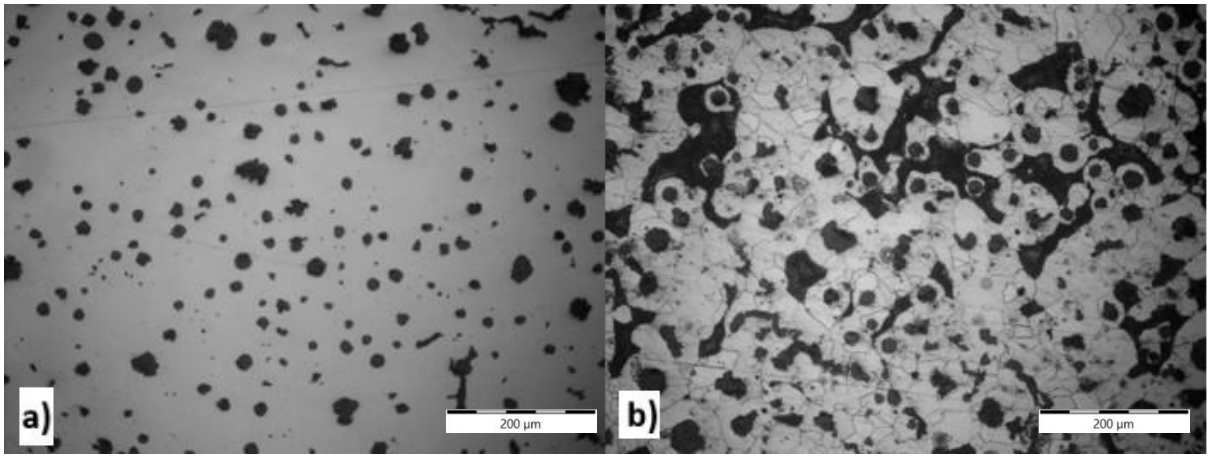


Figure 1. *Metallography of the sample 6 of investigated EN-GJS-400-15 ductile cast iron*
a) Polished condition, b) Etched condition

Figure 1a shows the polished state of the ductile cast iron sample 6, in which the shape and size of the graphite particles are analysed. A predominantly spheroidal shape (type VI) can be observed, but also the presence of some degenerated shapes (type V). The distribution of nodules is relatively homogeneous, but with significant deviation in partiles size (4-7). Figure 1b shows the microstructure after etching, where the grain boundaries of the matrix and the predominantly ferritic matrix are clearly visible. A characteristic ferrite “halo” or bullseye phenomenon is visible around a number of graphite nodules - a bright ring of ferrite formed by the diffusion of carbon from austenite into graphite during transformation. Bullseye occurs when the core of spheroidal graphite forms on inclusions or insufficiently stabilised nucleation sites, so that concentric rings of ferrite/pearlite form around it. Bullseye is caused by insufficient or inhomogeneous Mg treatment, weak inoculation of the melt, and the presence of undesirable elements and oxide/sulphide inclusions. Rapid or uneven cooling can further promote this graphite degeneration. The appearance of the bullseye structure indicates a lower metallurgical quality of the melt and can be associated with lower toughness and homogeneity of the microstructure.
Figures 2a and 2b show samples whose R-value is outside the target range. These samples exhibit an uneven microstructure, degraded graphite nodules and a ferrite/pearlite ratio that is outside the target range for the grade EN-GJS-400-15 ductile cast iron [51], [52].

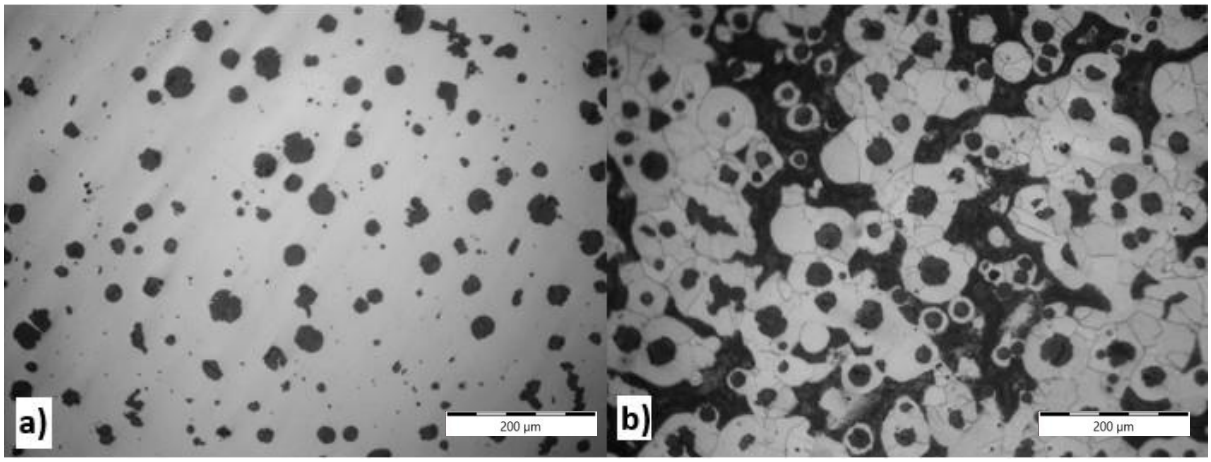


Figure 2. *Metallography of the sample 7 of investigated EN-GJS-400-15 ductile cast iron*
a) Polished condition, b) Etched condition

Figure 2a shows the polished state of ductile cast iron sample 7, in which the distribution and shape of the graphite particles are clearly visible. The graphite is present in the form of nodules of various sizes (4-7). When compared to Figure 1a, the graphite nodules are larger and more scattered, with the

degenerative form of graphite being more strongly represented. Figure 2b, after etching, shows the microstructure of the matrix with clearly expressed grain boundaries. The matrix has a higher pearlite content when compared to Figure 1b, althouth the average content is the same (Table 6). In contrast to Figure 1b, more bullseyes appear indicating more instable nucleation.
Achieving the desired mechanical properties requires balanced ferrite-pearlite matrix, high nodularity and controlled casting parameters. In this study, the mechanical properties of the cast samples were evaluated through Brinell hardness measurements, tensile strength tests, and elongation analysis, with the results compared to the standard specifications. Table 8 provides an overview of the mechanical properties for the EN-GJS-400-15 samples.

Table 8. *Mechanical properties for the EN-GJS-400-15 samples*

Sample	Hardness / [HBW]	Tensile strength (R_m) / [N/mm^2]	Elongation (A) / [%]
1	146.00	438.37	24.56
2	170.67	476.09	22.64
3	191.67	540.32	6.40
4	154.33	452.17	18.50
5	160.67	470.40	21.46
6	152.00	465.09	16.00
7	150.67	380.35	3.32

Sample 6 is most in line with requirement of EN 1563:2018 [9]. In contrast, the analysed values of sample 7 for tensile strength and elongation do not meet the requirements of EN 1563:2018 [9]. Sample 7 has a low R-value and insufficient thermal activity for the formation of graphite nodules. Samples 3 has an elongation value that does not comply with the requirements of 1563:2018 [9] for EN-GJS-400-15. Sample 3 has an extremely high tensile strength, but a very low elongation. The CEL of this sample is in the lower range of the eutectic value, its R is higher than recommended. The GRF1 and GRF2 indicate moderate graphitisation, although the ferrite/pearlite ratio and nodularity are good. A slightly lower CEL, high hardness and low elongation indicate degradation of the graphite nodules. The analysed values of samples 1, 2, 4, 5 and 6 comply with the standard EN 1563:2018 [9] for ductile cast iron of grade EN-GJS-400-15. These samples have a balanced ferrite/pearlite ratio and their R-values are within the recommended range. Although their matrix consists of Type V and Type VI graphite, a higher degree of graphitisation provided mechanical properties that comply with the EN 1563:2018 [9] standard.
Figure 3 shows the dependence of CEL from the C, Si and P content. The trend lines for each element illustrate their respective contribution to the CEL value. Trend line equation and R^2 values are shown in Table 9.

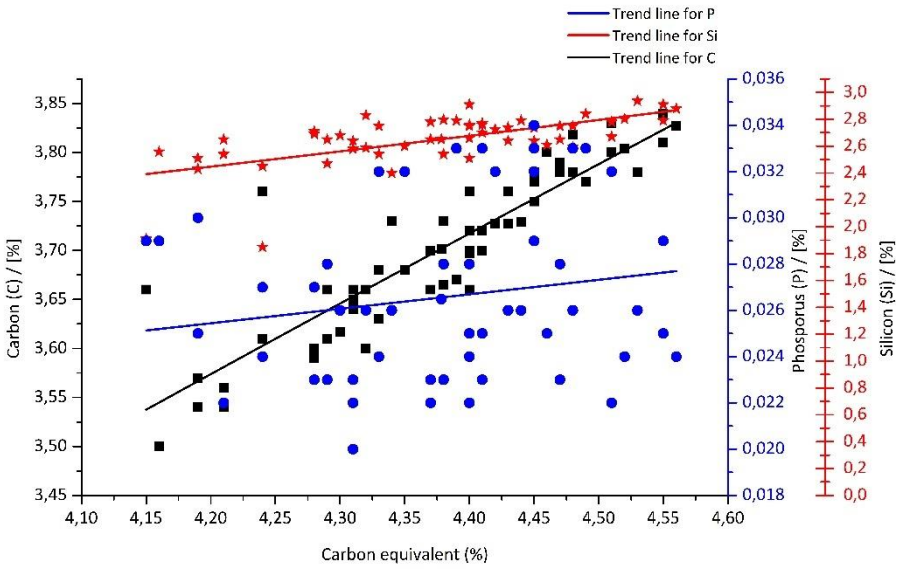


Figure 3. *The connection of CEL with C, Si and P content*

Table 9. *Equation and R2 values for trend lines from Figure 3*

Element	Equation	R^2
Carbon (C)	$y=0.978x-0.031x^2$	0.9999
Silicon (Si)	$y=0.045x+0.128x^2$	0.9967
Phosporus (P)	$y=0.00587x+0.00004x^2$	0.9815

As can be seen from Figure 3 and Table 9, the C content shows the strongest positive correlation with the CEL, which was to be expected based on its high R^2 coefficient. The trend line shows a steep increase, which confirms that the CEL value predominantly increases with increasing C content. Silicon also makes a positive contribution to the CEL value, albeit to a lesser extent due to its lower weighting factor (1/4). The red trend line shows a slight but constant upward trend, which indicates that higher Si values increase the CEL value. The P content shows the weakest correlation with CEL due to its generally low concentration. As previously mentioned, higher P content would increase CEL, but higher P content would lead to the formation of Fe_3P and significantly decrease mechanical properties [35], [36], [37], [38].

The influence of the CEL on the mechanical properties of the analysed samples is shown in Figure 4. Table 10 shows trend line equation and R^2 values for Figure 4.

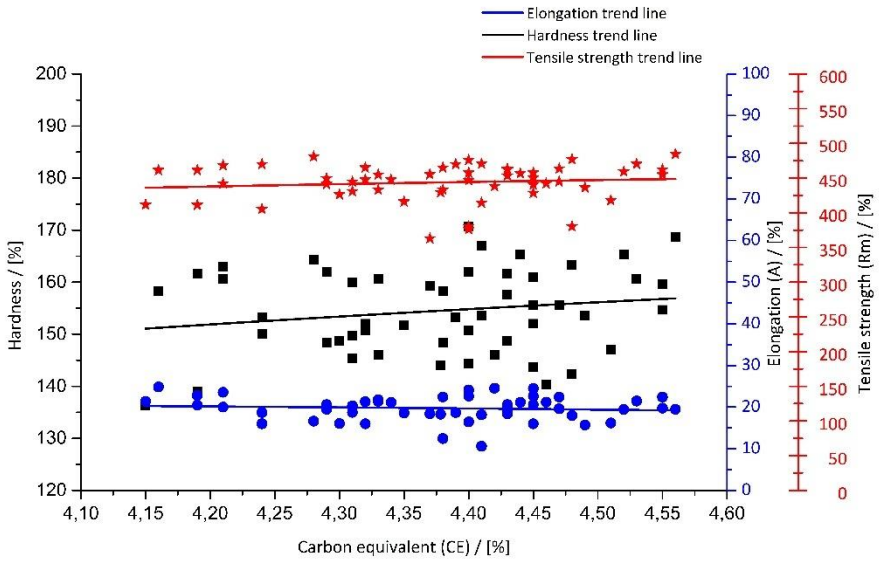


Figure 4. *The influence of the CEL content on the mechanical properties*

Table 10. *Equation and R^2 values for trend lines from Figure 4*

Element	Equation	R^2
Hardness	$y=56.6374x-4.8754x^2$	0.9976
Elongation	$y=11.6802x-1.6383x^2$	0.9810
Tensile strength	$y=172.2841x-16.2027x^2$	0.9961

The results indicate a slight increase in hardness and an almost constant tensile strength with increasing CEL, while elongation shows a decreasing tendency. This behaviour can be directly related to the microstructural parameters discussed in the previous section. Samples with higher CEL values (above 4.40%) showed signs of graphitisation defects, including the presence of chunky graphite and reduced secondary graphitisation factors (GRF2), leading to a significant reduction in elongation, despite favourable chemical parameters. Sample 7, for example, had a CEL of 4.40% but exhibited extremely low elongation due to pronounced acicularity and the presence of type V–VI graphite. In contrast, the samples with balanced CEL values and favourable thermal parameters (e.g. R < 6, GRF1/GRF2 in the target range) achieved mechanical properties in line with EN 1563:2018 [9] – with high nodularity, a predominantly ferritic matrix and an elongation of over 15%. The observed decrease in elongation with increasing CEL suggests that higher CEL values do not guarantee improved elongation. Instead, they can lead to structural irregularities if not compensated by suitable cooling conditions, the residual magnesium content and the graphite-forming potential of the melt. These results confirm the need for a comprehensive quality assessment that takes into account not only the chemical composition, but also the thermal behaviour and microstructural indicators of ductile iron.
Figure 5 shows the influence of nodularity on mechanical properties of the analysed samples. Table 11 shows trend line equation and R^2 values for Figure 5.

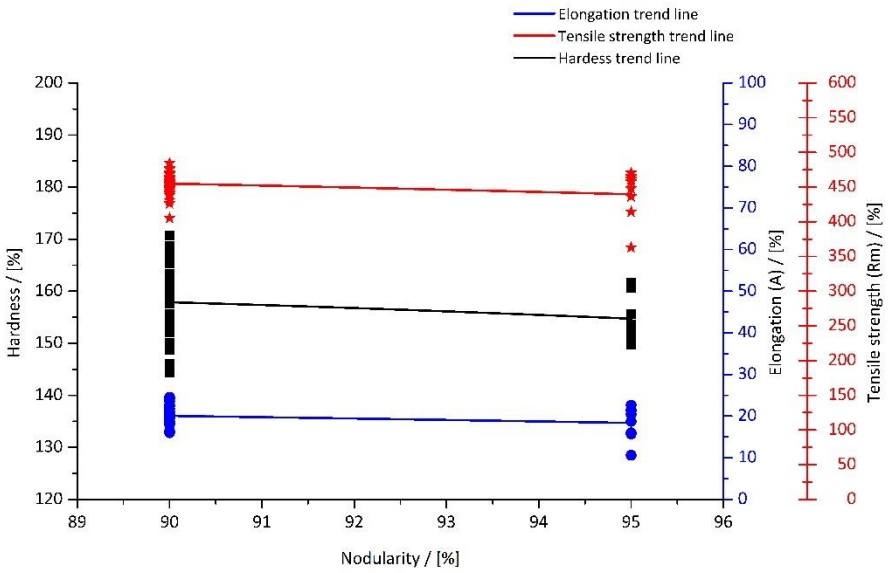


Figure 5. *The influence of nodularity on mechanical properties*

Table 11. *Equation and R^2 values for trend lines from Figure 5*

Element	Equation	R^2
Hardness	$y=4.0157x-0.0252x^2$	0.9982
Elongation	$y=0.7545x-0.0058x^2$	0.9799
Tensile strength	$y=12.7682x-0.0857x^2$	0.9977

Although higher nodularity is generally associated with improved elongation and tensile strength of ductile cast iron, the results of this study show that nodularity alone is not a sufficient indicator of casting quality. Samples with nodularity ≥95% showed lower elongation and higher hardness values, which contradicts the expected behaviour. This was primarily attributed to unfavourable graphite morphology (e.g. chunky graphite, type V) and increased acicularity (ACEL > 4.25) [9]. Furthermore, increased CEL and P contents (P > 0.025%), contributed to a degradation of the microstructure and the formation of brittle phases despite acceptable nodularity. Thermal analysis (ATAS) confirmed that increased recrystallisation (R > 6) [9], high eutectic start temperatures (T_{ES}) and rapid eutectic cooling rates (dT/dT_{ES} <–0.09) favoured unstable solidification and hindered proper graphite growth. The best mechanical properties were observed in samples with balanced CEL values, recalescence between 2–4.5, GRF1 and GRF2 within the target ranges and ACEL below 4.25 [9]. This emphasises the importance of integrating nodularity with chemical, thermal and microstructural parameters to reliably predict and achieve the desired mechanical performance of EN-GJS-400-15 ductile cast iron.

Figure 6 shows the influence of ferrite fraction on the mechanical properties. Table 12 shows trend line equation and R^2 values for Figure 6.

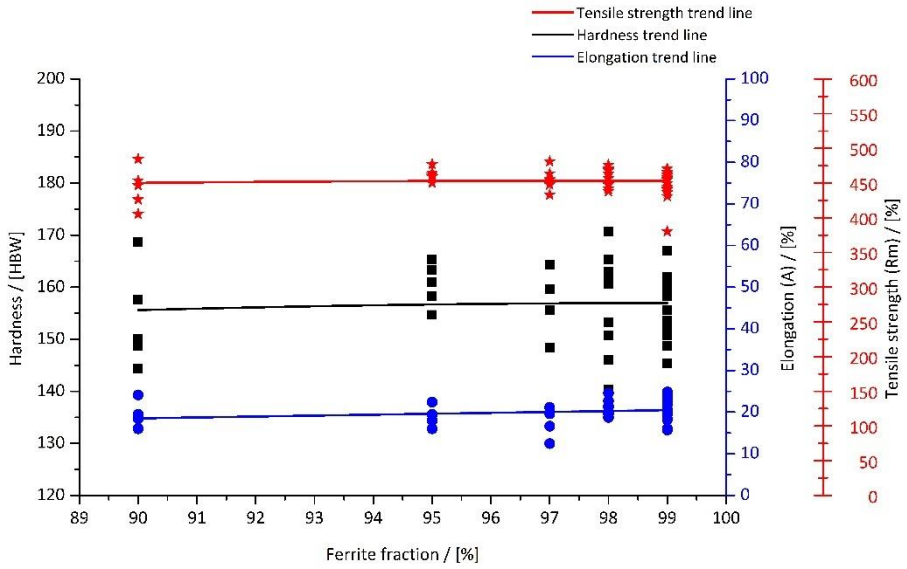


Figure 6. *The influence of ferrite fraction on the mechanical properties*

Table 12. *Equation and R^2 values for trend lines from Figure 6*

Element	Equation	R^2
Hardness	$y=3.1621x-0.0159x^2$	0.9978
Elongation	$y=0.19353x-0.00013x^2$	0.9813
Tensile strength	$y=9.2243x-0.0468x^2$	0.9981

Although a higher ferrite content generally increases elongation, the data shows that elongation increases only slightly with ferrite content, while tensile strength and hardness remain relatively constant over the entire range. This indicates that the ferrite content alone does not fully determine the mechanical behaviour. A further correlation with thermal and chemical parameters explains these trends more precisely. Samples with a high degree of recrystallisation (R > 6), a slightly increased P content and a slightly insufficient residual Mg content exhibit lower elongation and higher hardness, which can be attributed to impaired graphite morphology (chunky graphite) and incomplete nodularisation. In addition, rapid eutectic cooling rates ($dT/dT_{ES} < -0.09$) and low GRF2 values (<65) prevented proper graphite growth, even in samples with high ferrite content. The mechanical properties are therefore the result interactions between the solidification dynamics, the balance of the chemical composition and the morphology of the graphite. Optimising these factors, rather than focusing solely on the composition of the matrix, is crucial to achieving reliable mechanical properties of ductile cast iron.

4. Conclusions

The investigation of the quality of EN-GJS-400-15 ductile cast iron has shown that the control of the chemical composition alone is not sufficient to achieve the mechanical properties in line with EN 1563:2018. Although all samples analysed were within the prescribed chemical composition, there were significant variations in the microstructure and mechanical properties due to the thermal parameters and solidification dynamics. Optimum values were achieved for samples with a balanced carbon equivalent (~4.30), a residual magnesium content within the target range, and recalescence between 2–4.5.

The microstructural analysis confirmed a predominantly ferritic matrix with low pearlite content, high nodularity (>90%) and mainly graphite in type VI, which is in line with standard recommendations. However, the occurrence of degenerative graphite morphology (type V – chunky graphite) was also observed, resulting in lower mechanical properties despite high nodularity. The results clearly show

that high nodularity alone does not guarantee favourable mechanical properties. Rather, the combined effect of chemical, thermodynamic, and microstructural parameters must be taken into account.

The mechanical tests showed that samples with a balanced ferrite–pearlite matrix, stable thermal parameters (S_1 > 20, R within the target range), low acicularity and well-developed graphite nodules met the requirements of EN 1563:2018 and achieved a tensile strength of >400 N/mm² and an elongation of >15%. Conversely, samples with elevated CEL values (>4.40), insufficient thermal stability, and reduced secondary graphitisation factor (GRF2) exhibited lower elongation and did not meet the standard, although their chemical composition was acceptable. Although the chemical composition met the requirements of the standard, inconsistencies in the mechanical properties were observed due to variations in the microstructure, particularly with regard to the type and size of the graphite, the ferrite/pearlite ratio, and the occurrence of the bullseye phenomenon.

The results confirm that ensuring consistent quality of EN-GJS-400-15 ductile cast iron requires integrated monitoring of chemical composition, thermal analysis parameters, and microstructure. Key factors include control of CEL, residual magnesium content, phosphorus content, regulating the cooling rate, and optimising the graphite morphology. This shows that reliable production of ductile cast iron can only be achieved through a comprehensive approach that integrates chemical, thermodynamic, and microstructural features and ensures the stability and reproducibility of the mechanical properties required for industrial application.

Acknowledgments

The study was performed as part of the research topic “Design and characterisation of Innovative Engineering Alloys”, Code: FPI-124-ZZB funded by the University of Zagreb within the framework of financial support for research, a scientific research project Infrastructural scientific projects: Center for Foundry Technology—SIMET, code: KK.01.1.1.02.0020 and VIRTULAB—Integrated Laboratory for Primary and Secondary Raw Materials, code: KK.01.1.1.02.0022, financed by the European Regional Development Fund, Operational Programme Competitiveness and Cohesion 2014–2020.

References

[1] Mohd Nadeem, B., Afzal Khana, D.M., Singh, K.K., 2018. Effect of inoculation and nodularisation treatment temperature on recalescence and eutectic undercooling temperature in Spheroidal graphite (SG) cast iron, International Journal of Cast Metals Research, 31(5), 261-268. DOI: 10.1080/13640461.2018.1434987.

[2] Costanzo, B., Di Vittorio, C., Gregory, F., Francesco, I., Luca, S., 2019. Ductile cast irons: Microstructure influence on the fatigue initiation mechanisms, Fatigue and Fracture of Engineering Materials Structure, 42(9), 1-11. DOI:10.1111/ffe.13100.

[3] Moritz, R., Hergen Groß, S., Björn, P., Andreas, B.P., 2018. Influence of carbide-promoting elements on the pearlite content and the tensile properties of high silicon SSDI ductile iron, Inter Metalcast, 12, 106-112, DOI:10.1007/s40962-017-0146-7.

[4] Ji, Y., Tang, H., Lan, P., Shang, C., Zhang, J., 2017. Effect of Dendritic Morphology and Central Segregation of Billet Castings on the Microstructure and Mechanical Property of Hot-Rolled Wire Rods, Steel Res. Int., 88, DOI:10.1002/srin.201600426

[5] Zhou J Y., 2010. Colour metallography of cast iron: spheroidal graphite cast iron (I). China Foundry, 7(1): 76-88.

[6] Oluwasegun, K., Olawale, O., Ibitoye, S., 2016. Processing Techniques and Productions of Ductile Iron: A Review, International Journal of Scientific and Engineering Research, 7(9) 397-423, ISSN 2229-5518.

[7] Sertucha, J., Suárez, R., Izaga, J., Hurtado, L., Legazpi, J., 2006. Prediction of solid state structure based on eutectic and eutectoid transformation parameters in spheroidal graphite irons, Int. J. Cast Met. Res., 19, 315–322, DOI:10.1179/136404606X167114

[8] Abdellah, M. Y., Alharthi, H., Alfattani, R., Suker, D. K., Abu El-Ainin, H. M., Mohamed, A. F., Hassan, M. K., Backar, A. H., 2024. Mechanical Properties and Fracture Toughness Prediction of Ductile Cast Iron under Thermomechanical Treatment, Metals, 14(3), 352, DOI:10.3390/met14030352

[9] Founding - Spheroidal graphite cast irons EN 1563:2018

[10] Čanžar, P., Tonković, Z., Kodvanj, J., 2012. Microstructure influence on fatigue behaviour of nodular cast iron, Materials Science and Engineering: A, 556:88-99.

[11] Qing, J.J., Richards, V.L, Van Aken, D,C., 2016. Examination of spheroidal graphite growth and austenite solidification in ductile iron, Metallurgical and Materials Transactions A, 47:6197-6213.

[12] Liu J.C., Elliott R., 1999. The influence of cast structure on the austempering of ductile iron. Part 3. The role of nodule count on the kinetics, microstructure and mechanical properties of austempered Mn alloyed ductile iron, International Journal of Cast Metals Research, 12(3):189-195.

[13] Liu, Jh., Yan, Js., Zhao, Xb. et al. 2020. Precipitation and evolution of nodular graphite during solidification process of ductile iron. China Foundry 17, 260–271, DOI:10.1007/s41230-020-0042-2

[14] Boulifa, M., Ali, H., 2021. Study of the Influence of Alloying Elements on the Mechanical Characteristics and Wear Behavior of a Ductile Cast Iron, Frattura ed Integrità Strutturale, 15. 74-83, DOI:10.3221/IGF-ESIS.56.06.

[15] Tubić Bulat, B. Zovko Brodarac, Z., 2021. Influence of solidification and processing parameters on nodular cast iron microstructure- an overview, 19th IFC, Split.

[16] Shaprikov, I.A., 1992. Effect of Carbon Content On The Ductile Iron Quality, Foundry (Liteynoje Proizvodstvo), 11. 6-75,

[17] Darmawan, A., Purboputro, P., Yulianto, A., Anggono, A.D., Wijianto, W., Masyrukan, Setiawan, R., Kartika, N., 2020. Effect of Magnesium on the Strength, Stiffness and Toughness of Nodular Cast Iron, Materials Science Forum, 991. 17-23, DOI:10.4028/www.scientific.net/MSF.991.17.

[18] Yulianto, A., Anggono, A., Partono, D., Ngafwan, P., 2025. The Impact of Fe-Mg Inoculation with Nickel Addition on the Microstructure of Thin-Walled Ductile Cast Iron, Engineering Proceedings, 84(1), 64, DOI:10.3390/engproc2025084064

[19] Riposan, I., Denisa A., Iuliana S., Mihai C., Stelian S., 2022. Graphite Nodularity Evaluation in High-Si Ductile Cast Irons, Materials, 15, 21:7685. DOI:10.3390/ma15217685

[20] Pereira, I., Anjos, V., Alonso, G., et al., 2024. Damping Behaviour of High Silicon Nodular Cast Iron, Inter Metalcast., 18, 373–389, DOI:10.1007/s40962-023-01007-8

[21] Horbach, L., Gebhardt, C., Zhang, J., Joseph, B.D., Bührig-Polaczek, A., Broeckmann, C., 2023. The effect of silicon microsegregation on the mechanical properties of high silicon alloyed ductile cast iron under monotonous loading, Heliyon, Dec 20;10(1), DOI:10.1016/j.heliyon.2023.e23904

[22] Čatipović, N., Živković, D., Dadić, Z., 2018. The Effects of Molybdenum and Manganese on the Mechanical Properties of Austempered Ductile Iron, Tehnički vjesnik, 25(2) 635-642, DOI:10.17559/TV-20170124120729

[23] Azimijam, A., Kahalil-Allafi, J., Mehrvarz, A., Akbari, E., 2023. Effect of Manganese on Microstructural, Mechanical, and Electrochemical Properties of Ni-Resist Gray Cast Irons, International Journal of Metalcasting, 18(23), DOI:10.1007/s40962-023-01128-0

[24] Roula, A., Kosnikov, G., 2008. Manganese distribution and effect on graphite shape in advanced cast irons, Mater.Lett., 62(23), 3796–3799, DOI:10.1016/j.matlet.2008.04.056

[25] Riposan, I., Chisamera, M., Kelley, R., Usa, K., Barstow, M., Naro, R. L., 2003. Magnesium-Sulfur Relationships in Ductile and Compacted Graphite Cast Irons as Influenced by Late Sulfur Additions

[26] de Albuquerque Vicente, A., Sartori Moreno, J.R., de Abreu Santos, T.F., Romano Espinosa, D.C., Soares Tenório, J.A., 2019. Nucleation and growth of graphite particles in ductile cast iron, Journal of Alloys and Compounds, 775, 1230-1234, ISSN 0925-8388, DOI:10.1016/j.jallcom.2018.10.136

[27] Colin-García, E., Cruz-Ramírez, A., Reyes-Castellanos, G., Romero-Serrano, J.A., Sánchez-Alvarado, R.G., Hernández-Chávez, M., 2019. Influence of nickel addition and casting modulus on the properties of hypo-eutectic ductile cast iron, Journal of Mining and Metallurgy Section B Metallurgy, 55(00):23-23, DOI: 10.2298/JMMB181012023C

[28] Hernandez-Avila, J., Salinas-Rodriguez, E., Cerecedo-Saenz, E., Rivera-Landero, I., Cardoso-Legorreta, E., Flores-Badillo, J., Reyes-Valderrama, M.I., 2015. The effect of molybdenum on the microstructure of nodular iron, Europ. Sci. J., 11(36), 337

[29] Franzen, D., Pustal, B., Bührig-Polaczek, A., 2021. Mechanical Properties and Impact Toughness of Molybdenum Alloyed Ductile Iron, Inter Metalcast, 15, 983–994, DOI:10.1007/s40962-020-00533-z

[30] Mourad, M., Ibrahim, M., El-Hadad, S., 2024. Effect of Copper Addition on Microstructure and Mechanical Properties of Ductile Cast Iron, International Journal of Materials Technology and Innovation, 4(1), 75-79, DOI:10.21608/ijmti.2024.287146.1102

[31] Tsujikawa, M., Matsumoto, N., Nakamoto, K., Michiura, Y., 2010. Pearlite Stabilisation by Copper on Ductile Cast Iron, In Key Engineering Materials Trans Tech Publications, Ltd., 457, 151–156. DOI:10.4028/www.scientific.net/kem.457.151

[32] Górny, M., Kawalec, M. , 2013. Effects of Titanium Addition on Microstructure and Mechanical Properties of Thin-Walled Compacted Graphite Iron Castings, J. of Materi Eng and Perform., 22, 1519–1524, DOI:10.1007/s11665-012-0432-8

[33] Górny, M., Kawalec, M., Sikora, G., Lopez, H., 2014. Effect of Cooling Rate and Titanium Additions on Microstructure of Thin-Walled Compacted Graphite Iron Castings, ISIJ International, 54, 10, 2288-2293, DOI:10.2355/isijinternational.54.2288

[34] Li, H. B., Li, H. T., Li, C. J., Qu, L. J., 2012. The Effect of Cr Content on the Microstructure and Performance of Heat Resistant Nodular Cast Iron, Advanced Materials Research, 430–432, 273–276. DOI:10.4028/www.scientific.net/amr.430-432.273

[35] Zou, Jp., Shimizu, K., Cai, Qz., 2015. Effects of Cr Content and Annealing Temperature on Microstructure and Wear Characteristics of Cast Ausferrite Nodular Iron, J. Iron Steel Res. Int., 22, 1049–1054, DOI:10.1016/S1006-706X(15)30111-4

[36] Sudarshan, T., Srivatsan, T.S., 1992. Role of phosphorus content on porosity of cast irons, J Mater Sci., 27, 869–875, DOI:10.1007/BF01197635

[37] González-Martínez, R., Sertucha, J., Thébaut, Y. et al., 2025. Effect of Phosphorus on Intermediate Temperature Embrittlement of High Silicon Spheroidal Graphite Cast Irons, Metall Mater Trans A, 56, 2769–2785, DOI:10.1007/s11661-025-07804-6

[38] Bartlett, L.N., Rahman, R. Torres, A., 2018. Minimizing Phosphorus Pickup During Melting and Casting of Lightweight Fe–Mn–Al–C Steels, Inter Metalcast, 12, 164–181, DOI:10.1007/s40962-017-0152-9

[39] Abbasi, H.R., Bazdar, M., Halvaee, A., 2007. Effect of phosphorus as an alloying element on microstructure and mechanical properties of pearlitic gray cast iron, Materials Science and Engineering: A, 444(1–2) 314-317, DOI:10.1016/j.msea.2006.08.108

[40] Riposan, I., Chisamera, M., Stan, S. et al., 2011. Benefits of Residual Aluminum in Ductile Iron, J. of Materi Eng and Perform., 20, 57–64, DOI:10.1007/s11665-010-9640-2

[41] Gebhardt, C., Nellessen, J., Bührig-Polaczek, A., Broeckmann, C., 2021. Influence of Aluminum on Fatigue Strength of Solution-Strengthened Nodular Cast Iron, Metals, 11(2):311, DOI:10.3390/met11020311

[42] Shinde, V.D., Ravi, B., Narasimhan, K., 2012. Solidification behaviour and mechanical properties of ductile iron castings with varying thickness, International Journal of Cast Metals Research, 25(6), 364-373, DOI:10.1179/1743133612Y.0000000024

[43] Dwulat, R., Janerka, K., 2023. Evaluation of the Metallurgical Quality of Nodular Cast Iron in the Production Conditions of a Foundry, Journal of Manufacturing and Materials Processing, 7(1), 18. DOI:10.3390/jmmp7010018

[44] Stefanescu, D.M., Suarez, R., Kim, S.B., 2020. 90 years of thermal analysis as a control tool in the melting of cast iron, China Foundry 17, 69–84, DOI:10.1007/s41230-020-0039-x

[45] ATAS MetStar system, version 10.4.2.

[46] Heraeus Electro-Nite International N.V., **Thermal Analysis of Cast Iron**, Houthalen, Belgium 7-9, www.canfieldjoseph.com/assets/files/Foundry/Melt/Electro-nite-Thermal-Analysis-of-Cast-Iron.pdf

[47] Heraeus Electro-Nite, QuiK-Cup / QuiK-Lab E, Thermal Analysis of Cast Iron, datasheet, www.ibt.co.il/wp-content/uploads/2022/04/file1369985964_U5109-1.pdf

[48] Stefanescu, D., 2021. Analysis of the Rationale and Accuracy of the use of Carbon Equivalent and Thermal Analysis in the Quality Control of Cast Iron, International Journal of Metalcasting, 16, DOI:10.1007/s40962-021-00685-6

[49] Sertucha, J., Lacaze, J., Regordosa, A., 2025. Polynomial Description of the Fe–C–Si Stable Phase Diagram for up to 4.5 wt% Si, Including the Effect of Cr, Cu, Mn and P, Inter Metalcast, 19 1847–1856, DOI:10.1007/s40962-024-01428-z

[50] Lindqvist, S., Kuutti, J., Sirkiä, L., Forsström, A., 2024. Constraint effects on fracture toughness of ductile cast iron in the ductile regime, Engineering Fracture Mechanics, 306, 110202. DOI:10.1016/j.engfracmech.2024.110202

[51] Seidu, S., Sumaila, A., Adetunji, O., 2020. Effect of Cu-Ni and Cu-Ni-Mn on the Microstructural and Mechanical Behaviour of As-Cast Non-Inoculated Hypereutectic Grey Iron, Journal of Minerals and Materials Characterization and Engineering, (8) 27-46, DOI:10.4236/jmmce.2020.82003

[52] Kołakowski, J., Brzeżański, M., Burdzy, D., Sobieraj, J., Urbanowicz, M., Paruch, T., Janerka, K., 2022. The Effect of Successive Stages of the Melting Process on the Nucleation of Ductile Cast Iron, Archives of Foundry Engineering, 61-67, DOI:10.24425/afe.2023.144281

[53] Baer, W., 2020. Chunky Graphite in Ferritic Spheroidal Graphite Cast Iron: Formation, Prevention, Characterization, Impact on Properties: An Overview, Inter Metalcast, 14, 454–488, DOI:10.1007/s40962-019-00363-8

[54] ISO/TR 945-4:2020 Microstructure of cast irons – Part 4: Test method for evaluating nodularity in spheroidal graphite cast irons

[55] ISO 945-1:2019 Microstructure of cast irons – Part 1: Graphite classification by visual analysis

Design of the reconfigurable workstation for collaborative robot Franka

***Marko Mladineo*[1], *Pol Menou*[2], *Mate Buzov*[1] *and Luka Celent*[3]**

1) University of Split, Faculty of Electrical Engineering, Mechanical Engineering and Naval Architecture, R. Boskovica 32, 21000 Split, Croatia

2) Toulouse INP-ENSIACET, Allée Émile Monso 4 - CS 44362 - 31030 Toulouse CEDEX 4, France

3) University of Portsmouth, Faculty of Technology, School of Mechanical and Design Engineering, Portsmouth PO1 3DJ, UK

Corresponding author: mmladine@fesb.hr

Original scientific article

Abstract: The Industry 4.0 paradigm introduced new kind of robot designed to collaborate with human workers: collaborative robot (cobot). The cobots came more into the focus with introduction of Industry 5.0 paradigm and its human-centric aims. The cobots are usually very user friendly with intuitive programming interface and manual teaching of cobot movements. However, most of the cobots are not equipped with vision system, because the system requires additional training and cost. Without vision system, the problem occurs with workstation configuration. Cobot expects to have parts and products on the same spatial positions where they were during the programming and teaching. That means the workstation needs to be reconfigurable to support easy exchange of parts and cobot's program. In this research, conceptual design of a reconfigurable workstation has been selected, developed and constructed as the final product. The reconfigurable workstation with tooling plate has been constructed and successfully tested with collaborative robot Franka Panda on the computer RAM assembly/disassembly example.

Keywords: *collaborative robot; reconfigurable workstation; assembly; disassembly; Industry 4.0/5.0*

1. Introduction

Industry 4.0 now represents more than a decade of transformation of manufacturing through digital technologies, especially information-communication technology [1]. Smart factories now connect machines, systems, and people through the Internet of Things, artificial intelligence, and real-time data exchange. These technologies enable better decision-making, predictive maintenance, and system integration across entire production [2].

What makes Industry 4.0 different is its focus on collaboration with human worker rather than its replacement. While previous industrial revolutions often eliminated jobs, the goal of this transformation is to merge human creativity with machine precision and speed. This has created new challenges and opportunities in manufacturing. Companies need systems that are automated and flexible enough to work alongside human operators. This need for collaboration has led us to the development of collaborative robots, or cobots, which represent a key technology in Industry 4.0 evolution. This human-centric approach was especially emphasized with introduction of Industry 5.0 paradigm in 2021 ([3] and [4]).

1.1. From Autonomous Robots to Human-Robot Collaboration

Over the past decades, the implementation of robots has changed the way factories work. Traditional robots have reached unmatched accuracy and speed. However, these robots were built to operate alone, separated from human workers by safety cages, making them inappropriate for the flexibility and variability required by today's industries. Their lack of adaptability and the need for strict safety protocols limited their use in dynamic or human-involved processes.

This has led to a design of new type of robot, collaborative robots, also called cobots. To understand what a cobot is, it is important to understand the true meaning of this word. The term cobot is a mix

of the words robot and collaborative, this underlines the importance of the human in the process. The goal is no longer to replace human labour entirely, but rather to enhance human capabilities while decreasing the number of repetitive or demanding tasks. Cobots support the human by handling the mechanical aspects of a task, while the human brings adaptability. Their design includes advanced safety features, such as torque sensors, compliant joints, and intuitive interfaces, enabling safe and productive human–robot workstation [5].

Nowadays cobots have evolved to become safer and aren't only limited to the industrial sector, in consequence the definition also changed. So, the cobot is a collaborative robot designed to safely operate alongside humans in shared spaces and during joint tasks. It relies on environmental sensing and autonomous decision-making to interact effectively and securely [6]. This shift marks a critical evolution in robotics: from isolated automation to interactive collaboration.

1.2. Cobot in the Industry 4.0

After transitioning from classical robots to cobots, many adaptations were made, such as the integration of safety-rated sensors, force limiters, and speed monitoring systems to protect workers from unintended contact with the cobot's movements. These changes were mandatory to create a safe and collaborative environment for the human operator [5]. They allow cobots to detect and react to unexpected human movements, helping to avoid collisions and accidents in real time.

Today, cobots have found their place on the production line. They are commonly used to handle physically demanding or repetitive tasks, such as lifting and positioning heavy components. This not only reduces the risk of injury for human workers but also frees them to focus on more skilled or value-added operations. In addition, cobots can significantly improve workflow efficiency by transporting parts or assemblies more quickly and consistently than manual handling allows [7]. This collaboration between robots and operators leads us to better manufacturing time, productivity and reliability.

This synergy between human and robot contributes directly to the main objectives of Industry 4.0: improved productivity, real-time adaptability, and optimized use of human talent. But to fully unlock this potential, attention must also be paid to the physical configuration of the cobot's working environment. Without an appropriate workstation, even the most advanced cobot may fail to perform at its full potential.

1.3. Evolution of cobot workstation

Today the evolution of cobots is still a reality and it won’t stop soon. In this perspective the development of new working space is a requirement to enhance the robot and the worker collaboration. A well-designed workstation allows cobots to operate efficiently, safely, and without interruption, which is essential.

Moreover, the progress of cobot workstation is a step needed to transition from Industry 4.0 to Industry 5.0 [4]. While Industry 4.0 develops connectivity and automation, Industry 5.0 focuses more on human needs, customization, and sustainability. In this new context, workstations must be more intuitive, more ergonomic, and more adaptable [8] not only to improve productivity but also to reduce the physical and mental strain on workers. Unfortunately, many collaborative workstations still rely on simple flat tables, often improvised or carried over from earlier industrial setups. These surfaces rarely provide the precision and flexibility required for tasks that involve both humans and cobots especially when the robot does not use vision systems or external sensors to locate its working components. In such cases, even small misalignments can result in positioning errors, failed grasps, or unnecessary reprogramming. These issues can lead to inefficiencies, production delays, or even equipment damage.

This paper proposes the use of a tooling plate as the foundation of the reconfigurable workstation, instead of the most used T-slot plate (Figure 1). This represents a new type of modular platform with a regular grid of holes that allows parts to be securely and precisely mounted. This kind of approach enables reconfigurability. With this configuration, each element of the task can be placed exactly where it is needed repeatedly without manual realignment. This improves repeatability and workflow

for the cobot and the human. The reconfigurable workstation with tooling plate has been constructed for collaborative robot Franka Panda [9].

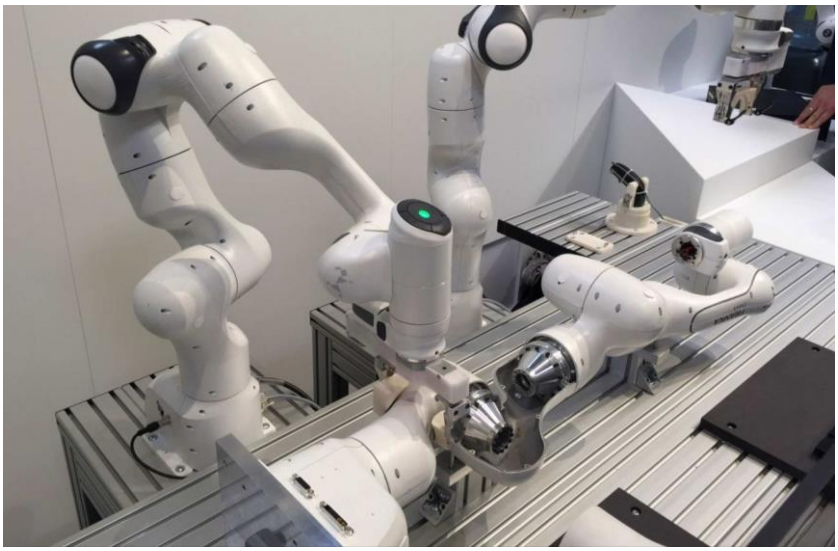


Figure 1. *Cobot workstation with aluminum T-slot plate [10]*

2. Methodology

2.1. Selection of the cobot workstation design

There are many possible designs for the robot/cobot workstation. It all depends on the final application. In this case, the workstation should have some kind of adaptability and easy reconfiguration, it should plug & play, as well. Meaning that no calibration is required after each setup. Furthermore, it shouldn’t be expensive and complex to assemble. At the end, the cobot workstation selection seems to be a multi-criteria problem which needs to be addressed by some multi-criteria analysis methods [11].

The multi-criteria analysis of the cobot workstations has been made in previous research [8]. The benchmarking was made, which resulted with to three basic designs (Figure 2): the robot station is attached to a workbench (RS1), the robot station is adjustable but without a workbench (RS2), and the robot station is a workbench with robot installed onto it (RS3).

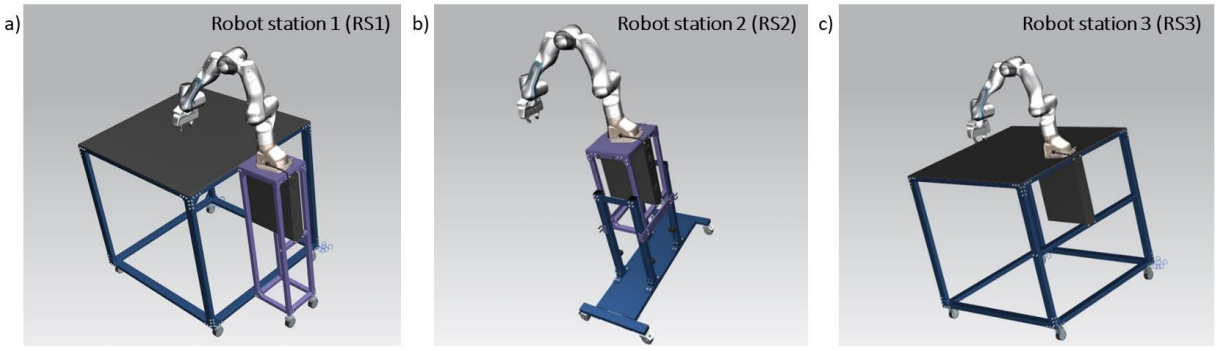


Figure 2. *Three variants of robot station design: a) Robot station 1 (RS1); b) Robot station 2 (RS2); c) Robot station 3 (RS3) [10]*

These three variants were alternatives submitted to multi-criteria analysis (TOPSIS and SAW), which resulted in selection of the third variant [8]: the robot station is a workbench with robot installed onto it (RS3). Therefore, the third variant (RS3) has been selected to be constructed and assembled as reconfigurable workstation for collaborative robot Franka.

2.2. Construction of the cobot workstation

After selection of the cobot workstation design, the next step was the construction of the cobot workstation. The workstation design was submitted to stress and displacement analysis by using FEM (Finite Element Method). The focus of analysis was the tooling plate which is a 5 mm thick steel plate (DD11 or DIN EN 10111) with more than 1200 holes. The tooling plate should carry all the parts that need to be assembled into the product. The idea was that product with all parts could weight up to 50 kg. The CAD model and FEM model of the tooling plate have been made (Figure 3).

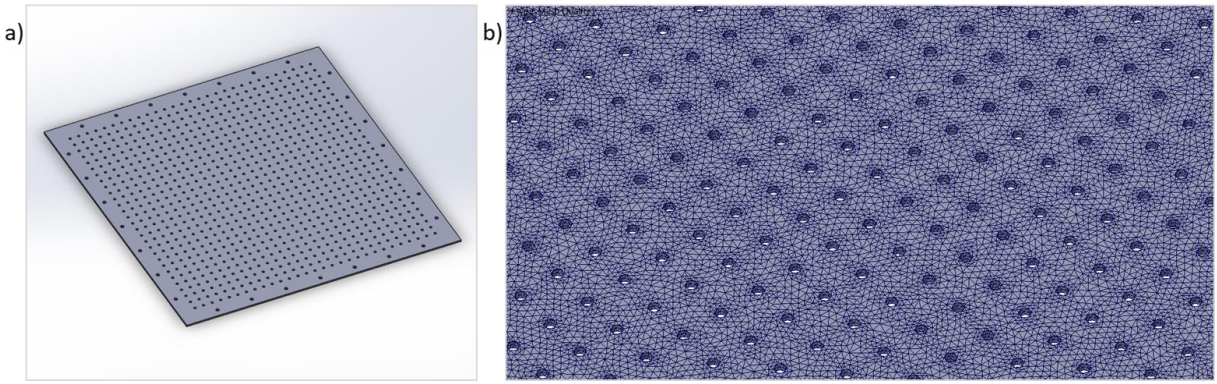


Figure 3. *Tooling plate: a) Tooling plate CAD model; b) Tooling plate FEM model*

The FEM analysis of the tooling plate resulted with highest stress of 134.5 MPa and largest displacement of 0.172 mm (Figure 4). Both values clearly demonstrate that tooling plate can uphold 50 kg without causing any fracture or deformation.

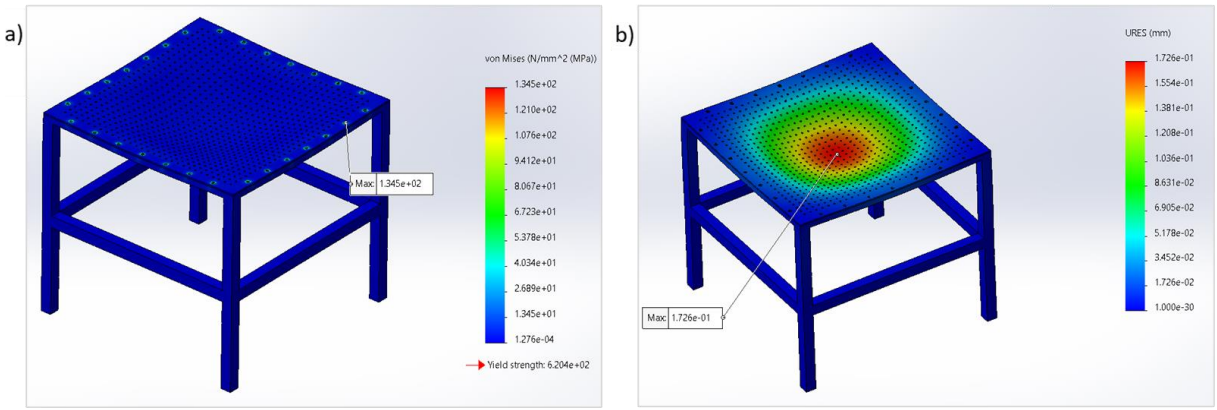


Figure 4. *FEM analysis of the tooling plate: a) Stress analysis; b) Displacement analysis*

3. Results

Since the workstation design was analysed and approved, the workstation has been constructed. Beside the steel tooling plate, the table frame was assembled by using aluminum profiles with rectangle T-slot cross section (Figure 5). The original design (Figure 2c) has been slightly modified, so the tooling plate upholds the parts and product only, not the cobot. Because the cobot Franka Panda itself has a weight of approximately 20 kg.

The final step was the testing of the new workstation, especially its reconfiguration abilities. A simple task was created: cobot takes out the RAM memory from the slot on the PC motherboard and then inserts it into the slot on the second PC motherboard. This task has both disassembly and assembly operations. The workplace configuration was first made in the document template (Figure 6a) and then the real workplace setup was made (Figure 6b). The workplace configuration template is a document that has a sketch of the tooling plate with all its holes. There is a defined enumeration of the holes like a custom coordinate system.



Figure 5. *Reconfigurable workstation for collaborative robot Franka*

It was very easy and intuitive to make a workplace setup by reading the documented configuration. Nevertheless, after removing the workplace setup, it was very easy to make a same workplace setup again. The whole process takes several minutes only, and no additional calibration of the cobot is needed.

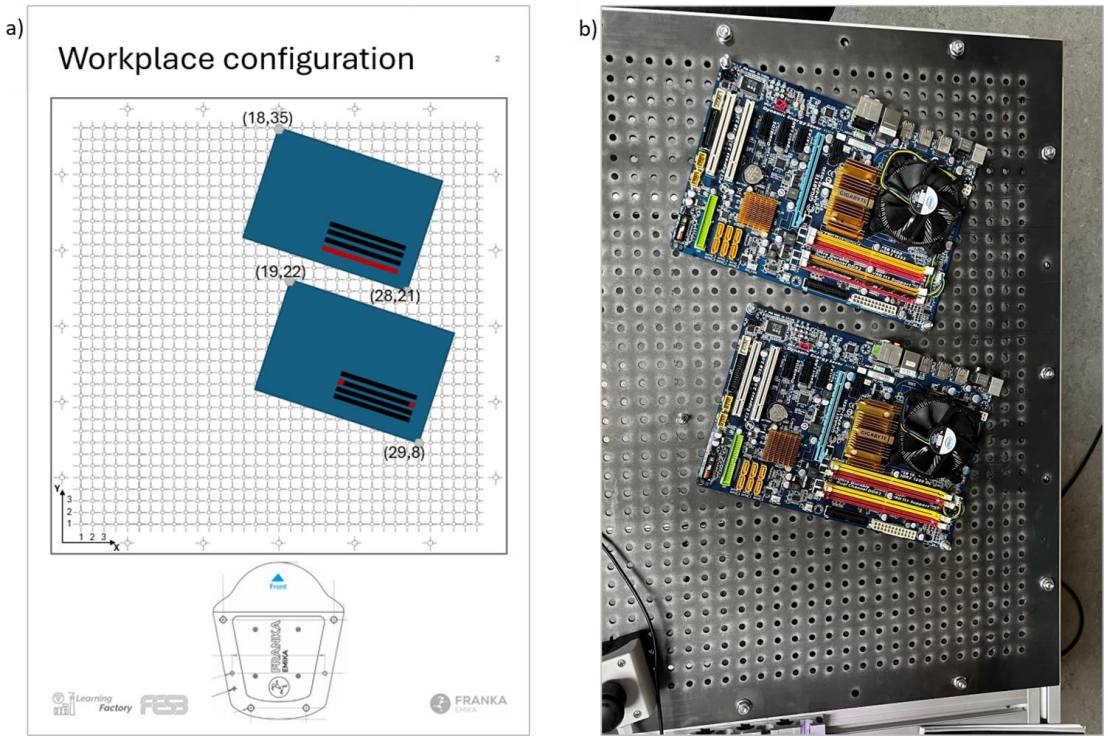


Figure 6. *Example of workplace configuration for computer RAM assembly/disassembly: a) Workplace configuration template; b) Workplace setup*

4. Conclusions

In the market, there are many different designs of the workstation for collaborative robot. Recently, the design with the tooling plate as a table is catching more attention. In this research, such a design was selected, and real workstation has been constructed and assembled. The design is allowing easy and intuitive reconfiguration of the workplace with no further cobot’s calibration required. It is a huge advantage not only for industrial application, but for educational purposes, as well. The cobot’s are allowing easy and intuitive change of its programmed tasks. However, sometimes it is very difficult to run some tasks, because they need proper and precise workstation configuration. The proposed design of the workstation is solving that issue. The future research will consist of testing more demanding and more precise tasks, to challenge the reconfigurability abilities of proposed design.

References

[1] Kagermann, H., Wahlster, W., Helbig, J., 2013. Recommendations for implementing the strategic initiative INDUSTRIE 4.0, Heilmeyer und Sernau, Berlin

[2] Bartodziej, C.J., 2017. The concept industry 4.0, Springer Gabler, Wiesbaden

[3] European Commission – Directorate-General for Research and Innovation, 2021. Industry 5.0 – Towards a sustainable, human-centric and resilient European industry, Publications Office of the European Union, Luxembourg

[4] Mladineo, M., Ćubić, M., Gjeldum, N., Crnjac Žižić, M., 2021. Human-centric approach of the Lean management as an enabler of Industry 5.0 in SMEs, MTSM 2021, Split

[5] Mariscal, M.A., González-Pérez, J., Azfar, K., Gutierrez-Llorente, J.M., García-Herrero, S., 2019. Risks management and cobots: Identifying critical variables, Proceedings of the 29th European Safety and Reliability Conference, Hannover

[6] Guertler, M., Tomidei, L., Sick, N., Carmichael, M., Paul, G., Wambsganss, A., Hernandez Moreno, V., Hussain, S., 2023. When is a robot a cobot? Moving beyond manufacturing and arm-based cobot manipulators. Proceedings of the Design Society, 3, 3889–3898.

[7] Ojstersek, R., Javernik, A., Buchmeister, B., 2021. The impact of the collaborative workplace on the production system capacity: Simulation modelling vs. real-world application approach. Advances in Production Engineering & Management, 16 (4), 431–442.

[8] Veza, I., Mladineo, M., Kutlesa, M., Gjeldum, N., Bilic, B., Crnjac Zizic, M., Aljinovic, A., Basic, A., 2022. Selection of the Cobot Workstation for the Learning Factory by Using the Multi-Criteria Analysis, Proceedings of the 12th Conference on Learning Factories (CLF 2022), Singapore

[9] Robohub, Switzerland, 2016. I am FRANKA: German collaborative robot can build itself. https://robohub.org/i-am-franka-german-collaborative-robot-can-build-itself/ (accessed 27 June 2025).

[10] Franka Robotics, Germany, 2025. Franka Research. https://franka.de/franka-research-3 (accessed 27 June 2025).

[11] Chu T.C., Lin Y.C., 2003. A Fuzzy TOPSIS Method for Robot Selection. International Journal of Advanced Manufacturing Technologies, 21, 284–290.

Stress-corrosion cracking of X70 steel for main pipelines in different corrosivity environments at cathodic polarization

***Lyudmila Nyrkova*[1], *Svetlana Osadchuk*[1], *Larysa Goncharenko*[1] *and Oleg Bratochkin*[1]**

1) E.O. Paton Electric Welding Institute of the National Academy of Sciences of Ukraine, 03150, Kyiv, Kazymyr Malevich Str., 11, Ukraine

Corresponding author: lnyrkova@gmail.com

Original scientific article

Abstract: A comparative studies of stress-corrosion cracking peculiarities of X70 steel for main pipelines in corrosive environments with pH from 5,6 to 9,6 at cathodic polarization using slow strain rate tests, voltametry, masometry, optical metallography, and SEM were carried out. It was established three mechanism of SCC depending on polarization potential – anodic dissolution (AD), hydrogen embrittlement (HE) and mixed mechanism with simultaneously running of AD and HE. The ranges of mixed mechanisms were identified: for near neutral pH solution NS4 – from -1.001 to -1.085 V; for high pH 9.6 solution – from -0.907 to -1.005 V; for low-acid pH solution 5.6 – from -0.816 to -0.949 V. Results indicate that maintaining of protective potential at the maximum level -1.05 V is not as dangerous as it can be, because it can lead to SCC by hydrogen embrittlement mechanism. So decision for choice of maximum protective potential have to accepted depending on corrosivity of the environment.

Keywords: *steel X70; slow strain rate tests; voltametry; SEM; stress-corrosion cracking; corrosion*

1. Introduction

Stress-corrosion cracking (SCC) in main gas pipelines has long posed a serious threat to their structural integrity [1]. To this day, a comprehensive understanding of its development remains incomplete, and practical methods of prevention have yet to be identified—making its study highly relevant. Based on global experience, two types of SCC of pipe steels are distinguished: "classic" high pH SCC occurring in concentrated carbonate-bicarbonate solutions (pH > 9.0) [2-4], and near-neutral pH SCC (at pH around 6.5) [5-10]. High pH SCC develops via local anodic dissolution mechanism (AD), though near-neutral pH SCC is caused by dissolution at the tip and back sides of crack and is accompanied by hydrogen permeation into the steel. However, the exact role of hydrogen in this mechanism requires further investigation [11]. Both high pH SCC and near-neutral pH SCC is strongly influenced by cathodic potential. Beavers [12] indicated that SCC initiates through anodic dissolution, while its propagation is driven by hydrogen-embrittlement mechanism (HE). In contrast, Lu et al. [13] reported that hydrogen has a limited effect on active dissolution of pipe steel in near-neutral pH groundwater, suggesting an incomplete understanding of the relationship between hydrogen effects and anodic dissolution. Liu et al. [14-20] demonstrated that hydrogen's combined influence in soil environments creates different electrochemical conditions between the tip and back sides of a crack. Notably, studies [21-25] confirm the hydrogen-induced plasticity effect in X70 steel at specific cathodic potential ranges in near-neutral pH and acidic pH solutions, which decreases susceptibility to SCC by reducing stress concentrations at crack formation sites. This enlarges the deformation zone ahead of the crack tip and subsequently lowers its intensity. However, the precise mechanism of hydrogen-induced plasticity and its connection to SCC under cathodic polarization remains unclear and demands further research. As noted in studies [15, 21], SCC susceptibility increases at potentials more negative than −920 mV. This presents a significant challenge for pipeline safety: protection systems must be installed without simultaneously increasing the risk of SCC.

Therefore, the aim of this work was to investigate the SCC susceptibility of X70 steel in a pH range from mildly acidic to mildly alkaline under cathodic polarization. This paper summarizes a series of studies focused on exploring SCC behavior of X70 steel in environments of varying corrosivity.

2. Experimental Details

The study was conducted on X70 steel, which is used for main gas pipelines. The chemical composition of X70 steel is shown in Table 1, and its microstructure is illustrated in Figure 1.

Table 1. *The chemical composition of X70 steel*

Specimen characteristic, regulatory documents requirements	C	Mn	Mo	V	Nb
X70 steel	0,096	1,71	0,03	0,06	0,052
Requirements of ISO 3183 [26]	0,280	1,40	Nb+Mo+V no more than 0,15		

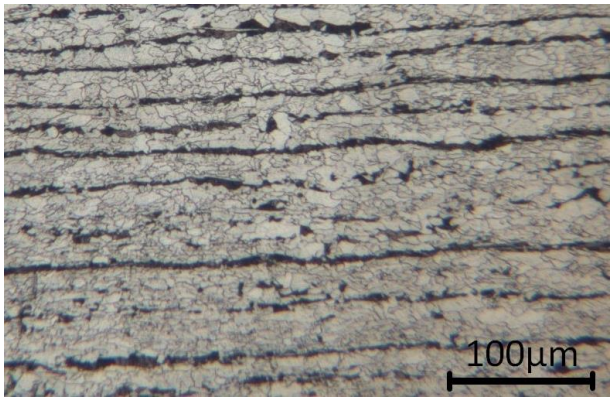


Figure 1*. Optical micrograph of the microstructure of the X70 test specimen*

The chemical composition and physical properties of the solutions used in the experiments are presented in Table 2.

Table 2*. The physical composition of the solutions*

	Solution composition	pH	Electro conductivity, Cm/cm
1	1,92 g/l HCOOH + 54,5 g/l HCOONa + 10 g/l KCNS	5,6	$37{,}3\times10^{-3}$
2	0,037KCl + 0,559 $NaHCO_3$ + 0,008$CaCl_2$ + 0,089 $MgSO_4$	8,2	$0{,}823\times10^{-3}$
3	0,1 M $NaHCO_3$ + 0,1 M Na_2CO_3	9,6	$18{,}3\times10^{-3}$

The solutions were prepared using distilled water and chemically pure reagents. To streamline the presentation and avoid repetition, the following terminology was adopted for the solutions: 1 – mildly acidic solution, 2 – near-neutral pH solution NS4, 3 – mildly alkaline solution.

Specimens for testing were cut from a steel sheet perpendicular to the rolling direction. Prior to testing, the surfaces were polished with 2500-grit abrasive paper, degreased using magnesium oxide, thoroughly rinsed, and dried.

Corrosion and electrochemical tests were carried out on rectangular specimens in size 50 × 50 × 1 mm. Corrosion rate was determined by gravimetric method using three specimens—based on mass loss per unit area over a period of 168 hours (1 week).

Potentiometric and voltammetric studies were performed using a clamping cell with a working area of 2.826×10^{-5} m². The working electrode was an X70 steel specimen; the reference electrode was a saturated silver chloride electrode (SSCE), and the auxiliary electrode was platinum wire. Corrosion potentials were measured during 1 hour. Polarization curves were recorded in potentiodynamic mode

at a scan rate of 10^{-3} V/s according to [27]. An MTech PGP-550F universal potentiostat/galvanostat with software was used. To determine the boundaries of the SCC mechanism transition, polarization curves were also recorded at scan rates of 0.5 mV/s and 100 mV/s.
Slow strain rate (10^{-6} s^{-1}) tests were performed an AIMA-5-1 machine, in the above solutions under cathodic polarization potentials of −0.750 V and −1.050 V (relative to SSCE). According to National Standart of Ukraine 4219 [28], the minimum and maximum protective potentials are −0.850 V and −1.150 V versus the copper sulfate reference electrode, which correspond to potentials of −0.750 V and −1.050 V versus SSCE.
A scheme of the specimens is shown in Figure 2.

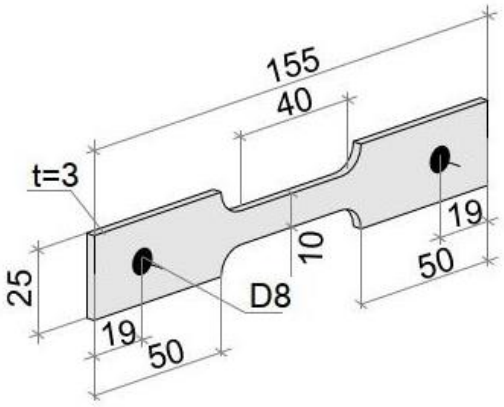


Figure 2. *Specimen for slow strain rate tests [29]. The dimensions are provided in millimeters.*

Stress corrosion studies were carried out by slow strain rate (10^{-6} s^{-1}) test method (SSRT) on an AIMA-5-1 machine, in solutions under cathodic polarization potentials of −0.750 V and −1.050 V. Figure 1 shows a schematic image of the specimen for SSRT.

3. Experimental results and discussion

3.1. Corrosion tests

The appearance of the specimen surfaces after corrosion tests is shown in Figure 3. It can be observed that dark, almost black corrosion products covered the surfaces of specimens tested in mildly acidic solution (Figure 3a) and in near-neutral pH solution (Figure 3b). The surface of specimens exposed to the mildly alkaline solution retained a metallic shine with localized reddish corrosion spots (Figure 3c).



a *b* *c*

Figure 3. *Appearance of specimens after 168-hour exposure at room temperature in mildly acidic solution (a), near-neutral pH solution NS4 (b), and mildly alkaline solution (c)*

The corrosion rates were as follows: in mildly acidic solution 0.079 mm/year, in near-neutral pH solution, 0.0536 mm/year, in mildly alkaline solution – 0.0008 mm/year (Figure 4).

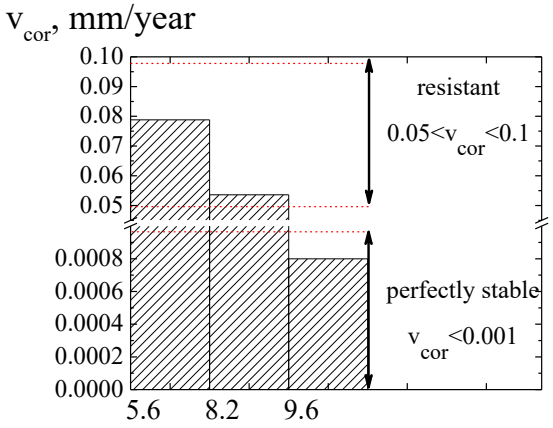
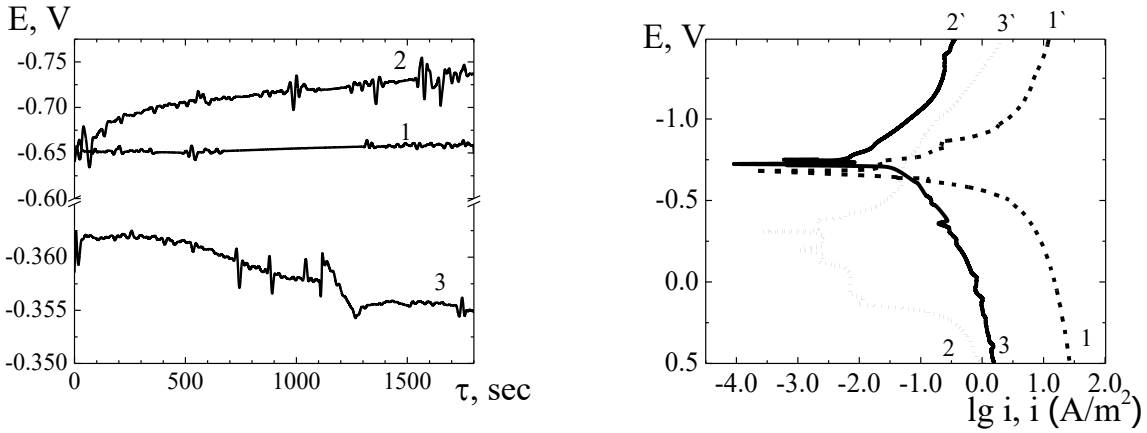


Figure 4. *Dependence of corrosion rate of X70 steel on solution pH.*

3.2. Electrochemical tests

Corrosion potential of X70 steel changes with solution pH levels change in the sequence 5.6 → 8.2 → 9.6, shifting from −0.649 V to −0.737 V to −0.365 V (Figure 5, a).



a *b*

Figure 5. Corrosion potentials (a) and polarization curves (b) of X70 steel: 1 – mildly acidic solution; 2 – near-neutral pH solution; 3 – mildly alkaline solution

The anodic dissolution currents decrease as the solution pH shifts from 5.6 to 9.6 (Figure 5b, curves 1, 2, and 3), which correlates with the observed corrosion rate values. The anodic Tafel slopes are 0.075 V, 0.063 V, and 0.105 V (Figure 5a), indicating on diffusion-controlled corrosion in aqueous solutions (Table 3).

Table 3*. Electrochemical properties of X70 steel*

Solution	E_{cor}, V	b_a, V	$E^1_{i=0}$, V	$E^1_{i=0}$, V	Range of mixed mechanism of SCC
1,92 g/l HCOOH + 54,5 g/l HCOONa + 10 g/l KCNS	-0.649	0.075	-0.816	-0.949	0.133
0,037KCl + 0,559 $NaHCO_3$ + 0,008$CaCl_2$ + 0,089 $MgSO_4$	-0.737	0.063	-1.001	-1.085	0.084
0,1 M $NaHCO_3$ + 0,1 M Na_2CO_3	-0.365	0.105	-0.907	-1.005	0.098

3.3. Slow strain rate tests

Fracture diagrams of specimens in various solutions are shown in Figure 6. Compared to the fracture curve in air, the rupture curves in solutions consistently occur with lower elongation values. Upon analyzing these curves, it is evident that the lowest relative elongation corresponds to the specimen tested in the mildly acidic solution (Figure 6, curve 4).

For assessing susceptibility to SCC, the descending parts of the fracture curves are particularly important. These sections provide preliminary insights into the final stage of crack evolution, which is especially relevant for analyzing the SCC process. As shown in Figure 6a, at a polarization potential of −0.750 V, the lengths of these segments are identical for both near-neutral pH and mildly alkaline solutions, while no descending section is present for the mildly acidic solution were observed (Figure 6a, curve 4). At a polarization potential of −1.050 V, the descending segment is longest for the specimens in the mildly alkaline solution, somewhat shorter for near-neutral pH solution, and practically absent in the case of mildly acidic solution (Figure 6b).

After specimen failure, the fracture surface area was assessed, and the SCC susceptibility coefficient was calculated [30, 31]:

$$K_S = \frac{S_0 - S_1^{air}}{S_0 - S_1^{sol}} = \frac{\psi^{air}}{\psi^{sol}} \quad (1)$$

where S_0 – cross-sectional area of the specimens before testing, mm^2;
S_1^{air} – cross-sectional area of the specimens after testing in air, mm^2;
S_1^{sol} – cross-sectional area of the specimens after testing in solution, mm^2;
ψ^{air} and ψ^{sol} – relative narrowing of specimens relatively in air and in solution.

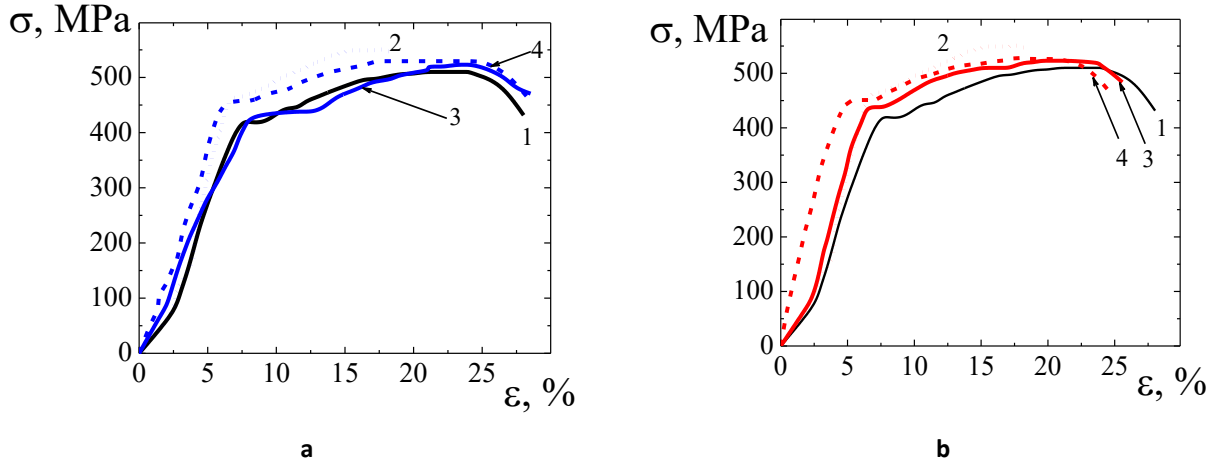


Figure 6. *Fracture curves of X70 steel specimens after SSRT in air (1) and corrosion-mechanical tests under polarization potential −0.750 V (a), and −1.050 V (b) in mildly acidic solution (2), near-neutral pH solution NS4 (3), and mildly alkaline solution (4)*

Figure 7 presents the dependence of the SCC susceptibility coefficient K_S on pH solution. This relationship is non-monotonic and differs for both minimum and maximum cathodic polarization potentials. From the curve analysis, it is noted that the lowest SCC susceptibility is observed in the near-neutral pH solution NS4, where the K_S values are 1.03 and 1.15, respectively, for the both polarization potentials.

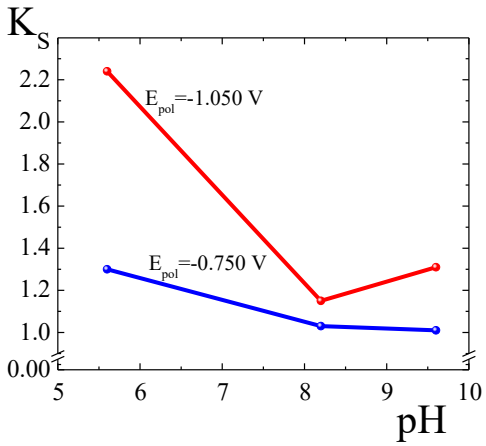


Figure 7. *Variation in SCC susceptibility of X70 steel specimens as a function of solution pH under different cathodic polarization potentials*

At the minimum protective potential -0.750 V, lowering the pH to 5.6 results in an approximately 21% increase in K_S; under maximum polarization -1.050 V, the increase is nearly twice. When the pH is raised to 9.6, K_S remains nearly unchanged at the minimum potential, but under maximum polarization potential, it increases by about 12%.

These trends indicate that even under the same protective potential, the SCC susceptibility of X70 steel varies depending on solution pH. It is also likely that susceptibility at constant pH may change depending on the solution's chemical composition, though this assumption requires further investigation.

3.4. SEM studies

The fracture surface of the specimen after failure in air shows distinct signs of plastic deformation (Figure 8a), which are especially noticeable in deep dimples corresponding in size to the steel grains. Alongside regions of ductile dimpled failure by detachment, fragments of ductile failure via shear are identified. Flat zones on the fracture surface are visible, resulting from the rupture of pearlitic bands under intense plastic strain.

Comparing the fracture surfaces of specimens polarized at −0.750 V, the following features are observed:

- in the mildly acidic solution (Figures 8b), near the specimen's edge, a ductile zone is formed through shear deformation and detachment of fine pores, with weakly developed rupture ridges. Beyond 50 µm from the edge, along with small dimples, quasi-brittle fragments up to 30 µm in size with flat bases appear, concentrated in regions containing pearlitic microstructure;
- in near-neutral pH solution, the fracture is predominantly dimpled, formed shear and detachment mechanisms, with shear facets resulting from pore coalescence under deformation (Figure 8c);
- -in the mildly alkaline solution, ductile fracture fragments by shear deformation alternate with discrete quasi-cleavage features up to 40 µm in diameter (Figure 8e).

Under a polarization potential of −1.050 V, the fracture characteristics differ notably:

- for the mildly acidic solution, part of the surface near the edge reveals shear planes and elongated dimples with rupture ridges. On another section, quasi-brittle fragments up to 50 µm in diameter with flat bases are present, along with cavities likely formed due to localized hydrogen permeation under cathodic polarization (Figures 8f);
- in the solution with near-neutral pH, the fracture is mixed: small dimples (5–20) µm appear alongside intergranular cleavage facets up to 30 µm in size. The proportion of dimpled ductile failure is significantly lower than that of brittle fracture (Figures 8g).

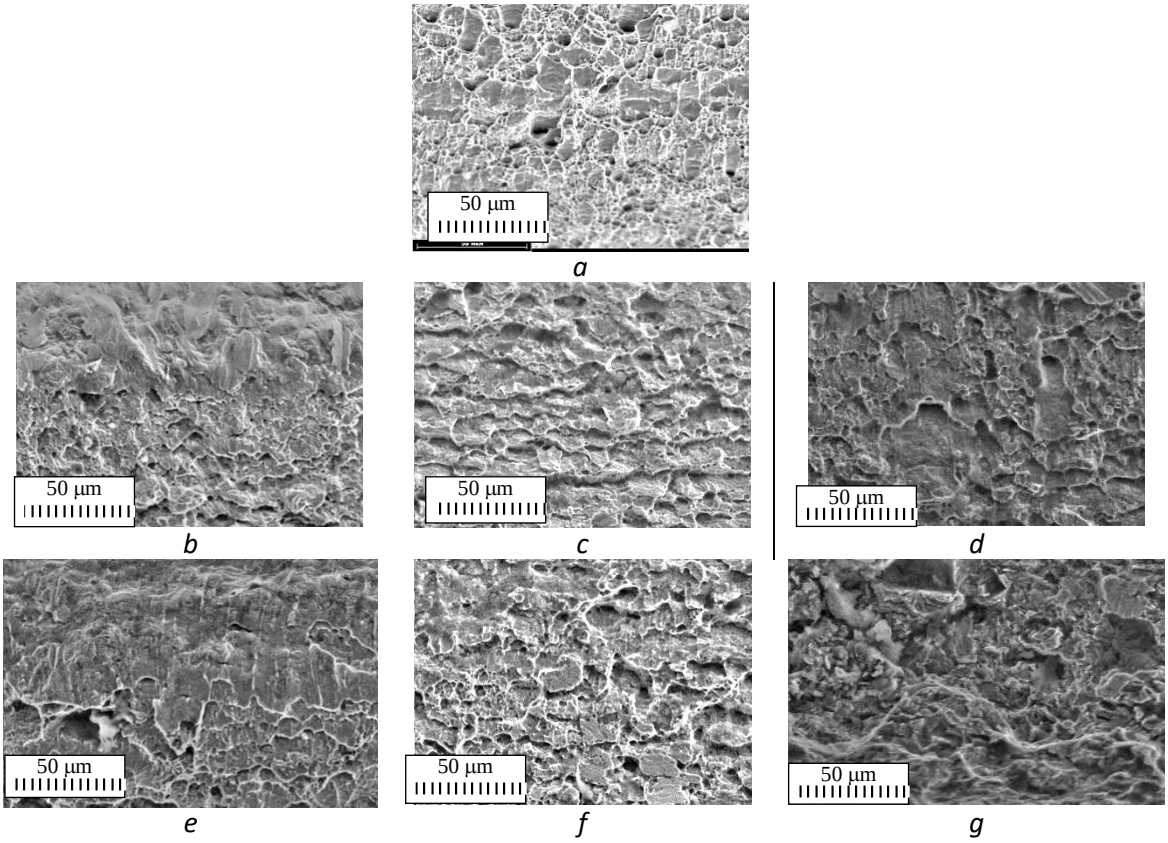


Figure 8. *Fracture surfaces of X70 steel specimens following mechanical testing in air (a), and corrosion-mechanical testing in solutions under cathodic polarization at −0.750 V (b, c, d) and −1.050 V (e, f, g): mildly acidic solution (b, e), near-neutral pH solution NS4 (c, f), and mildly alkaline solution (d, g)*

3.5. Voltametric curves under fast and slow potential scan rates

To elucidate the SCC mechanism, voltametric curves under fast and slow potential scan rates were investigated (Figure 9). According to Parkins’ theory [10, 15], the boundaries of cathodic polarization potentials at which the SCC mechanism of X70 steel shifts were identified. These potential boundaries are presented in Table 3.

Figure 10 presents an analysis of the potential ranges at which SCC mechanism changes depending on the pH of the solution. Both minimum and maximum protective potentials level are shown on the diagram. Based on the observed trends, the following patterns were established for the standardized protective potential range:

- at potentials more positive than −0.750 V, SCC of X70 steel proceeds via the anodic dissolution mechanism;
- within the normalized potential range from −0.750 V to −1.050 V and pH range of 5.6 to 9.6, the probable SCC mechanisms include anodic dissolution, mixed, and hydrogen embrittlement.

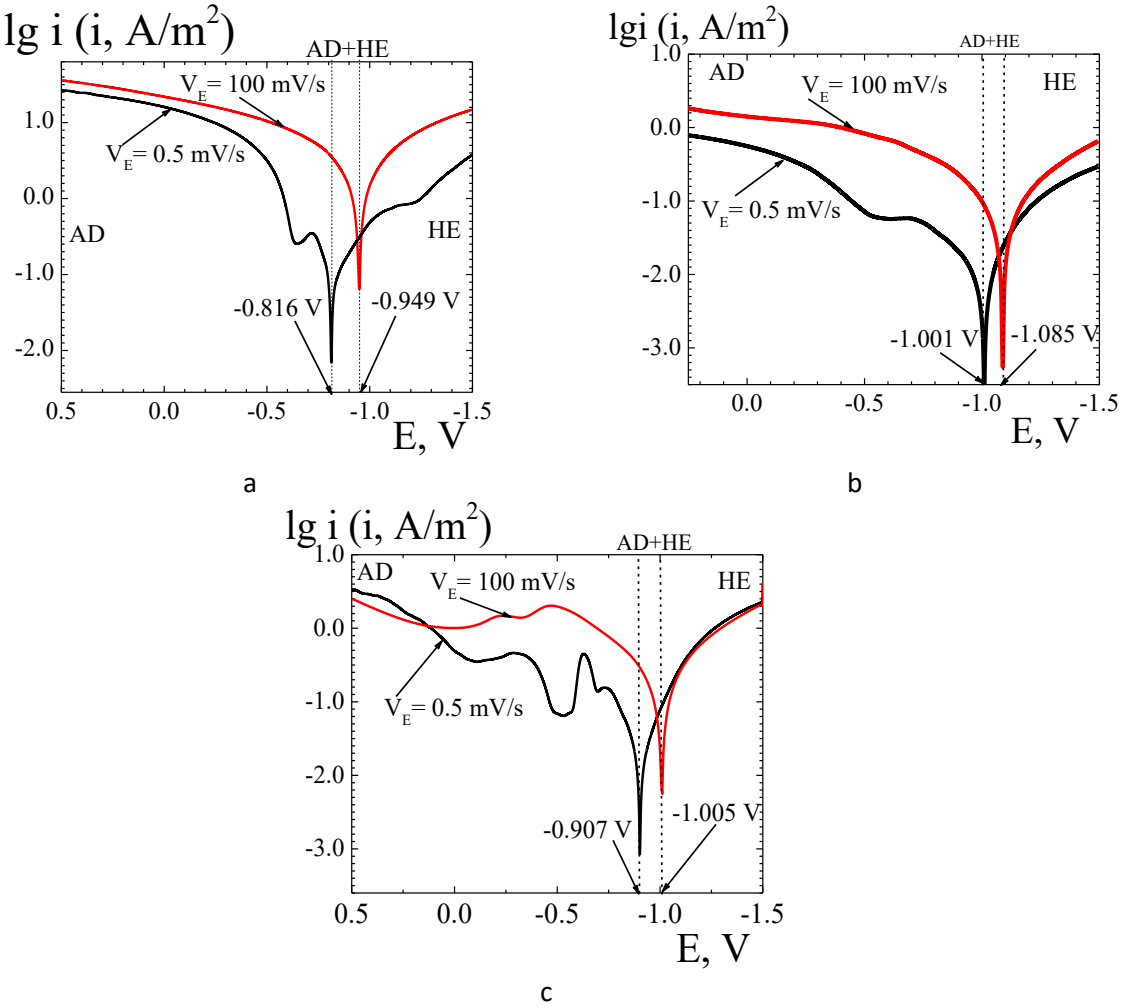


Figure 9. *Voltammetric curves of X70 steel under fast and slow potential scan rates in: (a) mildly acidic solution; (b) near-neutral pH solution NS4; (c) mildly alkaline solution*

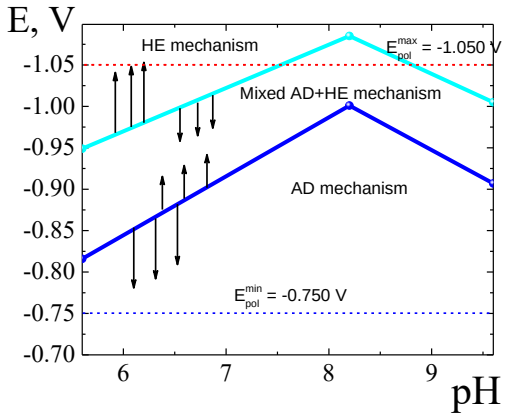


Figure 10. *Variation in the boundaries of SCC susceptibility ranges for X70 steel specimens depending on solution pH*

With changes in solution pH, the dominant SCC mechanisms also shift:

- in near-neutral pH solution (8,2), SCC occurs via the anodic dissolution and mixed mechanisms, correlating with fracture surface morphology (Figure 8c, f).
- in solutions with pH 5.6 and 9.6, all three mechanisms — anodic dissolution, mixed mechanism, and hydrogen embrittlement — are possible, as confirmed by the observed fracture surfaces (Figures 8b, e, and d, g).

These findings emphasize that selecting the maximum protective potential must be thoroughly justified, since excessive polarization in mildly acidic or mildly alkaline environments may trigger cracking by the hydrogen embrittlement mechanism.

4. Conclusions

It has been demonstrated that as the pH of the medium shifts from 5.6 to 9.6, the corrosion resistance of X70 steel increases. In mildly acidic and near-neutral pH solutions, the steel exhibits notable resistance (corrosion rate ranging from 0.05 to 0.1 mm/year according to corrosion resistance scale). In the mildly alkaline solution, the steel X70 shows perfectly resistance (with a corrosion rate lower than 0.1 mm/year according to corrosion resistance scale). The measured corrosion rates were: 0.0788, 0.0536, and 0.0008 mm/year, respectively.

It was established that within the pH range of 5.6 to 9.6, the lowest susceptibility to SCC occurs in the NS4 solution. The corresponding K_S values are 1.03 at a polarization potential of −0.750 V and 1.15 at −1.050 V. At the minimum protective potential, lowering the pH to 5.6 increases K_S to 1.3; under the maximum polarization, it nearly twice, to 2.24 when pH increases to 9.6; K_S equals to 1.01 and 1.31, respectively.

It was established that the ranges of potentials at which the SCC mechanism transitions are dependent on the pH of the solution. At pH 8.2, SCC within the −0.750 V to −1.050 V potential range occurs via anodic dissolution and mixed mechanisms. In solutions with pH 5.6 and 9.6, all three mechanisms—anodic dissolution, hydrogen embrittlement, and mixed—are presented, as approved by fracture surface morphology.

These patterns highlight that selecting the maximum protective potential must be carefully substantiated. Excessive polarization in environments with mildly acidic or mildly alkaline pH may lead to SCC development via the hydrogen embrittlement mechanism.

Acknowledgments

This scientific project was carried out by the support r the support of National Academy of Sciences of Ukraine in 2022-2024 (state registration number 0122U001188).

References

[1] Leis, B.N. & Eiber R.J., 1997. Stress-Corrosion Cracking on Gas-Transmission Pipelines: History, Causes and Mitigation, Proceedings of First International Business Conference on Onshore Pipelines, 1997, Berlin.

[2] Oskuie, A. A., Shahrabi, T., Shahriari, A., & Saebnoori, E., 2012. Electrochemical impedance spectroscopy analysis of X70 pipeline steel stress corrosion cracking in high pH carbonate solution. Corrosion Science, 61, 111-122. https://doi.org/10.1016/j.corsci.2012.04.024.

[3] Bordbar, S., Alizadeh, M., & Hashemi, S.H., 2013. Effects of microstructure alteration on corrosion behavior of welded joint in API X70 pipeline steel. Materials & Design, 45, 597–604. https://doi.org/10.1016/j.matdes.2012.09.051.

[4] Liang, P., Li, X., Du, C., & Chen, X., 2009. Stress corrosion cracking of X80 pipeline steel in simulated alkaline soil solution. Materials & Design, 30(5), 1712–1717. https://doi.org/10.1016/j.matdes.2008.07.012.

[5] Xu, L.Y. & Cheng, Y.F., 2012. An experimental investigation of corrosion of X100 pipeline steel under uniaxial elastic stress in a near-neutral pH solution. Corrosion Science, 59, 103–109. https://doi.org/10.1016/j.corsci.2012.02.022.

[6] Lu, B.T., Song, F., Gao, M., & Elboujdaini, M., 2010. Crack growth model for pipelines exposed to concentrated carbonate–bicarbonate solution with high pH. Corrosion Science, 52 (12), 4064–4072. https://doi.org/10.1016/j.corsci.2010.08.023.

[7] Eslami, A., Kania, R., Worthingham, B., Boven, G.V., Eadie, R., & Chen, W., 2011. Effect of CO_2 and R-ratio on near-neutral pH stress corrosion cracking initiation under a disbonded coating of pipeline steel. Corrosion Science, 53(6), 2318–2327. https://doi.org/10.1016/j.corsci.2011.03.017.

[8] Lu, B.T., Luo, J.L., Norton, P.R., & Ma, H.Y., 2009. Effects of dissolved hydrogen and elastic and plastic deformation on active dissolution of pipeline steel in anaerobic groundwater of near-neutral pH. Acta Materialia, 57(1), 41–49. https://doi.org/10.1016/j.actamat.2008.08.035.

[9] Parkins, R.N., Blanchard, W.K., & Delanty, B.S., 1994. Transgranular stress corrosion cracking of high-pressure pipelines in contact with solutions of near neutral pH. Corrosion, 50 (5), 394-408. https://doi.org/10.5006/1.3294348

[10] Gadala, I.M. & Alfantazi, A., 2014. Electrochemical behavior of API-X100 pipeline steel in NS4, near-neutral, and mildly alkaline pH simulated soil solutions. Corrosion Science, 82, 45–57. https://doi.org/10.1016/j.corsci.2013.12.020.

[11] Fang, B.Y., Atrens, A., Wang, J.Q., Han, E.H., Zhu, Z.Y., & Ke, W., 2003. Review of stress corrosion cracking of pipeline steels in “low” and “high” pH solutions. Journal of Materials Science, 38, 127–132. https://doi.org/10.1023/A:1021126202539.

[12] Beavers, J.A. & Harle, B.A., 1996, June. Mechanisms of high-pH and near-neutral-pH SCC of underground pipelines. In: International Pipeline Conference, Vol. 1, 555–568. New York: American Society of Mechanical Engineers.

[13] Lu, B.T., Luo, J.L., & Norton, P.R., 2010. Environmentally assisted cracking mechanism of pipeline steel in near-neutral pH groundwater. Corrosion Science, 52(5), 1787–1795. https://doi.org/10.1016/j.corsci.2010.02.020.

[14] Liu, Z.Y., Li, X.G., & Cheng, Y.F., 2012. Mechanistic aspect of near-neutral pH stress corrosion cracking of pipelines under cathodic polarization. Corrosion Science, 55, 54–60. https://doi.org/10.1016/j.corsci.2011.10.002.

[15] Liu, Z.Y., Lu, L., Huang, Y.Z., Du, C.W., & Li, X.G., 2014. Mechanistic aspect of non-steady electrochemical characteristic during stress corrosion cracking of an X70 pipeline steel in simulated underground water. Corrosion, 70(7), 678–685. https://doi.org/10.5006/1153.

[16] Liu, Z.Y., Li, X.G., & Cheng, Y.F., 2010. In-situ characterization of the electrochemistry of grain and grain boundary of an X70 steel in a near-neutral pH solution. Electrochemistry Communications, 12(7), 936–938. https://doi.org/10.1016/j.elecom.2010.04.025.

[17] Liu, Z.Y., Li, X.G., Du, C.W., & Cheng, Y.F., 2009. Local additional potential model for effect of strain rate on SCC of pipeline steel in an acidic soil solution. Corrosion Science, 51(12), 2863–2871. https://doi.org/10.1016/j.corsci.2009.08.019.

[18] Liu, Z.Y., Li, X.G., Du, C.W., Zhai, G.L., & Cheng, Y.F., 2008. Stress corrosion cracking behavior of X70 pipe steel in an acidic soil environment. Corrosion Science, 50(8), 2251–2257. https://doi.org/10.1016/j.corsci.2008.05.011.

[19] Zhiyong, L., Zhongyu, C., Xiaogang, L., Cuiwei, D., & Yunying, X., 2014. Mechanistic aspect of stress corrosion cracking of X80 pipeline steel under non-stable cathodic polarization. Electrochemistry Communications, 48, 127–129. https://doi.org/10.1016/j.elecom.2014.08.016.

[20] Javidi, M. & Horeh, S.B., 2014. Investigating the mechanism of stress corrosion cracking in near-neutral and high pH environments for API 5L X52 steel. Corrosion Science, 80, 213–220. https://doi.org/10.1016/j.corsci.2013.11.031.

[21] Liu, Z.Y., Wang, X.Z., Du, C.W., Li, J.K., & Li, X.G., 2016. Effect of hydrogen-induced plasticity on the stress corrosion cracking of X70 pipeline steel in simulated soil environments. Materials Science and Engineering: A, 658, 348–354. https://doi.org/10.1016/j.msea.2016.02.019.

[22] Murakami, Y., Kanezaki, T., & Mine, Y., 2010. Hydrogen effect against hydrogen embrittlement. Metallurgical and Materials Transactions A, 41, 2548–2562. https://doi.org/10.1007/s11661-010-0275-6.

[23] Miresmaeili, R., Liu, L., & Kanayama, H., 2012. A possible explanation for the contradictory results of hydrogen effects on macroscopic deformation. International Journal of Pressure Vessels and Piping, 99, 34–43. https://doi.org/10.1016/j.ijpvp.2012.08.001.

[24] Ren, X.C., Chu, W.Y., Su, Y.J., Li, J.X., Qiao, L.J., Jiang, B., & Chen, G., 2008. The effects of atomic hydrogen and flake on mechanical properties of a tyre steel. Materials Science and Engineering: A, 491(1–2), 164–171. https://doi.org/10.1016/j.msea.2008.02.002.

[25] Wu, S., Gao, Z., Liu, Y., & Hu, W., 2023. Effect of cathodic protection potential on stress corrosion susceptibility of X80 steel. Corrosion Science, 218, 111184. https://doi.org/10.1016/j.corsci.2023.111184.

[26] ISO 3183:2019 Petroleum and natural gas industries — Steel pipe for pipeline transportation systems

[27] ISO 17475:2005 Corrosion of metals and alloys — Electrochemical test methods — Guidelines for conducting potentiostatic and potentiodynamic polarization measurements

[28] National Standart of Ukraine 4219:2003. STEEL PIPE MAINS. General requirements for corrosion protection

[29] Nyrkova, L., Goncharenko, L., Osadchuk, S., Bratochkin, O., & Kovalenko, S., 2024. Mechanical Technologies and Structural Materials (Conference Proceedings), 317. https://www.strojarska-tehnologija.hr/img/pdf/Conference_Proceedings_MTSM_2024.pdf.31.

[30] Nyrkova L. Stress-corrosion cracking of pipe steel under complex influence of factors. Engineering Failure Analysis. 2020. Vol. 116. 104757.

[31] Nyrkova, L.I., Osadchuk, S.O., Rybakov, A.O., & Mel’nychuk, S.L., 2020. Methodical approach and a criterion for the evaluation of the susceptibility of pipe steel to corrosion cracking. Materials Science, 55(5), 625–632.

Improving chairlift operations with safety measures, technological innovations, and efficiency optimization

***Rosen Petrov*[1], *Milena Biserova*[1], *Aleksander Vulkov*[1] *and Nikolay Stoimenov*[1]**

1) Institute of Information and Communication Technologies at the Bulgarian Academy of Sciences, Sofia, Bulgaria

Corresponding author: nikistoimenow@gmail.com

Review article

Abstract: Chairlifts are a key element of the infrastructure of mountain resorts, providing convenient and efficient transport for tourists and skiers. However, these systems are exposed to various technical and operational problems that can lead to accidents, delays, and increased maintenance costs. This article examines the main challenges associated with chairlifts, in particular, how to use them by skiers, to prevent downtime and the intervention of responsible persons. Good practices for preventing malfunctions and innovative solutions to increase the safety and efficiency of these transport facilities are also analyzed. A method of localizing passenger flow is proposed to increase ski lift efficiency. One option is to position passengers correctly on the lift seat, which can prevent unwanted tilting. The method under consideration utilizes radar sensors, algorithms, and cameras. Light panels guide the skiers to the appropriate seating areas. The system provides visual guidance, improves organization, and enhances safety. The outcomes of this study demonstrate a reduction in the probability of accidents, an enhancement in reliability, and a reduction in service times.

Keywords: *chairlift; ski lift; light board; radar sensors; mountain transport; chairlift maintenance*

1. Introduction

Chairlifts are a type of ropeway used primarily in mountainous areas to transport people, most often in ski resorts, tourists, and nature parks. They consist of a system of ropes that drive a series of chairs suspended from them (Figure 1).



Figure 1. *Six-seater chair lift*

Chairlifts are composed of several main components:

- Support-rope system - the main element is the support rope, which moves along a track covered by support poles. The rope moves continuously in a closed loop, driven by a main engine or a backup engine, and seats are attached to the rope at equal distances [1].
- Seats - most often made of metal structures with plastic or soft padding for comfort. They are equipped with safety bars that prevent passengers from falling. Some are open, others are

equipped with cabins that protect against bad weather conditions. In some cases, seats are used, especially in luxury resorts.

- Support poles and stations - the poles are located at certain intervals and support the rope, reducing vibrations. There are two main stations: lower (initial) and upper (final), where passengers get on and off. The stations have mechanisms for speed control and possibly stopping the system [2].
- The classification of chairlifts is carried out according to the following criteria:
- Depending on the design and principle of operation, they can be single-seater (rarely found today, used mainly in old facilities), double-seaters and triple-seaters (common in smaller resorts), and quadruple-seaters, six-seaters, and eight-seaters (modern ski resorts use larger capacities to reduce queues).
- Depending on the method of joining the ropeway - fixed seats - attached directly to the moving rope, which means that the speed of the entire lift is relatively slow to facilitate boarding and disembarking, and detachable, automatically unfastened seats - upon reaching the station, the seats are disconnected from the main rope and move along a rail mechanism at a significantly lower speed, which makes boarding and disembarking easier and safer.

Chairlifts are one of the most popular means of transportation in mountain resorts, offering convenience and efficiency. They have a number of advantages, but also some disadvantages that can affect skier comfort.

Advantages:

- Speed and efficiency – especially with detachable seats, which reduce waiting times;
- Comfort and safety – thanks to safety mechanisms and modern technologies;
- Panoramic views – chairlifts offer unique views during the ascent;
- Environmental friendliness – they operate on electricity and have less environmental impact compared to other modes of transport in the mountains.

Disadvantages:

- Vulnerability to weather conditions – wind, heavy snow, or fog can limit the operation of the lift;
- Lack of protection against cold in some models – without windshields and heating, passengers can be exposed to low temperatures;
- Inconvenience when boarding and disembarking for inexperienced users – especially for novice skiers.

During their research into methods for optimizing passenger flow, the authors were unable to find applied devices of this nature. In the context of Bulgaria, there is an absence of a system that has been developed or implemented. It has been observed that certain ski lifts are accompanied by signs along the path, which is frequently covered by a layer of snow. A visual line has been incorporated into the design to indicate to skiers where they should stop, but not where they should board or how they should distribute themselves on the seats.

2. Common problems during chairlift operation

During the operation of chairlifts, various problems related to technical maintenance, safety, and weather conditions can arise. Here are some of the most common:

2.1. Technical Problems

One of the most common problems encountered in the operation of modern chairlifts is a failure of the drive system, which includes problems with the drive motor, rollers, or brake mechanisms, which can lead to an indefinite stop of the lift. Another problem can be the wear of the transport cable, which can deform, delaminate, or wear out mechanically. The problem with the roller mechanisms is also fundamental, as bearings wear out and fail, rollers can wear out or blocked, which affects the movement of the lift. Failures in monitoring and control systems, including sensors, control panels, or other electronic components, can also fail and lead to a stop of the facility.

2.2. Weather conditions

Weather conditions are of key importance for lift facilities, as they are exposed to external factors. Wind speed in many cases determines the stability of the system, and when the permissible standard speed is exceeded, the lift must be stopped.

Dense fog and reduced visibility are other challenges that can make the work of the staff difficult and affect the safety of passengers.

Icing of the rope and mechanical parts and heavy snowfalls also make normal technical operation difficult, as the accumulated ice and snow can lead to mechanical damage, stopping the lift and possible intervention by the technical staff.

2.3. Emergency situations

The main reason for interrupting the normal operation of the ski lift is the power outage, in which case the lift may remain blocked if there is no backup power supply. Other emergency situations that can lead to the shutdown of the facility are passenger incidents, such as falls from seats, stuck clothing or a problem with the closing mechanism. In the worst case, an evacuation may be necessary, if the lift cannot be restarted, users must be evacuated using additional equipment.

2.4. Operational errors

One of the most common operational errors is when boarding and disembarking passengers.

If skiers do not take the correct position, they may fall, which can slow down the lift and cause crowding.

Another reason for an emergency stop of the facility is overloading the lift, associated with too many passengers or incorrect weight distribution. Not following safety measures, such as improper passenger behavior, shaking the seat, or jumping, can create risks to the health and life of all users. Failure to use safety bars properly has been identified as a contributing factor to safety risks in chairlifts [3]. Observational studies have shown that compliance with safety bar use varies significantly among different skier demographics [4].

3. Human recognition systems

There is a range of technologies for remotely detecting human presence in each area, including:

Acoustic sensors - these are devices that detect, measure, and analyze sound waves and vibrations in various environments. They convert acoustic signals into electrical or digital data that can be used for monitoring, control, or analysis.

Acoustic sensors work on the principle of converting sound waves into mechanical or electrical signals. Depending on their type, they use different technologies, such as the piezoelectric effect, electromagnetic induction, and optical methods.

Real-time human presence analysis - Real-time human behavior in ski lifts is crucial to ensuring safety, efficiency, and automation. This includes using computer vision and AI to detect passengers, verify proper seating, monitor for incidents, and optimize operations at the ski resort [5].

By integrating human presence analysis technologies, a greater degree of safety and incident prevention can be achieved, automated monitoring, and increasing facility capacity by managing the flow of users.

Infrared sensors - these are devices that can detect people, monitor the occupancy of the lift facility, as well as improve its operational reliability in conditions of poor visibility (snow, fog, night).

This type of sensor is used to detect fallen or stuck passengers, an automatic emergency stop, in case of an incorrectly seated passenger. They also have the ability to work in adverse weather conditions, detect and register unauthorized access, monitor and analyze ski areas in order to avoid crowding. Infrared sensors play a crucial role in these applications, with their accuracy influenced by various technological factors [6].

Radar sensors - similar to infrared sensors, they work in all weather conditions, including snow, fog, and darkness, making them an excellent choice for reliable detection of people and objects. These

sensors work by emitting and receiving sound waves in different frequency ranges. Their main advantages are reliable operation in all conditions, the ability to detect objects from afar, real-time monitoring, and low energy consumption.
These sensors can detect fallen or stuck passengers, automatically stop the lift in case of an incorrectly seated passenger, and work in adverse weather conditions to improve operational reliability. Machine learning techniques have been employed to analyze chairlift operations and improve safety compliance [7].

4. Passenger distribution and seat balancing system

The passenger distribution and seat balancing system was developed to ensure even seating in the six-seater chairlift. Its main task is to prevent imbalance that can occur if skiers sit unevenly – for example, if they only occupy one side of the seat. This could lead to tilting, which increases the risk of accidents. Optimizing passenger distribution and balancing has been highlighted as a key factor in improving ski lift efficiency [8]. To avoid this problem, the system uses radar sensors to detect the number of passengers in the boarding area (Figure 2). In combination with a light board that provides clear instructions, it guides skiers to the optimal seating arrangement. This not only ensures passenger safety but also better organization of the flow of people, leading to faster and more efficient boarding (Figure 3).



Figure 2. *Radar sensor*

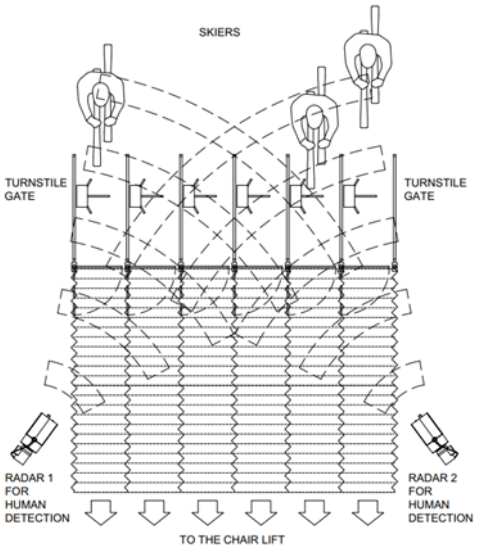


Figure 3. *Detection area*

When passing through the turnstile gates, skiers enter the waiting area, where radar sensors detect their number in real time [9]. The algorithm analyzes the input data and, depending on the number of people in the group, determines the optimal distribution of the seats. If the group is full (six people), the system does not take any additional actions, since all the seats are occupied and the weight is evenly distributed. In case the group is smaller, for example, three or five people, the algorithm distributes the passengers so that the weight is balanced on the seat, ensuring stability and safety.

When there are three people, for example, the system can place them in seats 3, 4, and 5 as shown in Figure 4.

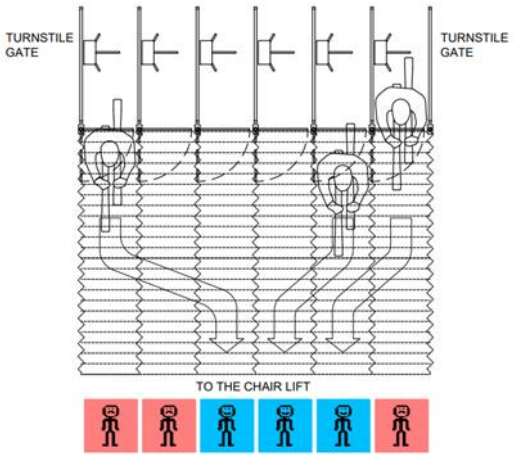


Figure 4. *Regrouping zone*

After the algorithm calculates the best placement, a signal is sent to the light board, which, using a visual signal, indicates to the skiers where to stand.

Once the system has calculated the optimal passenger seating, the light board located in front of the skiers displays blue and red graphics to guide skiers to the most appropriate seats, ensuring a balanced seating distribution and preventing one-sided seating, which can lead to accidents [10]. The presence of a light board with instructions provides several key advantages. It significantly increases the efficiency of the boarding process, reducing waiting times and making it easier for skiers to choose the right seats. This is especially important during busy periods when there are many passengers and there is a risk of delays. In addition, the light board creates clear and easy-to-understand communication between the system and skiers, eliminating the need for verbal instructions from staff. This reduces the workload of employees and at the same time increases the safety and accuracy of actions (Figure 5).

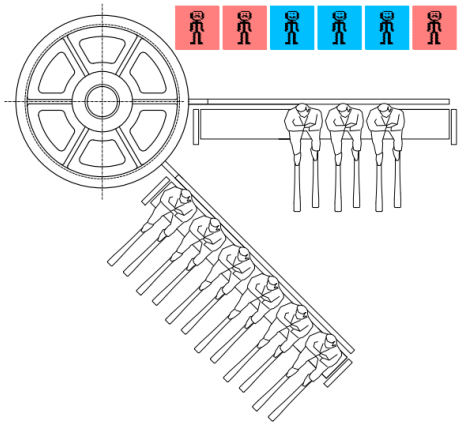


Figure 5. *Correct seating position*

To achieve more efficient operation of the ski facility, the system can be connected to the lift control, allowing operators to monitor the boarding process in real time. If, despite the instructions, the seat is occupied unevenly, the operator can receive a warning and take corrective measures.

5. Conclusion

The developed signaling system to increase the capacity and efficiency of chairlifts represents an innovative solution to address the operational challenges faced by these transport facilities. By

integrating radar sensors for monitoring the number of passengers and algorithms for optimal weight distribution on the seats, the system ensures even passenger seating and minimizes the risk of imbalance that can lead to accidents.

The application of light boards that guide skiers to the optimal seats improves operational efficiency by speeding up the boarding process and minimizing waiting times. This communication system also relieves staff by eliminating the need for verbal instructions and reducing the workload of the operator. Providing visual guidance through light arrows ensures better organization of passengers, while maintaining high levels of safety.

The integration of such a system allows real-time monitoring of passenger flow and making adjustments when necessary, such as warnings for incorrectly occupied seats. This contributes to more efficient management of skier flow and reduced potential for emergency situations. The system provides significant benefits, including reduced risk of accidents, improved operational reliability and reduced service times, leading to increased overall ski lift efficiency.

References

[1] Težak, S., Lep, M., 2019. Solutions for increasing the capacities of cable cars. Journal of Sustainable Development of Transport and Logistics, 4(1), 31-37. https://doi.org/10.14254/jsdtl.2019.4-1.4.

[2] Kiesel, A., Brandi, G., Schlatter, J., Langenberg, S., others,2024. Structural reuse of decommissioned ski lift steel trusses for load-bearing applications. Architecture, 4(4), 835-853

[3] Harley, E. M., Stepan, L. L., Scher, I. S, 2023. Factors that influence chairlift restraint bar use in the United States. https://doi.org/10.1016/j.jsampl.2023.100031

[4] Park, J. I., King, D. R., Jonas, R. K., Phillips, K. B., 2022. An observational study of skier and snowboarder chairlift lap bar, helmet, and snow goggle usage. Proceedings of the Human Factors and Ergonomics Society Annual Meeting, 66(1). https://doi.org/10.1177/1071181322661412

[5] Naser, A., Lotfi, A., Zhong, J., 2023. Towards human distance estimation using a thermal sensor array. Neural Computing and Applications, 35, 23357–23367. https://doi.org/10.1007/s00521-021-06193-2

[6] Tang, Z., Liu, Y., Cui, L., Hu, Z., et.al., 2024. The technological development of infrared sensors in substations and the key determining factors affecting the accuracy of measurement data. E3S Web of Conferences, 522, 01032. https://doi.org/10.1051/e3sconf/202452201032

[7] Alqasir, H., 2020. Deep Learning for Chairlift Scene Analysis: Boosting Generalization in Multi-Domain Context [Doctoral dissertation, Université de Lyon]. Retrieved March 19, 2025, from https://www.researchgate.net/publication/351245747_Deep_Learning_for_Chairlift_Scene_Analysis_Boosting_Generalization_in_Multi-Domain_Context

[8] Delibašić, B., Radovanovic, S., Jovanovic, M. Z., Suknović, M., 2020. Improving decision-making in ski resorts by analysing ski lift transportation—A review. In Advances in Operational Research in the Balkans. https://doi.org/10.1007/978-3-030-21990-1_16

[9] Li, L., Mu, X., Li, S., Peng, H., 2020. A review of face recognition technology. In IEEE Access. https://doi.org/10.1109/ACCESS.2020.3011028

[10] Jegham, I., Ben Khalifa, A., Alouani, I., Mahjoub, M. A., 2020. Vision-based human action recognition: An overview and real-world challenges. In LATIS - Laboratory of Advanced Technology and Intelligent Systems.

Feasibility study for damage analysis of a hip prosthesis made of Ti6Al7Nb alloy

***Massimo Rogante*[1] *and Luigi Arcangeli*[2]**

1) Rogante Engineering Office, Contrada San Michele 61, 62012 Civitanova Marche, Italy

2) Studio Lightbox, Via Civitanova 161/163, 62012 Civitanova Marche, Italy

Corresponding author: main@roganteengineering.it

Review article

Abstract: This feasibility study was conducted to investigate the potential causes of fracture at the proximal end of the femoral stem (also known as the prosthetic neck) in a right hip prosthesis made of Ti6Al7Nb alloy. The fracture occurred in a patient who had previously undergone total hip arthroplasty due to right-sided coxarthrosis, about 15 months after the arthroplastic intervent. During the procedure, a femoral stem, an acetabular component (comprising the acetabular cup and liner) and a ceramic femoral head were implanted.
The study begins with a review of the current state-of-the-art regarding such failures, with particular focus on design specifications and documented cases of mechanical failure. It then presents a feasibility analysis that includes visual inspection of the fracture surfaces and an overview of the selected spectroscopic, spectrometric, and neutron-based characterization techniques which could be adopted to carry out a full investigation.
The findings and considerations presented here aim to offer a methodological reference framework for analyzing similar cases of implant failure in the future.

Keywords: *Ti6Al7Nb; fracture; femoral stem; fatigue*

1. Introduction

Total hip arthroplasty (THA) is a widely performed orthopedic procedure designed to restore mobility and relieve pain in patients suffering from degenerative joint conditions such as coxarthrosis. The long-term success of THA relies heavily on the mechanical integrity and biocompatibility of the implant materials, as well as the design and manufacturing quality of the prosthetic components. Despite significant advances in implant technology and surgical techniques, instances of implant failure - particularly involving fractures of the femoral stem or neck - continue to be reported in clinical practice, though they remain relatively rare.
One such instance prompted the present study: a fracture at the proximal end of a femoral stem made of Ti6Al7Nb alloy in a right hip prosthesis. This case raised critical concerns regarding the mechanical performance of the alloy under in vivo loading conditions, as well as potential contributing factors such as material's defects, design flaws, patient-specific biomechanics or surgical variables. Ti6Al7Nb is known for its favorable combination of mechanical strength, corrosion resistance and biocompatibility. It has been adopted as an alternative to the more commonly used Ti6Al4V alloy due to concerns regarding vanadium toxicity. Fractures in Ti-based femoral components (particularly in the prosthetic neck region), however, suggest that material performance alone cannot ensure long-term reliability. Fracture of a component generally occurs when the stresses that develop within it to balance external forces exceed the limit of the component's constituent material.
Understanding the root causes of such failures is essential for improving implant designs and material selection and for developing standardized diagnostic protocols, in order to assess and mitigate risk in future cases. This calls for a comprehensive analysis that integrates clinical, mechanical and materials science perspectives.
Establishing a robust methodological framework for post-failure evaluation, moreover, could greatly benefit surgeons, manufacturers and regulatory agencies by enabling a more systematic approach to

implant assessment. In this context, the present feasibility study sets out to explore the potential origins of fracture in the femoral neck of a Ti6Al7Nb prosthesis. Building on a review of existing literature concerning mechanical failures of hip implants, we outline a set of experimental techniques - ranging from the visual inspection already carried out to advanced spectroscopic, spectrometric and neutron-based methods - that could be employed to conduct a full damage assessment. While the current work does not include a complete forensic analysis, it seeks to define the scope and practicality of such an investigation, providing a preliminary foundation for further studies. The results and methodological insights presented here aim to contribute to a growing body of knowledge on implant failure mechanisms and to support the development of improved diagnostic and preventive strategies in orthopedic implantology.

2. Traumatic event and current state of the art

The patient, while standing and bending over to pick up an object approximately 40 cm from the ground, suddenly suffered a collapse of his right limb, experiencing pain and functional impairment, and then fell to the ground. Subsequent radiological examination revealed a fracture of the neck of the femoral component, so the patient underwent a revision surgery with replacement of the damaged prosthesis stem only, as the acetabular component had been found to be stable. The considered hip prosthesis sample and the related documentation were preliminarily examined, with reference to the constituent materials and type, with the aim of formulating this methodological approach and identifying both the techniques and the most suitable instrumentation to carry out the potential investigation.

2.1. Hip replacement

The hip joint is composed of the following parts: the acetabulum or cup, the femoral head, the greater trochanter, the lesser trochanter and the femoral neck. The femoral head, together with the joint, forms the so-called “ball and socket joint” necessary for walking. This joint is characterized by a wide range of motion, albeit limited by ligaments and muscles. A hip prosthesis, also called a “biomorphic” prosthesis because it reproduces the model found in nature, is the first replacement of parts of the musculoskeletal system. This artificial joint can be made of metal alloys, plastic materials and ceramics. Referring to Figure 1, a hip prosthesis consists of a dome or cup, also called the “acetabular cup”, a head and a stem. The cup, in turn, is composed of a hemispherical metal part - also called “metal back” - and a ceramic or ultra-high-molecular-weight polyethylene (UHMWPE) insert.

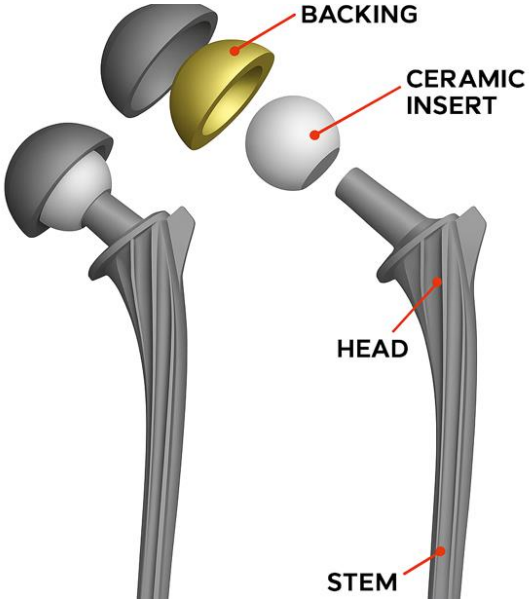


Figure 1. *Schematic representation of hip replacement.*

The cup is positioned inside the acetabulum (or “acetabular cavity”) of the pelvis after preparing the bone seat using special reamers, so that it covers the old bone surface. The cup includes the ceramic articular insert, which fits between the metal hemispherical portion and the articular head.
The stem is positioned at the upper end of the medullary canal of the femur, after appropriate resection of the femoral head and preparation of the seat using appropriate rasps. A prosthetic articular head, made of metal or ceramic, is assembled onto the stem, which articulates with the internal surface of the cup. The neck of a total hip replacement coincides with the upper end of the femoral stem, which is connected to the femoral or prosthetic head via a conical coupling between the stem with a male taper and the head with a female taper. In “standard” prostheses, the neck is an integral part of the femoral stem, which is always made of a metal alloy. Table 1 lists some of the metal materials used to make the femoral stem.

Table 1. *Metallic materials used for the construction of the femoral stem [1]*

Material	Young modulus (GPa)	Ultimate tensile strength (MPa)	Breaking elongation (%)	Density (g/cm^3)
Ti6Al4V	110	900	10	4,5
Inox AISI 316L (forged)	200	1000	9	7,9
CoCrMo (cast)	230	660	8	8,3
CoNiCrMo (forged)	230	1800	8	9,2

In the case of the Ti6Al4V alloy, since V it is not particularly absorbed, it can be replaced with Nb. To produce osteoinductive activity (i.e., the bone graft's ability to stimulate undifferentiated stem cells - or osteoprogenitor cells - from surrounding tissues to differentiate into osteoblasts), a Ti coating obtained using plasma spray technology is sometimes applied to the stem. This coating increases the roughness of the stem, enhancing osteoinductive activity, improving fatigue characteristics and reducing the likelihood of defects.
The forces applied to the hip depend on the type of support, which can be bipedal or monopedal. In the former case, the body weight is applied to the body's center of gravity - which is located on the axis of symmetry - so that two equal forces act on the hips. In the second case, relating to walking, the centre of gravity is shifted along the axis of the raised limb, so (as supported by experimental research [2]) it appears that the force applied to each hip, at each gait cycle, can reach values close to approximately 300 kg. Considering the various types of walking, including running, or going up/down stairs, the inertial force involved varies or other muscles are activated that are unloaded on the hip, with a general increase of 5 to 7 times the body weight. The stresses involved are those of presso-flexion that affect the bone structures and those of friction generated on the joint surfaces in contact. All loads are cyclic, so while bone remodelling phenomena occur in the bone structures, the prostheses in turn are subject to fatigue.

2.2. Design requirements for a hip prosthesis

The design specifications for a hip prosthesis can generally be summarized as follows:
a) Preservation of Natural Kinematics: the prosthesis must allow for the degrees of rotational freedom typical of the natural joint, minimizing the risk of dislocation.
b) Load-Bearing Capability: the implant must withstand the significant loads encountered during gait (see Section 2.1.), ensuring both static and dynamic (especially fatigue) reliability.
c) Fatigue Resistance: due to cyclic loading during walking, the prosthesis must demonstrate high fatigue strength. In an individual with normal activity, the hip joint undergoes approximately 1,000,000 cycles per year. The femoral stem, being unshielded by bone, is the most fatigue-sensitive

component. Currently, the minimum requirement for market approval is resistance to at least 20 years of cyclic loading [2].
d) Wear Resistance of Articulating Surfaces: articulating components must resist wear or be designed such that wear does not compromise functionality or induce adverse tissue reactions.
e) Use of Biocompatible Materials: materials must be biocompatible to prevent harmful tissue reactions or alterations. They should also promote a stable mechanical interface between stem and femur, and between acetabular cup and pelvis. High mechanical strength, particularly under bending-compression fatigue, is required. Additionally, materials must be sterile to support healthy bone growth and prevent necrosis.
f) Mechanical Stability of Bone-Implant Interfaces: long-term mechanical stability of the interfaces mentioned in (e) must be ensured, both immediately post-implantation and over time.
g) Surgical Feasibility: the prosthesis should be easy to implant, requiring minimally invasive procedures and preserving ligamentous structures.
h) Ease of Revision: in the event of damage or functional failure, the prosthesis should be easily replaceable, with minimal bone loss during removal.
i) Preservation of Biomechanical Integrity: the prosthesis should not compromise the overall mechanical behavior of the pelvis-femur system. The implant assembly (stem, head and cup) is significantly stiffer than the natural joint, potentially transmitting harmful impulsive loads.
j) Favorable Stress Distribution in Bone: the implant should promote physiological bone remodeling, particularly in the femur, avoiding stress shielding, bone resorption or abnormal growth.

2.3. Cases of damage

Forces 3.3 to 4.3 times the human body weight have been measured in prosthetics applied to subjects during normal walking or running: these forces are applied approximately 700 times for every kilometer traveled. Even during a sedentary lifestyle, body weight is loaded onto each leg 5,000 to 10,000 times a day, or more than 1,000,000 times a year. These conditions, given the resistant cross-sections of the implants, can cause fatigue, so the prostheses in question must be designed and manufactured with these conditions in mind.
In Italy, e.g., over 200,000 hip and knee replacements are currently installed each year; in the United States, e.g., over 400,000 hip replacements are reported, but approximately 10% of implant failures are reported, mostly not due to prosthesis fractures, but rather to loosening, infection, dislocation or patient-specific factors. Table 2 shows hip replacement surgeries in Italy (divided into total, partial, and revision replacements), data taken from the Hospital Discharge Form (HDF) for the period 2001-2010.

Table 2. *Hip replacement surgery in Italy between 2001 and 2010*

	2001	2002	2003	2004	2005	% (#)
total replacement	45.656	48.672	51.241	54.349	55.516	3,0
partial replacement	20.732	21.331	20.981	21.627	22.380	1,6
replacement review	5.969	6.451	6.494	6.683	6.913	2,3
Total	72.357	76454	78.716	82.659	84.809	2,6
	2006	2007	2008	2009	2010	
total replacement	57.521	58.555	58.679	59.397	595.631	3,0
partial replacement	22.386	22.289	23.034	22.506	23.916	1,6
replacement review	7.170	7.229	7.164	7.264	7.342	2,3
Total	87.077	88.073	88.877	89.167	90.889	2,6
(#) average annual increase						

Modern hip and knee replacements, as statistically reported [3], are expected to function for 10 to 20 years in 90% of patients. The following cases concern prosthesis failures reported in the literature and news reports in recent years.
The main causes of hip prosthesis revisions in recent years is highlighted in Table 3, which generally represents the causes of hip replacement revisions in the period considered.

Table 3. *Main Causes of Hip Prosthesis Revisions in Recent Years*

Period / Source	Aseptic Loosening	Infection (PJI)	Periprosthetic Fracture	Instability / Dislocation	Wear / Osteolysis	Other Causes (e.g., metal reaction, debris)
Italy (2001–2015, Ministry of Health) [4]	8.3%	10.5%	not reported	"Mechanical failure" 31.5% (includes instability)	included in mechanical failure	–
Single Center (2011–2020, 803 revisions) [5]	66.6%	11.0%	5.5%	3.5%	6.0%	Increasing osteolysis, acetabular wear, instability
USA Center (2001–2015, 3450 cases) [6] and [7]	~80% (loose) / ~19% of total revisions septic	~19.2% septic revisions	not specified	included in other categories	wear decreasing; infection rising	local tissue reactions ~7%
Regional Center (2015–2020, 189 patients) [8]	52%	17%	18%	12%	not separated	–
UK (NJR report, up to 2021) [9] and [10]	~9,962 cases (~21% of revisions)	~6,159 (~15%)	~6,355 (~22%)	~7,028 (~22%)	wear/debris ~5,991 (~21%)	includes metal debris/tissue reaction, pain

Figure 2 shows, e.g., a hip prosthesis stem failure, with the following causes reported: failure, incorrect initial implant and material errors.
Several other cases of hip prosthesis failure were reported between 2006 and 2009, specifically following failure of the prosthetic neck; these cases required identifying the causes of the prosthetic failure, which were hypothesized to be defects in construction, materials used, and structural typology, whether or not compliant with guidelines. Among the various failures reported in the news, one example is the "breakage of the prosthetic neck of the left hip" while the patient was walking, an event attributed to a manufacturing defect in the prosthesis: according to the opinion of the relevant technical expert, in fact, the breakage of the prosthetic neck, which occurred approximately three years after installation, was not attributable to errors in surgical technique, but rather to a manufacturing defect and wear of the material used [11].

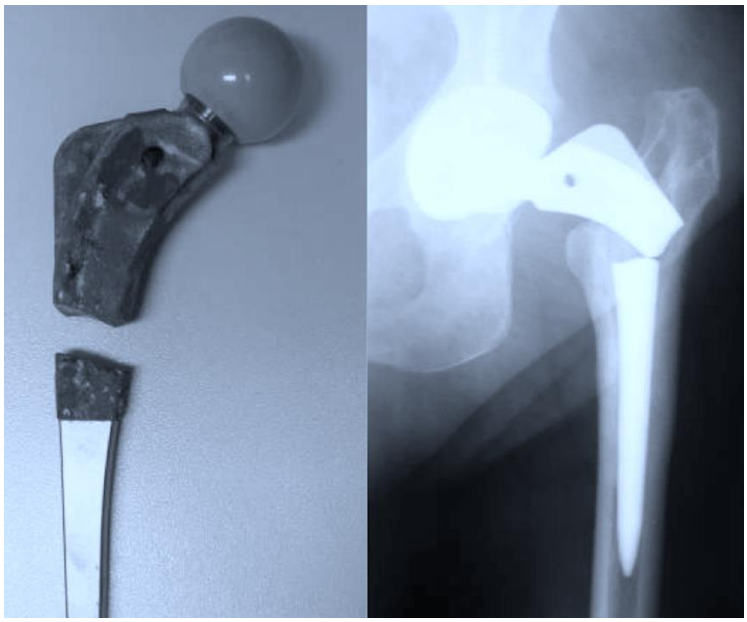


Figure 2. *An example of hip replacement stem fracture.*

The ruling of the Court of Ravenna, Italy, dated 20/03/2017 relating to the civil case of First Instance registered under no. R.G. 2453/2013, similarly concerns the breakage of the prosthetic neck approximately 18 months after installation, likely due to a manipulation event or a hypothetical accidental fall of the prosthesis during the phases represented by packaging, sterilization, transport, storage or handling before surgery, such as to originate a micro-irregularity on the surface that then led to the fatigue failure of the prosthesis itself ([12] and [13]).

Warnings of a high risk of fracture of the prosthetic neck (stem) have been issued, as reported in [14], regarding couplings of prosthetic stems with femoral heads having certain femoral neck lengths, since the requirements regarding implant loads foreseen by the ISO 7206-6:2013-11 [15] standard are not met. The risk of breakage is higher the longer the prosthetic neck used.

An analysis of six cases of femoral neck fracture in Ti6Al4V alloy is reported in [16], where the conditions for the formation of superficial cracks after long-term dynamic fatigue are mentioned. Another research published in 2010 concerns the database of the Federal Drug Administration Manufacturer and User Facility Device Experience (FDA MAUDE) from 01/01/2000 to 19/05/2009, where 37 cases of femoral neck prosthesis fracture were traced. Among these, one case in particular was described, for which corrosion fatigue phenomena were given as reasons [17]. The case described in publication [18] instead concerns the fracture of the neck of the femoral component of a total hip prosthesis in Ti6Al4V alloy in a 64-year-old patient. The reported cause of the fracture is material fatigue.

Other cases of fracture of the femoral component of hip prosthesis are reported in [19], [20], [21], [22] and [23], while other types of prosthesis failure are reported in the literature as follows.

Failures - static fractures - have been reported, for example, in the ceramic part (fragmentation due to fragility and the presence of very heavy loads, such as those caused by tripping, which increase the load) [2]. Fracture of the ceramic femoral head has been reported, in particular, in [24] (where it is reported that this type of fracture is statistically found in the range 0.8÷1.7% of ceramic/ceramic implants).

Among the causes of hip prosthesis failure highlighted in [2], long-term structural fatigue failure of the acetabular component is mentioned, which is of modest size and has a small arm, therefore the flexion determined by the acetabulum is very limited. Especially due to pressure loads, crash failure can occur in the case of ceramic heads or ceramic-ceramic couplings, where static failures due to the acetabular component appear, leading to the onset of creaking of the prosthesis.

3. Feasibility analysis and selected characterization techniques

3.1. Description of the considered femoral stem

This is a primary implant femoral stem used in hip reconstruction surgeries, in combination with a femoral head and an acetabular cup (or a dual-mobility cup). It is indicated in cases of advanced joint degeneration, primarily due to primary coxarthrosis or post-traumatic degenerative conditions. The device is implanted without the use of bone cement. Key features include:

- Femoral neck angle (CCD – Centrum-Collum-Diaphyseal angle): 131°
- Taper: 12/14
- Length: 160 mm
- Offset: 41.3 mm
- Reduced-diameter neck to allow a greater human Range of Motion (ROM): 11 mm
- Rough microstructured surface
- Tapered distal end to prevent localized contact points.

The implant is made from a forged titanium-aluminum-niobium alloy (Ti6Al7Nb, ISO 5832-11), which is free of ferromagnetic materials. The surface finish consists of a rough microstructured texture achieved through corundum blasting.

3.2. Visual analyses and preliminary failure interpretation

Figures 3 and 4 show the fractured prosthesis following the failure.



Figure 3. *The fractured prosthesis following the failure.*

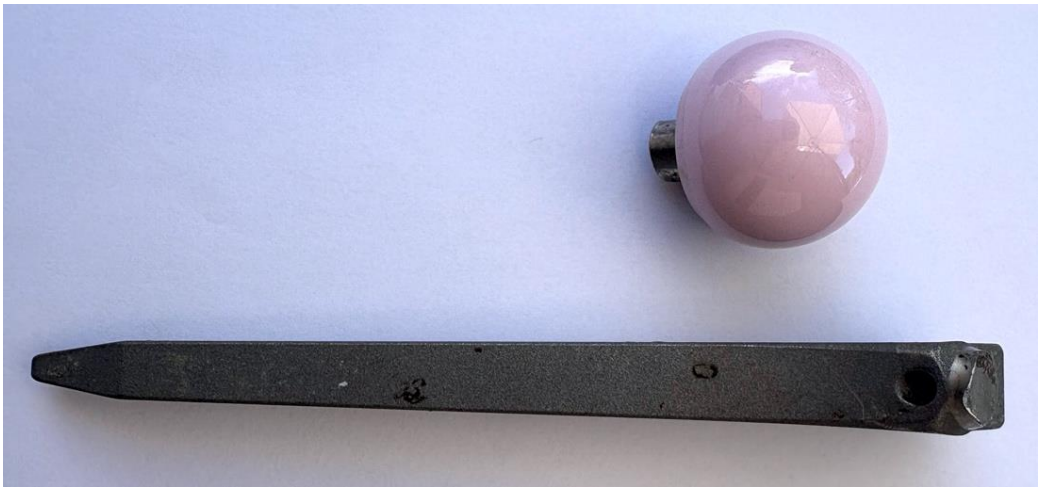


Figure 4. *The fractured prosthesis following the failure.*

Figures 5 to 8 refer to the fracture surface at the neck region of the femoral component, associated with the main body of the femoral stem.

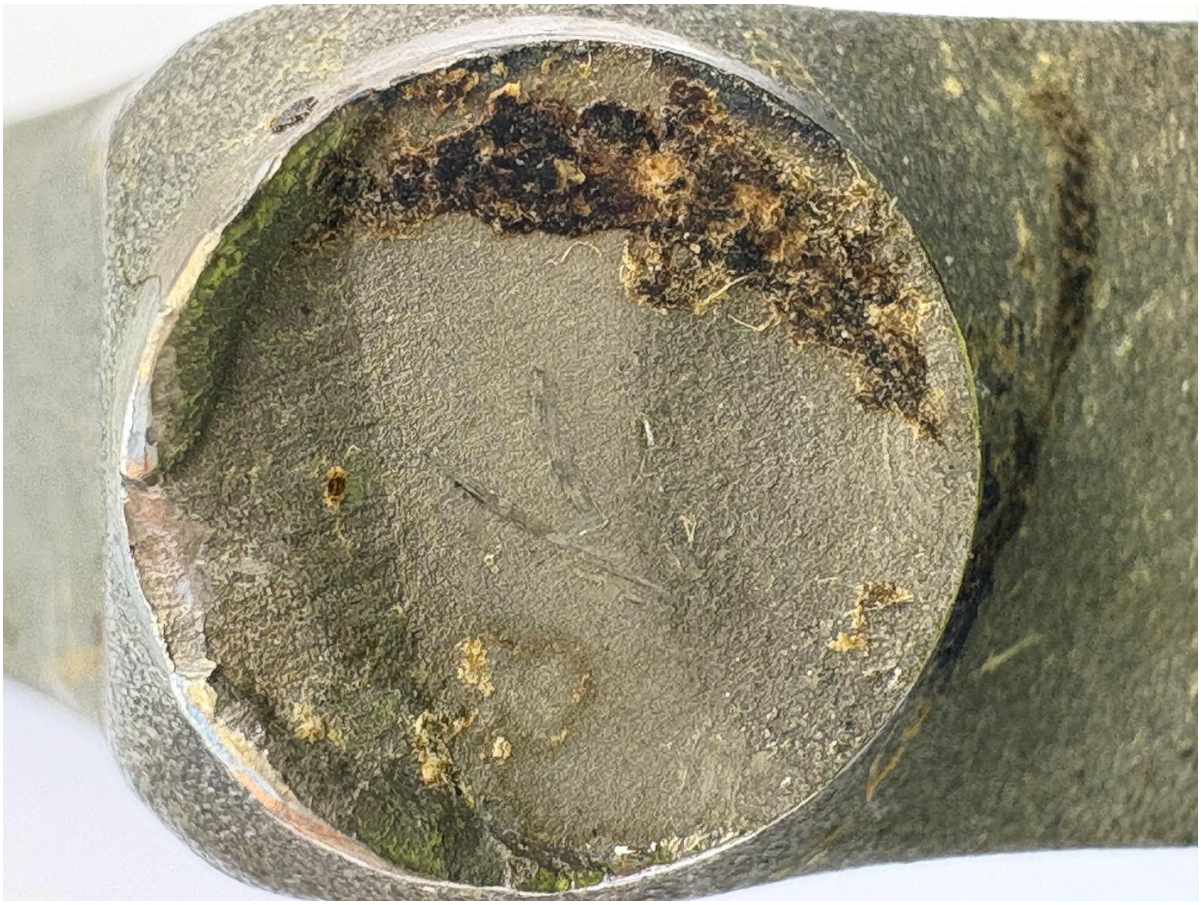


Figure 5. *Fracture surface of the neck of the femoral component, belonging to the femoral stem.*



Figure 6. *Fracture surface of the neck of the femoral component, belonging to the femoral stem.*

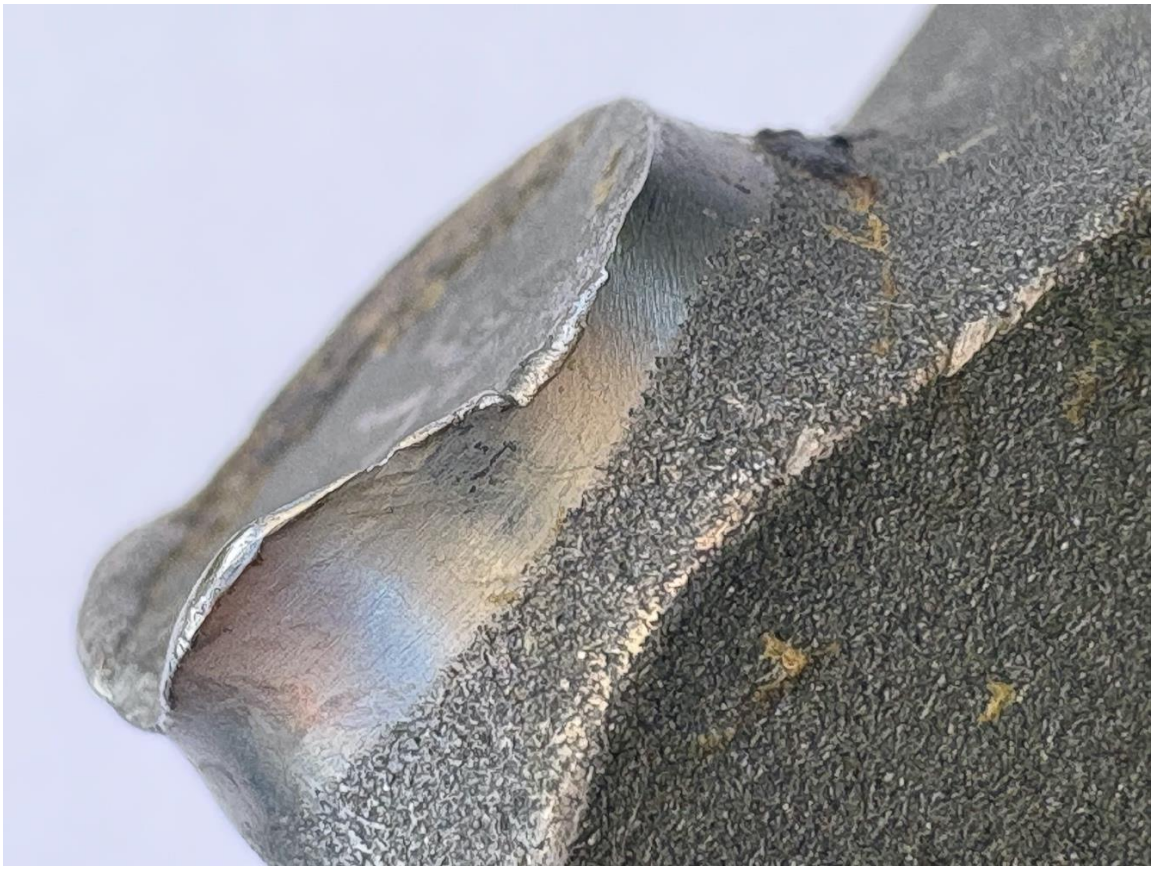


Figure 7. *Fracture surface of the neck of the femoral component, belonging to the femoral stem.*



Figure 8. *Fracture surface of the neck of the femoral component, belonging to the femoral stem.*

Figures 9 to 11 refer to the fracture surface at the neck region of the femoral component, belonging to the upper end of the femoral stem connected to the femoral head.



Figure 9. *Upper end of the femoral stem fixed in the ceramic insert (femoral head): the fracture surface is highlighted.*

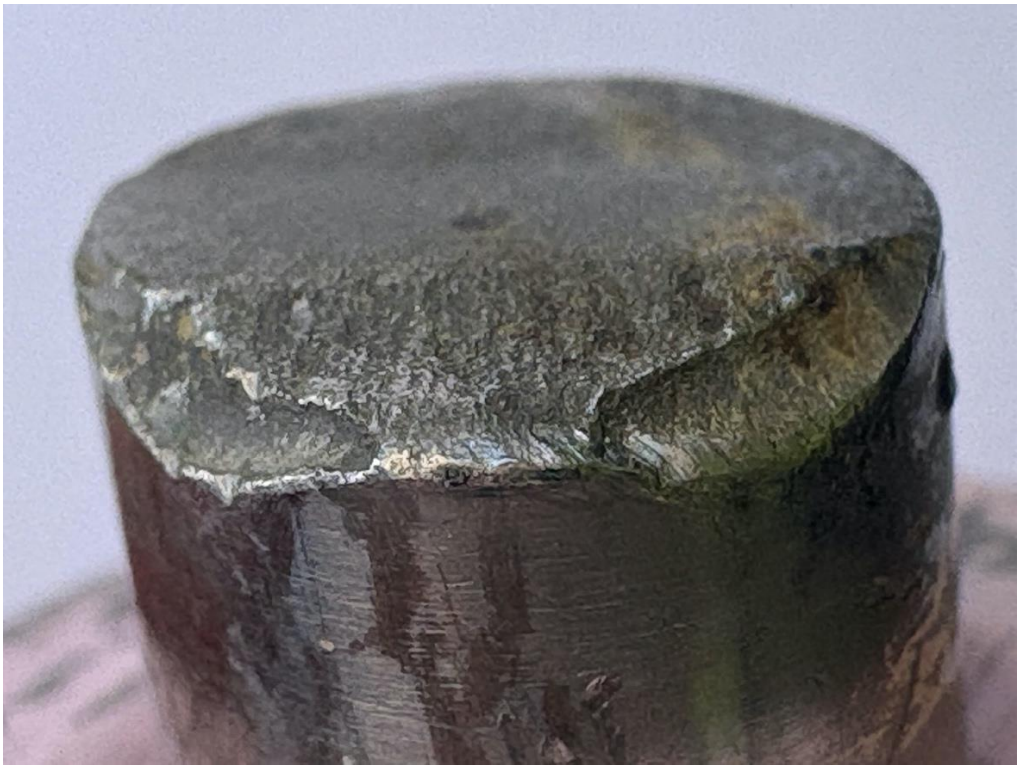


Figure 10. *Upper end of the femoral stem fixed in the ceramic insert (femoral head): the fracture surface is highlighted.*



Figure 11. *Upper end of the femoral stem fixed in the ceramic insert (femoral head): lateral view.*

The fracture surface of the retrieved femoral stem, illustrated in Figures 5 and 6, reveals macroscopic and microscopic features consistent with fatigue failure in a ductile metallic alloy, specifically Ti6Al7Nb. The overall morphology delineates three distinct zones: crack initiation, progressive propagation, and final catastrophic failure. These characteristics are typical of high-cycle fatigue mechanisms occurring under subcritical stress conditions.

A notable feature is the dark, crescent-shaped (lunette-like) region located near the periphery of the fracture surface. Its curvilinear geometry and marginal position suggest it served as the fatigue crack initiation site. This conclusion is further supported by the darker coloration and evidence of surface oxidation and corrosion products, which are indicative of prolonged exposure to the physiological environment prior to ultimate failure. Such features are consistent with slow, progressive crack advancement rather than sudden overload.

The inclined fracture plane, oriented at approximately 45° relative to the axis of the component (see Figures 6 and 7), is indicative of ductile overload. This region lacks oxidation and presents a brighter, more granular appearance, suggesting it corresponds to the final fracture event that occurred once the remaining cross-sectional area was insufficient to support the applied loads. This is a classic manifestation of shear failure following the degradation of structural integrity due to fatigue propagation.

Further evidence of fatigue failure is provided by the opposing fracture surface (Figures 9 and 10), which exhibits a smooth zone with visible fatigue striations. This observation confirms the presence of a fatigue mechanism operating over an extended period prior to failure.

It is important to emphasize that, based on clinical records and the mechanical loading history reconstructed from patient activity, the applied loads were within the expected range for which the prosthesis was designed. No evidence suggests abnormal use or overload due to patient behavior. Therefore, the failure cannot be attributed to negligence or inappropriate mechanical loading on the part of the patient.

Given these findings, the origin of the fracture should be investigated from a materials science and engineering perspective. A detailed metallurgical examination is warranted to assess the presence of intrinsic microstructural anomalies, such as inclusions, porosity, grain boundary defects, or processing-induced discontinuities. Such features may act as local stress concentrators and initiate premature crack nucleation. The role of surface treatments, manufacturing processes, and design geometry should also be evaluated to determine their potential contribution to the failure.

In conclusion, the fractographic evidence supports a failure mechanism driven by high-cycle fatigue in a ductile alloy, exacerbated by localized defects or material heterogeneities rather than patient-related mechanical overload. The case highlights the critical importance of comprehensive failure analysis to identify the root cause and to inform future improvements in implant design and material processing.

3.3. Ti6Al7Nb alloy

The Ti6Al7Nb alloy - specifications: ISO5832/11 (ref. published standard valid at the time of installation of the femoral stem in question [25]); ASTM F1295; UNS R56700 - is one of the new generation implant materials with regard to the replacement of vanadium with niobium in its chemical composition, due to the presumed cytotoxicity of vanadium in the human body [26]. Thanks to this modified composition, this alloy is characterized by a more advantageous set of mechanical properties [27] and by higher corrosion resistance and biotolerance compared to the commonly used Ti6Al4V alloy ([28] and [29]). The main uses are in endoprostheses (hip, knee, shoulder, osteosynthesis), bone screws, bone plates, nails, spinal systems and oral implants [30], as well as applications in the dental [31] and aeronautical sectors. The compositional limits of this alloy are reported in Table 4.

Table 4. *Composition limits of the Ti6Al7Nb alloy according to ISO 5832-11 [32]*

Element	Maximum Composition Limit (% by weight)
Ti	balance
Al	5.5 - 6.5
Nb	6.5 – 7.5
Fe	≤ 0.25
O	≤ 0.20
C	≤ 0.08
N	≤ 0.05
H	≤ 0.009
Ta (optional)	≤ 0.50
Other elements (each)	≤ 0.10
Other elements (total)	≤ 0.40

It is, in particular, an α-β Ti alloy with excellent biocompatibility and high strength, made of a hexagonal α-phase, stabilized with Al, and a regular central body β-phase, stabilized with Nb. Its mechanical properties depend significantly on the morphology and volume fractions of these phases, which in turn are determined by manufacturing process parameters ([32] and [33]). A combination of mechanical properties such as plasticity and toughness with significant strength, as well as hardness and elasticity, therefore, is essential for components made using Ti6Al7Nb alloy. These properties depend not only on the composition and size of the initial powder particles, but also on the design of the internal structure and the presence of defects in the final product determined by process parameters and manufacturing strategy [34]. The most important microstructural parameter determining the mechanical properties is the α-colony size. By decreasing this dimension, the yield strength, the ductility, the resistance to crack nucleation (HCF resistance) and the resistance to micro-cracks propagation are improved - determining, together with the resistance to crack nucleation, the resistance to slow cycle fatigue (LCF or low cycle fatigue) -; in parallel, only for the resistance to macro-cracks propagation and including the fracture resistance, a high size of the α colony (which

corresponds to a high crack front roughness) is desirable [32]. Table 5 summarizes the main mechanical properties.

Table 5. *Main mechanical properties of the Ti6Al7Nb alloy*

Parameters	*Min. value*	*Max.value*	*Unit of measurement*
Density	4.51	4.53	g/cm^3
Hardness	2700	2900	MPa
Melting point	1800	1860	K
Latent heat of fusion	360	370	kJ/kg
Specific heat	540	560	J/kg°K
Elastic limit	895	905	MPa

Niobium, which belongs to the same group as vanadium in the periodic table, acts as a stabilizing α-β element (similar to the vanadium alloy Ti6AL4V), but the strength of the Nb alloy is slightly lower than that of the Ti6AL4V alloy. The main difference between Ti6Al7Nb and Ti6AL4V is related to several factors such as solid solution strengthening, structural refinement provided by the refined two-phase structure, and the difference in microstructure between the two alloys.

This alloy is normally fabricated by conventional ingot metallurgy, forging bulk material. Powder metallurgy techniques [35], moreover, can be used to achieve specific properties: by changing processing parameters such as sintering temperature, it is possible to vary the level of porosity and customize the final properties. The most common powder metallurgy methods are hot pressing, metal injection forming, and mixing and pressing. In the production of Ti6Al7Nb, a sintering temperature in the range of 900÷1400 °C is commonly used. Altering the sintering temperature imparts different properties, such as different porosity and microstructures, as well as a different composition of the α, β, and α+β phases. In recent years, processes for producing this alloy have been considered using various 3D printing techniques such as selective laser melting and electron beam melting [26].

Heat treatments can influence the microstructure, improving characteristics such as ductility, machinability, and structural stability based on the differences in microstructures and cooling rates between the α and β phases [36]. The cooling rate also impacts the morphology. The size of the α colony is the most important microstructural property due to its influence on the fatigue properties and deformation mechanics of the transformed α+β alloys.

3.4. Spectroscopic techniques and estimation of possible obtainable results

The chemical composition (in weight %) of the damaged femoral stem under examination can be determined by spectroscopy methods, in order to help verify the elemental content (which can be done in conjunction with other techniques considered here) and whether this content is in accordance with the ISO 5832-11 standard valid at the time of installation of the considered femoral stem [25]. This standard provides the characteristics of the corresponding test methods for the wrought titanium alloy known as titanium6-aluminium7-niobium alloy (titanium6-Al7-Nb) for use in the manufacture of surgical implants; published in 1994, it was improved in its new edition in 2014 [37].

Scanning Electron Microscopy (SEM) ([38], [39] and [40]) enables high-resolution observation of material samples, offering magnification and resolution up to 1000 times greater than traditional optical microscopy, due to the much shorter wavelength of electrons compared to photons. The technique involves generating a high-energy electron beam in a vacuum, which is focused and deflected to scan selected areas of the sample. As the beam interacts with the sample, it generates various signals - such as secondary electrons, backscattered electrons and X-rays - that are detected

and processed to form grayscale images. The penetration depth of the electron beam depends on the atomic number of the material: it is greater in lighter elements and shallower in heavier ones. The intensity of backscattered electrons, consequently, correlates with the material’s density and hardness. SEM systems are often equipped with Energy Dispersive X-ray Spectroscopy (EDS or EDX) detectors, which allow for non-destructive microchemical analysis by capturing characteristic X-rays emitted from the sample when bombarded by electrons. A combined SEM–EDX setup typically includes a scanning electron microscope and a silicon-lithium (Si(Li)) detector cooled with liquid nitrogen (77 °K). This configuration enables simultaneous morphological and compositional characterization, including elemental mapping, concentration profiling, and quantitative chemical analysis. In this context, SEM can be applied to fracture surface analysis, particularly to investigate crack initiation and propagation areas using secondary and backscattered electron imaging. EDX microanalysis (also known as EDAX) can be used to assess the local surface chemical composition.

Fractography is a technique used to examine fracture surfaces at high magnification, typically with optical or electron microscopy, to assess surface morphology and determine the fracture mechanism. The main fracture types include brittle, ductile, fatigue, and creep. Brittle fracture typically proceeds in three stages: dislocation accumulation during plastic deformation; formation of microcracks at regions of high dislocation density; microcrack propagation, which may be intergranular (along grain boundaries) or intragranular (along specific crystallographic planes known as cleavage planes).

In ductile fracture, the sequence involves nucleation of microvoids, microvoid coalescence (often oriented at 90°) and final fracture along a 45° shear plane due to material strain hardening.

Fractographic analysis begins with a preliminary inspection using a stereomicroscope to evaluate macroscopic features such as plastic deformation or faceted surfaces typical of brittle fracture. This is followed by scanning electron microscopy (SEM) to observe surface morphology in greater detail. In such analysis, secondary electrons are used for topographic imaging, as backscattered electrons are less suited for morphological assessment. SEM images can reveal features like cleavage planes, providing further insight into brittle fracture mechanisms.

Particle-induced X-ray emission (PIXE) is a spectrometric technique applicable as a non-destructive analysis of the constituent elements of objects and samples. Bombardment of the target with high-energy ions, usually protons with energies in the MeV range, creates ionizations of the internal structure. Outer structure electrons descend and fill vacancies in the internal structure. When an internal vacancy is filled, an X-ray photon of characteristic energy for the target atom is emitted [41]. An energy-dispersive detector is then applied to measure the emitted characteristic X-rays, the X-ray spectrum is analyzed off-line, and the characteristic X-ray intensities are converted to elemental concentrations ([42] and [43]). The corresponding instrumentation chosen for the possible analysis campaign of the considered femoral stem is a PIXE facility of a 5MV Van De Graaff accelerator, which consents to determine the elemental composition of the base material in the 10 μm thick layer of the analyzed object. This instrumentation uses a correctly collimated 2.5 MeV proton beam, and the window-target distance for the measurements is selectable; a distance of 10 mm, for example, corresponds to a beam diameter of approximately 1.5 mm. Sensitivity ranges from 50 to 1000 ppm, varying depending on the elements and also depending on the matrix composition. Since the proton beam on the target can be small (i.e., in the range 0.8 to 3 mm), even small spots and selected features on the samples can be analyzed. This spectrometric technique can help verifying the content of the constituent elements of the considered femoral stem. The investigation would be carried out at the surface level, providing information complementary to that acquired by other techniques considered here, in order to better verify whether: this content is in accordance with the standard; there are inhomogeneities in the composition (investigating different areas of the sample) between the surface and the internal part of the investigated component (the latter analysis, carried out using PGAA, see par. 3.5), such inhomogeneities being indicative of possible problems related to internal stresses in the examined material, potentially co-responsible for the failure event.

In particular, the fracture surface of the femoral stem highlighted in Figures 5 and 6 (which, as already mentioned, exhibits a dark, crescent-shaped spot) should be considered here for an in-depth analysis

in relation to the fracture surface belonging to the upper end of the femoral shaft connected to the femoral head (Figures 9 and 10).

3.5. Neutron techniques and estimation of possible obtainable results

In recent years, neutron techniques have increasingly provided a valuable contribution to the solution of industrial problems ([44], [45] and [46]). Neutrons are elementary particles, essentially devoid of electrical charges, which together with protons constitute the atomic nucleus. The characteristic of not interacting electrically with electrons and nuclei in matter has the advantage of being able to penetrate materials in depth. While X-rays offer excellent resolution, but are easily absorbed by matter (only managing to penetrate superficial layers), neutrons, having a linear absorption coefficient approximately 1000 times weaker than the former, penetrate up to several centimetres (approximately 1-2 cm for steel, approximately 5-6 cm for aluminium and its alloys). Neutrons are created by continuous sources (nuclear reactors) or by pulsed sources (accelerators). In continuous sources, they are produced by the fission reaction of heavy nuclei such as 235U or 239Pu and are initially characterized by very high energy; they are subsequently slowed to thermal energies by moderators, then subjected to collisions that slow them further to bring them into thermal equilibrium with the surrounding medium. Finally, special guide tubes are used to transfer the neutrons produced from within the core to the various instruments (e.g., diffractometers and spectrometers).

The Rogante Engineering Office has developed specific methodological approaches and data processing procedures for the industrial applications of neutron techniques, aimed at obtaining information on relevant parameters responsible of material’s performance.

Neutron diffraction (ND) is a non-invasive technique used for qualitative and quantitative analysis of phase composition and structural properties of materials on a macroscopic and atomic scale. It allows the study of dynamic behavior, crystallographic texture, and internal residual stresses (RS), which are stress states within materials not caused by external loads but by processes such as manufacturing or thermal treatments. ND can probe several millimeters beneath the surface, enabling 3D mapping of RS - unlike X-ray diffraction, which only reaches a few microns. RS analysis is critical for improving production, quality, safety, and understanding phase transformations. ND employs high-resolution time-of-flight (TOF) diffractometers using thermal neutron beams and velocity selectors. The TOF-ND technique provides detailed insights into structure, phase, texture, and internal variations across samples, all without damaging them. It is especially useful in evaluating crystallographic texture evolution and detecting sample inhomogeneities compared to reference materials. This technique has already been used to verify the evolution of the crystallographic texture of titanium alloys following heat treatment ([47] and [48]), and it is suggested to investigate the considered femoral component.

Prompt Gamma Activation Analysis (PGAA) is an innovative, non-destructive technique for determining the elemental composition of materials, including both major and trace elements. Unlike conventional analytical methods (e.g., XRF, INAA, ICP-MS), which are often destructive and surface-limited, PGAA enables volumetric analysis without damaging the sample. Using a low-intensity neutron beam, it induces gamma radiation from the sample’s nuclei, allowing detection of multiple elements simultaneously with varying sensitivities. PGAA requires no sample preparation and can analyze entire objects or specific parts. Thanks to the high neutron penetration and minimal background noise, it provides an average internal composition, making it suitable for large or complex samples. Measured concentrations can be normalized to the total mass without external standards, and data can be further analyzed (e.g., via Principal Component Analysis) to detect similarities or differences between samples ([49] and [50]). PGAA is particularly useful for verifying the composition of industrial components - such as the considered femoral stem - ensuring conformity with standards (e.g., [37]) and detecting any inhomogeneities.

3.6. Additional techniques

Hardness tests (e.g., Vickers HV1) can be performed to verify whether the hardness values are in line with those expected for the alloy type.

4. Discussion and conclusions

This feasibility study addressed the fracture of a Ti6Al7Nb alloy femoral stem at the proximal neck region, occurring 15 months after total hip arthroplasty. The fracture surface analysis, supported by macroscopic and microscopic observations, clearly points to a fatigue-driven failure mechanism, marked by typical signs of crack initiation, progressive propagation and final ductile overload. The goal of this study was to investigate the cause of failure and also to propose a methodological framework for analyzing similar cases of orthopedic implant failures.

Visual and microscopic inspection of the fracture surface revealed hallmark features of high-cycle fatigue in ductile metals, such as a crescent-shaped initiation zone, fatigue striations and a final rupture zone with a 45° inclined fracture plane. The fatigue origin was located at the outer edge of the prosthetic neck, where oxidation and corrosion products were present, suggesting prolonged in vivo crack propagation under physiological conditions.

The mechanical loading history, reconstructed from clinical documentation and patient activity, did not show evidence of excessive or abnormal stress. It is reasonable to conclude, hence, that the implant operated within its expected mechanical limits and the failure cannot be attributed to patient misuse.

Attention must therefore turn to potential material and design-related contributors. The implant, manufactured from a forged Ti6Al7Nb alloy with a rough, microstructured surface finish, is designed to provide enhanced biocompatibility and mechanical integrity. Nonetheless, the possibility of intrinsic microstructural defects (e.g., inclusions, porosity, or segregation), manufacturing-induced surface anomalies, or geometric stress risers warrants further investigation.

To this end, a comprehensive suite of analytical techniques was identified, including SEM, EDX, fractography, PIXE, neutron diffraction and PGAA. These methods were selected to ensure a multi-scale and complementary approach capable of evaluating both surface and subsurface features of the alloy.

The review of state-of-the-art literature confirmed that fractures in hip prosthetic components, though relatively rare, have been documented in various clinical and engineering contexts. The analysis conducted in this study supports the hypothesis that such failures may stem from complex interactions between material properties, manufacturing processes and implant design geometry, rather than from patient-induced overload.

Among the various techniques considered, neutron-based methods have emerged as particularly valuable due to their non-destructive nature and capacity to probe larger volumes of material. These techniques enable the detection of bulk defects, internal stresses and degradation phenomena that might remain hidden to surface-sensitive or destructive methods like SEM, TEM, or X-ray analysis.

Neutron techniques complement traditional methodologies by offering statistically robust data, as the measurements average over a larger material volume. This makes them especially suited for detecting subtle yet critical anomalies - such as internal microstructural inconsistencies or stress gradients - that could initiate or accelerate fatigue damage in service.

The analytical strategies and findings presented here offer a framework for future investigations into implant failures involving Ti6Al7Nb alloys or similar materials. These methodologies can be adapted to assess components used in various clinical scenarios, especially where long-term mechanical integrity and material performance are of critical concern.

In conclusion, the fracture of the Ti6Al7Nb femoral stem in this case was primarily driven by fatigue-related degradation mechanisms, not by overload or user-related factors. The evidence indicates that intrinsic material imperfections or process-related defects played a pivotal role in crack initiation and propagation.

The proposed analytical framework - combining conventional surface analysis with advanced, non-destructive neutron techniques - provides a robust, interdisciplinary approach to understanding the root causes of such failures. The insights gained from this case study can inform future design improvements, material selection criteria and quality control processes, thereby enhancing the longevity and reliability of orthopedic implants.

This work lays the groundwork for a standardized diagnostic protocol for implant failure analysis, offering valuable reference points for both clinical and materials science communities in the ongoing pursuit of safer, more durable biomedical devices.

References

[1] Park, J., Lakes, R.S., 2010. Biomaterials: An Introduction, Third Edition, Springer, New York

[2] R. Guagnano, Protesi d'anca, Biomedicahelp, Report, http://www.biomedicahelp.altervista.org/Magistrale/Biomechanics/BBB_PrimoAnno/Endoprotesi/Endoprotesi_AppuntiProtesiGinocchio.docx (accessed 21 July 2025).

[3] Il fallimento di una protesi articolare: la chirurgia di revisione - quando ne ho bisogno?, Report, Ortopedia Traumatologia Borgotaro, 2017 https://ortopediaborgotaro.it/otb-news-per-il-paziente-ortopedia-borgotaro/164-il-fallimento-di-una-protesi-articolare-la-chirurgia-di-revisione-quando-ne-ho-bisogno (accessed 21 July 2025).

[4] Longo, U.G., Papalia, R., Salvatore, G., Tecce, S.M., Jedrzejczak, A., Marcozzi, M., Piergentili, I., Denaro, V., 2022. Epidemiology of revision hip replacement in Italy: a 15-year study (2001–2015)**.** BMC Surgery, 22, 355.

[5] Feng, X.**,** Gu, J.**,** Zhou, Y., 2022. Primary total hip arthroplasty failure: aseptic loosening remains the most common cause of revision - a retrospective review of 803 cases from 2011 to 2020. American Journal of Translational Research, 14(10), 7080-7089.

[6] Bozic, K.J., Kurtz, S.M., Lau, E., Ong, K., Vail, T.P., Berry, D.J., 2009. The epidemiology of revision total hip arthroplasty in the United States**.** Journal of Bone and Joint Surgery – American Volume, 91(1), 128–133.

[7] Jafari, M.S., Coyle, C., Mortazavi, J.S.M., Sharkey, P.F., Parvizi, J., (2010). Revision hip arthroplasty: Infection is the most common cause of failure. Clinical Orthopaedics and Related Research, 468(8), 2046-2051.

[8] RIPO – Registro dell’Impiantologia Protesica Ortopedica Emilia-Romagna, 2024. Trends and failure causes of THA in a cohort of 142,113 patients (2000-2020). MDPI Prosthesis, 6(6), 96.

[9] Lenguerrand, E., Whitehouse, M.R., Beswick, A.D., Jones, S.A., Porter, M.L., Blom, A.W., 2017. Revision for prosthetic joint infection following hip arthroplasty: evidence from the National Joint Registry**.** Bone & Joint Research, 6(6), 391–398.

[10] National Joint Registry (NJR), 2021. 18th Annual Report – Hip, Knee, Ankle, Elbow and Shoulder Arthroplasty. https://reports.njrcentre.org.uk/ (accessed 21 July 2025).

[11] Zanin, R., 2013. Si rompe la protesi: causa da 130 mila €. Tribuna di Treviso, 02 Ottobre 2013. https://www.tribunatreviso.it/cronaca/si-rompe-la-protesi-causa-da-130-mila-o5vuqoo5 (accessed 21 July 2025).

[12] Responsabilità Medica, 2017. L’ospedale risponde anche per il difetto della protesi impiantata. https://www.rivistaresponsabilitamedica.it/lospedale-risponde-anche-difetto-della-protesi-impiantata/ (accessed 21 July 2025).

[13] Tribunale di Ravenna, 2017. Sentenza, 20/03/2017. https://www.rivistaresponsabilitamedica.it/wp-content/uploads/2017/06/Trib.-Ravenna-7-marzo-2017-gu-Vicini.pdf (accessed 21 July 2025).

[14] AAP implantate AG, 2015. Informativa urgente sulla sicurezza relative allo stelo retto SM. http://www.salute.gov.it/imgs/C_17_AvvisiSicurezza_6340_files_itemFiles_0_azione_itemAzione_0_fileAzione.pdf (accessed 21 July 2025).

[15] ISO, 2013. ISO 7206-6:2013 – Implants for surgery – Partial and total hip joint prostheses — Part 6: Endurance properties testing and performance requirements of neck region of stemmed femoral components, International Organization for Standardization, Geneva.

[16] Fokter, S.K., Rudolf, R., Moličnik, A., 2016. Titanium alloy femoral neck fracture - clinical and metallurgical analysis in 6 cases. Acta Orthopaedica, 86, 197-202.

[17] Dangles, C.J., Altstetter, C.J., 2010. Failure of the modular neck in a total hip arthroplasty. J. Arthroplasty, 25(7), 1169.E5-1169.E7.

[18] Grivas, T.B., Savvidou, O.D., Psarakis, S.A., Bernard, P.F., Triantafyllopoulos, G., Kovanis, I., Alexandropoulos, P., 2007. Neck fracture of a cementless forged titanium alloy femoral stem following total hip arthroplasty: a case report and review of the literature. Journal of Medical Case Reports, 1(174).

[19] Morgan-Hough, C.V., Tavakkolizadeh, A., Purkayastha, S., 2004. Fatigue failure of the femoral component of a cementless total hip arthroplasty. Journal of Arthroplasty, 19, 658–660.

[20] Gilbert, J.L., Buckley, C.A., Jacobs, J.J., Bertin, K.C., Zernich, M.R., 1994. Intergranular corrosion-fatigue failure of cobalt-alloy femoral stems. A failure analysis of two implants. Journal of Bone and Joint Surgery, 76A, 110–115.

[21] Burstein, A.H., Wright, T.M., 1985. Neck fractures of femoral prostheses. Journal of Bone and Joint Surgery, 67A, 497.

[22] Rand, J.A., Chao, E.Y., 1987. Femoral implant neck fracture following total hip arthroplasty: a report of three cases. Clinical Orthopaedics and Related Research, 221, 255–259.

[23] Vatani, N., Comando, D., Acune, J., Prieto, D., Caviglia, H., 2002. Faulty design increases the risk of neck fracture in hip prosthesis. Acta Orthopaedica Scandinavica, 73, 513–517.

[24] Rambaldi, R., 2011. Un affare medico-legale da 6.000.000 di euro: case report di una revisione protesica. Acta Orthopedica Italica, 35, 143–146.

[25] ISO, 1994. ISO 5832-11:1994 – Implants for surgery – Metallic materials – Part 11: Wrought titanium 6-aluminium 7-niobium alloy, International Organization for Standardization, Geneva.

[26] Bolzoni, L., Hari Babu, N., Ruiz-Navas, E.M., Gordo, E., 2013. Comparison of microstructure and properties of Ti-6Al-7Nb alloy processed by different powder metallurgy routes. Key Engineering Materials, 551, 161–179.

[27] Liu, X., Chu, P.K., Ding, C., 2004. Surface modification of titanium, titanium alloys, and related materials for biomedical application. Materials Science and Engineering: R, 47, 49–121.

[28] Chlebus, E., Kuźnicka, B., Kurzynowski, T., Dybała, B., 2011. Microstructure and mechanical behaviour of Ti-6Al-7Nb alloy produced by selective laser melting. Materials Characterization, 62, 488–495.

[29] López, M.F., Gutiérrez, A., Jiménez, J.A., 2002. In vitro corrosion behaviour of titanium alloys without vanadium. Electrochimica Acta, 47, 1359–1364.

[30] Fellah, M., Labaïz, M., Assala, O., Dekhil, L., Taleb, A., Rezag, H., Iost, A., 2014. Tribological behavior of Ti-6Al-4V and Ti-6Al-7Nb alloys for total hip prosthesis. Advances in Tribology, 2014, Article ID 451387, 13 pages.

[31] Kobayashi, E., Wang, T.J., Doi, H., Yoneyama, T., Hamanaka, H., 1998. Mechanical properties and corrosion resistance of Ti-6Al-7Nb alloy dental castings. Journal of Materials Science: Materials in Medicine, 9, 567–574.

[32] Lütjering, G., 1998. Influence of processing on microstructure and mechanical properties of (α + β) titanium alloys. Materials Science and Engineering A, 243, 32–45.

[33] Ajeel, S.A., Alzubaydi, T.L., Swadi, A.K., 2007. Influence of heat treatment conditions on microstructure of Ti-6Al-7Nb alloy as used surgical implant materials. Engineering and Technology, 25, 431–442.

[34] Yadroitsev, I., Thivillon, L., Bertrand, Ph., Smurov, I., 2007. Strategy of manufacturing components with designed internal structure by selective laser melting of metallic powder. Applied Surface Science, 254, 980–983.

[35] Rogante, M., 2017. Metallurgia delle polveri per la produzione di componenti. Stampi, Tecniche Nuove Ed., Milano, 8, 58–65.

[36] Sercombe, T., Jones, N., Day, R., Kop, A., 2008. Heat treatment of Ti-6Al-7Nb components produced by selective laser melting. Rapid Prototyping Journal, 14 (5), 300–304.

[37] ISO, 2014. ISO 5832-11:2014 – Implants for surgery – Metallic materials – Part 11: Wrought titanium 6-aluminium 7-niobium alloy. International Organization for Standardization, Geneva.

[38] Smith, K.C.A., Oatley, C.W., 1955. The scanning electron microscope and its fields of application. British Journal of Applied Physics, 6 (11), 391–399.

[39] Goldstein, G.I., Newbury, D.E., Echlin, P., Joy, D.C., Fiori, C., Lifshin, E., 1981. Scanning Electron Microscopy and X-ray Microanalysis. Plenum Press, New York, p. 673.

[40] Rinaldi, R., 1985. Microanalisi·X: recenti sviluppi e aspetti pratici. Rendiconti della Società Italiana di Mineralogia e Petrologia, 40, 241–254.

[41] Johansson, T.B., Akselsson, R., Johansson, S.A.E., 1970. X-ray analysis: elemental trace analysis at the 10^{-12} g level. Nuclear Instruments and Methods, 84, 141–143.

[42] Maenhaut, W., Malmqvist, K.G., 2002. Particle-induced X-ray emission analysis. In: Handbook of X-ray Spectrometry, 2nd ed., U.S.A., 719–810.

[43] Mandò, P.A., Przybyłowicz, W.J., 2009. Particle-Induced X-ray Emission (PIXE). In: Encyclopedia of Analytical Chemistry, John Wiley & Sons, U.S.A., 47.

[44] Rogante, M., 2008. Applicazioni industriale delle tecniche neutroniche. Atti del 1° Workshop Nazionale per l'Industria “Applicazioni Industriale delle Tecniche Neutroniche®”, Civitanova Marche, Italia, 12–14 Giugno 2008, 40–120.

[45] Rogante, M., Rosta, L., 2005. Nanoscale characterisation by SANS and residual stresses determination by neutron diffraction related to materials and components of technological interest. Proc. of SPIE, 5824, Opto-Ireland 2005: Nanotechnology and Nanophotonics, Eds. Blau, W.J., Kennedy, D., Colreavy, J., SPIE, Bellingham, WA, 294–305.

[46] Studio d’Ingegneria Rogante, Italy, Determinazione delle tensioni residue mediante diffrazione neutronica. http://www.roganteengineering.it/pagine_servizi/servizi1.pdf (accessed 21 July 2025).

[47] Bhattacharyya, D., Viswanathan, G.B., Vogel, S.C., Williams, D.J., Venkatesh, V., Fraser, H.L., 2006. A study of the mechanism of α to β phase transformation by tracking texture evolution with temperature in Ti–6Al–4V using neutron diffraction. Scripta Materialia, 54, 231–236.

[48] Lonardelli, I., Gey, N., Wenk, H.R., Humbert, M., Vogel, S.C., Lutterotti, L., 2007. In situ observation of texture evolution during α → β and β → α phase transformations in titanium alloys investigated by neutron diffraction. Acta Materialia, 55, 5718–5727.

[49] Studio d’Ingegneria Rogante, Italy, Prompt Gamma Activation Analysis per l’investigazione di materiali e componenti industriali. http://www.roganteengineering.it/pagine_servizi/servizi3.pdf (accessed 21 July 2025).

[50] Révay, Zs., Belgya, T., Kasztovszky, Zs., Weil, J.L., Molnár, G.L., 2004. Cold neutron PGAA facility at Budapest. Nuclear Instruments and Methods B, 213, 385–388.

Structural and operational dynamics of small-to-medium cast-iron foundries in Italy: a 2025 perspective

Massimo Rogante[1]

1) Rogante Engineering Office, Contrada San Michele 61, 62012 Civitanova Marche, Italy

Corresponding author: main@roganteengineering.it

Review article

Abstract: This paper examines the structural characteristics of a small-to-medium-sized cast iron foundry in Italy, highlighting its evolution, operational phases and technological advancements.
The study initially traces the development of such foundries from the mid-20th century to the present, emphasizing the integration of automation and adherence to modern safety and environmental standards.
A block diagram illustrating the main manufacturing phases is presented, then, providing a visual overview of the production workflow. This is followed by detailed analyses of the key operational departments, with particular emphasis on the automatic moulding process and the combustion systems utilized in the casting department.
The paper concludes with an overview of the foundry's manufacturing capabilities, underscoring its role in the contemporary industrial landscape.

Keywords: *cast iron; foundry operations; automated moulding; industrial processes.*

1. Introduction

The Italian foundry industry has long been a cornerstone of the nation's manufacturing sector, with small-to-medium-sized enterprises (SMEs) playing a pivotal role in producing cast iron components for various applications.
Cast iron foundries have been integral to Italy’s industrial heritage, particularly in regions like the Marches, where artisanal craftsmanship has long coexisted with industrial innovation. These foundries, indeed, have historically been characterized by their adaptability, expertise and integration of traditional techniques with modern technologies. Over the decades, these metalworks have evolved from traditional manual operations to incorporate semi-automated and automated processes, aligning with global trends towards efficiency, precision and sustainability. The transformation of a typical small-to-medium-sized Italian cast iron foundry reflects this broader industrial shift.
In the 1950s, Italian foundries largely relied on manual moulding techniques, with limited mechanization. But the manual moulding was carried out with great skill and concerned in particular large castings. One of the first foundries of the Marches region as well as of the Adriatic area was the “Fonderia Marchigiana”, a cast iron, bronze and aluminum foundry created by Mr. Luigi Ninonà. Figure 1 shows some images of the production process of this foundry at the time. A rare video from 1955, filmed at the original headquarters of this foundry in Civitanova Marche, illustrates the main stages of its production process and is presented in [1]. This foundry served various industrial sectors, from automotive to winemaking, from agriculture to instrumental mechanics and mechanical engineering. Figure 2 shows one of the patents for industrial inventions made within the same foundry. It is a machine equipped with a crumbling and amalgamating apparatus, with oscillating pins, which sifts and mixes the materials constituting the foundry sand with separation of foreign and harmful materials and a mechanical sieve, and which precedes the “sand launcher” machine already on the market at the time [2]. Among the patented industrial inventions developed within the said foundry is also a horizontal casting system for manufacturing rollers used in winemaking equipment. The

innovation enabled accurate centering of the roller pin during the casting process, thereby obviating the need for post-casting alignment corrections [3].

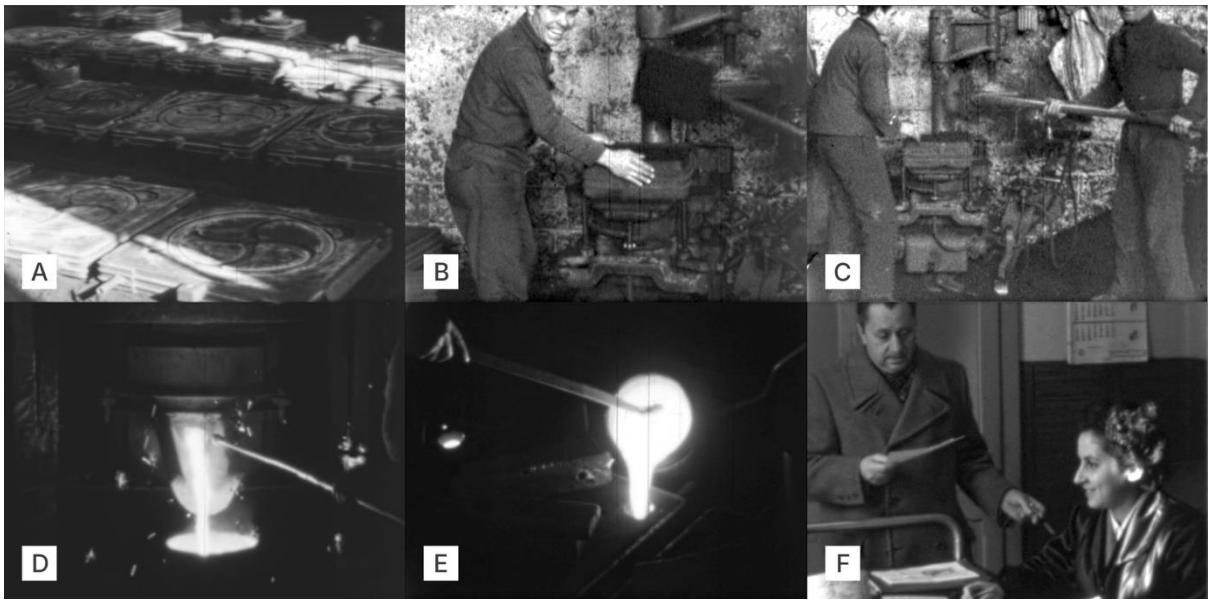


Figure 1. *Some rare images of the production process of the Italian foundry “Fonderia Marchigiana” in the year 1955: a) mouldings prepared with the sand for fusion, for the production of flywheels for wine-making machines; b, c) operating the moulding machine; d) pouring of liquid cast iron from the cupola furnace into the ladle; e) subsequent pouring of the liquid cast iron into the mould; f) the administration office.*

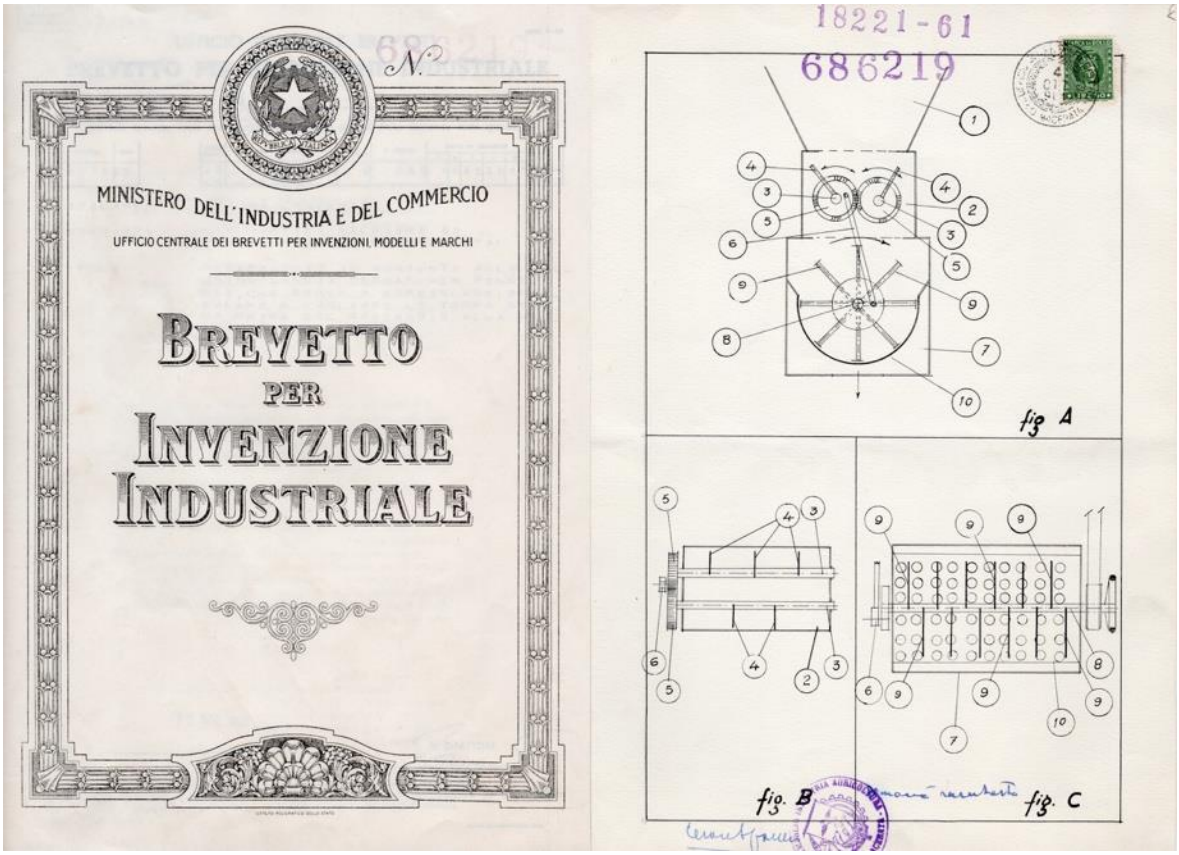


Figure 2. *Italian Patent of a machine for the preparation of foundry sand, equipped with a crumbling and amalgamating apparatus featuring oscillating pins, a mechanical sieve and a system for separating foreign and harmful materials. The machine was designed to operate upstream of the "sand launcher" already available on the market at the time [2].*

By the 1980s, advancements in automation and computer-aided design began to influence the sector. The introduction of semi-automatic moulding machines, such as those used in the semi-automatic moulding plant of a typical small Italian cast iron foundry, marked a significant step forward. These machines, featuring hydraulic compression and shot and compression systems, allowed for increased production rates and improved dimensional accuracy. This evolution has been driven by the need to enhance productivity, ensure consistent quality and meet the growing demands of industries such as automotive, construction and machinery manufacturing [4].

In recent years, the global foundry landscape has faced several challenges, with economic uncertainties, rising energy costs and stringent ecological regulations. Italian foundries, in particular, have been impacted by these factors, necessitating strategic adaptations to maintain competitiveness. The focus has also shifted towards enhancing energy efficiency, reducing environmental impact and improving worker safety. The adoption of automated systems, such as stack molding and vibratory sand handling equipment, has enabled foundries to optimize resource utilization and reduce manual labor, as well as to improve workplace safety. Moreover, the integration of digital tools and data analytics has facilitated real-time monitoring and quality control, ensuring that products meet stringent industry standards.

Environmental considerations, in particular, have become increasingly prominent, with foundries implementing measures to minimize emissions, manage waste and comply with European Union directives. The emphasis on sustainability has led to the exploration of alternative materials, energy-efficient processes and recycling initiatives within the industry [4].

Various Italian cast iron foundries, currently, feature advanced automation systems to boost efficiency and quality, with further developments anticipated in the coming years. Key technologies include automated molding lines, robotic core making and insertion, induction furnaces with controlled alloy dosing and precise automatic pouring systems. Finishing processes use robotic grinding and shot blasting, while 3D scanning, X-ray and real-time monitoring ensure quality. Integrated MES platforms and IoT systems manage production, maintenance and energy use. Environmental controls like sand reclamation and dust extraction support eco-friendly operations. These systems place these Italian foundries at the forefront of Industry 4.0.

This paper aims to provide a comprehensive overview of the structure and operations of a small-to-medium-sized cast iron foundry in Italy, illustrating how traditional practices have been adapted to meet contemporary industrial demands. By examining the manufacturing phases, the departmental functions and the technological advancements, this work offers insights into the dynamic nature of Italy's foundry sector and its responsiveness to global industrial trends.

2. Production departments

A small-to-medium-sized cast iron foundry in Italy tipically employs approximately 10-20 individuals, including production managers, sales/purchase managers and administrators. In Figure 3 the manufacturing phases are represented schematically.

The production process is divided into four main departments:

- Automatic Moulding Process Department, which utilizes semi-automatic moulding machines to produce moulds efficiently
- Resin Hand Moulding Department, focusing on producing smaller or more intricate castings using resin-bonded sand
- Core Shop Department, i.e. manufactures cores that define internal features of castings
- Casting Department, which involves melting and pouring cast iron into moulds, followed by cooling and shake-out processes.

A pattern shop, moreover, is also included.

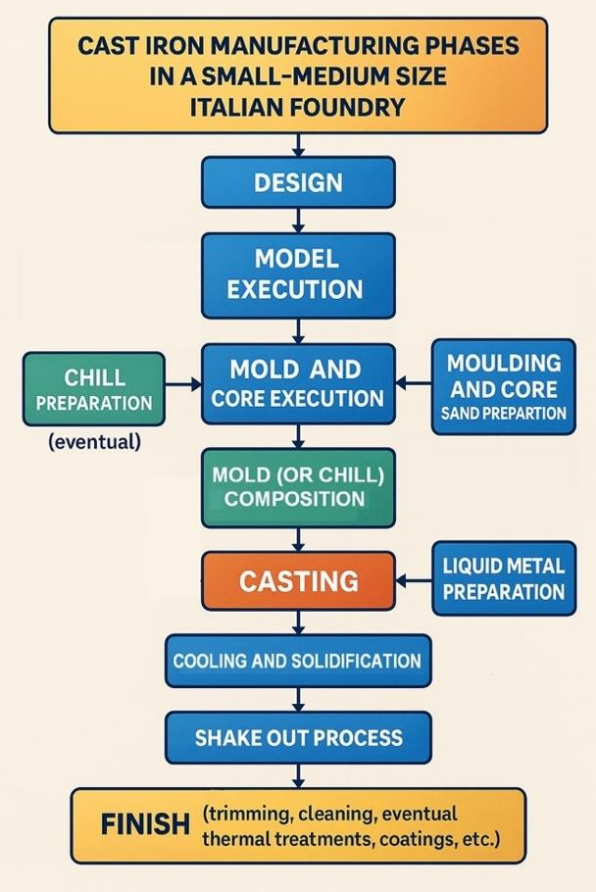


Figure 3. *Schematic representation of the manufacturing workflow in a small- to medium-scale Italian foundry producing cast iron components [5].*

2.1. Automatic Moulding Process Department

The considered cast iron foundry features a semi-automatic moulding facility. This department operates through the following three-phase automated sequence.

a) Moulding Sand Preparation and Distribution

The preparation of the moulding sand mixture is performed using a muller (Figure 4).



Figure 4. *Console and muller.*

The sand is then distributed to the moulding machines via specialized conveyor belts. The sand composition includes siliceous material, water, and a 5% non-flammable pre-mixed additive comprising 60% bentonite and 40% foundry-grade mineral blacking.

b) Mould Production

This phase includes mould formation using semi-automatic machines, assembly of the moulds, and coupling of the upper and lower halves.

c) Mould Filling and Shake-Out

Liquid cast iron is poured into the moulds, followed by a shake-out process after solidification.

The department is typically served by two compressed air storage tanks with capacities of approximately 2000 and 1000 litres, respectively.

The semi-automatic plant is designed to consolidate key operational areas-core placement, casting, and shake-out-enabling enhanced process control. The smallest standard moulding box dimensions are 700 x 600 x (240 + 240) mm. Production rates typically range from 50-60 moulding boxes per hour. In this setup, each simple moulding machine operates on a single line and produces either the upper or lower half of the mould box. The main functional areas include moulding, casting, and cooling.

The moulding machine generally features two stations with a translating pattern plate carrier, enabling efficient pattern cleaning and replacement. These modular machines support the following multiple moulding systems depending on production needs: hydraulic compression; high-frequency ramming with hydraulic compression; shock and hydraulic compression; shot and hydraulic compression; air impulse; vacuum-assisted moulding. The central moulding zone includes a volumetric hopper for sand feeding, a pressing and forming unit (configurable per foundry requirements), a feedback header and a hydraulically driven pattern withdrawal system (from top to bottom).

The pattern plate carrier rotates 180° to alternately position the upper and lower halves in the moulding zone (Figure 5).



Figure 5. *A typical pattern plate carrier system used in small-scale Italian cast iron foundries.*

An external transfer unit enables rapid exchange of pattern plate carriers. An example of moulding machine’s technical specifications is the following:

- moulding type: shot and compression
- feedback header: flat
- compression force: 42 tons
- maximum pattern draw stroke: 220 mm

- cycle time per half mould box: 30 seconds
- pattern plate change system: hydraulic, controlled via an integrated console.

Figure 6 depicts a moulding machine installed in a semi-automatic moulding plant typical of small Italian foundries.

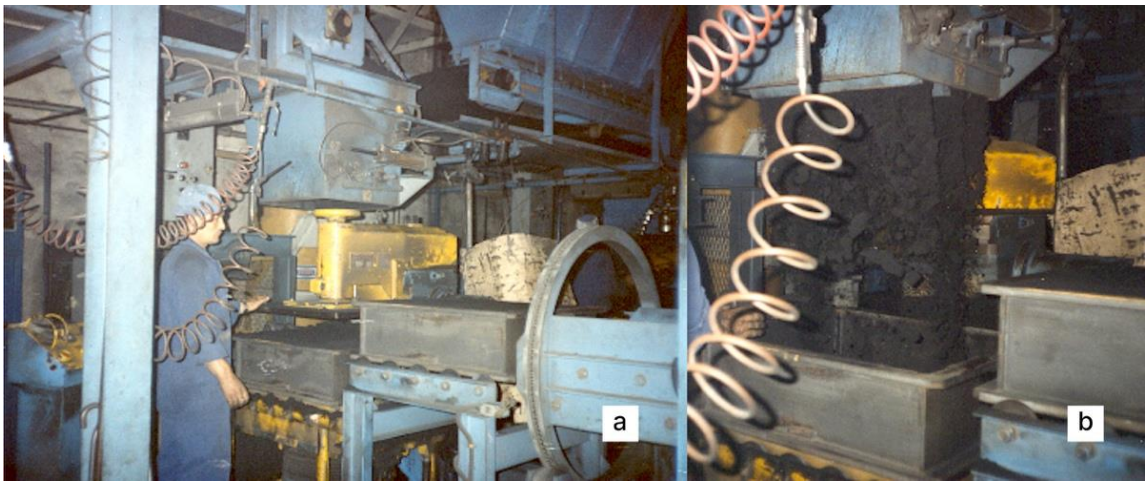


Figure 6. *Moulding machine within a semi-automatic moulding facility of a representative small-scale Italian cast iron foundry: a) overview; b) filling the moulding boxes.*

A dedicated work and inspection line allows operators to place cores and perform real-time quality checks. On the upper half-moulding line, a milling unit for cutting the pouring hole (adjustable location) and a turnover system for rotating the half-mould boxes to facilitate core placement and inspection, are installed as auxiliary systems. An automatic coupling system joins the upper and lower half-moulds from the assembly line. The coupling device, equipped with pneumatic cylinders and mechanical jaws, precisely aligns and locks the mould halves into place.

All components are mounted on a robust, electro-welded steel frame compliant with current Italian safety regulations. The support rails for mould box transfer extend from the stripping zone to the coupling station.

Dedicated casting and cooling lines, built to withstand thermal and mechanical stress, handle the moulds post-assembly. Lateral safety guards prevent damage from accidental metal spills. Figure 7 shows, e.g., the casting and cooling areas.



Figure 7. *Casting and cooling line arrangement in a small-to-medium-sized Italian foundry engaged in cast iron manufacturing.*

An automatic stripping system extracts castings and residual sand. The system features a mobile press that pushes mould boxes against a break plate, releasing sand and castings. Residual sand is removed by rotating brushes inside the mould box.
A continuous vibratory grid collects castings, including those of larger dimensions. Its frame is engineered for high capacity and reliability, driven by dual vibrators with adjustable centrifugal force to control vibration amplitude. A sand hopper with an extractor belt, typically holding up to 3 m^3 of sand, is located above the moulding machine. The plant uses hydraulic actuators to ensure consistent speed and high power with minimal spatial footprint. These actuators offer secure positional locking, including emergency stops, enhancing operational safety and control.
The hydraulic system includes pumps, motors, filters, manometers, electric and safety valves-designed with a safety margin to guarantee continuous, reliable operation.
All system components are coordinated via a programmable logic controller (PLC). Operational sequences are stored to allow seamless restarting from any interruption point without requiring a reset. The control console typically also integrates motor feeds, valves, and remote switches for complete automation and diagnostics.

2.2. Resin Hand Moulding Department

This department focuses on producing smaller or more intricate castings using resin-bonded sand. The process involves preparing a mixture of dry sand, resin and hardener, followed by hand moulding. In some cases, surfaces are coated with a special plaster based on diluted graphite to enhance resistance. Currently, the resin hand moulding process in small-to-medium cast iron foundries continues to play a critical role in the production of complex and low-volume castings. The operational workflow within this department can be broadly segmented into the following phases:

a) Mixture Preparation:

A continuous mixer is used to prepare a homogeneous moulding mixture composed of dry silica sand, furan resin, and a cold-setting hardener. The furan resin employed is non-flammable and complies with current EU REACH regulations concerning volatile organic compounds (VOCs). The hardener, typically based on sulfonic acids, is likewise non-flammable and is formulated for cold-box moulding systems, enabling ambient-temperature curing.

b) Manual Mould Assembly:
Skilled operators manually shape the moulds using the prepared mixture. Upon exposure to ambient air, the mixture undergoes polymerization and solidifies. In specific cases, to enhance the mould’s surface hardness and finish, a coating is applied, consisting of a fine graphite suspension in a volatile carrier mixture of isopropanol and methanol. While this coating significantly improves surface integrity and casting quality, its high flammability necessitates strict safety controls.

c) Pouring and Stripping:
Once the mould is fully prepared and inspected, it is filled with molten cast iron. After cooling and solidification, the casting is removed (stripped) from the mould manually or with mechanical assistance, depending on the size and complexity of the part.

Safety and Environmental Controls:
Due to the flammability of the graphite-alcohol coating, storage and handling are performed under stringent conditions. Only minimal quantities required for immediate use are maintained within the production area. These are stored in a sealed, water- and gas-tight container equipped with a compressed-air delivery system that feeds a spray gun, ensuring precise and safe application.
Bulk quantities of the coating are stored in a designated, ventilated storage unit located outside the main production facility. This storage area is constructed with horizontal and vertical fireproof partitions, designed according to the anticipated fire load based on maximum plausible material

quantities. The structure complies with current Italian and EU fire safety codes (e.g., UNI EN 13501 [6]), and is equipped with appropriate fire suppression systems, spill containment features, and real-time atmospheric monitoring for alcohol vapors.

Modernization Trends:
Several foundries are currently transitioning toward semi-automated mould preparation systems and real-time quality monitoring via embedded sensors, reducing operator exposure to volatile substances and improving consistency. Additionally, there is a growing shift toward bio-based or low-emission binders and coatings to comply with tightening EU environmental regulations and to support workplace health and safety initiatives.

2.3. Core Shop Department

The Core Shop remains a central unit in the casting process, responsible for producing cores essential to forming internal cavities and complex geometries in cast iron components. In small-to-medium Italian foundries currently operating, the department employs two primary core-making technologies:

a) Shell Moulding Cores

This process uses high-purity dry French sand pre-coated with furan resin. The coated sand is introduced into a heated metal core box, where the thermal activation causes the resin to polymerize, forming a rigid shell around the cavity walls. This method is favored for its dimensional precision and is typically used for producing smaller cores with high thermal stability.

b) Cold-Box Cores

Cold-box technology remains prevalent for medium to complex cores due to its high productivity and superior core strength. The process involves mixing dry French sand with furanic resin and a gaseous hardener—typically dimethylethylamine (DMEA) or trimethylamine (TMA) with a purity of ≥99% and water content ≤2%. These hardeners are flammable and require strict handling procedures. Upon injection of the amine gas into the core box, rapid curing occurs at room temperature, allowing for fast cycle times and precise geometry.
Due to the high flammability and volatility of the amine-based hardeners, safety protocols have been currently aligned with ISO 45001 [7] and the EU's latest CLP and REACH regulations:

- Only small quantities of the gaseous hardener are stored within the production area, in certified pressure-rated, explosion-proof containers equipped with leak detection sensors and temperature monitoring.
- Excess quantities are stored in an external, fire-rated chemical storage facility. This facility is constructed with gas-tight insulation, automatic fire suppression systems, and complies with the EU ATEX directive for environments with potentially explosive atmospheres.
- Ventilation and air purification systems are installed both at the point of use and in the storage zones to prevent amine vapor accumulation and ensure occupational exposure remains below the Threshold Limit Values (TLVs) specified by the European Chemicals Agency (ECHA).
- Operator workstations are equipped with local exhaust ventilation and personal protective equipment (PPE), including gas masks with activated charcoal filters, where necessary.

Driven by regulatory pressure and corporate sustainability goals, some foundries have begun transitioning to low-emission core binders, including polyurethane-based systems and bio-derived amine alternatives. Additionally, automation of sand mixing and dosing, combined with digital controls for gas injection, has enhanced both safety and process repeatability. Sensor-integrated core boxes now allow for real-time quality control, reducing defect rates and material waste.
Figure 8 shows the core installation phase in mould preparation for iron casting - operations within the Core Shop.

2.4. Casting Department

The casting department houses the main melting and pouring facilities, which in small-to-medium foundries are typically based on rotary furnaces equipped with hydraulically actuated tilting mechanisms for controlled pouring. These rotary melting furnaces are designed for flexibility, energy efficiency and operational safety, aligned with current European standards (e.g., EN ISO 13577 for industrial thermal processing equipment [8]).

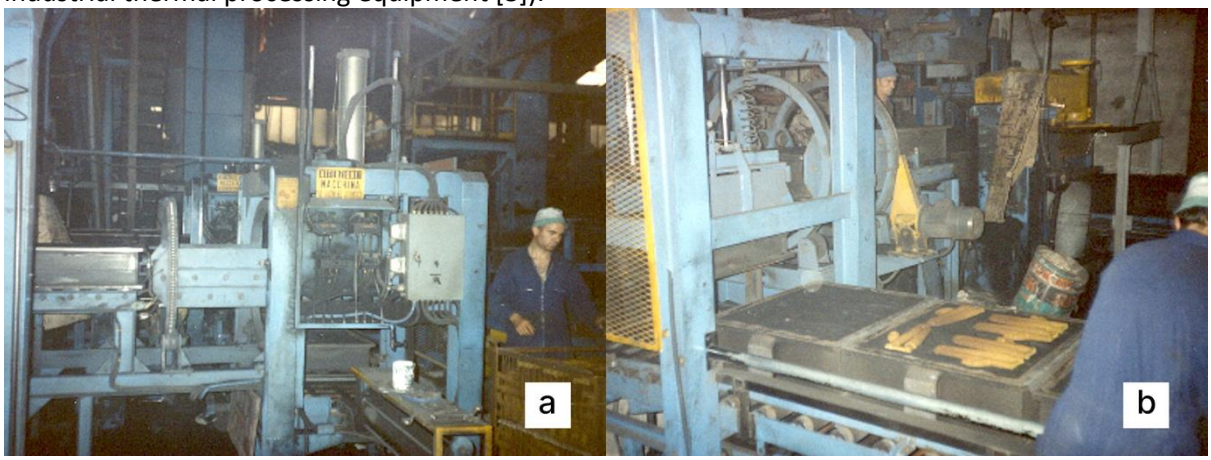


Figure 8. *Positioning of sand cores in mould assemblies for iron casting production - Core Shop Department: a) overview; b) detail.*

2.5. Casting Department

The casting department houses the main melting and pouring facilities, which in small-to-medium foundries are typically based on rotary furnaces equipped with hydraulically actuated tilting mechanisms for controlled pouring. These rotary melting furnaces are designed for flexibility, energy efficiency and operational safety, aligned with current European standards (e.g., EN ISO 13577 for industrial thermal processing equipment [8]).
The standard energy source for these systems remains a high-efficiency oxy-fuel combustion setup, using oxygen and methane gas as the primary feedstocks. The combustion system is engineered for high thermal efficiency, reduced emissions (notably NO_x and CO_2), and precise control over melting conditions. The key components are described as follows:

a) <u>Burner System</u>
The main burner is a dual-jacket assembly that incorporates:
- Outer and inner steel jackets to house and thermally insulate the combustion zone.
- Flexible connections (oversleeves) for high-pressure fluid lines-oxygen, methane, and cooling oil-with flame- and temperature-resistant fittings.
- Flame detection probe to monitor the presence of the ignition flame (pilot flame or “pennon”)
- Ignition system with an electronic igniter and dedicated pilot flame, ensuring safe startup sequences.

b) Combustion Control and Regulation System

The regulation and monitoring setup ensures safe and optimal combustion through the following components:

- Oxygen and methane regulation groups, each comprising:
  - high-pressure reducers, to maintain a constant downstream pressure (typically 1 bar for methane) to ensure stable burner operation.
  - fine control valves, for pressure stabilization and flow modulation.
- Flow measurement unit, equipped with:
  - calibrated mass flowmeters, to monitor real-time oxygen/methane ratios
  - pressure switches for automatic warning and shutdown in case of insufficient flow or delivery pressure anomalies.
- On-off pneumatic safety valves, integrated with programmable logic controllers (PLCs), perform:
  - range verification and automated shut-off in the event of burner malfunction, combustion imbalance, or emergency stop
  - control over three operational flame intensities:
    - minimum flame for startup and ignition
    - medium flame for holding temperature
    - maximum flame for full-load melting.
- Manual bypass valves, used to:
  - preselect gas flow levels during manual operation or emergency conditions
  - override automated sequences when needed to prevent furnace damage due to unexpected solidification of molten metal.

c) Control Console and Automation

A centralized furnace control console governs all operational sequences, with PLC-based logic and user interfaces. Its main functions include:

- cooling system control (start/stop, temperature regulation)
- furnace air-purging prior to ignition
- pilot and main burner ignition sequences
- alarm management with both acoustic and visual signals for abnormal events such as pressure loss, ignition failure, or power outage
- programmable cooling cycle control, ensuring safe shutdown and thermal protection.

d) Piping and Infrastructure

- Oxygen Supply Line
  Material: Carbon steel
  Diameter: 1 ½ inches
  Designed to withstand high-pressure feed and thermal cycling.
- Methane Supply Line
  Material: AISI 304 stainless steel (selected for its corrosion resistance)
  Fabrication: Seamless, head-welded joints
  Routing: From the reduction and measurement group to the mixing chamber at the burner inlet
  Safety Feature: an inline emergency shutoff valve automatically activates upon detection of pressure loss (e.g., due to pipe rupture), preventing gas leaks and minimizing ignition risks.

The combustion system, as installed, complies with the ATEX directives (ATmosphères Explosives, for explosive atmospheres), PED (Pressure Equipment Directive) and ISO 12100 [9] (machine safety principles, a norm expected to be replaced by ISO/DIS 12100 within the coming months), ensuring high levels of operational safety, system reliability, and environmental compliance.

Energy and Emissions Optimization

Advances in burner design, real-time combustion analytics and AI-driven process control enable modern foundries to reduce fuel consumption and Greenhouse gas (GHG) emissions significantly. Many plants currently incorporate oxygen-enrichment optimization algorithms, remote diagnostics and predictive maintenance tools, in order to enhance furnace performance and to extend equipment life.

Figure 9 shows examples of patterns, filled moulding boxes and castings representative of typical workflows in small-to-medium Italian cast-iron foundries. These visuals illustrate key stages in the production process, highlighting operational practices analyzed in the study.



Figure 9. *Some patterns (a, b), filled moulding boxes (b) and castings (c).*

2.6. Pattern shop

The pattern shop is a core component of the cast-iron manufacturing process, particularly in small-to-medium-sized foundries where flexibility, responsiveness and product customization are key operational requirements. In modern facilities, Computer Numerical Control (CNC) workstations and 3D printing technologies – mainly, adopting Acrylonitrile Butadiene Styrene (ABS) - are increasingly deployed for the rapid prototyping of patterns.

These 3D-printed models serve a variety of purposes depending on customer specifications: currently, they represent the highest quality standard for pattern production. Their appeal lies in their versatility and the ability to rapidly produce components with high morphological accuracy, including fine geometric features defined during the design phase. The effectiveness of 3D printing in model production, highlighting the optimization between speed and surface quality, is described in [10] and [11].

Advanced metrology tools, such as contact measurement systems and 3D laser scanners, contribute significantly to achieving a high degree of dimensional precision. The main capabilities of a modern pattern shop typically include:

- CAD/CAM Design, i.e. implementation of sophisticated 3D software platforms to develope highly accurate patterns and core boxes
- Computer-controlled milling centers to fabricate patterns from materials such as resin, wood or aluminum
- Pattern storage and maintenance: in structured system and dedicated spaces for model upkeep and modifications.
- Production Flexibility, manufacturing both individual prototypes and small-to-medium production runs, following the diverse client requirements
- Coordination with the technical office, in order to optimize designs for casting performance and downstream machinability.

For the production of prototypes and limited-run components, low-density resins are commonly employed. These materials are selected for their cost-effectiveness, fast processing times and superior surface finish. Even for large-sized patterns, this approach ensures time and cost savings without compromising quality.

Conversely, high-density resins are adopted to create patterns devoted to large-scale production. These resins offer various advantages, including enhanced abrasion resistance, excellent surface

integrity and high dimensional stability. Patterns produced using such resins ensure durability, operational efficiency and consistent quality standards across standard foundry operations.

3. Manufacturing Capabilities

The manufacturing capabilities of small-to-medium-sized cast-iron foundries in Italy have evolved considerably to align with the demands of an increasingly competitive, environmentally conscious, and digitally integrated global market. These foundries represent a blend of traditional metallurgical knowledge and advanced technological adaptation, playing a pivotal role in Italy’s industrial base and its export-oriented economy.

3.1. Materials and Casting Range

Italian foundries in this category are capable of producing a wide spectrum of cast iron grades, including austempered ductile iron (ADI), grey (lamellar) iron, malleable iron, Ni-resist alloys, spheroidal graphite (nodular) iron, and compacted graphite (vermicular) iron. These materials support applications in sectors ranging from automotive and agricultural machinery to energy and railway systems. Casting weights are typically classified as follows:

- small castings, from 0.5 kg up to 100 kg;
- medium castings, from 100 kg to 1,000 kg;
- large castings, from 1,000 kg up to approximately 10 metric tons.

Moreover, many foundries maintain in-house capabilities for the design and prototyping of pattern equipment using CAD/CAM systems and 3D printing, facilitating rapid iteration and close collaboration with clients during the development phase.

3.2. Melt Capacity and Energy Considerations

Standard melt capacity ranges from 100 to 200 metric tons or more per day, typically sustained over three shifts. Modern plants are increasingly integrating energy-efficient induction furnaces, energy recovery systems and advanced process controls, in order to reduce emissions and meet EU carbon-reduction targets under the Green Deal framework. Foundries are also beginning to adopt digital energy management systems, to monitor consumption and optimize melt scheduling in real time.

3.3. In-House Laboratory and Digital Quality Control

To guarantee metallurgical consistency and full traceability, foundries operate comprehensive laboratory facilities with both traditional and digital instruments. These typically include:

- computer-controlled optical emission spectrometers for elemental analysis
- real-time sulphur and carbon analyzers
- universal testing machines for tensile and impact strength
- metallographic preparation stations with automated polishing and etching units
- ultrasonic and radiographic non-destructive testing (NDT) systems
- digital stereo microscopes with AI-assisted image analysis
- Brinell and Rockwell hardness testers with digital readouts
- optical and infrared pyrometers integrated with process control software
- "Maxi-labs" strategically located at melting and holding furnace stations for fast decision-making during production.

Additionally, with the rise of Industry 4.0, various foundries now employ digital twin simulations, machine learning for defect prediction, and cloud-based quality monitoring platforms. Standard test bars are cast and dispatched to certified laboratories for independent mechanical testing, in cases requiring third-party verification.

Modern cast iron grades are suitable for numerous applications where it is essential to detect the presence of defects in the material (even below the surface) and to determine the exact metallographic structure. Neutron beam techniques, which are non-destructive and non-invasive, are

particularly useful for interpreting the structural basis for physical properties and improving the quality of the material under consideration ([12], [13] and [14]).

3.4. Multi-Stage Inspection and Traceability

Casting inspection is currently a multi-layered process combining traditional methods with modern digital tools. Components are routinely inspected at multiple checkpoints - often including post-casting, post-machining and pre-shipment stages. Dimensional checks are increasingly carried out using coordinate measuring machines (CMMs), laser scanners and automated vision systems. All inspection data is logged digitally to ensure traceability, auditability and to supply a rapid response to client specifications or complaints.

3.5. Compliance with International Standards and Market Requirements

Italian foundries operate under strict adherence to a range of international quality and safety norms, including UNI (Italy), ISO, DIN (Germany) and ASTM (United States) standards. In light of increasing global integration, many foundries are currently also certified under ISO 14001 [15] (environmental management), ISO 45001 [16] (occupational health and safety) and ISO 50001 [17] (energy management). Compliance with REACH regulations and alignment with EU taxonomy requirements for sustainable activities are becoming key discriminators in the marketplace.

4. Discussion and conclusion

This research has provided an exploration of the structural and operational dynamics of small-to-medium-sized cast-iron foundries in Italy, offering insights into how these enterprises are traversing a period of significant transition. The analysis has shown that, while these foundries vary in size, technological maturity and market orientation, they share common challenges arising from evolving regulatory frameworks, global economic pressures and shifts in customer expectations. Over the past decade, the enforcement of stricter safety and environmental standards has played a pivotal role in reshaping production practices. For many operators, this has required important financial investment in equipment upgrades and process optimization, as well as a cultural shift toward more proactive compliance and sustainability strategies.

Despite these pressures, cast iron has retained its strategic role in the industrial landscape. Its robust mechanical properties, combined with cost-efficiency and versatility, make it always indispensable in a wide array of applications, from automotive components and heavy machinery to civil infrastructure and energy systems.

As the industry looks ahead to the coming years, in addition to the needed technological enhancements the broader challenge lies in reconciling the heritage of Italian foundry craftsmanship with the demands of a rapidly changing industrial context. The following key themes are among those expected to shape the future of this sector.

a) Environmental sustainability and regulatory adaptation

The green transition is a present necessity, thus foundries will be increasingly expected to demonstrate measurable progress in emissions reduction, resource efficiency and responsible waste management. Transitioning toward circular production models - emphasizing the reuse of scrap material, energy recovery and minimal environmental footprint - will likely become a defining factor in securing both public trust and market access.

b) Integration of digital technologies

The adoption of digital tools is emerging as a central pillar of modernization. From predictive maintenance and real-time process monitoring to digital simulation and quality control via machine learning, the digitalization of operations offers opportunities to significantly enhance productivity and responsiveness. This transformation requires organizational readiness, digital skills development and a willingness to rethink traditional workflows.

c) Workforce evolution and knowledge retention
The demographic profile of the foundry workforce is shifting, with many experienced technicians approaching retirement. Preserving artisanal knowledge while cultivating a new generation of skilled workers will be a major concern. Addressing this will call for a dual strategy: on one hand, fostering technical education and apprenticeships tailored to the sector’s needs; on the other, creating attractive, forward-looking career paths that integrate digital and environmental competencies alongside traditional metallurgical expertise.

d) Market diversification and global positioning
Global supply chains are probably becoming more unpredictable, thus localized resilience is gaining importance. Foundries must therefore look beyond traditional markets, seeking niche opportunities where their blend of quality, customization and flexibility can offer a competitive advantage. Cooperations with public and private research institutions, active participation in innovation clusters and a stronger digital presence may help position these companies as reliable players also in a fragmented global market.

In conclusion, while small-to-medium cast-iron foundries face undeniable challenges, they also stand on the threshold of significant opportunity. Their deep-rooted expertise, combined with targeted innovation and an openness to change, can serve as the foundation for long-term sustainability and renewed competitiveness. The years ahead will test the sector’s capacity to adapt and to lead within a broader movement toward cleaner, smarter and more resilient manufacturing. Ensuring success will require coordinated action from industry stakeholders, policymakers and the research community alike, working together to support a sector that continues to contribute meaningfully to industrial identity and economic fabric.

Acknowledgments

The author wishes to point out that this article includes historical references to the “*Fonderia Marchigiana*”, a prominent industrial enterprise located in the Marche region, which played a vital role in Italy’s reconstruction following the World War II. This foundry, which remained operational until the second half of the 1990s, holds particular significance to the author, who served as its Sole Director for a period of nearly two years. The documentary materials cited herein - including archival sources and an original film from 1955 featuring exclusive content - are presented for scholarly and historical purposes. Their inclusion aims to contribute to the preservation, dissemination and appreciation of Italy’s industrial heritage, with particular regard to the legacy of small- to medium-sized foundries that have contributed in shaping the nation’s economic and cultural landscape.

References

[1] Rogante Engineering Office, 2025. La Fonderia Marchigiana nel 1955. Filmato storico su pellicola Ferrania 8mm, Civitanova Marche. https://www.youtube.com/watch?v=kEmB0ohPp_U (accessed 30 June 2025).

[2] Ninonà, L., 1965. Apparecchio, in aggiunta alla macchina “lancia terra” per fonderia che serve a sgretolare, amalgamare e vagliare la terra stessa prima del passaggio alla macchina lancia terra. Italian Patent for Industrial Invention n. 686219, Italian Ministry of Industry and Commerce, Rome

[3] Ninonà, L., 1967. Sistema di fusione orizzontale per la formazione di rulli per machine enologiche che permette la centratura perfetta del perno del rullo senza ulteriori correzioni di centratura. Italian Patent for Industrial Invention n. 739112, Italian Ministry of Industry and Commerce, Rome

[4] Global Grow Market, India 2025. Dimensioni, quota, crescita e analisi del mercato di ghisa e getti in ghisa, per tipologia (stampaggio verticale, stampaggio orizzontale), per applicazioni coperte (settore automobilistico, settore della metallurgia ferrosa, settore della produzione di macchinari, settore della

lavorazione degli stampi, altri), approfondimenti regionali e previsioni fino al 2033. https://www.globalgrowthinsights.com/market-reports/cast-iron-cast-iron-castings-market-106809 (accessed 30 June 2025).

[5] Rogante, M., 2001. Structure of a small-medium size cast iron foundry in Italy, MATRIB 2001, Vela Luka, Korčula

[6] UNI - Italian Standards Body, Italy, 2018. EN 13501-1:2018 - Fire classification of construction products and building elements - Part 1: Classification using data from reaction to fire tests. https://store.uni.com/en-13501-1-2018 (accessed 30 June 2025).

[7] International Organization for Standardization, Switzerland, 2018. ISO 45001:2018 Occupational health and safety management systems - Requirements with guidance for use. https://www.iso.org/standard/63787.html (accessed 30 June 2025).

[8] International Organization for Standardization, Switzerland, 2016. EN ISO 13577-1:2016 - Industrial furnaces and associated processing equipment - Safety - Part 1: General requirements. https://www.iso.org/standard/68019.html (accessed 30 June 2025).

[9] International Organization for Standardization, Switzerland, 2010. ISO 12100:2010 - Safety of machinery - General principles for design - Risk assessment and risk reduction. https://www.iso.org/standard/51528.html (accessed 30 June 2025).

[10] Thiel, J., Ravi, S., Bryant, N., 2016. Advancements in materials for three-dimensional printing of mold and cores. International Journal of Metalcasting, 11(1), 3–13.

[11] Upadhyay, M., Sivarupan, T., El Mansori, M., 2017. 3D printing for rapid sand casting – a review. Journal of Manufacturing Processes, 29, 211–220.

[12] Čatipović, N., Rogante, M., Avdušinović, H., Grgić, K., 2023. Influence of a Novel Double Tempering Process on the Microstructure and Mechanical Properties of Cu-Alloyed Austempered Ductile Iron with Possible Nano (Micro)-Characterization using Neutron Beam Techniques. Crystal, 13(9), 1359.

[13] Rogante, M., 2008. Applicazioni Industriali delle Tecniche Neutroniche, 1st Italian Workshop for Industry "Industrial Applications of Neutron Techniques", Civitanova Marche, Italy

[14] Rogante, M., 2003. Industrial applications of neutron techniques: a recent overview related to materials and components of technological interest, MATRIB 2003, Vela Luka, Korčula

[15] International Organization for Standardization, Switzerland, 2015. ISO 14001:2015 - Environmental management systems - Requirements with guidance for use. https://www.iso.org/standard/60857.html (accessed 30 June 2025).

[16] International Organization for Standardization, Switzerland, 2018. ISO 45001:2018 - Occupational health and safety management systems - Requirements with guidance for use. https://www.iso.org/standard/63787.html (accessed 30 June 2025).

[17] International Organization for Standardization, Switzerland, 2018. ISO 50001:2018 - Energy management systems - Requirements with guidance for use. https://www.iso.org/standard/69426.html (accessed 30 June 2025).

Further reading

[1] Jolly, M., 2005. Prof.John Campbell’s Ten Rules for Making Reliable Castings. JOM: the journal of the Minerals, Metals & Materials Society, 57 (5), 19–28.

[2] Schleg, F., 2000. Guide to casting and molding processes. Engineered Casting Solutions, 2 (3), 18–27.

[3] Lobenhofer, R., 2002. Small Foundry Management. Modern casting, 92 (4), 58–60.

[4] Lehmhus, D., 2024. Advances in Metal Casting Technology: A Review of State of the Art, Challenges and Trends-Part II: Technologies New and Revived. Metals, 14 (3), 334.

[5] European Commission, Bruxelles 2020. A New Industrial Strategy for Europe. https://eur-lex.europa.eu/legal-content/EN/TXT/?uri=CELEX:52020DC0102 (accessed 30 June 2025).

Characterization of bipolar plates for hydrogen fuel cells manufactured using additive manufacturing technology

***Anđela Rohtek*[1], *Nikša Čatipović*[1], *Željko Penga*[1], *Jure Penga*[1], *Mišo Jurčević*[1] *and Petra Bagavac*[1]**

1) University of Split, Faculty of Electrical Engineering, Mechanical Engineering and Naval Architecture, R. Boškovića 32, 21000 Split, Croatia

Corresponding author: arohte00@fesb.hr

Original scientific article

Abstract: This study investigates the suitability of materials fabricated using additive manufacturing technology for application in bipolar plates of hydrogen fuel cells. The material selected for evaluation was Protopasta, which was 3D printed into various sample geometries. The primary objective of the research was to characterize the thermal and mechanical properties of the samples, with particular emphasis on thermal conductivity, tensile strength, and hardness. These properties were assessed to evaluate the material’s capability for heat dissipation and its mechanical resilience under operational conditions typical of fuel cell environments.

Keywords: *additive manufacturing; bipolar plates; hydrogen fuel cells; thermal conductivity; mechanical properties*

1. Introduction

Fuel cells are electrochemical devices that enable the direct conversion of chemical energy into electrical energy. Each fuel cell consists of two electrodes — a positive electrode (cathode) and a negative electrode (anode) — along with an electrolyte, a catalyst, and a current collector. Fuel cells operate based on an electrochemical reaction, where hydrogen is used as the fuel at the anode side, and oxygen or air serves as the oxidant at the cathode side, as illustrated in Figure 1. At the anode, hydrogen molecules are split into protons and electrons with the aid of a catalyst. The protons pass through the membrane, while the electrons are directed through an external electrical circuit, thereby generating electric power. At the cathode, the protons, electrons, and oxygen recombine to form water [1].

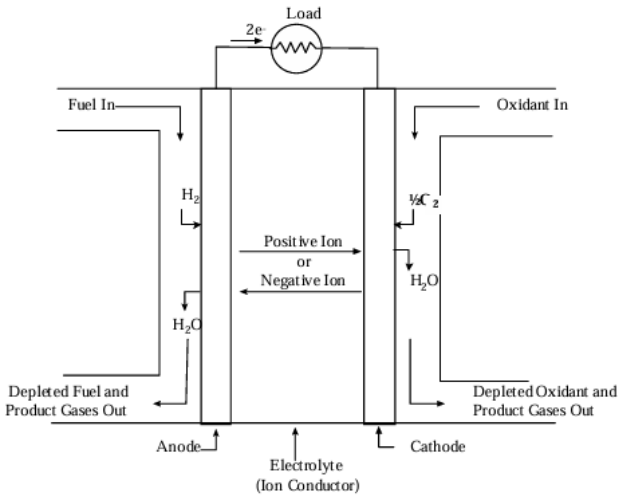


Figure 7. *Basic Structure of a fuel cell [1]*

1.1. The role of bipolar plates

Bipolar plates play a crucial role in the operation of a fuel cell stack, significantly influencing its efficiency, durability, and overall cost. One of their primary functions is the distribution of reactants, such as hydrogen and oxygen (or air), to the active electrode surfaces where electrochemical reactions take place. The design of the plates incorporates flow channels that enable uniform distribution of reactants across the membrane surface, ensuring stable and efficient reaction conditions.

In addition to gas distribution, bipolar plates serve as conduits for the transfer of electrical current between individual cells in the stack. Due to their dual-sided configuration, one side of the plate conducts electrons toward the cathode of one cell, while the other side conducts electrons from the anode of the adjacent cell. This function necessitates the use of materials with high electrical conductivity to minimize energy losses.

A third essential function of bipolar plates is thermal management. During fuel cell operation, heat is generated as a byproduct of the electrochemical processes. If not properly managed, this heat can lead to system overheating. Therefore, bipolar plates must efficiently conduct heat away from the active regions toward the cooling system, thereby maintaining optimal operating temperature and reducing the risk of membrane and catalyst degradation [2]. Consequently, thermal conductivity is one of the key material properties to consider in the design and manufacturing of bipolar plates.

Traditional materials used for bipolar plates, such as graphite and metals, although exhibiting good electrical and thermal conductivity, face several limitations. Graphite is known for its corrosion resistance but is expensive and brittle, making handling and machining more challenging. Metallic plates, on the other hand, offer high strength and conductivity but are prone to corrosion and significantly increase the overall weight of the system [3]. These challenges have driven the development of new, innovative materials and technologies, such as additive manufacturing, which offer the potential to reduce costs, enhance material properties, and increase flexibility in the design of fuel cell components.

1.2. The role of additive manufacturing

Additive manufacturing, also known as 3D printing, plays an important role in enhancing both the materials and design of bipolar plates for hydrogen fuel cells. This technology enables the fabrication of complex geometries and flow field patterns that are difficult or costly to achieve using conventional manufacturing methods. The use of advanced materials, including polymer composites and specialized alloys, allows for improvements in the thermal conductivity and mechanical strength of bipolar plates. Additionally, additive manufacturing contributes to cost reduction by optimizing material usage and minimizing production waste.

1.3. Research objective

The objective of this study was to investigate the thermal conductivity and related heat transfer characteristics of cylindrical specimens manufactured from Protopasta using additive manufacturing technology, in order to assess their suitability for use in bipolar plate fabrication. Additionally, the study aimed to evaluate the mechanical properties of test specimens produced in the same manner.

2. Materials and methods

2.1. Additive manufacturing of materials

The samples were printed using *Electrically Conductive Composite PLA* filament, 1.75 mm / 500 g (CDP11705). This filament is a composite material combining finely milled carbon fibers with a high-temperature PLA matrix, offering enhanced durability and dimensional stability. While it provides excellent layer adhesion and minimal warping even without a heated bed, its abrasive nature may require periodic nozzle replacement and first-layer calibration during prolonged use.

The filament is based on PLA with an addition of 10% high-purity milled carbon fibers. It has a density of approximately 1.24 g/cc and a volume resistivity of 15 ohm-cm for molded resin, 30 ohm-cm along the print layers (x/y direction), and 115 ohm-cm across layers (z direction). Recommended print

settings include a nozzle temperature of 215 °C, a heated bed temperature of 60 °C, and a print speed ranging between 25–45 mm/s.
The test specimens were fabricated using a Creality Ender 3 V3 SE 3D printer, shown in Figure 2. For thermal conductivity testing, two cylindrical samples were printed using a 0.2 mm nozzle and two using a 0.4 mm nozzle. For mechanical property evaluation, six standardized tensile specimens were printed—three with a 0.2 mm nozzle and three with a 0.4 mm nozzle. In addition, two tablet-shaped specimens (one per nozzle size) were fabricated for supplementary analysis.



Figure 8. *Creality Ender 3 V3 SE*

Initial calibration of the 3D printer was performed using a 0.2 mm nozzle with the *Creality 4.8* slicing software. Key print parameters were adjusted as follows: material flow was reduced to 80% to control the output volume, and the layer height was set to 0.1 mm. During calibration, a deviation of 0.25 mm was observed along all three axes (x, y, and z) on a 20 × 20 × 20 mm calibration cube. To compensate for dimensional discrepancies, *Horizontal Expansion* was applied with an offset of +0.25 mm in both the x and y directions. No specific adjustment option was available for the z-axis.
Layer height was reduced from the default 0.2 mm to 0.1 mm to accommodate the finer 0.2 mm nozzle. *Line Width* was also adjusted, reduced from 0.4 mm to 0.2 mm. A successful 5 mm high printed specimen measured 4.5 mm in height post-printing, while the width remained accurate at 10.5 mm. Infill settings for the first specimen were configured with 80% infill for both the interior and outer shell. For the second specimen, the outer shell infill remained at 80%, while the internal infill was increased to 100%.
Cylindrical geometry was chosen for thermal conductivity testing due to its simplicity and suitability for surface-based thermal measurements. The intended dimensions for the printed cylinders were 50 mm in diameter and 21 mm in thickness, leaving a 0.5 mm margin on each side for post-processing and surface refinement. The final printed specimens had a measured diameter of 49.5 mm (considered negligible deviation) and a thickness of 21 mm, which was reduced to 20 mm after sanding.
Surface preparation began with 180-grit sandpaper, followed by progressive finishing with 600-, 1200-, and 2000-grit sandpapers to achieve a smooth, uniform surface required for thermal testing. The samples were subsequently polished for improved measurement accuracy.
For tensile strength testing, standardized test specimens with a square cross-section were fabricated, as shown in Figures 4 and 5. Each specimen measured 150 mm in length and 4 mm in thickness. These

dimensions align with standardized protocols for tensile testing, ensuring comparability of mechanical property results with existing literature and standards.

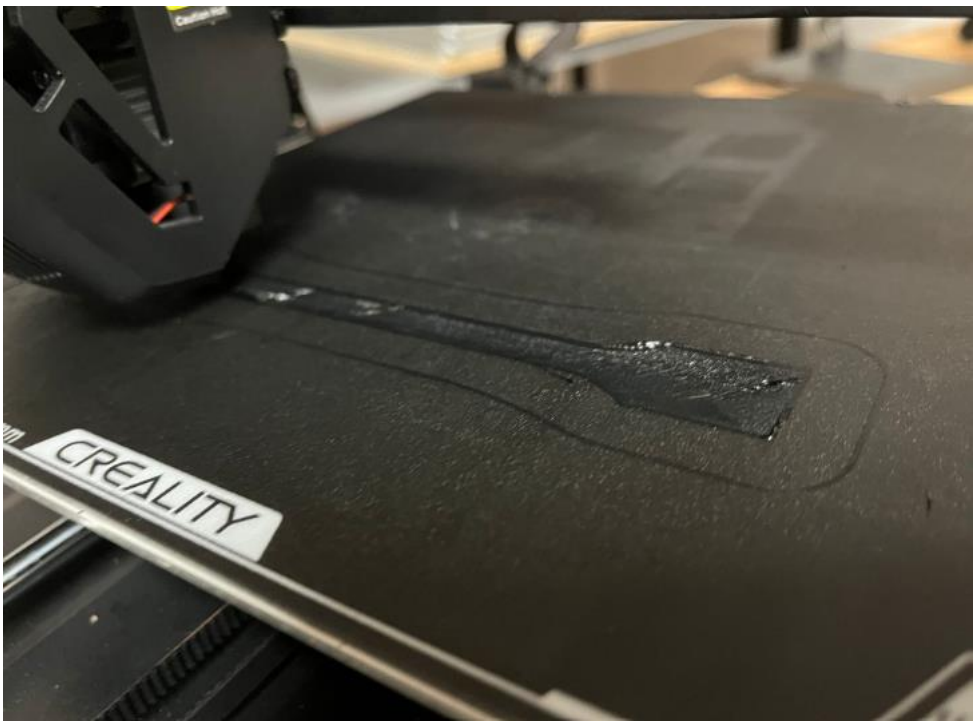


Figure 9. *Additive Manufacturing of test specimens*

Three specimens were produced with each nozzle size in order to obtain statistically more reliable results and to enable the calculation of the arithmetic mean. Regarding the hardness testing, two tablet-shaped specimens with a diameter of 30 mm and a thickness of 10 mm were fabricated for testing simplicity. Multiple measurements were performed on each specimen to determine the average value.



Figure 10. *Specimens fabricated using the 0.4 mm nozzle*

2.2. Methods for measuring thermal properties

There are various methods used to measure specific thermal properties, typically classified into steady-state and transient methods. While steady-state methods are still widely used in testing, transient methods are simpler, faster, and relatively more accurate. Additionally, the entire measurement process is typically computer-controlled. Steady-state methods include instruments based on measuring plates according to Poensgen and Bock, cylindrical devices based on Van Rinsum, as well as spherical devices following Nusselt’s principle. On the other hand, transient methods include devices based on Fitch’s approach, which measures the temperature difference between two points on a material over a fixed time interval during a defined phase. In contrast to measuring temperature at multiple points over a fixed time period (as in Fitch's method), commonly used transient methods also include the flash method and the transient plane source (TPS) method. The flash method uses a rapid heat pulse to track temperature change over time, while the transient plane source method involves heating a disk-shaped sensor with electrical current and recording the corresponding temperature evolution [4, 5].

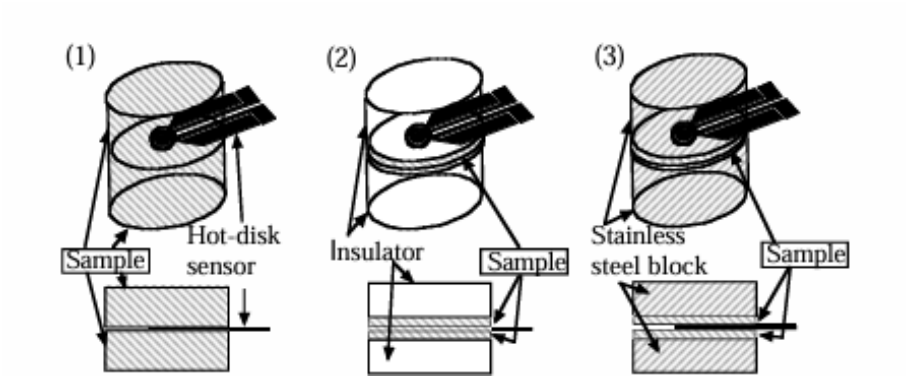


Figure 11. *Methods for measuring thermal properties [5]*

2.3. Methods for measuring mechanical properties

Tensile strength represents the maximum stress a material can withstand before breaking under tensile loading. The most commonly used method for determining tensile strength is tensile testing in accordance with standards such as HRN, EN, and ISO 6892-1. This method involves the preparation of test specimens, typically in the form of standardized tensile bars, and placing them into testing machines that apply a controlled tensile load. The load is gradually increased until the specimen fractures. Based on parameters such as stress and strain, the tensile strength of the material is determined [6].

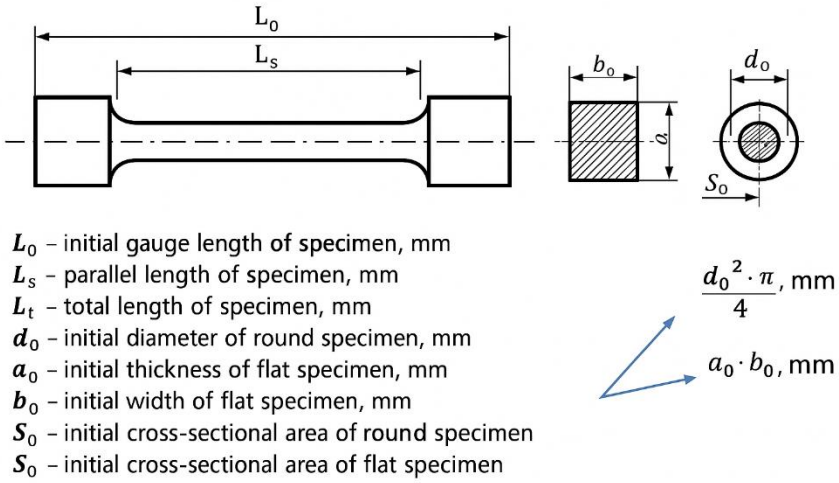


Figure 12. *Standards for test specimens in tensile strength testing [6]*

2.4. Material characterization

2.4.1. Thermal properties

Thermal conductivity of the samples was measured using the Transient Plane Source (TPS) method with a Hot Disk sensor. The TPS method is employed for precise measurement of the thermal properties of materials. It is an absolute method that not only determines temperature but also how heat propagates through a material.

The core component of the method is the Hot Disk sensor, which is designed as a double-spiral element and heated by an electric current. This sensor is placed between two pieces of the material being tested. As the material heats up, the system records temperature changes as a function of time. This measurement configuration allows for the analysis of thermal conductivity, thermal diffusivity, and specific heat capacity of various materials, including metals, plastics, liquids, and biomaterials.

Thermal measurements using this method can be conducted over a wide temperature range—from cryogenic conditions up to high temperatures, reaching as much as 1800 K [5].

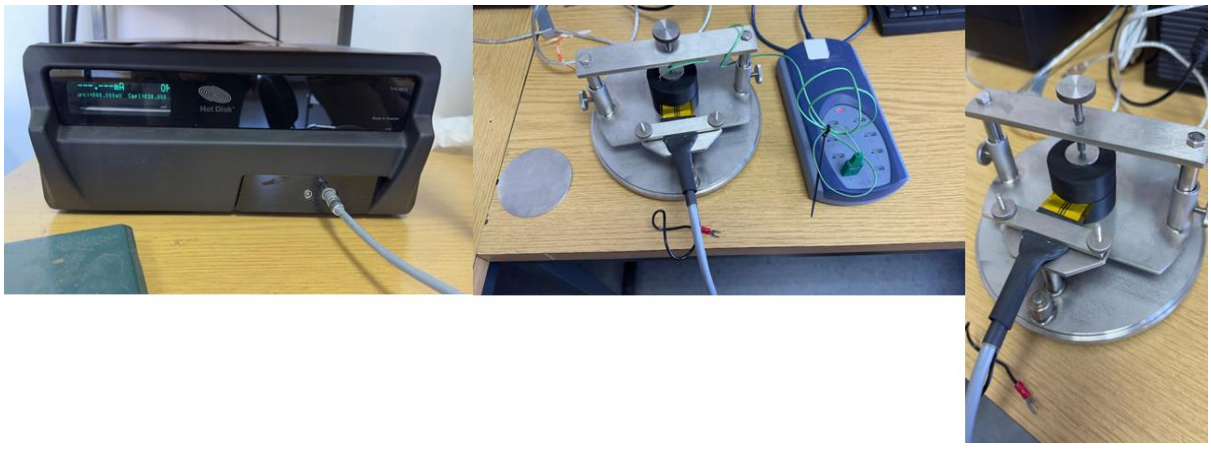


Figure 13. *Thermal conductivity measurement of samples*

2.4.2. Mechanical properties

To measure the hardness of the material, a digital Shore D durometer was used (shown in Figure 8). A durometer is a device used to determine a material’s resistance to localized deformation—more precisely, to measure its hardness. In addition to the D version, there are also Shore A and Shore C versions of the durometer, each designed for testing materials with different characteristics.

The Shore A durometer is used for soft materials such as natural and synthetic rubber, elastomers, wax, soft PVC, and leather. It applies a lower spring force (8.065 N) and is suitable for low-hardness materials. The Shore C durometer is intended for medium-hard materials like cellular rubber, foamed plastic parts, and medium-hard elastomers. It uses a higher spring force (44.5 N) than Shore A and is applicable when the material is neither completely soft nor fully hard.
The durometer used in this study was a Shore D type, specifically intended for hard materials such as rigid plastics, resins, acrylics, glass, and fibers. It applies the same spring force as the Shore C durometer (44.5 N), but is designed for testing high-hardness and more resistant specimens.



Figure 14. *Hardness measurement of samples using a Shore D Durometer*

For tensile strength testing, an Instron 8801 testing machine was used (shown in Figure 9). This device is designed for evaluating the mechanical properties of materials under various types of loading, including tensile, compressive, and flexural forces. It enables precise testing in accordance with international standards and is commonly used for testing metals, plastics, composites, and other engineering materials.



Figure 15. *INSTRON 8801 Device for Tensile Strength Testing*

The sample is placed between two grips that firmly hold it in place, while either the upper or lower head of the machine moves, stretching the sample at a controlled speed until fracture occurs, as shown in Figure 10. During testing, the device continuously measures the applied force and the corresponding deformation of the sample. Based on the collected data, the tensile strength is calculated—defined as the maximum stress the material can withstand before breaking.
Measurement and data processing are carried out using dedicated computer software that controls the testing machine and enables detailed analysis of the recorded data through a force–elongation diagram.



Figure 16. *Tensile Strength Testing Procedure for Samples*

3. Results

3.1. Thermal conductivity testing

For each sample, measurements were performed four times, each lasting 40 seconds with a power of 80 mW. There was a 10-minute pause between each measurement. The sample temperature was maintained at 24°C. Measurements began after 30 minutes to allow the sample temperature to stabilize. Upon completion of each test, data were obtained for thermal conductivity, thermal diffusivity, and specific heat capacity. Thermal conductivity refers to the material’s ability to conduct heat—higher conductivity indicates better heat transfer capability. Thermal diffusivity describes the rate at which heat spreads through a material; higher diffusivity means faster thermal response. Specific heat capacity is the amount of heat required to change the temperature of a unit mass of the material.

A higher specific heat capacity means the material can absorb more heat without a significant rise in temperature.

For the tested samples, the desired results include:

– High thermal conductivity, for more efficient heat transfer through the material

– High thermal diffusivity, to ensure the material quickly responds to temperature changes

– Lower specific heat capacity, to facilitate rapid thermal adaptation

The results obtained from the samples printed with the 0.2 mm nozzle are shown in Table 1.

Table 1. *Thermal conductivity testing of samples fabricated using a 0.2 mm nozzle*

Measurement number	Temperature	Thermal conductivity	Thermal diffusivity	Specific heat capacity	Measurement penetration depth
1.	24 °C	0.1894 W/mK	0.1904 mm^2/s	0.9945 MJ/m^3K	5.52 mm
2.	24 °C	0.1878 W/mK	0.1845 mm^2/s	1.018 MJ/m^3K	5.44 mm
3.	24 °C	0.1901 W/mK	0.1912 mm^2/s	0.9937 MJ/m^3K	5.53 mm
4.	24 °C	0.1899 W/mK	0.1910 mm^2/s	0.9939 MJ/m^3K	5.53 mm
Average value	24 °C	0.1893 W/mK	0.1893 mm^2/s	1.0000 MJ/m^3K	5.51 mm

For the testing of samples fabricated using a 0.4 mm nozzle, the results obtained are presented in Table 2.

Table 2. *Thermal conductivity testing of samples fabricated using a 0.4 mm nozzle*

Measurement number	Temperature	Thermal conductivity	Thermal diffusivity	Specific heat capacity	Measurement penetration depth
1.	24 °C	0.1955 W/mK	0.1682 mm^2/s	1.162 MJ/m^3K	5.19 mm

2.	24 °C	0.2048 W/mK	0.1906 mm²/s	1.074 MJ/m³K	5.53 mm
3.	24 °C	0.2040 W/mK	0.1875 mm²/s	1.088 MJ/m³K	5.48 mm
4.	24 °C	0.2081 W/mK	0.1982 mm²/s	1.050 MJ/m³K	5.63 mm
Average value	24 °C	0.2031 W/mK	0.1861 mm²/s	1.094 MJ/m³K	5.46 mm

3.2. Hardness testing

For the purpose of hardness testing, two disc-shaped test specimens (tablets) with a diameter of 30 millimeters and a thickness of 10 millimeters were planned to be fabricated using the 3D printer employed in this study, utilizing two different nozzle sizes: 0.4 mm and 0.2 mm. However, only the specimen printed with the 0.4 mm nozzle was successfully produced.

Although the smaller 0.2 mm nozzle is, in theory, better suited for precise printing of intricate details and thinner layers, it proved incompatible with the requirements of hardness testing in this case. Due to its very narrow opening and reduced material flow rate, extrusion irregularities occurred, leading to pressure buildup in the hot end, interrupted material flow, and insufficiently homogeneous layer formation. As a result, the print using the 0.2 mm nozzle lacked consistency and surface quality, making it unsuitable for further hardness testing.

The hardness test was conducted using a digital Shore D durometer, and measurements were taken three times on the same specimen to obtain a representative value through arithmetic averaging. The first reading was 060.5 HD. Since the results showed good consistency, the second and third readings were 059.8 HD and 060.2 HD, respectively. The arithmetic mean of the three measurements was 60.17 HD.



Figure 17. *Result of the first hardness measurement*

3.3. Tensile strength testing

Tensile strength testing was initially planned for samples fabricated using two different nozzle diameters: 0.4 mm and 0.2 mm. The samples were intended to be produced using a Creality Ender 3 V3 SE 3D printer. However, during the preparation phase, it became evident that fabricating tensile test specimens with the 0.2 mm nozzle was not feasible due to a mismatch between the testing requirements and the capabilities of the printer.

Although the 0.2 mm nozzle allows for more detailed printing, it significantly increases print time and makes it difficult to achieve the mechanical stability needed for larger and functional geometries, such as standardized tensile specimens. Attempts to fabricate such samples resulted in warping, layer delamination, or excessive brittleness, rendering the specimens unsuitable for mounting in the testing machine.

As a result, only the samples produced with the 0.4 mm nozzle were used for tensile testing, as they provided sufficient mechanical strength and dimensional accuracy.



Figure 18. *Fracture behavior observed in three samples during tensile testing*

A total of three specimens were tested, all fabricated under identical conditions using a 0.4 mm nozzle. The testing was carried out using a tensile testing machine, with continuous monitoring of force and displacement until the point of specimen fracture. The collected experimental data were processed using the corresponding software tool, which enabled numerical analysis and the generation of both tabular and graphical outputs for each specimen. The obtained results were interpreted and are presented in the following sections of this paper.

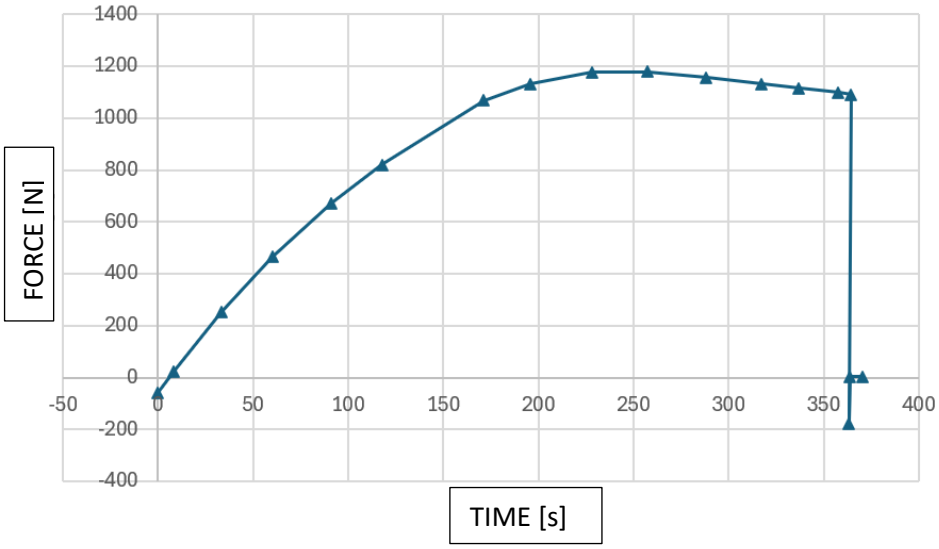


Figure 19. *Tensile strength testing of the first sample*

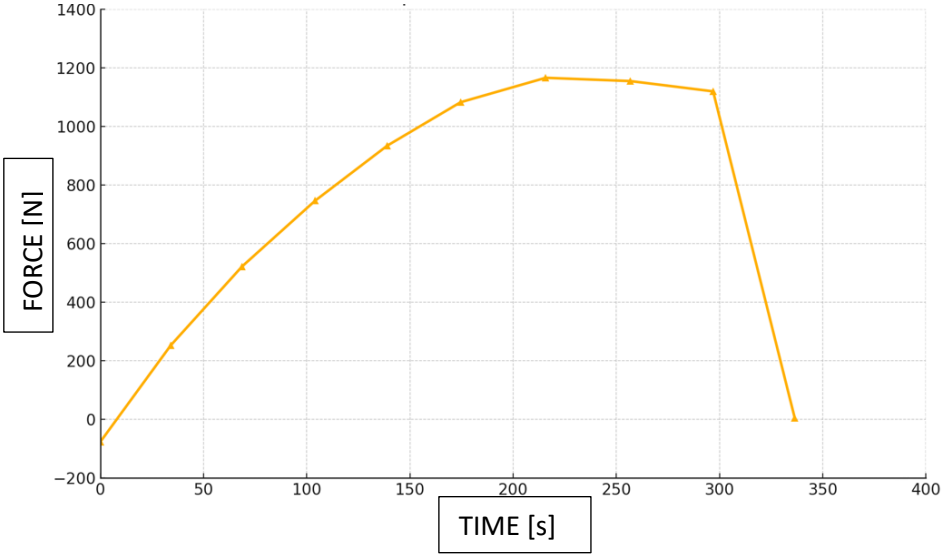


Figure 20. *Tensile strength testing of the second sample*

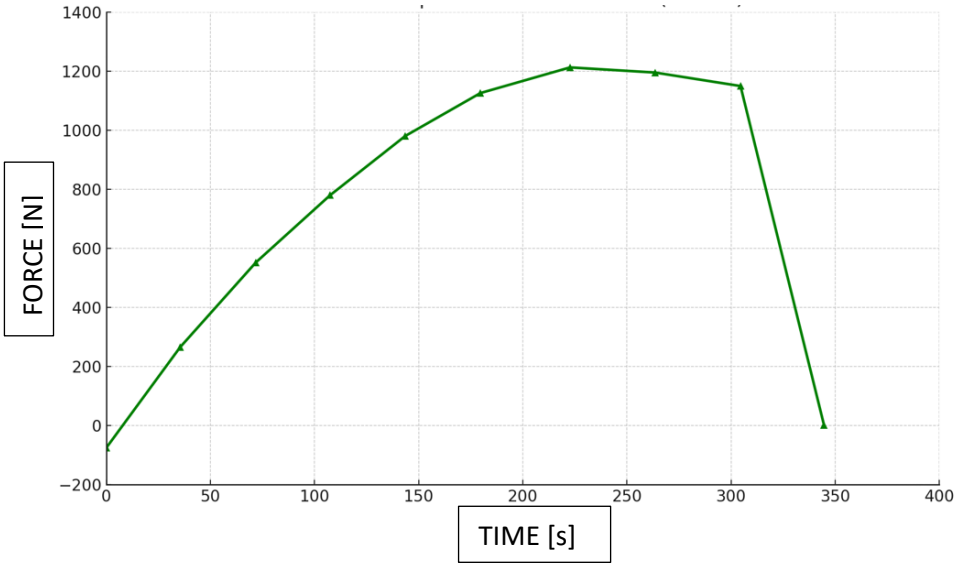


Figure 21. *Tensile strength testing of the third sample*

4. Discussion

A comprehensive characterization of the thermal and mechanical properties of additively manufactured samples was conducted to assess their suitability for the fabrication of bipolar plates in fuel cells. The testing focused on thermal conductivity, hardness, and tensile strength, with an emphasis on using an economical and functional material. The material used in this research was Protopasta Conductive PLA, a relatively low-cost filament, making it attractive for experimental prototyping at high volumes with minimal expense. Protopasta was selected to explore the possibility of economically producing functional components—such as bipolar plates—without significant investment in expensive composite materials.

It was essential to determine whether such an affordable material could meet the basic mechanical and thermal stability requirements expected of bipolar plates under real-world operating conditions. Despite its conductivity and acceptable mechanical properties, the material proved to be most reliable when processed using a 0.4 mm nozzle.

Due to the complexity of geometries and functional demands, two nozzles—0.2 mm and 0.4 mm—were tested to compare their performance in fabricating test specimens. However, the samples produced using the 0.2 mm nozzle were found unsuitable for reliable testing due to issues with layer quality, excessive brittleness, and unstable extrusion. In contrast, the 0.4 mm nozzle samples demonstrated significantly better dimensional stability and mechanical coherence. The results of thermal conductivity measurements showed that the 0.4 mm nozzle samples had slightly higher thermal conductivity than those produced with the 0.2 mm nozzle, likely due to a more homogeneous internal structure and better interlayer bonding. In particular, the average thermal conductivity of the specimens fabricated with the 0.4 mm nozzle was 0.2031 W/mK, compared to 0.1893 W/mK for those printed with the 0.2 mm nozzle. Although the numerical difference appears small, it clearly indicates that the larger nozzle produced samples with improved heat transfer capability, most likely due to enhanced interlayer bonding and reduced internal defects. This quantitative comparison confirms that nozzle diameter directly affects thermal conductivity, supporting the conclusion that the 0.4 mm nozzle is more suitable for achieving consistent thermal performance. For comparison, conventional bipolar plates fabricated from graphite typically exhibit thermal conductivity values in the range of 80–120 W/mK, while metallic plates (such as stainless steel or aluminum alloys) achieve values exceeding 15 W/mK. Composite plates generally fall between 5 and 25 W/mK, depending on filler content and matrix type. Although the measured thermal conductivity of Protopasta (0.19–0.20 W/mK) is significantly lower, the material still demonstrates sufficient heat transfer capacity for early-stage evaluation of flow-field designs and functional concepts.

Hardness was measured only on samples produced with the 0.4 mm nozzle, as the 0.2 mm samples lacked a sufficiently smooth and consistent surface for precise measurements. The recorded Shore D hardness value of 60.17 confirms the material's acceptable resistance to localized deformation.

Based on Figures 13, 14, and 15 for the three tensile specimens, differences in their mechanical behavior can be observed. Sample 1 (blue line) demonstrated the highest tensile resistance, achieving a maximum force of approximately 1220 N and elongating up to 340 seconds before sudden fracture. This curve indicates high tensile strength and relatively brittle failure at the point of fracture.

Sample 2 (orange line) displayed similar deformation behavior, but with a slightly lower maximum force (1180 N) and shorter time to fracture (330 seconds), suggesting marginally lower tensile strength while retaining similar fracture characteristics.

Sample 3 (green line) showed the lowest peak force (~1210 N) and the shortest deformation time (between 300 and 310 seconds). However, it was distinguished by a more gradual decline in force after the peak, indicating the possibility of some plastic deformation prior to final fracture.

Overall, tensile strength testing of the three Protopasta specimens produced by additive manufacturing revealed maximum force values ranging from 1180 N to 1220 N, indicating adequate load-bearing capacity under tensile stress. While bipolar plates in fuel cells are not typically subjected to significant tensile loads, but rather mechanical and chemical influences, the results suggest that this material, despite its lower strength compared to metals or composites, may still be suitable due

to advantages such as ease of processing, low weight, design flexibility, and corrosion resistance. When expressed in terms of ultimate tensile strength, these maximum forces correspond to values between 73.8 MPa and 76.3 MPa, based on the 4 × 4 mm² cross-sectional area of the specimens. Reporting the results in stress units allows for direct comparison with literature data, and it confirms that the material exhibits mechanical performance in the typical range expected for PLA-based composites. While the absolute thermal and mechanical values are lower than those of traditional bipolar plate materials, Protopasta offers unique advantages such as low weight, corrosion resistance, and simple processing through additive manufacturing. These attributes make it a suitable choice for producing prototypes and conducting conceptual testing, where rapid manufacturing and cost efficiency are prioritized over peak performance.

For comparison, a study by F. Parmaksiz et al. (2023) aimed to analyze different PLA filament compositions (PLA + CF, Tough PLA, PLA Wood, etc.) using layer thicknesses of 0.1, 0.2, and 0.3 mm. In the case of PLA+CF, thermal conductivity increased by 11.84% with a 0.3 mm layer thickness, confirming that larger layers (and more effective material flow) enhance thermal properties. They also concluded that hardness remains practically unchanged with varying layer thicknesses, which aligns with the findings of this study, regardless of the larger nozzle used [7].

In another 2023 study, it was confirmed that the mechanical properties of PLA materials are highly sensitive to print settings—subtle variations in geometry, speed, and layer thickness significantly affect interlayer cohesion. The authors emphasized that using finer nozzles such as 0.2 mm increases the risk of under-extrusion and internal defects, which corresponds with the issues encountered in the current study [8].

Additionally, research published in Entropy, titled "Specific Heat Capacity and Thermal Conductivity Measurements of PLA-Based 3D Printed Parts with Milled Carbon Fiber Reinforcement" (Blanco et al., 2022), provides a detailed analysis of the thermal properties of PLA filaments with 10%, 20%, and 30% milled carbon fiber (MCF) content. Their findings showed that adding fibers increased both thermal diffusivity and, consequently, thermal conductivity. However, they also noted that porosity and internal structural defects—especially in materials with higher fiber content—can limit improvements in thermal conductivity. This supports the observations from the present study: by optimizing printing parameters and reducing defects, improved homogeneity and more reliable heat transfer can be achieved [9].

5. Conclusion

In conclusion, the results of this study confirm that affordable materials such as Protopasta can serve as a valid basis for the development of functional components within fuel cell systems, provided that the printing process is properly optimized. Although the initial plan included testing samples produced with a 0.2 mm nozzle, technical difficulties prevented reliable testing of those specimens. On the other hand, samples fabricated using a 0.4 mm nozzle demonstrated better mechanical consistency and satisfactory thermal and tensile properties.

The results of thermal conductivity, hardness, and tensile strength measurements were consistent with values reported in the literature, confirming the reliability of the experimental procedures. For experimental prototyping, research validation, and basic functional testing, the use of cost-effective composite materials such as Protopasta Conductive PLA has proven to be both justified and beneficial. Although its performance is inferior to graphite, metals, or high-performance composites, the ease of production, reduced cost, and corrosion resistance make Protopasta a practical option for rapid prototyping of bipolar plates. This positions the material as a valuable tool in early-stage development of hydrogen fuel cells, particularly for conceptual validation and preliminary performance assessments. Its low cost, ease of processing through additive manufacturing, and satisfactory mechanical and thermal performance make it highly suitable for the rapid development and testing of conceptual designs.

References

[1] jj Fuel Cell Handbook (7th edition), 2004. U.S. Department of Energy, Morgantown

[2] Hoogers, G., 2003. Fuel Cell Technology, Handbook (1st edition), Florida

[3] Tomić, A. Z., 2022. Metode ispitivanja trajnosti membranskih elektrolizatora, Fakultet elektrotehnike, strojarstva i brodogradnje, Split

[4] Gustafsonn, S. E., 1991. Transient plane source techniques for thermal conductivity and thermal diffusivity measurements of solid materials

[5] Nagai, H., Hirao, K., Shimizu, T., Kusano, D., 2012. Application of Hot-disk Method to Thermal-Conductivity Measurement at High Temperature

[6] Kladarić, I. Mehanička svojstva materijala – vlačni pokus

[7] Parmaksiz, F., Anac, N., Kocar, O., Erdogan, B., 2023. Investigation of mechanical properties and thermal conductivity coefficients of 3D printer materials

[8] Kumar, M. S., Farooq, M. U., Ross, N. S., Yang, C., Kavimani, V., Adediran, A. A., 2023. Achieving effective interlayer bonding of PLA parts during the material extrusion process with enhanced mechanical properties

[9] Blanco, I., Cicala, G., Recca, G., Tosto, C., 2022. Specific Heat Capacity and Thermal Conductivity Measurements of PLA-Based 3D-Printed Parts with Milled Carbon Fiber Reinforcement

Comparison of the optimization results of a polyamide crane support obtained through numerical simulation and testing under operating conditions

***Amra Talić-Čikmiš*[1], *Kenan Šabanović*[1] *and Aida Imamović*[2]**

1) Faculty of Mechanical Engineering, University of Zenici Fakultetska 1, 72 000 Zenica, Bosnia and Herzegovina

2) Faculty of of Engineering and Natural Sciences, University of Zenici, Bosnia and Herzegovina

Corresponding author: amra.talic.cikmis@unze.ba

Professional article

Abstract: Building upon the numerical optimization of the polyamide support for the overhead crane control system, this paper investigates the performance of the redesigned component under real operating conditions. The improved support was installed on a fully functional crane and subjected to field testing in order to validate the previously simulated performance improvements. Additionally, the paper presents the development of an injection mold and the determination of optimal process parameters for manufacturing the component using polyamide material. The results confirm the structural reliability and efficiency of the optimized support in real-world applications, as well as the cost-effectiveness and technical viability of the proposed production method.

Keywords: *ANSYS Structural Optimization; conditions comparison of results; mass reduction; testing in working*

1. Introduction

he combination of numerical simulations and experimental validation has become a standard approach in the optimization of engineering components. Recent research on polymer structures [1,2] and crane systems [3] demonstrates how these methods can enhance reliability, reduce weight, and improve overall performance, providing a strong basis for the present study. In the previous study[4], special attention was given to the polyamide support of the overhead crane control system, a component whose function is to ensure safe access for workers regardless of the position of other crane elements. This independence of the control system from the crane’s moving components is crucial, as it allows operators to manage the system from any position within the workspace. However, due to frequent impacts at the ends of the crane guides, this support was identified as a critical point of failure, with the potential risk of severing the main control cable during operation (Figure 1). Building on these findings, the present work extends the analysis by subjecting the redesigned support to experimental testing and comparing the obtained results with numerical simulations in order to validate the reliability and accuracy of the proposed improvements.

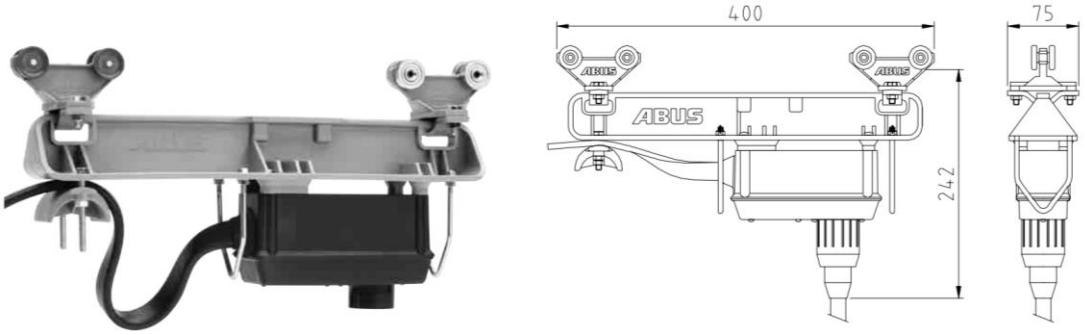


Figure 1. *Design of the observed support and its load [4]*

The manufacturer states in the characteristics of these supports that their carrying capacity is a maximum of 22 kg [5].
Furthermore, the adopted model is presented in comparison with the initial design, showing reduced mass and increased load-bearing capacity. For clarity, graphical representations of both the original and optimized models are provided (Figure 2).

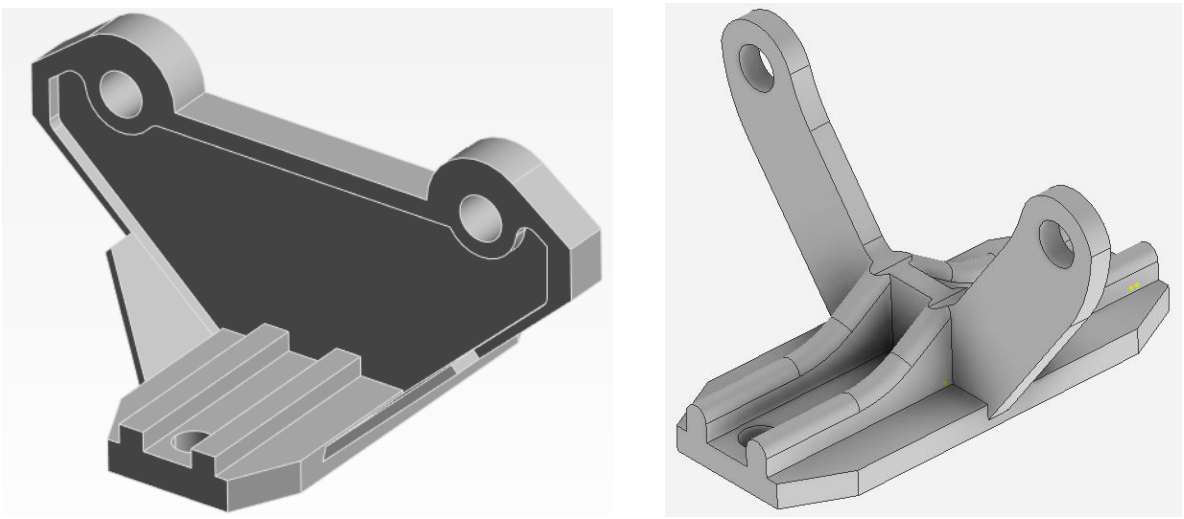


Figure 2. *Original support (left) Final support (right)*

2. Comparison of results and adoption of the load-bearing capacity of the optimized support

For easier comparison of the obtained results of numerical simulations for the original and optimized support model, it is first necessary to compile all obtained values of maximum equivalent stress, deflection, and safety factor against plastic deformation for the same load values and generally identical simulation settings into a single table (Table 1).

Table 1. *Overview of the obtained results for the original and optimized support model*

Model	Parameter	Static case	Static & Dynamic case
Original	Equivalent Stress	26,20 MPa	34,06 MPa
Optimized	Equivalent Stress	19,07 MPa	26,78 MPa
Original	Vertical Deformation	1,22 mm	1,22 mm
Optimized	Vertical Deformation	0,87 mm	0,87 mm
Original	Safety Factor	2,18	1,68
Optimized	Safety Factor	2,99	2,13

From the tabulated data, it can be observed that the obtained optimized support model is significantly more durable compared to the initial one. For the same applied load, both the equivalent stress and vertical displacement in both loading cases show a considerable reduction, while the safety factor against plastic deformation has correspondingly increased.
The obtained safety factors for the optimized support under a load of 30 kg — approximately 3 in the case of static force only, and around 2 in the case of combined static and dynamic forces — are more than satisfactory. However, it is necessary to take into account the possibility of improper use of the support, i.e., potential overloading in real conditions, the weight of components that represent permanent loads not included in the prescribed load capacity, the transfer of load by one side of the support in case of failure of the other, as well as possible lateral impacts. Considering all of these aspects, the optimal load-bearing capacity of the optimized support is adopted as 30 kg.

3. Experimental testing of the support under load

To confirm the results of the numerical analysis[4], experimental testing of both the original and optimized support was carried out, and the results were compared with the expected numerical values. The supports were 3D-printed using Nylon 66(Table 2), the same material applied in the numerical simulations [6]. Triangular infill patterns were used, as they represent the most geometrically resistant shapes. The following figures show the preparation for printing of the original and optimized support (Figure 3 i Figure 4).

Table2. *Mechanical properties of Nylon White [8]*

Property	Test Standard	Onyx	Nylon White
Tensile Strength (MPa)	ASTM D638	36	51
Tensile Modulus (GPa)	ASTM D638	1.4	1.7
Tensile Strain at Break (%)	ASTM D638	58	150
Flexural Strength (MPa)	ASTM D790*	81	50
Flexural Modulus (GPa)	ASTM D790*	3.6	1.4
Flexural Strain at Break (%)	ASTM D790*	N/A**	N/A**
Heat Deflection Temperature (°Celsius)	ASTM D648 Method B	145	41
Density (g/cm^3)	N/A	1.2	1.1

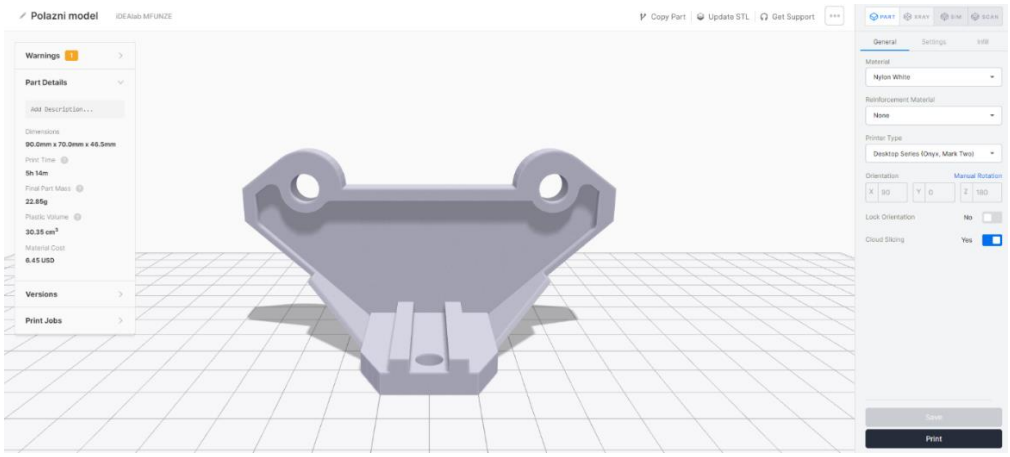


Figure 3. *Preparation of the original support model for 3D printing*

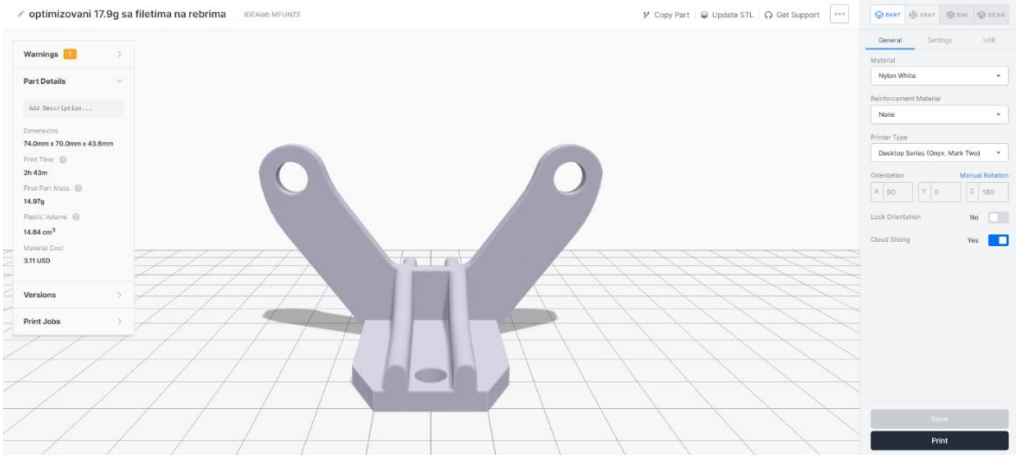


Figure 4. *Preparation of the optimized support model for 3D printing*

It is important to note a problem that occurred during the printing setup: due to the geometry of the original model, a complete internal infill was not possible, and a maximum of 55% infill was allowed. Therefore, this infill percentage was adopted for both support models to ensure the validity of the results. With this infill, the 3D-printed original support has a mass of 22.85 g (Figure 3) instead of the designed 25.60 g, while the optimized support has a mass of 14.97 g (Figure 4) instead of the designed 17.96 g. The 3D-printed supports are shown in the following figure (Figure 5).

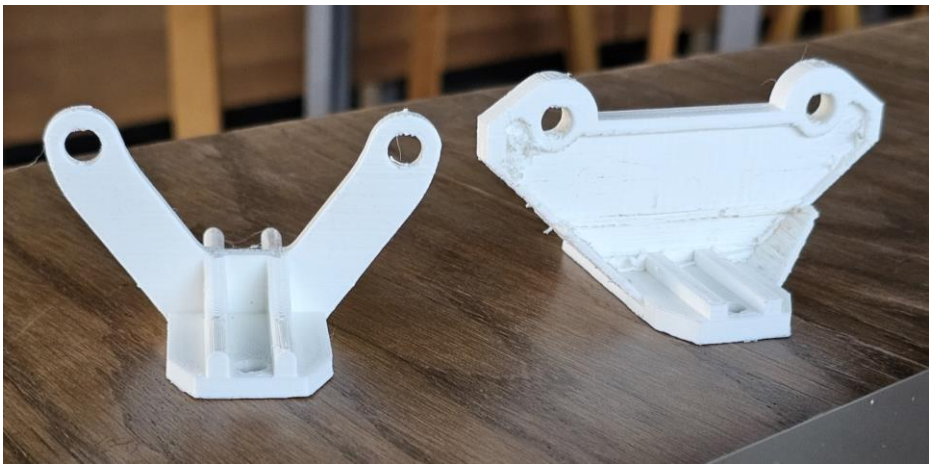


Figure 5. *3D-printed plastic supports – optimized (left) and original (right)*

The loading experiment of the supports was conducted using an improvised setup(Figure 6). In addition to the previously mentioned issue with the infill during the printing process, another problem arose due to equipment limitations. The initial plan was to load the fully printed supports with their prescribed load capacities and then with increased loads, and subsequently compare the obtained results with the expected numerical values. However, due to the lack of appropriate weights to simulate the load, the supports were tested with only a single load, which was lower than originally planned.

The supports were loaded on each side with one weight of 9.5 kg, giving a total load of 19 kg. The weights were attached to hooks connected to a fixture, as shown in the figure below. Due to the very specific geometry, it was nearly impossible to correctly place measuring tapes to capture the maximum stress resulting from the applied load. Therefore, the measured parameter was the deflection, i.e., the vertical displacement of the free end of the support. The deflection was measured using a displacement sensor positioned so that its probe was located at the very end of the support, in order to capture the deflection as accurately as possible.

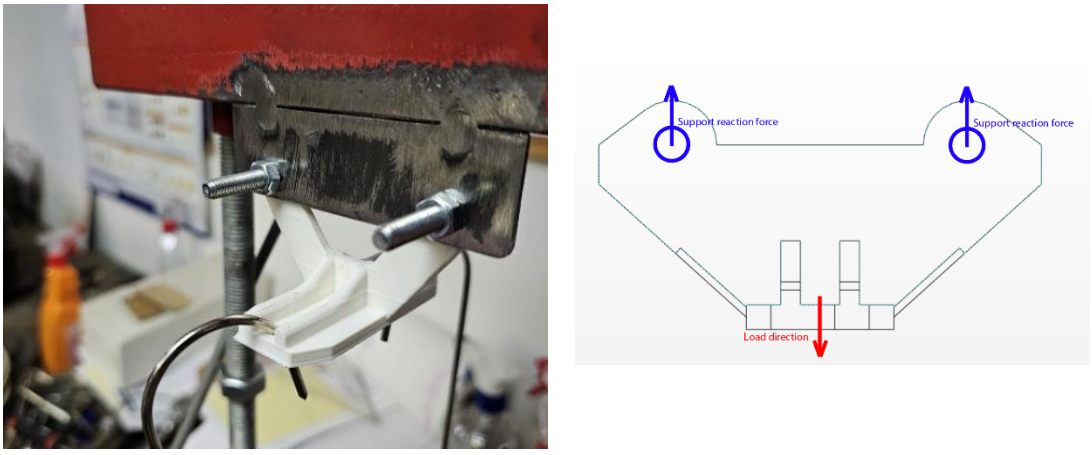
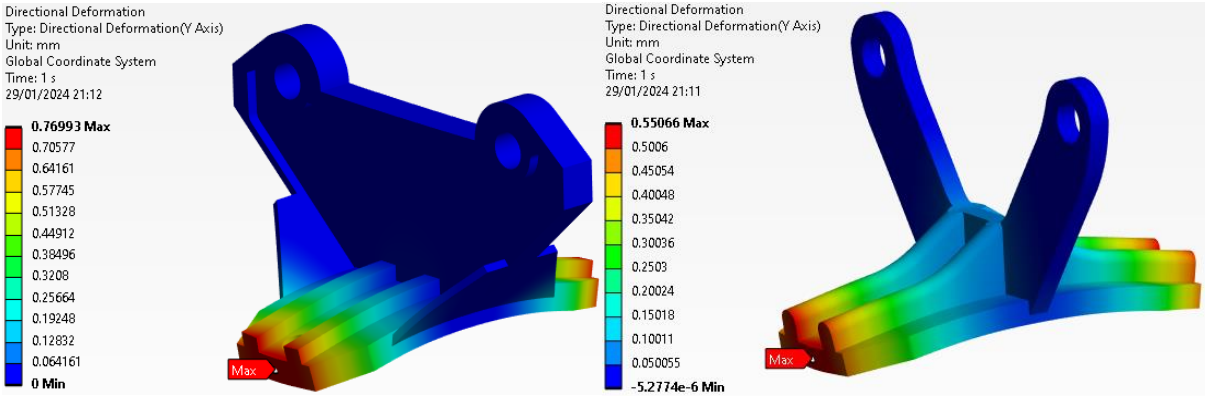


Figure 6. *Scheme of settings for conducting the experiment and the device on which the experiment was performed*

The LDR linear displacement sensor with an external controller is characterized by a short, compact design and a small diameter of only 8 mm. It has only one half-bridge coil. The plunger, which moves freely inside the sensor housing, is directly attached to the measuring object.
The measuring ranges are 10 mm, 25 mm, and 50 mm. The compact design of the sensor and its small diameter allow the installation of measuring systems in confined spaces.
Given the changed circumstances compared to the initial experimental plan, it was necessary to perform additional numerical simulations in order to have a basis for comparison with the experimentally obtained results. Therefore, simulations of the original and optimized supports were carried out under a vertical load of 19 kg, corresponding to a force of:

$$F_e = m_e \cdot g = 19\ kg\ \cdot 9{,}81\ \mathrm{m}/s^2 = 186{,}39 \qquad (1)$$

However, since, as previously mentioned, the supports were 3D-printed with 55% infill, the experimental results cannot exactly match the numerical ones, because the simulation software does not allow modeling of partially filled structures and assumes a fully solid infill. Therefore, the numerical analysis here is only used to determine the expected percentage reduction in deflection of the optimized support compared to the original one. The deflection results are presented in Figure 7.



a) *b)*

Figure 7. *Deflection of the original model a) under a load of 19 kg and b) Deflection of the optimized model under a load of 19 kg*

From the figures, it can be seen that the optimized support is expected to have approximately 28% lower deflection compared to the original support. The experimental results show a deflection of 0.99 mm for the original model, while the optimized support exhibited a deflection of 0.74 mm, representing a reduction of 0.25 mm, or 25.25%, compared to the original support.
The obtained result is excellent in relation to the expected value and confirms that the optimized support indeed experiences smaller deflections. The complete output from the displacement sensor, which measured the deflection, is provided as experimental evidence in the appendices of this work for both the original and optimized supports. Only the values at the final moment should be considered, as the load is stabilized at that point and the actual deflection is obtained.
The Table 3 presents an overview of the expected and experimentally obtained deflections for both supports under a load of 19 kg.

Table 3. *Overview of the obtained results for the original and optimized support under a 19 kg load*

Parameter	Original support	Optimized support	Deviation optimized/ original support
Deformation – numerical	0,77 mm	0,55 mm	-28,57 %
Deflection – experimental	0,99 mm	0,74 mm	-25,25 %

Its optimization was carried out, specifically through the improvement of its geometry, resulting in a significant increase in load-bearing capacity of approximately 36%, while simultaneously reducing the mass by about 30%, as shown in the Table 4. Through the optimization, the prescribed load capacity of the support was increased from 22 kg to 30 kg. The actual load capacity is even higher, but a lower prescribed value is adopted to ensure a safety margin against potential load increases.

Table 4. *Comparison of characteristics of the original and optimized support*

Characteristic	Original support	Optimized support	Deviation
Mass	25,60 g	17,96 g	-29,84 %
Load capacity	22 kg	30 kg	36,36 %

4. Conclusion

The aim of this study was to optimize the polyamide support of the overhead crane control system using numerical simulations, with validation provided through experimental testing. The results confirmed that the redesigned support achieved significant improvements in both strength and efficiency, while simultaneously reducing weight.

This work illustrates the value of combining simulation-driven optimization with experimental verification, showing that numerical models can reliably predict real structural behavior[1,2,3,7]. The applied approach not only improved the performance of the investigated component but also demonstrated a methodology that can be extended to other elements of crane systems and similar engineering applications.

References

[1] Sommer, D. et al., 2024. Optimization of Mechanical Properties and Evaluation of Fatigue Behavior of Selective Laser Sintered Polyamide-12 Components’, Polymers, 16(10)

[2] Al Rashid, A., Koç, M., 2022. Experimental validation of numerical model for thermomechanical performance of material extrusion additive manufacturing process: Effect of process parameters, Polymers, 14(17), Article 3482

[3] Bretotean Pinca, C., Tirian, G. O., Josan, A.,2009. Application of finite element method to an overhead crane bridge, WSEAS Transactions on Applied and Theoretical Mechanics, 4(2), pp. 64–73.

[4] ABUS Komponenten, Germany, 2019.

https://www.abus-kransysteme.de/download/de/91/abus_komponenten_a.pdf (accessed 15 February 2024).

[5] Talić-Čikmiš, A ., Šabanović, K., Barlov, A., Imamović, A., 2024. Optimization of polyamide support of the overhead crane control system, MTSM 2024, Split

[6] Ertalon 66 SA, UK, 2011.

https://www.theplasticshop.co.uk/plastic_technical_data_sheets/nylon_66_technical_data_sheet.pdf (accessed 15 February 2024).

[7] Imamović, M., Hadžikadunić, F., Talić-Čikmiš, A., Bošnjak, A., 2019. Examples of kinematic analysis of complex mechanism using modern software applications, IRMES 2019, Research and Development of Mechanical Elements and Systems Participation, Kragujevac, Serbija

[8] https://support.markforged.com/portal/s/article/Nylon-White (accessed 15 July 2025).

Electrocoagulation and hybrid electrocoagulation for wastewater treatment: strength, challenges and future prospects

***Ladislav Vrsalović*[1], *Senka Gudić*[1], *Nediljka Vukojević Medvidović*[1], *Sandra Svilović and Mario Nikola Mužek*[1]**

1) University of Split, Faculty of Chemistry and Technology, Ruđera Boškovića 35, 21000 Split, Croatia

Corresponding author: ladislav@ktf-split.hr

Review article

Abstract: Electrocoagulation (EC) is an electrochemical method used for water treatment, based on the electrochemical generation of coagulants from sacrificial metal electrodes, typically aluminium or iron. The process involves the anodic dissolution of the metal in parallel with the cathodic hydrogen evolution, generating hydroxide anions. This process leads to the in situ formation of metal hydroxides in the bulk solution, which act as primary agents for the destabilisation and agglomeration of colloidal and dissolved pollutants. As a method that integrates electrochemical principles with classical coagulation mechanisms, EC is increasingly recognised as a technologically viable alternative aligned with the demands for sustainable and energy-efficient wastewater treatment. This paper outlines the principles and applications of EC and hybrid EC systems, the strengths and limitations of the technology, along with the key directions for future research and development.

Keywords: *electrocoagulation; waste water treatment; organic polutants; inorganic polutants; hybrid processes*

1. Introduction

The challenges related to the availability and quality of water resources have intensified considerably over the past decades. These issues are primarily attributed to the growth of the global population, which is accompanied by deforestation, rapid urbanisation, industrialisation, and climate change. Consequently, existing aquatic environments have become increasingly loaded by diverse pollutants—ranging from heavy metals to structurally complex organic compounds—whose presence poses significant threats to both ecosystems and public health. The growing demand for clean water is closely related to the ongoing demographic expansion, underscoring the urgency for sustainable water management strategies [1-3]. Wastewater management remains the utmost challenge to environmental sustainability and public health.

Conventional wastewater treatment approaches rely on a wide range of established technologies, including physicochemical methods, biological treatments, adsorption techniques and more recent innovations such as advanced oxidation processes (AOPs) and membrane filtration [3-13]. Physico-chemical treatments usually require substantial chemical input, which not only elevates operational expenditure but also complicates downstream treatment steps and increases the risk of secondary pollution [14]. AOP-s typically rely on highly reactive oxidising agents, which, while effective, impose significant operational costs and raise safety concerns due to the handling of hazardous chemicals [15]. Biological treatment systems, although environmentally favourable, require tightly regulated environmental conditions, long treatment time and extensive treatment facilities [16,17]. Moreover, biological treatment sometimes results in the generation of undesirable metabolic byproducts. Emerging methods such as membrane filtration and adsorption alone frequently prove insufficient without robust pretreatment stages. Otherwise, membrane filtration methods tend to suffer from declining performance due to membrane fouling or pore blockage, leading to reduced permeate flux and overall inefficiency [18,19]. In light of these challenges, electrochemical processes have gained considerable attention in recent years as a promising alternative. They offer notable advantages in terms of process controllability, pollutant removal efficiency, and the potential for integration with

renewable energy sources, making them increasingly attractive for advanced wastewater treatment applications. Some of disadvantages of electrocoagulation are: possibility of electrode passivation during EC process which reduces surface area, increases resistance and lowers efficiency; need for periodical cleaning and replacing of the electrodes; operational complexity at large scale industrial applications which requires sophysticaded parameters monitoring and automatization; variation of energy consumption depending on the conditions; inadeqeuacy for highly polluted water without pretreatment, etc. [20-22].

This mini-review paper will present the general mechanism of the electrocoagulation process, highlight the advantages and disadvantages of the method, as well as the potential for combining it with other wastewater treatment techniques, with particular emphasis on the research conducted at the Faculty of Chemistry and Technology, University of Split.

2. Principles of electrocoagulation

In the simplest configuration, an electrocoagulation setup consists of two metallic electrodes, connected to a rectifier that serves as the power source. The electrode connected to the positive pole of the rectifier is called the anode, and the electrode connected to the negative pole of the rectifier is called the cathode. These electrodes are immersed in the electrochemical reactor filled with the wastewater (Figure 1 a) and b)). In a laboratory condition, a magnetic stirrer is typically used to ensure the movement of the electrolyte inside the reactor, thereby eliminating concentration and temperature gradients and achieving a uniform distribution of electrogenerated coagulants. Mixing improves mass transport of reactants to the electrode surfaces, thereby increasing the efficiency of electrochemical reactions, and also enhances collisions between destabilised colloids, resulting in the formation of larger flocs that are easier to remove via sedimentation, flotation, or filtration.

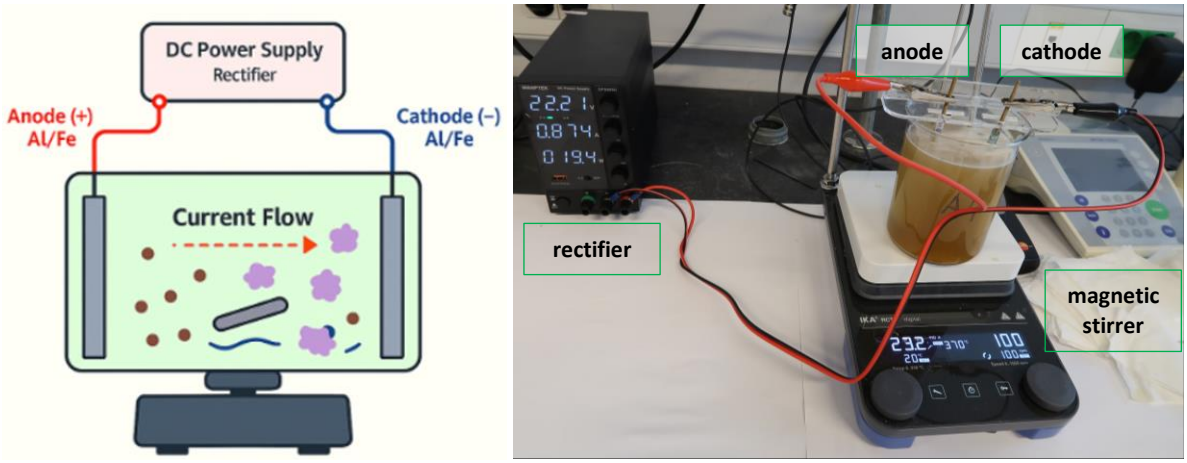


Figure 1. *Basic setup for electrocoagulation process a) schematics, b) photo from the laboratory*

When a direct current is applied, the oxidation reaction is evolved on the anode, which results in its dissolution and the formation of metal cations:

$$M_{(s)} \rightarrow M^{n+}_{(aq)} + ne^- \quad (1)$$

If the anode potential is sufficiently high, the secondary anodic reaction - oxygen evolution reaction can also occur:

$$2H_2O_{(l)} \rightarrow 4H^+_{(aq)} + O_{2(g)} + 4e^- \quad (2)$$

On the cathode, the hydrogen evolution reaction, as a cathodic reaction is taking place:

$$2H_2O_{(l)} + 2e^- \rightarrow H_{2(g)} + 2OH^-_{(aq)} \quad (3)$$

Depending on the pH of the solution, the oxygen reduction reaction can also take place in neutral or alkaline solutions:

$$O_{2(g)} + 2H_2O + 4e^- \rightarrow 4OH^- \quad (4)$$

In electrocoagulation processes, aluminium (Al) and iron (Fe) alloys are most commonly used as electrode materials due to their electrochemical, economic, and environmental advantages.
Electrocoagulation relies on the anodic dissolution of the metal, which releases metal ions that form hydroxides (e.g., $Al(OH)_3$, $Fe(OH)_3$) in aqueous solution. These hydroxides act as coagulants – agents that destabilise colloids and suspended particles. Formation of Al and Fe hydroxides can be described with the following equations (5-9):

Aluminium:

$$Al_{(s)} \rightarrow Al^{3+}_{(aq)} + 3e^- \quad (5)$$

$$Al^{3+}_{(aq)} + 3OH^- \rightarrow Al(OH)_3 \quad (6)$$

During the anodic dissolution of aluminium, other ionic species are also formed, and the situation is more complex than what is suggested by the simple chemical equations. Thus, formed Al^{3+} cations, further react and transform into various monomeric and polymeric ionic forms such as $Al(OH)^{2+}$, $Al(OH)_2^+$, $Al_2(OH)_2^{4+}$, and $Al(OH)_4^-$, $Al_6(OH)_{15}^{3+}$, $Al_7(OH)_{17}^{4+}$, $Al_8(OH)_{20}^{4+}$, $Al_{13}O_4(OH)_{24}^{7+}$, and $Al_{13}(OH)_{34}^{5+}$ along with the low soluble amorphous species such as $Al(OH)_3$ and Al_2O_3, which depend on the initial pH of the solution [23-25].

Iron:

$$Fe_{(s)} \rightarrow Fe^{2+}_{(aq)} + 2e^- \quad (7)$$

$$Fe^{2+}_{(aq)} + 2OH^- \rightarrow Fe(OH)_2 \quad (8)$$

$$Fe^{3+}_{(aq)} + 3OH^- \rightarrow Fe(OH)_3 \quad (9)$$

In acidic solution, the dominant cation is the Fe^{2+} ion, which in neutral solutions hydrolyses to $FeOH^+$ and $Fe(OH)_2(aq)$ and can finally precipitate in the form of $Fe(OH)_2(s)$. Anionic complexes, such as $Fe(OH)_3^-$ and $Fe(OH)_4^{2-}$have been observed in alkaline solutions. Regarding the iron(III), in acidic solutions the aqueous complex Fe^{3+} forms and further hydrolyses to $FeOH^{2+}$, $Fe(OH)_2^+$, $Fe(OH)_3(aq)$ with the rise of solution pH, and the possibility of forming several polynuclear complexes [26,27].
$Al(OH)_3$ and $Fe(OH)_3$ exhibit amorphous, flocculent structures that efficiently remove suspended solids, organic pollutants, and heavy metals.
Aluminium and iron are cost-effective, abundant, and well-established materials in industry. Their affordability makes them suitable for large-scale wastewater treatment. The oxidation products of Al and Fe do not produce toxic byproducts. The resulting metal hydroxides have a high adsorption capacity, enabling secondary immobilisation of contaminants.

3. Application of electrocoagulation in wastewater treatment – examples

Synthetic dyes present dangerous water pollutants as they are widely used in significant quantities in different branches of industries such as textile, leather, paper, plastics, food, cosmetics, printing, and dye manufacturing industries [28-30]. They are highly stable organic compounds persistent to different chemical and photolytic processes, and therefore potentially pose a bioaccumulation risk in the natural environment. Hence, the treatment of dye-contaminated wastewater presents one of the most challenging tasks [31,32]. Electrocoagulation presents an efficient method for their removal from the wastewater. Gudić et al. [33] investigated the possibility of removing Crystal Violet dye (CV) from synthetic wastewater solutions by electrocoagulation using AA2007 aluminium alloy electrodes in a current density range of 0.016 to 0.032 A/cm^2 and initial pH values ranging from 3.2 to 7.0. The concentration of the dye was determined using a spectrophotometer. Dye removal increased with the increase in current density and process duration, yielding the best results at an initial solution pH of 5.5. At the maximum applied current density of 0.032 A/cm^2 results is almost 100% colour removal after 40 minutes. Figure 2 shows solution colour changes as a function of electrocoagulation time.

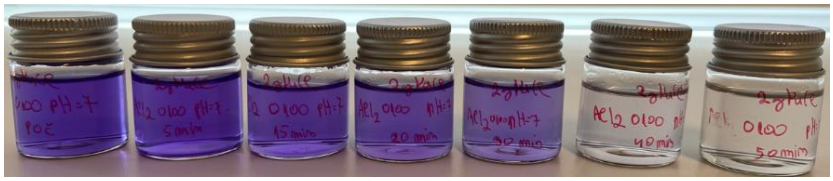


Figure 2. *Changes in the colour intensity as a function of electrocoagulation time*

Similarly, the electrocoagulation method was used for the removal of Tartrazine Yellow (TY) azo dye, using the same experimental setup, and the process optimisation was performed using response surface methodology [34]. The effects of current density, *i* (0.008–0.024 A/cm^2), initial solution pH (3.0–7.0), and treatment time, t (10–50 min) on main process parameters like pH, temperature (T), TY dye concentration (c) and removal efficiency (R), changes in the mass of anode, and sludge characterisation were studied. The experimental plan was developed using Design-Expert software. High removal efficiency is achieved more quickly with an increase in current density and a decrease in initial pH. The final removal efficiency of the TY dye was in the range between approx. 28% and 99% as a function of the experimental conditions (current density, initial pH, and treatment time) (Figures 3 and 4) [34,35].

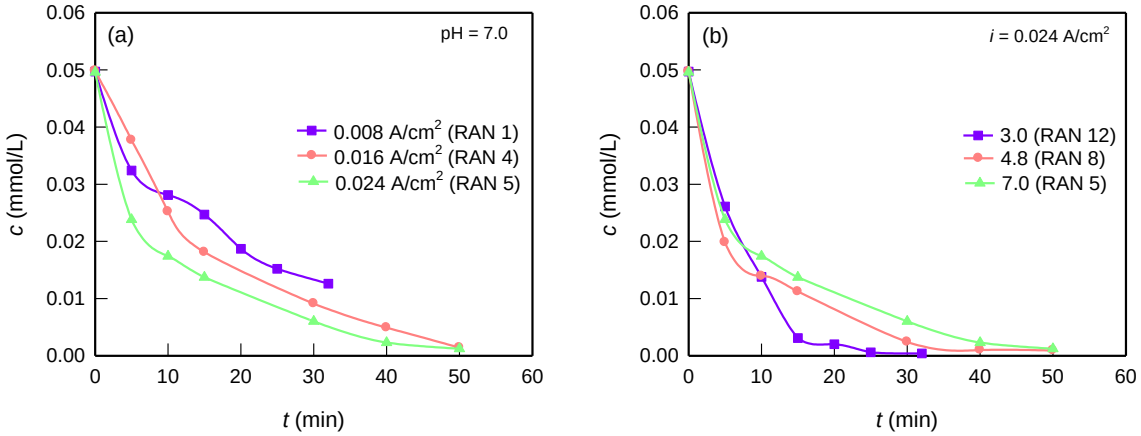


Figure 3. *TY concentration changes during the EC process: a) at different initial pH of the solution, b) at different current densities [34,35]*

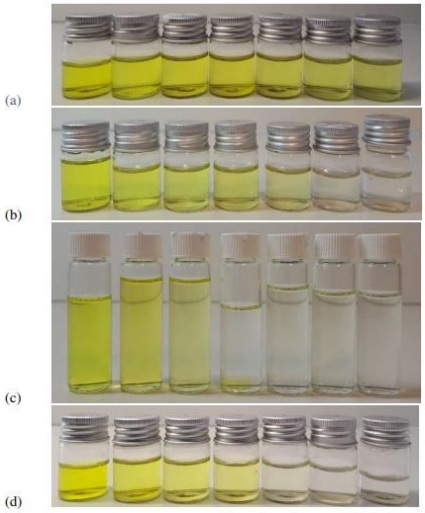


Figure 4. *TY samples collected after different times of EC process: a) i = 0.008 A/cm^2, pH = 7.0, b) i = 0.024 A/cm^2, pH = 7.0, c) pH = 3.0, i = 0.024 A/cm^2 and d) pH = 4.8, i = 0.024 A/cm^2 [34,35]*

Diaz et al. [36] investigated electrocoagulation-adsorption processes for the removal of the cationic dye malachite green (MG) and the anionic dye Remazol yellow (RY). They have found that the

continuous electrocoagulation-adsorption system was more efficient for removing dyes than electrocoagulation alone. To investigate the remediation of real complex wastewater solutions using electrocoagulation, compost lachetate solutions with varying initial chemical oxygen demand (COD) concentrations (ranging from 381.52 to 1675.80 mg O_2/L) were used [37]. The experiments were performed in the electrochemical batch-type reactor with different operating parameters such as the electrode material (Fe, Al, Zn), initial pH (4, 6 and 8), the addition of NaCl electrolyte (0.5, 1, and 1.5 g/L), and addition of zeolite (15, 20 and 25 g/L). The results show that high removal for both COD and turbidity was obtained with all of the electrode materials investigated (Table 1).

Table 1. *Final values and removal efficiency of turbidity and chemical oxygen demand (COD) in suspension after ECZ experiments are planned according to Taguchi's L9 orthogonal array design [37].*

Exp. No.	Experiment mark	Final values Turbidity, NTU	COD, mg/L	TS, g/L	Turbidity	Removal percentage COD
1	ECZ-Fe, pH=4, 0.5 g/L NaCl, 15 PZ g/L	2.04±0.08	40.550±1.84	0.84±0.11	98.78	92.97
2	ECZ-Fe, pH=6, 1.0 g/L NaCl, 20 PZ g/L	2.45±0.09	62.669±3.19	1.25±0.18	98.53	89.14
3	ECZ-Fe, pH=8, 1.5 g/L NaCl, 25 PZ g/L	1.55±0.05	81.101±3.69	1.76±0.15	99.07	85.94
4	ECZ-Al, pH=4, 1.0 g/L NaCl, 25 PZ g/L	0.23±0.01	33.178±1.84	1.25±0.18	99.86	94.25
5	ECZ-Al, pH=6, 1.5 g/L NaCl, 15 PZ g/L	0.77±0.01	55.296±3.69	1.76±0.16	99.54	90.42
6	ECZ-Al, pH=8, 0.5 g/L NaCl, 20 PZ g/L	0.29±0.04	40.550±1.84	0.96±0.12	99.83	92.97
7	ECZ-Zn, pH=4, 1.5 g/L NaCl, 20 PZ g/L	36.3±0.10	62.669±3.19	1.84±0.16	78.26	89.14
8	ECZ-Zn, pH=6, 0.5 g/L NaCl, 25 PZ g/L	13.89±0.02	58.982±3.69	0.86±0.14	91.68	89.78
9	ECZ-Zn, pH=8, 1.0 g/L NaCl, 15 PZ g/L	47.50±0.30	66.355±1.84	1.50±0.18	81.56	88.50

The anode consumption was changed in order: Zn > Fe > Al, and analysis of the electrode surfaces using an optical microscope revealed pitting, general or uniform corrosion, along with partial surface coverage by a layer of corrosion products, depending on the experimental conditions [37]. The results of this study confirm that Fe, Al, and Zn can be used as electrodes by electrocoagulation combined with zeolite (ECZ) in the treatment of compost leachate, resulting in a significant improvement in water quality. ECZ has proven to be an effective method for treating compost leachate, especially in reducing the COD and turbidity in moderately polluted compost leachate, achieving a COD reduction of 85–92%, and a turbidity removal of 78–99%.

In their subsequent investigation, Vukojević Medvidović et al. [38] compared the treatment efficiency of biowaste compost leachate with electrocoagulation and electrocoagulation in the presence of zeolite (ECZ) at different stirring speeds, electrode distances, and the addition of electrolytes. The leachate was obtained from the composting mass in an open container. The natural zeolite used in this study originated from the Zlatokop deposit in Vranjska Banja, Serbia, with a zeolite particles size of 0.1–0.5 mm. Electrodes were made from AA2007 aluminium alloy. The results have shown that the stirring speed, electrode distance, addition of zeolite, and electrolyte influence the efficiency of COD and TNK removal. In contrast, turbidity removal is very high, independently of the investigated experimental conditions (Table 2).

Table 2. *Final values and removal efficiency of turbidity, chemical oxygen demand (COD), total Kjeldahl nitrogen (TNK), and total solids (TS) in suspension after EC experiments [38].*

Exp. No.	Experiment	Final Values				Removal Percentage, %		
		Turbidity, NTU	COD, mg/L	TN_K, mg/L	TS, g/L	Turbidity	COD	TN_K
1	$EC_{70rpm+EL}$	3.38	88.47	14.01	1.165	96.12	68.21	54.55
2	$EC_{200rpm+EL}$	2.29	62.67	0.56	1.175	97.37	77.48	98.18
3	$EC_{400rpm+EL}$	0.77	25.81	5.60	1.165	99.12	90.73	81.82
4	EC_{70rpm}	3.26	51.61	14.01	0.16	96.27	81.46	84.55
5	$ECZ_{70rpm+EL}$	0.88	47.92	30.82	1.045	99.00	82.78	0.00
6	$ECZ_{200rpm+EL}$	0.99	22.12	8.40	0.98	98.86	92.05	72.73
7	$ECZ_{400rpm+EL}$	1.43	22.12	11.21	1.08	98.37	92.05	63.64
8	ECZ_{70rpm}	2.78	7.37	8.40	0.30	96.82	97.35	72.73
9	$EC_{1.5cm+EL}$	0.50	14.75	30.82	1.70	99.43	94.70	0.00
10	EC_{3cm+EL}	0.59	0.00	5.60	1.53	99.33	100.00	81.82
11	$EC_{4.5cm+EL}$	3.38	88.47	5.60	1.165	96.12	68.21	81.82
12	$EC_{1.5cm}$	1.61	3.69	5.60	0.295	98.15	98.68	81.82
13	$ECZ_{1.5cm+EL}$	0.38	147.46	5.60	1.545	99.56	47.02	81.82
14	ECZ_{3cm+EL}	0.39	40.55	19.61	1.68	99.56	85.43	36.36
15	$ECZ_{4.5cm+EL}$	0.88	47.92	30.82	1.045	99.00	82.78	0.00
16	$ECZ_{1.5cm}$	0.45	7.37	2.80	0.32	99.48	97.35	90.91

Investigations have shown that zeolite particles increase treatment efficiency in the ECZ process. Additionally, zeolite in solution affects the electrode surface by cleaning the formed surface layers during mixing, thereby reducing fouling and electrode passivation, and contributing to the uniform dissolution of the anodes [37,38].

Vukojević Medvidović et al. [39] continued their research by investigating the influence of synthetic zeolite (SZ) particle size (<90, 90–160, and 160–600 μm) on ECZ treatment of compost leachate with a high organic load. The results have shown that the largest zeolite particle size, ranging from 160 to 600 μm, generally results in a lower increase in pH and temperature, as well as a higher decrease in COD and turbidity. A significant effect on the measured parameters also depends on the electrode type, current density, and contact time [39].

The electrocoagulation method, combined with zeolite in a single step, was efficiently applied to treat municipal wastewater with saline water infiltrate [40]. For this experiment, municipal wastewater was collected from the wastewater treatment plant Stupe, Croatia, and analysed in terms of determining electrical conductivity, pH, turbidity, chemical oxygen demand (COD), total Kjeldal nitrogen (TKN) and biochemical oxygen demand (BOD5). The electrocoagulation was performed with AA2007 aluminium alloy electrodes. Approximately 12 experiments were conducted to investigate the influence of the initial pH values of the solution, the addition of zeolite (20 g/L), and electrolyte (1 g/L NaCl) on the efficiency of electrocoagulation at a contact time of t = 60 min. The results show that adjusting the initial pH values and adding zeolite have no significant effect on reducing electrical conductivity, and the removal efficiency varies in the range of 53.26–65.79%. The highest turbidity reduction is achieved (97.14%) at pH = 4, while the addition of zeolite under the same conditions results in a lower turbidity removal efficiency (62.14%). Overall, reductions in electrical conductivity (in the range of 17.00–65.79%), turbidity (in the range of 61.28–97.44%), COD (in the range of 77.08–92.71%), and total Kjeldahl nitrogen (in the range of 33.33–90.48%) were observed. The application of electrocagulation for municipal wastewater treatment was also studied by other researchers [41-43].

Ascon found out that the electrocoagulation process can significantly reduce the existence of bacteria *Echerichia colly* in municipal wastewater. With the experimental setup of neutral pH of 7, amperage of 3 A, and treatment time of 60 min, he achieved the highest *E. coli* removal efficiency of 99.9% [44]. Cutting-oil emulsions are used as lubricants and coolants in metalworking processes. Due to its complex composition, used cutting-oils have potential for high levels of contamination and rancid odours due to the presence of emulsifiers, corrosion inhibitors, extreme pressure agents, biocides or antifoam compounds [45,46]. Therefore, it should be removed from the wastewater, most commonly with micro and ultrafiltration, but in combination with an effective pretreatment method, which will prevent the occurrence of irreversible fouling on membrane pores. Electrocoagulation has been shown as an excellent pretreatment process for cutting-oil emulsion removal [47].

The electrocoagulation process can be efficiently used in the removal of heavy metals from wastewater. Thus, Bacry et al. [48] have studied the removal of lead, cadmium, zinc, chromium, nickel, manganese, and copper as individual elements and in mixtures of synthetic and real wastewater by electrocoagulation, using aluminium electrodes as anodes and stainless steel electrodes as cathodes. A complete removal (100%) was achieved for Pb after 20 min at 5 mA/cm^2, for Ni after 40 min at 5 mA/cm^2, for Cu at 40 min at 5 mA/cm^2, while for other elements the percentage of removal was 98% for Cd after 40 min at 15 mA/cm^2, 98% for Zn after 40 min at 5 mA/cm^2, 98% for Cr after 60 min at 5 mA/cm^2, 98% for Mn after 60 min at 15 mA/cm^2. Kumar et. al. [49] have shown that electrocoagulation can be successfully performed for more than 99% removal of arsenic in contaminated drinking water using iron electrodes. Pikna et al. have shown the possibility of complete chromium removal using the electrocoagulation method with steel electrodes [50,51]. New investigations have shown its applicability in the removal of microplastics [52,53].

These examples have shown the versatility of electrocoagulation process application in wastewater treatment.

4. Balancing Efficiency and Sustainability in EC Process Design

Designing an effective EC or hybrid EC process requires more than simply achieving high pollutant removal from the aqueous phase. A truly optimized process must strike a balance between treatment efficiency and long-term sustainability. This involves a comprehensive evaluation of multiple interrelated factors that influence both performance and operational feasibility. One of the key parameters is electrode consumption, which is particularly important due to passivation or corrosion behaviour. The second key important parameter is electrical energy demand. Namely, high energy consumption can compromise the environmental and economic viability of the treatment system, while excessive electrode degradation can lead to reduced process efficiency and increased material costs.

Equally important are the settling characteristics of the floccules generated during treatment. Floccules with poor sedimentation behaviour may result in inadequate solid–liquid separation, requiring additional post-treatment steps and increasing sludge handling complexity.

Therefore, process optimization must take into account:

- Operational parameters (current density, treatment time, pH, electrode configuration),
- Resource consumption (electrode wear, energy use),
- Effluent quality (residual turbidity, pollutant concentrations),
- Sludge properties (volume, settling rate, dewaterability).

Advanced optimization tools such as design of experiments (DoE), response surface methodology (RSM), or Taguchi are often employed to systematically investigate the interactions among these variables and to identify optimal conditions. Ultimately, a balanced EC process design ensures not only high removal efficiency but also operational robustness, cost-effectiveness, and environmental compatibility—key criteria for real-world applications.

5. Further developments in the electrocoagulation and hybrid EC processes

Traditional EC systems face challenges related to energy consumption, operational cost, and sustainability. Therefore, ongoing research and technological development will be focused on enhancing process efficiency, economic viability, and environmental sustainability. Three significant directions for further improvement include:

1. Utilization of waste or recycled metals as electrode materials**,**
2. Integration of renewable energy sources such as wind and solar power**,**
3. Implementation of hybrid systems combining EC with complementary treatment technologies**.**

A promising strategy for increasing the sustainability of EC is the substitution of conventional sacrificial electrodes (commonly aluminium or iron) with waste or recycled metal materials. This approach contributes to circular economy principles, reduces raw material costs, and mitigates environmental impacts related to mining and metal processing. Studies have demonstrated that electrodes fabricated from scrap iron, recycled aluminium cans, and industrial metal waste can perform comparably to commercial electrodes in pollutant removal, including heavy metals, dyes, and organic contaminants [54-56]. However, issues such as impurity content, structural uniformity, and electrode longevity must be addressed through proper material pre-treatment and system optimization.

EC, in addition to enabling the removal of a wide range of pollutants, has demonstrated promising potential as a sustainable technology for simultaneous hydrogen production, a clean and renewable energy carrier. In the EC process, the anode undergoes dissolution under the influence of electric current, releasing metal ions that act as coagulants. Simultaneously, water is reduced at the cathode, resulting in the evolution of hydrogen gas (H_2). If properly captured, the hydrogen generated at the cathode can be utilized as a clean energy source, effectively transforming the EC process into a dual-function system—for both wastewater purification and green hydrogen production [57,58].

This innovation further closes the resource loop: waste is repurposed into electrodes that treat wastewater while simultaneously producing hydrogen. Such an approach exemplifies circular economy principles and sustainable engineering, where waste is redefined as a resource with added value. The integration of water treatment and energy production within a single system represents an attractive pathway toward the development of hybrid technologies for resource recovery, especially in the context of carbon footprint reduction and increased energy efficiency in both industrial and municipal settings.

Conventional EC systems rely on grid electricity, often derived from fossil fuels. Transitioning to renewable energy sources—notably solar and wind energy—represents a crucial step toward greener operation. Off-grid EC systems powered by photovoltaic panels or wind turbines have been successfully deployed in remote or energy-scarce regions, particularly for small-scale wastewater

treatment. Solar-powered EC units can be directly coupled with photovoltaic (PV) panels using DC current, simplifying system design and reducing energy conversion losses [59-61]. Furthermore, hybrid energy systems that combine solar and wind power can offer greater reliability by compensating for intermittency in energy supply.
Combining EC with other treatment technologies can significantly improve treatment efficiency, reduce chemical demand, and lower sludge production [62,63].

6. Conclusions

Electrocoagulation (EC) has emerged as a promising, efficient, and environmentally friendly method for treating a wide range of wastewater types, including those contaminated with synthetic dyes, heavy metals, organic matter, bacteria, and microplastics. The underlying principle, based on the in situ generation of metal hydroxides via anodic dissolution, ensures the effective destabilization of colloids and the removal of suspended and dissolved pollutants.
The experimental studies reviewed and conducted at the Faculty of Chemistry and Technology, University of Split, have confirmed the high applicability of EC in the treatment of synthetic and real wastewater samples. Notably, the enhancements achieved through the hybridization of EC with natural and synthetic zeolites (ECZ) have improved pollutant removal efficiency, reduced sludge formation, and mitigated electrode fouling.
Furthermore, the integration of EC systems with renewable energy sources, as well as the use of recycled electrode materials, and use of produced hydrogen represents a strategic step toward sustainable and circular wastewater management. These directions align well with global trends in green technology and resource efficiency.
Despite the demonstrated potential, challenges persist in optimizing operational parameters, understanding the long-term behaviour of electrode materials, and minimizing energy consumption.
Electrocoagulation—especially in its hybrid forms—offers a robust, adaptable, and sustainable solution to the complex challenge of modern wastewater treatment.

References

[1] Uddin, Md.G., Nash, S., Olbert, A.I., 2021. A review of water quality index models and their use for assessing surface water quality. Ecological Indicators, 122, 107218.

[2] Tahreen, A., Jami, M.S., Ali, F., 2020. Role of the electrocoagulation in wastewater treatment: A developmental review. Journal of Water Process Engineering, 37, 101440.

[3] Nishat, A., Yusuf, M., Qadir, A., Ezaier, Y., Vambol, V., Khan, M.I., Moussa, S.B., Kamyab, H., Sehgal, S.S., Prakash, C., Yang, H.-H., Ibrahim, H., Eldin, S.M., 2023. Wastewater treatment: A short assessment on available techniques. Alexandria Engineering Journal, 76, 505–516.

[4] Tóth, A.J., Fózer, D., Mizsey P., Sabev Varbanov, P., Klemeš, J.J., 2023. Physicochemical methods for process wastewater treatment: powerful tools for circular economy in the chemical industry. Reviews in Chemical Engineering, 39 (7), 1123–1151.

[5] Mužek, M.N., Omanović, D., Đulović, A., Burčul, F., Svilović, S., Blažević, I., 2020. The Garden Candytuft (*Iberis umbellata* L.): At the Crossroad of Copper Accumulation and Glucosinolates. Processes, 8 (9), 1116.

[6] Bikić, F., Pašalić, A., 2016. Influence of Soil pH and Addition of a Complexing Agent on the Cadmium Content in Certain Plants. Kemija u industriji, 65 (7-8), 375–378.

[7] Ugrina, M., Čeru, T., Nuić, I., Trgo, M., 2020. Comparative Study of Mercury(II) Removal from Aqueous Solutions onto Natural and Iron-Modified Clinoptilolite Rich Zeolite. Processes, 8 (11), 1523.

[8] Kaczmarzyk, I., Jeleniewska, Z., Onyshchenko, O., Ślepski, P., Pieczyńska, A., Kozłowska-Tylingo, K., Bogdanowicz, R., Ryl, J., Prześniak-Welenc, M., 2025. High-Performance Ceramic-Carbon Composite Electrodes for Sustainable Wastewater Remediation: A Comparative Study of Catalytically-active Nanoparticle Loading. Electrochimica Acta, 530, 146404.

[9] Sarkale, P.S., Chougale, S.T., Jadhav, A.S., 2024. Removal of antibiotic residue from aqueous solution by advanced oxidation process. The Holistic Approach to Environment, 14 (3), 91–100.

[10] Gopalakrishnan, G., Jeyakumar, R.B., Somanathan, A., 2023. Challenges and Emerging Trends in Advanced Oxidation Technologies and Integration of Advanced Oxidation Processes with Biological Processes for Wastewater Treatment. Sustainability 15 (5), 4235.

[11] Zelić, I.E., Tomašić, V., Gomzi, Z., 2023. Removal of Neonicotinoid Insecticides in a Flat-plate Photoreactor. Kemija u industriji, 72 (9-10), 537–544.

[12] Ezugbe, E.O., Rathilal, S., 2020. Membrane Technologies in Wastewater Treatment: A Review. Membranes, 10 (5), 89.

[13] Štrkalj, A., Glavaš, Z., Matijašić, G., 2014. Adsorption of hexavalent chromium from an aqueous solution of steel-making slag. Materiali in Tehnologije, 48 (5), 619–622.

[14] Crini, G., Lichtfouse, E., 2019. Advantages and disadvantages of techniques used for wastewater treatment. Environmental Chemistry Letters, 17 (1), 145–155.

[15] Mukherjee, J., Lodh, B.K., Sharma, R., Mahata, N., Shah, M.P., Mandal, S., Ghanta, S., Bhunia, B., 2023. Advanced oxidation process for the treatment of industrial wastewater: A review on strategies, mechanisms, bottlenecks and prospects. Chemosphere, 345, 140473.

[16] Nag, M., Lahiri, D., Ghosh, S., Sarkar, T., Pati, S., Das, A.P., Ram, D.K., Bhattacharya, D., Ray, R.R., 2024. Application of microorganisms in biotransformation and bioremediation of environmental contaminants: A review. Geomicrobiology Journal, 41 (4), 374–391.

[17] Kuppan, N., Padman, M., Mahadeva, M., Srinivasan, S., Devarajan, R., 2024. A comprehensive review of sustainable bioremediation techniques: Eco friendly solutions for waste and pollution management. Waste Management Bulletin, 2 (3), 154–171.

[18] Wang, J., Zhou, X., Chen, Y., Hu, Y., 2018. Pretreatment in membrane processes for ultra-pure demineralized water production from secondary effluent. Desalination and Water Treatment, 109, 36–44.

[19] Satyam, S., Patra, S., 2024. Innovations and challenges in adsorption-based wastewater remediation: A comprehensive review. Heliyon, 10 (9), e29573.

[20] Mollah, M.Y.A., Morkovsky, P., Gomes, J.A.G., Kesmez, M., Parga, J., Cocke, D.L., 2004. Fundamentals, present and future perspectives of electrocoagulation. Journal of Hazardous Materials, 114 (1–3), 199–210.

[21] Chen, G., 2004. Electrochemical technologies in wastewater treatment. Separation and Purification Technology, 38 (1), 11–41.

[22] Graça, N.S., Rodrigues, A.E., 2022. The Combined Implementation of Electrocoagulation and Adsorption Processes for the Treatment of Wastewaters. Clean Technologies, 4, 1020–1053.

[23] Sharma, D., Chaudhari, P.K., Dubey, S., Prajapati, A.K., 2020. Electrocoagulation treatment of electroplating wastewater: A review. Journal of Environmental Engineering, 146 (10), 03120009.

[24] Rakhmania, Kamyab, H., Yuzir, M.A., Abdullah, N., Quan, L.M., Riyadi, F.A., Marzouki, R., 2022. Recent Applications of the Electrocoagulation Process on Agro-Based Industrial Wastewater: A Review. Sustainability, 14 (4), 1985.

[25] Łuba, M., Mikołajczyk, T., Pierożyński, B., Smoczyński, L., Wojtacha, P., Kuczyński, M. 2020. Electrochemical degradation of industrial dyes in wastewater through the dissolution of aluminum sacrificial anode of Cu/Al macro-corrosion galvanic cell. Molecules, 25 (18), 4108.

[26] Dubrawski, K.L., Mohseni, M., 2013. *In-situ* identification of iron electrocoagulation speciation and application for natural organic matter (NOM) removal. Water Research, 47 (14), 5371–5380.

[27] Ingelsson, M., Yasri, N., Roberts, E.P.L., 2020. Electrode passivation, faradaic efficiency, and performance enhancement strategies in electrocoagulation – a review. Water Research, 187, 116433.

[28] Mishra, D.P., Sahu, P.K., Acharya, B., Mishra, S.P., Bhati, S., 2024. A review of the synthesis and application of azo dyes and metal complexes for emerging antimicrobial therapies. Results in Chemistry, 10, 101712.

[29] Rotaru, A., Moantă, A., 2016. Azoic dyes: From thermal properties to a wide range of applications. In Advanced Engineering Materials; Recent Developments for Medical, Technological and Industrial Applications; Academica Greifswald: Greifswald, Germany, Chapter 4.

[30] Leulescu, M., Rotaru, A., Pălărie, I., Moanţă, A., Cioateră, N., Popescu, M., Morîntale, E., Bubulică, M.V., Florian, G., Hărăbor, A., Rotaru, P., 2018. Tartrazine: Physical, thermal and biophysical properties of the most widely employed synthetic yellow food-colouring azo dye. Journal of Thermal Analysis and Calorimetry, 134, 209–231.

[31] Gudelj, I., Hrenović, J., Landeka Dragičević, T., Delaš, F., Šoljan, V., Gudelj, H., 2011. Azo boje, njihov utjecaj na okoliš i potencijal biotehnološke strategije za njihovu biorazgradnju i detoksifikaciju. Arhiv za Higijenu Rada i Toksikologiju, 62, 91–101.

[32] Selvaraj, V., Swarna Karthika, T., Mansiya, C., Alagar, M., 2021. An over review on recently developed techniques, mechanisms and intermediate involved in the advanced azo dye degradation for industrial applications. Journal of Molecular Structure, 1224, 129195.

[33] Gudić, S., Vrsalović, L., Medvidović Vukojević, N., Svilović, S., Ivančić, S., 2024. Removal of Crystal Violet Dye by Electrocoagulation – Analysis of Electrode and Solution Changes. Kemija u industriji, 73 (3-4), 109–117.

[34] Gudić, S., Čatipović, N., Ban, M., Svilović, S., Vukojević Medvidović, N., Rotaru, A., Vrsalović, L., 2025. Efficient Removal of Tartrazine Yellow Azo Dye by Electrocoagulation Using Aluminium Electrodes: An Optimisation Study by Response Surface Methodology. Applied Sciences, 15 (10), 5563.

[35] Ban, M., 2024. Removal of Tartrazine Yellow dye from aqueous solution by electrocoagulation, Diploma thesis, University of Split, Faculty of Chemistry and Technology, Split.

[36] Castañeda-Díaz, J., Pavón-Silva, T., Gutiérrez-Segura, E., Colín-Cruz, A., 2017. Electrocoagulation-Adsorption to Remove Anionic and Cationic Dyes from Aqueous Solution by PV-Energy. Journal of Chemistry, 2017, 5184590.

[37] Svilović, S., Vukojević Medvidović, N., Vrsalović, L., Kulić, A., 2022. Combining natural zeolite and electrocoagulation with different electrode materials – electrode surface analysis and Taguchi optimization. Applied Surface Science Advances, 12, 100330.

[38] Vukojević Medvidović, N., Vrsalović, L., Svilović, S., Bobanović, A., 2022. Electrocoagulation vs. Integrated Electrocoagulation-Natural Zeolite for Treatment of Biowaste Compost Leachate—Whether the Optimum Is Truly Optimal. Minerals, 12 (4), 442.

[39] Vukojević Medvidović, N., Vrsalović, L., Svilović, S., Magaš, K., Jozić, D., Čović, A., 2023. Electrocoagulation Combined with Synthetic Zeolite—Does the Size of Zeolite Particles Matter? Minerals, 13 (9), 1141.

[40] Vrsalović, L., Vukojević Medvidović, N., Svilović, S., Pavlinović, A. 2023. Taguchi method in the optimization of municipal wastewater treatment by electrocoagulation integrated with zeolite. Energy Reports, 9, 59–76.

[41] Maćerak, A.L., Duduković, N., Kiss, F., Slijepčević, N., Pešić, V., Bečelić-Tomin, M., Kerkez, Đ., 2024. Electrocoagulation in treatment of municipal wastewater– life cycle impact assessment. Chemosphere, 355, 141701.

[42] Kumari, S., Naresh Kumar, R., 2020. Electrocoagulation for COD, turbidity, ammonia and phosphate removal from municipal wastewater. Journal of Indian Chemical Society, 97, 527–532.

[43] Bote, M.E., Desta, W.M., 2022. Removal of turbidity from domestic wastewater using electrocoagulation: optimization with response surface methodology. Chemistry Africa 5, 123–134.

[44] Aguilar-Ascon, E., 2019. Removal of *Escherichia coli* from domestic wastewater using electrocoagulation. Journal of Ecological Engineering, 20 (5), 42–51.

[45] Singh Lodhi, A.P., Kumar, D., Kaur, T., Singh, N., 2021. Development of lubricious, non-toxic, and corrosion-resistant metalworking fluid: A possible replacement for mineral oil-based fluids. Journal of Cleaner Production, 323, 129173.

[46] Jozić, S., Vrsalović, L., Bajić, D., Gudić, S., 2022. Investigation of different cutting conditions in the machining of steel — Towards cleaner production. Journal of Cleaner Production, 356, 131881.

[47] Milić, J.K., Dražević, E., Košutić, K., Simonič, M., 2016. Microfiltration of cutting-oil emulsions enhanced by electrocoagulation. Desalination and Water Treatment, 57, 10959–10968.

[48] Bacry, S.A., Matta, M.E., Noureldin, A.M., Zaher, K., 2024. Performance evaluation of electrocoagulation process for removal of heavy metals from wastewater using aluminum electrodes under variable operating conditions. Desalination and Water Treatment, 318, 100396.

[49] Kumar, P.R., Chaudhari, S., Khilar, K.C., Mahajan, S.P., 2004. Removal of arsenic from water by electrocoagulation. Chemosphere, 55 (9), 1245–1252.

[50] Pikna, L’., Heželová, M., Morillon A., Algermissen D., Milković O., Findorák R., Cesnek M., Briančin J., 2020. Recovery of Chromium from Slags Leachates by Electrocoagulation and Solid Product Characterization. Metals, 10, 1593.

[51] Pikna, L’., Heželová, M., Remeteiová, D., Ružičková, S., Findorák, R., Briančin, J.A., 2023. Comprehensive View of the Optimization of Chromium (VI) Processing through the Application of Electrocoagulation Using a Pair of Steel Electrodes. Materials, 16, 3027.

[52] Elkhatib, D., Oyanedel-Craver, V., Carissimi, E., 2021. Electrocoagulation applied for the removal of microplastics from wastewater treatment facilities. Separation and Purification Technology, 276, 118877.

[53] Shen, M., Zhang, Y., Almatrafi, E., Hu, T., Zhou, C., Song, B., Zeng, Z., Zeng, G., 2022. Efficient removal of microplastics from wastewater by an electrocoagulation process. Chemical Engineering Journal, 428, 131161.

[54] Bani-Melhem, K., Al-Kilani, M.R., Tawalbeh, M., 2023. Evaluation of scrap metallic waste electrode materials for the application in electrocoagulation treatment of wastewater. Chemosphere, 310, 136668.

[55] Nippatla, N., Philip, L., 2020. Electrochemical process employing scrap metal waste as electrodes for dye removal. Journal of Environmental Management, 273, 111039.

[56] Kazim, H., Sabri, M., Al-Othman, A., Tawalbeh, M., 2024. Utilizing scrap metals in electrocoagulation: Revolutionizing water treatment with AI applications for enhanced resource recovery. Journal of Resource Recovery, 2, 1024.

[57] Pratiwi, R., Slamet, S., Muttaqin, R., Dilla, D.S., 2023. The opportunity of using hydrogen produced from electrocoagulation process of hospital liquid waste as renewable energy source. AIP Conference Proceedings, 2667, 030006.

[58] Vasconcelos da Silva, L.T., Gadelha de Oliveira, A., Ribeiro, J.P., Lopes, A.F., Costa, R.S., Neto, E.F.A., Carvalhod, T.V., Romero, F.B., Sales, J.V.S., Correia de Souza, F.T., Ferreira do Nascimento, R., 2024. Electrocoagulation cell for the production of hydrogen without carbon emission and simultaneous treatment of textile wastewater. International Journal of Hydrogen Energy, 64, 906–913.

[59] Çetinkaya, A.Y., 2025. Integration of electrocoagulation and solar energy for sustainable wastewater treatment: a thermodynamic and life cycle assessment study. Environmental Monitoring and Assessment, 197, 224.

[60] Jeon, S.-B., Kim, S., Park, S.-J., Seol, M.-L., Kim, D., Chang, Y.K., Choi, Y.-K., 2016. Self-powered electro-coagulation system driven by a wind energy harvesting triboelectric nanogenerator for decentralized water treatment. Nano Energy, 28, 288–295.

[61] Dermentzis, K., Marmanis, D., Cristoforidis A., Moumtzakis, A., 2015. Photovoltaic electrocoagulation process for remediation of chromium plating wastewaters. Desalination and Water Treatment, 56 (5), 1413–1418.

[62] Asfaha, Y.G., Zewge, F., Yohannes, T., Kebede, S. 2022. Application of hybrid electrocoagulation and electrooxidation process for treatment of wastewater from the cotton textile industry. Chemosphere, 302, 134706.

[63] Twizerimana, P., Wu, Y., 2024. Overview of integrated electrocoagulation-adsorption strategies for the removal of heavy metal pollutants from wastewater. Discover Chemical Engineering, 4, 14.

Structural features of welded joints of special-purpose steel with increasing number of fatigue load cycles

***Olga Kushnarova*[1], *Olena Berdnikova*[1], *Tetyana Alekseienko*[1], *Svitlana Grigorenko*[1], *Valeriy Pozniakov*[1], *Aleksandr Gaivoronskiy*[1], *Anatoliy Zavdoveev*[1] *and Massimo Rogante*[2]**

1) Paton Electric Welding Institute of NAS of Ukraine, K.Malevicha 11, 03150 Kiev, Ukraine

2) Rogante Engineering Office, Contrada San Michele n.61, 62012 Civitanova Marche, Italy

Corresponding author: avzavdoveev@gmail.com

Original scientific article

Abstract: The paper considers the patterns of formation of the structure of welded joints of special-purpose steel using austenitic (A) type welding wire after welding and operational cyclic loads. Welded joints were obtained by arc welding, which was carried out without preliminary heating in a protective gas environment. Cyclic loads of welded joints were performed at σ = 60 MPa with a different number of cycles. The features of grain, subgrain and dislocation structures were studied using light and transmission electron microscopy. Based on complex studies, experimental data were obtained at different structural levels, an analytical assessment was made of the contribution of structural-phase components and their parameters formed in welded joints to the level of structural strengthening of the metal of the heat-affected zone after welding and operational load.

Keywords: *special purpose steel; welded joint; cyclic loading; microstructure; microhardness; substructure; bainite; martensite; dislocation density; structural strengthening*

1. Introduction

At the present stage of manufacturing critical welded assemblies of metal structures operating in difficult operating conditions, high-strength steels [1-6] are widely used. At the same time, the operational characteristics of metal welded joints, such as hardness, strength, corrosion and wear, etc., are significantly affected by the processes of structure formation in the metal of welded joints [7-10]. It is known that most welded joints in high-strength steel structures are affected by cyclic loads during operation [11-14]. Such loads cause the development of fatigue processes in the material, which can lead to the accumulation of microdamage, a decrease in strength characteristics, the formation of microcracks, fatigue cracks and, finally, to the destruction of structures 15 - 18. With an increase in the number of load cycles, the probability of fatigue crack initiation increases, which necessitates the study of structure formation processes. Particular attention should be paid to the study of structural-phase transformations at all levels - grain, subgrain and dislocation, as well as to the assessment of the influence of these parameters on the ability of the welded joint metal to relax internal stresses. These factors largely determine not only crack resistance, but also other operational properties of welded joints [19, 20]. Therefore, studies of the influence of structural factors on the crack resistance of welded joints of structural steels, including special-purpose steels in the structures of light armored vehicles are extremely relevant [21, 22].

Objective: study of structural changes in the metal of welded joints of special-purpose structural steel after welding and fatigue cyclic loading depending on the number of load cycles and determination of the influence of structural factors on the strength characteristics of the metal.

2. Materials and research methods

The article considers the patterns of formation of the structural-phase composition and properties of welded joints of Armox 500 armor steel (0.24% C; 0.25% Si; 0.84% Mn; 0.5% Cr; 0.97% Ni; 0.33% Mo; 0.016% P; 0.016% P; austenitic type Sv-08Kh20N10T (0.1% C; 10.0% Ni; 20.0% Cr; 1.0% Si; 8.0% Mn; 0.9% Ti; 0.018% S; 0.035% P) after welding and operational loads. Welding was performed without

preliminary heating in an Ar + CO_2 shielding gas environment at the following mode: I = 180 A; U = 25 ... 26 V; V = 18 m /hour. Cyclic loads of welded joints were performed at σ=60 MPa with the number of cycles Nc=1080000, Nc=1450000, Nc=1800000.
The structure was studied using light microscopy (Versamet-2, Neophot-32 microscopes), electron transmission microscopy (JEM-200CX, JEOL). Microhardness (HV) was measured on a LECO M-400 microhardness tester with a load of 100 g.

3. Results and discussion

3.1. Microstructure

Using the world microscopy methods, it was established that an austenitic structure with a grain size of Dз=20...90 μm and a microhardness of HV=1700...2450 MPa is formed in the weld metal of Armox 500 armor steel, Figure 1a. After operational loads, compared to the initial state, the grain size decreases on average by 1.3, 1.5 and 1.6 times, while the microhardness increases by 10–20%, respectively, with an increase in the number of cycles Nц=1,080,000, 1,450,000, 1,800,000, Figure 1. At the same time, a uniform level of microhardness of the austenitic structure with an almost unchanged grain size is maintained in the weld metal of each version of the welded joints.

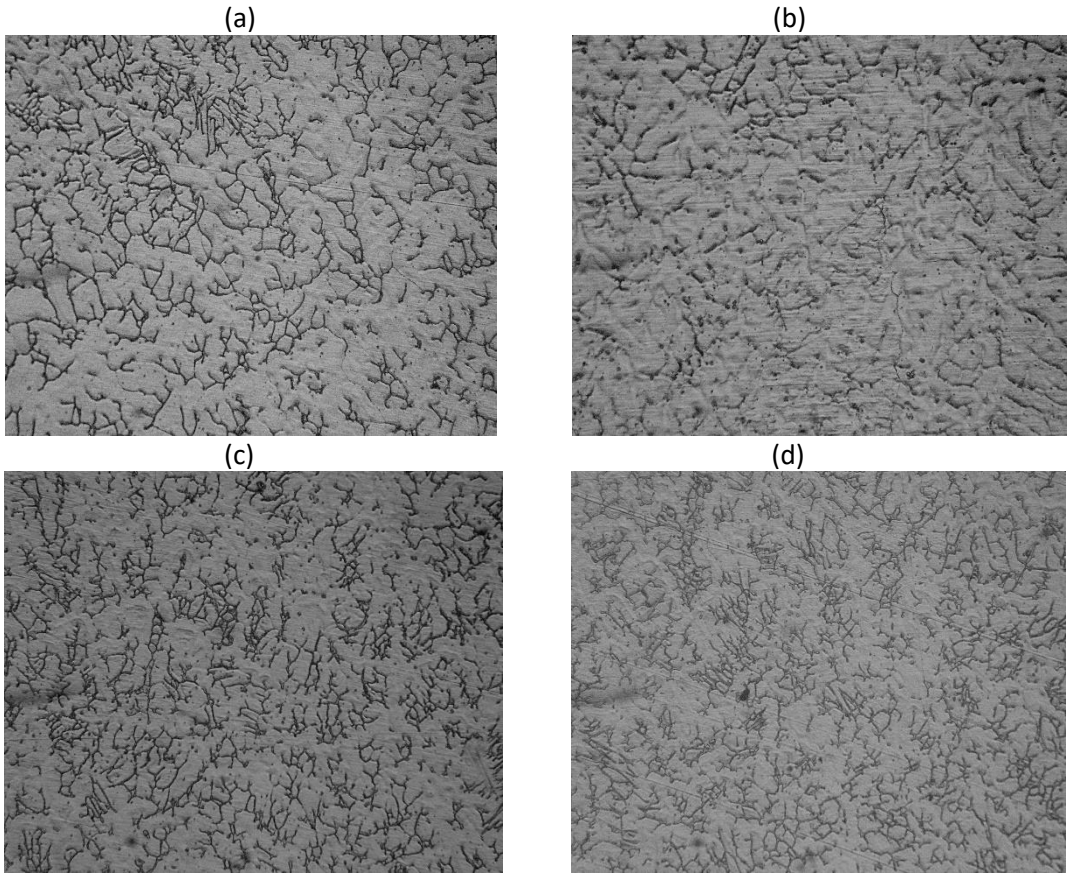


Figure 1. *Microstructure of the weld metal in a welded joint of Armox 500 armor steel using Sv-08Kh20N9G7T wire after welding and operational load (σ=60 MPa): a) – initial state; b) – number of cycles Nц=1080000; c) – Nц=1450000; d) – Nц=1800000 (× 500)*

In the heat-affected zone (HAZ) in the initial state, a martensitic-bainite structure is formed. In the overheating region, the grain size is Dz = 80...200 μm at HV = 4010...4640 MPa, and in the area of complete recrystallization - Dz = 25...65 μm at HV = 4640...5140 MPa, Figure 2 a. With an increase in the number of load cycles, the microhardness of the HAZ metal increases by about 20%, which is due to the uniform refinement of the packet martensitic-bainite structure by 1.25-1.6 times, Figure 2 b-d.

Thus, it was established that in the weld metal of the welded joints of Armox 500 armor steel after welding both in the initial state and after operational loads (Nц=1080000, 1450000, 1800000 microhardness of the austenitic structure to increase the grain load with increasing grain load. refinement of the martensite-bainitic structure.

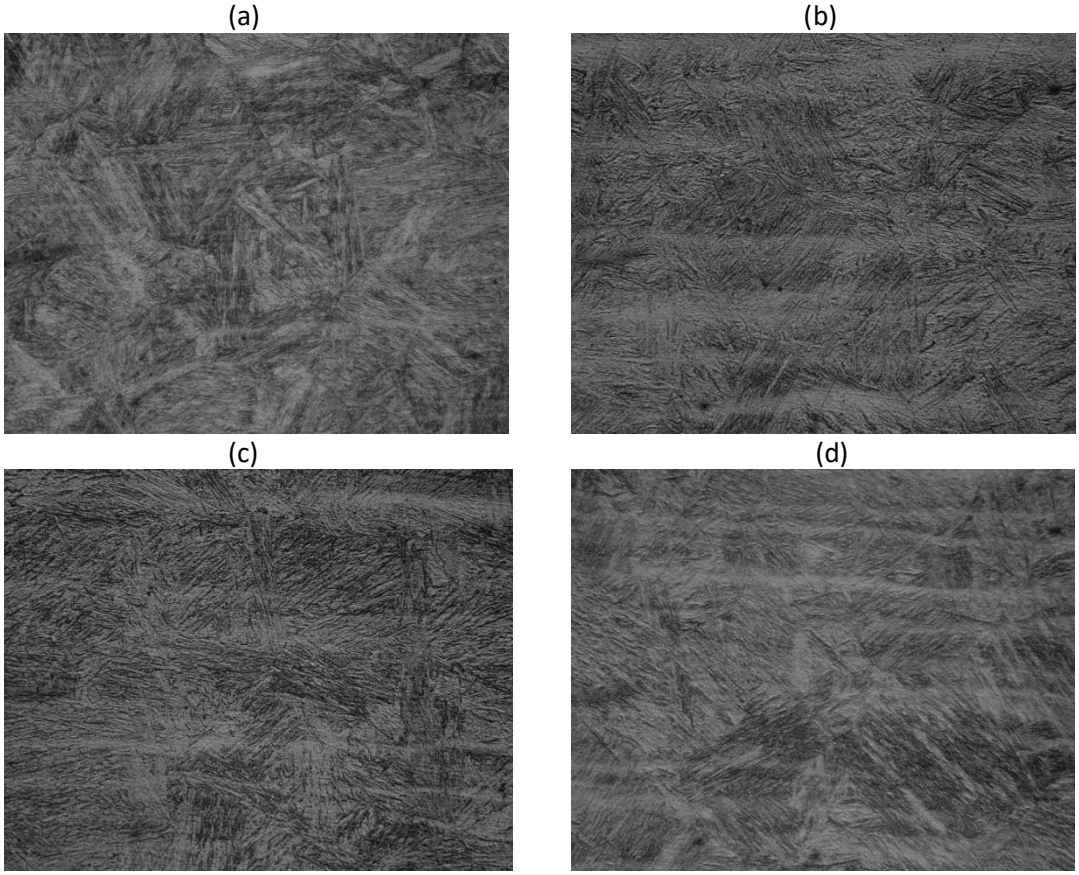


Figure 2. *Microstructure of the thermite attack zone (HAZ) in a welded joint of Armox 500 armor steel using Sv-08Kh20N9G7T wire after welding and operational load (σ=60 MPa): a) – initial state; b) – number of cycles Nц=1080000; c) – Nц=1450000; d) – Nц=1800000 (× 500)*

3.2. Dislocation structure

Further examination of welded joints of Armox 500 steel and after operational loading was carried out using transmission electron microscopy. In the initial state, the formation of an austenitic substructure with a size of dc = 0.35…0.9 μm was established in the weld metal, Figure 3 a. A lath structure of the bainitic-martensitic type is observed in the heat-affected zone, Figure 3 b-d. The width of the rails is: for lower bainite (Bn) hp = 0.27…1.4 μm, for upper bainite (Bv) hp = 0.25…1.3 μm, for tempered martensite (Mvid) hp = 0.4…1.6 μm. The substructural parameters are: for Bn dc = 0.2…1.45 μm, for Bv dc = 0.2…1.37 μm, for Mvid dc = 0.31…2.0 μm. The average dislocation density of these structural components is $\rho = 3…8.5\times10^{10} cm^{-2}$.

After the operational load (σ = 60 MPa) with the increase in the number of cycles (Nц = 1,080,000 and 1,450,000), a uniform increase in the dislocation density by 1.4–1.5 times is observed in the weld metal compared to the initial state: $\rho = (3…7)\times10^{9}$ cm^{9} cm^{9} cm^{-2}, respectively, Figure 4 a-b. No sharp gradients in the dislocation density were detected in the HAZ. Compared to the initial state, the dislocation density in the HAZ increases on average by 1.17–1.2 times to $\rho = (5\times10^{10}…1\times10^{11})$ cm^{-2} (at Nц = 1,080,000) and $\rho = (5.5\times10^{10}…1.4\times1x10^{11})$. In this case, the substructure is refined by 1.15–1.2 times: for Nc = 1,080,000 – dc(Bn) = 0.17…1.3 μm, dc(Bv) = 0.15…1.2 μm, dc(Mvid) = 0.25…1.6 μm; for Nc = 1,450,000 – dc(Bn) = 0.15…1.12 μm, dc(Bv) = 0.12…1.0 μm, dc(Mvid) = 0.2…1.45 μm, Figure 4 c-f. Thus, the formation of substructural components in the absence of sharp dislocation density

gradients ensures an increase in crack resistance and additional strengthening of the weld metal and HAZ at the specified numbers of cycles.

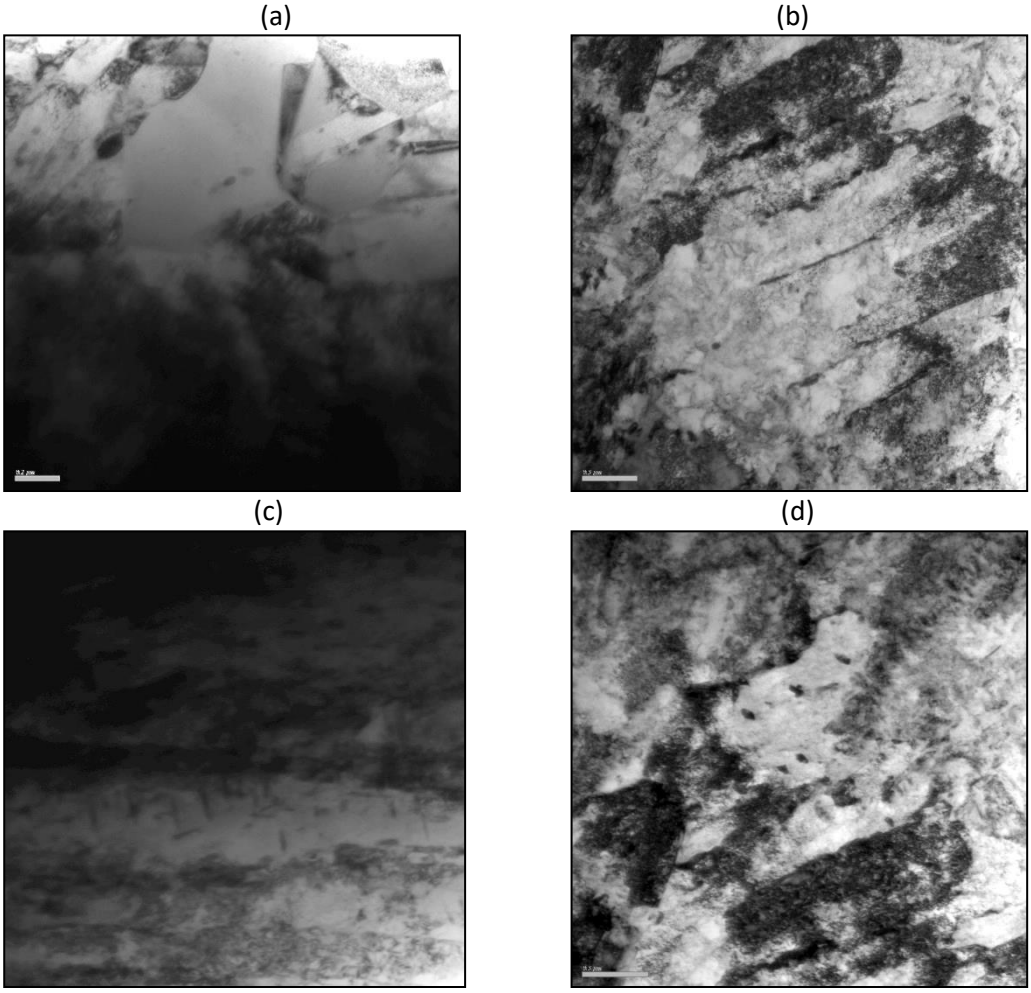


Figure 3. *Fine structure of the weld metal (a) and the first zone of the HAZ (b-c) of the welded joint of Armox 500 armor steel with Sv-08Kh20N9G7T wire after welding (initial state), (a - ×25000; b - ×18000; c - ×22000; d - ×25000)*

In the weld metal after the operational load at Nц = 1800000, pronounced gradients of dislocation density are observed, which can contribute to the initiation of microcracks 23, 24. In the austenitic structure of the weld metal, the size of substructural elements decreases by 1.5 times compared to the initial state to dc = 0.12…0.6 μm, while the dislocation density increases by 4 times — to ρ = (5×10^{9}…2×10^{10}) cm^{-2} with its non-uniformity. In the heat-affected zone, the substructure also becomes finer by 1.5 times: for lower bainite dc = 0.1…0.95 μm, for upper bainite dc = 0.1…0.86 μm, for tempered martensite dc = 0.15…1.25 μm. The dislocation density in these structural components increases by 2.3 times - up to ρ = (4×10^{10}…2×10^{11}) cm^{-2}, and sharp gradients of their distribution between the volume of grains and their limits are noted, Figure 5 b-d.

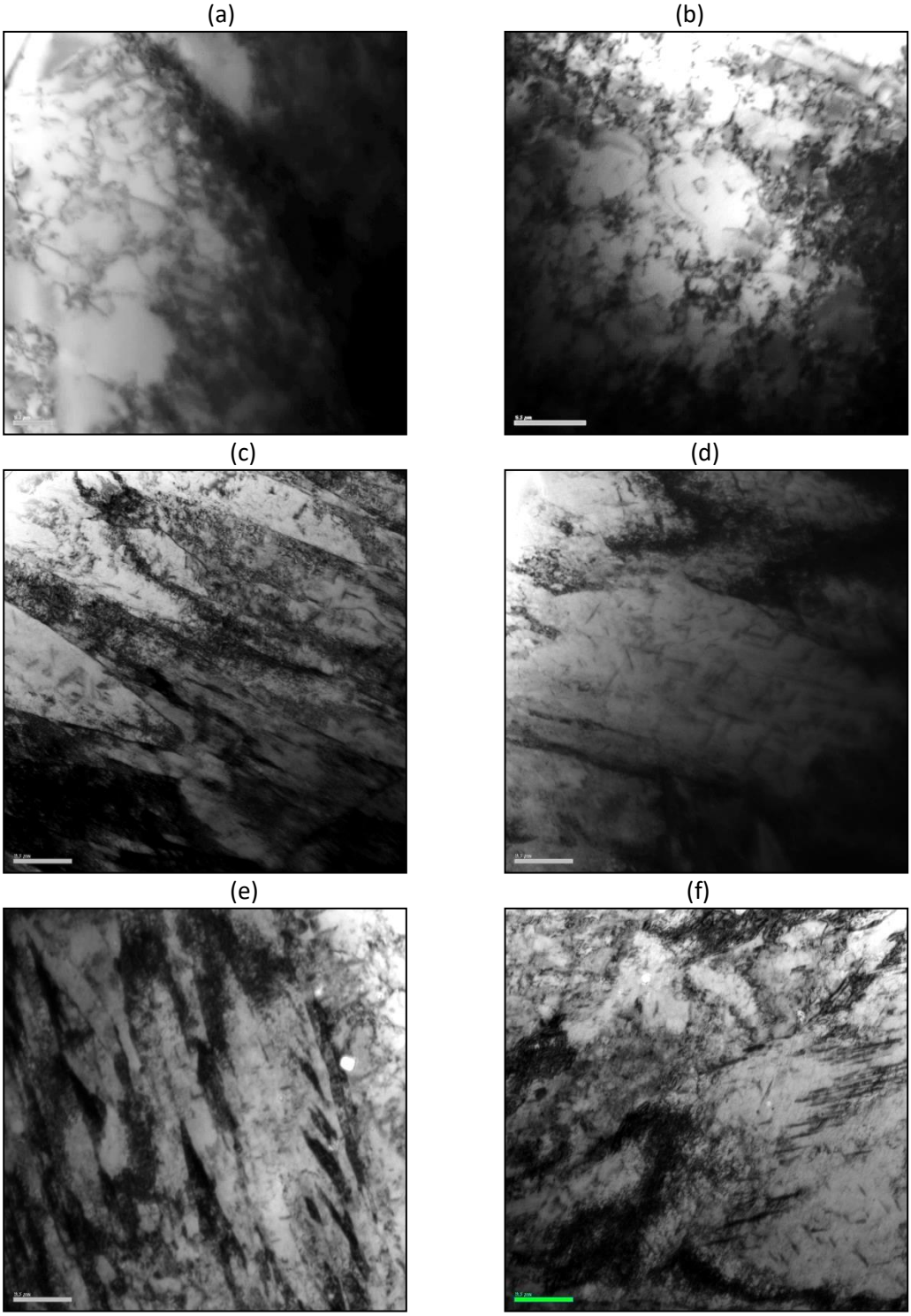


Figure 4. *Fine structure of the weld metal (a, b) and the first zone of the HAZ (c-f) of the welded joint of Armox 500 armor steel with Sv-08Kh20N9G7T wire after welding and loading (=60MPa) Nc=1080000 (c, d) and Nc=1450000 (e, f), (a - ×35000; b - d - ×25000; e - f - ×22000)*

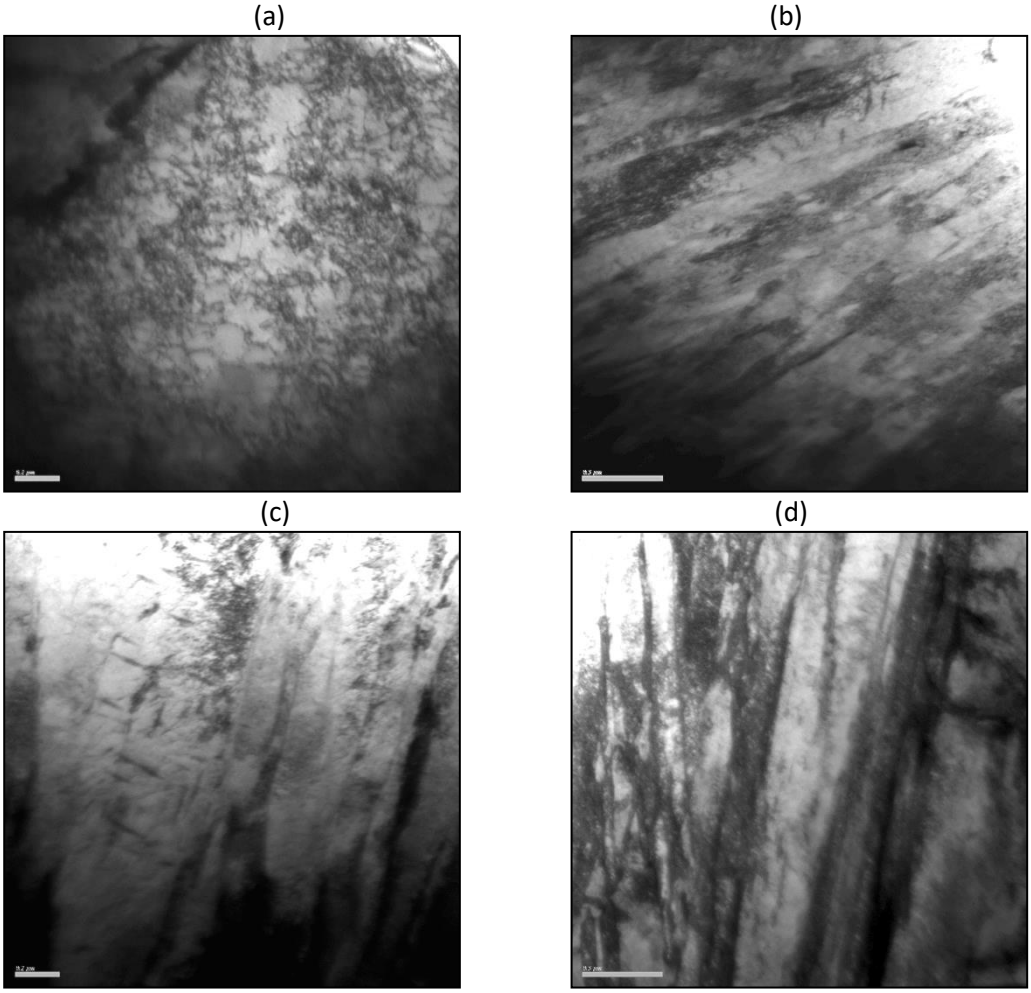


Figure 5. *Fine structure of the weld metal (a) and HAZ (b-d) of a welded joint of Armox 500 armor steel with Sv-08X20N9G7T wire, welding and loading □=60MPa with Nc=1800000, (a, d - ×35000; b, c - ×25000)*

Thus, it was established that in the metal of the welded joint of the Armox 500 armor steel after operational loading (σ = 60 MPa) at the number of cycles Nц = 1080000 – 1450000 in the weld metal and HAZ only insignificant gradients of dislocation density and formation of substructural components are observed. This will ensure crack resistance during strengthening of the metal of the welded joints [23, 24]. At Nц = 1800000, noticeable gradients of the dislocation density distribution are recorded. This will lead to a decrease in crack resistance due to an increase in the probability of microcrack nucleation

3.3. Analytical Evaluation of Structural Hardening

Based on experimental studies of welded joints of special armor steel Armox 500 after welding and operational loading (cyclic load □=60 MPa) with the number of cycles Nc=1080000; 1450000; 1,800,000, analytical evaluations of changes in the structural strengthening index (□σT) of the metal and HAZ (overheating area) were carried out, taking into account the contribution of each of the structural parameters.

Quantitative evaluations of strengthening for each of the structural parameters (grain size, subgrain size, phase particles, dislocation density) were performed according to Hall-Petch, Orowan, etc. [19, 23]. Similar assessments of structural strengthening were tested on steels of different strength classes, alloys, their welded joints, coatings, etc. [24-30]. The results of analytical evaluations of the mechanical properties of materials were obtained and verified.

Analytical estimates of the structural strengthening (□σT) of the metal of the first section of the HAZ (overheating section) taking into account the contribution of each of the structural parameters show

that in the welded joint of Armox 500 armor steel after welding (initial state) the main contribution is provided by substructural (□□c =). (□□t.r. = 285 MPa) and dislocation (□□d = 272 MPa) strengthening, Figure 6.

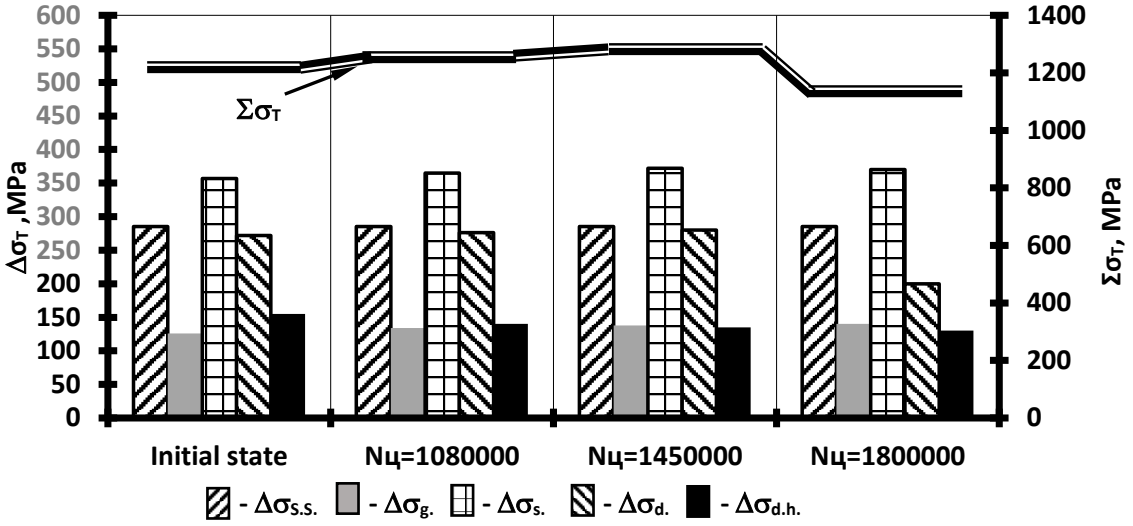


Figure 6. *Contribution of structural components to the calculated value of strengthening (ΣΔσT) of the I zone of the HAZ of special armor steel Armox 500 using Sv-08X20N9G7T wire after welding and operational load Nц=1080000, Nц=1450000, Nц=1800000*

In a welded joint of Armox 500 armor steel after welding and operational load at Nc=1080000 in the HAZ metal, the main contribution is provided by substructural (Δσc. = 365 MPa), dislocation (Δσд = 276 MPa) and hardness. MPa) strengthening, Figure 6. In the HAZ metal after Nc=1450000, the main contribution is provided by substructural (Δσs. = 372 MPa), solid-soluble ($\Delta\sigma_{ss}$ = 285 MPa) and dislocation (Δσd. In the HAZ metal after the load Nc=1800000, the main contribution to ΣσT is provided, as in the previous cases, by substructural (Δσs. = 370 MPa), solid-soluble (Δσss = 285 MPa) and dislocation (Δσσ).

It should be noted that in welded joints of Armox 500 armor steel after welding and operational load Nc=1080000, Nc=1450000, Nц=1800000 the highest structural hardening indices in the HAZ metal are provided by the structural components of lower March bainite. The metal is contributed by the solid solution, substructural and dislocation components.

Under cyclic loading, materials undergo tiring processes that can lead to a decrease in strength characteristics. Microdamage at the structure level can accumulate, which can ultimately reduce the strength of the metal. It should also be noted that under long-term cyclic loading, microcracks can form, increasing with each cycle. Such processes are observed in the welded joint at Nц=1800000.

4. Conclusion

In the weld metal of Armox 500 steel welded joints obtained using Sv-08Kh20N9G7T wire, an austenitic structure with a stable grain size and a uniform level of microhardness is formed, which is preserved both in the initial state and in each version of the joints after cyclic loading with a number of cycles. In the metal of the heat-affected zone (HAZ) of welded joints, a martensitic-bainitic structure is formed. With an increase in the number of loading cycles, structural changes are observed in the metal of welded joints of Armox 500 armor steel: refinement of austenitic grains (in welds) and packages of martensitic-bainitic structure (in HAZ) and an increase in microhardness, especially in areas of overheating and complete recrystallization.

Studies of the fine structure of the HAZ metal of welded joints of Armox 500 steel have established that with the number of cycles Nц=1080000; 1450000, there is a uniform increase in the dislocation

density and refinement of the substructure, which will ensure crack resistance and strengthening of the weld metal and HAZ.
With the greatest number of overload cycles (Nц=1800000), gradients of the dislocation density are observed. This can contribute to the nucleation of microcracks and, accordingly, a decrease in the crack resistance of the metal.
It has been established that under moderate cyclic loads in welded metals of Armox 500 armor steel joints, a uniform level of dislocation density is observed. This will ensure their crack resistance. Analytical assessments of the structural strengthening of the HAZ metal have shown that the main contribution to the overall level of strengthening is provided by the substructural, solid-soluble and dislocation components. The key role belongs to the following structural components of lower bainite and tempered martensite.

References

[1] Paton, B.E., 2008. Selected proceedings. Kiev, PWI, 256p

[2] Science of materials, achievements, prospects. Ed. by L.M. Lobanov. Kyiv, Akademperiodyka, 2018, Vol. 2.

[3] Kasatkin, B.S., Musiyachenko, V.F., Low alloy steels of high strength for welded structures. . – M.: Technology , 1970. – 188 p.

[4] Zherbin, M.M. High-strength construction steels . Kiev: Stroitel , 1974. – 159 p.

[5] Potok, Ya.M. High-strength steels. – Metallurgy, 1972. – 207 p.

[6] Gorynin, I., 1980. Weldable hoigh strength steels, Naukova dumka, , pp.120-131.

[7] Lobanov, L., Kostin, V., Makhnenko, O., Zukov, V., Kostenevych, O., 2019. Forecasting of structural transformations in heat affected zone steel of 15KH2NMFA at anti-corrosion cladding. Problems of Atomic Science and Technology, 126, 89 - 96

[8] Grigorenko G.M., Kostin V.A., 2018. Criteria for evaluating the weldability of steels. Welding International, 27 (10), pp. 815 – 820.

[9] Madej, K., Świdergoł, S., Jakubiec, P., 2015. Analysis of Cracks in Welded Joints of Pipes with Eyes made of S890QL1 Steel. Jakubiec, Biuletyn Instytutu Spawalnictwa, 6: - P.11-22.

[10] Nyrkova L.I., Goncharenko L.V., Lisovyi P.E., Osadchuk S.O., Klymenko A.V., Kostin V.A., 2022. Stress-corrosion cracking of steels for main gas pipelines. Mechanical Technology and Structural Materials, 120– 130

[11] Ostash O.P., Andreiko I.M., Kulyk V.V., Babachenko O.I. and Vira V.V., 2009. Influence of the Mode of Thermal Treatment and Load Ratio on the Cyclic Crack-Growth Resistance of Wheel Steels. Fiz.-Khim. Mekh. Mater. 45(2), 63-70.

[12] Babinets, A.A., Ryabtsev, I.A., 2016. Fatigue life of multilayer hard-faced specimens. Welding International, 30, 4, 305-309. https://doi.org/10.1080/01431161.2015.1058004

[13] Ryabtsev, I.O., Knysh, V.V., Babinets, A.A. et al., 2020. Fatigue life of specimens after wear-resistant, manufacturing and repair surfacing. The Paton Welding J., 9, 19-25.

[14] Nyrkova L., Lisovyi P., Gonchasrenko L., Osadchuk S., Kharchenko Y., Klymenko A., Kostin V., 2023. Investigation of stress-corrosion cracking of welded joint of X70 steel under cathodic polarization in near neutral environment. Materials Protection, 64 (1), pp. 96 – 106.

[15] Makhnenko, V.I., 2006. Safe service life of welded joints and assemblies of modern structures. Kyiv, Naukova Dumka, 178p.

[16] Ryabtsev I.O., Knysh V.V., Babinets A.A., Solovej S.O., Ryabtsev I.I., Lentyugov I.P., 2024. Features of origination and propagation of fatigue cracks under cyclic mechanical loads of deposited plates. Avtomatychne Zvaryuvannya" (Automatic Welding), 1, 2024, pp. 3-7..

[17] Knysh V.V., Solovej S.O., Ryabtsev I.O., Babinets A.A., 2021. Fatigue life of specimens from 40KH steel after wear-resistant. "Avtomatychne Zvaryuvannya" (Automatic Welding), 8, pp. 3-8.

[18] Nyrkova L.I., Lisovyi P.E., Goncharenko L.V., Osadchuk S.O., Kostin V.A., Klymenko A.V., 2017. Regularities of Stress-Corrosion Cracking of Pipe Steel 09G2S at Cathodic Polarization in a Model Soil. Environment Physics and Chemistry of Solid State, 22, 828 - 836

[19] Krasovsky A.Ya., 1977. Physical foundations of strength. Naukova Dumka, 117 p.

[20] Kotrechko S.A., 2008. Ultimate strength. Crystals, metals, structures. Naukova Dumka, 296p.

[21] Kostin V.A., Grigorenko G.M., Poznyakov V.D., Zuber T.O., 2020. Structural Transformations of the Metal of Heat-Affected Zone of Welded Joints of High-Strength Armor Steels. Materials Science, 55 (6), pp. 863-869.

[22] Kostin V. A., Poznyakov V. D., Berdnikova O. M., Zhukov V. V., Alekseyenko T. O., 2021. Influence of Structural Transformations on the Mechanical Properties of Welded Joints of Armor Steels. Materials Science, 56, 472 – 480.

[23] Trefilov V. I., 1978. Deformation strengthening and destruction of polycrystalline metals. Naukova dumka, 248 p.

[24] Markashova, L.I., Poznyakov, V.D., Gaivoronskii, A.A., Berdnikova, E.N., Alekseenko, T.A., 2012. Estimation of the strength and crack resistance of the metal of railway wheelsafter long-term operation. Materials Science, 47(6), pp. 799–806

[25] Markashova L., Berdnikova O., Bernatskyi A., Sydorets V., Bushma O., 2019. Crack Resistance of 14KhGN2MDAFB High-Strength Steel Joints Manufactured by Laser Welding. IOP Conference Series: Earth and Environmental Science, 224, 012013.

[26] Berdnikova O., Kushnarova O., Bernatskyi, A. Alekseienko, T., Polovetskiyi, Y., Khoklov. M., 2020. Structure Peculiarities of the Surface Layers of Structural Steel under Laser Alloying. 2020 IEEE 10th International Conference Nanomaterials: Applications & Properties (NAP), pp. 02IT01-1-02IT01-4.

[27] Berdnikova O. M., Tyurin Yu. M., Kolisnichenko O. V., Kushnarova O. S., Polovetskiyi Y. V., Titkov Y. P., and Eremeeva L.T., 2022. Nanoscale structures of detonation metal-ceramic coatings of the Ni-Cr-Fe-B-Si system. Nanosystems, nanomaterials, nanotechnologies., 20 (1), pp. 97-109.

[28] Berdnikova O., Kushnarova O., Bernatskyi A., Polovetskyi Y., Kostin V., and Khokhlov M., 2021. Structure features of surface layers in structural steel after laser-plasma alloying with 48(WC-W2C)+48Cr+4Al powder. 2021 IEEE 11th International Conference Nanomaterials: Applications & Properties (NAP), 01-04.

[29] Kushnarova O., Berdnikova O., Alekseienko T., Sokolovskyi M., Siora O., Lukashenko V., Bernatskyi A., 2025. Influence of the substructure on the change of mechanical properties in the surface layers of structural steel during laser and laser-plasma alloying. Molecular crystals and liquid crystals, 769, 695-705.

[30] Berdnikova O., Kushnarova O., Bernatskyi A., et al., 2020. Structure Peculiarities of the Surface Layers of Structural Steel under Laser Alloying. IEEE 10th International Conference Nanomaterials: Applications & Properties (NAP), pp. 02IT01-1-02IT01-4

Anton Paar

Anton Paar GmbH Group

Founded in 1922 in Graz, Austria, by Mr. Anton Paar, the company is a global market leader in density and concentration measurement, rheometry and viscometry, and dissolved carbon dioxide determination. Anton Paar also offers cutting-edge technologies, such as Raman spectroscopy, X-ray diffraction (XRD), particle size analysis, and surface analysis. Anton Paar's customers include most of the major beer and soft drink manufacturers worldwide, and companies active in the food, chemicals, petroleum, and pharmaceutical industries, as well as leading academic institutions.

Anton Paar GmbH is part of the Anton Paar GmbH Group, which has 39 sales subsidiaries and eight producing sites. The Anton Paar GmbH Group is, in turn, part of the Anton Paar Group AG, owned by the charitable Santner Foundation. The company now employs more than 4,200 people in areas such as research and development, production, sales, and service. In recent years, Anton Paar GmbH has invested up to 14.5 % of its annual turnover in research and development. In 2023, the Anton Paar GmbH Group generated net sales revenue of € 587 million.

In addition to its focus on research and development, Anton Paar's growth is driven by strategic acquisitions.

In 2007, the company acquired Dr. Kernchen GmbH near Hannover, Germany (specializing in optical metrology; now Anton Paar OptoTec). This was followed in 2012 by the acquisition of the Petrotest Group, Germany (petroleum industry measurement technology; now Anton Paar ProveTec), and in 2014 by CSM Instruments SA, Switzerland (surface analysis; now Anton Paar TriTec). In 2016, Anton Paar acquired a product line of Raman benchtop devices from BaySpec Inc. (California, USA) and licensed handheld Raman technology from SciAps Inc. (Massachusetts, USA). In 2017, the company integrated particle size analysis technology acquired from Cilas (France) into its product portfolio.

Further expansion came with the acquisition of Quantachrome Instruments (USA) in February 2018 – now operating as Anton Paar QuantaTec – and AXO Dresden (Germany) in February 2019, enhancing capabilities in pore and porous material characterization and X-ray optics. Most recently, in 2023, Anton Paar acquired Brabender GmbH & Co. KG (Germany), now operating as Anton Paar TorqueTec, adding specialized solutions for characterizing kneading properties and lab-scale extrusion.



The Main Building and the Technology Center at the headquarters in Graz, 2024

ANSAR-ANALITIKA
ANALYTICAL EQUIPMENT

Ansar-analitika is company dedicated to consulting, sales and aftersales of scientific, analytical and general laboratory instruments and supplies. We are actively on market since 2009. From that time, we delivered, installed and doing a maintenance of hundreds of instruments and devices.

Advanced research and material characterization

Life science areas of research and quality control

Control and analytical laboratories in the food and agricultural sector

avantor delivered by VWR | KERN | BICASA We lead lab | TEMPER | LINSEIS

witeg GERMANY | JASCO | agar scientific | SCION INSTRUMENTS | RENISHAW apply innovation

Nabertherm | KPM | OXFORD INSTRUMENTS | ThermoFisher SCIENTIFIC | ECOSAFE ZERO WASTE

OPSIS

ANSAR-ANALITIKA
ANALYTICAL EQUIPMENT

Contact

Zagrebačka cesta 164a, 10 000 Zagreb

ansar@ansar-analitika.hr
+385 1 7980 857

Links

Privacy policy
Terms and conditiones

Follow us

BELMET 97 distributes high-quality measuring instruments and scientific research equipment.

Over the years, the company has grown thanks to the ambitions of our staff and the technical knowledge and expertise.



VISION

Our vision is to be the company that best understands the needs of clients in search of advanced measurement solutions and technology.



MISSION

BELMET 97 pushes the boundaries in measurement, research and experimentation technology. Working together with our clients, safely and responsibly, we bring experience, methods, motivated teams and world-class equipment to IMAGINE the possible, THINK to find a solution and ACT to deliver.







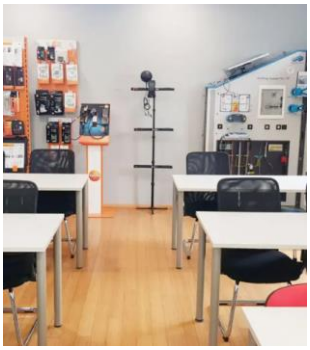












BELMET 97 doo

Hrvatsko proljeća 34
10040 Zagreb
Croatia

phone: *+385 (0)1 2959 900*
fax: *+385 (0)1 2959 910*
info@belmet97.hr

Working hours:
Monday – Friday, 8am-4pm



SPREMNI NA SVE IZAZOVE



INTUITIVNO
SUČELJE



SPREMNI ZA
INDUSTRIJU 4.0



SVESTRANI
I PO MJERI

OSLOBODI SVOJ POTENCIJAL U ZAVARIVANJU

Eurotehnika

Susedsko polje 2B
10000 Zagreb

+385 (0)1 2404 356
+385 (0)1 2404 359

info@eurotehnika.hr
www.eurotehnika.hr

INTELLIGENT
REVOLUTION

M.TEH DISTRIBUTION

HIOKI

KEYSIGHT TECHNOLOGIES

RIGOL
Possibilities and More

EXFO

ITECH
YOUR POWER TESTING SOLUTION

SUMITOMO ELECTRIC

optimize! softing

www.MTEH.hr

TOPOMATIKA

METROLOGY SOLUTIONS IN ONE PLACE



DISPLACEMENT AND DEFORMATION ANALYSIS



AUTOMATED MEASURING



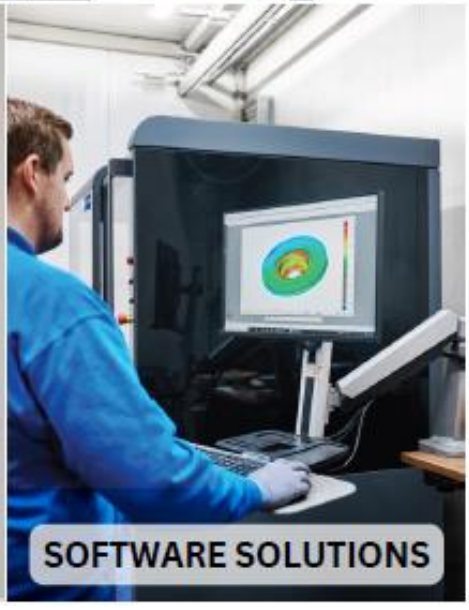
VISUAL INSPECTION



3D SCANNING AND MEASURING



CT SCANNING AND INSPECTION



SOFTWARE SOLUTIONS